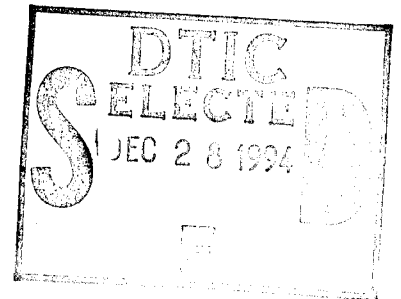
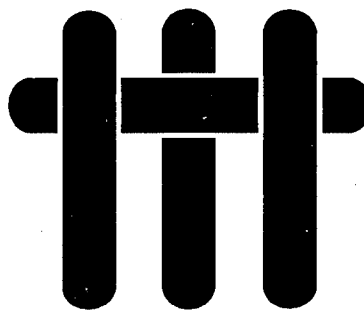


ANNUAL REPORT
Office of Naval Research

Contract. No. N00014-93-I-0213
January 1, 1994 - December 31, 1994



M A T E R I A L S



**BIMATERIAL INTERFACES
AND THEIR ROLE
IN THE MECHANICAL PERFORMANCE
OF THE IN-SITU COMPOSITES**

This document has been approved
for public release and sale; its
distribution is unlimited.

by

A. G. Evans

Materials Department
College of Engineering
University of California
Santa Barbara, California 93106-5050

and

Division of Applied Sciences
Harvard University
Cambridge, MA 02138

19941219 109

REPORT DOCUMENTATION PAGEForm Approved
OMB No. 0705-0188

1. AGENCY USE ONLY (Leave blank)		2. REPORT DATE 931231	3. REPORT TYPE AND DATES COVERED ANNUAL REPORT 940101 TO 941231	
4. TITLE AND SUBTITLE Bimaterial Interfaces and Their Role in the Mechanical Performance of the In-Situ Composites			5. FUNDING NUMBERS N00014-93-I-0213	
6. AUTHOR(S) Evans, Anthony G.				
7. PERFORMING ORGANIZATION NAME(S) AND ADDRESS(ES) MATERIALS DEPARTMENT COLLEGE OF ENGINEERING UNIVERSITY OF CALIFORNIA SANTA BARBARA, CA 93106-5050			8. PERFORMING ORGANIZATION REPORT NUMBER	
9. SPONSORING/MONITORING AGENCY NAME(S) AND ADDRESS(ES) OFFICE OF NAVAL RESEARCH MATERIALS DIVISION 800 NORTH QUINCY STREET ARLINGTON, VA 22217-5000			10. SPONSORING/MONITORING AGENCY REPORT NUMBER	
11. SUPPLEMENTARY NOTES				
12A. DISTRIBUTION/AVAILABILITY STATEMENT See Distribution List			12B. DISTRIBUTION CODE	
13. ABSTRACT (Maximum 200 words) The annual report of the Office of Naval Research grant at UCSB on Bimaterial Interfaces and their role in the Mechanical Performance is concerned basically with the mechanical properties of ceramic/metal bonded systems and with establishing criteria for interface decohesion, for sliding and for cracking across interfaces. Please refer to the executive summary for further details.				
14. SUBJECT TERM Bimaterial Interfaces, Mechanical Performance, In-Situ Composites			15. NUMBER OF PAGES 390	
			16. PRICE CODE	
17. SECURITY CLASSIFICATION OF REPORT UNCLASSIFIED	18. SECURITY CLASSIFICATION OF THIS PAGE UNCLASSIFIED	19. SECURITY CLASSIFICATION OF ABSTRACT UNCLASSIFIED	20. LIMITATION OF ABSTRACT	

Section 2 PAPERS

	<u>TITLE</u>	<u>AUTHOR</u>
Article 1.	A New Procedure for Measuring the Decohesion Energy for Thin Ductile Films on Substrates	A. Bagchi G. E. Lucas Z. Suo A. G. Evans
Article 2.	The Cracking Resistance of Nanoscale Layers and Films	D. K. Leung M. Y. He A. G. Evans
Article 3.	The Thermomechanical Integrity of Thin Films and Multilayers	A. G. Evans J. W. Hutchinson
Article 4.	A Fracture Resistance Measurement Method for Bimaterial Interfaces Having Large Debond Energy	M. R. Turner B. J. Dalgleish M. Y. He A. G. Evans
Article 5.	Analysis of the Double Cleavage Drilled Compression Specimen for Interface Fracture Energy Measurements over a Range of Mode Mixities	M. Y. He M. R. Turner A. G. Evans
Article 6.	Stress Redistribution in Ceramic/Metal Multilayers Containing Cracks	Q. Ma M. C. Shaw M. Y. He B. J. Dalgleish D. R. Clarke A. G. Evans
Article 7.	Fatigue Crack Growth and Stress Redistribution at Interfaces	M. C. Shaw D. B. Marshall B. J. Dalgleish M. S. Dadkhah M. Y. He A. G. Evans
Article 8.	The Structure and Thermomechanical Properties of Mo/Al ₂ O ₃ Interfaces	M. R. Turner J. P. A. Löfvander J. B. Davis A. G. Evans
Article 9.	Preliminary Assessment of Mica as a High-Temperature Fiber Coating for SiC Composites	A. M. Segadaes P. D. Warren A. G. Evans

1	<input checked="" type="checkbox"/>
2	<input type="checkbox"/>
3	<input type="checkbox"/>
7 Codes	
and/or	
Total	

	<u>TITLE</u>	<u>AUTHOR</u>
Article 10.	Structure and Properties at the Ferroelectric/Electrode Interface Between Lead Zirconate Titanate and Copper	H. C. Cao M. DeGraef A. G. Evans
Article 11.	Effects of Composite Processing on the Strength of Sapphire Fiber-Reinforced Composites	J. B. Davis J. Yang A. G. Evans
Article 12.	A Simple Method for Measuring Surface Strains Around Cracks	D. J. Wissuchek T. J. Mackin M. DeGraef G. E. Lucas A. G. Evans
Article 13.	Cracking and Damage Mechanisms in Ceramic/Metal Multilayers	M. C. Shaw D. B. Marshall M. S. Dadkhah A. G. Evans

Section 1: EXECUTIVE SUMMARY

A microelectronics-based method for measuring the debond energy for thin metal films on dielectric substrates has been developed and used to determine the debonding of Cu from various dielectrics such as SiO₂, SiN_x and polyimide. It uses a vapor deposited Cr superlayer, subject to 'intrinsic' tensile stress, to provide the energy release rate for decohesion. The Cr layer and the Cu film are patterned into strips and then severed (by dry etching) in order to establish the critical thickness at which spontaneous decohesion occurs. This critical thickness is explicitly related to Γ_i . The influence of mode mixity angle on Γ_i has been investigated by depositing a third thin layer of Cu onto the Cr, prior to severing. The fracture energies for electron-beam evaporated Cu films having thicknesses between 50 and 500 nm are found to be of order 1 Jm⁻². There are small (but significant) effects of film thickness and mode mixity. The sequence from lowest to highest Γ_i is found to be Cu/SiN_x → Cu/SiO₂ → Cu/polyimide. Values of ~ 1 Jm⁻² are similar to the thermodynamic work of adhesion, measured for liquid Cu on SiO₂ and Si₃N₄. They are much lower than Γ_i values obtained for Cu diffusion bonded to oxides and nitrides. However, Γ_i for thin Cu films was shown to be considerably enhanced (to > 6Jm⁻²) by using a thin (10nm) Cr interlayer. The specific role of this interlayer is being investigated.

The mechanical characteristics of nanoscale Si/Cu films and multilayers have been investigated in order to identify thin layer effects. This system is a prototypical brittle/ductile multilayer having well-bonded interfaces. It has been found that these nanoscale layers are stronger but less damage tolerant than thicker layers. The principal mechanism that governs both behaviors involves the propagation of flaws in the thin Si layers by tunneling and channeling. Accordingly, the strains needed to cause cracking increase with the inverse of the layer thickness and can exceed 2% when the layers are thin (~100 nm). The critical strains also increase as either the stiffness or yield strength of the substrate increase. Consequently, brittle layer cracking is insensitive to pre-existing flaws and occurs over a narrow range of strains. Such behavior contrasts with the stochastic nature of cracking in thicker layers. The inevitable consequence is that cracks in nanoscale multilayers become unstable and propagate across successive brittle layers causing inferior damage tolerance. This behavior occurs despite extensive plastic flow in the metal layers: because plastic deformation has minimal effect on alleviating the frontal stress concentration. An alternative approach for suppressing unstable

cracking and promoting damage tolerance has been explored. It involves the use of weak interfaces that cause debonding. This effect has been demonstrated by interposing thin Au interlayers between the Si and Cu. In this case, debonding occurs and cracks that form in the Si are indeed found to be stabilized. Qualification of this behavior is in progress.

A new method of measuring Γ_i for well bonded metal/ceramic interfaces has been devised. It is an adaptation of the Double Cantilever Drilled Compression (DCDC) Specimen. A comprehensive analysis of the specimen has been performed. Its application has been demonstrated on several metal/oxide interfaces having fracture energies up to 100 Jm^{-2} . The method allows direct observation of fracture mechanisms by optical microscopy (over a range of mode mixities) because the DCDC specimen enables cracks to extend stably, as the load is increased. Videos of extending cracks have been taken to demonstrate debonds nucleating on the interface ahead of the crack front. This is found to occur at grain boundaries and small precipitates. A systematic study to understand the associated mechanisms is in progress.

The DCDC specimen will be used to perform a systematic study of crack propagation along several well-bonded interfaces. These include interfaces comprising Al_2O_3 with Cu, Ni and Pt as well as SiC and AlN with W, Al and Cu. The emphasis will be on the interface sites that act as nuclei for debonds ahead of the crack. In some cases, various nuclei will be deliberately introduced prior to bonding, particularly voids, precipitates and grain boundaries. The role of segregants, such as C and O, and of interplanes, such as NiAlO_4 in $\text{Ni/Al}_2\text{O}_3$, will be investigated. The studies on the $\text{Ni/Al}_2\text{O}_3$ interface will be related to the performance of functionally graded and multilayer systems, by classifying the role of controlled interface decohesion on cracking and damage tolerance.

Fluorescence spectroscopy will be used to study the stresses around cracks on metal/ceramic interfaces. For this purpose, a Au/Ge eutectic will be sputtered onto Al_2O_3 substrates with a Cr doped surface layer. Thermal cycling will be used to controllably change the residual stress. Interface debonds will also be introduced by thermal cycling. Stress will be measured in the Al_2O_3 near the interface, around the debond front. These stress measurements will be used to understand the nature of the plasticity in the metal occurring near the crack tip. The results will be compared with calculations by Hutchinson that include strain gradient plasticity effects. This study will lead to a basic understanding of the influence of plasticity on Γ_i . The results will also be used for

modelling adhesion in multichip modules and thyristors where brazing is used to attach the Si chips to the ceramic dielectric.

Section 2

PAPERS

A new procedure for measuring the decohesion energy for thin ductile films on substrates

A. Bagchi, G. E. Lucas, Z. Suo, and A. G. Evans

Materials Department, College of Engineering, University of California–Santa Barbara, Santa Barbara, California 93106-5050

(Received 15 July 1993; accepted 24 March 1994)

A novel testing technique has been developed capable of measuring the interfacial fracture resistance, Γ_i , of thin ductile films on substrates. In this technique, the thin film on the substrate is stressed by depositing onto the film a second superlayer of material, having a large intrinsic stress, such as Cr. Subsequent processing defines a precrack at the interface between the film and the substrate. The strain energy available for driving the debond crack is modulated by varying the thickness of the Cr superlayer. Spontaneous decohesion occurs for superlayers exceeding a critical thickness. The latter is used to obtain Γ_i from elasticity solutions for residually stressed thin films. The technique has been demonstrated for Cu thin films on silica substrates.

I. INTRODUCTION

The decohesion of interfaces between metals and nonmetals is a critically important technological issue.^{1,2} Many of the basic phenomena have been identified, particularly the role of the interface debond energy, Γ_i , and its dependence on the loading mixity, Ψ (Fig. 1).^{3,4} The latter is a measure of the relative shear to tensile opening of the interface crack surfaces near the tip. Methods for measuring Γ_i have also been devised and calibrated (Fig. 2).⁴⁻⁶ However, these methods typically require specimens made by using a high homologous temperature (T/T_m) processing step, such as the diffusion bonding of sandwich specimens: T and T_m denote the processing temperature and the metal melting point, respectively (Fig. 2). For interfaces that have experienced only low temperatures upon fabrication, there are many tests for the qualitative ranking of the interface fracture resistance. These include scratch,⁷ microscratch,^{8,9} peel,^{10,11} and blister tests.^{12,13} However, the full quantification of most of these tests has not usually been possible because of the complex elastic/plastic stress fields involved. For example, models for the microscratch test⁹ are based on simplifying assumptions regarding the stress state and the decohered area. One exception is the peel test, which has been quantified.^{10,11} Even then, deconvolution of Γ_i from the peel force is complex and subject to appreciable uncertainties. Moreover, this test has a mode mixity that differs in sign and magnitude from that associated with most practical decohesion problems.³ Blister tests are more readily interpreted but also provide mode mixities having inappropriate sign.^{12,13} Such tests have further limitations when applied to thin, opaque, ductile films. There are two practical problems. The pressure imposed to induce decohesion increases the stress in the film and may cause yielding.

Moreover, the perimeter of the decohered zone is difficult to measure. A preferred test method for ductile films would be one in which the stresses in the film diminish as the decohesion extends and also have an energy release rate G independent of the decohered length.

The present article addresses the deficiencies by devising a new test that has the following attributes. The method can be used for ductile thin films deposited onto substrates at low T/T_m . It has a mode mixity typical of that associated with thin film decohesion ($\Psi \approx 0^\circ$ – 50°) and G independent of decohesion length. Moreover, the

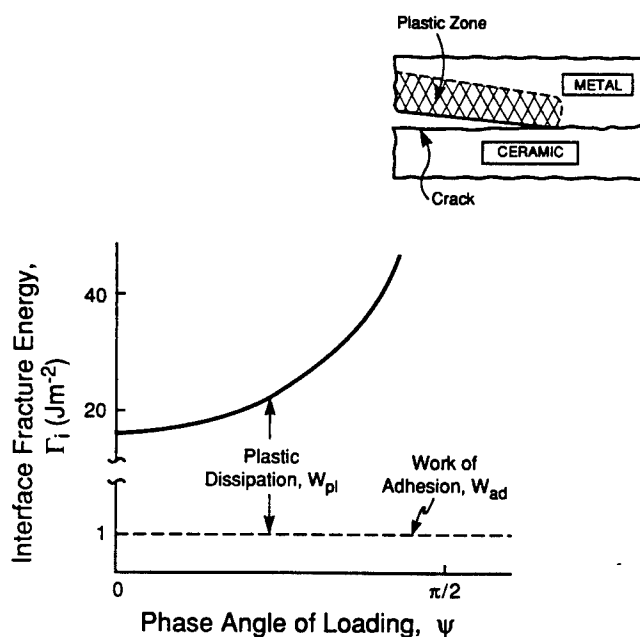


FIG. 1. A schematic indicating the effect of loading mixity on the interface fracture energy, Γ_i . The values used are typical for metal/oxide interfaces. Also shown is a schematic of crack growth with plastic dissipation.

AVAILABLE TESTS TO MEASURE Γ_i

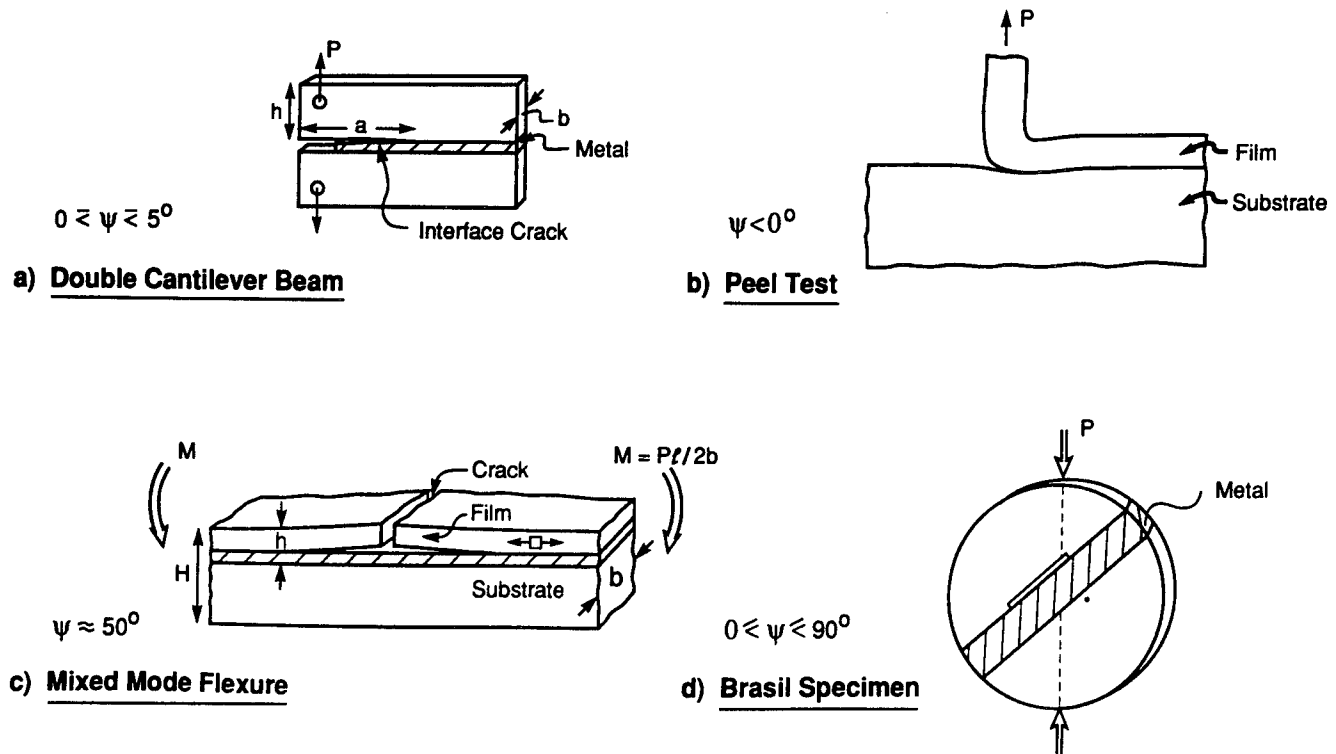


FIG. 2. Some test methods used to measure the interface fracture energy.

stress in the film decreases as decohesion proceeds. The procedure can also be implemented in a conventional microelectronics fabrication facility.

Interface decohesion occurs subject to several dissipation mechanisms.¹⁴⁻¹⁶ The fundamental mechanism involves the work of adhesion, W_{ad} , which represents the basic separation energy for the bonds across the interface. In general, plastic dissipation W_{pl} also occurs within a plastic zone in the metal, as the decohesion extends along the interface (Fig. 1). This contribution scales with W_{ad} .^{15,16} It also varies with crack extension, Δa , leading to a resistance curve.¹⁶ This curve, in turn, depends on the ratio of the peak decohesion stress, $\hat{\sigma}$, to the yield strength of the metal, σ_0 (Fig. 3). Moreover, W_{pl} may increase as the film thickness becomes larger and as the mode mixity angle increases (Fig. 1). In some cases, when the interface is nonplanar, frictional effects can also contribute to Γ_i .³ The new test method has been devised with the intent of systematically exploring these effects for metal thin films on nonmetallic substrates.

II. SOME BACKGROUND MECHANICS

The relevant mechanics of thin film decohesion consider a thin film subject to residual tension, σ_f , on

a thick substrate (Fig. 4). The energy release rate associated with an interface decohesion, originating from an edge (or discontinuity), attains a steady-state value, G_{ss} , provided that the decohesion length, a_0 , exceeds the film thickness. Moreover, since all of the stress in the film

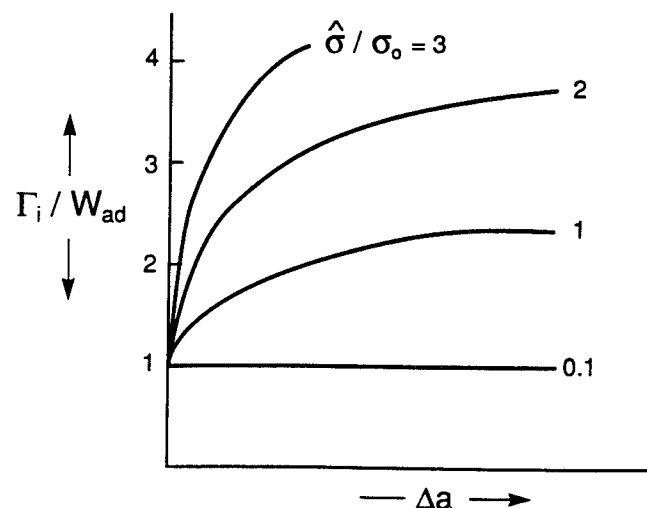


FIG. 3. Effect of metal yield strength on the interface fracture energy: σ_0 is the yield strength, $\hat{\sigma}$ the bond strength, and Δa the crack extension.¹⁶

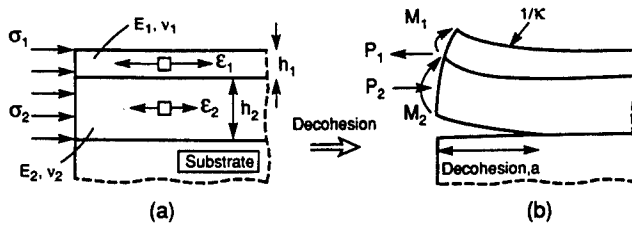


FIG. 4. A schematic showing the behavior of a bilayer film subject to residual tension as it decoheres from the substrate. The stresses σ_1 and σ_2 (a) are the misfit stresses, which provide the forces P_i and the moments M_i (b) in the metal bilayer above the decohesion crack. The curvature of the decohered bilayer film is κ .

above the decohesion is released, the nondimensional energy release rate for a thin strip is^{3,17}

$$G_{ss} E_f / \sigma_f^2 h_f = 1/2, \quad (1)$$

where E_f is Young's modulus for the film and h_f is the film thickness. The corresponding mode mixity is $\Psi = 52^\circ$. The thin film test method should duplicate this mode mixity. For a wide strip (width $w > h_f$), the residual stresses are biaxial and the revised steady-state energy release rate is³

$$G_{ss} E_f / \sigma_f^2 h_f = 1 - \nu_f, \quad (2)$$

where ν_f is Poisson's ratio of the film. At smaller decohesion lengths ($a_0 < h_f$), the energy release rates depend on the details at the edge.^{3,17} The preferred test method should avoid these edge problems by using only decohesion precracks within the steady-state range.

For a bilayer film, interface decohesion leads to bending, whereupon some energy is stored in the film above the decohesion. Consequently, the steady-state energy release rate is reduced. The new value, as derived in the Appendix, is

$$G_{ss} = \sum_i \frac{\sigma_i^2 h_i}{E_i'} - \sum_i \frac{1}{E_i'} \left[\frac{P^2}{h_i} + \frac{12M_i^2}{h_i^3} \right], \quad (3)$$

where $i = 1, 2$ refer to the two materials in the bilayer. The load P associated with the residual tension σ_i in each layer (Fig. 4) can be expressed in terms of the curvature of the decohered bilayer, κ , the film thickness, h_i , and the biaxial elastic moduli, $E_i' = E_i / (1 - \nu_i)$, as¹⁸:

$$P = \left[\frac{E_1' h_1^3 + E_2' h_2^3}{6(h_1 + h_2)} \right] \kappa \quad (4)$$

with κ given by

$$\kappa = \frac{6(h_1 + h_2)(\epsilon_1 - \epsilon_2)}{[h_1^2 + E_2' h_2^3 / E_1' h_1 + E_1' h_1^3 / E_2' h_2 + h_2^2 + 3(h_1 + h_2)^2]}, \quad (5)$$

where $\epsilon_i = \sigma_i / E_i'$. The bending moment, M_i (Fig. 4), is given by

$$M_i = E_i' \kappa, \quad (6)$$

where I_i is the moment of inertia, $I_i = h_i^3 / 12$.

III. THE METHOD

A key consideration for development of a method concerns the mode mixity, Ψ . In order to maintain Ψ in the requisite range, there are few options for loading the system. Among these, the only approach that appears to be straightforward involves the use of a residual stress which essentially duplicates the problem of interest. However, for typical thin films ($h_f < 1 \mu\text{m}$), and representative residual stress levels ($\sigma_f^R < 100 \text{ MPa}$), the residual stress-induced energy release rate is small [Eq. (1)], of the order, $G_{ss} \approx 0.1 \text{ Jm}^{-2}$. Most interfaces with practical interest would have a debond energy substantially larger than this.¹⁴ Consequently, decohesion would not be induced. The preferred test method must identify a procedure that substantially increases G_{ss} , without changing Ψ , while also preserving the structure and microstructure of the interface.

A method that increases the energy release rate, at essentially constant Ψ , involves deposition of an additional material layer onto the film. This superlayer increases the total film thickness and also elevates the total residual stress without changing the interface. In order to accomplish this, the additional layer must be deposited in accordance with the following three characteristics. Deposition must be conducted at ambient temperature. The layer must not react with the existing film. The layer must have a large residual tension upon deposition. A Cr film, deposited by electron beam evaporation, meets all three criteria.¹⁹

The new test method has the following three features: (i) A decohesion precrack is created, with length $a_0 > h_f$. (ii) The film is patterned to form narrow strips. (iii) The Cr film thickness is varied in order to produce a range of energy release rates. To provide these features, a thin strip of carbon is first deposited. This layer is the source of the interface precrack (Fig. 5). The film of interest is then deposited. Subsequently, a Cr layer with the requisite thickness is deposited onto the film. Thereafter, the bilayer is patterned to form strips orthogonal to the carbon lines. Finally, the strips are severed above the C. The latter step creates the edge needed to induce an energy release rate (Fig. 5). The half-width of the carbon line, a_0 , defines the precrack length. When the strips decohere after severing, the energy release rate exceeds the debond energy; i.e., $G_{ss} > \Gamma_i$. Conversely, when the film remains attached, $G_{ss} < \Gamma_i$. Consequently, Γ_i is determined from the critical Cr layer thickness above

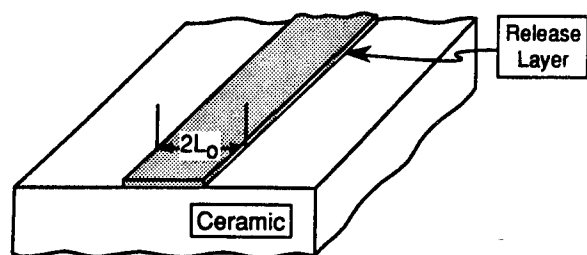
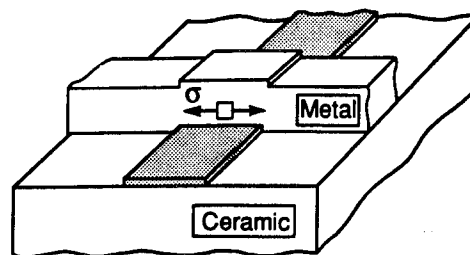
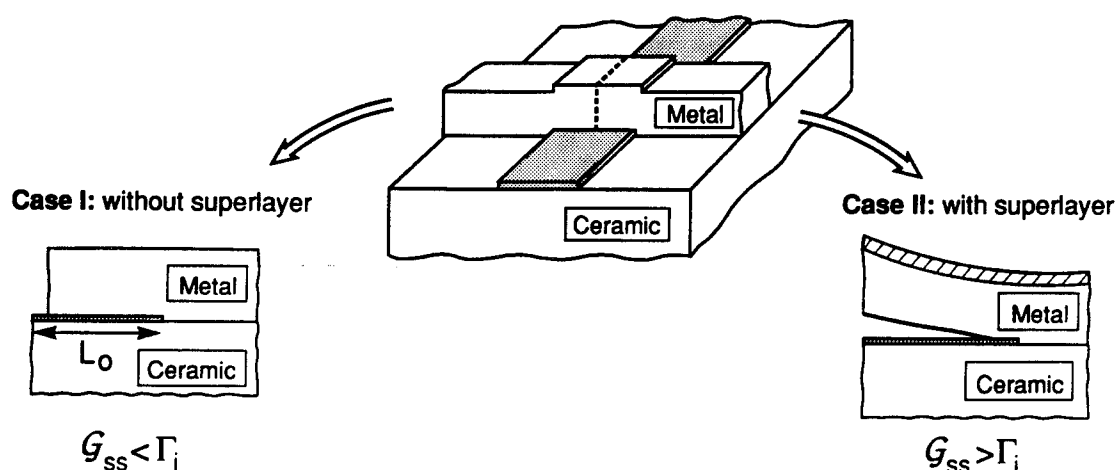
STEP I Release Layer Deposition**STEP II** Metal Layer & Superlayer Deposition**STEP III** Bilayer Cut

FIG. 5. The procedure used to measure the debond energy of the interface.

which decohesion always occurs, designated h_c . The bilayer solution [Eq. (3)] then relates Γ_i to the critical Cr thickness by using the equalities: $G_{ss} = \Gamma_i$ and $h_1 = h_c$.

IV. EXPERIMENTAL PROCEDURE

A flow chart of the overall procedure is presented in Fig. 6. Deposition and photolithography are conducted in a clean room facility. Residual stresses are measured from beam deflections. Then, film severing above the precrack is conducted. The films are inspected to assess the critical thickness, h_c . Finally, this critical thickness is used to determine Γ_i .

A. Deposition and patterning

Preliminary experiments have been carried out by using evaporated copper films and glass substrates. The choice of copper is particularly attractive due to its emerging importance as an interconnect material. It is expected to replace aluminum for deep submicron metal linewidths, because of its superior conductivity and higher resistance to electromigration.²⁰ All processing steps are carried out in Class 100 and Class 10 000 clean room facilities. Careful substrate cleaning is essential.

For this purpose, the glass substrates (Corning 0211) are solvent cleaned in trichloroethylene, acetone, and isopropyl alcohol in order to remove organic contaminants. Then, they are water cleaned, followed by etch-cleaning in buffered hydrofluoric acid, in order to remove all inorganic contaminants. Finally, they are rinsed in de-ionized water and dried. The carbon release layer is thermally evaporated (thickness ~ 200 Å) onto the substrate and patterned to the desired geometry (Fig. 5) by using a bilayer photolithography technique. Pure copper (99.999%) is then deposited by electron beam evaporation at a background pressure $\approx 8 \times 10^{-7}$ Torr. Thereafter, the chromium superstructure layer (99.9% pure) is evaporated. An *in situ* quartz monitor is used to control the deposition rate (Cu ~ 10 Å/s, Cr ~ 1 Å/s) and the film thickness. Subsequent lift-off defines the metal line geometry. Finally, a through cut is made in the metal bilayer by wet etching. An optical micrograph of a processed test specimen is shown in Fig. 7.

B. Residual stress measurement

The residual stress is measured by using a standard procedure that relies on determination of the

FLOW CHART

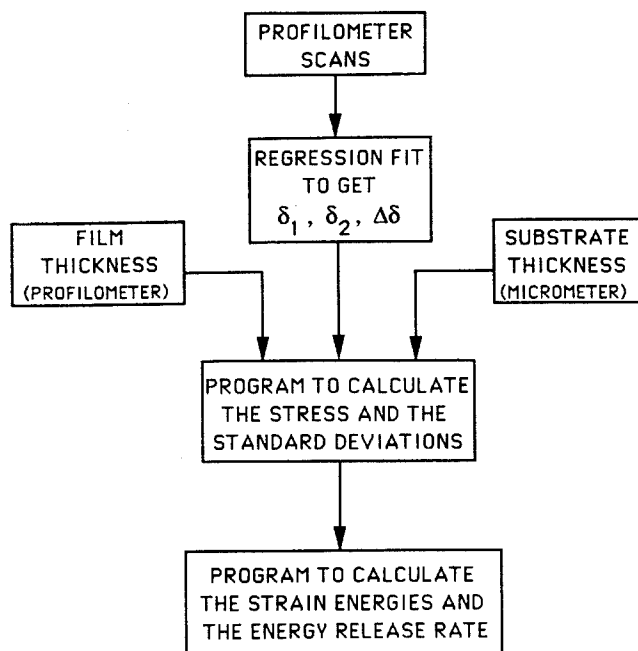


FIG. 6. A flow chart indicating the sequence used to measure the debond energy.

film/substrate system.²¹ For this purpose, a profilometer is used to measure substrate curvature.²² The profilometer uses a metallic stylus, which is horizontally scanned while its vertical movement is converted to an electrical signal. The substrate often has an initial curvature. Therefore, two scans are made in order to measure the bending deflection of the substrate. These are made both with (δ_1) and without (δ_2) the film attached. The residual

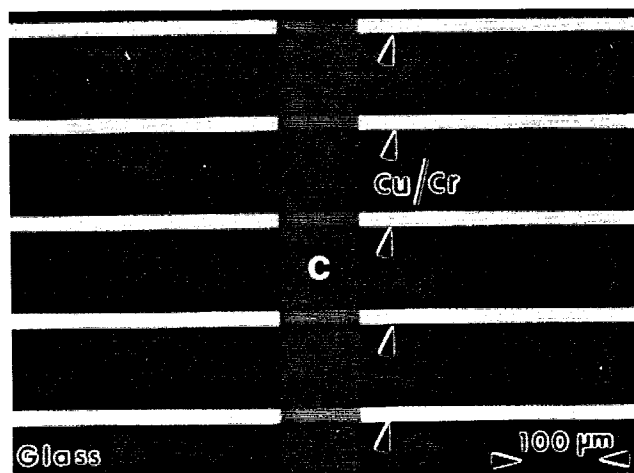


FIG. 7. An optical micrograph of the processed test specimen.

stress in the film is related to these displacements by:

$$\sigma^R = \frac{4E_s(\delta_1 - \delta_2)h_s^2}{3(1 - \nu_s)L^2h_f}, \quad (7)$$

where L is the length of the profilometer scan, h_s is the substrate thickness, and E_s , ν_s are the substrate Young modulus and Poisson's ratio, respectively. This procedure is used to evaluate the residual stress in the Cu and then the residual stress in the Cr deposited onto the Cu. The total stress, σ_{tot} , associated with both is

$$\begin{aligned} \sigma_{tot} &= \sigma_{Cr}H_{Cr} + \sigma_{Cu}H_{Cu} \\ &= \sigma_{Cu} + (\sigma_{Cr} - \sigma_{Cu})H_{Cr}, \end{aligned} \quad (8)$$

where H is the relative layer thickness,

$$H = h/(h_{Cu} + h_{Cr}).$$

Consequently, if the stresses are essentially independent of the film thicknesses, there would be a linear dependence of the total stress on the relative thickness, H . This approach is used to assess the experimental results.

V. RESULTS

A. Residual stress

Residual stress measurements have been performed on a batch of four samples with the same nominal Cu thickness (4425 Å) and with four Cr thicknesses: 220 Å, 445 Å, 660 Å, and 900 Å. On each sample, five profilometer scans were made before and after removing the film from the substrate. A least square regression fitting to the data gives the deflections (δ_1 and δ_2) and their respective standard deviations. The film thickness is also obtained from the scans. The substrate thickness is measured with a digital micrometer. The stresses obtained in this manner are plotted in Fig. 8. A linear fit appears to obtain, consistent with stresses in each separate layer being independent of thin film thickness

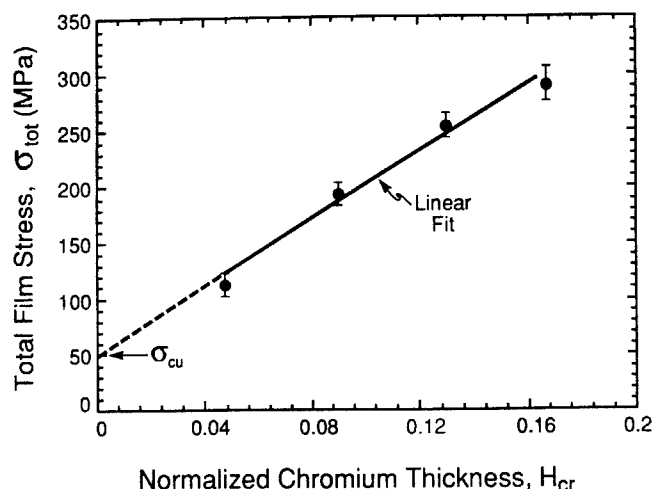


FIG. 8. A plot of the total film stress with the normalized Cr layer thickness.

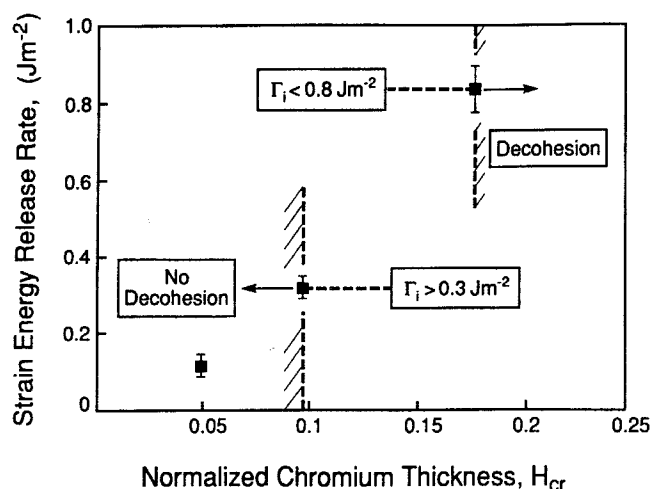


FIG. 9. A plot of the calculated energy release rates with the normalized Cr layer thickness. Also shown are the lines separating the film that decohered from that which remained attached and associated bounds in the interface fracture energy.

[Eq. (8)]. This fit indicates that the residual stresses in the Cu and Cr layers are 50 MPa and 1575 MPa, respectively, with standard deviations $\sim 3\%$. The former is consistent with the yield strength of Cu films, and both values are within the range measured by others.²³

B. Interfacial fracture energy

For a glass substrate with a $0.44 \mu\text{m}$ thick Cu film, the results are summarized in Fig. 9. When the Cr superlayer was either 22 nm or 45 nm thick, the bilayer remained attached to the substrate (Fig. 10(a)). Conversely, when the Cr layer was 90 nm thick, decohesion occurred, followed by curling of the film (Fig. 10(b)). Consequently, h_c is between 45 nm and 90 nm. By introducing these values into the energy release rate formula for the bilayer [Eq. (3)], bounds are placed on

the interface fracture energy. For this purpose, the elastic modulus of the film is needed. Generally, polycrystalline thin films can have a lower modulus than the bulk material, because of porosity at the boundaries of the columnar grains. Consequently, for completeness, independent measurement of E_f would be needed. Such measurements have yet to be performed in this study. Instead, literature values of polycrystalline Cu and Cr thin films are used ($E_f = 120 \text{ GPa}$ ²⁴ and 93 GPa ,²⁵ respectively). With these choices for E_f , the bounds on the interface fracture energy are $0.3 \leq \Gamma_i \leq 0.8 \text{ Jm}^{-2}$. Earlier study of Cu/glass interfaces, produced by diffusion bonding and annealing, indicated that Γ_i usually ranged between 0.14 and 4 Jm^{-2} (the highest being 8 Jm^{-2}).²⁶ The scatter was attributed to surface contaminants, which influenced the bonding. The present results are at the lower end of this range. Such results are consistent with the absence of an annealing step, in the present study, leading to a more pronounced influence of minor contaminants. These, in turn, reduce the potential for a contribution to Γ_i from plastic dissipation in the Cu. The present values are comparable with the work of adhesion ($W_{ad} = 0.5 \text{ Jm}^{-2}$) for liquid Cu on SiO_2 .²⁷ This suggests that there is a minor contribution to Γ_i from plastic dissipation, perhaps because the Cu film is relatively thin.

VI. CONCLUDING REMARKS

A new test procedure for measuring the interface decohesion energy Γ_i of metallic thin films on nonmetallic substrates has been devised, analyzed, and demonstrated. The procedure duplicates the conditions found upon decohesion induced by residual stress. The measured values of Γ_i may thus be used directly, in conjunction with the mechanics of thin films in order to predict such factors as the critical film thickness. Moreover,

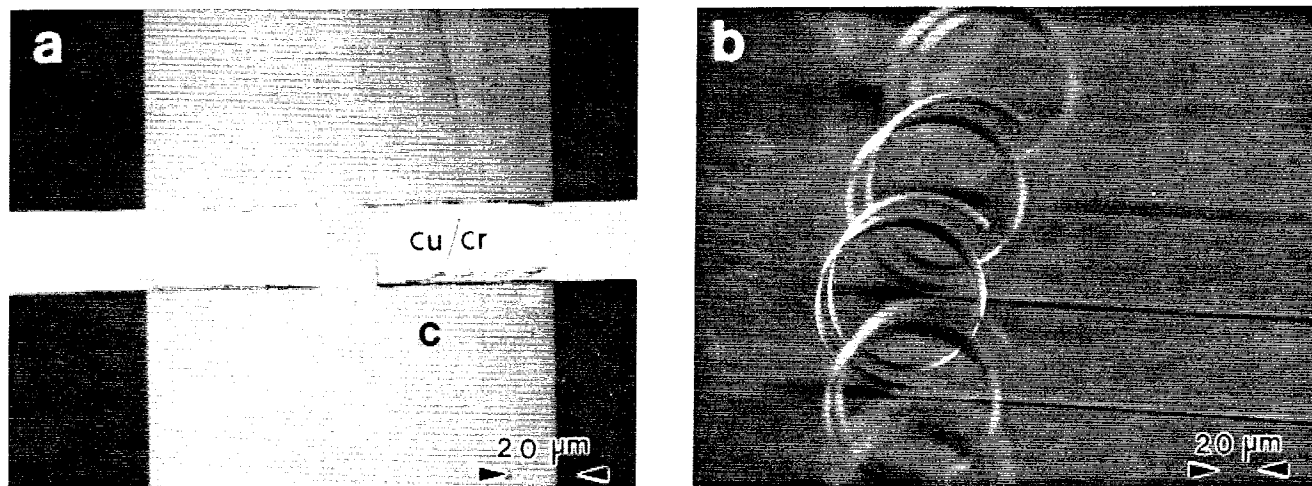


FIG. 10. Specimens providing the lower and upper bounds in the fracture energy, with the Cr superlayer thickness (a) $h_1 = 450 \text{ \AA}$, below the critical thickness, and (b) $h_1 = 900 \text{ \AA}$, above the critical thickness.

the method allows a systematic study of trends in Γ_i with the key deposition and postdeposition variables. These include the effect of contaminants, of active metal layers, of annealing, electric fields, etc. Studies are now in progress which will apply the new method to these basic issues.

Finally, since the value of Γ_i obtained from these tests is subjected to knowledge of the elastic properties of the bilayer film, simple acoustic procedures for measuring these properties are being implemented.

ACKNOWLEDGMENT

Financial support was provided by the Office of Naval Research under ONR Contract N00014-93-I-0213.

REFERENCES

1. P. S. Ho, *Appl. Surf. Sci.* **41–42**, 559 (1989).
2. M. D. Thouless, *J. Vac. Sci. Technol. A* **9**, 2510 (1991).
3. J. W. Hutchinson and Z. Suo, *Adv. Appl. Mech.* **29**, 63 (1992).
4. A. G. Evans, M. Rühle, B. J. Dalgleish, and P. G. Charalambides, *Metall. Trans.* **21A**, 2419 (1990).
5. P. G. Charalambides, J. Lund, A. G. Evans, and R. M. McMeeking, *J. Appl. Mech.* **56**, 77 (1989).
6. J. S. Wang and Z. Suo, *Acta Metall. Mater.* **38**, 1279 (1990).
7. J. Ahn, K. L. Mittal, and R. H. MacQueen, *Adhesion Measurement of Thin Films, Thick Films, and Bulk Coatings*, ASTM STP 640, edited by K. L. Mittal (American Society for Testing and Materials, 1978), p. 134.
8. T. W. Wu, *J. Mater. Res.* **6**, 407 (1991).
9. S. Venkataraman, D. L. Kohlstedt, and W. W. Gerberich, *J. Mater. Res.* **7**, 1126 (1992).
10. K.-S. Kim and N. Aravas, *Int. J. Solids Struct.* **24**, 417 (1988).
11. K.-S. Kim and J. Kim, *J. Eng. Mat. Tech.* **110**, 266 (1988).
12. M. G. Allen and S. D. Senturia, *J. Adhesion* **25**, 303 (1988).
13. M. G. Allen and S. D. Senturia, *J. Adhesion* **29**, 219 (1989).
14. A. G. Evans and B. J. Dalgleish, *Acta Metall. Mater.* **40**, Suppl., S295 (1992).
15. M. L. Jokl, V. Vitek, and C. J. McMahon, Jr., *Acta Metall. Mater.* **28**, 1479 (1980).
16. V. Tvergaard and J. W. Hutchinson, *J. Mech. Phys. Solids* **41**, 1119 (1993).
17. M. D. Drory, M. D. Thouless, and A. G. Evans, *Acta Metall. Mater.* **36**, 2019 (1988).
18. S. Timoshenko, *J. Opt. Soc. Am.* **11**, 223 (1925).
19. M. S. Hu and A. G. Evans, *Acta Metall. Mater.* **37**, 917 (1989).
20. S. S. Wong, J. S. Cho, H. K. Kang, and C. H. Ting, *Electronic Packaging Materials Science V*, edited by E. D. Lillie, P. S. Ho, R. Jaccodine, and K. Jackson (Mater. Res. Soc. Symp. Proc. **203**, Pittsburgh, PA, 1991), p. 347.
21. G. G. Stoney, *Proc. R. Soc. London Ser. A* **82**, 172 (1909).
22. M. E. Thomas, M. P. Hartnett, and J. E. McKay, *J. Vac. Sci. Technol. A* **6**, 2570 (1988).
23. R. Abermann, *Thin Films: Stresses and Mechanical Properties III*, edited by W. D. Nix, J. C. Bravman, E. Arzt, and L. B. Freund (Mater. Res. Soc. Symp. Proc. **239**, Pittsburgh, PA, 1992), p. 25.
24. J. A. Ruud, D. Josell, F. Spaepen, and A. L. Greer, *J. Mater. Res.* **8**, 112 (1993).
25. M. Janda, *Thin Solid Films* **142**, 37 (1986).
26. R. M. Cannon, R. M. Fisher, and A. G. Evans, *Thin Films—Interfaces and Phenomena*, edited by R. J. Nemanich, P. S. Ho, and S. S. Lau (Mater. Res. Soc. Symp. Proc. **54**, Pittsburgh, PA, 1986), p. 799.
27. J. G. Li, *J. Mater. Sci. Lett.* **11**, 903 (1992).

APPENDIX

The strain energy release rate

Interfacial decohesion, motivated by residual stresses in deposited thin film layers, occurs subject to the steady-state strain energy release rate, G_{ss} , when the interfacial flaw size, a_0 , exceeds the film thickness.³ Moreover, since the film stress diminishes as the interface decoheres, this energy release behavior is entirely controlled by elasticity, even when the film has yielded upon prior thermal processing.³ For thin film systems a strain energy balance may be used to calculate G_{ss} , wherein two elements, having width Δa , are chosen far ahead and far behind the growing interfacial crack (Fig. A1). If U_a and U_b denote the strain energies in these volume elements, then

$$G_{ss}\Delta a = U_a - U_b \quad (A1)$$

This result applies provided that the substrate thickness is much larger than the film thickness. The element far ahead of the crack tip is in biaxial plane stress:

$$\begin{aligned} \sigma_x^i &= \sigma_y^i = \sigma_i, \\ \sigma_i &= \varepsilon_i E_i / (1 - \nu_i) = \varepsilon_i E_i', \\ \sigma_z^i &= \tau_{xy}^i = \tau_{yz}^i = \tau_{zx}^i = 0 \quad (i = 1, 2), \end{aligned} \quad (A2)$$

where σ_1, σ_2 are the residual stresses in the two layers and $\varepsilon_1, \varepsilon_2$ the corresponding residual strains. The elastic strain energy density associated with each layer ($i = 1, 2$), per unit width, is

$$\Delta U_a^i / h_i \Delta a = \frac{\sigma_i^2}{E_i'} \quad (A3)$$

where E_i' is the biaxial modulus of the film layers. Consequently, for a bilayer,

$$U_a \equiv \sum \Delta U_a^i = \left[\frac{\sigma_1^2 h_1}{E_1'} + \frac{\sigma_2^2 h_2}{E_2'} \right] \Delta a \quad (A4)$$

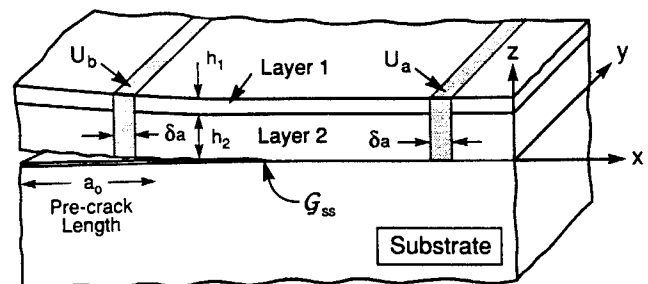


FIG. A1. A schematic describing the energy balance approach to find the strain energy release rate for a bilayer thin film.

When both layers are in residual tension (as in the present experiment) and when $\varepsilon_1 > \varepsilon_2$, the film bends upward after decohesion in an attempt to relax the strains (Fig. 4). The resultant stresses in each layer can be related to the forces, P_i , moments, M_i , and curvature, κ , defined in Fig. 5, by¹⁸:

$$\begin{aligned}\sigma_i(z) &= P_i/h_i + zE'_i\kappa \\ M_i/I_i &= E'_i\kappa \\ I_i &= h_i^3/12,\end{aligned}\quad (\text{A5})$$

where z now denotes the vertical distance from the neutral axis in each separate layer, whereas I_i is the sectional modulus. The strain energy is then³

$$U_b = \sum_i \frac{1}{E'_i} \left[\frac{P_i^2}{h_i} + \frac{M_i^2}{I_i} \right] \Delta a \quad (\text{A6})$$

It is now required to provide expressions that relate P_i , M_i , and κ to the stresses and the film thicknesses, by using beam theory. For a bilayer, this procedure provides five linear equations involving the five unknowns, namely P_1 , P_2 , M_1 , M_2 , and κ . Equilibrium dictates that, for a bilayer,

$$\begin{aligned}\sum P_i &= 0; \rightarrow P_1 = P_2 = P \\ \sum M_i &= 0; \rightarrow M_1 + M_2 = P \left(\frac{h_1 + h_2}{2} \right)\end{aligned} \quad (\text{A7})$$

Geometry requires that

$$\begin{aligned}M_1 &= E'_1 I_1 \kappa \\ M_2 &= E'_2 I_2 \kappa\end{aligned} \quad (\text{A8})$$

Strain compatibility at the interface gives

$$-\varepsilon_1 + \frac{P_1}{E'_1 h_1} + \frac{h_1 \kappa}{2} = -\varepsilon_2 - \frac{P_2}{E'_2 h_2} - \frac{h_2 \kappa}{2} \quad (\text{A9})$$

In this case, analytical solutions for P , M_i , and κ are obtained as¹⁸:

$$\begin{aligned}M_i &= E'_i I_i \kappa \\ P &= \left[\frac{E'_1 h_1^3 + E'_2 h_2^3}{6(h_1 + h_2)} \right] \kappa\end{aligned}$$

and

$$\kappa = \frac{6(h_1 + h_2)(\varepsilon_1 - \varepsilon_2)}{[h_1^2 + E'_2 h_2^3/E'_1 h_1 + E'_1 h_1^3/E'_2 h_2 + h_2^2 + 3(h_1 + h_2)^2]} \quad (\text{A10})$$

The strain energy release rate is then ($i = 1, 2$)

$$G_{ss} = \sum_i \frac{\sigma_i^2 h_i}{E'_i} - \sum_i \frac{1}{E'_i} \left[\frac{P_i^2}{h_i} + \frac{12M_i^2}{h_i^3} \right] \quad (\text{A11})$$

The above result can be generalized for a multilayer film ($i = 1, 2, 3, \dots, n$). The number of unknowns is $2n + 1$, because each layer has two (a force, P_i , and a moment, M_i), in addition to the curvature, κ , of the film after decohesion. The solution requires $2n + 1$ linear equations. The first two stem from equilibrium considerations:

$$\sum \text{force} = 0; \rightarrow P_1 + P_2 + \dots + P_n = 0 \quad (\text{A12})$$

$$\begin{aligned}\sum \text{moment} &= 0; \rightarrow \sum_{i=1}^n M_i = \sum_{i=1}^{n-1} P_i \\ &\quad \times \left(\frac{h_i + h_n}{2} + \sum_{k=i+1}^{n-1} h_k \right)\end{aligned} \quad (\text{A13})$$

The next n equations relate the moments to the curvature ($i = 1, 2, \dots, n$)

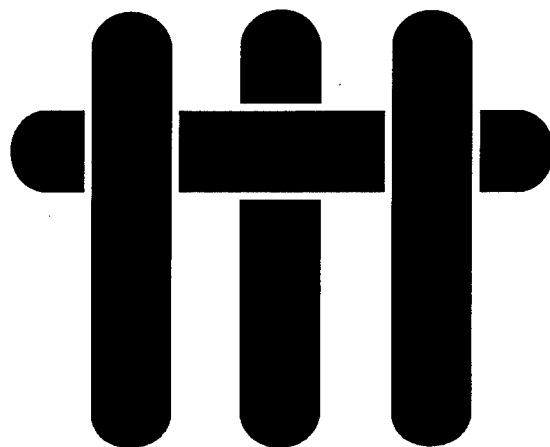
$$M_i = E'_i I_i \kappa. \quad (\text{A14})$$

Finally, the remaining $n - 1$ equations involve strain compatibility at the $n - 1$ interfaces. For the r th interface from the top, this can be expressed as ($r = 1, 2, \dots, n - 1$):

$$\varepsilon_r + \frac{P_r}{E'_r h_r} + \frac{h_r \kappa}{2} = \varepsilon_{r+1} + \frac{P_{r+1}}{E'_{r+1} h_{r+1}} - \frac{h_{r+1} \kappa}{2}. \quad (\text{A15})$$

A program needed to solve these equations has been developed using MATLAB. (The mode mixity may also be calculated.³ For the present experiments, $\Psi \approx 0^\circ$.)

M A T E R I A L S



THE CRACKING RESISTANCE OF NANOSCALE LAYERS AND FILMS

by

D.K. Leung, M.Y. He and A.G. Evans
Materials Department
College of Engineering
University of California, Santa Barbara
Santa Barbara, California 93106-5050

ABSTRACT

Thin film cracking has been studied for a nanometer brittle/ductile layered system consisting of Si and Cu. Single Si films and Cu/Si/Cu trilayers were fabricated by physical vapor deposition. The films were deposited onto a ductile substrate consisting of stainless steel with a thin polyimide interlayer. Straining of the substrate induced cracking of the Si. Cracking strains $\geq 1\%$ were observed, particularly in layers ≤ 100 nm thick. The critical cracking strain was found to depend upon the Si layer thickness, as well as the thickness and elastic/plastic properties of the adjacent ductile layers. Si cracking was suppressed by the presence of adjacent Cu layers. The measured strains were compared with lower-bound critical strains for tunnel and channel cracking. Comparisons indicated that these mechanisms control the critical strain found in trilayers, because trilayer fabrication introduces edge flaws larger than the Si layer thickness. Conversely, for Si films, the measured critical strains exceed the channel cracking strain, because the flaws in these films are relatively small.

1. INTRODUCTION

Multilayers made from constituents with widely differing physical properties have been advocated as materials with exciting new thermomechanical properties.¹⁻³ The concepts are founded on the unusual behavior of naturally occurring materials, such as shells.⁴ The approach has been to combine a hard, brittle material with a softer, ductile material in order to achieve an optimal combination of damage tolerance, stiffness and strength. Generally, this has involved combinations of a ceramic with a polymer or metal and an intermetallic with a metal.¹⁻⁸ Research on ceramic/metal and intermetallic/metal multilayers has provided some instructive principles.⁵⁻⁸ One of the critical performance requirements is the attainment of damage tolerance while maintaining high strength.⁸ The principal mode of damage consists of crack formation in the brittle layers.⁸ The variables that influence such cracking are addressed in this study. Particular emphasis is placed on the role of the layer *thickness* and the mechanical characteristics of the adjoining material, such as *modulus* and *yield strength*.

Theoretical work on brittle layer damage has identified tunnelling or channelling modes of crack extension^{9,10} (Fig. 1). These modes operate when flaws pre-exist and propagate in steady-state along the layers. They provide a criterion for the lower bound critical strain, ϵ_c , with resulting implications for the fail-safe design of multilayers.^{9,11} The criterion is manifest as a cracking number Z given by⁹

$$Z = \Gamma_b / t_b \epsilon_c^2 E_b \quad (1)$$

where t_b is the layer thickness, E_b its modulus and Γ_b its fracture energy. The cracking number is of order unity, but depends somewhat on the elastic properties and yield strengths of the materials comprising the layers. A central implication of Eqn. (1) is that ϵ_c *increases* when the layer thickness becomes *small*. Thin layers in the *nanometer* range

should thus be particularly resistant to damage. This prediction is experimentally evaluated in the present study.

2. PHILOSOPHY AND APPROACH

Multilayer materials having layer thicknesses in the nanometer range can be produced by only a limited set of processing methods, especially when one constituent is metallic. Physical vapor deposition (PVD) is the preferred method. The materials of choice for the brittle and ductile constituents are Cu and Si, respectively, because both can be controllably deposited by PVD.

Thin nanoscale multilayers are difficult to test for their mechanical performance without inducing instabilities. Controlled deformation and damage responses are best explored by depositing the multilayer onto a *ductile substrate* and then introducing the strain by deforming the substrate. For this purpose, a 'multi-strain' specimen configuration has been developed (Fig. 2). It consists of a polished stainless steel beam with a compliant polyimide interlayer and Si/Cu multilayers. The specimen has two unique features. (i) Photolithographic techniques can be used to pattern the films or multilayers into thin strips, parallel to the beam axis. (ii) The beam can be placed in four-point flexure with the multilayers *on the side*. Then each strip, being thin and narrow relative to the beam, experiences a *uniaxial* tensile strain having the same magnitude as that in the steel substrate, at the same location. The reference strain may be calibrated by attaching a strain gauge to the tensile face of the substrate. Then, because of the linearity in strain between the neutral plane and the tensile surface, the strains within each strip can be obtained by interpolation. Each strip can be considered as an individual tensile sample, subject to a different strain level. Consequently, the minimum strain needed to induce layer damage can be determined from a *single test*. The damage having principal relevance is the cracking of the Si. Residual strains in the

multilayer that derive from deposition (intrinsic), as well as from thermal expansion¹² must be known in order to interpret the results.

The polyimide interlayer serves two purposes. (i) It redistributes strain concentrations that arise from slip bands which protrude from the substrate surface when the steel is strained plastically during testing. (ii) It has a low elastic modulus and allows the layers to deform with little constraint.

3. EXPERIMENTAL APPROACH

3.1 Multilayer Fabrication and Testing

Stainless steel beams ($\sim 3.2 \times 3.2 \times 42$ mm) were polished to an optical finish. After thorough washing, the beams were further cleaned in a Class 10,000 clean room. A standard degreasing procedure was used. This process consisted of ultrasonication for 5 minutes each in 1,1,1-trichloroethane, acetone and isopropanol, followed by drying with N_2 . This cleaning step ensured proper adhesion of the polyimide layer to the stainless steel.

The polyimide layer was deposited onto the clean surface. The formulation used was type PI2545, supplied by Du Pont (Wilmington, Delaware). This is a high-elongation PMDA-ODA (pyromellitic dianhydride oxydianiline) polyimide capable of sustaining high strain. The layer was applied by spin-coating the polyamic acid solution at a speed of 6000 rpm for 30 s. The heat treatment prescribed by the manufacturer was used to cure the polymer.

Initial experiments showed that a polyimide layer thickness of $\sim 5 \mu\text{m}$ was needed to ensure a substrate with a surface roughness amplitude < 50 nm after straining. Each spin-coating cycle yielded a cured film $\sim 1.6 \mu\text{m}$ thick, as measured by profilometry. Thus, the beams were spin-coated three times.

Microelectronics processing techniques of photolithography and photoresist lift-off were used to pattern the films and multilayers into the configurations required for the multi-strain specimen. A quartz photomask plate which contains the specifications of the 'multi-strain' specimen configuration was designed. The layout consisted of a series of 8 mm long strips, each either 20 or 30 μm wide. The center of each strip was spaced 50 μm from the next, so that approximately 60 fit on a 3.2 mm-wide beam substrate. The strips were also partitioned into 16 segments along their length. Subdividing allows for each location identification on the specimen surface.

All photoresist processing was done inside a Class 100 environment. Positive photoresists, which dissolve upon exposure to UV light, were used with the mask to create a structure suitable for film lift-off. Prior to photoresist deposition, the surfaces of the polyimide-coated substrates were again solvent cleaned. Photoresist layers (AZ P4110 or P4210, Shipley, Newton, Massachusetts) were deposited and processed using conditions recommended by the manufacturer. Optical printing, consisting of mask alignment, photoresist exposure, and development was the next processing step. A mask aligner was used to manipulate the polyimide-coated substrate to the proper position underneath the mask and to hold it in close physical contact during exposure. After exposure a developer solution was used to dissolve the exposed photoresist. The specimens were then rinsed in running deionized water for at least 15 min.

A single-gun electron beam evaporation unit was used to deposit all films. A cryopump was used to evacuate the chamber to a base vacuum of $\leq 7 \times 10^{-7}$ torr prior to evaporation. Film thicknesses and deposition rates were determined using a quartz crystal monitor, and later verified by profilometry. Deposition rates of 2.0 and 0.4 nm/s were used for Cu and Si, respectively.* Various layers of Si, Cu and Cr were deposited.

* The Cu films are polycrystalline, with grain sizes on the order of the film thickness, while the Si films are amorphous.

In all cases, a thin (10 nm) Cr layer was first deposited onto the polyimide. Variations were made in the subsequent Si and Cu layer thicknesses.

Subsequently, the beam was introduced into a four-point flexure fixture with the coated surfaces *on the side*. A bending moment was applied. During this process, each strip, being very thin and narrow compared with the stainless steel beam, experiences a *uniaxial* tensile strain having the same magnitude as that in the steel substrate, at the same location (Fig. 2). The surface displacements were recorded by using strain gauges. The responses were monitored as a function of the distance from the neutral axis of the beam. The strains within each strip are readily obtained from the strain gauge measurements, because of the linearity in strain between the neutral plane and the surface. Observations were performed by interrupting the tests and then transferring the specimen to either the scanning electron microscope (SEM) or an optical microscope.

3.2 Residual Strains

A standard bending procedure was used to assess the residual strain.¹⁴ A thin glass cover slip substrate was prepared and a polyimide layer spun on. Si was deposited by employing deposition conditions identical to those used for producing the multilayers. The curvature of the substrate was measured using a profilometer.¹⁵ The Si was then removed and the curvature measured again. The differential in curvature was used to obtain the residual stress in the Si, knowing the elastic modulus of the glass and the Si layer thickness. (Fig. 3) The stress has been separated into intrinsic and thermal components. This differentiation allows the residual stress for Si deposited on other substrates, such as stainless steel, to be deduced. This is achieved by measuring the temperature change during deposition by placing a thermocouple in contact with the substrate surface. The thermal residual stress is determined from the thermal expansion coefficients.

4. LAYER PROPERTIES

The substrate bending experiments for Si films on polyimide-coated glass consistently gave tensile residual stresses in the range 270 ± 30 MPa for thicknesses between 100 and 300 nm. The substrate temperature change during deposition was measured to be $\Delta T = 40^\circ\text{C}$. The thermal residual stress in the Si is given by

$$\sigma_R^t = \Delta\alpha\Delta TE_s/(1-\nu_s) \quad (2)$$

where ν_s is Poisson's ratio for the Si, $\Delta\alpha$ is the thermal expansion mismatch with the substrate and E_s is the Young's modulus for the Si.[‡] The thermal stress in the Si, calculated from Eqn. (2) for Si on polyimide-coated glass (parameters summarized in Table I), is $\sigma_R^t = -20$ MPa. The 'intrinsic' residual stress in the Si is thus, $\sigma_R^i = 290$ MPa. The intrinsic stresses are usually insensitive to the choice of substrate.¹⁵ It is thus assumed that σ_R^i is the same for Si on polyimide or Si on Cu.

For thin Si films or multilayers on a *thick* stainless steel substrate, the thermal residual stresses are controlled exclusively by the thermal expansion mismatch between Si and steel (Table I). The thermal stresses in the Si would thus be, $\sigma_R^t = -57$ MPa. Consequently, the total residual stress (intrinsic plus thermal) is, $\sigma_R = 230$ MPa. The corresponding residual strain is, $\epsilon_R = \sigma_R/E_S = 0.002$. For all data reported below, this strain is superposed onto the applied strains.

[‡] E_s is considered to be the same as that for polycrystalline Si ($E_s = 107$ GPa). Because Si films deposited by PVD are amorphous, the potential for overestimation caused by this assumption is assessed to be about 10%.

5. LAYER CRACKING MEASUREMENTS

5.1 Si Films

The experiments revealed that those strips closest to the neutral plane which were subject to strains below a critical value, ϵ_c , were everywhere uncracked. At locations further from the neutral plane, where the tensile strains exceeded ϵ_c , multiple cracks were present (Fig. 4) and the crack spacing decreased as the strain increased. Conversely, there were no cracks on the compressive side of the neutral plane. The strain ϵ_c becomes the critical cracking strain. The strain was obtained for a range of Si film thicknesses. The trends in ϵ_c with Si film thickness, t_{Si} , are plotted on Fig. 5. Note that ϵ_c remains almost constant with film thickness and that relatively large strains are needed to cause cracking.

5.2 Trilayers

The behavior of Cu/Si/Cu trilayers with Cr interlayers differs substantially from that for the Si films (Figs. 6 and 7). In this case, the critical strains have an appreciable dependence on Si layer thickness and, at small thicknesses, substantially exceed the cracking strains required for the Si films. Moreover, there is a strong influence of the Cu layer thickness on ϵ_c , with larger thicknesses resulting in higher critical strains. Note that there is extensive plastic distortion of the Cu around the cracks in the Si, with rupture of the Cu occurring in some instances (Fig. 7).

6. CRITICAL CRACKING STRAINS

6.1 Energy Release Rates

The cracking of thin brittle layers is subject to a lower bound critical strain ϵ_c . This bound is associated with either *tunneling* in embedded layers or *channeling* in surface

films. This critical strain applies when the layer contains initial flaws that *exceed* the film thickness. Such flaws are often present in thin films, particularly at edges. They are usually introduced during fabrication. The strain ϵ_c thus becomes an important parameter for the fail-safe design of multilayers.^{9,11}

Tunneling and channeling cracks extend subject to a steady-state energy release rate, G_{ss} . The strain ϵ_c can thus be calculated by evaluating G_{ss} and equating it to the fracture energy for the brittle material, Γ_b . In turn, G_{ss} can be determined from plane strain solutions for the average opening displacement $\bar{\delta}$ experienced by an existent layer crack, as the tensile stress σ is increased, in accordance with (Fig. 8)⁹

$$G_{ss} = \int_0^{\sigma} \bar{\delta} d\sigma \quad (3)$$

The problem thus reduces to calculation of $\bar{\delta}(\sigma)$. For this purpose, a simplification is made to facilitate analytical solutions. It is assumed that slip is confined to a thin boundary layer at the interface between the Si and the Cu. The remaining material is regarded as elastic (Fig. 8). This approach has provided considerable insight into related problems in layered materials.¹⁷ With this idealization, the calculations can be performed using an integral equation formulation, elaborated elsewhere.¹⁷ The initial step is to evaluate the length of the zone that slips. Then, the crack opening displacements are evaluated and the average value $\bar{\delta}$ determined. The present calculations are performed for layers having the same elastic properties (a good approximation for Si and Cu) and by assigning a slip resistance τ to the boundary layer. In turn, τ is related to the uniaxial yield strength of the Cu (designated σ_0) by, $\tau = \sigma_0/\sqrt{3}$. The specific solutions generated are for trilayers of Cu and Si, according to the following logic. The polyimide layer between the trilayer and the substrate has

such a low modulus that the elastic displacements at the interface should be closely similar to those expected at a free surface.

The displacements calculated for trilayers having a range of thicknesses are plotted on Fig. 8. Note that the displacements increase as τ decreases and as the relative outer layer thickness decreases, leading to larger values of G_{ss} . The specific trends in G_{ss} are plotted on Fig. 9.

6.2 Critical Strain

By equating G_{ss} to Γ_{si} , the critical strain for tunnel cracking, ϵ_t , can be determined from Fig. 9 as

$$\frac{2\Gamma_{si}}{\pi(1-\nu^2)\epsilon_t^2 t_{si} E} = F\left(\frac{E\epsilon_t}{\tau}, \frac{t_{si}}{t_{cu}}\right) \quad (4)$$

when F is the function represented by Fig. 9 and ϵ_t is the *total* strain (applied plus residual). The function F can be expressed by the following approximate formulae:

when $\epsilon_t > 2.5 \tau/E$,

$$F \approx \left(\frac{\epsilon_t E}{\tau} - 2.5\right) g(t_{si}/t_{cu}) \quad (5a)$$

where

$$g \approx \frac{t_{si}/t_{cu} + 0.6}{t_{si}/t_{cu} + 3}$$

and, when $\epsilon_t < 2.5\tau/E$,

$$F \approx 1 \quad (5b)$$

Inserting F from Eqn. (5a) into Eqn. (4) and rearranging gives

$$(E\epsilon_t/\tau)^3 + \left[\frac{1-2.5g}{g} \right] (E\epsilon_t/\tau)^2 = \frac{2E\Gamma_{Si}}{\pi\tau^2 t_{Si} g} \quad (6)$$

This formula can be used to plot the normalized critical strain $E\epsilon_c/\tau$ against the cracking number, $\pi\tau^2 t_{Si}/2E\Gamma_{Si}$, for various t_{Cu}/t_{Si} (Fig. 10). These curves are compared with the measured critical strains in the following section.

7. ANALYSIS

7.1 Si Films

The experimental measurements of the critical strain (Fig. 5) are compared with predicted values for channel cracking, ϵ_{ch} . For this purpose, the polyimide is considered to behave as an elastic material with a Young's modulus, $E \approx 3$ GPa. The Si is considered to have a fracture energy $\Gamma_{Si} \approx 6$ Jm⁻² and a Young's modulus, $E = 107$ GPa. These predictions (Fig. 5) give critical strains *smaller* than those found in the experiments, with the discrepancy increasing as the Si film thickness increases. Recalling that ϵ_{ch} should represent a *lower bound* that applies when flaws pre-exist in the film (having length in excess of the film thickness),⁹ the discrepancy can be attributed to the nature of the flaws in the Si.

Since the measured ϵ_c is *independent* of film thickness, the flaws in the Si are inferred to have *fixed size*, a_0 , for all films in the thickness range probed by the present experiments ($t_{Si} > 50$ nm). If the flaws in the Si are considered to exist at the edge, as schematically illustrated in Fig. 5, surface flaw solutions may be used to calculate the

critical strain for flaw controlled cracking. Since the polyimide has a very low modulus, the edge crack in the Si is considered to be able to displace freely at the Si/polyimide interface. Then, the standard surface flaw solution may be used to estimate the critical strain,¹⁷

$$\epsilon_c \approx \frac{1}{(1.12\sqrt{\pi})} \sqrt{\frac{\Gamma_{Si}}{Ea_0}} \quad (7)$$

This formula is found to be consistent with the experimental measurements (Fig. 5) on the assumption that edge flaws exist having length, $a_0 \approx 100$ nm. Edge flaws in this size range are too small to attain the lower bound channel cracking situation (which requires that $a_0 \gtrsim t_{Si}$).⁹ The flaw size is thus consistent with the measured critical strain being *larger* than ϵ_{ch} . Moreover, close approach to this bound should arise when $t_{Si} \approx 100$ nm, consistent with the finding that the predictions for channel and flaw controlled cracking coincide at $t_{Si} \approx 50$ nm (Fig. 5).

7.2 Cu/Si/Cu Trilayers

Analysis of the trilayer results uses the tunnel cracking strain, ϵ_t (Fig. 10), upon assuming the presence of edge flaws in excess of the Si layer thickness. For this purpose, the uniaxial yield strength of the Cu is considered to be the same for all layer thicknesses and have magnitude, $\sigma_0 \sim 350$ MPa.¹³ The predictions made using Fig. 9 with $\Gamma_{Si} = 6 \text{ Jm}^{-2}$, are plotted on Figs. 10 and 11 for a range of relative layer thicknesses, t_{Cu} / t_{Si} . The experimental measurements from Fig. 6 are superposed on both Figs. 10 and 11. For specimens with relatively thick Cu layers, $t_{Cu} \geq 300$ nm, the critical strain, ϵ_c , measurements appear to be consistent with the predicted values. However, at $t_{Cu} \leq 200$ nm, ϵ_c is below the lower-bound tunnel cracking prediction. This discrepancy may be due to the simplified assumption used in the model that the

Cu behaves in a linearly elastic manner, except for the yielding boundary layers. In fact, large-scale plastic deformation of Cu always occurs, sometimes resulting in rupture of the layer (Fig. 7). In consequence, for thin layers, extensive distortion and rupture of the Cu appears inevitable, causing ϵ_c to diminish below predicted values.

8. CONCLUSION

The strain needed to crack thin Si layers depends on three factors: the layer thickness, the properties and thickness of the neighboring layers and the magnitude of edge flaws introduced during fabrication. In almost all cases, solutions for either channel cracking of the films or tunnel cracking in thin layers provide an explicit lower bound for the critical strain. In some cases, pre-existing edge flaws are sufficiently small that the cracking strains can appreciably exceed the lower bound.

The critical strains in the Si/Cu system are significantly higher than that for Si/polyimide. This situation arises because the high modulus of the Cu (relative to polyimide) elevates the critical strain for tunnel cracking. Moreover, because of this effect, the critical strain increases appreciably as the Si layer thickness decreases, especially when $t_{si} = 100$ nm or less.

The tunnel cracking concepts would further suggest that the critical cracking strain for Si layers could be even larger if either the yield strength of the Cu could be increased or a metal with a larger modulus were used. Validation of this prediction would require further research.

TABLE I

Material Properties

Material	E [GPa]	α [$\times 10^{-6}/^{\circ}\text{C}$]
Si	107	3
Cu	124	17
Glass (Corning 0211)	74	7.4
Stainless Steel (AISI 304)	200	16
Polyimide (DuPont PI2545)	~ 3	~ 30

REFERENCES

- 1) F.E. Heredia, M.Y. He, G.E. Lucas, A.G. Evans, H.E. Dève and D. Konitzer, "The Fracture Resistance of Directionally Solidified Dual-Phase NiAl Reinforced with Refractory Metals," *Acta Metall. Mater.* **41**[2], 505–511 (1993).
- 2) H.C. Cao, J.P.A. Löfvander, A.G. Evans and R.G. Rowe, "Mechanical Properties of an *in-situ* Synthesized Nb/Nb₃Al Layered Composite," accepted by *Mater. Sci. and Eng. A*.
- 3) Z. Cheng and J.J. Mecholsky, Jr., "Toughening by Metallic Lamina in Nickel/Alumina Composites," *J. Am. Ceram. Soc.* **76**[5] 1258–1264 (1993).
- 4) P. Calvert, "Biomimetic Ceramics and Composites," *MRS Bull.*, **17**[10] 37–40 (1992).
- 5) H.C. Cao and A.G. Evans, "On Crack Extension in Ductile/Brittle Laminates," *Acta Metall. Mater.* **39**[12], 2997–3005 (1991).
- 6) G.R. Odette, B.L. Chao, J.W. Sheckherd and G.E. Lucas, "Ductile Phase Toughening Mechanisms in a TiAl-TiNb Laminate Composite," *Acta Metall. Mater* **40**[9], 2381–2389 (1992).
- 7) M.Y. He, F.E. Heredia, D.J. Wissuchek, M.C. Shaw and A.G. Evans, "The Mechanics of Crack Growth in Layered Materials," *Acta Metall. Mater.* **41**[4] 1223–1229, (1993).
- 8) M.C. Shaw, D.B. Marshall, M.S. Dadkhah and A.G. Evans, "Cracking and Damage Mechanisms in Ceramic/Metal Multilayers," *Acta Metall. Mater.* **41**[11] 3311–3322 (1993).
- 9) S. Ho and Z. Suo, "Tunneling Cracks in Constrained Layers," *J. Appl. Mech.* **60**[4] 890–894 (1993).
- 10) J.W. Hutchinson and Z. Suo, "Mixed Mode Cracking in Layered Materials," *Adv. in App. Mech.* **29** 63–191 (1992).
- 11) A.G. Evans and J.W. Hutchinson, "The Thermomechanical Performance of Thin Films and Multilayers, *Acta Metall. Mater.*, in press.
- 12) R.W. Hoffman, "The Mechanical Properties of Thin Condensed Films," *Physics of Thin Films*, **3**, p. 211, Academic Press Inc., New York, 1966.
- 13) M.D. Merz and S.D. Dahlgren, "Tensile Strength and Work Hardening of Ultrafine-grained High-purity Copper," *J. of Appl. Phys.* **46**[8] 3235–3237 (1975).
- 14) D.S. Campbell, "Mechanical Properties of Thin Films," *Handbook of Thin Film Technology*, edited by L.I. Maissel and R. Glang, Chapter 12, McGraw-Hill, New York, 1970.

- 15) M.E. Thomas, M.P. Hartnett and J.E. McKay, "The Use of Surface Profilometers for the Measurement of Wafer Curvature," *J. Vac. Sci. Technol. A* 6[4] 2570-2571 (1988)
- 16) W.D. Nix, "Mechanical Properties of Thin Films," *Met. Trans. A*, 20A[11] 2217-2245 (1989).
- 17) K.S. Chan, M.Y. He and J.W. Hutchinson, "Cracking and Stress Redistribution in Ceramic Layered Composites," *Mater. Sci. and Eng. A*, 167[1-2] 57-64, (1993).
- 18) H. Tada, P.C. Paris and G.R. Irwin, *The Stress Analysis of Cracks Handbook*, Del Research Corporation (1973).

FIGURE CAPTIONS

- Fig. 1. A schematic of the tunnel cracking phenomenon in layered systems.
- Fig. 2. A schematic showing the configuration used for imposing defined strains on thin multilayer strips. The substrate is stainless steel and the strain varies linearly with distance from the neutral plane.
- Fig. 3. The bending that occurs for a thin residually stressed Si film on a polyimide-coated glass substrate .
- Fig. 4. Multiple cracks present in thin strip Si films at strains above the critical value.
- Fig. 5. The influence of Si film thickness on the critical strain. Also shown are values calculated for channel cracking and for flaw-controlled cracking. The edge flaw size for the latter is ~ 100 nm.
- Fig. 6. Critical strains for Si layers within Cu/Si/Cu trilayers for various Cu and Si thickness combinations.
- Fig. 7. Cracks within a Cu/Si/Cu trilayer at a strain above ϵ_c . Note the yielding and rupture of the Cu layers in addition to cracking of the Si.
- Fig. 8. A plot of relative crack opening displacement as a function of normalized stress σ/τ for trilayers having different thicknesses.
- Fig. 9. A plot of normalized steady state energy release rate G_{ss} as a function of normalized stress σ/τ for trilayers having different thicknesses.
- Fig. 10. A plot of normalized critical strain $E\epsilon_t/\tau$ against the cracking number $\pi \tau^2 t_{si} / 2 E_{si} \Gamma_{si}$, for various t_{si} / t_{cu} . The measured values are superposed.
- Fig. 11. A comparison of measured and predicted critical strains for various t_{si} / t_{cu} (assuming $\sigma/\tau = 10$).

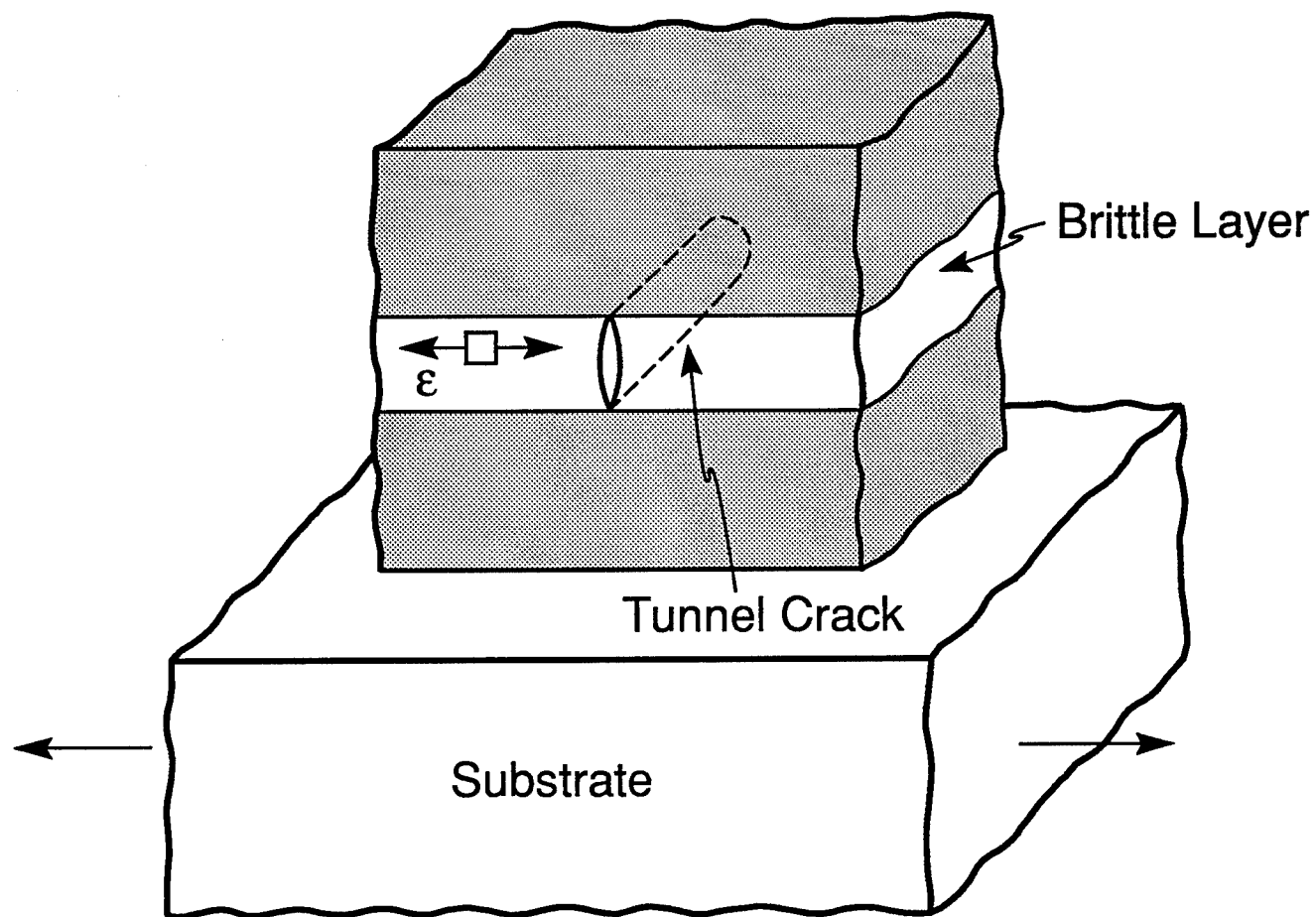


Figure 1

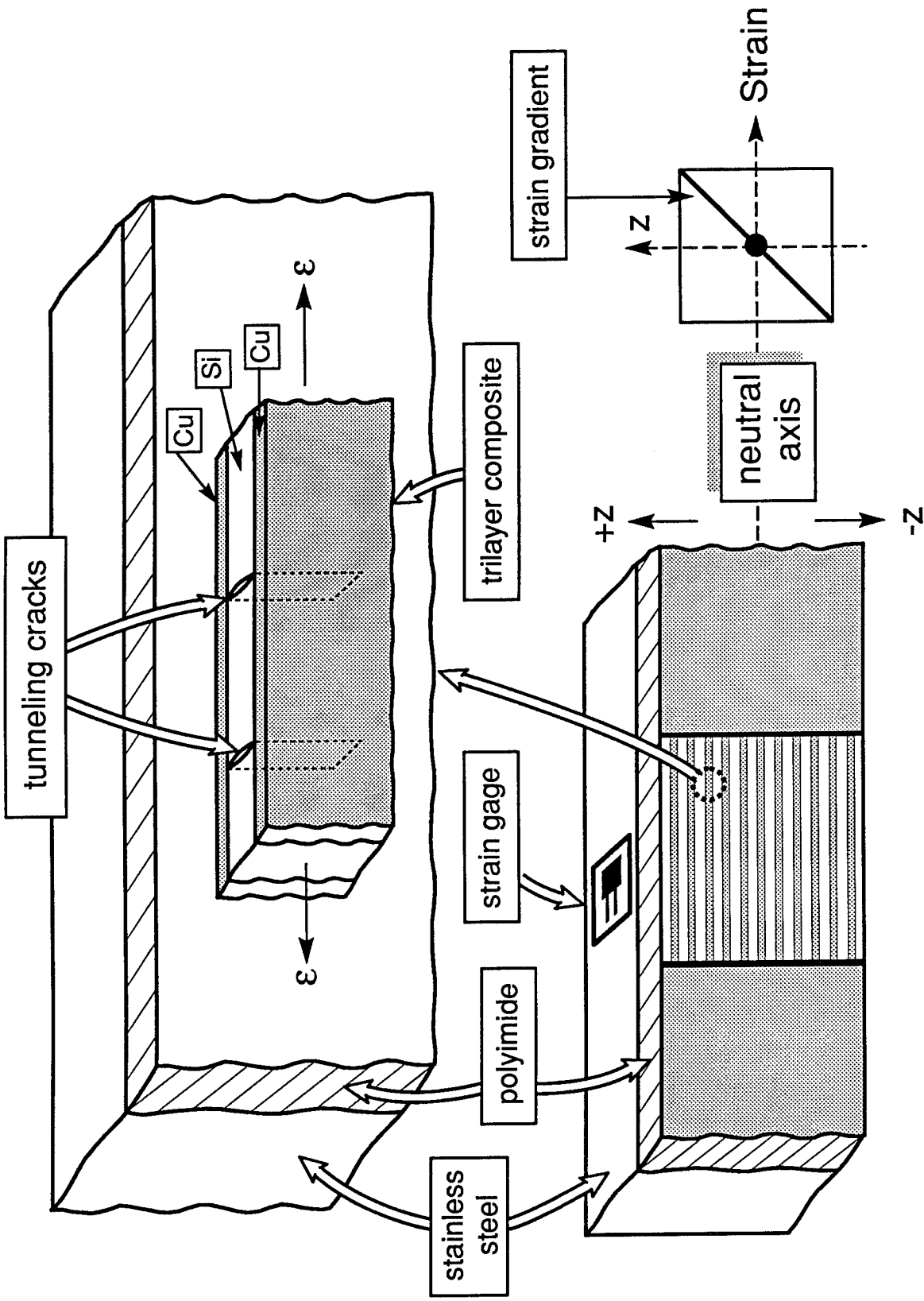
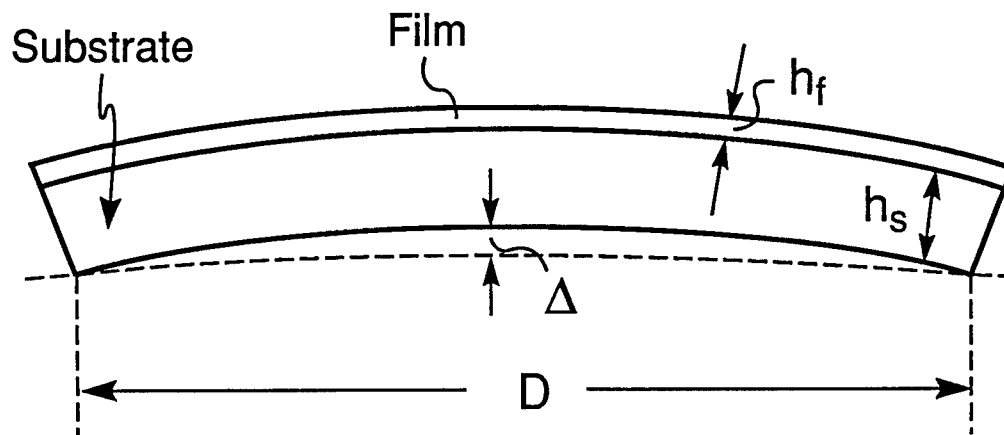


Figure 2



$$\sigma_f = [E_s \Delta h_s^2] / [3 (1-\nu_2) D^2 h_f]$$

Figure 3

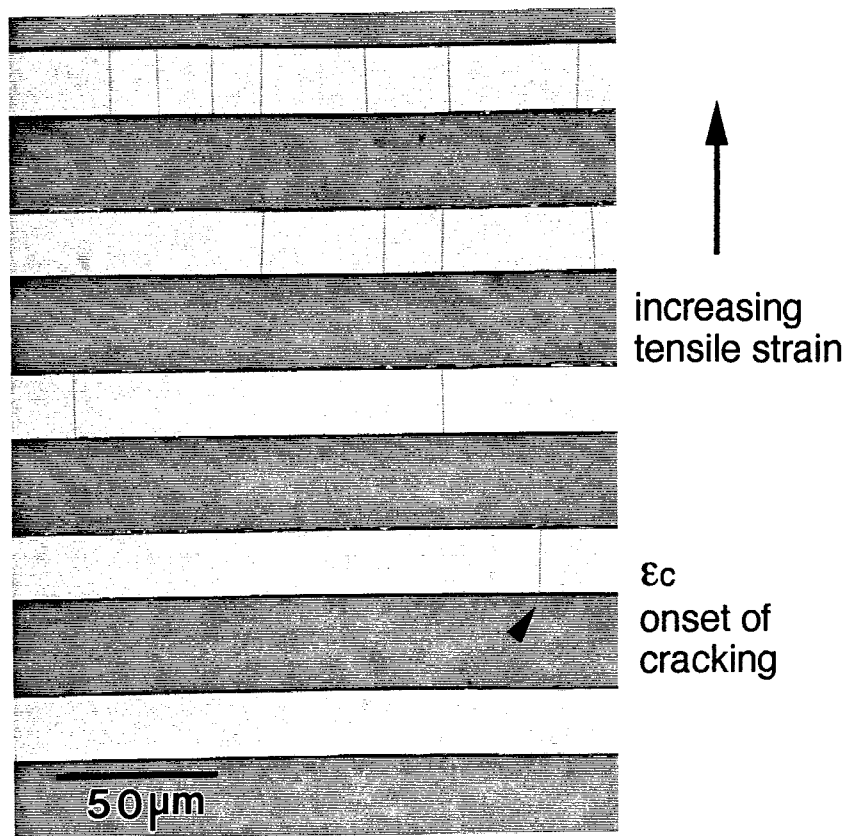


Figure 4

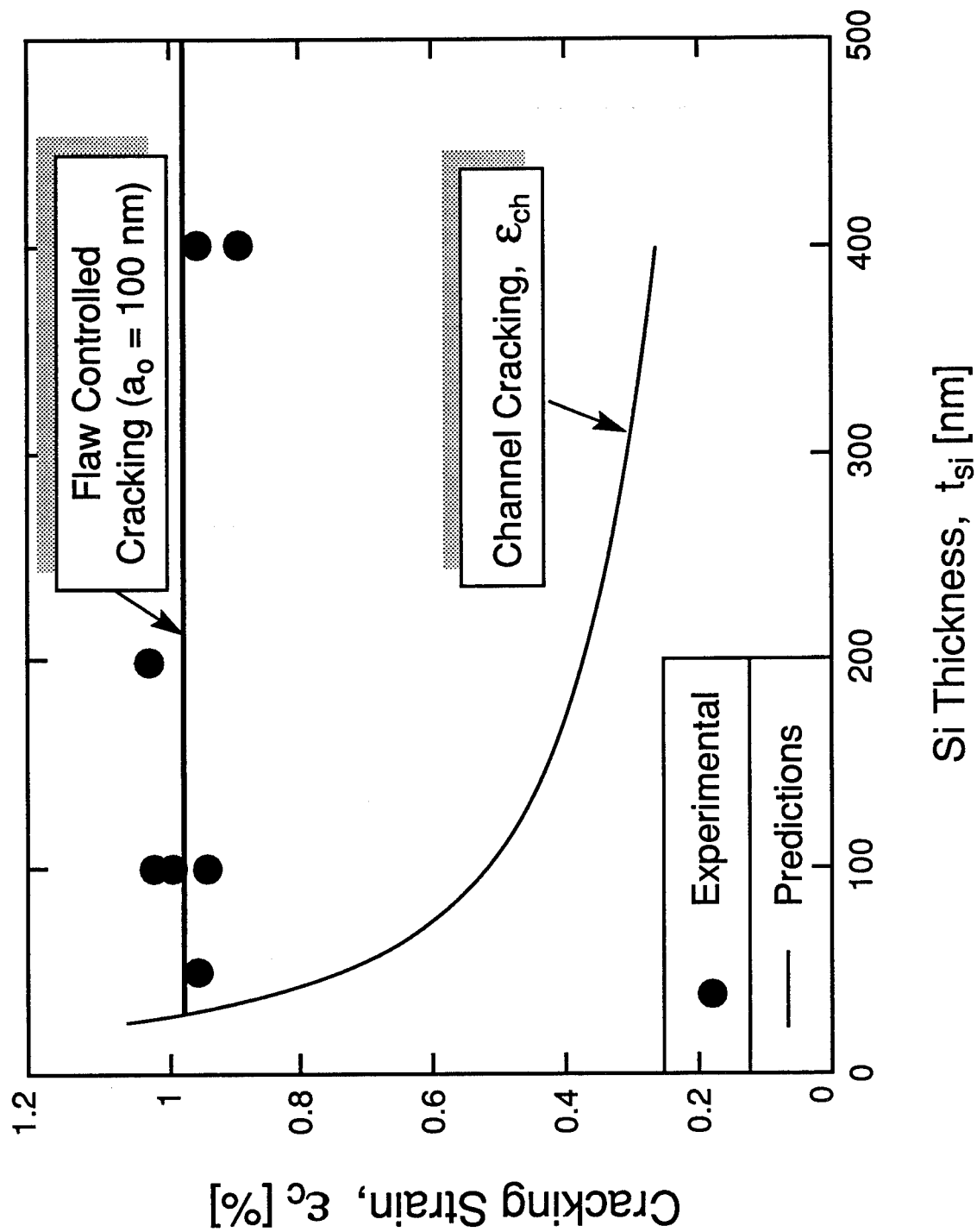


Figure 5

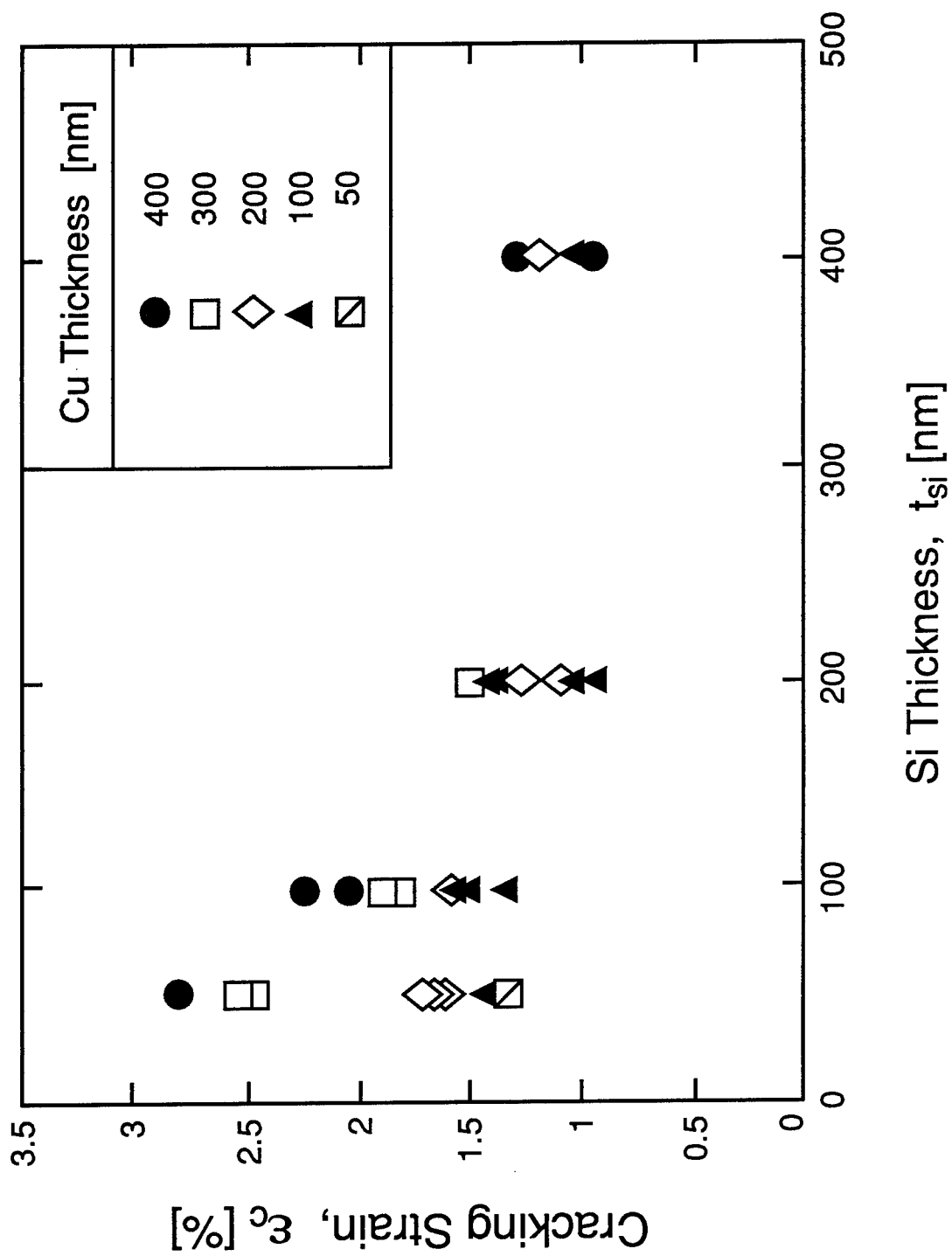


Figure 6

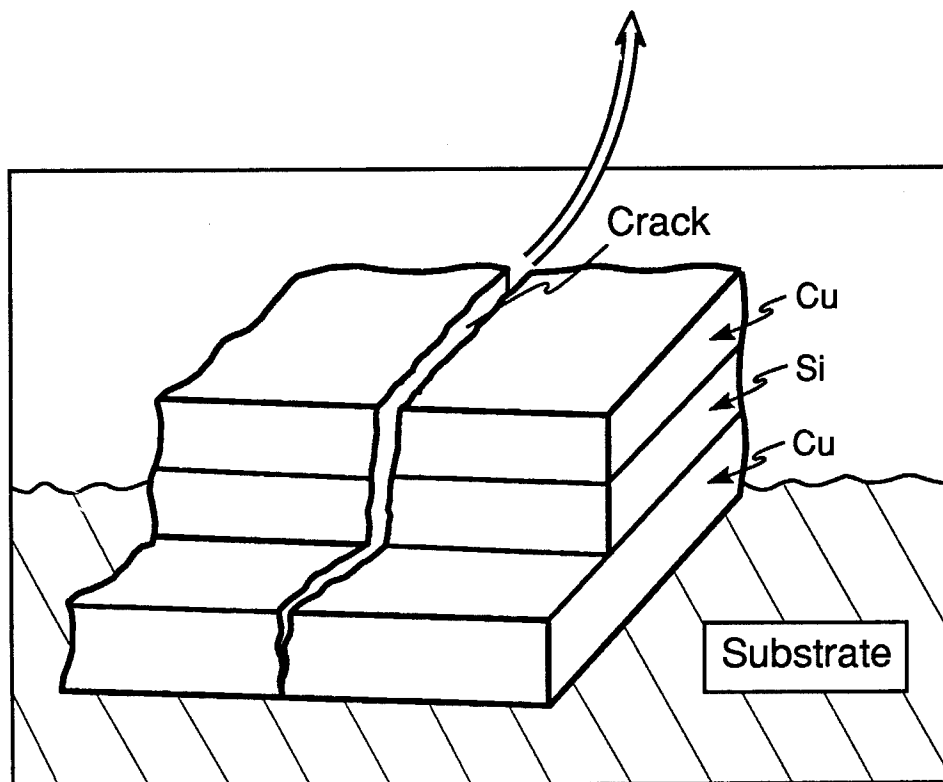
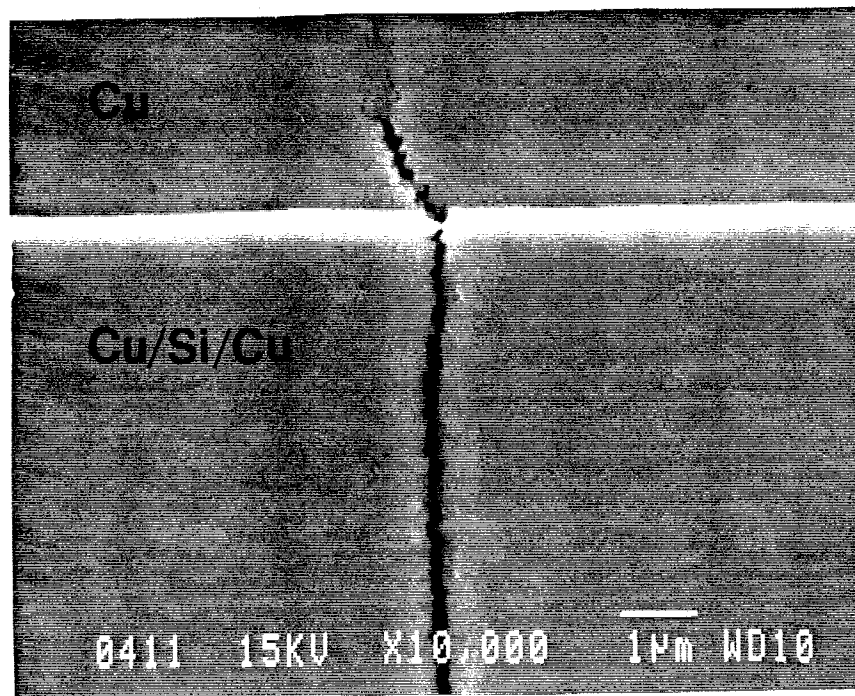


Figure 7

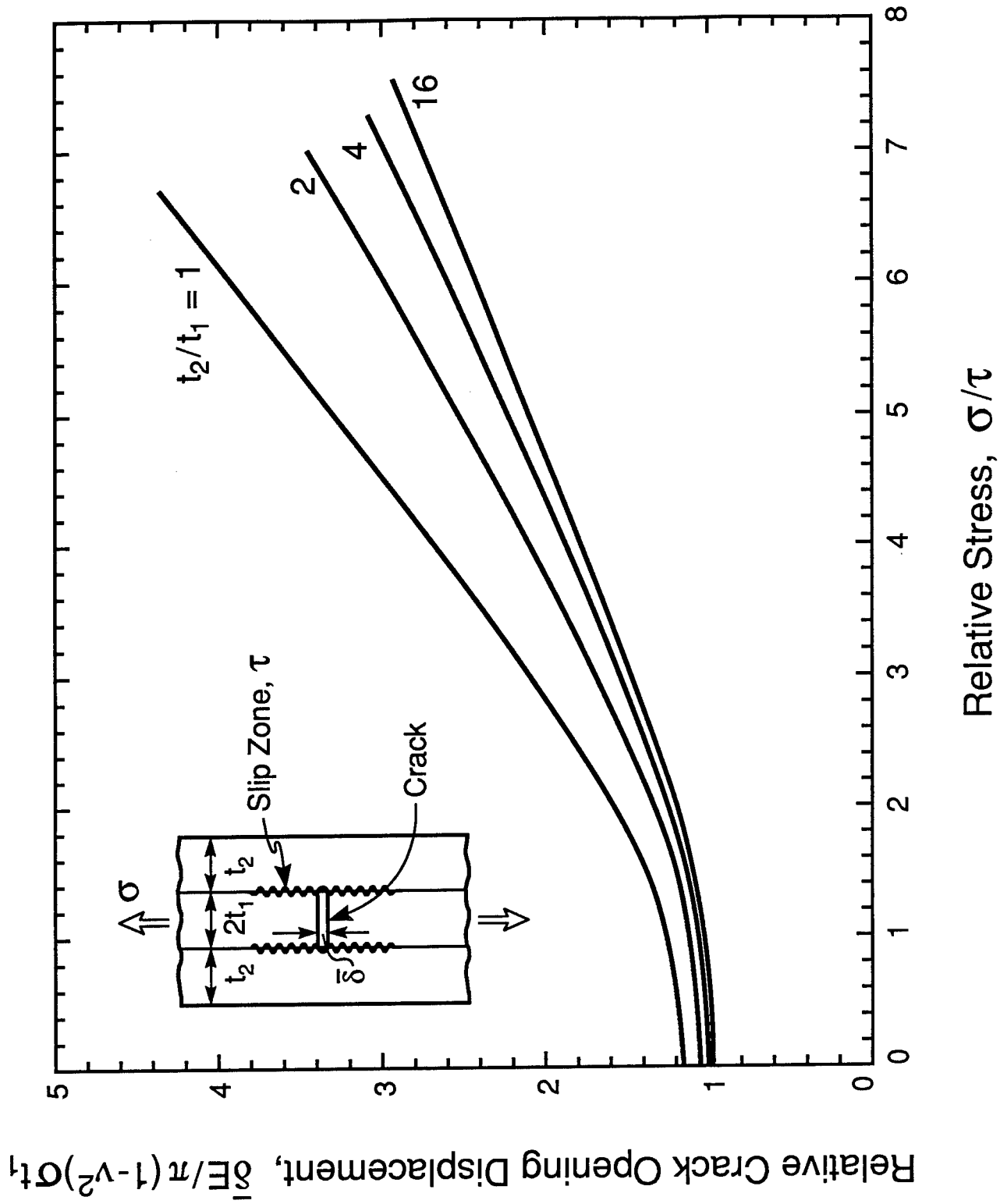


Figure 8

Steady State Energy Release Rate, $2E G_{ss} / \pi(1-\nu^2) \sigma^2 t_1$

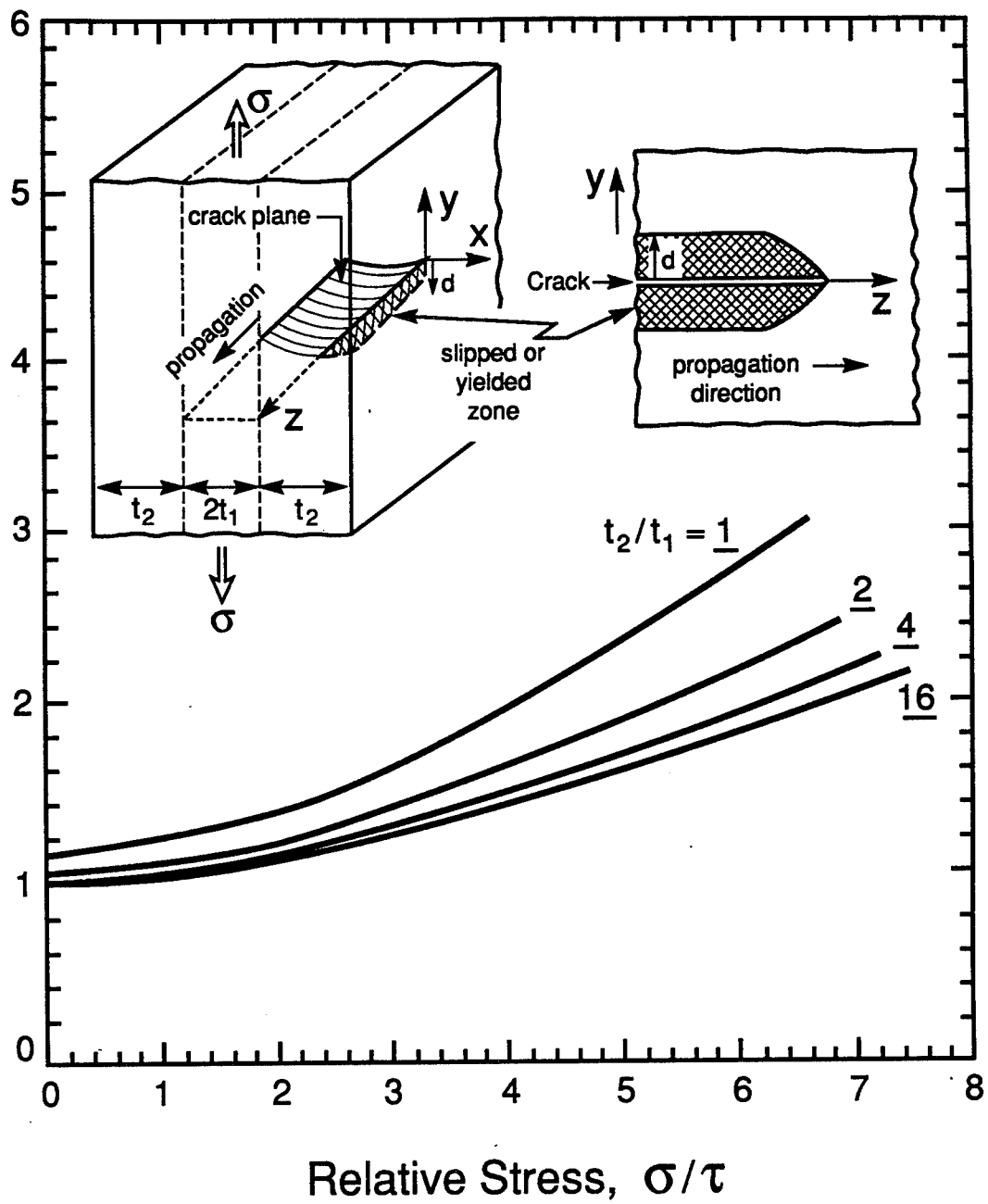


Figure 9

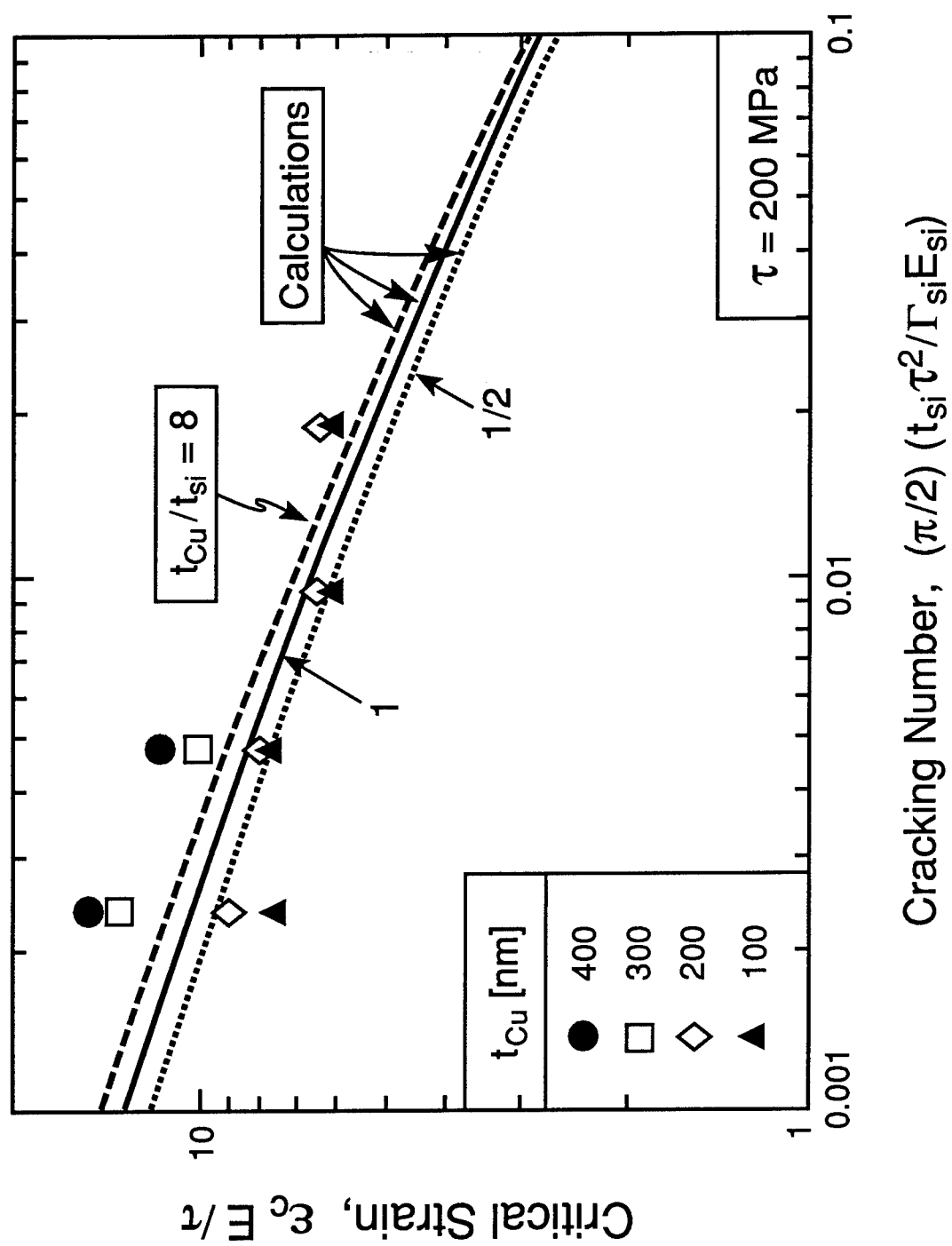


Figure 10

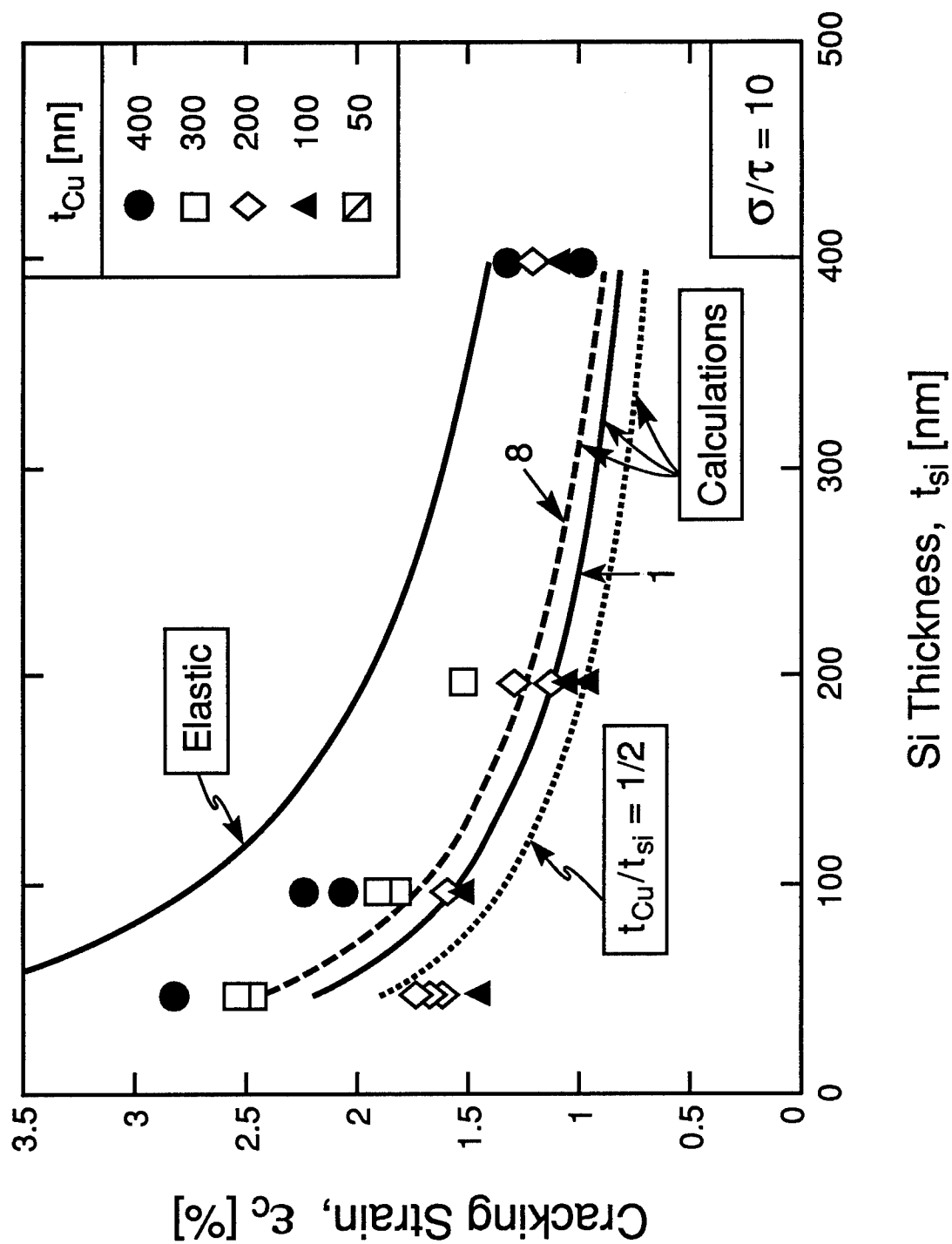
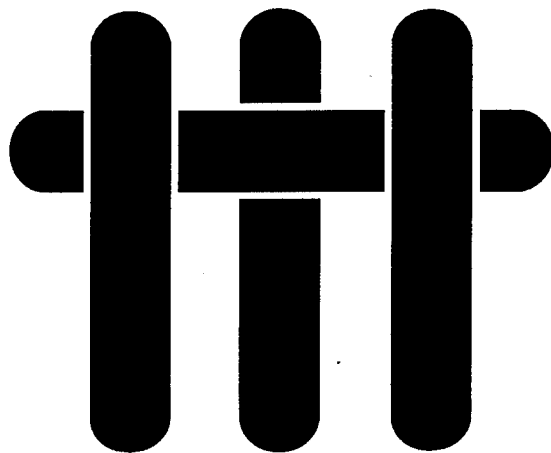


Figure 11

M A T E R I A L S



THE THERMOMECHANICAL INTEGRITY OF THIN FILMS AND MULTILAYERS

by

A.G. Evans
Materials Department
College of Engineering
University of California, Santa Barbara
Santa Barbara, California 93106-5050

and

J.W. Hutchinson
Division of Applied Sciences
Harvard University
Cambridge, Massachusetts 02138

TABLE OF CONTENTS

1.	INTRODUCTION.....	4
2.	RESIDUAL STRESSES	6
2.1	Basic Features.....	6
2.2	Stress Redistribution	8
2.2.1	Edges and Surfaces.....	9
2.2.2	Bending	10
2.3	Measurements Methods	12
2.3.1	Beam Deflection.....	12
2.3.2	Lattice Strain	13
2.3.3	Localized Methods	14
3.	INTERFACES.....	14
3.1	Concepts	14
3.2	Measurement Methods.....	16
3.3	Interface Separation Criteria.....	17
3.4	Plastic Dissipation	19
3.5	Friction	20
3.6	Cyclic Effects	20
3.7	Layer Thickness Effects	21
3.8	Fracture Energy Measurements	21
4.	CRACKING AND DECOHESION	23
4.1	Mechanics Concepts: Steady-State Cracking.....	23
4.1.1	Decohesion and Spalling.....	24
4.1.2	Layer Cracking.....	27
4.1.3	Crack Paths.....	28
4.2	Mechanics Concepts: Stress Redistribution.....	29
4.3	Experimental Measurements	31
4.4	Fail-Safe Design Concepts.....	32
4.5	Damage Modes	33
4.6	Some Practical Problems	35
5.	THERMOMECHANICAL FATIGUE.....	36
6.	THIN LAYER EFFECTS	38
7.	DESIGN METHODOLOGY.....	39
APPENDIX I		
	Intrinsic Stresses In Vapor Deposited Films.....	42
	MECHANISMS.....	43
1.	Grain Growth.....	43
2.	Point Defect Annihilation.....	44
3.	Sintering.....	46

ABSTRACT

Thin films and multilayers comprised of different classes of material are often used for various functional requirements. As these become relatively large in section and geometrically more complex, thermomechanical integrity is a major concern. It influences performance, yield and reliability. A methodology for thermomechanical design is needed that complements procedures used for circuit design. This article elaborates the principles of fail-safe thermomechanical design, based on the damage mechanisms known to occur in these systems. Among the important mechanisms are delamination and crazing of brittle layers, thermomechanical fatigue of metallic constituents and interface decohesion.

The damage mechanisms are generally activated by residual stress, both thermal and 'intrinsic.' The origins of these stresses are discussed, as well as stress redistribution effects that arise because of bending, discontinuities, etc. Emphasis is given to measurement methods which provide those data needed for implementation of the fail-safe design methodology.

1. INTRODUCTION

There are many technologies that use thin layers of dissimilar materials in order to achieve functional requirements. Some of the important areas include: electronic packaging¹ and ferroelectric actuators,² as well as coatings used for either thermal protection³ or for abrasion,⁴ oxidation and corrosion resistance. An example of a multilayer used for electronic packaging is shown in Fig. 1.1, to illustrate the variety of geometric arrangements that arise.¹ The dissimilar nature of the constituents presents challenges concerning the thermomechanical integrity and reliability,⁵ especially when at least one of the constituents is brittle: ceramic, semiconductor, glass, or certain polymers. Two dominant factors causing reliability problems are the mismatch in thermal expansion coefficient between the materials, which causes residual stress, and the decohesion resistance of the interfaces. When one of the constituents is metallic, an additional factor is boundary layer shear that arises as a result of plasticity. Other significant phenomena include stress redistribution and thermomechanical fatigue. The intent of this article is to establish the principles governing the thermomechanical integrity of multilayers and to provide a methodology for designing fail-safe systems. It complements three other review articles: one on residual stress,⁶ a second on the mechanics of decohesion in multilayers⁷ and a third on thin films.⁸

Interfaces have a special significance in multilayer systems, because they are both numerous (Fig. 1.1) and susceptible to decohesion and sliding. A thermomechanical description of interfaces is provided, with an emphasis on decohesion and sliding characteristics. A particular challenge is the design and implementation of test procedures that measure interface properties. Few methods provide rigorous results which can also be readily implemented on actual multilayer configurations (Fig. 1.1). The methods which satisfy these requirements are emphasized and typical results discussed.

Residual stresses arise because of either thermal expansion differences between the constituents or defect annihilation subsequent to deposition.^{6,8} They are modified by various relaxation and redistribution effects that occur as a result of creep and yielding, in addition to debonding and sliding at interfaces. There are also important effects on the stress of thermal cycling, especially when one constituent is metallic and when the temperature range is large enough to cause yielding. Redistribution phenomena are prevalent near edges and corners and in the presence of microcracks in the brittle layers. In consequence, the stresses cannot generally be predicted. Experimental procedures are needed to measure them. Moreover, the residual stresses are configuration dependent, because the plastic strains occur in response to the deviatoric stresses. There are particularly large differences between the stress magnitudes in planar layers compared with built-in cylindrical features, such as vias in electronic packages⁹ (Fig. 1.1). Residual stress measurement techniques amenable to multilayers are described in this article.

The cracking and decohesion events expected in a multilayer system can be predicted, subject to knowledge about residual stresses, their redistribution, and the external loads, as well as the interface response. Many of these phenomena and the associated mechanics have been comprehensively addressed in a recent review.⁷ In this article, an overview is given, including some additional phenomena. The primary importance of the mechanics is to define *fail-safe multilayer designs*. Such designs refer to multilayers that are incapable of thermostructural failure from the residual stresses existing in the system.

It is a common misconception that to ensure reliable performance, it is sufficient to have the brittle material be subject to in-plane compression. Such stresses indeed suppress cracking through the layer, *normal* to the interface, often referred to as crazing. But cracking may still occur *parallel* to the interface, resulting in delamination.⁷ While both crazing and delamination can be suppressed by diminishing the residual stress, this is not always either possible or desirable, because the choice of materials and the

processing are dictated by functionality considerations. Moreover, in principle, susceptibility to damage can also be diminished by reducing layer thicknesses.⁷ But, this approach often introduces additional interfaces which frequently cause other problems, such as interface decohesion, dielectric breakdown, etc.⁵ In general, therefore, it is important to have a procedure for designing thermostructurally fail-safe multilayer systems, when there are functionality constraints on both the choice of materials and the layer thicknesses.

In many cases, the loading is cyclic and thermomechanical fatigue effects arise.¹⁰⁻¹³ Among the important cyclic phenomena are shakedown and ratcheting, as well as the nucleation and growth of cracks near the interfaces. It is critically important to include these effects in the design methodology for multilayers.

2. RESIDUAL STRESS

2.1 Basic Features

One source of residual stress is the thermal expansion mismatch between constituents. This mismatch leads to stresses when the temperature changes. There are other sources of residual stress when the layers are either vapor deposited or structurally modified at low homologous temperatures. These are often referred to as 'intrinsic' stresses. Such stresses develop as a consequence of diffusional effects in previously deposited sections of the film. They involve mechanisms which *eliminate defects* having an associated 'free volume.'⁶ These defects include grain boundaries, vacancies, interstitials, voids and gas molecules. Diffusion allows the number density of previously created defects to reduce, by grain growth, dislocation climb, annihilation, etc., resulting in a misfit as the film attempts to either contract or expand. However, since the in-plane misfit displacements are constrained by the attached substrate, elastic strains develop in the film. For films that deposit with a high defect density, these

diffusional effects can be rapid, leading to large 'intrinsic' stresses, in the GPa range. Some of the mechanisms and the associated stresses are discussed further in Appendix I. These stresses can be either tensile or compressive. The residual stresses can also be redistributed by plastic deformation and creep.⁶

In multilayers produced at high temperatures, by either co-sintering or diffusion bonding, the residual stresses derive primarily from thermal expansion misfit. The stresses are relatively uniform, with minimal gradients through the layers. Conversely, the mechanisms of 'intrinsic' stress development do not operate homogeneously as the film deposits. There is usually a change in stress with film thickness and a stress gradient within the film.⁶ Typically, the first layers to deposit have the largest stress. Such behavior is generally found for inorganic films, such as oxides, nitrides, diamond, etc. Metallic films which yield upon cooling experience stress relaxation and, in consequence, are subject to a more uniform residual stress.

The residual stresses have scaling characteristics based on a reference stress, designated the *misfit stress*, σ^T , such that the actual residual stress, σ_R , can always be expressed in the form,

$$\sigma_R / \sigma^T = q \quad (2.1)$$

where q is a non-dimensional function that depends on geometry, elastic properties, etc. Several examples are presented below. In general, for the reasons indicated above, σ^T cannot be predicted from models, even when the mechanisms are known. It must be measured.

When the constituent materials and the interfaces respond to changes in temperature in an *elastic* manner, the misfit stress is defined by,

$$\sigma^T = E_1 \Delta \alpha (T_R - T) / (1 - \nu_1) \quad (2.2)$$

where T is the temperature, T_R the reference temperature at which the stress is zero (Fig. 2.1a), $\Delta\alpha = \alpha_1 - \alpha_2$ is the mismatch in thermal expansion between the layers, E_1 is Young's modulus of the reference layer and ν_1 its Poisson's ratio. The quantity σ^T is the stress which would be induced in a thin film of material #1 attached to an *infinite substrate* of material #2. (Results for a one-dimensional layered system, which neglects in-plane Poisson effects, can be retrieved by setting ν_1 to zero.)

Inelastic deformation in one of the constituents changes the misfit stress (Fig. 2.1b) and the reference temperature, T_R (Fig. 2.1a). A typical stress/temperature cycle, when the film yields^{6,8} (Fig. 2.1a,b), indicates that the reference temperature can be *translated* by thermal cycling. The subsequent behavior is elastic within a range of temperature referred to as the shakedown range, ΔT_s (Fig. 2.1a and Section 5). In the absence of an applied transverse stress, ΔT_s is given by¹⁰

$$\Delta T_s \approx 1.4 \sigma_o / E_m |\Delta\alpha| \quad (2.3)$$

where σ_o is the uniaxial cyclic yield strength, and E_m is the Young's modulus of the yielding constituent.

2.2 Stress Redistribution

When physical discontinuities are present, stress redistribution occurs. This influences q in Eqn. (2.1) and has implications for the thermomechanical integrity. The effects are particularly important when appreciable external loads are imposed, possibly leading to complete rupture of a system which would otherwise survive. The phenomenon exists at edges and surfaces and in the presence of cracks. It is also caused by bending. The presence of interfaces provides two major mechanisms of stress redistribution: (i) plastic deformation in a boundary layer near the interface and

(ii) debonding at the interface, sometimes accompanied by friction. Some useful analytical results for the stress redistribution magnitudes are presented below. These are augmented later by numerical solutions for stress redistribution around cracks.

2.2.1 Edges and Surfaces

At an edge or surface, the normal and shear stresses must become zero. This requirement causes stress redistribution and typically, generates normal and shear stresses at the *interface*, near the edge. The magnitude and extent of the stresses depend on whether the interface is elastic or whether debonding/slip occur. A typical elastic result (Fig. 2.2) illustrates the development of interface shear and normal stresses in thin films. Yielding or slip along a boundary layer near the interface induces a slip zone (Fig. 2.2), of length L , given approximately by,^{14,15}

$$L/h \approx \sigma^T/\tau_o \quad (2.4)$$

where τ_o is the shear resistance of the interface. Within this zone, the residual stress in the film σ_R acting parallel to its plane (σ_{yy}) varies linearly with distance, z , from the edge ($z < L$),

$$\sigma_R(z) \approx \tau_o(z/h) \quad (2.5a)$$

or

$$\sigma_R/\sigma^T = z/L \quad (2.5b)$$

A component normal to the interface, σ_{zz} , also exists very near the edge, as shown.

2.2.2 Bending

One important phenomenon in multilayers is bending because of the moments of stress associated with the residual field. The consequences are most vividly illustrated for an elastic *bilayer*, subject to misfit stress, σ^T defined above. Consider the geometry shown in Fig. 2.3 and let

$$\Sigma = \frac{E_1/(1-\nu_1)}{E_2/(1-\nu_2)} \quad \text{and} \quad \xi = \frac{h_1}{h_2} \quad (2.6)$$

The average residual stress σ_R in layer #1, $\bar{\sigma}$, is related to σ^T by

$$\bar{\sigma}/\sigma^T = \frac{1 + \Sigma\xi^3}{(\Sigma\xi^2 - 1)^2 + 4\Sigma\xi(\xi + 1)^2} \quad (2.7a)$$

The residual stress σ at the top surface of layer #1 is

$$\sigma/\sigma^T = \frac{[1 - 3\Sigma\xi^2 - 2\Sigma\xi^3]}{(\Sigma\xi^2 - 1)^2 + 4\Sigma\xi(\xi + 1)^2} \quad (2.7b)$$

The curvature of the bilayer caused by bending is

$$\kappa = \frac{6\xi^2(1+\xi)}{(\Sigma\xi^2 - 1)^2 + 4\Sigma\xi(1+\xi)^2} \left[\frac{(1-\nu_2)\sigma^T}{E_2 h_1} \right] \quad (2.8)$$

and the deflection δ (Fig. 2.4) is

$$\delta = -\kappa D^2/8 \quad (2.9)$$

where D is the plate diameter or length. For thin films on a thick substrate ($\xi \ll 1$), Eqn. (2.8) reduces to¹⁶

$$\kappa = \frac{6h_1(1-\nu_2)\sigma^T}{E_2 h_2^2} \quad (2.10)$$

The above results indicate that the *average* residual stress is essentially the misfit stress, σ^T , when the film is *thin* ($\xi \ll 1$), but is reduced to a fraction of σ^T when the film and substrate have comparable thicknesses, as plotted in Fig. 2.3 for three values of Σ . Bending has its maximum effect when the two layers have about equal thickness, resulting in substantial redistribution of the misfit stress. Specifically, and most importantly, the stress at the top of layer #1 develops the *opposite sign* from the misfit stress and becomes substantially larger in magnitude than the average stress in that layer, $\bar{\sigma}$,¹⁷ as seen in Fig. 2.3. The key features brought out in Fig. 2.3 are summarized as follows: (a) When layer 1 is sufficiently thin, ($\xi \ll 1$), the residual stress in this layer is everywhere approximately the misfit stress σ^T . (b) Conversely, when layer 2 is relatively thin, ($\xi \rightarrow \infty$), the stress throughout layer 1 approaches zero. (c) Yet, in the intervening range of ξ , the stress σ at the top surface of layer #1 can have the opposite sign to σ^T and can be large compared to $\bar{\sigma}$. In particular, tensile stresses can arise at the surface of a film that would be in compression in the absence of bending. The range of ξ corresponding to such tensile stresses is of direct relevance to the crazing mode of film cracking. From Eqn. (2.7b) it is seen that a tensile stress will exist at the top surface for all thickness ratios ξ greater than that satisfying $3\Sigma\xi^2 + 2\Sigma\xi^3 = 1$. For small Σ , the *minimum* ξ corresponds to $\xi \cong (1/2\Sigma)^{1/3}$; for $\Sigma = 1$, $\xi = 1/2$; while for large Σ , $\xi \cong (1/3\Sigma)^{1/2}$. This example for the bilayer illustrates the importance of the configurational details mentioned earlier.

2.3 Measurements Methods

There are two basic approaches for determining residual stress. One approach measures either the misfit stress σ^T by averaging information over a substantial area away from edges and discontinuities. Beam bending is an example. The other approach involves localized measurements of displacements in order to examine the redistributed stress. Moiré interferometry exemplifies the latter.

2.3.1 Beam Deflection

The preferred approach for measuring the misfit stress is the beam deflection method.¹⁶ This approach measures the deflection (Fig. 2.4) and infers the residual stress from Eqn. (2.9). For systems in which the film is thin compared with the substrate, the curvature is given by Eqn. (2.10). As discussed in connection with Fig. 2.3, σ^T can be identified with the average residual stress in the upper layer (i.e., the film) when $\xi \ll 1$. (Just how thin the film must be for the method to be accurate can be seen in Fig. 2.3. For $\Sigma = 1$, ξ must be less than about 0.03, and for $\Sigma = 10$, ξ must be less than about 0.003.) Thus, the method can be used to measure the average residual film stress whether that stress arises from thermal expansion mismatch, or from intrinsic stresses (or combinations of the two). This remains true even when the intrinsic film stresses are nonuniform through the thickness, as long as σ^T is interpreted as the average film stress. Note that none of the properties of the film need to be known in order to measure σ^T , except its thickness. The method gives a rigorous measure of σ^T provided that $D \gg h_2$, and that the substrate is elastic. Interface decohesion from the ends would be a problem, unless the decohesion length is small.

The deflection δ needed to obtain σ^T can be measured with excellent precision by using either a laser interferometer or a mechanical profilometer. Measurement systems

based on lasers have been established at many laboratories. Some are capable of continuous measurements as the temperature is varied.

Since only the average of the film stress contributes to the curvature for films which are thin compared to the substrate, stress gradients normal to the surface have no effect. Should gradients exist and be important, alternative procedures are necessary to measure them.

2.3.2 *Lattice Strain*

Several other methods for measuring the residual stress rely on determination of the lattice strain. The strains are then converted into stresses if the elastic properties are known (not always trivial). The strains are typically determined from the shift in intensity peaks that relate to the lattice spacings (Fig. 2.5). X-ray and neutron diffraction methods are commonly used, as well as Raman microscopy.¹⁸⁻²⁰ The strain tensor is ascertained from the shifts in either the diffraction peaks or the fluorescence. It is usually necessary to calibrate the peak shifts by imposing a known load onto the body being interrogated. In organic materials, the characteristic Raman peaks displace when a strain is imposed.¹⁹ Such displacements can be used to measure strain with high spatial resolution ($\sim 1 \mu\text{m}$). Alternately, dopants in certain inorganic crystals give rise to fluorescence peaks when subject to laser illumination (Fig. 2.5). These peaks also displace when a strain is imposed.²¹ The best known example is the Cr fluorescence peak in an Al_2O_3 host lattice.²⁰ This fluorescence spectroscopy approach can measure strains with a spatial resolution $< 20 \mu\text{m}$.

Beam absorption represents both an opportunity and a problem. When absorption occurs, particularly with X-rays, the measured lattice strain is a weighted average over the beam penetration depth,¹⁸ which is not precisely known. However, the penetration does depend on the beam orientation and its wavelength. The associated variations in penetration may, in principle, be used to assess gradients in stress normal to the surface.

2.3.3 Localized Methods

Localized stress redistribution in thin films, multilayers and fibers can be experimentally assessed from three basic measurements. (i) *Lattice strains* can be measured by either fluorescence spectroscopy¹² or microfocus X-ray methods. (ii) *Surface displacements* can be determined by moiré interferometry or strain mapping methods.²²⁻²⁵ (iii) *Stresses* can be evaluated by using the thermoelastic effect.²⁶⁻²⁵ Some results are presented in Section 4.

3. INTERFACES

3.1 Concepts

Interfaces between dissimilar materials are susceptible to debonding and sliding. These responses need to be understood through rational models, before thin film and multilayer behavior can be predicted. There are two basically different interface responses: 'strong' and 'weak'.²⁸ In principle, these can be differentiated upon subjecting the interface plane to a uniform normal tensile stress. Should one of the constituent materials fail prior to interface rupture, the interface would be designated 'strong.' Conversely, should failure occur by interface separation, the interface would be considered 'weak.' However, it is not trivial to conduct such an experiment, devoid of spurious edge effects. Indirect measures are typically used to differentiate 'strong' and 'weak' interfaces.

When interfaces are 'strong,' they may be susceptible to *slip* occurring in the metal within a boundary layer around the interface. Such slip is an important source of stress redistribution.

'Weak' interfaces are represented by a model that allows for simultaneous fracture and deformation (Fig. 3.1). Sometimes friction is also involved.^{28,29} Fracture along the

interface is characterized by a critical value of the energy release rate for the interface crack. For this purpose a mixed mode characterization of the crack tip loading is required and two special elastic mismatch parameters, called the Dundurs parameters, have a central role. For cases under consideration (each layer is isotropic), the Dundurs mismatch parameters are⁷

$$D_\alpha = \frac{\bar{E}_1 - \bar{E}_2}{\bar{E}_1 + \bar{E}_2} \quad \text{and} \quad D_\beta = \frac{1}{2} \frac{\mu_1(1-2\nu_2) - \mu_2(1-2\nu_1)}{\mu_1(1-\nu_2) + \mu_2(1-\nu_1)} \quad (3.1)$$

where $\bar{E} = E/(1-\nu^2)$ and $\mu = E/(2(1+\nu))$. With K_I and K_{II} denoting the mode I and mode II stress intensity factors for the interface crack, the energy release rate \mathcal{G} is given by⁷

$$\mathcal{G} = \frac{1}{2}(1-D_\beta^2) \left(\frac{1}{\bar{E}_1} + \frac{1}{\bar{E}_2} \right) (K_I^2 + K_{II}^2) \quad (3.2)$$

The phase angle ψ is used throughout this review as the measure of the relative amount of mode II to mode I loading at the interface. When $D_\beta = 0$, it is defined by⁷

$$\psi = \tan^{-1}(K_{II}/K_I) \quad (3.3)$$

When $D_\beta \neq 0$, the definition of ψ is slightly more complicated, involving a length scale.⁷ The definition (Eqn. 3.3) suffices for the purposes of this review, since in most instances the effects of small nonzero values of D_β are small.

The condition for a crack to advance along the interface is $\mathcal{G} = \Gamma_i(\psi)$, where Γ_i is the interfacial fracture energy measured in units of energy per unit area. The associated decohesion energy Γ_0 represents one of the three possible contributions to Γ_i . A second

contribution derives from plastic deformation, which often accompanies crack extension. A third involves friction along contacting crack faces.

The plasticity contribution is expressed through a multiplicative dissipation function \mathcal{P} .^{30,31} The most important variables are,

$$\Gamma_i = \Gamma_o \mathcal{P}(\hat{\sigma}/\sigma_o, N, h/R_o) \quad (3.4)$$

Here, σ_o is the uniaxial yield strength of the metal which deforms plastically, N is its strain hardening exponent, $\hat{\sigma}$ is the peak stress needed to cause interface separation (Fig. 3.1), h is the metal layer thickness and R_o is a dimension that governs the plastic zone size, given by

$$R_o = E\Gamma_o/3\pi(1-\nu^2)\sigma_o^2 \quad (3.5)$$

The function \mathcal{P} is discussed in Section 3.3, below.

In some cases, there is a third contribution, which occurs when the fracture surfaces come into contact behind the debond front. Such behavior is most likely when the applied loading has a substantial mode II component. Its magnitude is governed by roughness and the friction coefficient for the debonded interface.^{29,32}

3.2 Measurement Methods

One of the present limitations is the paucity of good measurements of the interface debond energy. Such measurements are difficult to obtain under conditions that provide controlled, stable growth of a debond crack. The major experimental problems are as follows: (i) Introducing a well-defined, debond crack at the interface.

(ii) Allowing for the contribution to the energy release rate from the residual stress.

(iii) The design of methods that provide measurements over a range of mode mixity

relevant to practical problems. (iv) The avoidance of uncharacteristic dynamic effects that arise upon unstable crack growth.

Most of the test methods that provide satisfactory data on technologically relevant interfaces involve sandwich configurations. These must be produced by diffusion bonding at relatively high homologous temperatures and are thus restricted to certain types of interface. Moreover, there are physical size limitations on configurations that can be realistically used. In consequence, the test specimens depicted in Fig. 3.2 have been found to be most useful, because interface cracks can be extended in a stable manner, with optical monitoring of the debond.^{11,28,33} Phase angles between $\psi = 0$ and $\sim 90^\circ$ can be accessed with these specimens.

Measurements are even more difficult for thin film interfaces produced at relatively low homologous temperatures (by sputtering, evaporation, etc.). In this case, loading the film in a controlled manner in order to evaluate \mathcal{G} at the relevant phase angle is problematic. Peel tests are widely used, but there are two fundamental limitations with this test.³⁴ (a) It is difficult to deconvolute the force measurements to determine Γ_i . (b) The phase angle is not representative of that for typical decohesion problems.⁷ Procedures in which residual stresses provide the energy release rate appear to be more satisfactory. One such method is depicted in Fig. 3.3. It uses a superposed Cr layer deposited by sputtering.³⁵ Such layers have a large 'intrinsic' residual tensile stress. When the layer has sufficient thickness, spontaneous decohesion occurs at the metal/ceramic interface. The critical Cr layer thickness needed for this purpose gives Γ_i . Moreover, this Γ_i is measured at phase angles, ψ between 0° and 50° , typical of those involved in many decohesion phenomena.⁷

3.3 Interface Separation Criteria

There are several basic mechanisms of interface separation that govern Γ_0 and $\hat{\sigma}$ (Fig. 3.4). In some cases, separation occurs by plastic hole coalescence in a metal

boundary layer in accordance with a *ductile fracture mechanism*²⁸ (Fig. 3.5). The stress within the separation zone is a multiple (typically about 3) of the uniaxial yield strength of the metal, σ_0 . The separation displacement scales with the spacing ℓ , between the hole nuclei on the interface,³⁶ such that the decohesion energy is,

$$\Gamma_o \approx \sigma_o \ell / 2 \quad (3.6)$$

The holes usually form at a spacing related to the interface microstructure, especially the grain size.³⁷ Consequently, Γ_o is microstructurally sensitive and its magnitude encompasses a wide range. The lower limit, $\Gamma_o \approx 40 \text{ Jm}^{-2}$, is exemplified by pure Al bonded to a fine grained oxide. The largest values measured without prematurely failing one of the constituents are in the range, $\Gamma_o \approx 10^3 \text{ Jm}^{-2}$.

When *brittle interphases* or reaction products exist, decohesion often occurs *within* this phase, and the separation energy Γ_o is related to that of the interphase itself, Γ_p .^{28,38} A practical example is the amorphous silicate phase that often exists at oxide/metal bonds (Fig. 3.6).^{28,39} In such cases, $\Gamma_o \approx \Gamma_p \approx 5\text{--}10 \text{ Jm}^{-2}$. There is also some dependence on the mode mixity, related to changes in crack morphology.⁴⁰ In mode I, the crack is relatively planar whereas, in mode II, *en echelon* microcracking (Fig. 3.7) is the preferred failure mechanism.³⁸

Brittle debonding can also occur by rupture of the bonds at the interface plane (Fig. 3.1).^{41,42} The equilibrium separation energy is then given by the work-of-adhesion, W_{ad} . The rupture stress $\hat{\sigma}$ is the peak value associated with the atomic separation law⁴⁴ (Fig. 3.1). This mechanism usually operates when the bond plane contains either contaminants or segregants. It is most prevalent for bonds produced at low homologous temperatures, wherein contaminants control W_{ad} and $\hat{\sigma}$.¹¹ Bonds produced at higher homologous temperatures by diffusion bonding are less susceptible to contaminants, because carbon, hydrogen and oxygen typically dissolve in the metal and diffuse away

from the interface. However, the segregation of impurity species to the interface may still affect W_{ad} and $\hat{\sigma}$.⁴²

3.4 Plastic Dissipation

The plastic dissipation is leveraged by the stress $\hat{\sigma}$ acting within the separation zone and by the separation energy Γ_o (Eqn. 3.4). It may also be affected by the layer thickness. Computations of the debond resistance have been made by assuming that each element of metal deforms in accordance with the laws of continuum plasticity.^{30,31} The results for thick layers are summarized in Fig. 3.8 for three values of the strain hardening exponent N . The effects of layer thickness are shown on Fig. 3.9. There are three important implications:

- (i) Plastic dissipation is negligible when $\hat{\sigma} < 3 \sigma_o$. All of the energy is dissipated by bond separation and $\Gamma_i \approx \Gamma_o$.
- (ii) When $\hat{\sigma}$ exceeds 3 to 5 σ_o (depending on N), the plastic dissipation becomes so large in thick layers that the debond cannot propagate by interface separation. In this case, other fracture mechanisms intervene. However, when the layers become thin, $h/R_o \lesssim 5$, the constraint on the plastic flow allows much larger stresses to develop. In consequence, crack growth at the interface can occur, even when $\hat{\sigma}/\sigma_o > 5$. In this range, quite large values of Γ_i/Γ_o can be achieved. Moreover, the scaling with layer thickness is given by

$$\Gamma_i/\Gamma_o = (h/R_o)f(\hat{\sigma}/\sigma_o, N) + 1 \quad (3.7)$$

where f is a function that can be estimated from Fig. 3.9.

(iii) There is a major influence of the mode mixity on the plastic dissipation, even when the separation energy itself is independent of phase angle, ψ .³¹ In many cases, this effect accounts for the practical difficulty found in propagating mode II debonds along interfaces.

3.5 Friction

When the interface crack is non-planar and subject to a relatively large phase angle, contacts may exist along the crack surface.^{29,32} Friction operates at these contacts, giving rise to frictional shear tractions. These tractions reduce the energy release rate at the crack tip and lead to dissipation as the debond propagates. Consequently, the debond resistance increases and is strongly influenced by the phase angle (Fig. 3.10). This frictional effect is particularly important for mode II loadings. The best known application is fiber pull-out in composites. Here, a constant friction stress τ_0 acting along the interface behind a separation zone with a designated debond energy has been used as an acceptable representation (Fig. 3.11).³² Such interfaces are characterized by a combination of a mode II debond energy, Γ_i , and a frictional sliding resistance, τ_0 .

3.6 Cyclic Effects

Cracks on interfaces can propagate upon cyclic loading, even on those interfaces designated to be 'strong.' A good example is the $\text{Al}_2\text{O}_3/\text{Al}$ interface, which only ruptures by a ductile mechanism when loaded monotonically, but can debond by fatigue upon cyclic loading.^{11,12} Crack growth occurs by the same basic mechanism that operates in the monolithic metal. It is accompanied by crystallographic striations on the metal side of the cyclic debond crack (Fig. 3.12). In most instances, the crack growth rates, da/dN , are somewhat larger than those found in the alloy itself, as revealed by the crack growth measurements made for $\text{Al}_2\text{O}_3/\text{Al}$ in Fig. (3.13). The larger crack

growth rates probably arise because of the larger amplitude shear stress reversals that occur near the crack tip, when located at the interface.⁴⁸

There are no data for mode II fatigue crack growth along the interface, but there are indications that da/dN is appreciably *less* than that in mode I, as also found in the alloy itself. Such trends in mixity are similar to those found upon monotonic loading, with regard to the fracture energy, Γ_i , as described above.

3.7 Layer Thickness Effects

When plastic dissipation in one of the constituents contributes to the interface fracture energy, there is an influence of layer thickness on Γ_i , given by Eqn. (3.6). This situation arises for either thin films or multilayer, when their thickness, h , is smaller than the plastic zone width, R_0 . In this case, the plastic zone is limited by the layer width and the plastic dissipation diminishes as h reduces.^{31,41,49} The trend in Γ_i with h depends on the mode mixity, as well as differing for thin films and embedded thin layers, because of the different constraints on plastic flow. Predictions have been obtained for a sandwich system loaded in mode I (Fig. 3.9) by using continuum plasticity to represent the deformation in the ductile layer.⁴⁹ When the layer is sufficiently thin compared to R_0 , most of the plastic dissipation is eliminated and Γ_i approaches Γ_0 . Once the layer thickness exceeds the size of the plastic zone (which is larger than R_0 for $\hat{\sigma}/\sigma_0 > 3$), no further increase in Γ_i occurs.

3.8 Fracture Energy Measurements

The most complete sets of data are those for an epoxy/glass interface (Fig. 3.14) obtained using a specially designed specimen and loading device.⁴³ These data demonstrate the strong influence of mode mixity on Γ_i . In this case, plastic dissipation in the epoxy dictates $\Gamma_i(\psi)$.⁴³ Unfortunately, this loading device could not be used for metal/ceramic bi-material systems, which have significantly larger elastic moduli.

Consequently, the results for metal/ceramic interfaces do not encompass a complete range of variables. Most of these data are for Al_2O_3 bonded to various metals at relatively high homologous temperatures. For 'strong' interfaces, a ductile fracture mechanism operates, particularly when Al and Cu are used. In tests performed on these interfaces, plastic hole growth and coalescence in the metal near the interface leaves ridges of metal on the oxide fracture surface^{28,37} (Fig. 3.5). These findings are qualitatively consistent with the prediction (Fig. 3.8) that brittle interface crack cannot occur when $\hat{\sigma}/\sigma_o$ is large. Instead, holes are generated at the interface, leading to a debond energy given by Eqn. (3.6). These interfaces have a sufficiently large Γ_i that fracture often proceeds preferentially in the oxide.⁴⁰

For 'weak' systems, the interface between the metal and the oxide can physically separate, with metal exclusively on one debond surface and oxide on the other.^{41,42} For these interfaces, the values of Γ_i measured range between $\sim 4 \text{ Jm}^{-2}$ for $\text{Al}_2\text{O}_3/\text{Mo}$ ⁴⁴ to $> 10^3 \text{ Jm}^{-2}$ for $\text{Al}_2\text{O}_3/\text{Nb}$.⁴⁵ There is evidence indicating effects on Γ_i of stress corrosion, segregation, strain-rate, phase angle and metal layer thickness. Resistance curve behavior also exists,⁴¹ involving plastic dissipation. A rigorous explanation for the occurrence of decohesion by bond rupture at these interfaces, rather than hole growth, has yet to be provided. The segregation of impurities near the interface, which influences local plasticity and the bond separation stress, $\hat{\sigma}$, is probably important.

Two sets of data are briefly examined: one for $\text{Al}_2\text{O}_3/\text{Ag}/\text{Nb}$ ⁴² and the other for $\text{Al}_2\text{O}_3/\text{C}/\text{Au}$.⁴¹ The study of Ag segregation to the $\text{Al}_2\text{O}_3/\text{Nb}$ interface (Fig. 3.15) has shown that the fracture energy can be substantially affected by segregants. There are also effects of the Nb orientation, which affects the plasticity. Such behavior is qualitatively consistent with Eqn. (3.4).

In the $\text{Al}_2\text{O}_3/\text{Au}$ system, effects of metal layer thickness on Γ_i have been found,⁴¹ as anticipated by Eqn. (3.4). However, the estimate of $\hat{\sigma}/\sigma_o$ obtained from Fig. 3.9 is relatively small, $\hat{\sigma}/\sigma_o \approx 4.5$, inferring an unrealistically low bond strength,

$\hat{\sigma} \approx 600 \text{ MPa}$.⁴⁶ In this system, C segregates to the interface, and reduces the bond strength, but probably not to such low levels. Moreover, plasticity occurring at the submicron scale in the vicinity of the debond tip probably causes the local stresses to substantially exceed those predicted by the continuum model.²⁸ The significance of this effect can be appreciated from calculations that simulate interface crack growth by interposing a thin elastic layer between the debond and the plastic zone⁴⁷ (Fig. 3.16). The implication is that Γ_i/Γ_o can be of order 10^2 or larger, with considerable plastic dissipation, while still allowing crack growth by bond rupture at the interface.

4. CRACKING AND DECOHESION

4.1 Mechanics Concepts: Steady-State Cracking

The basic mechanics needed to predict the onset of either interface debonds or cracks in the ceramic have been established.⁷ The limitation has been poor quality data, particularly on the interface properties and the plastic flow resistance of thin layers. A fundamental discovery from the mechanics is that many of the cracking and decohesion problems in stressed multilayer structures are subject to a steady-state energy release rate, G_{ss} . When this energy release rate is equated to the relevant fracture energy, a *lower bound* condition for cracking is found. This condition is associated with a *critical layer thickness*, h_c having non-dimensional form^{7,50}

$$h_c (\sigma^T)^2 / E \Gamma = \lambda \quad (4.1)$$

where λ is a configuration dependent, non-dimensional *cracking number* (of order unity) and Γ is the relevant fracture energy (ceramic or interface). The significance of this result is appreciated upon noting that, when $h < h_c$, there is insufficient strain energy to propagate a crack or debond to any appreciable distance. It thus represents a *fail-safe*

condition. It has particular significance for systems that require high reliability. The incidence of cracking and decohesion when $h > h_c$ is probabilistic in nature and dependent on manufacturing defects. Some fundamental solutions for the cracking number are illustrated in Fig. 4.1. For surface cracking and channeling (also called craze cracking), the relevant toughness Γ in (4.1) is the film toughness, provided that there is no debonding at the interface. For debonding, it is the interface toughness Γ_i (at $\psi \approx 50^\circ$). For spalling, Γ is the mode I substrate toughness. The substrate damage mode involves both the film and the substrate toughnesses.

These solutions rely on two fundamental mechanics problems: (i) *Decoctions* or cracks that originate from edges and propagate either along or parallel to the *interfaces*, and (ii) Cracks *normal* to the plane of the film or layer which originate from interior or edge flaws and propagate across the film or layer. Selected results on these two problems applicable to steady-state behavior are presented.

4.1.1 *Decohesion and Spalling*

Decoctions along the interface, and spalling cracks propagating parallel to the interface, derive their energy release rate from the changes in stresses ahead and behind the crack tip (Fig. 4.2). Steady-state conditions are attained once the crack has extended a distance from the left edge in Fig. 4.2 equal to several times the smaller of either h or H . In steady-state, the energy-release can be obtained by a relatively elementary analysis accounting for the difference in elastic energy stored well ahead and well behind the crack tip. By equating G_{ss} to Γ at the appropriate ψ , solutions to most of the important decohesion and substrate cracking problems have been derived. The phase angle ψ characterizing the mode mix requires a more complicated analysis, but complete numerical results are now available.⁷

The steady-state solution for the geometry and loadings shown in Fig. 4.2 permits the solution to a wide variety of cases. In a given application, the magnitudes and signs

of the load and moment quantities (each defined per unit thickness perpendicular to the plane of the figure), P_i and M_i , are calculated from stress distributions in the layers in a manner illustrated for a number of examples in Ref. 7. The energy-release rate is given by[†]:

$$2\bar{E}_2\bar{G}_{ss} = \frac{P_1^2}{hA_1} + \frac{M_1^2}{h^3I_1} + \frac{P_2^2}{h(\xi - \xi_1)} + \frac{12M_2^2}{h^3(\xi - \xi_1)^3} - \frac{P_3^2}{hA} - \frac{M_3^2}{h^3I} \quad (4.2)$$

where the loads and moments (per unit thickness) are defined on Fig. 4.2, $\xi = H/h$, $\xi_1 = H_1/h$ and now $\Sigma = \bar{E}_1/\bar{E}_2 = (1 + D_\alpha)/(1 - D_\alpha)$ with $\bar{E} \equiv E/(1 - \nu^2)$

$$A = \xi + \Sigma$$

$$I = \Sigma \left[(\Delta - \xi)^2 - (\Delta - \xi) + 1/3 \right] + \Delta \xi (\Delta - \xi) + \xi^3/3$$

$$\Delta = \frac{\xi^2 + 2\Sigma\xi + \Sigma}{2(\xi + \Sigma)}$$

A_1 , I_1 and Δ_1 have the same definitions, but with ξ replaced by ξ_1 and Δ replaced by Δ_1 . The expression for the energy-release rate holds whether the crack is on or off the interface.

If the crack is off the interface, as depicted in Fig. 4.2, the mode mixity is given by

$$\tan \psi = \frac{\sin \omega - (M/hP) \sqrt{U/V} \cos(\omega + \gamma)}{\cos \omega + (M/hP) \sqrt{U/V} \sin(\omega + \gamma)} \quad (4.3)$$

[†] The notation of Ref. 7 is retained in Eqns. (4.2) and (4.3). Note that the definition of ξ in these equations differs from its use earlier in the paper. The expressions for Δ and Δ_1 given here correct misprints in those in Ref. 7.

where

$$P = P_1 - C_1 P_3 - C_2 M_3/h$$

$$M = M_1 - C_3 M_3$$

with

$$C_1 = A_1/A, C_3 = I_1/I$$

$$C_2 = (A_1/I)[(\xi - \Delta) - (\xi_1 - \Delta_1)]$$

The geometric factors are

$$1/U = 1/A_1 + 1/(\xi - \xi_1) + 12 \frac{[\Delta_1 + (\xi - \xi_1)/2]^2}{(\xi - \xi_1)^3}$$

$$1/V = 1/I_1 + 12/(\xi - \xi_1)^3$$

$$\sin \gamma / \sqrt{UV} = 12 \frac{[\Delta_1 + (\xi - \xi_1)/2]}{(\xi - \xi_1)^3}$$

The only quantity not specified by these formulae is ω . It is an angle, tabulated in Ref. 51, having a weak dependence on ξ, ξ_1 and the moduli mismatch parameters D_α and D_β . For no modulus mismatch and for deep substrates, $\omega \approx 52^\circ$. The above expression for ψ holds without modification when the crack lies on the interface provided that there is no elastic mismatch. With mismatch, whenever D_β can be neglected, the only modification is that the quantity ω has a small jump from its value for a crack just below the interface (depending on D_α). Values of ω for the interface crack

are given in Ref. 7. When D_β is not insignificant, there is a slightly more complicated interpretation of ψ .⁷

4.1.2 Layer Cracking

Cracks that form *within* thin *brittle* layers, extend normal to the principal tensile stress and interact with the interfaces. The interaction leads to *tunnelling* or *channeling* modes of crack extension (Fig. 4.3). These modes also have a steady-state energy release rate which can be obtained from the solution to the 2-dimensional plane strain problem for the cracked layer well behind the propagating crack front (Fig. 4.3). Let \mathcal{G}_{ss} be the energy-release rate averaged over the tunneling crack front. An energy balance accounting for the release of energy per unit advance of the crack front under steady-state conditions gives $2h\mathcal{G}_{ss}$. It is the work done by the tractions acting across the plane of the layer crack, in the plane strain problem, as those tractions are reduced to zero. With σ denoting the stress in the layer prior to cracking and $\bar{\delta}$ as the average crack opening displacement ($2h\bar{\delta} = \int_0^{2h} \delta dx$), the steady-state energy-release rate of the tunneling crack is

$$\mathcal{G}_{ss} = \int_0^\sigma \bar{\delta}(\tilde{\sigma}) d\tilde{\sigma} \quad (4.4)$$

The fundamental result for a crack tunneling through a layer of thickness $2h$ is

$$\mathcal{G}_{ss} = \frac{\pi(1-\nu^2)\sigma^2 h}{2E} f(D_\alpha, D_\beta) \quad (4.5)$$

where E and ν pertain to the layer. If there is no elastic mismatch between the layer and the adjoining layers the function, $f = 1$. Otherwise, it depends somewhat on the elastic

mismatch parameters.⁵¹⁻⁵³ This result also assumes that no debonding, sliding or plastic yielding occurs where the crack intersects the neighboring layers. Either sliding or yielding along the interface, as depicted in Fig. 4.3, increase the average opening displacement of the crack and thereby increase the steady-state energy release rate.¹⁴ Equation (4.5) also applies to channeling, or crazing, cracks in a thin film of thickness h . Then, $f = 1.258$ in the absence of both elastic mismatch and interface relaxation.^{52,53}

4.1.3 Crack Path

A decision to be made concerns the preference for either interface debonding or ceramic cracking. To facilitate this decision, steady-state cracks are first assumed to exist either in the ceramic or at the interface. The crack within the ceramic is located on a plane having a zero mode II stress intensity factor ($K_{II} = 0$), because this is the preferred crack trajectory in brittle polycrystalline materials. The energy release rates are then sequentially calculated and compared with the corresponding fracture energies. The mode I value is used for the ceramic, Γ_c . For the interface, the debond energy Γ_i must be specified at the appropriate phase angle, ψ , which must be calculated. Alternately, the choice of trajectory is determined by whether a pre-existing interface crack prefers to continue along the interface or *kink* into the ceramic.^{7,54} For this purpose, the relative energy release rates for continued extension of the debond and for a kink into the ceramic provide the basic mechanics. As expected, there is a strong influence of the loading-phase ψ . The decision about the preferred crack path is made by equating the energy release rates to the respective fracture energies, resulting in a kinking diagram (Fig. 4.4).

When the crack does not extend along the interface, but instead, propagates into the ceramic, the crack path is determined exclusively by the criterion, $K_{II} = 0$.⁷ When the brittle layers are in *compression*, such paths exist *parallel* to the interfaces, at a characteristic distance from the interface.⁷ An important feature of the mechanics is the

appreciable configuration dependence. Namely, results for thin layers on semi-infinite substrates become inapplicable at a surprisingly large value of the substrate thickness (Fig. 4.5). This aspect of the solutions arises because bending of the material both above and below the decohesion plane has a considerable influence on both the energy release rate and the mode mixity. This bending reduces G_{ss} , because it limits the strain energy available for crack growth. It also, usually, reduces ψ , by inducing a larger opening at the crack faces. Consequently, while the solutions for semi-infinite substrates provide the necessary insight about decohesion and delamination (as well as the correct order), rigorous fail-safe predictions for actual configurations require additional analysis.

4.2 Mechanics Concepts: Stress Redistribution

When cracks tunnel through one of the brittle layers, simultaneous slip or debonding at the interface can increase the steady-state energy release rate, as discussed above, and thereby lower the resistance of that layer to cracking. However, these same effects reduce the stress concentration in adjacent layers, suppressing the spread of cracks out of a given layer. These other mechanisms of stress redistribution must be considered in the design of effective multilayers.

Before examining the stress solutions, it is useful to relate the extent of either slip or debonding to the constituent properties. There are two ranges governed by the ratio of the slip length, L , to the half-crack size, h . When L/h is small (e.g., ≤ 0.5), a small-scale yielding (SSY) result applies:¹⁴

$$L/h = 0.052\pi[\sigma^T/\tau_o]^2 \quad (4.6)$$

where σ^T is considered to be uniform and τ_o is the shear resistance of the slipping material. When L/h is large (≥ 1), numerical analysis gives¹⁴ (Fig. 4.6),

$$L/h \approx [\sigma^T/\tau_o] - 1 \quad (4.7)$$

This result differs slightly from the analytical solution (Eqn. 2.4).

Two basic stress solutions provide the key insights. (i) The asymptotic near tip solution for a semi-infinite crack impinging on an interface (Fig. 4.7). (ii) The full-field solution for a cracked layer designated the H-crack problem (Fig. 4.8).

The *asymptotic problem*¹⁴ (i) is applicable when the extent of debonding or slipping is small compared to the length of the crack itself. Let K denote the stress intensity factor of the crack in the absence of either debonding or slipping. It plays the role of the load. Solutions for the stress ahead of the crack are plotted in Fig. 4.7 for two cases: (1) with debonding extending a distance d along the interface on either side of the main crack and (2) with slip along the interface governed by a critical shear stress τ_o acting on the interface. In case (1), the interface crack is open and thus frictional effects are not expected to come into play. Case (2) models slip due plastic yielding of a vanishingly thin ductile adhesive layer along the interface. The interface remains closed and the distance over which slipping occurs is given by Eqn. (4.6). The normal stress acting on the plane ahead of the main crack tip plotted in Fig. 4.7. It is normalized by the elastic solution in the absence of either debonding or slip (i.e., by $K/\sqrt{2\pi x}$). The abscissa in this figure is the distance from the interface x normalized by the debonding or slipping distance L . Thus, values of the ordinate less than unity represent stress levels which have been reduced by sliding or slip. Note that debonding is more effective than yielding in redistributing the stress ahead of the crack.

Full-field solutions (ii) for the embedded crack extending across a layer (Fig. 4.8) are valid when the sliding or slip zones extend above the crack by distances comparable or greater than the thickness of the layer itself. These results exhibit some of the same basic features seen above and provide additional detail suitable for comparison with experimental measurements. One feature which does change involves the debonding

interface. For this case, the interface crack is *closed* when the debond zone length L exceeds roughly $(1/4)h$. The solutions are thus similar to those for *slip*, with τ_0 becoming the friction stress, τ_s . The consequence is that debonding is not necessarily such an effective means of stress redistribution.

A different situation arises when a *surface crack* exists in the outermost layer, an example of which is shown in Fig. 4.9. The debonds generated from the crack are mixed mode ($\psi \approx 50^\circ$), such that the cracked interface is open and the crack tip attains a steady-state energy release rate (G independent of interface crack length under constant bending moment) for L greater than several times h_1 . The debond can thus extend without limit, whenever the energy release rate reaches the mixed-mode interface toughness, Γ_i . Such debonding evidently eliminates stress concentrations at the point where the layer crack first meets the interface.¹² However, should the debond arrest because the loading is not pure bending, there are stress concentrations near the debond tip, associated with the magnitude of Γ_i .

4.3 Experimental Measurements

Experimental measurements on multilayers have been made using the $\text{Al}_2\text{O}_3/\text{Al}$ and $\text{Al}_2\text{O}_3/\text{Cu}$ systems, subject to imposed plus residual stresses.^{12,25} These systems, which have 'strong' interfaces upon monotonic loading, may be used to assess the effects of slip on stress redistribution. For this purpose, surface cracks have been introduced into the outermost Al_2O_3 layer and the system loaded in four-point flexure. The moiré interferometry and fluorescence spectroscopy methods have been used to probe the displacements and lattice strains, respectively. The extent of slip is best visualized by moiré interferometry after loading and unloading (Fig. 4.10). The residual displacements caused by slip in the metal boundary layer are then readily discerned. The extent of slip is completely consistent with analysis (Fig. 4.11).

While under load, moiré interferometry can also be used to obtain displacement measurements at high spatial resolution²⁵(~ 1 μm). A typical result is shown in Fig. 4.12. Strains in the Al_2O_3 layers are obtained directly from the displacement vectors. A comparison of measured strains with those calculated for 'H-cracks' subject to uniform tensile loading, at the corresponding L/a (Fig. 4.8) indicate good correspondence. Moreover, it is noted that the strains are quite closely represented by the solution for an elastically homogeneous, isotropic body, even though there has been considerable slip in the Al.²⁵ Fluorescence spectroscopy measurements confirm this behavior¹² (Fig. 4.13). The important conclusion, as noted earlier, is that the slip lengths have to be considerable before there is an appreciable reduction in the stress concentration around a crack.

When the same interfaces are debonded by cyclic loading (to a distance, $L/a \approx 2$), Fig. 4.14, the stress concentration, measured by fluorescence spectroscopy, is eliminated¹² (Fig. 4.13). As already noted, debonding from a surface crack is mixed mode, such that relief of the normal stresses occurs, causing a substantial reduction in the stress concentration. The measured stresses are consistent with those calculated for a multilayer in bending with a debonded interface¹² (Fig. 4.9).

4.4 Fail-Safe Design Concepts

In multilayer systems with at least one brittle layer, there are three competing modes of thermomechanical damage: (i) tunnel cracking or crazing, (ii) spalling or delamination, (iii) interface decohesion. A fail-safe concept ensures that *none* of these three damage modes may operate. The concept can be illustrated for a *bilayer*, following a scheme first proposed by Spearing *et al.*¹⁷ One of the layers is metallic, designated m, and the other is a brittle material, designated c.

Fail-safe conditions arise upon considering the steady-state solutions for each of the three brittle damage modes (Fig. 4.15). *Delamination* and interface decohesion reflect the

steady-state behavior represented by Eqn. (4.1), but involving different values of Γ and λ . The results can be plotted in space represented by the cracking numbers and Γ_i / Γ_c , with Γ_c being the fracture energy for the brittle material. The delamination behavior involves a determination of the location of the crack in the brittle layer, using Fig. 4.5, which, in turn, influences the magnitude of λ . When the brittle substrate is not thin compared to the metal layer, there is no mode I path located within the brittle material. In this range, delamination is not a viable damage mode. However, interface decohesion is still possible, in mixed mode, whenever Γ_i is relatively small.

Crazing of the brittle film has a steady-state governed by channeling, again given by Eqn. (4.4) or (4.5) such that the same space can be used to represent the craze susceptibility. A conservative solution for channel crack growth is obtained by assuming that the tensile stress in the brittle layer is uniform and given by σ at the top of the film (Eqn. 2.7b). The incidence of crazing then reflects the influence of thickness ratio on σ . A less conservative solution can be generated by accounting for the stress gradient by using Eqn. (4.4).

Fail-safe behavior is represented by the lower *envelope* of the three failure modes. It is sensitive to the ratio, Γ_i / Γ_c (Fig. 4.15). However, it is only necessary that $\Gamma_i / \Gamma_c \gtrsim 1$ to ensure that interface decohesion does not limit integrity. At larger values of Γ_i , delamination and crazing of the brittle layers are the limiting damage modes. Crazing is most relevant at small relative thicknesses ($\xi \lesssim 10$), whereas delamination limits integrity at larger thicknesses.

4.5 Damage Modes

The manner in which damage may progress across a multilayer is strongly dependent on the redistribution of stress by slip or decohesion at the interface discussed in §4.2. A particularly important distinction occurs when a crack already exists in one of the brittle layers. This crack may extend in a coplanar manner into the next brittle layer,

leading to the formation of a dominant crack with essentially brittle behavior when externally loaded. Alternatively, other cracks may form elsewhere in other brittle layers, in a strictly stochastic manner. This latter *damage* behavior results in inelastic strains and structurally superior performance. This distinction is analogous to a well-known phenomenon found in fiber composites, referred to as either global load sharing (GLS) (distributed fiber damage) or local load sharing (LLS) (dominant crack).^{55,56} The transition between GLS and LLS is clearly related to the stresses in layers adjacent to the layer containing the crack. However, a criterion for further cracking is also needed. This criterion has been based on probabilistic aspects of the tensile strengths of the brittle layers, subject to the stress distribution that occurs in the layers around the crack. However, there are no definitive probabilistic solutions, because of the complexity of re-evaluating the stress distribution as each crack forms within a stochastic simulation.

When conditions exist that result in distributed damage, GLS analysis relates the ultimate tensile strength (UTS) of a loaded multilayer to the constituent properties of the layers. The key feature is that the gauge length relevant to the stochastic analysis becomes $\sim 2L$ (Eqn. 4.7) such that the layers have a characteristic strength S_c . This behavior arises because cracks separated by distances $\gtrsim 2L$ do not have interacting stress fields. A consequent scaling relationship for the UTS, designated S_u , is⁵⁶

$$S_u \sim f S_o [\tau L_o / h S_o]^{1/(m+1)} \quad (4.8)$$

where m is the shape factor, f the volume fraction of brittle layers, S_o the scale factor in the layer strength distribution and L_o is a reference length.

Local load sharing conditions that result in the growth of a dominant crack lead to behavior governed by the stresses in the intact layer ahead of the crack. By equating the peak tensile stress to the characteristic layer strength, S_c , a renucleation stress intensity factor, K_{N_r} , can be obtained.²⁵ For example, when there are no ligaments present and

slip is the preferred interface response, the elastic solution still applies in the range, $L/a \gtrsim 5$; then,

$$K_N \approx S_c \sqrt{2\pi h} \quad (4.9)$$

where h is the layer half-thickness. At larger slip lengths, K_N increases. Moreover, as the crack extends and ligaments develop, the crack growth resistance, K_R , increases. Some typical experimental results³¹ demonstrating these behaviors are summarized in Fig. 4.16. Note that thick layers enhance both K_R and K_N . However, special thin layer effects can arise in the submicron range, which may cause reversions in behaviors as h reduces.

4.6 Some Practical Problems

When multilayers consisting of several different materials are designed to be fail-safe against decohesion and delamination, initially a simple procedure is needed to establish the most likely decohesion site and the associated steady-state energy release rate. For this purpose, it is recalled that cracking of one of the brittle constituents parallel to the interface occurs on a plane having $K_{II} \approx 0$. An analysis for locating this plane in an arbitrary multilayer represents the first important requirement. Then G_{ss} on that plane is needed for comparison with the fracture energy of the brittle material, Γ_c . Simultaneously, it is necessary to evaluate G_{ss} and the associated mode mixity at *each of the interfaces*. These must be compared with $\Gamma_i(\psi)$.

It is important to appreciate that the solutions are configuration dependent, because of the strong influence of bending on both G_{ss} and ψ . As emphasized before, analytical results for semi-infinite substrates can, therefore, be misleading. Experimental results may indicate the absence of decohesion and delamination in one configuration. Yet, another configuration made from the same materials may be prone to these

phenomena, and vice versa. The design of experiments to validate fail-safe systems requires careful analysis to ensure that the appropriate values of G_{ss} and ψ actually obtain at the most failure-prone layers and interfaces. An example is given in Fig. 4.17 for a metal/ceramic system, in which the interface is 'strong.' As a bilayer, a $K_{II} = 0$ plane exists in the ceramic parallel to the interface, as indicated on Fig. 4.5. The associated energy release can cause the ceramic to delaminate, whenever $G_{ss} > \Gamma_c$. Such behavior is found in the Cu/AlN system, when the Cu exceeds a critical thickness. However, ceramic failure is not inevitable. It can be suppressed if the bilayer is bonded or brazed to a metallic substrate having the appropriate thermal expansion coefficient. In particular, if the substrate has essentially the same thermal expansion coefficient as Cu and a high yield strength, the $K_{II} = 0$ plane is displaced into the substrate. A crack that begins in the AlN will thus deviate into the bond plane rather than propagate in the ceramic parallel to the interface. The system will thus sustain thermostructural integrity provided that the bond to the substrate is itself 'strong.'

5. THERMOMECHANICAL FATIGUE

Various cyclic effects can operate in thin films and multilayer systems, because of the dissimilar thermophysical properties of the constituents. These are thermal and mechanical in nature. They cause changes in stress and may introduce damage, which eventually leads to failure. All of these phenomena are embedded in the fundamentals of cyclic plastic deformation, occurring at various physical scales. It is convenient to separately address the phenomena that occur with and without cracks being present.

Before cracks form in the film or multilayer, thermal cycling may modify the residual stresses and can cause either damage or ratcheting. A thermal fatigue diagram¹⁰ (Fig. 5.1) indicates the ranges in which these phenomena occur, when a

transverse stress is also applied to the system. When this stress, σ_T , is *fixed* as the temperature cycles, by ΔT , the shakedown range is¹⁰

$$\sigma_T/\sigma_s + \Delta T/\Delta T_s = 1 \quad (5.1)$$

where $\sigma_s = 1.3 \sigma_o$. Within a range bounded by ΔT_s and σ_o , *shakedown* occurs. In this range, the stresses adjust to a new level, as thermal cycling proceeds, such that all subsequent behavior is *elastic*. Thereafter, the system is dimensionally stable and the stresses are predictable. Outside this range, various detrimental phenomena arise. With predominantly thermal loading, the plastic deformation that occurs with each cycle typically leads to cracking and interface debonding. When *transverse* loads are also present, ratcheting may occur, whereby plastic strain accumulates with each thermal cycle. The strain per cycle then increases as either ΔT or σ increase above the shakedown threshold values ΔT_s and σ_s .

When cracks begin to form in the brittle layers, additional fatigue effects arise. The cracks may either extend by fatigue into the metal, in mode I, or debond the interface (Fig. 5.2).^{11,12} The choice depends upon two ratios: the energy release rate range, ΔG and the crack growth rates, da/dN , at the relevant mode mixity. For a *surface crack*, debonds are mixed mode ($\psi \approx 50^\circ$), as already discussed. The *mixed-mode* interface da/dN should be compared with the *mode I* growth rate in the alloy (Fig. 3.13), at the relevant ΔG . The energy release rate for interface growth is less than that for growth into the alloy, by a factor ranging between 4 (initial) and 2π (steady state).⁷ If the interface growth rate is larger than the alloy growth rate, at this reduced ΔG (Fig. 5.3), then cyclic interface debonding is preferred, and vice versa. For Al_2O_3/Al multilayers, it is found that debonding from a surface crack occurs in preference to crack growth through the alloy¹² (Fig. 5.3), consistent with the larger da/dN at the interface.

The converse behavior obtains when a long crack is present, bridged by intact metal ligaments¹² (Fig. 5.4). Then, mode I fatigue cracking of the alloy occurs in preference to interface debonding. For this case, the energy release rate ratio is essentially the same as that for the surface crack.⁷ However, the debond growth rate along the interface is lower, because it is subject to mode II loading, with accompanying frictional resistance. The preference is thus for growth of a fatigue crack through the alloy, causing rupture of the ligaments.^{12,57} An embedded crack is expected to behave in a similar manner, but there have been no experimental measurements.

6. THIN LAYER EFFECTS

When the films or layers have submicron thickness, some special thin layer effects arise. One is related to the *threading* of dislocations through the ductile material. Another is governed by the elevation of the *tunnel cracking* resistance.

The threading of a dislocation through a thin layer occurs at a critical stress σ_c (Fig. 6.1) inversely dependent on the layer thickness, h , in accordance with the non-dimensional formula⁸

$$\sigma_c h / G_f b = \chi \quad (6.1)$$

where G is the shear modulus and b is the Burgers' vector, with χ being a threading number. For a thin film with an oxide layer on the surface, χ is given by

$$\chi = \frac{\tan \phi}{2\pi(1-\nu)\cos \theta} \left[\frac{G_s}{(G_f + G_s)} \ln \left(\frac{2.6h}{b} \right) + \frac{G_o}{(G_f + G_o)} \ln \left(\frac{17.5h_o}{b} \right) \right] \quad (6.2)$$

with G_o being the shear modulus of the oxide layer and h_o its thickness, while ϕ and θ are the angles that define the slip plane and slip direction, respectively, within the film. The threading predictions are consistent with the flow strengths measured for metal films having sufficiently small thickness that σ_c exceeds the bulk yield strength, σ_o .⁸ This thickness is typically, $h \approx 1 \mu\text{m}$. At larger thicknesses, the bulk behavior applies, subject to the equivalent microstructure. Namely, grain size effects must be included, through the Hall-Petch effect.⁸

A comparison of the dislocation threading result with the tunnel cracking formula relevant to the brittle layer (Eqn. 4.1) provides some useful insight. Upon equating the threading strength (Eqn. 7.1) to the tunnel cracking resistance (Eqn. 4.1), a critical thickness, h_* , is derived as

$$h_* = \left(\frac{E b^2}{\Gamma} \right) \frac{\chi^2}{4\lambda(1+\nu)^2} \quad (6.3)$$

At layer thickness $h > h_*$, dislocation threading occurs more readily than cracking and vice versa. This result suggests a tendency toward more brittle behavior as the layer thickness decreases.

7. DESIGN METHODOLOGY

The preferred design methodology would (i) use the minimum number of experiments needed to determine the relevant constituent properties and residual stresses and (ii) provide a software program that identified the most likely sites of delamination and cracking, as well as computing the associated energy release rates and mode mixities. Most applications are for either thin layers generated by vapor deposition or thick layers formed by post firing or co-sintering. These are often attached

to other systems, either by subsequent adhesive bonding or brazing. Frequently, electroplated layers are also present. The residual stresses and the fracture energies need to be measured, preferably, on the actual multilayers, following each of the major steps in the fabrication cycle. In some cases, the elastic properties also need to be determined, because the films contain porosity, particularly along columnar grain boundaries in vapor deposited material.

Residual stress measurements on either vapor deposited thin films or sintered thick films are most reliably achieved by simultaneously applying the same film to a *reference substrate*, within the same fabrication run. Then, either beam bending or fluorescence spectroscopy measurements can be made on the reference system. In some cases, these measurements can be made on standard substrates, such as Si and sapphire, in order to obtain the reference temperature, T_R , as well as the shakedown range ΔT_s when yielding occurs. Such measurements often provide enough information to calculate the residual stresses expected when other substrates and multilayers are used. For this purpose, it is necessary to use the reference tests to (i) evaluate the 'lock-in' temperature for films fabricated at high temperature (but otherwise are elastic), (ii) obtain the strength profile $\sigma_o(T)$ for films that yield on cooling (Fig. 2.1), (iii) determine creep relaxation rates $\sigma^T(T, \dot{T})$ for films that experience high homologous temperature subsequent to their fabrication.

Interface fracture energies can be influenced by each thermal cycle in the fabrication sequence, because of segregation and interdiffusional effects. Γ_i should be measured either on the actual multilayer or on representative thin layers subjected to thermal cycles that simulate the fabrication sequence. The preferred approach is to deposit a thick superlayer of either Cr or Cu onto the layer of interest, until the critical thickness that causes spontaneous decohesion is reached.³⁵ If the brittle material is found to delaminate, the interface is considered to be 'strong' enough and explicit

measurements of Γ_i are not necessary.[‡] Otherwise, the procedure described in Section 3 (Fig. 3.2) may be used to explicitly evaluate Γ_i (at $\psi \approx 50^\circ$). When a superlayer sufficiently thick to achieve delamination cannot be vapor deposited, a layer may be added by brazing, provided that the braze has been adequately characterized. Each interface can be assessed in this manner. In cases where Γ_i is needed at very different mode mixities, superstructures can be designed to give smaller values of ψ at the interface.

This overview has summarized existing knowledge about the thermomechanical characteristics of multilayers. Some areas have benefited from appreciable recent progress, such as the mechanics of cracking and decohesion. Other areas have only been dealt with in a superficial manner. Critical areas for future endeavors concern the details of the thermomechanical response, leading to fail-safe design codes. Also there is still much to be learned about interface debonding, particularly the interplay between segregation and the plastic flow properties of the metal in thin layers,

[‡] When substrate delamination occurs rather than interface decohesion, this method may be used to obtain the mode I fracture energy of the substrate when other data are unavailable.

APPENDIX I

Intrinsic Stresses in Vapor Deposited Films

When a vapor-deposited polycrystalline film is grown on a substrate having an incoherent interface, there is no obvious mechanism for generating stress in the surface layer *as it deposits*. Surface diffusion allows atom displacements which relax strains as they attempt to develop. This situation differs from that for coherent, single crystal films which incur coherency strains.

Intrinsic stresses usually develop as a consequence of subsequent diffusional effects that occur in previously deposited sections of the film.⁶ This involves mechanisms which eliminate those defects present in the film which have an associated 'free volume.' The one exception concerns the stresses associated with surfaces and interfaces, discussed below.

Vapor deposited films typically have a thin, equiaxed polycrystalline layer close to the interface. Above this layer, a columnar grain structure develops with a preferred crystallographic orientation. A common experience is that the equiaxed layer has a higher residual stress than the columnar material,⁶ resulting in bending when the film is removed from the substrate.

Intrinsic stresses in films are generally in the range 0.5 to 4 GPa. They can be tensile or compressive. They are also superposed on thermal expansion mismatch stresses. The mechanisms to be considered emphasize phenomena capable of giving GPa level stresses. Furthermore, the defects that give rise to the stresses, as they are eliminated by diffusion, must have sufficient density to provide the misfit strain, ϵ_T , which governs the intrinsic stress, σ_I , through the relation

$$\sigma_I = E\varepsilon^T/(1-\nu) \quad (\text{A1})$$

MECHANISMS

1. Grain Growth

The grain boundary is a source of 'free-volume' that diminishes as the grains grow, *subsequent to deposition*. As a small grain disappears (Fig. A1), stresses develop. ⁶These stresses provide a strain energy contribution to the chemical potential of the atoms on the two sides of a grain boundary. The transformation strain ε^T associated with the process (depicted in Fig. A1) is,

$$\varepsilon^T = 6 \left(\frac{1}{d} - \frac{1}{d_0} \right) \Delta a \quad (\text{A2})$$

where d is the actual grain size, d_0 is the initial value as the film deposits, Δa is the grain boundary free volume per unit area (which is of order the atomic dimension). The contribution of the strain energy to the chemical potential difference is

$$\Delta\mu_s = \frac{1}{2} E\Omega(\varepsilon^T)^2 \quad (\text{A3})$$

where Ω is the atomic volume and E is Young's modulus. This potential adds to that from the grain boundary curvature, given by

$$\Delta\mu_b = (2\gamma_b/d)\Omega \quad (\text{A4})$$

where γ_b is the grain boundary energy.

By setting the potential difference to zero, there is an equilibrium residual stress, σ_{eq}^R , which occurs at an equilibrium grain size, d_{eq} . Of course, the temperature needs to be large enough to allow grain boundary diffusion at a sufficiently rapid rate to attain this equilibrium. The equilibrium values are obtained by equating $\Delta\mu_s$ and $\Delta\mu_b$ to give

$$\sigma_{eq}^R = 3\gamma_b/2(\Delta a) \quad (A5a)$$

and

$$d_{eq} = \frac{3(1-\nu)d_o^2\gamma_b}{4E(\Delta a)^2} \quad (A5b)$$

Note that these stresses develop with time at temperature, by *grain boundary diffusion*. Moreover, the stresses *cannot* be eliminated by heat treatment. Higher stresses are more likely in fine grained material, which has a higher initial motivation for grain growth. *Only tensile stresses* arise.

For this mechanism to apply to vapor deposited films, it would be necessary for the initial grains that form during deposition to be quite small and then grow into the classical columnar configurations found when deposition is complete. The misfit strain required to achieve the equilibrium strain is of order, $\epsilon \approx 5 \times 10^{-3}$. Such strains can be achieved by removing at least one grain boundary from each $\sim 0.5 \mu m$ of film. The initial grains would need to be of order $0.2 \mu m$ or less and grow to twice their initial size as deposition proceeds.

2. Point Defect Annihilation

If point defects are trapped in the film as it grows, they have a 'free volume.' Their subsequent elimination at either grain boundaries or dislocations must cause 'intrinsic'

stress.⁶ The annihilation of vacancies or interstitials is well-simulated by analysis of dislocation climb (Fig. A2). The chemical potentials in the system are given by

$$\mu = \sigma_n \Omega + kT \ln C/C_o + \mu_o \quad (A6)$$

where C/C_o is the excess point defect concentration, μ_o is the reference potential, and σ is the stress normal to the dislocation. There is an equilibrium 'intrinsic' stress which obtains when, $\mu - \mu_o = 0$. It is given by,

$$\sigma_{eq}^R = \left(\frac{kT}{\Omega} \right) \ln(C/C_o) \quad (A7)$$

For example, if the excess defect concentration, $C/C_o \approx 2$, then $\sigma_{eq}^R \approx 2\text{GPa}$. This stress again develops with time at temperature. It requires lattice diffusion and thus occurs *slowly*. Once present, the stress cannot be eliminated. Instead, they may increase upon annealing. These stresses can be *either tensile* (vacancies) *or compressive* (interstitials). There is no obvious grain size effect on the stress. However, the stresses develop more rapidly in small grained films, because the diffusion distances are smaller.

In order to develop equilibrium level intrinsic stresses, misfit strains of $\sim 10^{-3}$ must be possible. This requires an original point defect concentration in the film, as it grows, $C \approx 10^{-3}$. This represents a high defect supersaturation, which should be detectable by experiment.

3. Sintering

Voids present on the grain boundaries upon deposition can be eliminated by subsequent sintering to create a residual tensile stress (Fig. A3). This stress has a maximum value given by the radius of curvature R of the as-deposited voids,

$$\sigma_{eq}^R = 2\gamma_s/R \quad (A8)$$

where γ_s is the surface energy. Typical values range between 20 MPa for 0.1 μm voids to 2 GPa for 1 nm voids. To achieve the required misfit stress, a void volume fraction $f \approx 10^{-3}$ would be needed on the as-deposited grain boundaries.

4. Grain Boundary Stress

Finally, it is noted that there is a stress associated with the grain boundaries. This stress is given by

$$\sigma^R \approx \gamma_b/d \quad (A9)$$

It is typically 1 GPa for 1 nm size grain, but only 1 MPa for 1 μm grains.

REFERENCES

- [1] *IBM Journal of Research and Development*, **36** (1992) 817-955.
- [2] S. Winzer, N. Shanker and A.P. Ritter, *J. Am. Ceram. Soc.*, **21** (1989) 2246.
- [3] G.W. Goward, *Proceedings of Workshop on Coatings for Advanced Heat Engines*, July 1987, NTIS, Springfield, VA.
- [4] *Journal of Hard Materials*, **2** (1991) 3-154.
- [5] A.T. English and C.M. Melliar-Smith, *Ann. Rev. Mat. Sci.*, **8** (1978) 459.
- [6] M.F. Doerner and W.D. Nix, *CRC Critical Reviews In solid States and Materials Sciences*, **14** (1988) 224.
- [7] J.W. Hutchinson and Z. Suo, *Advances in Appl. Mech.*, **29** (1992) 63.
- [8] W.D. Nix, *Met. Trans.*, **20A** (1989) 2217.
- [9] C.H. Hsueh and A.G. Evans, *J. Am. Ceram. Soc.*, **68** (1985) 120.
- [10] S. Jansson and F.A. Leckie, *J. Mech. Phys. Solids*, **40** (1992) 593.
- [11] R.M. Cannon, B.J. Dalgleish, R.K. Dauskhart, T.S. Oh and R.O. Ritchie, *Acta Metall. Mater.*, **39** (1991) 2145.
- [12] M.C. Shaw, M.Y. He, B.J. Dalgleish, D.B. Marshall and A.G. Evans, *Acta Metall. Mater.*, to be published.
- [13] S. Suresh, *Fatigue of Materials*, Cambridge University Press (1991).
- [14] K.S. Chan, M.Y. He and J.W. Hutchinson, *Mat. Sci. Eng.*, **A167** (1993) 57.
- [15] H.C. Cao and A.G. Evans, *Acta Metall. Mater.*, **39** (1991) 2997.
- [16] D.S. Campbell, *Handbook of Thin Film Technologies*, McGraw-Hill, NY (1970).
- [17] S.M. Spearing, M.A. Tenhover, D.B. Lucko, L. Viswenathan and D.K. Hollen, *MRS Publication*, in press.
- [18] M. Murakami, T.S. Kuan and I.A. Bleck, *Treatise on Material Science and Technology*, **24** (1982) 163.
- [19] R.J. Young, R.J. Day, M. Zakakhini and I.M. Robinson, *Comp. Sci. Tech*, **34** (1989) 243.
- [20] Q. Ma and D.R. Clarke, *J. Am. Ceram. Soc.*, **76** (1993) 1433.

- [21] L. Grabner, *Jnl. Appl. Phys.*, **49** (1978) 580.
- [22] D.R. Williams, D.L. Davidson and J. Lankford, *Eng. Mech.*, **20** (1980) 4.
- [23] M.S. Dadkhah, F.X. Wang and A.S. Kobayashi, *Eng. Tech.*, **7** (1988) 28.
- [24] M.R. James, W.L. Morris and B.N. Cox, *Exp. Mech.*, **30** (1990) 60.
- [25] M.C. Shaw, D.B. Marshall, M.S. Dadkhah and A.G. Evans, *Acta Metall. Mater.*, **41** (1993) 3311.
- [26] N. Harwood and W.M. Cummings, *Thermoelastic Stress Analysis*, Adam Hilger, IOP (1991).
- [27] A.K. Wong, J.G. Sparrow and S.A. Dunn, *J. Phys. Chem. Solids*, **49** (1988) 395.
- [28] A.G. Evans and B.J. Dalgleish, *Acta Metall. Mater.*, **40** (1992) 5295.
- [29] A.G. Evans and J.W. Hutchinson, *Acta Metall.*, **37** (1989) 909.
- [30] V. Tvergaard and J.W. Hutchinson, *J. Mech. Phys. Solids*, **40** (1992) 1377.
- [31] V. Tvergaard and J.W. Hutchinson, *J. Mech. Phys. Solids*, **41** (1993) 1119.
- [32] J.W. Hutchinson and H. Jensen, *Mech. of Mtls.*, **9** (1990) 139.
- [33] P.G. Charalambides, J. Lund, A.G. Evans and R.M. McMeeking, *J. Appl. Mech.*, **101** (1989) 77.
- [34] N. Aravas and K.S. Kim, *Intl. Jnl. Solids Structures*, **24** (1988) 417.
- [35] A. Bagchi, G.E. Lucas, Z. Suo and A.G. Evans, *J. Mater. Res.*, in press.
- [36] A.G. Varias, Z. Suo and C.F. Shih, *J. Mech. Phys. Solids*, **40** (1992) 485.
- [37] B.D. Flinn, C.S. Lo, F.W. Zok and A.G. Evans, *J. Am. Ceram. Soc.*, **73** (1993) 369.
- [38] A. Bartlett and A.G. Evans, *Acta Metall. Mater.*, **41**, (1993) 497.
- [39] M. De Graef, B.J. Dalgleish, M.R. Turner and A.G. Evans, *Acta Metall. Mater.*, **40** (1992) 5333.
- [40] R.M. Cannon, R.O. Ritchie and B.J. Dalgleish, *Acta Metall. Mater.*, in press.
- [41] I.E. Reimanis, B.J. Dalgleish and A.G. Evans, *Acta Metall. Mater.*, **39** (1991) 3133.
- [42] D. Korn, G. Elssner, H.F. Fischmeister and M. Rühle, *Acta Metall. Mater.*, **40** (1992) S355.
- [43] K.M. Liechti and Y.S. Chai, *J. Appl. Mech.*, **59** (1992) 295.

- [44] M.R. Turner, J.B. Davis, J.P.A. Löfvander and A.G. Evans, *Acta Metall. Mater.*, in press.
- [45] N.P. O'Dowd, C.F. Shih and M.G. Stout, *Intl. Jnl. Solids Structures*, **29** (1992) 571.
- [46] J.R. Smith, H. Schlosser and J. Ferrante, *Metal/Ceramic Interfaces*, (Ed. M. Rühle *et al*) Pergamon (1989) p. 15.
- [47] Z. Suo, C.F. Shih and A.G. Varias, *Acta Metall. Mater.*, **41** (1993) 1551.
- [48] C. Woeltjen, C.F. Shih and S. Suresh, *Acta Metall. Mater.*, **41** (1993) 2317.
- [49] V. Tvergaard and J.W. Hutchinson, *Phil. Mag.*, in press.
- [50] A.G. Evans, M.S. Hu and M.D. Drory, *J. Mater. Res.*, **3** (1988) 1043.
- [51] Z. Suo and J.W. Hutchinson, *Intl. Jnl. Solids Structures*, **25** (1989) 1337.
- [52] J.L. Beuth, *Intl. Jnl. Solids Structures*, **29** (1992) 155.
- [53] T. Ye, Z. Suo and A.G. Evans, *Intl. Jnl. Solids Structures*, **29** (1992) 2639.
- [54] M.Y. He and J.W. Hutchinson, *J. Appl. Mech.*, **56** (1989) 270.
- [55] M.Y. He, A.G. Evans and W.A. Curtin, *Acta Metall. Mater.*, **41** (1993) 871.
- [56] W.A. Curtin, *J. Am. Ceram. Soc.*, **74** (1991) 2837.
- [57] K.T. Rao, G.R. Odette and R.O. Ritchie, *Acta Metall. Mater.*, **40** (1992) 353.

FIGURE CAPTIONS

- Fig. 1.1 A multilayer electronic package.
- Fig. 2.1 Variations in the misfit stress upon temperature cycling when the film is subject to yielding: a) schematic, b) results for Al thin films (590 nm) on Si.
- Fig. 2.2 A schematic of stress redistribution effects near edges.
- Fig. 2.3 Trend in residual stress with relative layer thickness, h_1/h_2 , for bilayers having several modulus ratios, Σ .
- Fig. 2.4 Beam deflection caused by a thin film subject to residual compression.
- Fig. 2.5 A typical fluorescence spectroscopy measurement of the residual stress from the shift in the R_2 fluorescence peak for Cr dopants.
- Fig. 3.1 A schematic of interface fracture by bond rupture, accompanied by plastic dissipation.
- Fig. 3.2 Examples of sandwich test configurations used to evaluate the interface toughness over a range of phase angles: b, c and d give stable crack growth.
- Fig. 3.3 A test method for measuring the debond energy for thin ductile films on a substrate.
- Fig. 3.4 A schematic showing mechanisms of interface failure.
- Fig. 3.5 Ductile fracture of an interface showing ridges of metal attached to the ceramic side of the debond.
- Fig. 3.6 An amorphous silicate on the Al_2O_3 side of a debond surface between Pt and Al_2O_3 . The silicate layer is outlined by the light ridge across the grain facets.
- Fig. 3.7 Failure of a thin brittle layer in shear by *en echelon* microcracking: a) schematic, b) experimental observation for Ti/ Al_2O_3 .
- Fig. 3.8 Effects of plastic dissipation on the interface fracture energy.
- Fig. 3.9 Effects of metal layer thickness on the interface fracture energy.

- Fig. 3.10 Effect of mode mixity on the frictional contribution $\Delta\Gamma_o$ to the nominal interface fracture energy. H is the roughness amplitude.
- Fig. 3.11 A cell model for a fiber in a brittle matrix with a matrix crack, showing a mode II debond with frictional sliding along the debonded surfaces.
- Fig. 3.12 Fatigue striations caused by an interface crack in $\text{Al}_2\text{O}_3/\text{Al}$, (a) within a single grain, (b) across a grain boundary.
- Fig. 3.13 A comparison of fatigue crack growth rates for the $\text{Al}_2\text{O}_3/\text{Al}$ interface in mixed mode ($\psi = 50^\circ$) with the mode I growth rate found for Al alloys.
- Fig. 3.14. Effects of phase angle on the interface fracture energy for epoxy/glass interfaces. (See Ref. 7 for the choice of ψ .)
- Fig. 3.15 Effects of Ag segregation on fracture energy for the $\text{Al}_2\text{O}_3/\text{Nb}$ system for two Nb orientations (110) and (100).
- Fig. 3.16 Effect of the elastic layer thickness D on the plastic dissipation that accompanies interface crack growth by bond rupture.
- Fig. 4.1 Some fundamental cracking and decohesion problems, indicating magnitudes of the cracking number, λ .
- Fig. 4.2 A schematic showing forces P and moments M created by residual stress or external loading in a bilayer.
- Fig. 4.3 A schematic of crack growth by tunnelling with slip or debonding at the interface.
- Fig. 4.4 A kinking diagram indicating conditions that either give interface crack growth or cause cracking of the ceramic.
- Fig. 4.5 The predicted crack plane ($K_{II} = 0$) in the substrate for films in residual tension on a brittle substrate.
- Fig. 4.6 The variation in slip length with applied stress showing the small-scale yielding and shear lag regimes.

- Fig. 4.7 Asymptotic solution for stress redistribution by slip and debonding from a crack tip, as a function of slip/debond length.
- Fig. 4.8 Full-field solutions for stress redistribution around an embedded crack, by slip, for various shear resistances.
- Fig. 4.9 A surface crack illustrating mixed-mode debonding. Also shown are the stresses when the multilayer is in bending.
- Fig. 4.10 A moiré interferometry image of the slip band formed in $\text{Al}_2\text{O}_3/\text{Al}$ multilayers. The band initiates at the precrack tip and spreads vertically.
- Fig. 4.11 A comparison of plastic zone size measurements for $\text{Al}/\text{Al}_2\text{O}_3$ multilayers with calculations for a shear yield strength, $\tau_0 = 20 \text{ MPa}$.
- Fig. 4.12 Moiré interferometry images of displacements around a surface crack in $\text{Al}_2\text{O}_3/\text{Al}$ multilayers at eight different values of the nominal stress intensity factor, K . The precrack is at the top in the center.
- Fig. 4.13 Fluorescence spectroscopy measurements of σ_{kk} stress around a surface crack in $\text{Al}_2\text{O}_3/\text{Al}$ multilayers for a strongly bonded, slipping interface and an interface debonded by fatigue.
- Fig. 4.14 Optical image of a debond created by fatigue in an $\text{Al}_2\text{O}_3/\text{Al}$ multilayer.
- Fig. 4.15 A fail-safe diagram for a bilayer, reflecting the three brittle damage modes.
- Fig. 4.16 Resistance behaviors found in two layered materials.
- Fig. 4.17 A schematic showing the configuration dependence of delamination cracking in a multilayer.
- Fig. 5.1 A thermal fatigue diagram for a multilayer.
- Fig. 5.2 A schematic comparing fatigue debonding at the interface with cyclic crack growth through the alloy.
- Fig. 5.3 A schematic illustrating the criterion governing the fatigue crack trajectory.
- Fig. 5.4 Fatigue failure of a bridging alloy ligament.

- Fig. 6.1 A schematic of a threading dislocation in a thin film with an oxide layer.
- Fig. A1 A schematic of the potentials that cause grain growth and the consequent residual tensile stress in the film.
- Fig. A2 The potential for point defect annihilation at edge dislocations leading to climb.
- Fig. A3 Flexure involved in the removal of voids at the grain boundaries by sintering.
- Fig. A4 The grain boundary stresses in the thin film.

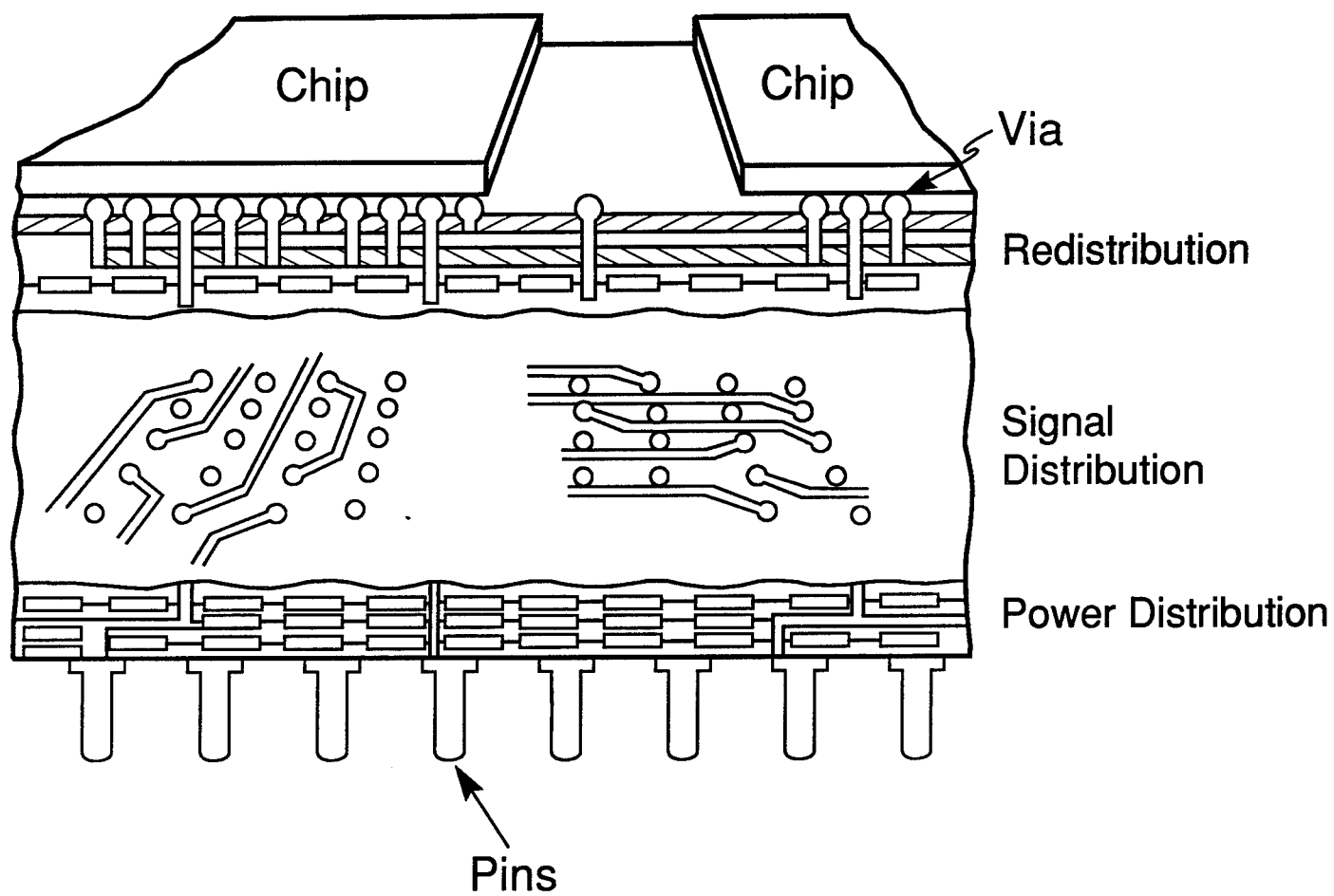
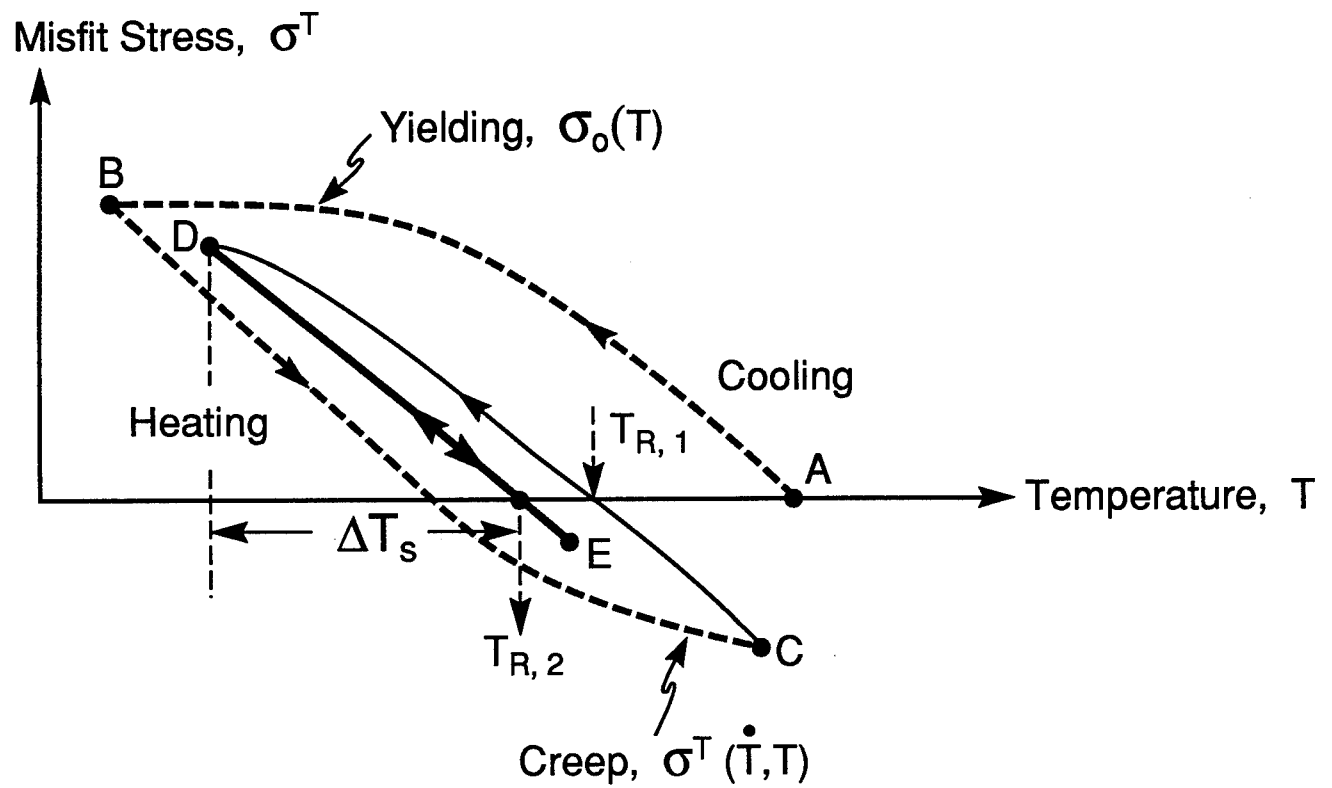


Figure 1.1



a) Schematic of Temperature Cycling : $A \rightarrow B \rightarrow C \rightarrow D \rightarrow E \leftrightarrow D$

Figure 2.1a

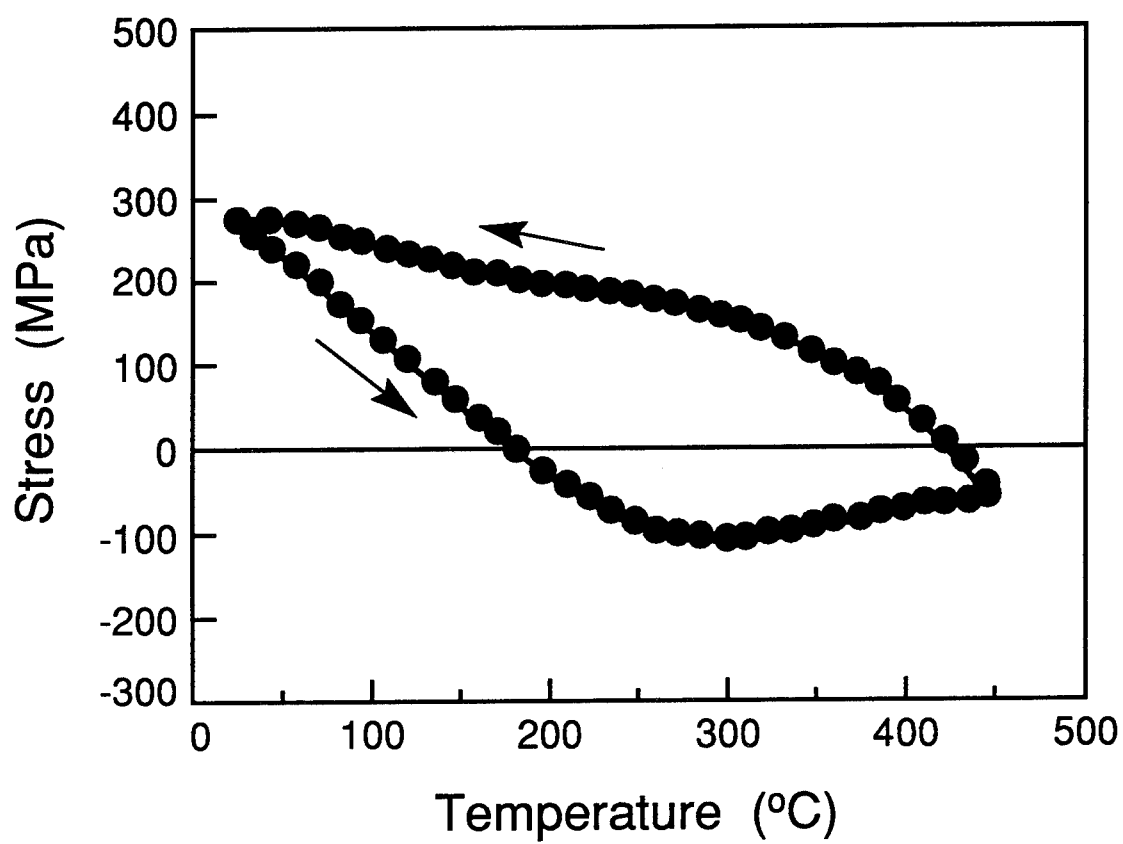


Figure 2.1b

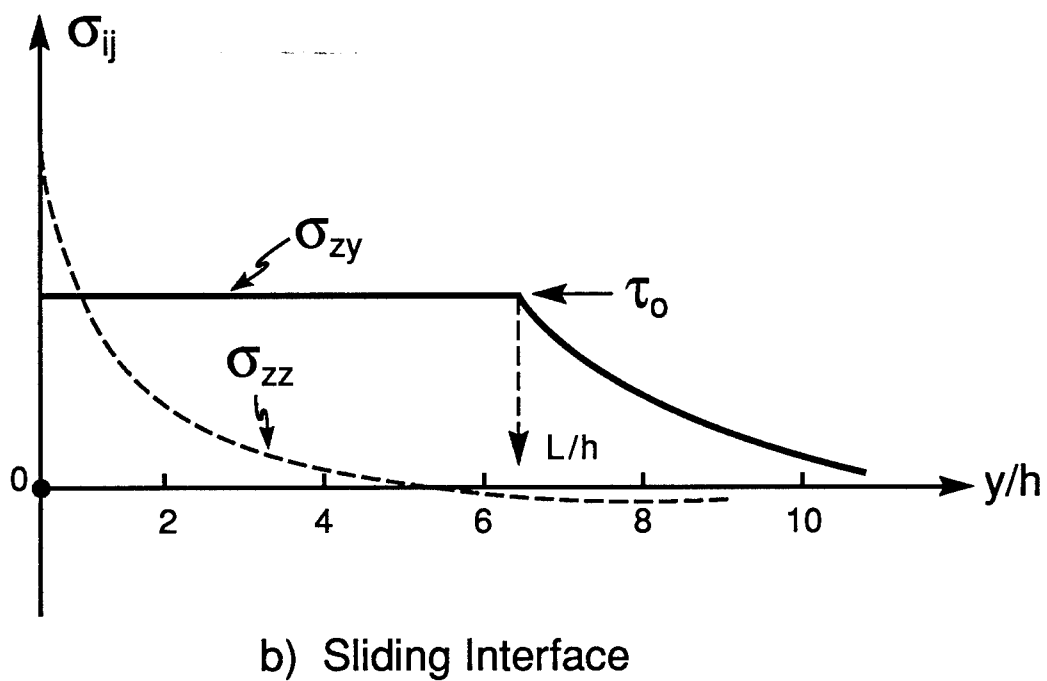
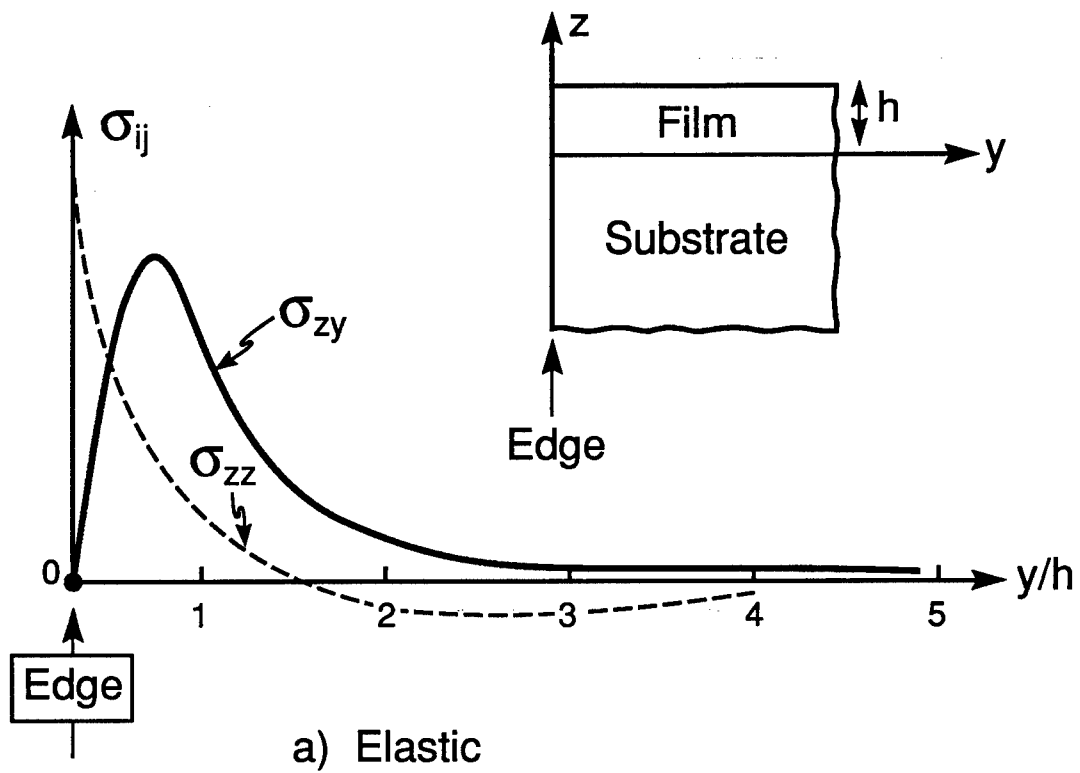


Figure 2.2

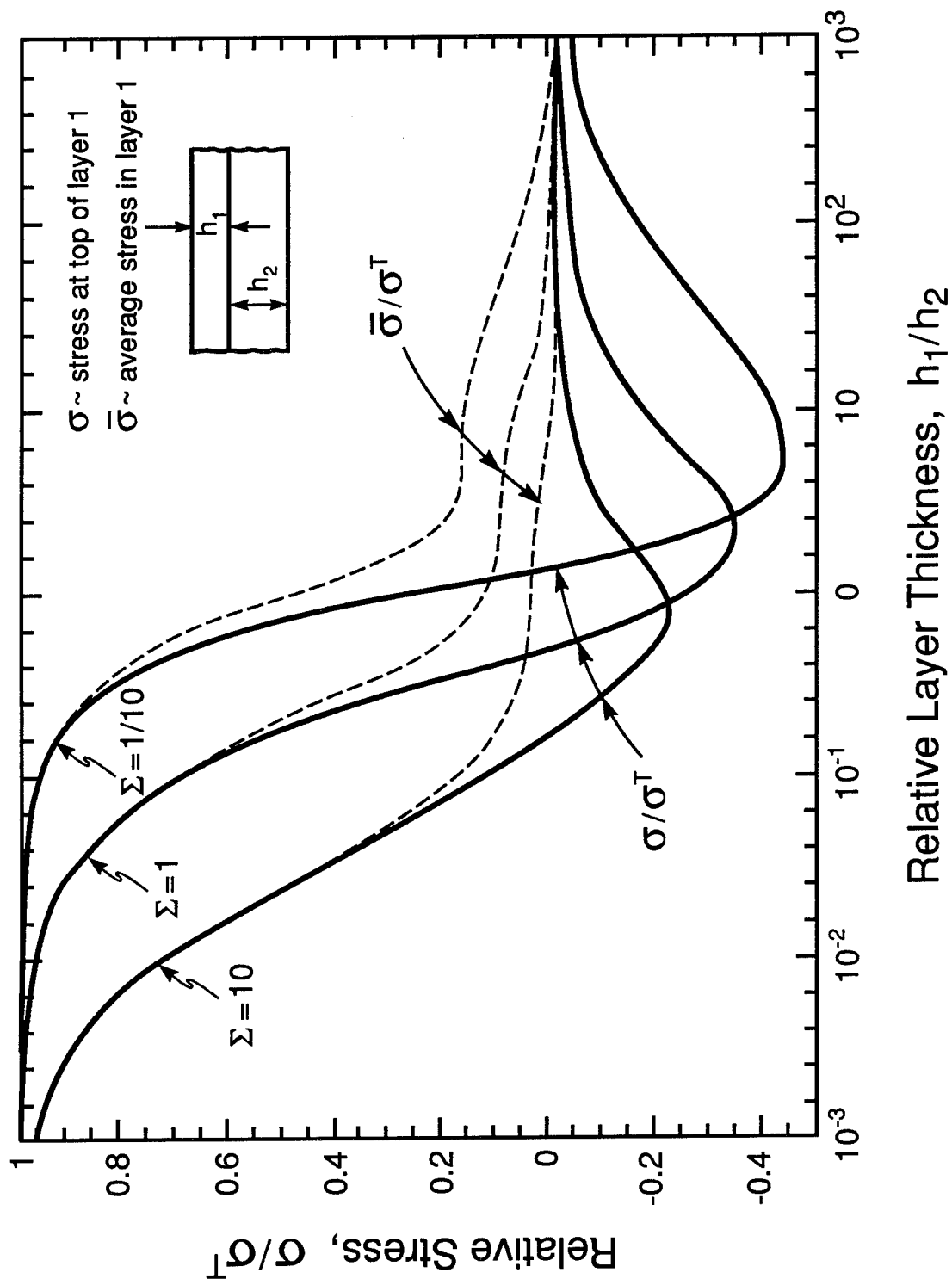


Figure 2.3

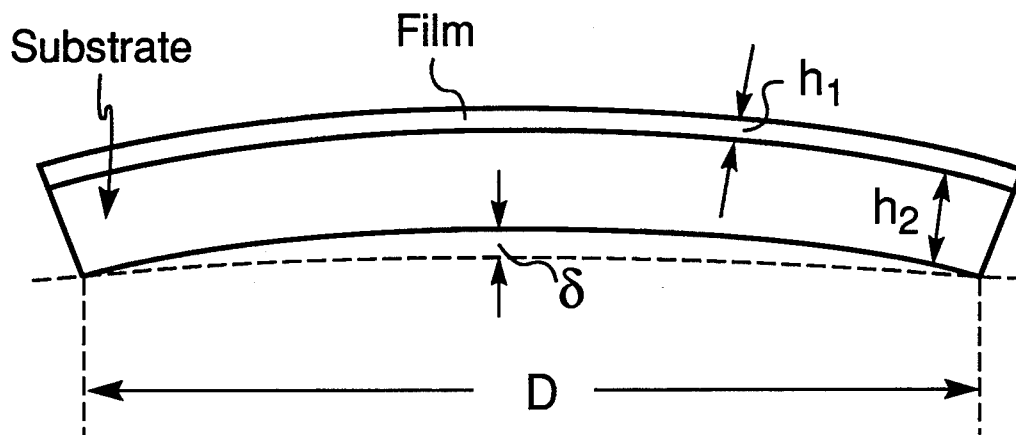


Figure 2.4

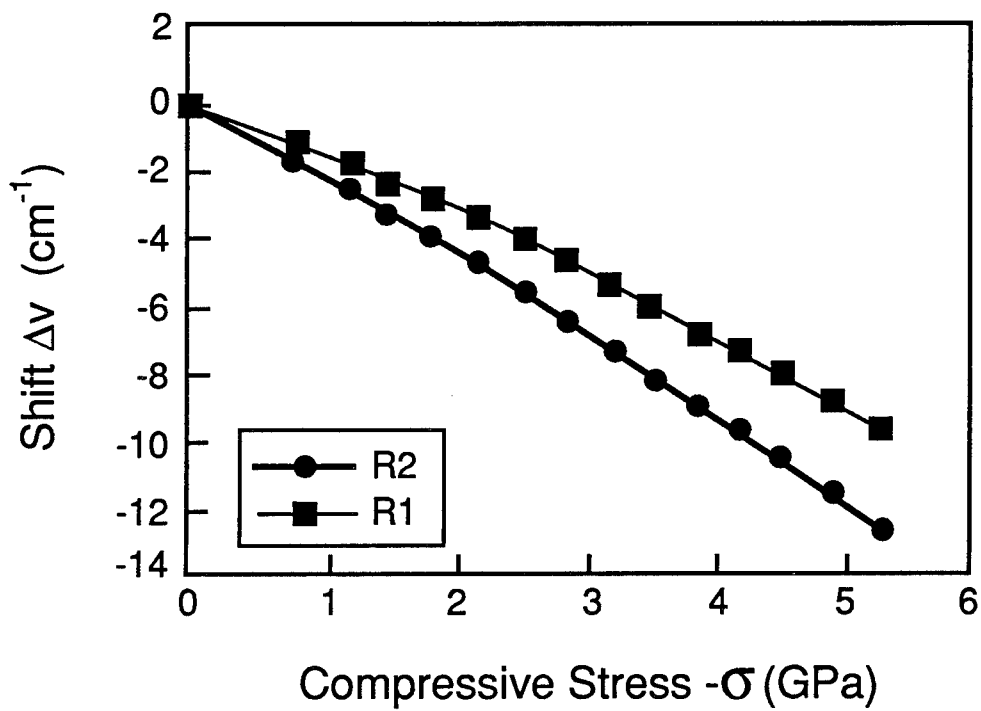
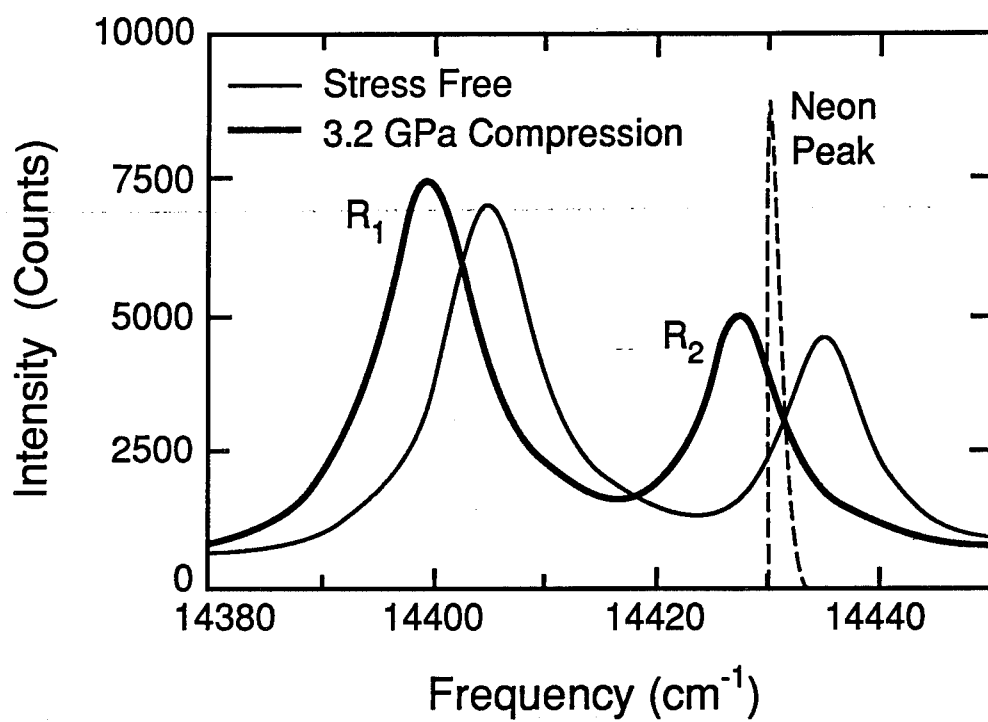


Figure 2.5

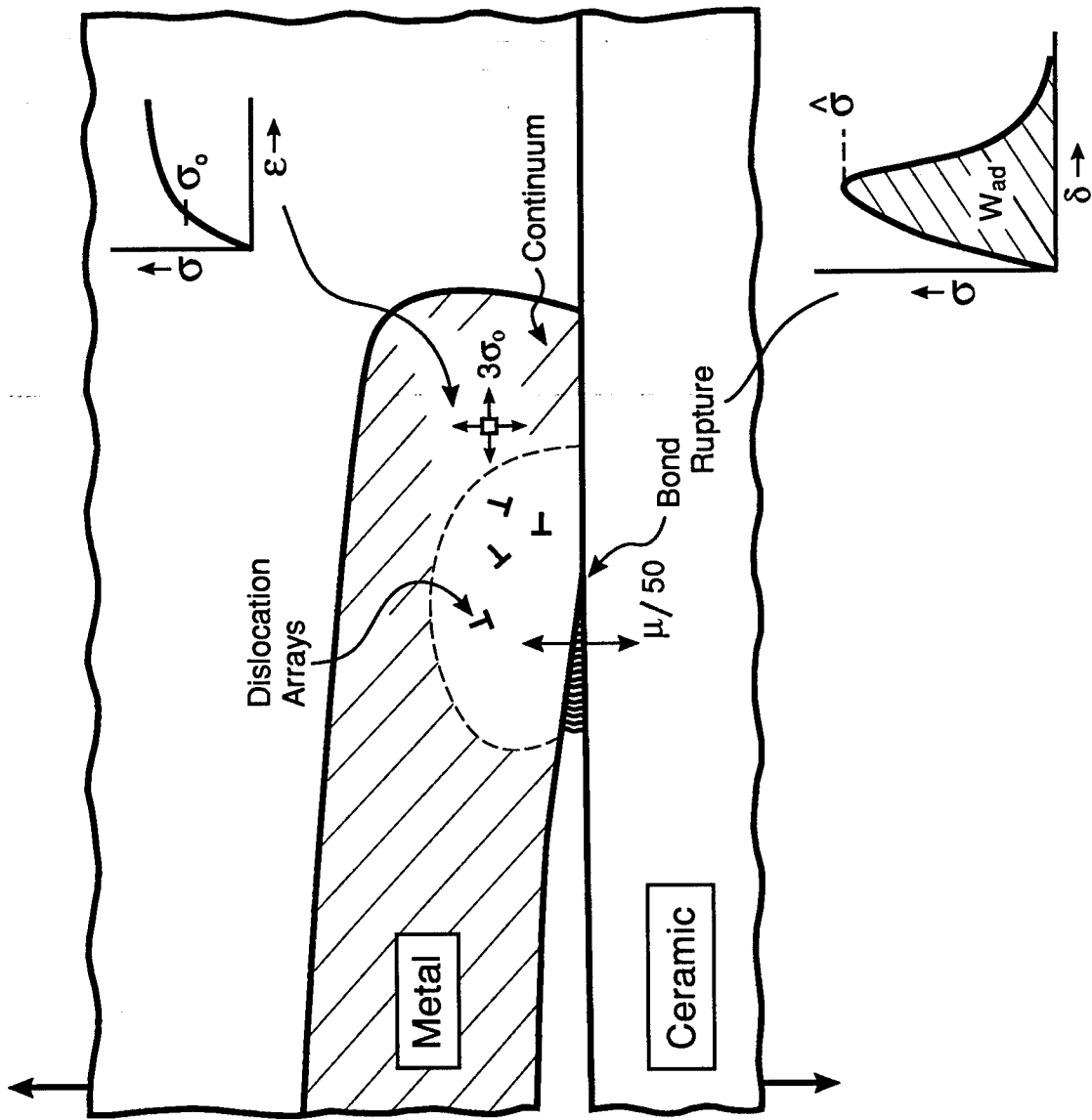


Figure 3.1

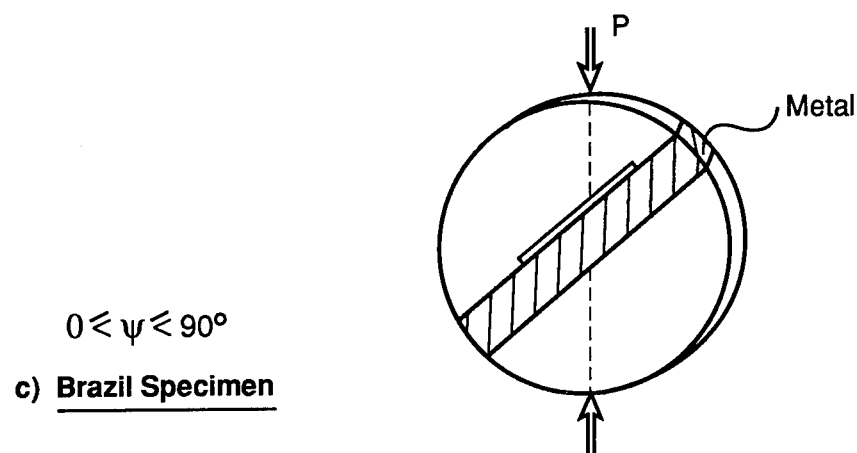
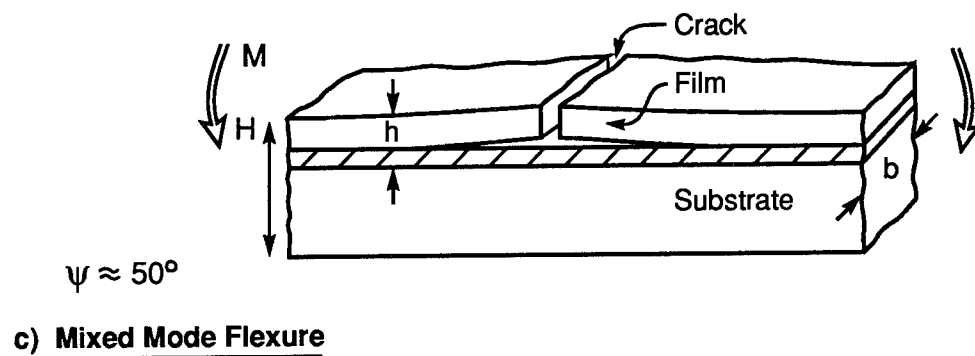
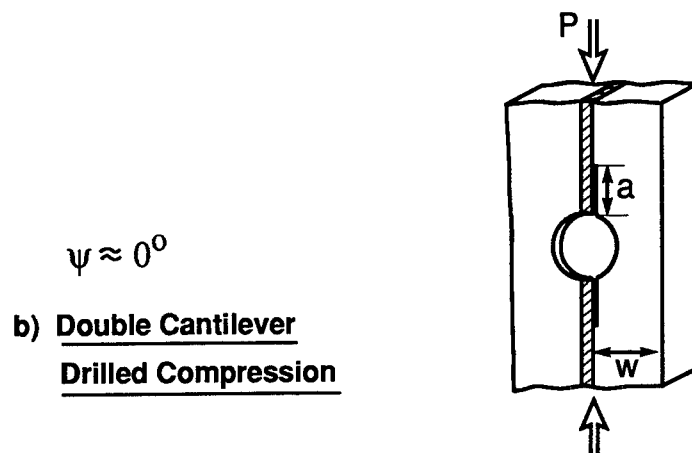
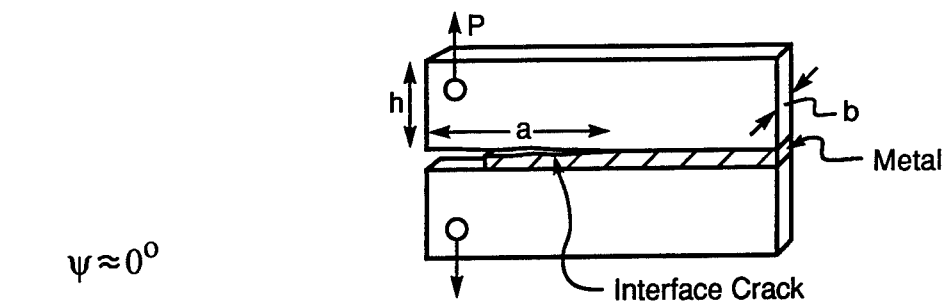


Figure 3.2

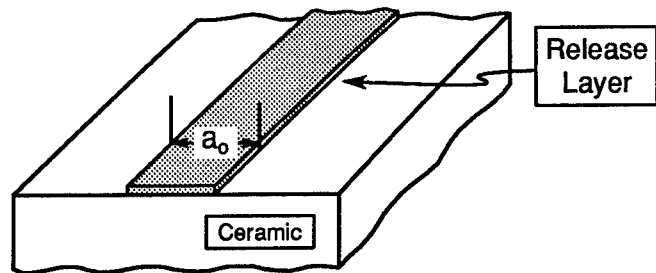
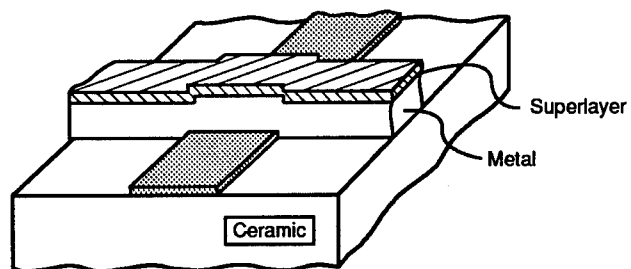
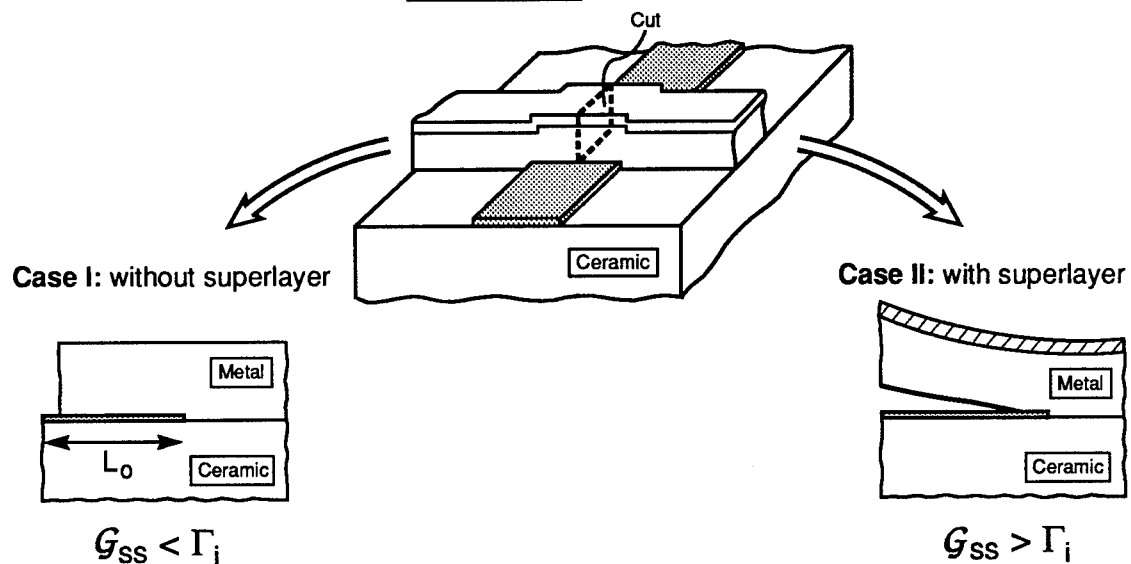
STEP IRelease Layer Deposition**STEP II**Metal Layer & Superlayer**STEP III**Bi-Layer Cut

Figure 3.3

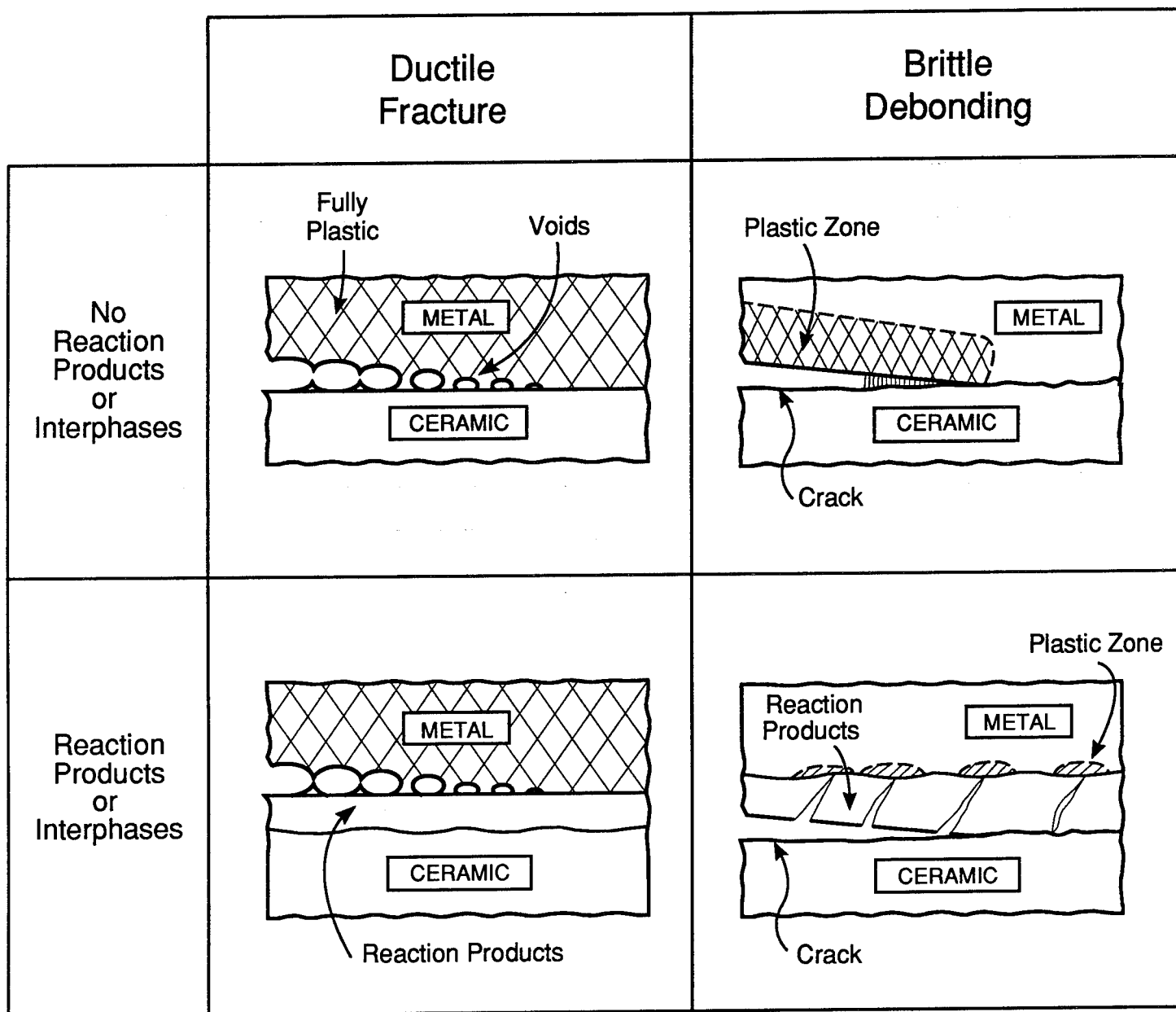


Figure 3.4

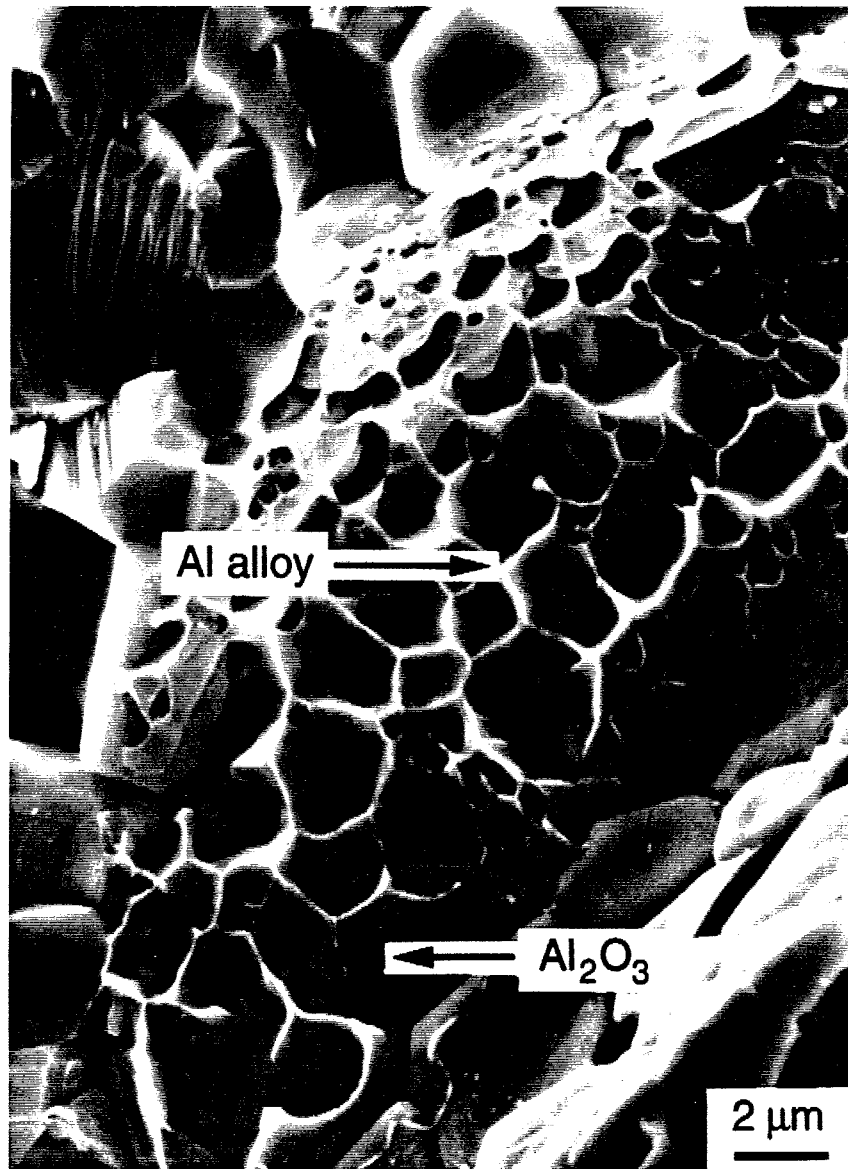


Figure 3.5

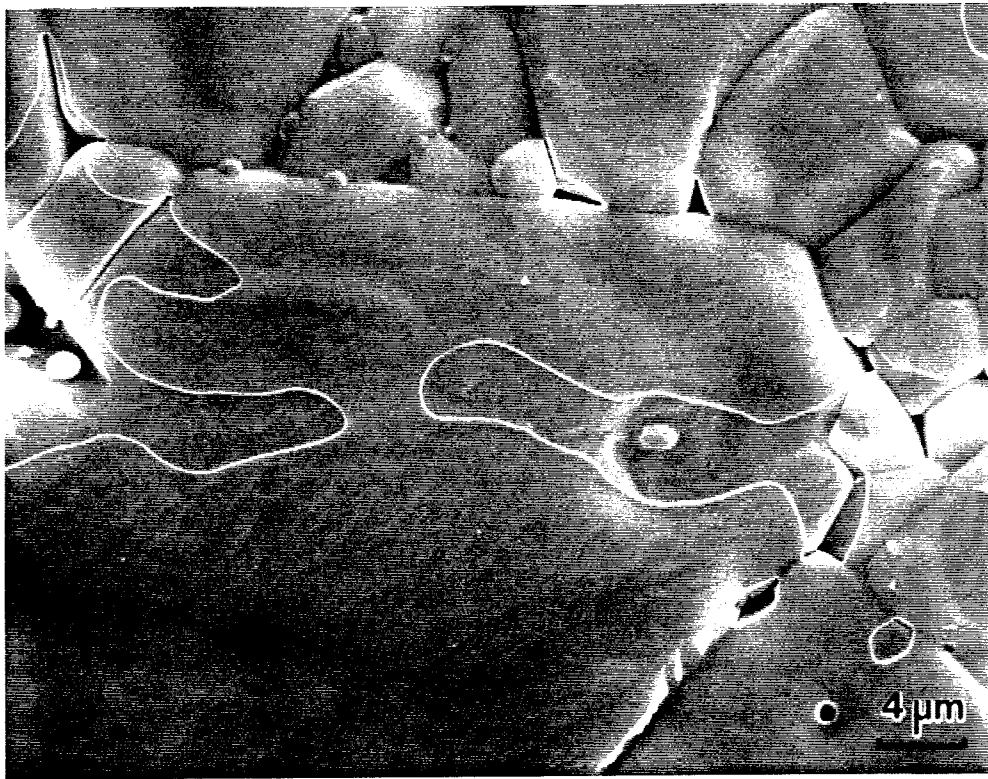


Figure 3.6

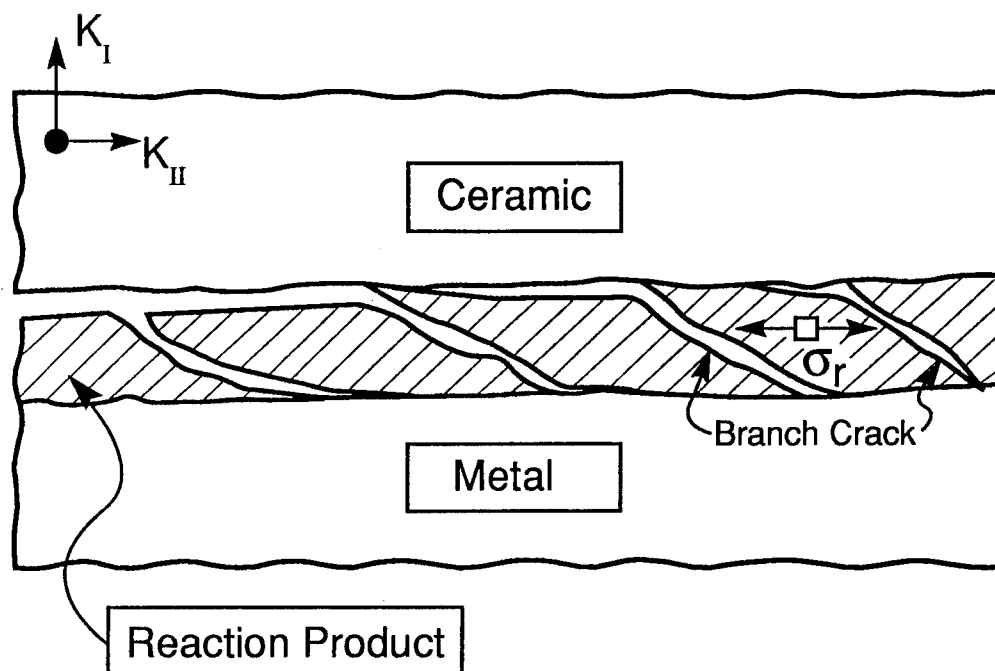


Fig. 3.7a

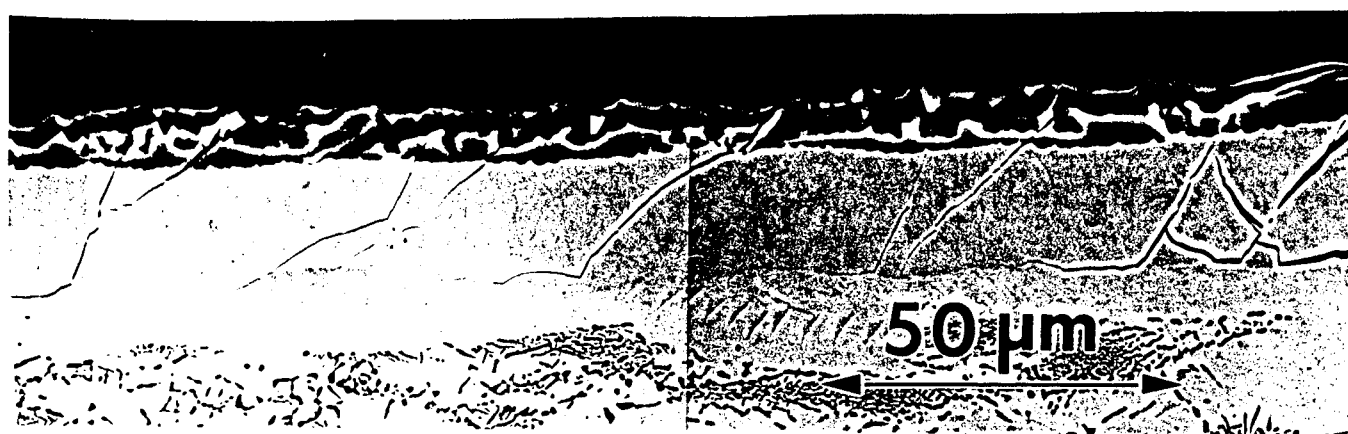


Figure 3.7b

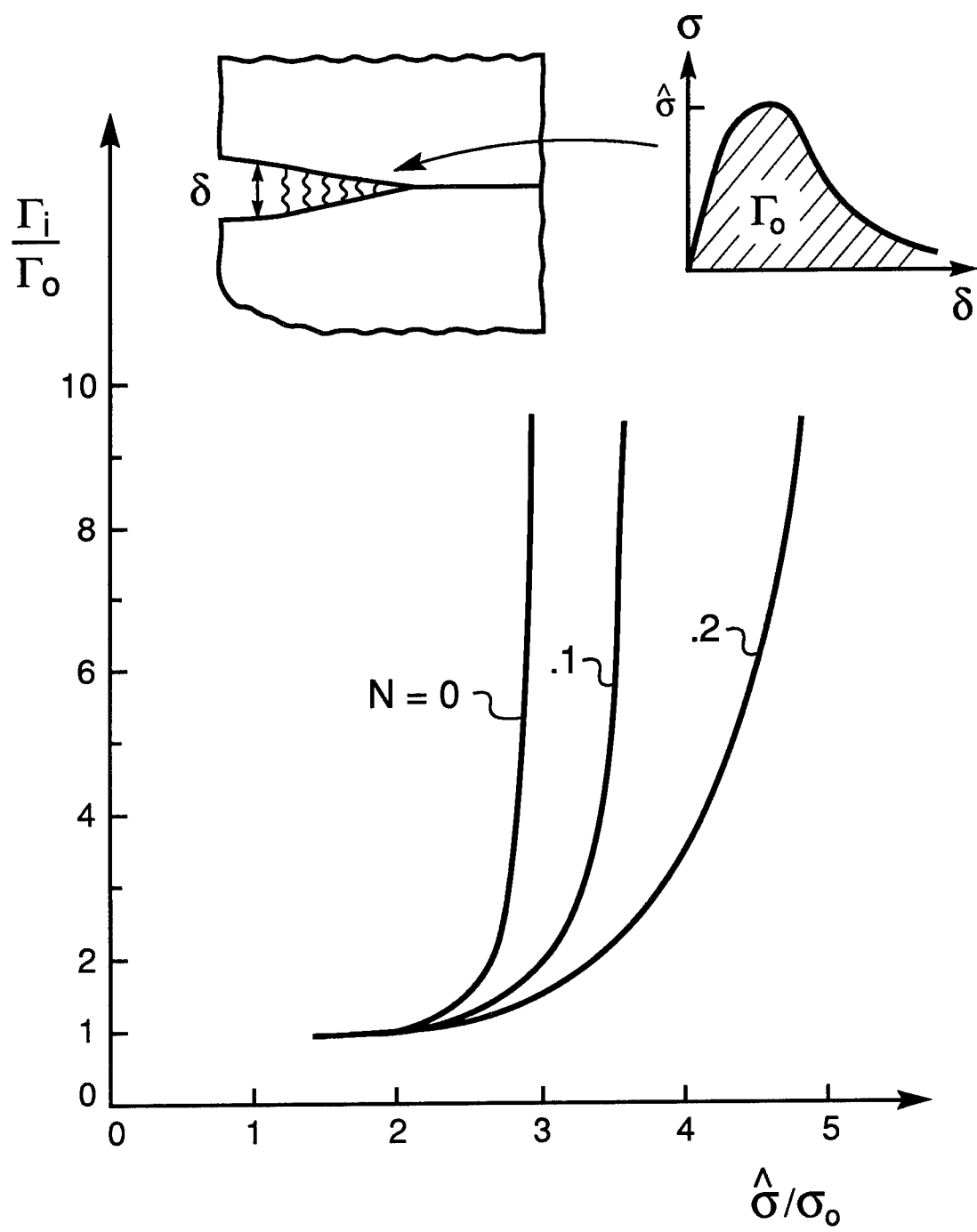


Figure 3.8

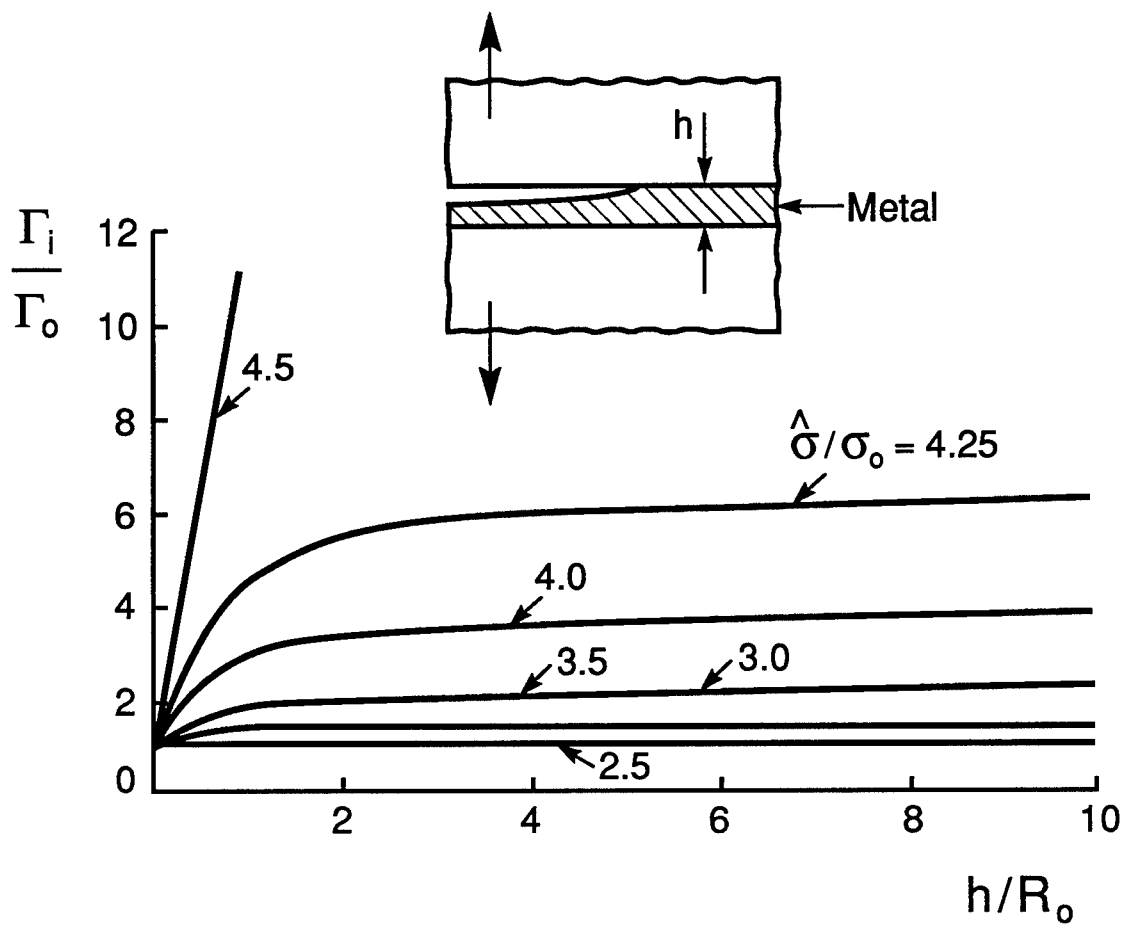


Figure 3.9

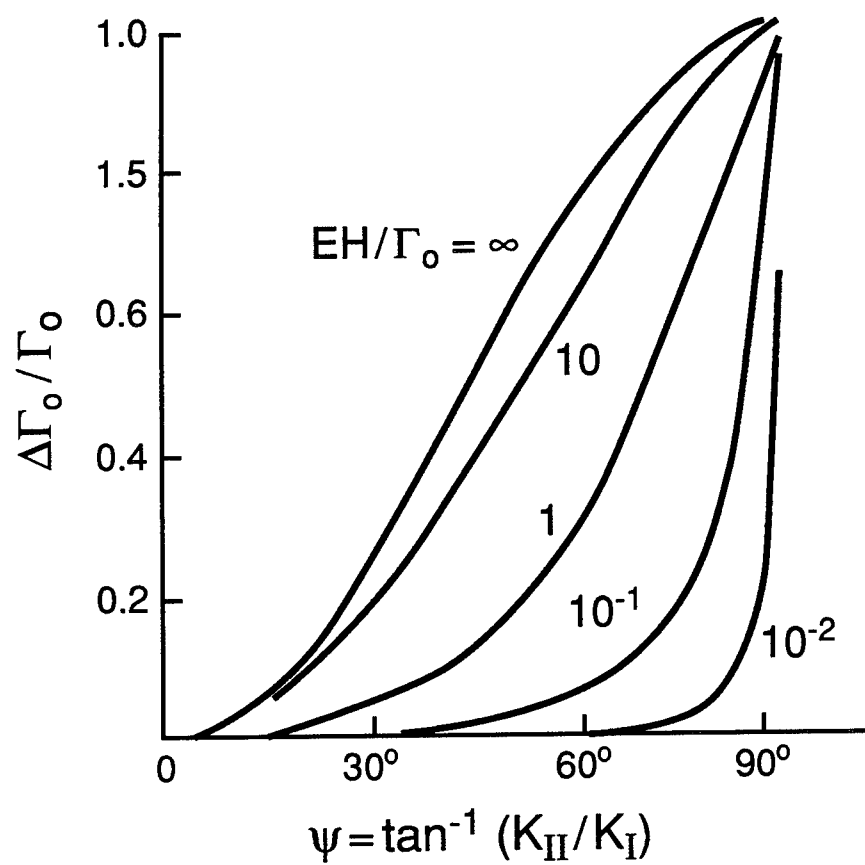


Figure 3.10

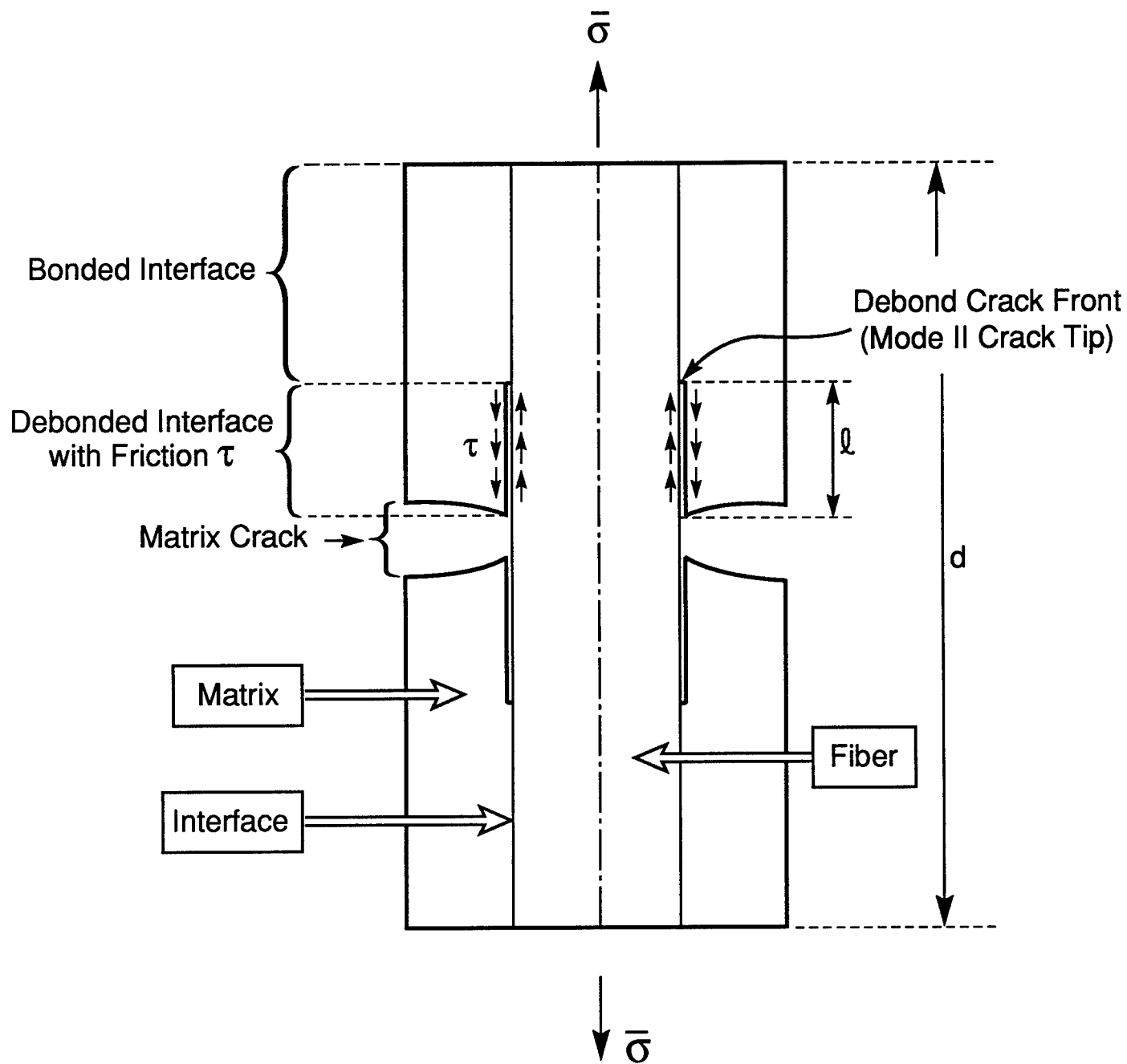
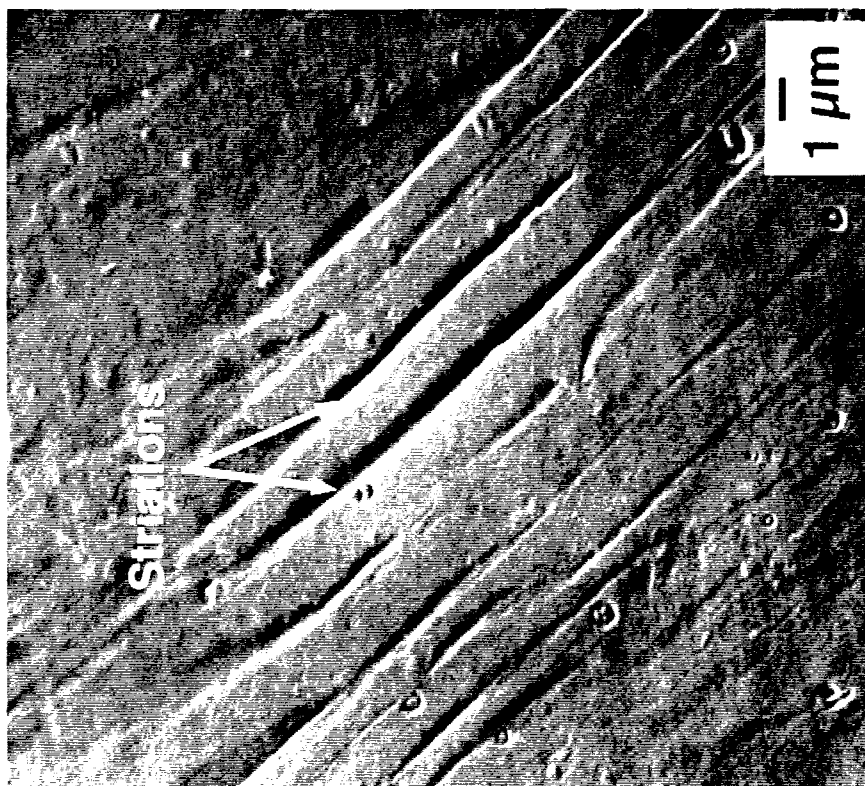
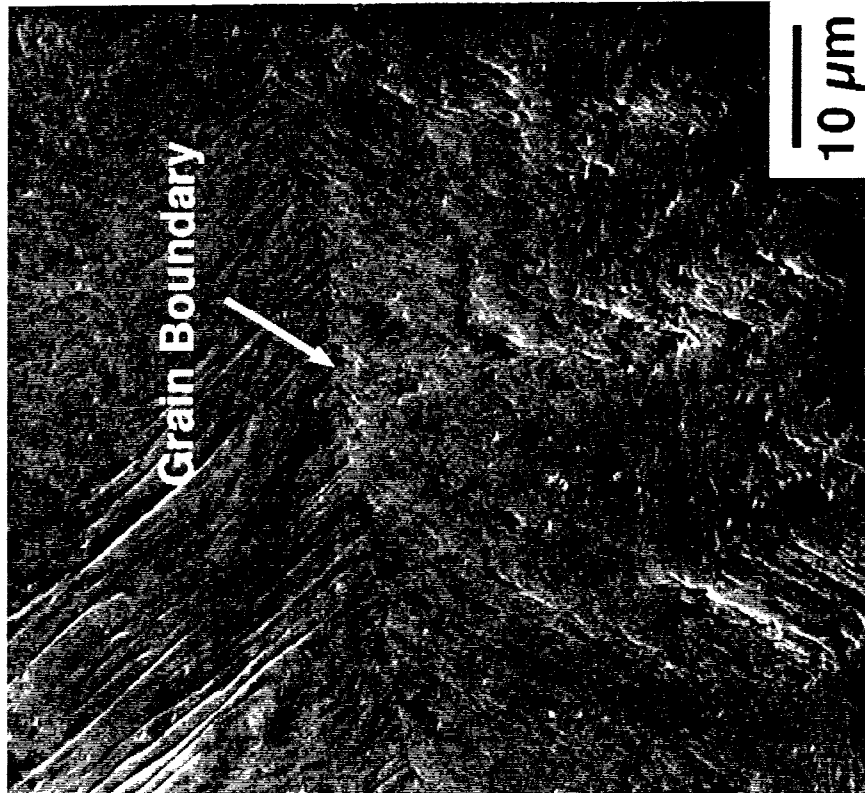


Figure 3.11



(a)



(b)

Figure 3.12

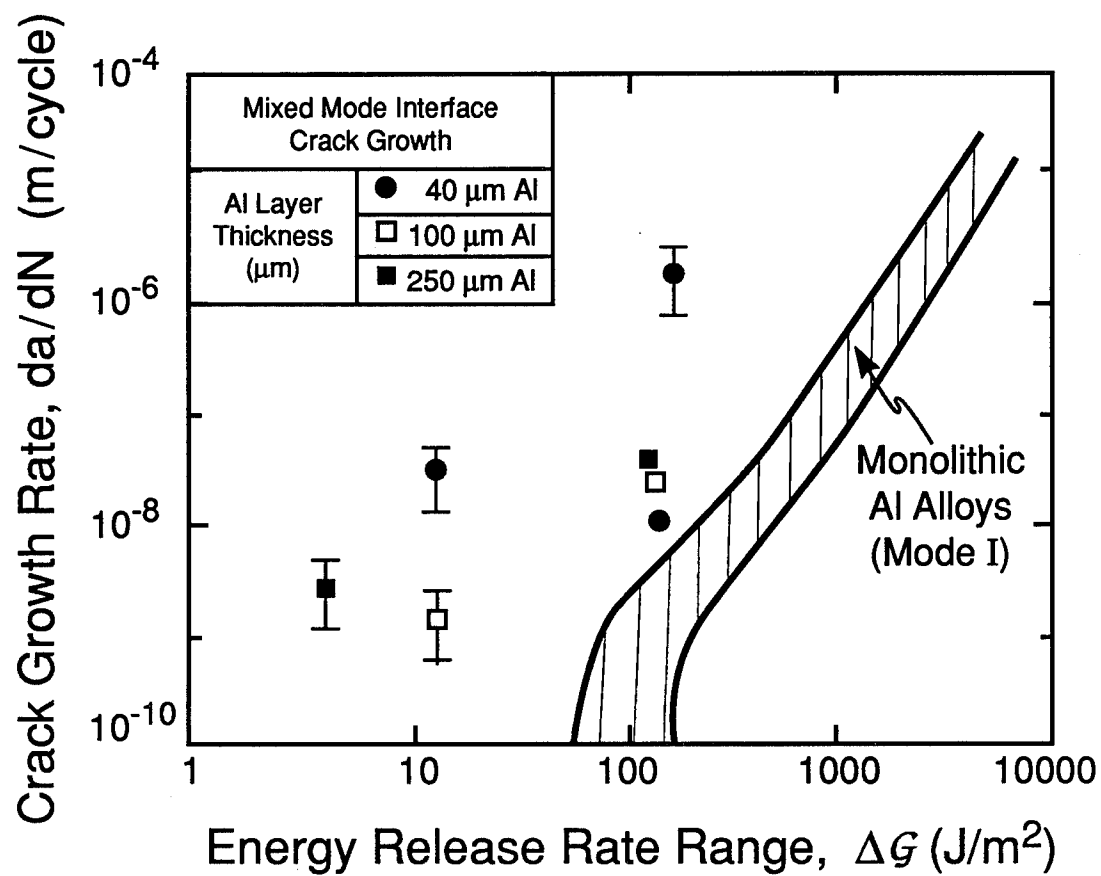


Figure 3.13

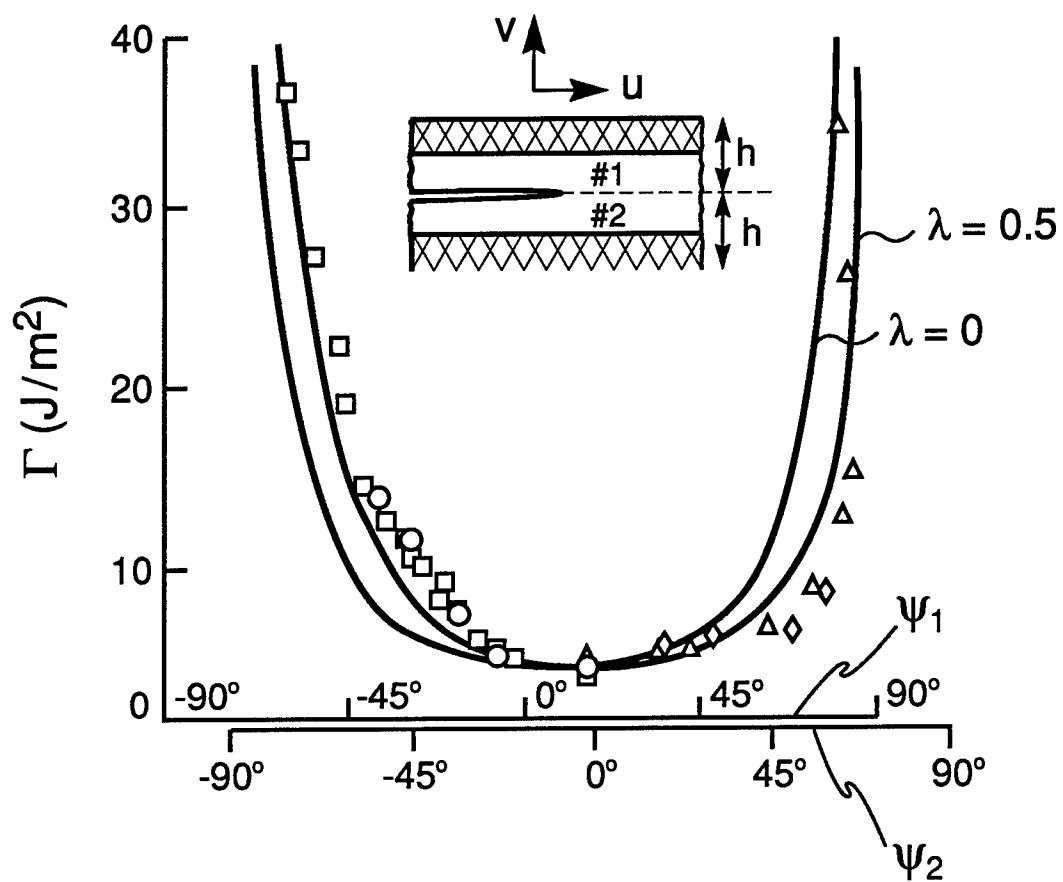


Figure 3.14

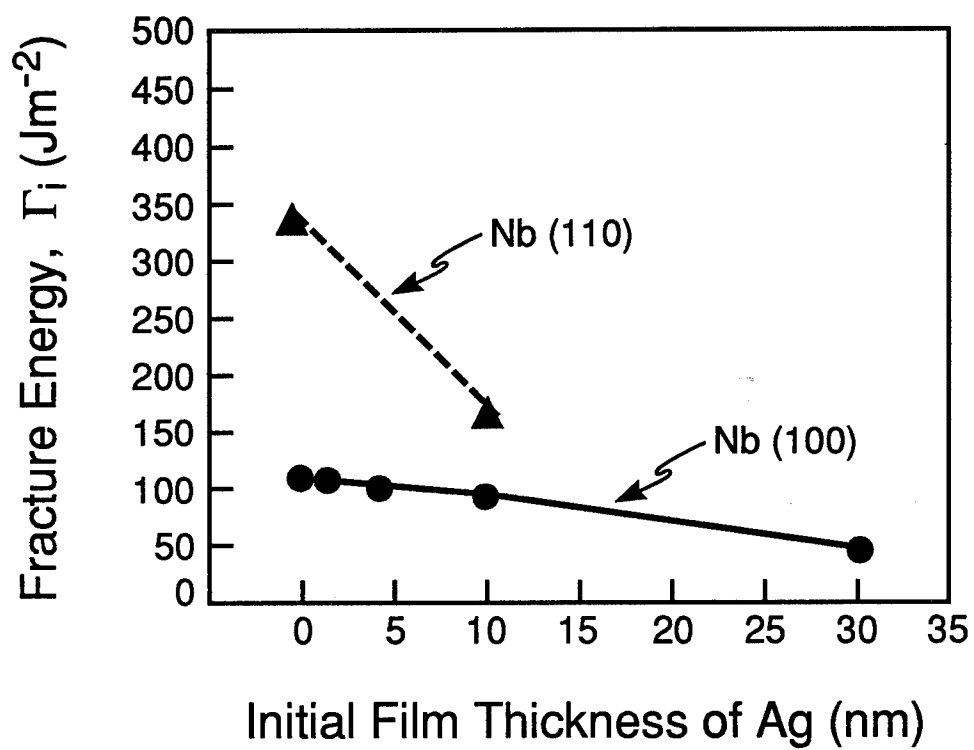


Figure 3.15

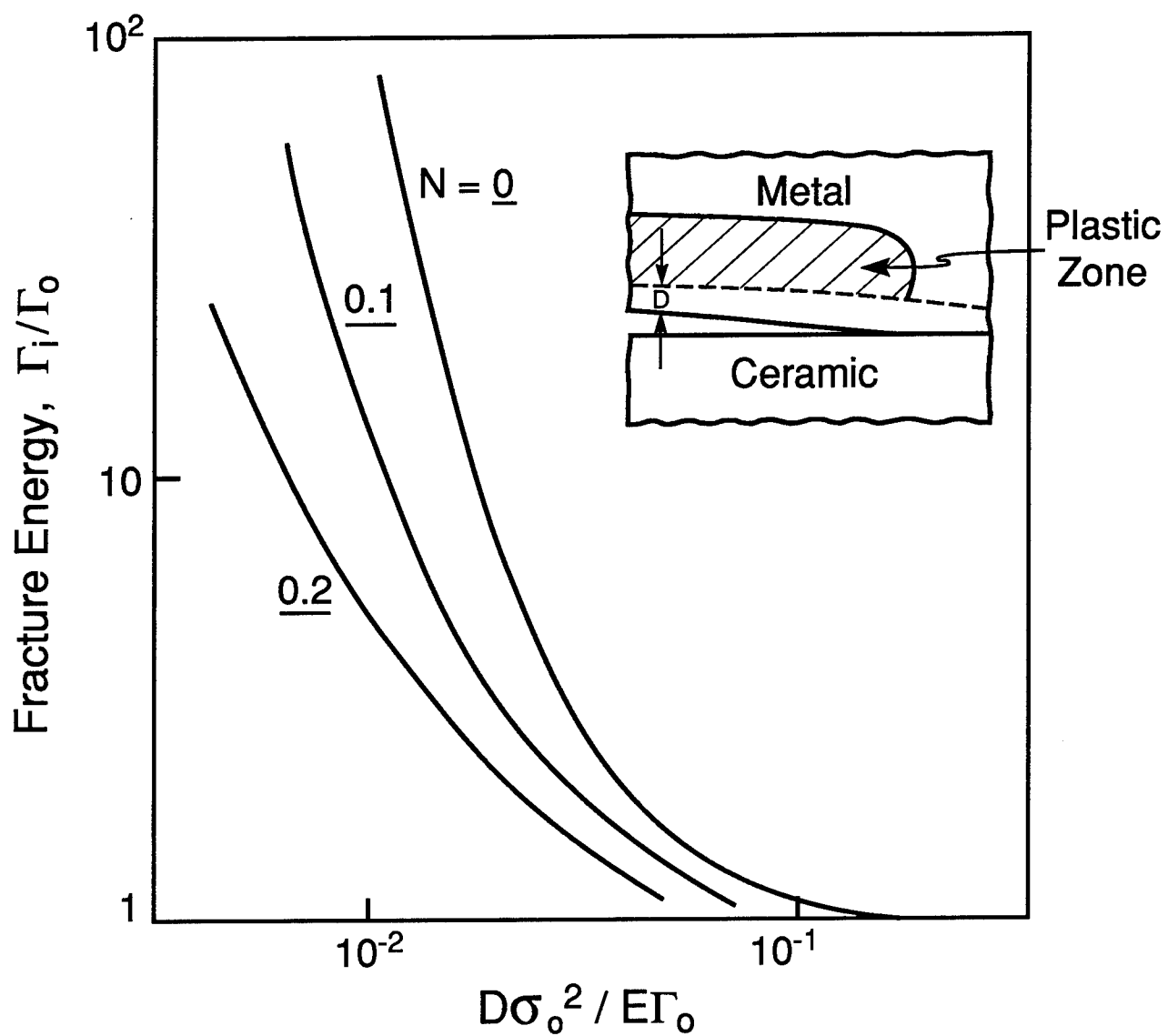
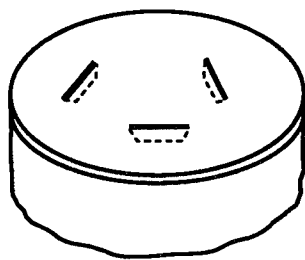


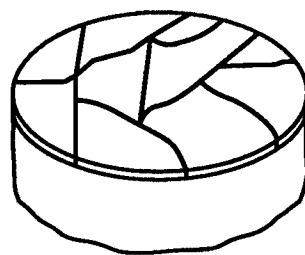
Fig. 3.16

Cracking Patterns

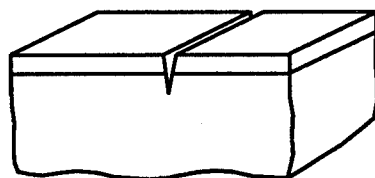
Cracking Number, λ



Surface Crack
3.95



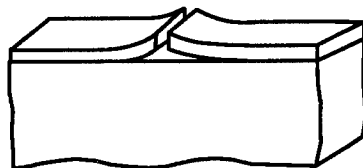
Channeling
1.98



Substrate Damage
3.95



Spalling
0.34



Debonding
1.03 (initiation)
0.5 (steady - state)

Figure 4.1

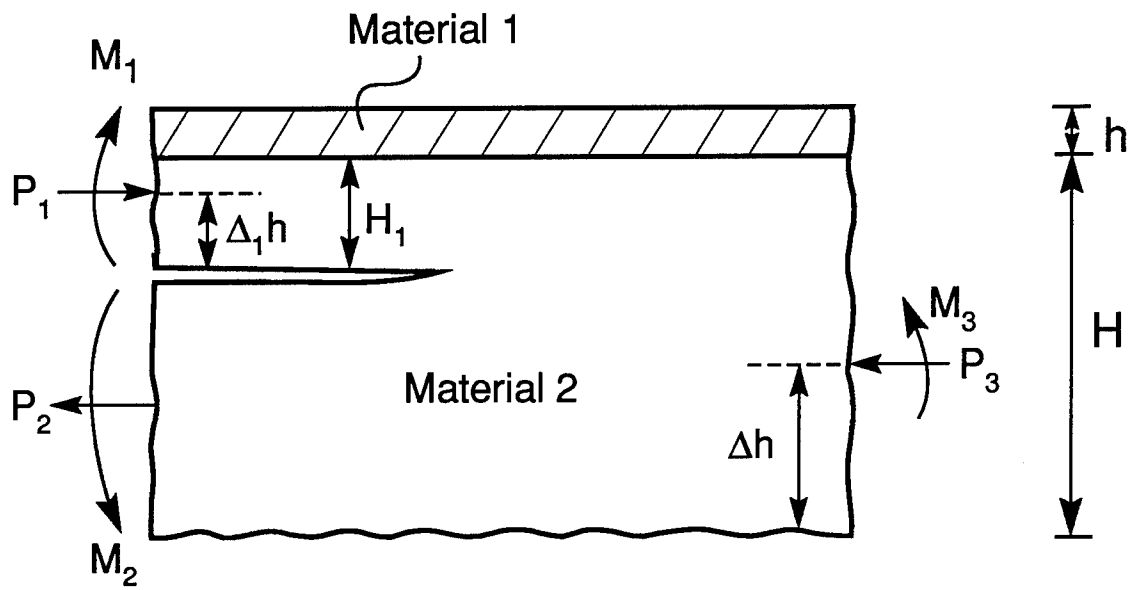
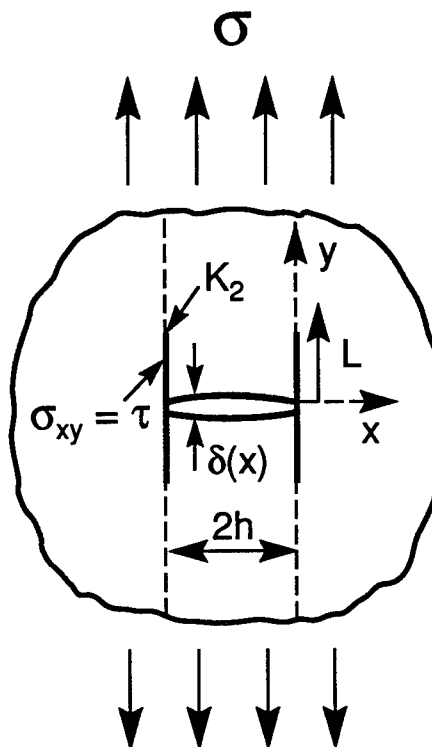


Figure 4.2



Evans.URI-4/94•amk•D51#1356-5

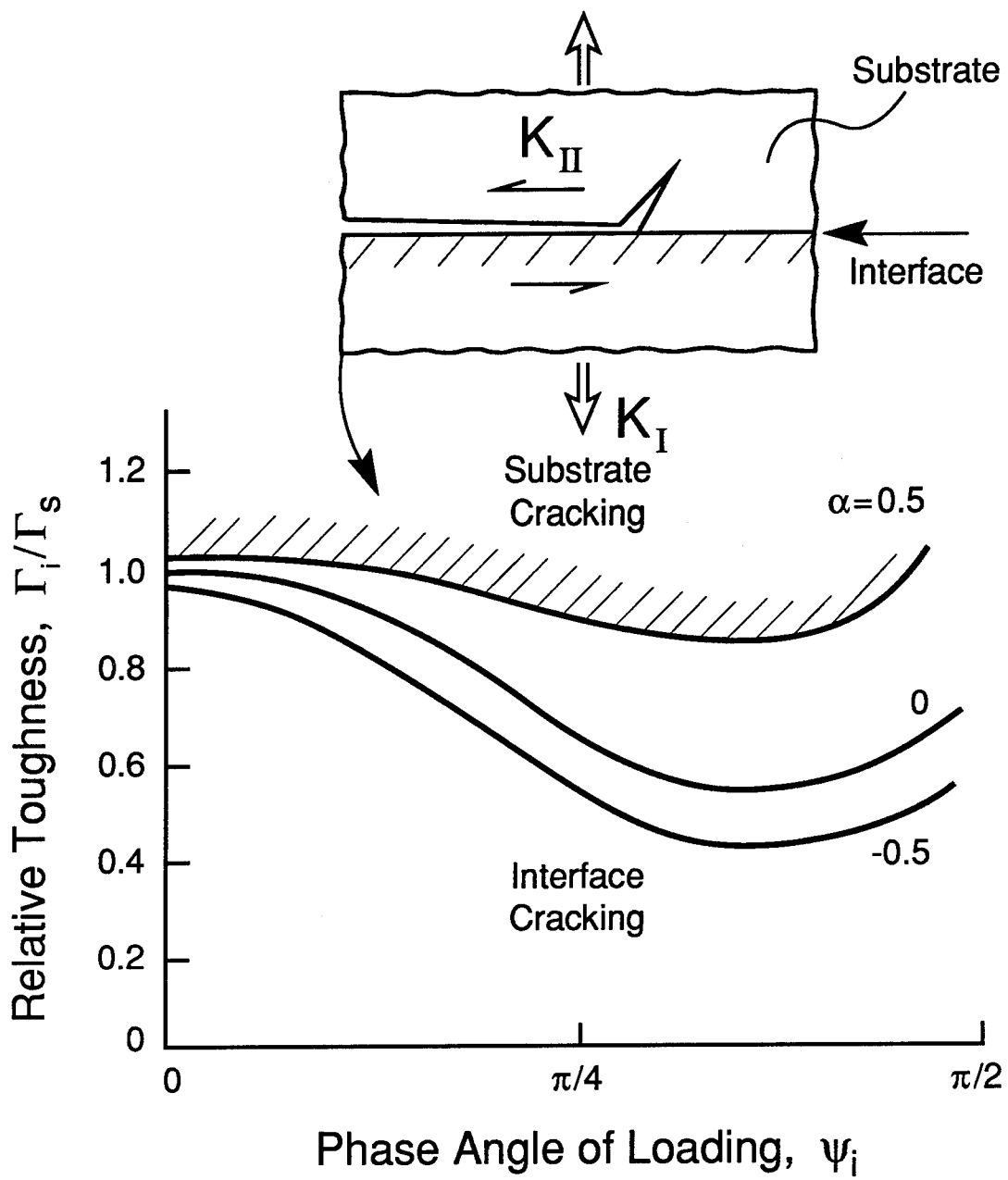


Figure 4.4

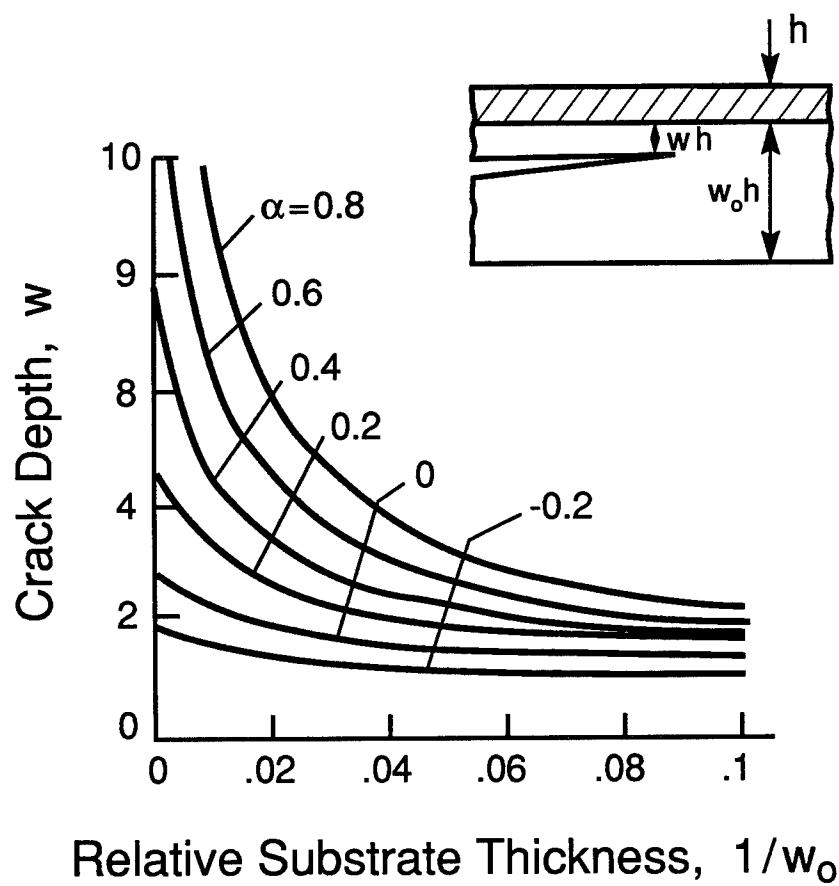


Figure 4.5

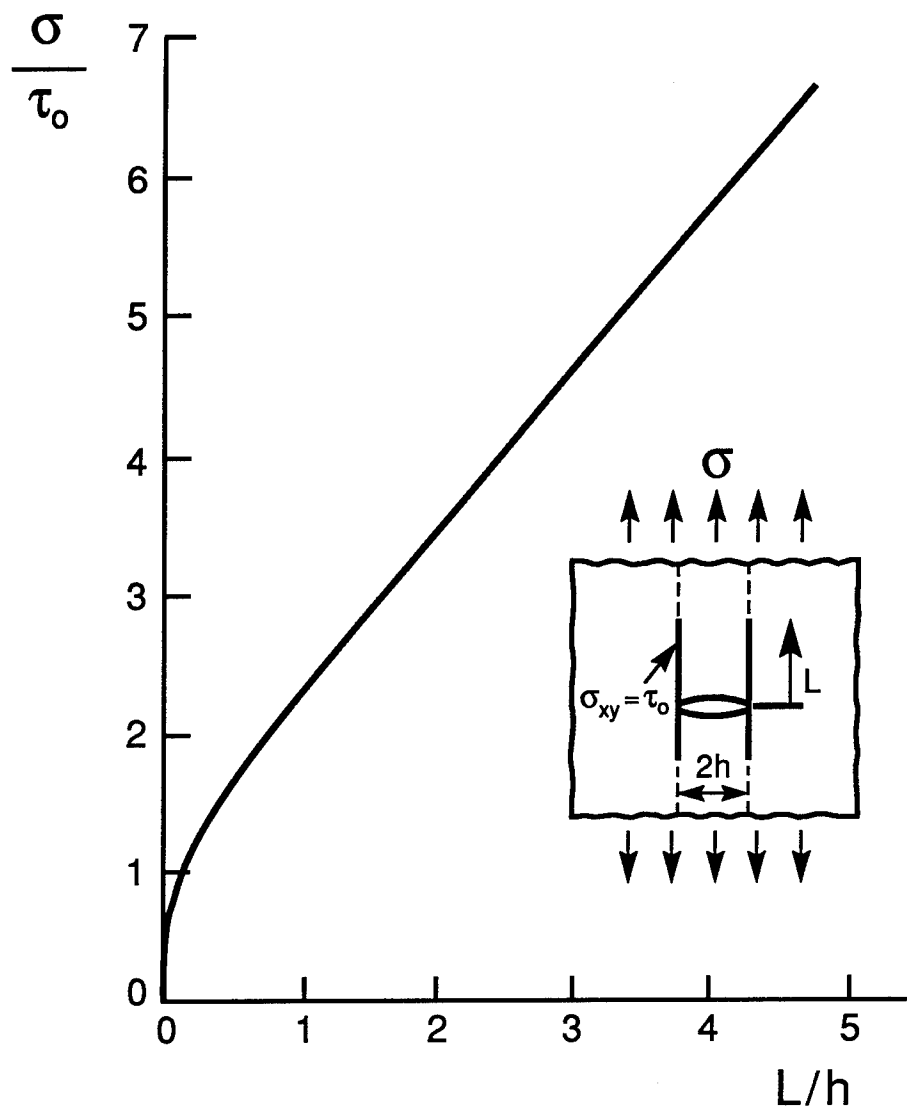


Figure 4.6

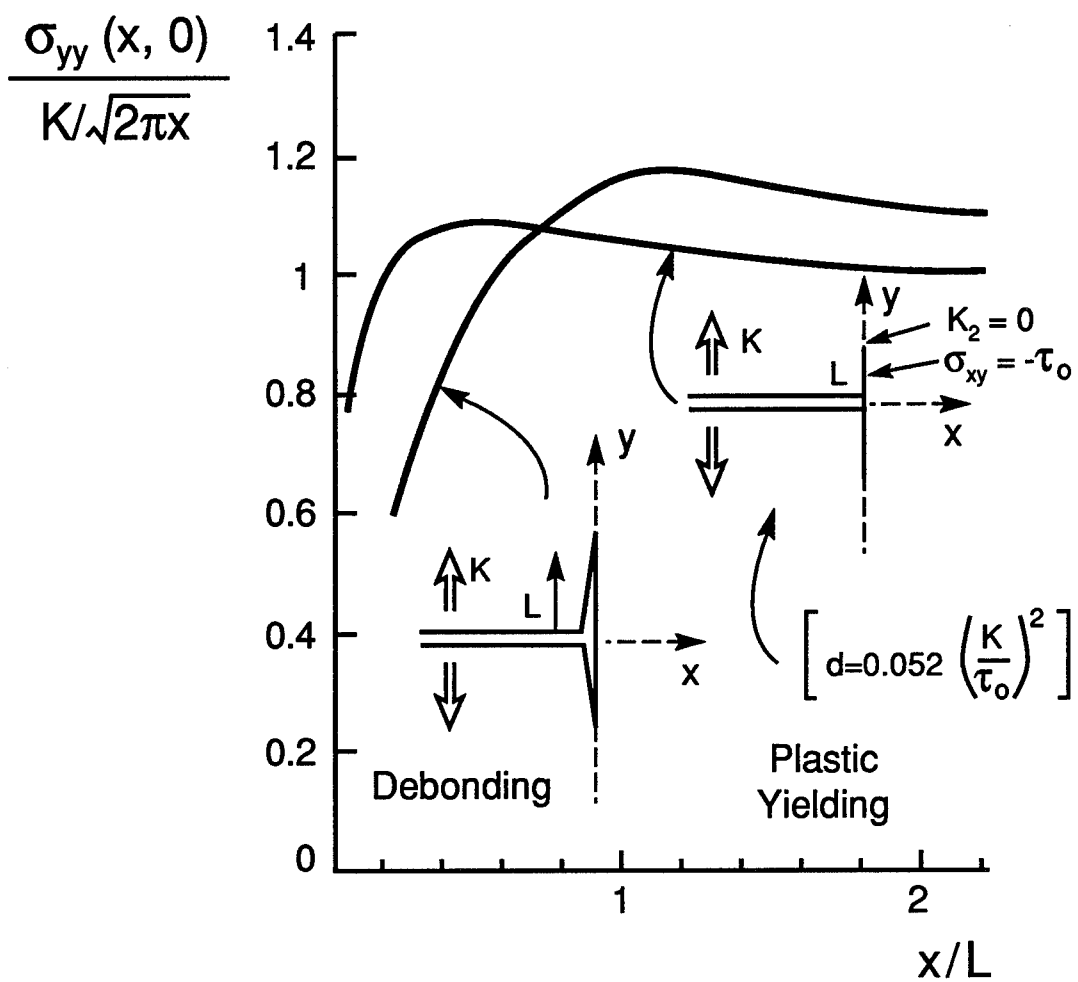


Figure 4.7

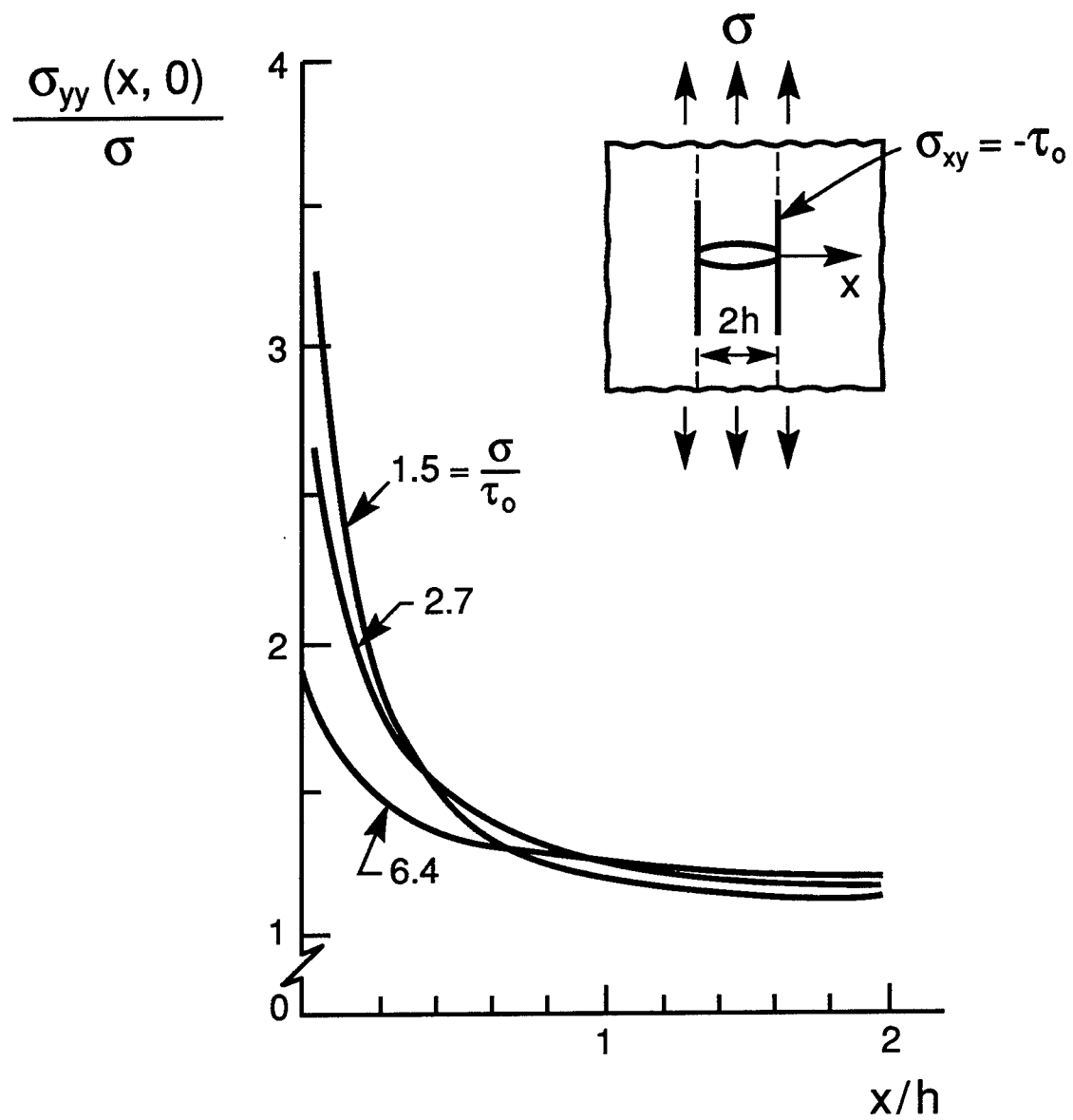


Figure 4.8

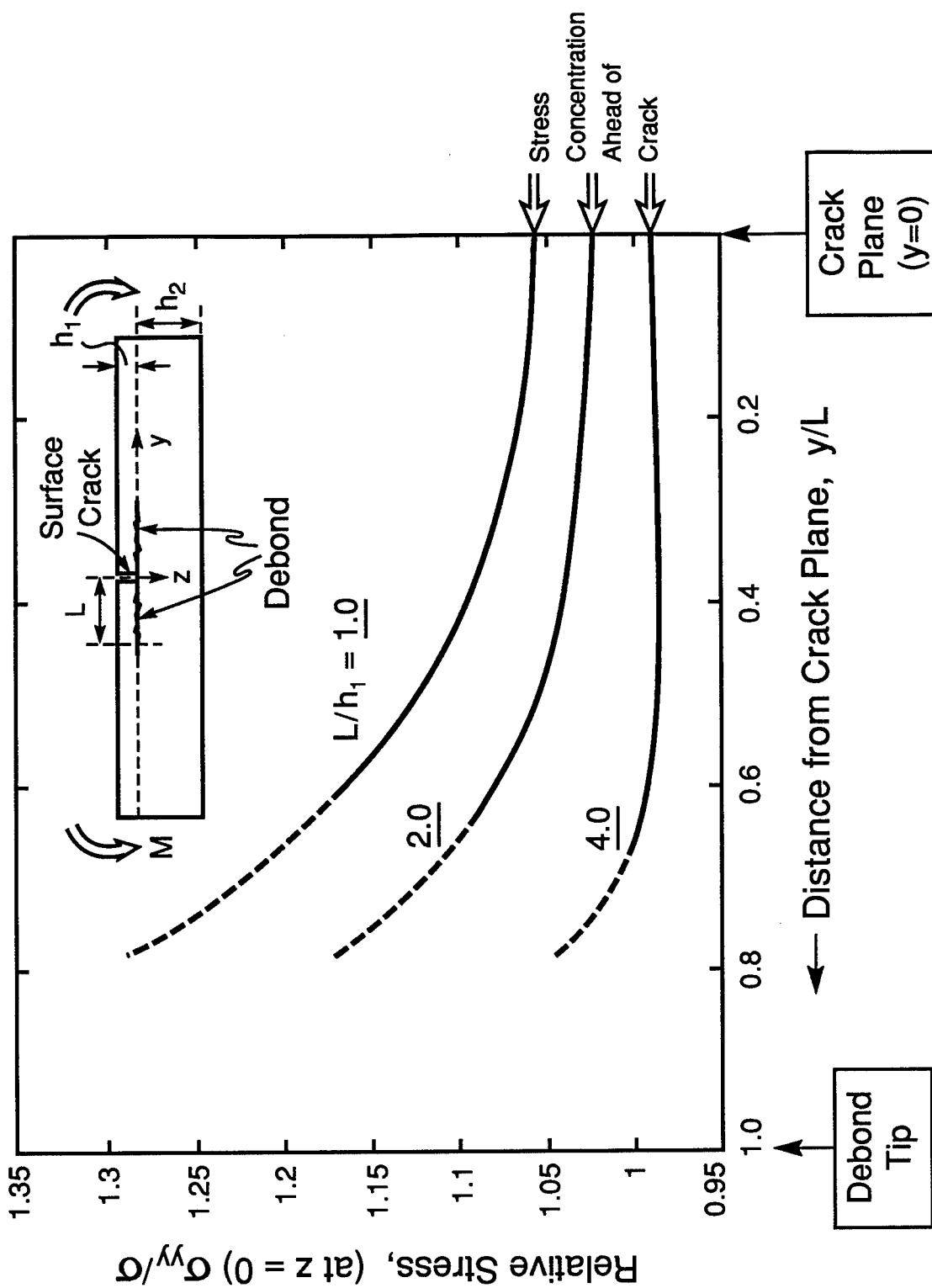


Figure 4.9

Precrack →

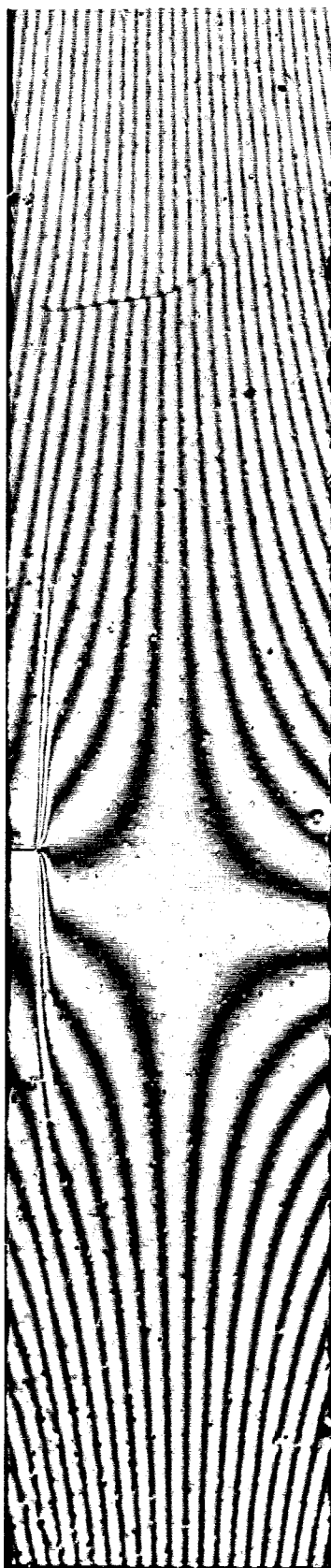


Figure 4.10

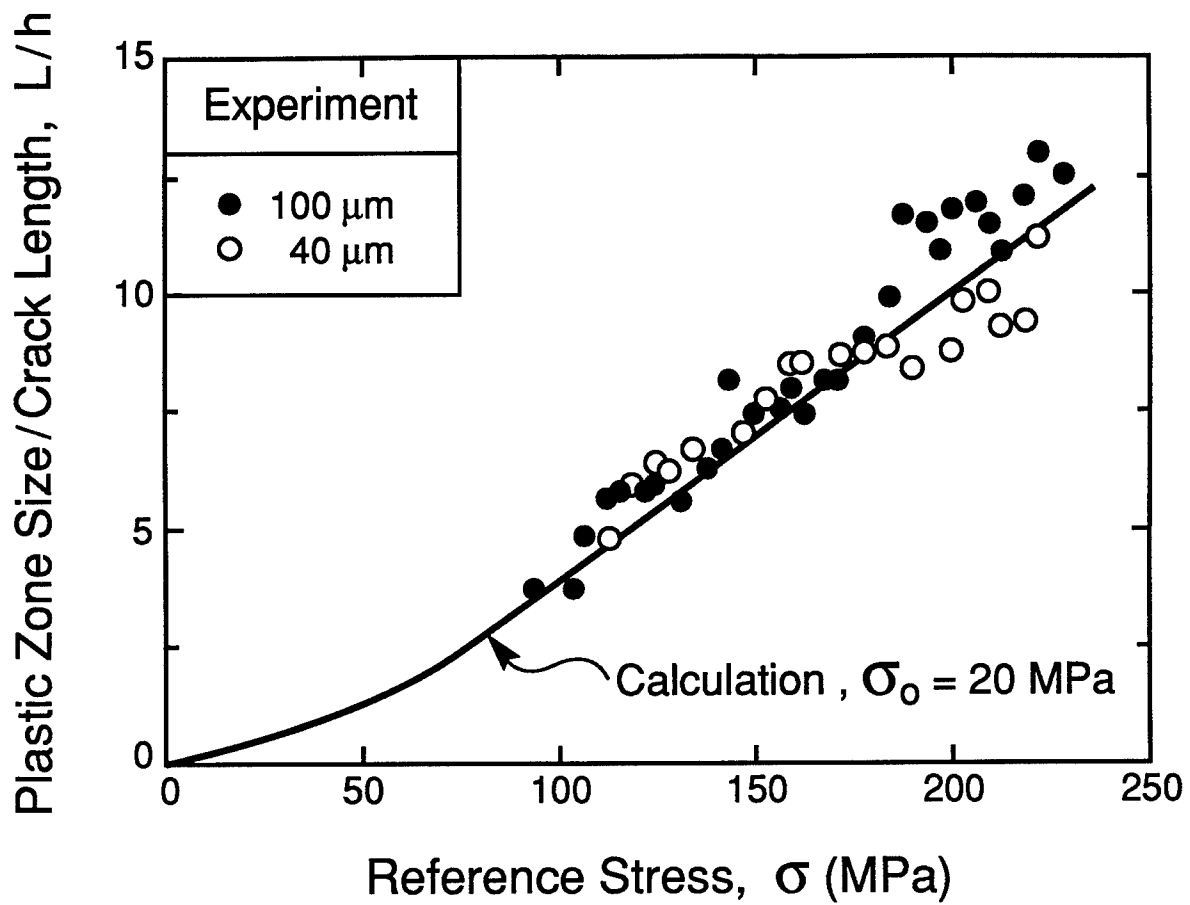


Figure 4.11

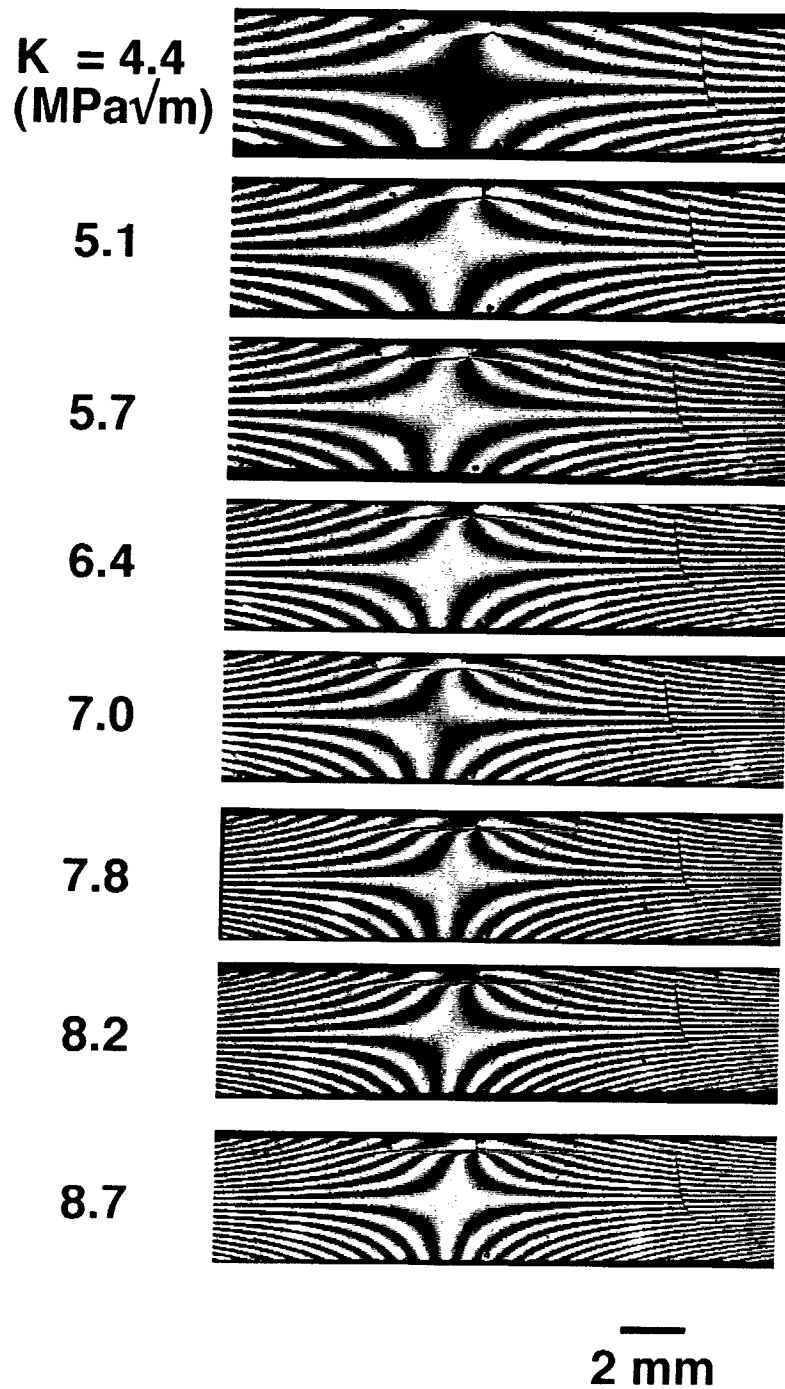


Figure 4.12

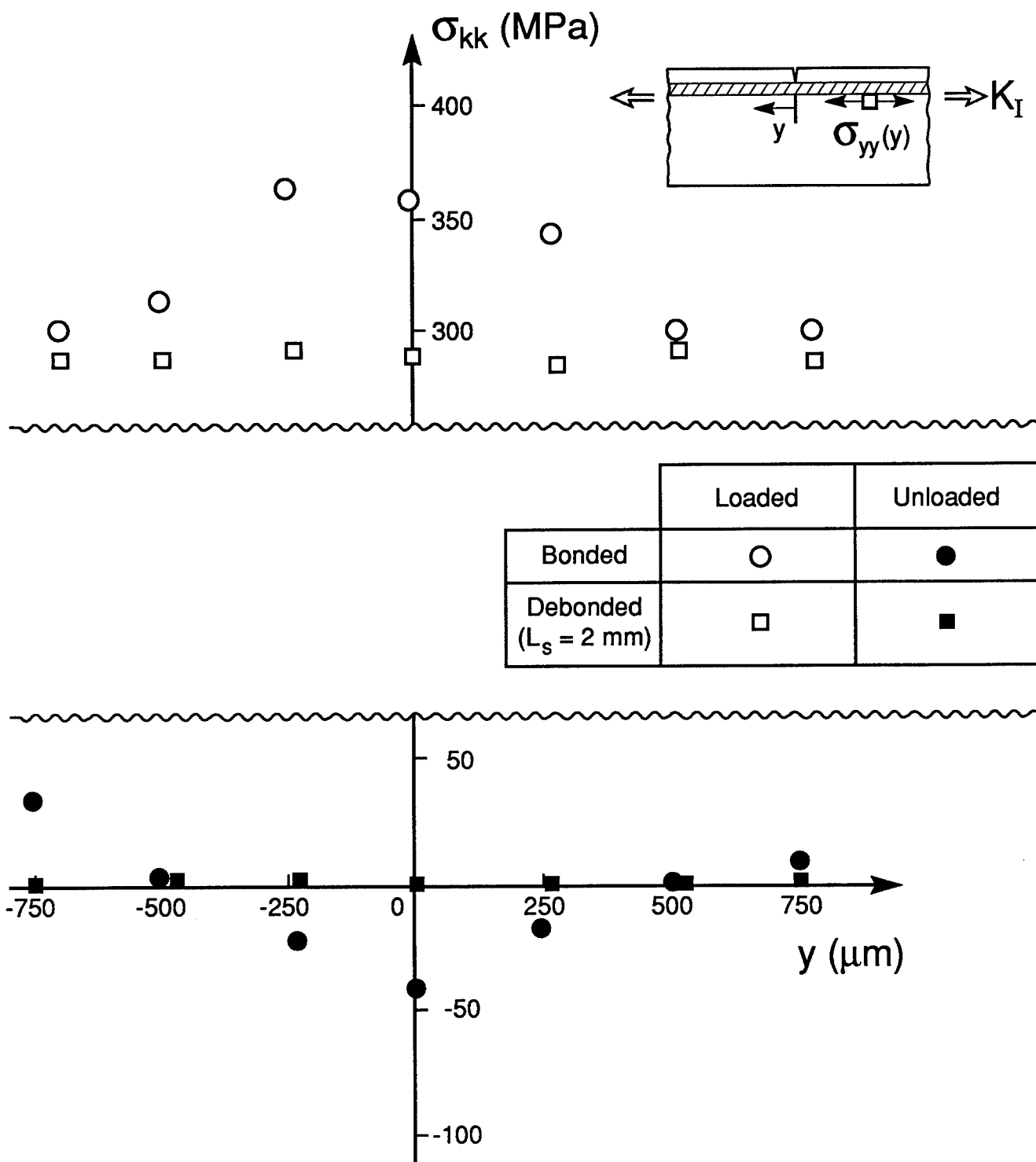
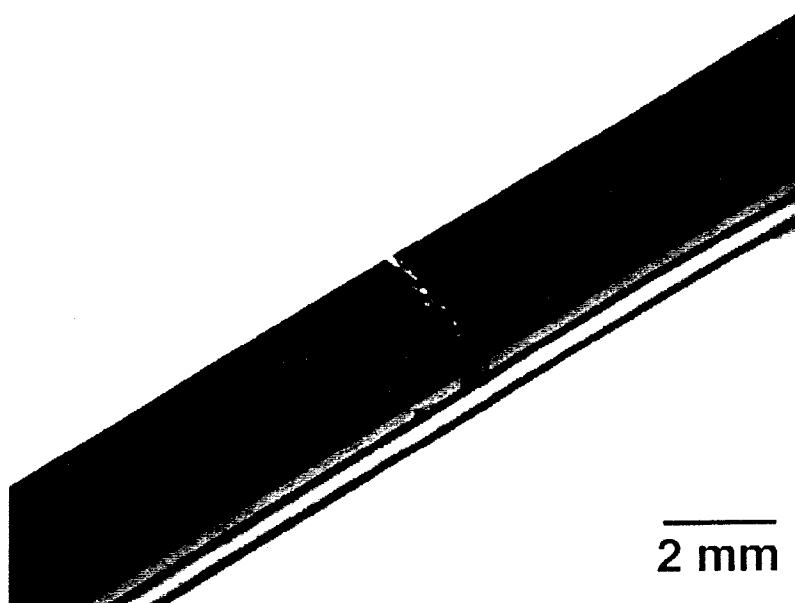
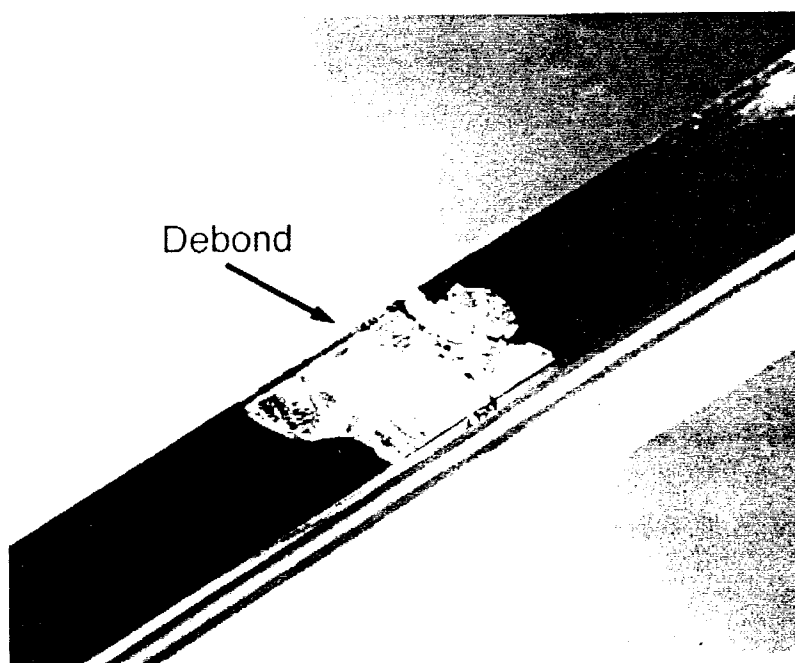


Figure 4.13



1 Load Cycle



50,000 Load Cycles

Figure 4.14

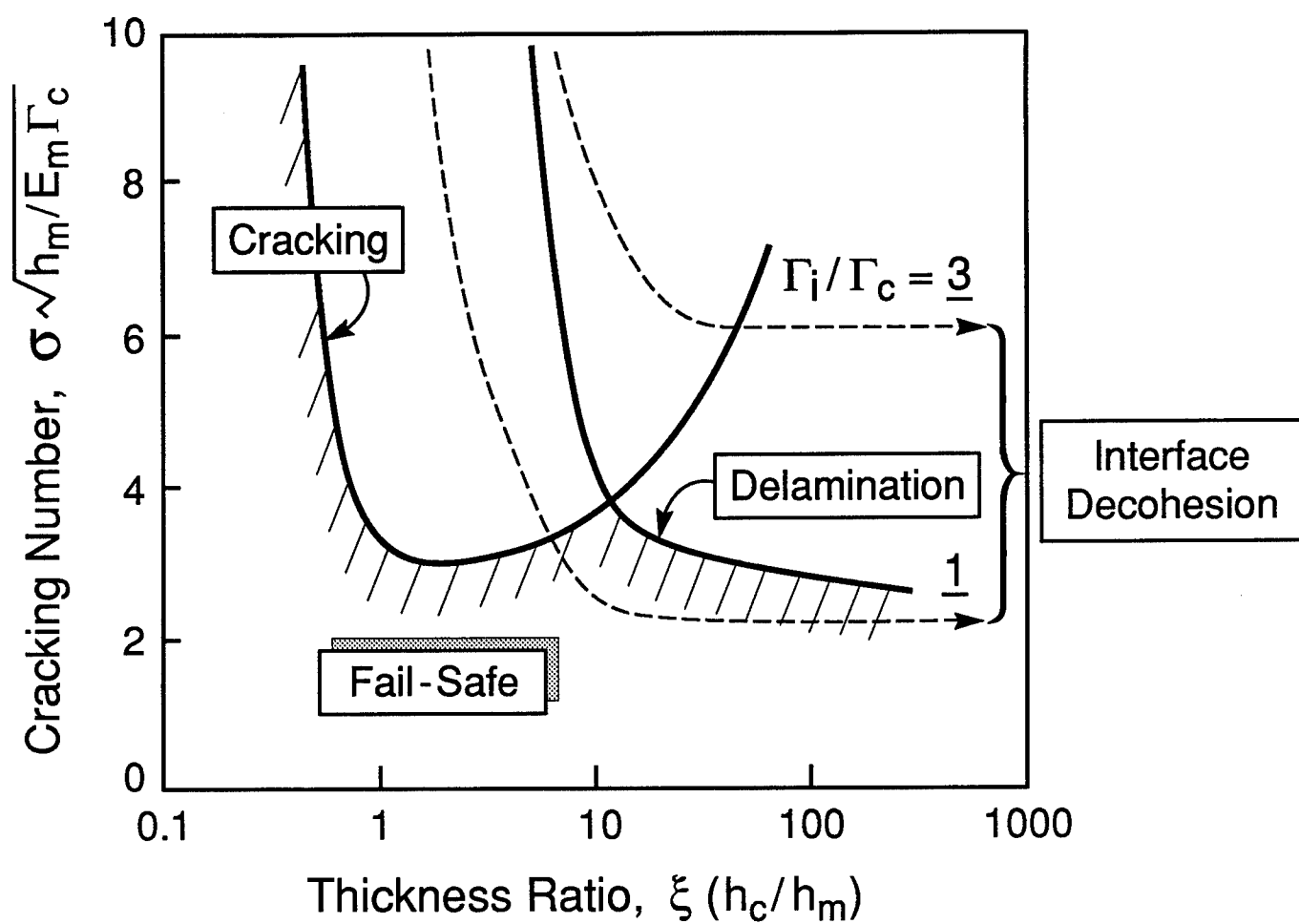


Figure 4.15

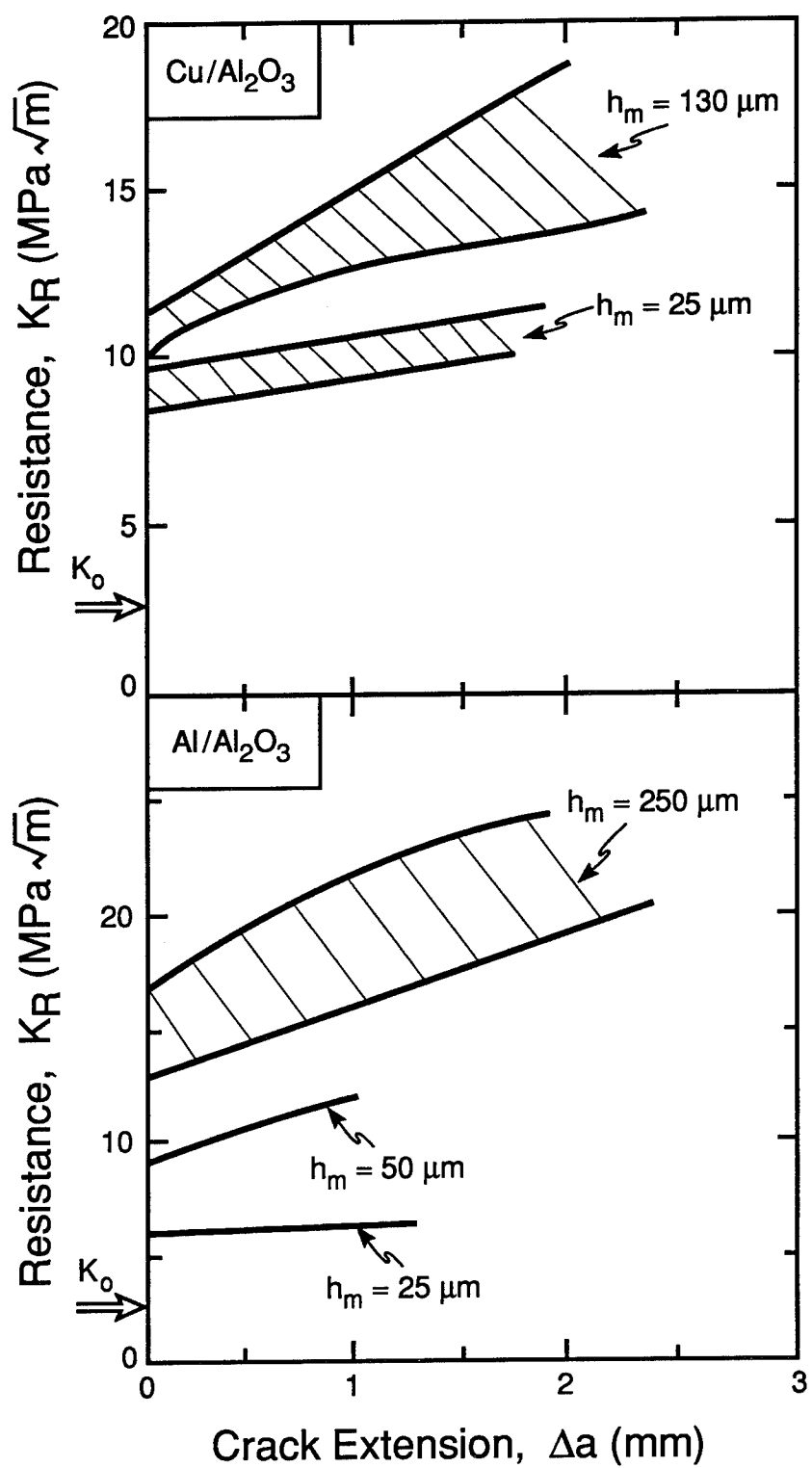
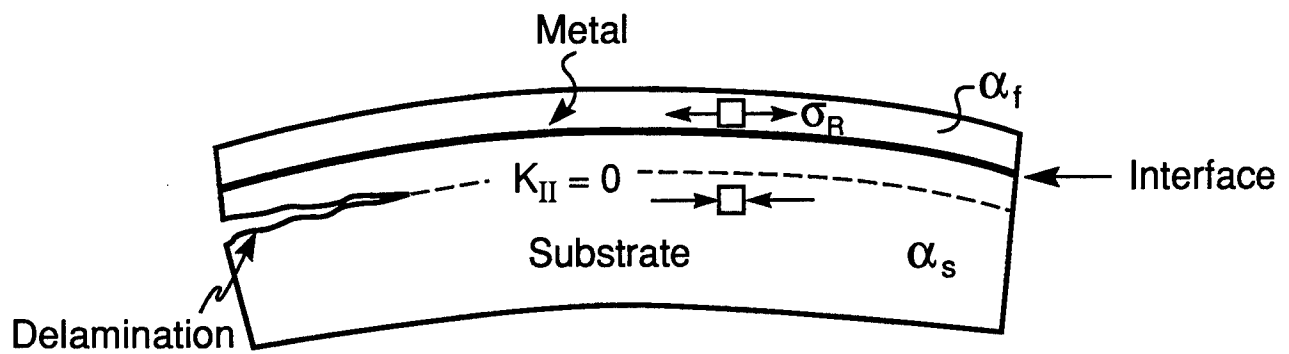
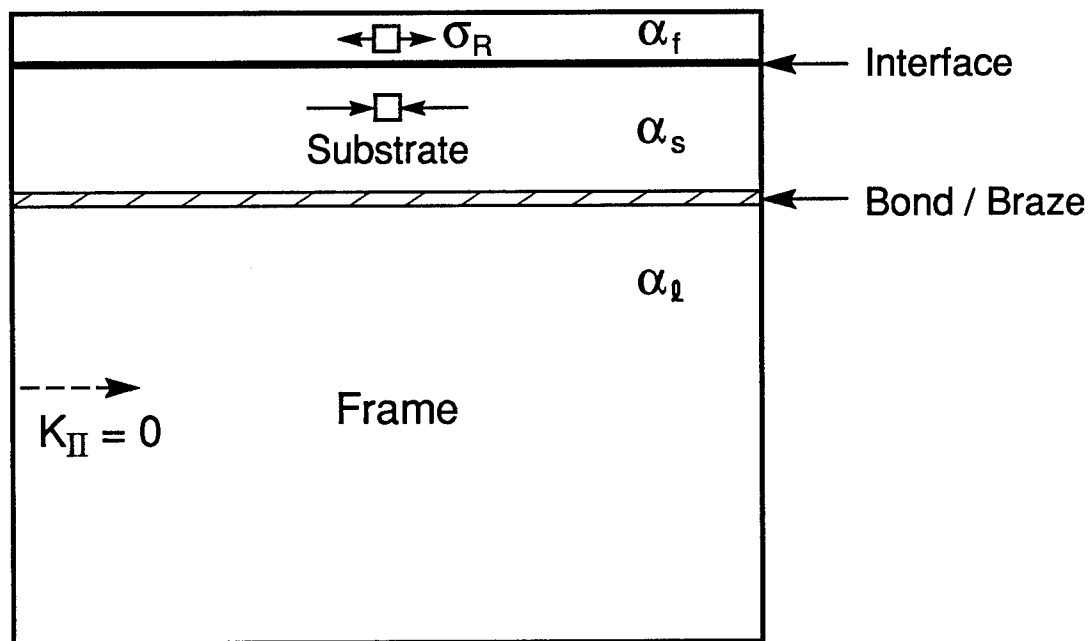


Figure 4.16



a) Bilayer ($\alpha_f > \alpha_s$)



b) Multilayer. ($\alpha_f \approx \alpha_l > \alpha_s$)

Fig. 4.17

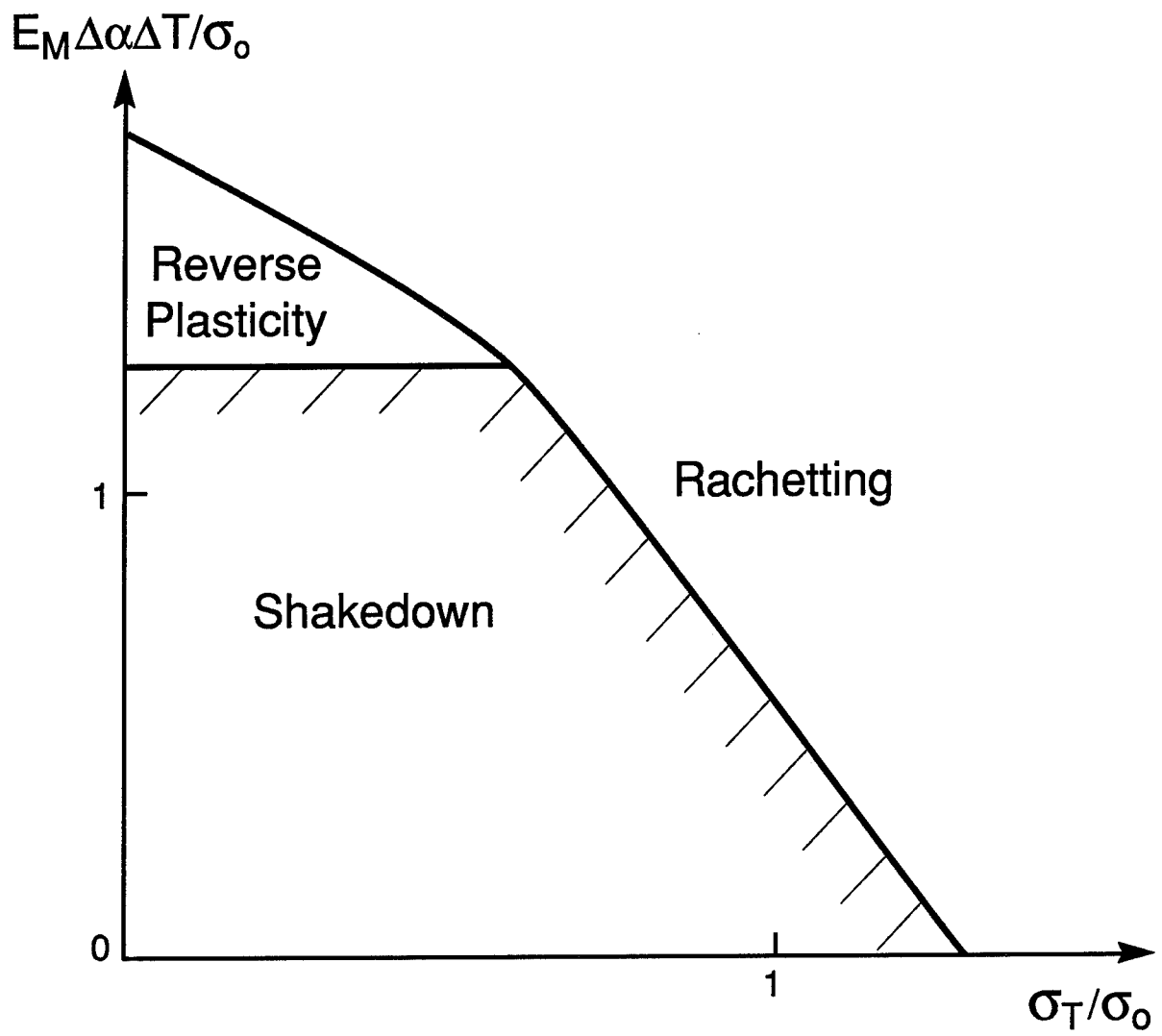
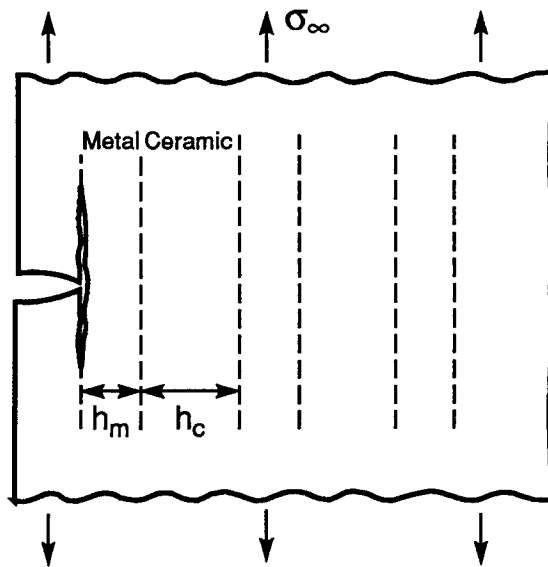
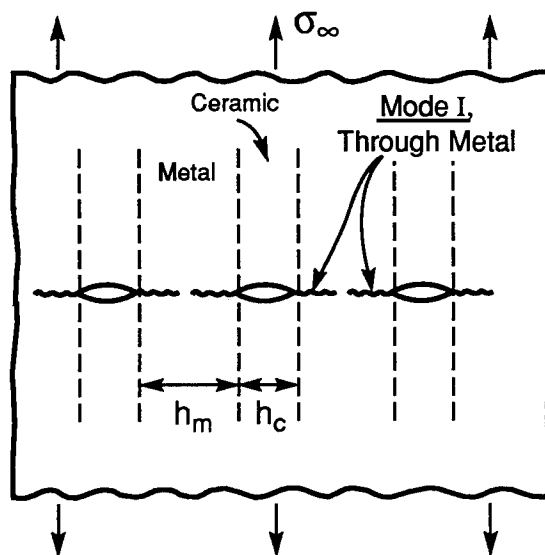


Figure 5.1

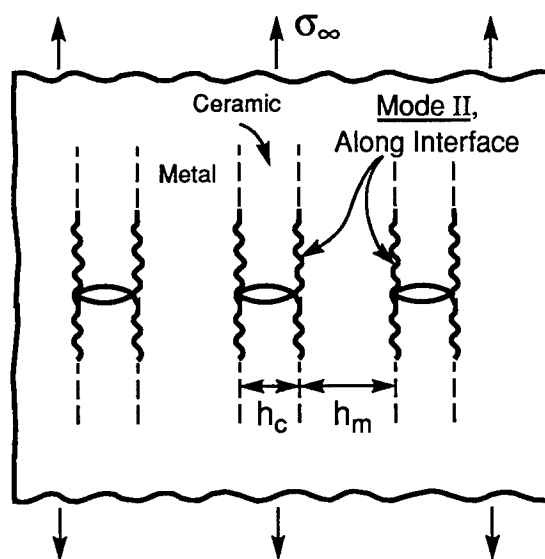
Mixed Mode
($\psi \cong 50^\circ$),
Along Interface



(a)



(b)



(c)

Fig. 5.2

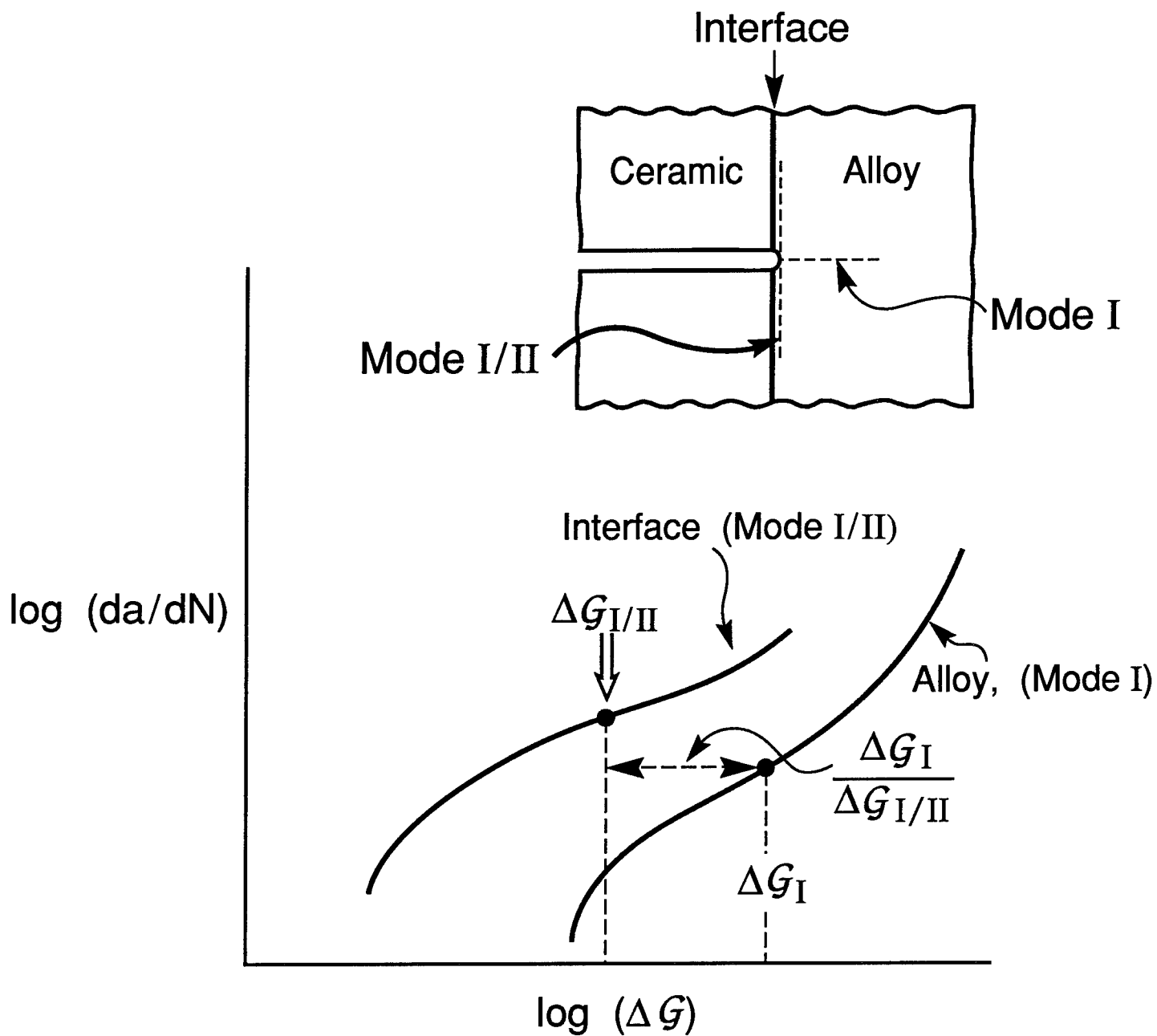


Figure 5.3



Figure 5.4

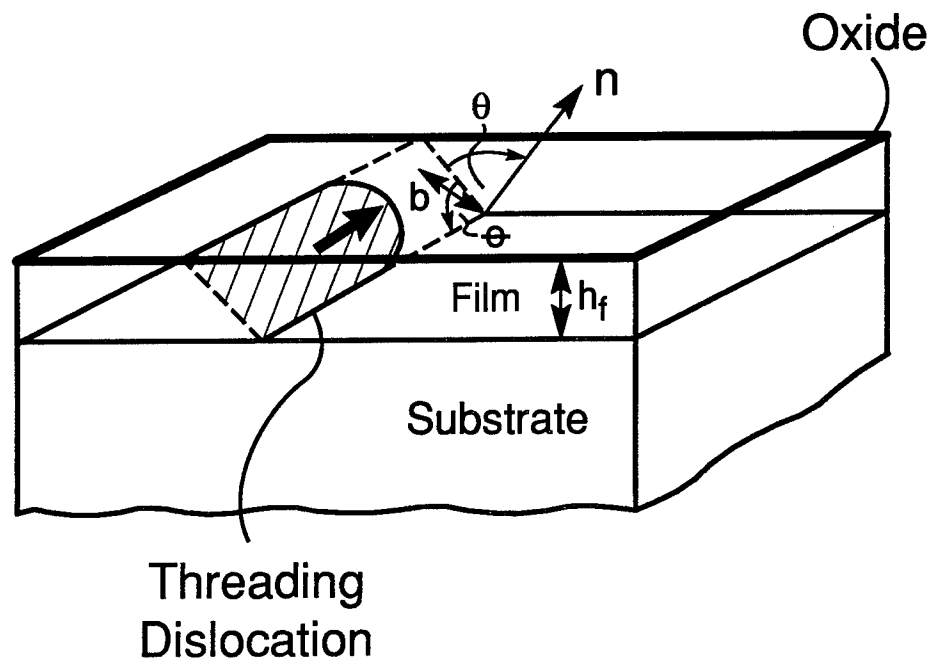


Fig. 6.1

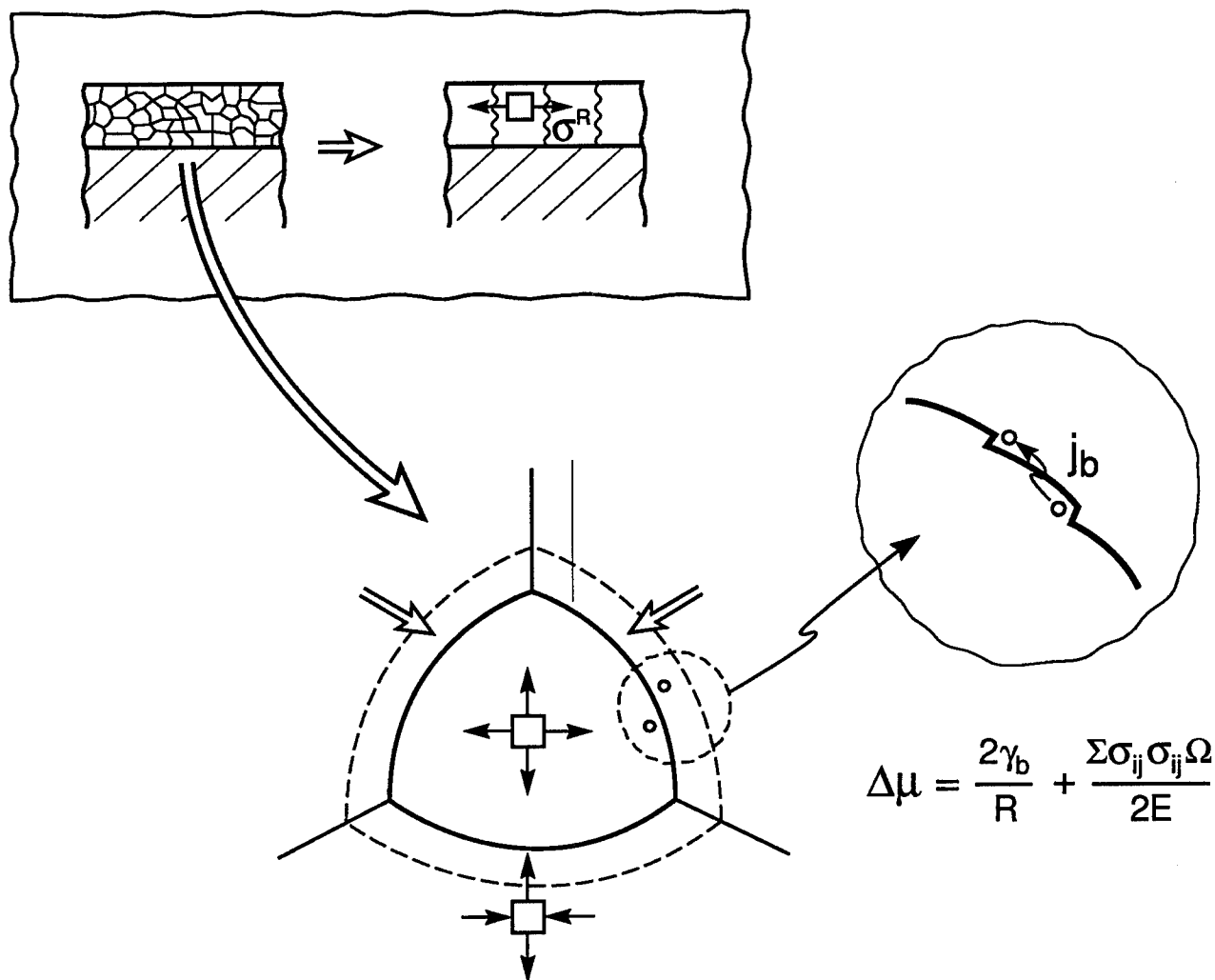


Fig. A1 Grain Growth Mechanism

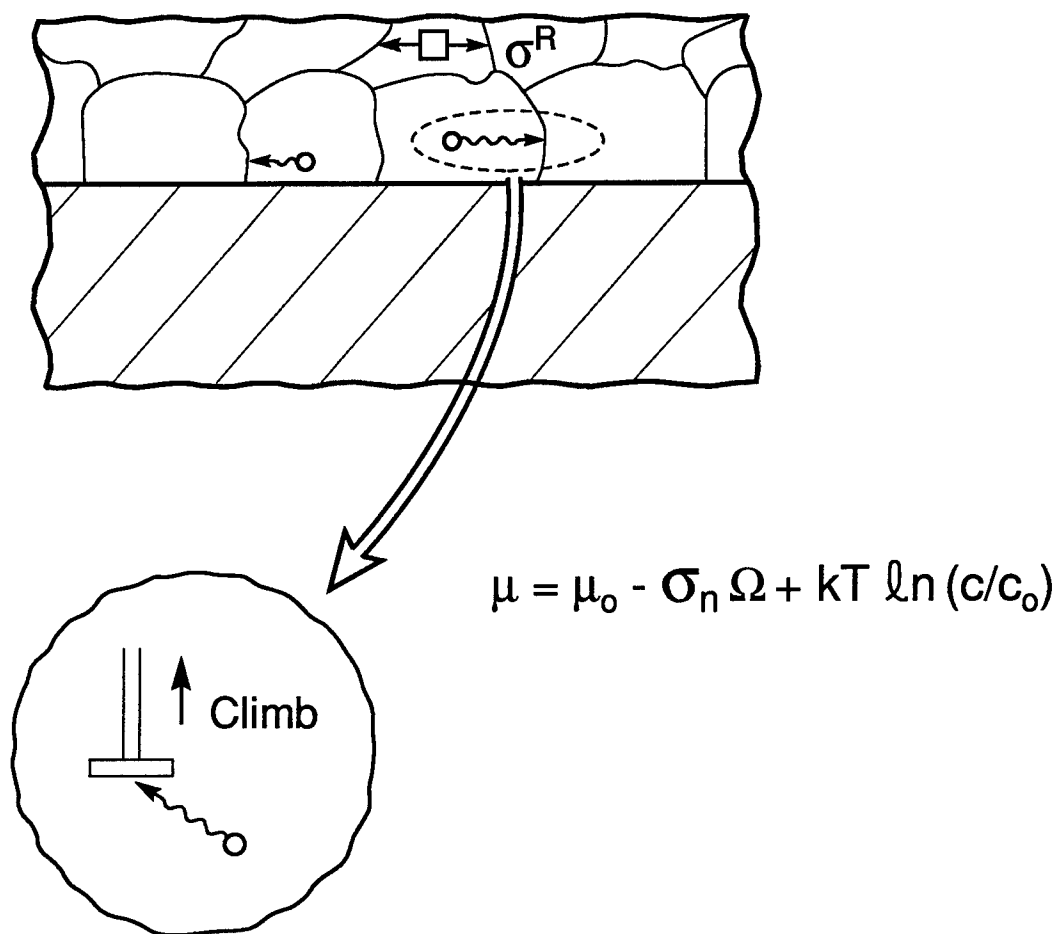


Fig. A2 Point Defect Anihilation Mechanism

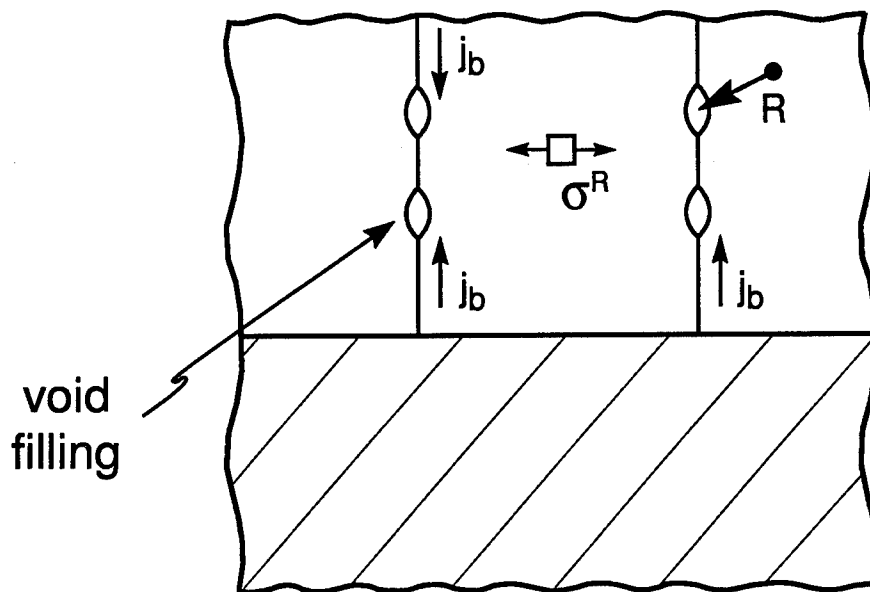


Fig. A3 Sintering

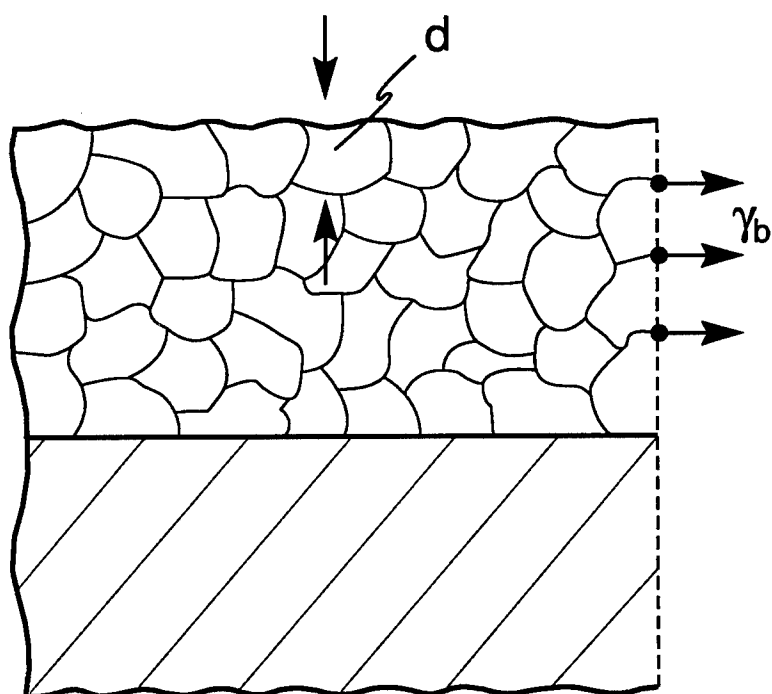
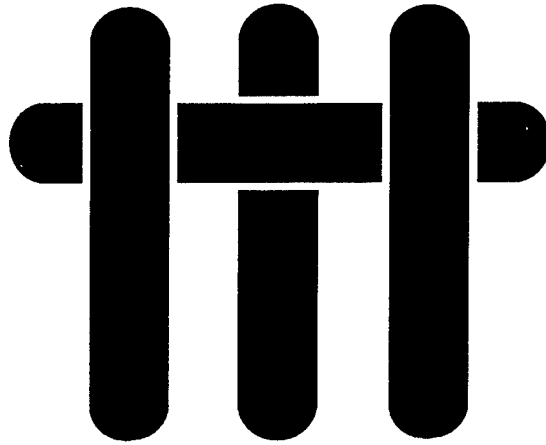


Fig. A4 Grain Boundary Stress

M A T E R I A L S



A FRACTURE RESISTANCE MEASUREMENT METHOD FOR BIMATERIAL INTERFACES HAVING LARGE DEBOND ENERGY

by

M.R. Turner, B.J. Dalglish, M.Y. He and A.G. Evans

Materials Department
College of Engineering
University of California, Santa Barbara
Santa Barbara, California 93106-5050

ABSTRACT

Experimental results obtained for the DCDC specimen demonstrate its capabilities for measuring the mode I fracture energy, Γ_I , of bimaterial interfaces. Two specific characteristics have been highlighted. (i) For interfaces characterized by a steady-state, Γ_I , the ability to obtain high-fidelity measurements over many millimeters of crack extension has been validated. The demonstrations have been made for glass/resin and sapphire/Au interfaces. Moreover, a concomitant ability to monitor interactions between the growing crack and the microstructure, including interface defects, has been presented. (ii) For interfaces that have differing mechanisms of crack growth *initiation* and *propagation*, such as sapphire/Pt, an ability to distinguish the initiation and arrest fracture energies has been illustrated. The corresponding capacity to monitor the associated mechanisms by optical microscopy has also been demonstrated.

1. INTRODUCTION

A range of different test methods for measuring the debond energy of metal/ceramic interfaces Γ_i has been developed¹⁻⁵ (Fig. 1). These methods encompass a range of mode mixities, with phase angles ψ ranging between 0 (mode I) and 90° (mode II). They have been widely exploited for interfaces having relatively low fracture energies, compared with that for the adjoining ceramic, Γ_c . However, they have limited applicability when Γ_i is significantly larger than Γ_c , because the cracks originally introduced at the interface tend to preferentially propagate through the ceramic.⁵ The phenomenon is characterized by a crack kinking diagram^{6,7} (Fig. 2) which indicates the expected crack path, as functions of Γ_i / Γ_c and ψ . It is evident from Fig. 2 that a negative phase angle encourages the crack to remain at the interface. The preferred test method should have this feature. The method should also allow the *stable* extension of the interface crack, subject to increasing loads. This situation leads to improved data fidelity, compared with specimens that cause unstable growth from a precrack.

The proposed method (Fig. 3) uses compressive loading to satisfy these two criteria. This method, referred to as the Double Cleavage Drilled Compression (DCDC) specimen,⁸⁻¹¹ has previously been used for monolithic brittle materials. The specimen geometry consists of a rectangular beam with a hole drilled in the center (Fig. 3). The beam is compressively loaded. A comprehensive analysis of this specimen is given in a companion paper.¹² Compressive loading causes tensile stresses to develop at the poles of the hole. Cracks then nucleate, extend from the poles and propagate axially in mode I ($\psi \approx 0$). At a constant applied load, the stress intensity diminishes upon crack extension, resulting in *stable crack propagation*. A non-dimensional relationship for the energy release rate is^{9,10,12}

$$\frac{1}{\sigma} \sqrt{\frac{EG}{R}} = F(a/R, w/R) \quad (1)$$

where R is the hole radius, E is Young's modulus, a is the crack length (Fig. 3), $2w$ is the plate width and F is a non-dimensional function given by¹²

$$F = (\sqrt{\pi} R/w) / [1 + (a/R)(0.235 - 0.259 R/w)] \quad (2)$$

In the DCDC specimen, when cracks attempt to form in the ceramic (at off-axis locations) rather than at the interface, such cracks are subject to a substantial mode II loading. Such loadings deflect the cracks *back toward the interface*.^{6,7,12} The consequence is a strong preference for interface fracture, even at relatively large Γ_i / Γ_c .¹²

The present study applies this specimen to the study of interface fracture by using a sandwich geometry, with a thin metal (Pt, Au) or polymer layer between two ceramic (Al_2O_3) or glass beams. Since the metal or polymer layers are thin compared with the specimen dimensions, the interface crack has almost the same energy release rate as that for the monolithic body¹² (Eqns. 1 and 2), with E being the Young's modulus of the *ceramic*. For the specific materials used in the present study, the energy release rate deviates from Eqn. (2) by less than 5%.¹² Moreover, the crack is still essentially mode I ($\psi \approx 0$). Specifically, the phase angle varies between $\sim 5^\circ$ for thermoset resin-bonded glass, down to $\sim 1^\circ$ for Al_2O_3 /Pt.¹² Such small changes from mode I should not have a significant influence on the interface fracture energy.^{5,13-17}

Finally, a technique for measuring the crack length a from the crack opening displacement, δ_o , is presented. It relies on the results of a numerical analysis,¹² which gives

$$E\delta_o/\sigma R = \Delta(a/R, w/R) \quad (3)$$

where Δ is a non-dimensional coefficient.¹²

2. EXPERIMENTAL

2.1 Materials

The initial investigation, plus the specimen validation, have been conducted on a model system consisting of glass bonded with thermoset resin. Additional results are presented for two oxide/metal interfaces prepared by diffusion bonding: sapphire/Au and sapphire/Pt. For preparation of these specimens, sandwich discs consisting of (a) soda lime glass bonded with a thermoset resin and (b) sapphire diffusion bonded with either 25 μm of platinum¹⁴ or 10 μm of gold^{15,16} have been prepared using procedures described elsewhere.¹³⁻¹⁶ To establish an interfacial precrack in the glass/thermoset resin specimens, a thin layer of vacuum grease was placed on the glass plate prior to bonding.

After bonding, the discs were cut into beams using diamond wheels, to achieve the specimen dimensions (Fig. 3); $L/w = 10$; $w/h = 1.2$. A hole was then introduced at the beam center, by diamond drilling, followed by reaming, such that, $w/R = 2 \rightarrow 3$. Finally, the ends of the beams were ground flat and parallel to ensure uniform transmission of compressive loads into the beams, upon testing.

2.2 Test Procedures

The platens to be used for compression loading consisted of ground alumina plates. A tungsten carbide hemisphere placed on the upper platen provided uniform loading when minor misalignments existed. A high-resolution optical microscope, equipped with a video system, was used to provide optical monitoring of interface debonds. In most cases, the debond could be readily identified by using either oblique,

reflected or transmitted illumination. In some instances, a red dye penetrant was used to highlight the debond region.

Loads were applied using a conventional hydraulic testing system. For the glass/epoxy and $\text{Al}_2\text{O}_3/\text{Au}$ specimens, precracks were introduced by monotonic loading in a wet atmosphere that encouraged stress corrosion.¹⁵ For the $\text{Al}_2\text{O}_3/\text{Pt}$ interfaces, cyclic loading was used with a maximum-to-minimum stress ratio, $R = 0.1$, and a frequency of 0.25 – 1.0 Hz. The peak load was chosen such that it did not exceed the interface fracture energy (based on preliminary estimation of Γ_i). After precracking to a crack length, $a \approx 3\text{--}4 R$, monotonic loading was used to extend the crack and thereby, evaluate the interface fracture resistance.

A crack opening displacement (COD) gage was also connected to the specimen after establishing an interfacial precrack. This was used to monitor the compliance and hence, provide an independent estimate of the crack length.

3. EXPERIMENTAL RESULTS

3.1 Glass/Thermoset

The initial crack growth from the precrack comprised debonds in the form of fingers (Fig. 4). Then, at a crack extension, $\Delta a/R \approx 6$, a well-delineated crack front developed. Subsequent crack growth occurred through the advancement of this crack front (Figs. 5a–d). The debond resistance Γ_R was thereby obtained as a function of crack extension, Δa (Fig. 6). This was achieved by using Eqn. (1) (upon equating \mathcal{G} to Γ_R) with the crack lengths evaluated by optical measurements and with F given by Eqn. (2). Crack lengths were also estimated from the crack opening displacement, δ_o . It is apparent from Fig. 6 that Γ_R is essentially *independent of crack extension*. Hence, interface decohesion can be represented by an explicit fracture energy Γ_i , in the range,

$\Gamma_i = 24 \pm 4 \text{ Jm}^{-2}$. Note that these Γ_i are substantially larger than the fracture energy of glass ($\Gamma_c \approx 8 \text{ Jm}^{-2}$).

3.2 Sapphire/Gold

The initial growth of the precrack again occurred by fingering. To obtain a well-delineated precrack front, the specimen was held at a constant load with water injected into the crack. This caused the ligaments between the fingers to debond by stress corrosion,^{15,16} resulting in a precrack, $a_0 \approx 3\text{--}4R$. Upon subsequent loading, stable crack extension occurred (Figs. 7a–d). Most specimens gave a constant mode I interfacial fracture energy, $\Gamma_i = 10 \pm 2 \text{ J/m}^2$ independent of crack extension.^{15,16} (Fig. 8).

The crack extension velocity and trajectory were influenced by the interface porosity, with the debonds being attracted by the porosity ahead of the crack front,²⁰ as noted in earlier studies conducted in mixed mode.^{15,16}

3.3 Sapphire/Platinum

After precracking by fatigue, monotonic loading resulted in debond nucleation *ahead of the crack front*, at interfacial voids. These voids coalesced in the vicinity of grain boundaries in the Pt (Fig. 9). Upon increasing the load, void coalescence lead to the formation of *debond patches*. At a maximum load, rapid coalescence of the debonded regions occurred, resulting in abrupt crack growth, followed by crack arrest. There was a corresponding drop in load. Such behavior has many similarities to crack growth by ductile fracture.^{5,18} Yet, examination of the fracture surfaces by scanning electron microscopy and EDS indicated that there was no Pt (and no impurities or contaminants) on the sapphire fracture surface. A discussion of the associated fracture mechanisms is presented elsewhere.²⁰

Based on the precrack length and the maximum load, the mode I initiation toughness was obtained from Eqns. (1) and (2) as $\Gamma_i^\circ \approx 52 \text{ J/m}^2$. The corresponding

arrest toughness was $\Gamma_i^a \approx 30 \text{ J/m}^2$. These values are appreciably larger than the fracture energy of the sapphire ($\Gamma_c = 10\text{--}20 \text{ Jm}^{-2}$, dependent on orientation).¹⁹ This finding again affirms the postulate that the DCDC specimen is capable of measuring interface fracture energies that exceed the fracture energy of the adjoining material.¹²

4. REMARKS

The present experimental study, in conjunction with the companion analysis,¹² has demonstrated the unique capabilities of the DCDC specimen for measuring the mode I fracture toughness of bimaterial interfaces. Data for glass/resin and sapphire/Au interface have demonstrated that high-fidelity information can be obtained, when Γ_i is invariant with crack extension. This ability obtains because the crack extends in a *stable manner* and *remains at the interface*. In consequence, continuous measurements of Γ_i can be made as the crack propagates. This enables interactions with the microstructure to be carefully probed, as elaborated elsewhere.²⁰

The measurements of interface cracking for the sapphire/Pt interface have indicated additional opportunities associated with the DCDC test protocol. Initiation fracture energies can be measured with good accuracy when the crack growth mechanism involves the nucleation and coalescence of voids *ahead of the crack* (by mechanisms similar to ductile fracture).¹⁸ Moreover, measurements are possible, even though the fracture energy substantially exceeds that of adjoining material. The further ability to achieve crack arrest and to obtain the arrest toughness has been demonstrated. There is a concomitant potential for studying the mechanisms of crack extension by direct optical microscopy.

These preliminary observations have implications for evaluation of the mechanisms of crack growth at bimaterial interface. The mechanistic details (and their

consequences) are discussed elsewhere.²⁰ The emphasis of this study has been on test method development and validation.

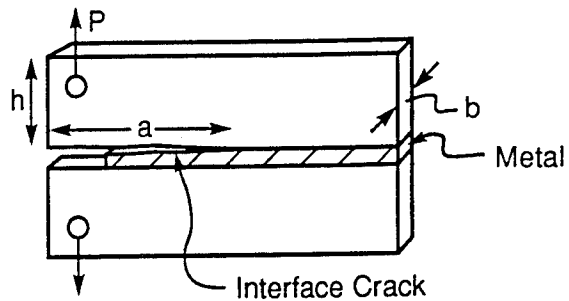
REFERENCES

- [1] R.M. Cannon, B.J. Dalgleish, R.K. Dausthart, T.S. Oh and R.O. Ritchie, *Acta metall. mater.*, **39**, 2145 (1991).
- [2] N.P. O'Down, C.F. Shih and M.G. Stout, *Int. J. Solids Struct.*, **29**, 571 (1992).
- [3] J.-W. Wang and Z. Suo, *Acta metall. mater.*, **38**, 1279–90 (1990).
- [4] P.G. Charalambides, J. Lund, R.M. McMeeking and A.G. Evans, *J. Appl. Mech.*, **111**, 77 (1989).
- [5] A.G. Evans and B.J. Dalgleish, *Acta metall. mater.*, **40**, S295 (1992).
- [6] M.Y. He and J.W. Hutchinson, *J. Appl. Mech.*, **56**, 270–78 (1989).
- [7] M.Y. He, A. Bartlett, A.G. Evans and J.W. Hutchinson, *J. Am. Ceram. Soc.*, **74**, 767–71 (1991).
- [8] C. Janssen, *Proc. Xth Int'l. Congress on Glass*, Kyoto, Japan, 23–30 (1974).
- [9] T.A. Michalske, W.L. Smith and E.P. Chen, *Engr. Frac. Mech.*, **4S**, 637–42 (1993).
- [10] Hongda Cai, F.T. Faber and E.R. Fuller, Jr., *J. Am. Ceram. Soc.*, **75**, 3111–17 (1992).
- [11] T.A. Michalske and E.R. Fuller, Jr., *J. Am. Ceram. Soc.*, **68**, 586–90 (1985).
- [12] M.Y. He, M.R. Turner and A.G. Evans, *Acta metall. mater.*, to be published.
- [13] H.C. Cao and A.G. Evans, *Acta metall. mater.*, **7**, 295 (1989).
- [14] M. De Graef, M.R. Turner, B.J. Dalgleish and A.G. Evans, *Acta metall. mater.*, **40**, S333–S344 (1992).
- [15] I.E. Reimanis, B.J. Dalgleish and A.G. Evans, *Acta metall. mater.*, **39**, 3133–41 (1991).
- [16] I.E. Reimanis, B.J. Dalgleish, M. Brahy, M. Rühle and A.G. Evans, *Acta metall. mater.*, **38**, 2645–52 (1990).
- [17] J.W. Hutchinson and Z. Suo, *Adv. Appl. Mech.*, **28**, (1991).
- [18] J.R. Rice and M.A. Johnson, *Inelastic Behavior of Solids*, M.F. Kanninen, *et al.*, eds., McGraw-Hill (1970).
- [19] S.M. Wiederhorn, *J. Am. Ceram. Soc.*, **52**, 485 (1969).
- [20] M.R. Turner and A.G. Evans, to be published.

FIGURE CAPTIONS

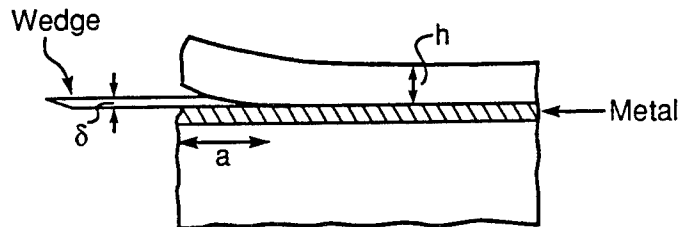
- Fig. 1. Test methods used to evaluate the interface fracture energy.
- Fig. 2. A kinking diagram indicating the loadings that induce the crack to deviate from the interface.
- Fig. 3. A schematic of the DCDC specimen used for interface toughness measurements.
- Fig. 4. Finger-like extension of the initial precrack at the resin/glass interface.
- Fig. 5. The evolution of a well-delineated crack at the resin/glass interface. The elliptical mark provides a reference.
- Fig. 6. The interface fracture resistance for the resin/glass system as a function of crack extension. Each set of results is obtained on one specimen. Results for four specimens indicate typical specimen-to-specimen variability.
- Fig. 7. Stable crack growth at the sapphire/Au interface.
- Fig. 8. Fracture resistance measurements for the sapphire/Au interface as a function of crack extension. Results for two different specimens are shown.
- Fig. 9. a) Schematic demonstrating the debonding process ahead of the precrack in the sapphire/Pt system. The debond patches occur at grain boundaries and other defects, such as precipitates.²⁰
b) *In situ* micrograph of a region ahead of the crack front, displaying debond patches.

$$0 \leq \psi \leq 5^\circ$$



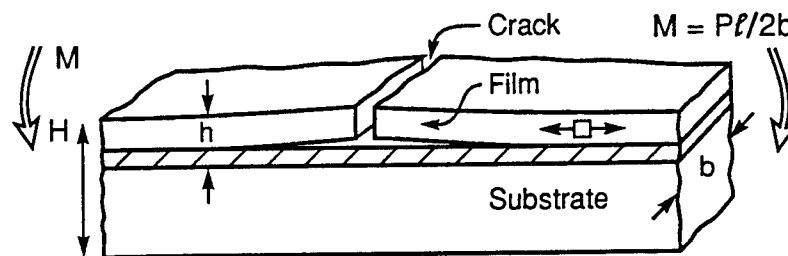
a) Double Cantilever Beam

$$\psi \approx -50^\circ$$



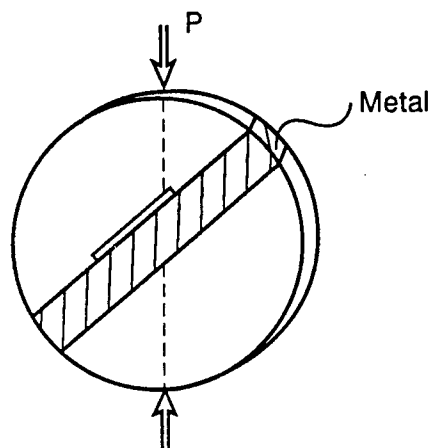
b) Wedge Loaded Peel Test

$$\psi \approx 50^\circ$$



c) Mixed Mode Flexure

$$0 \leq \psi \leq 90^\circ$$



d) Brasil Specimen

Figure 1

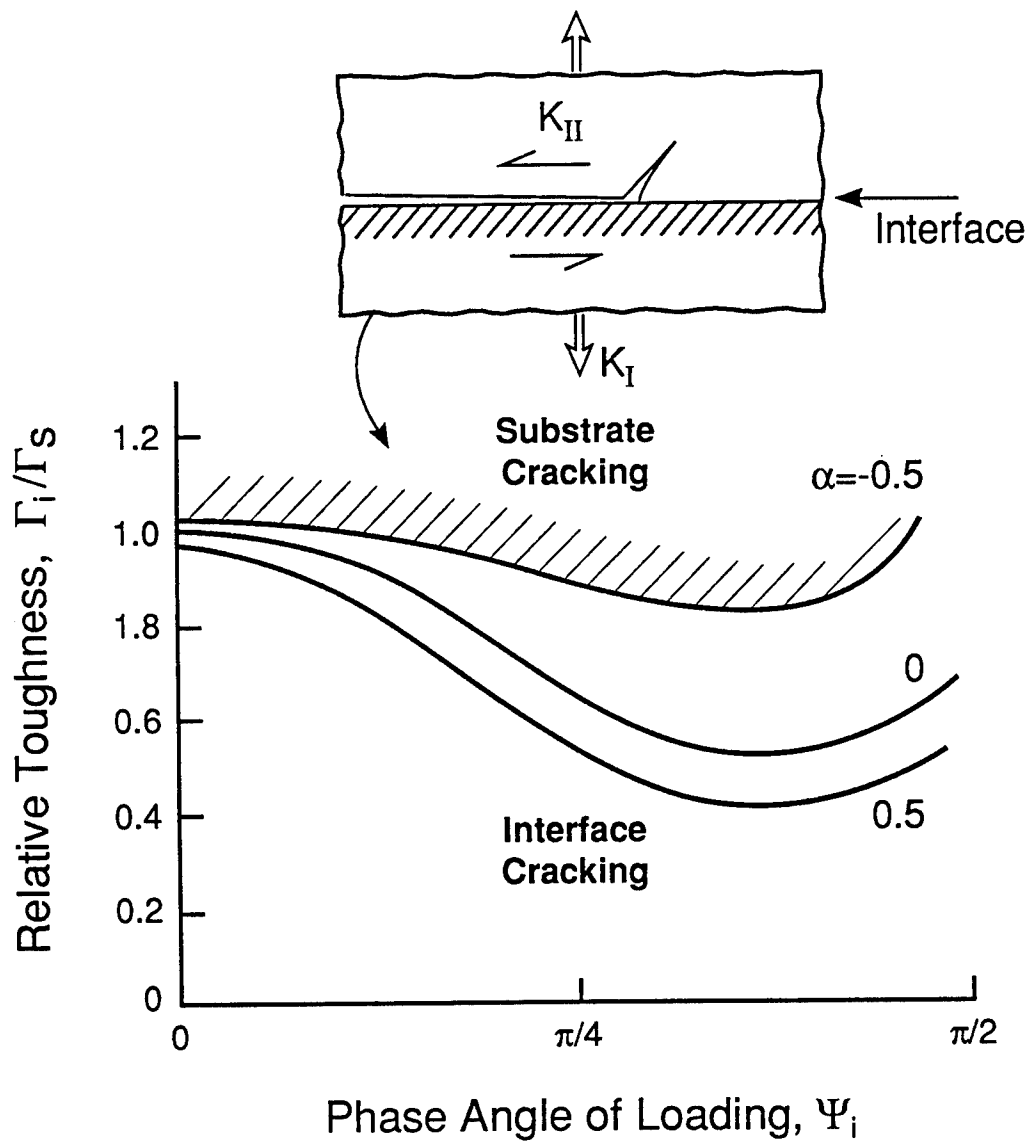


Figure 2

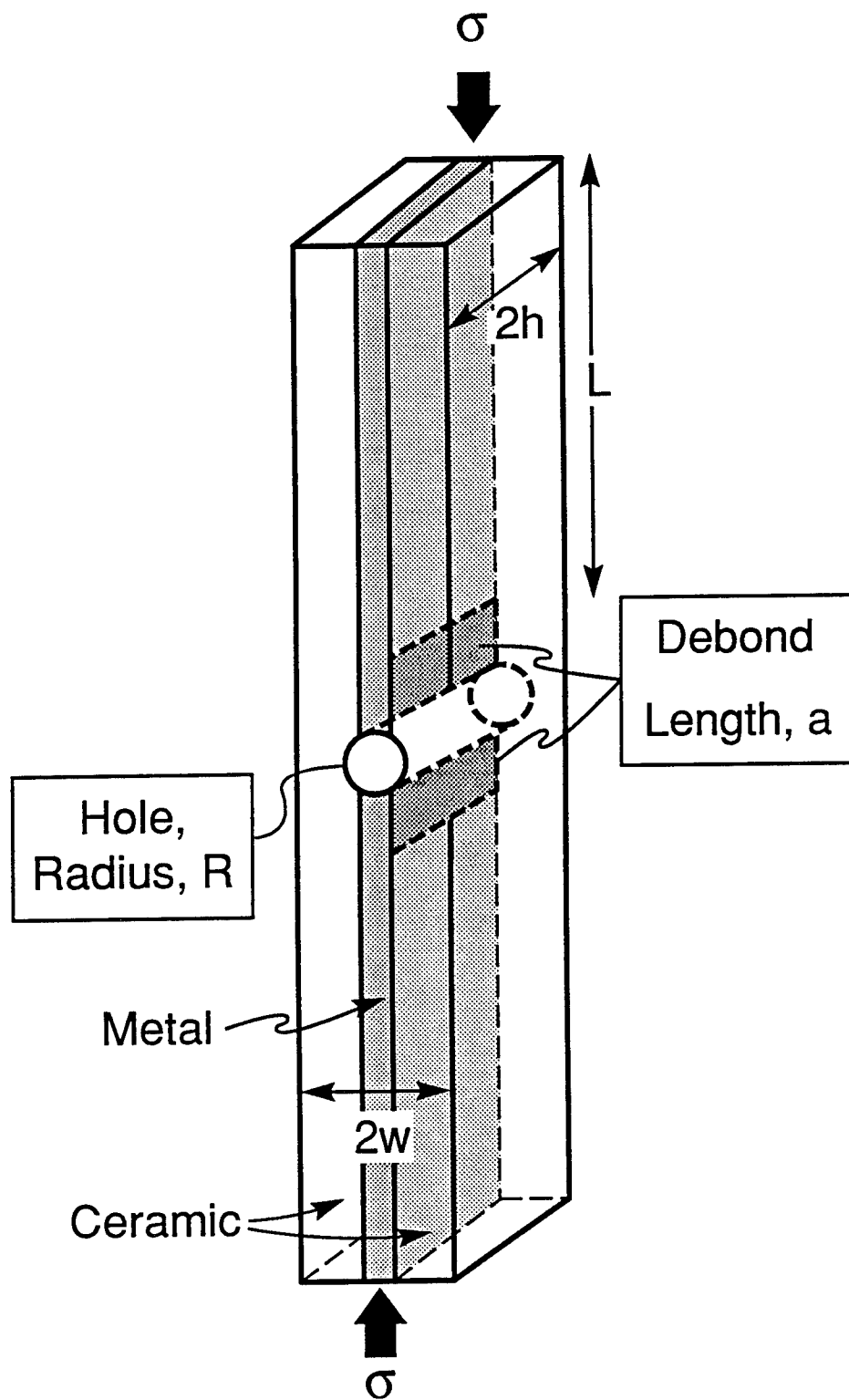


Figure 3

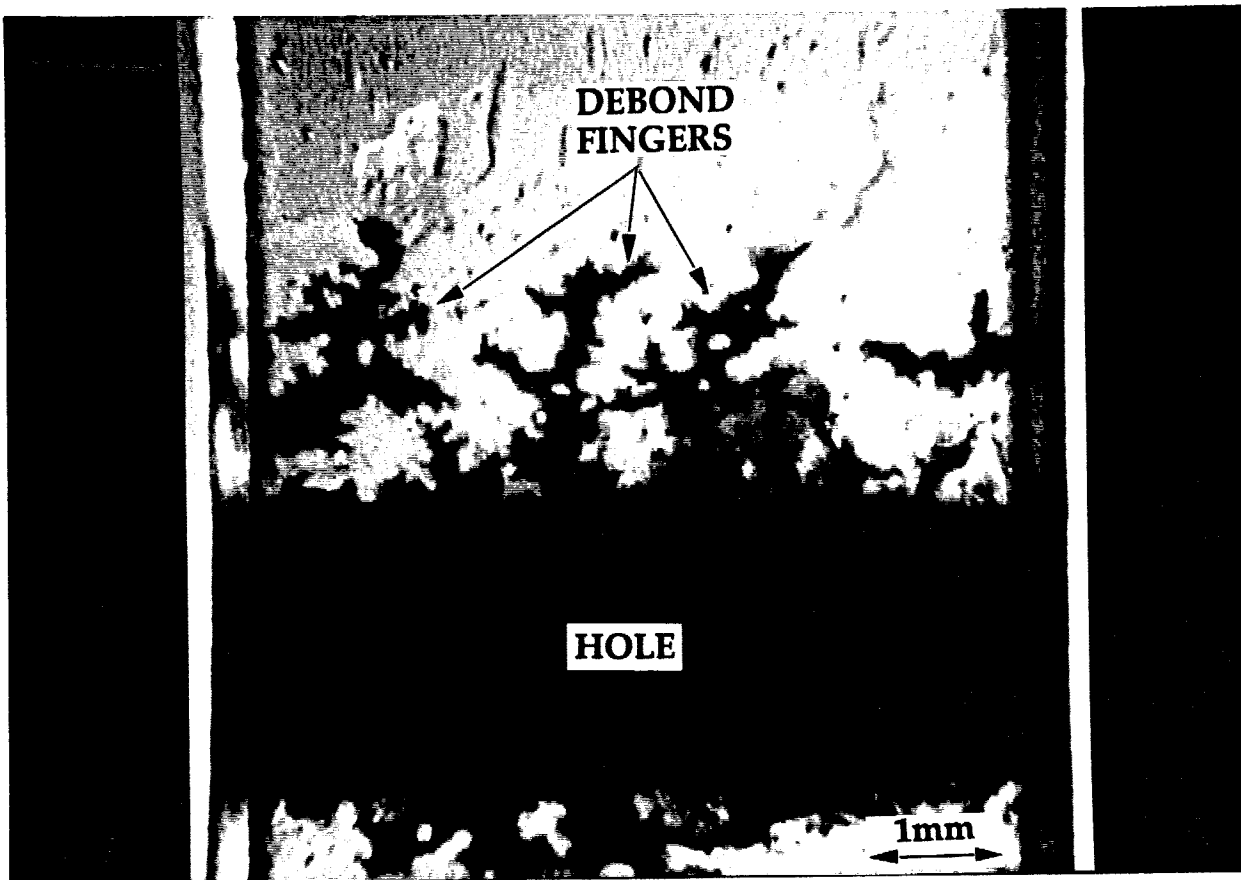


Figure 4

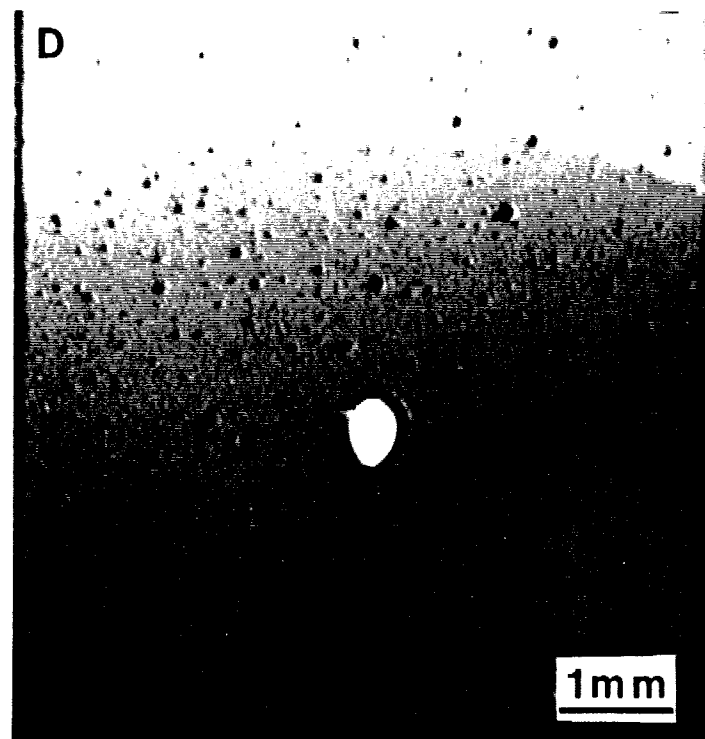
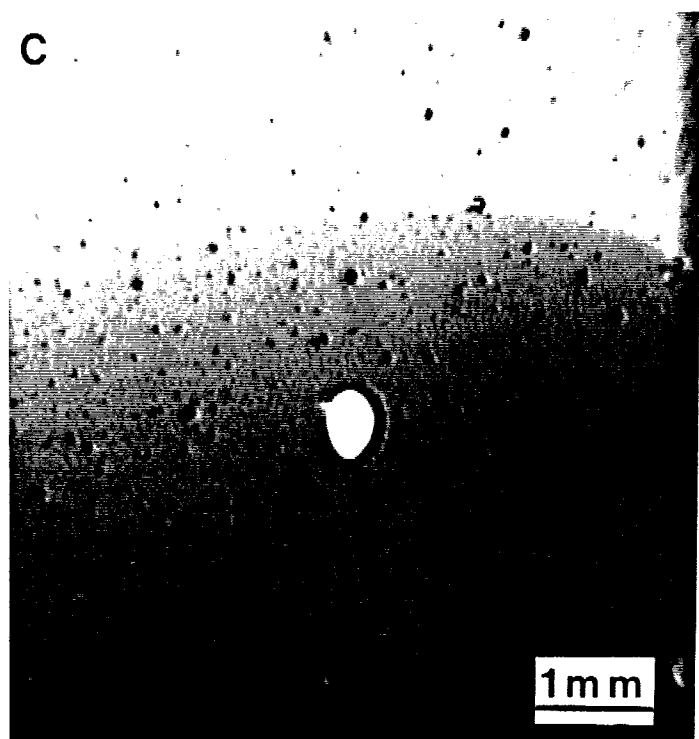
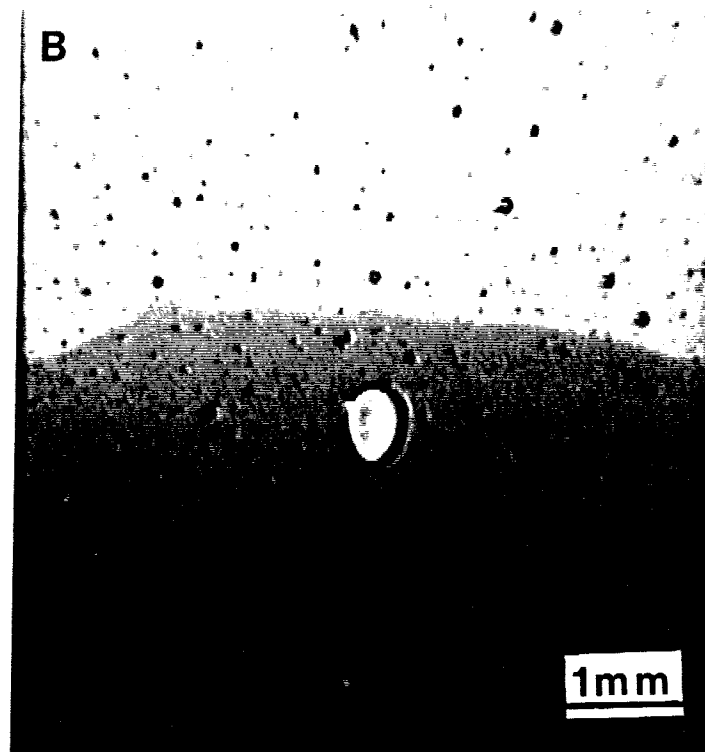
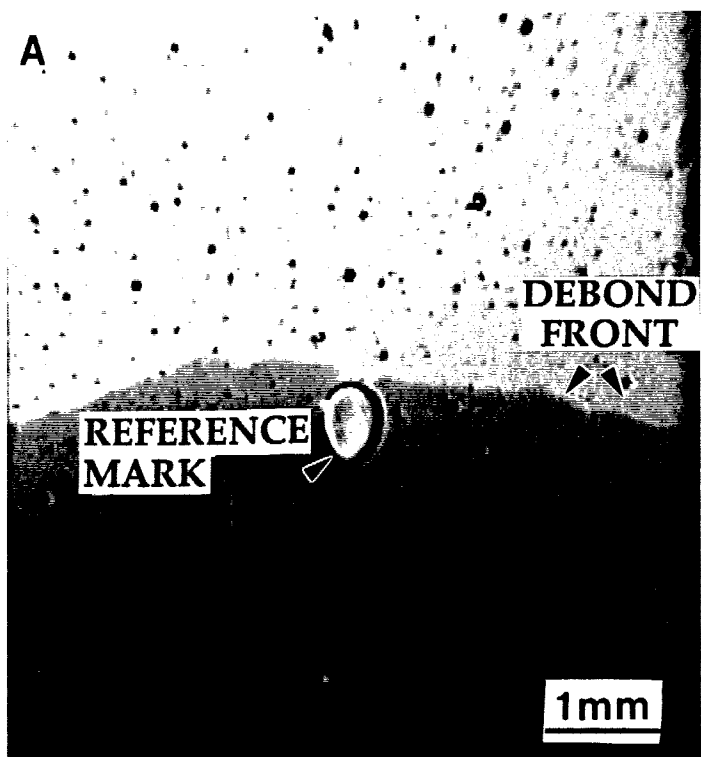


Figure 5

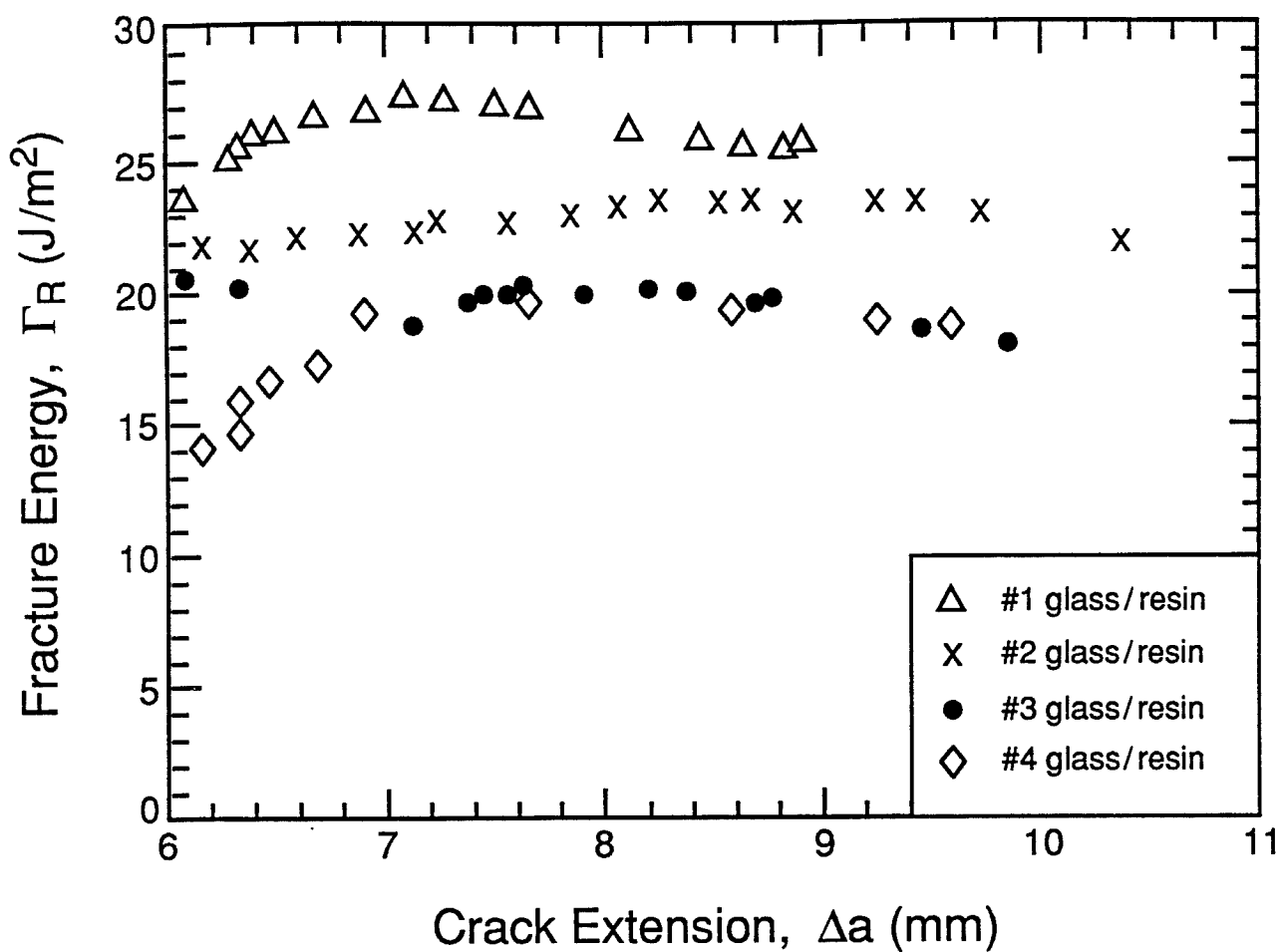
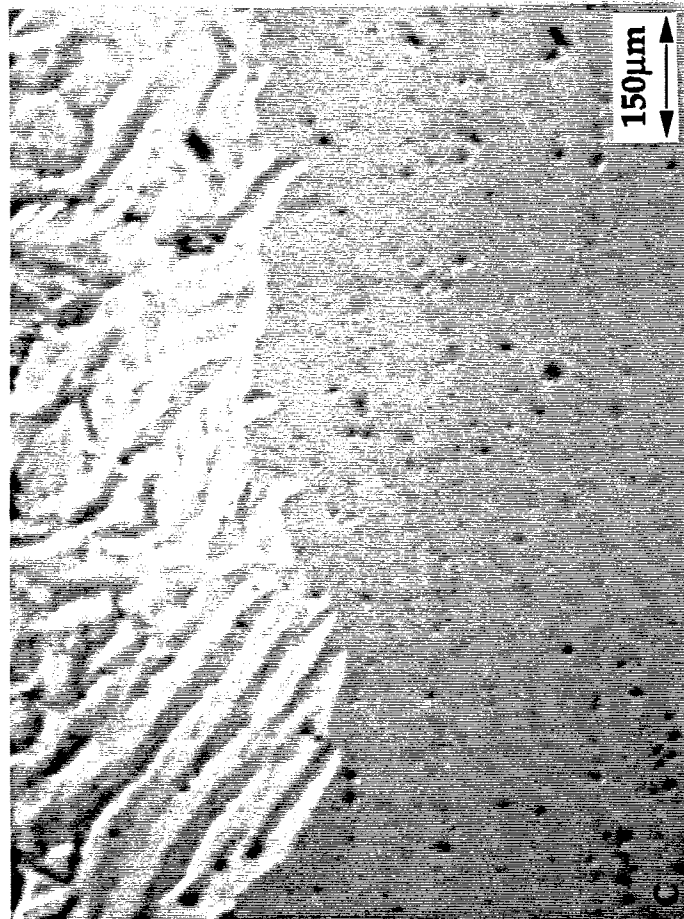
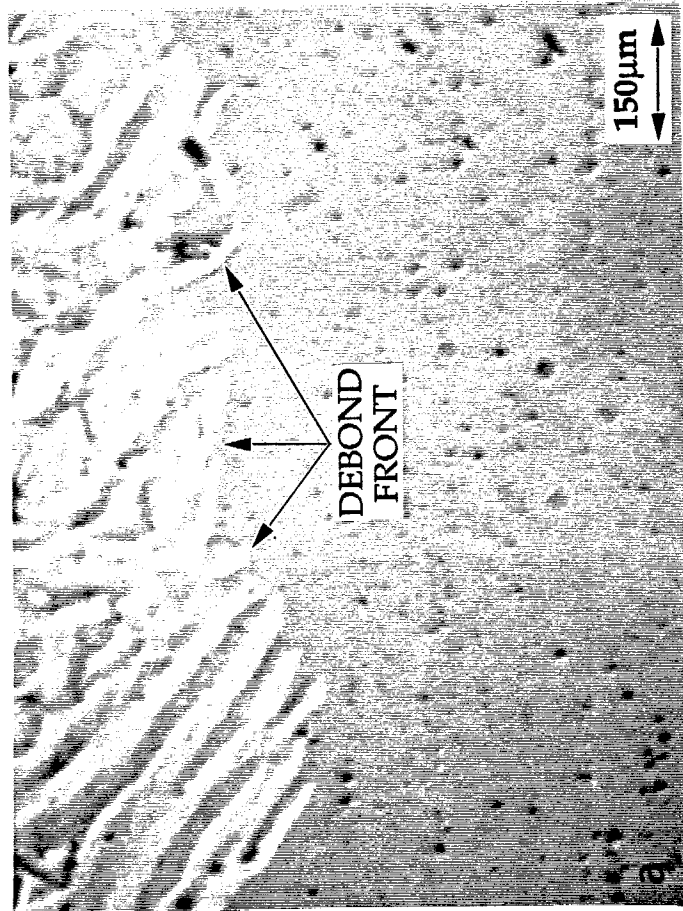
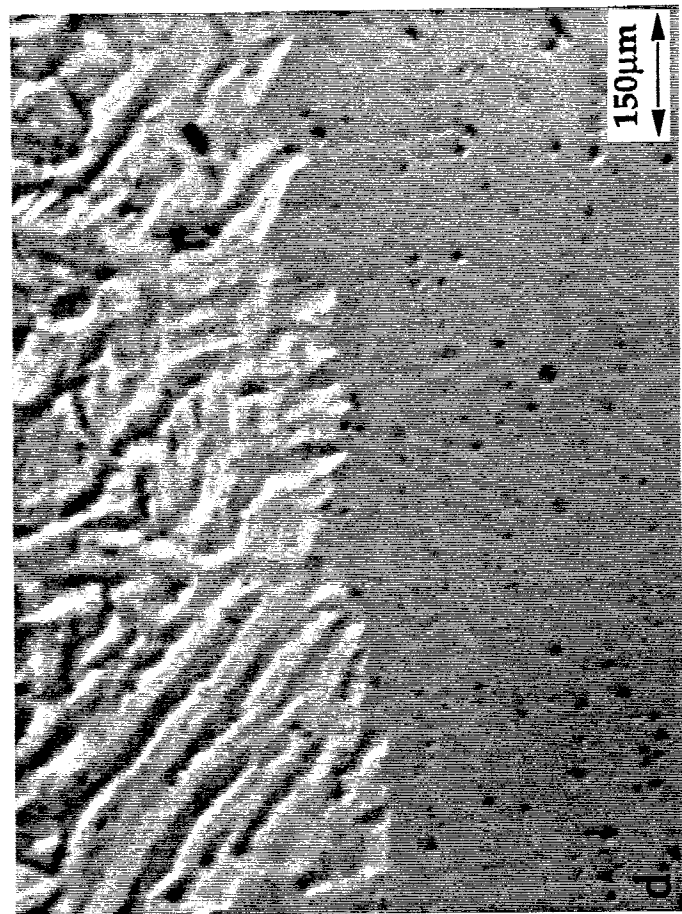
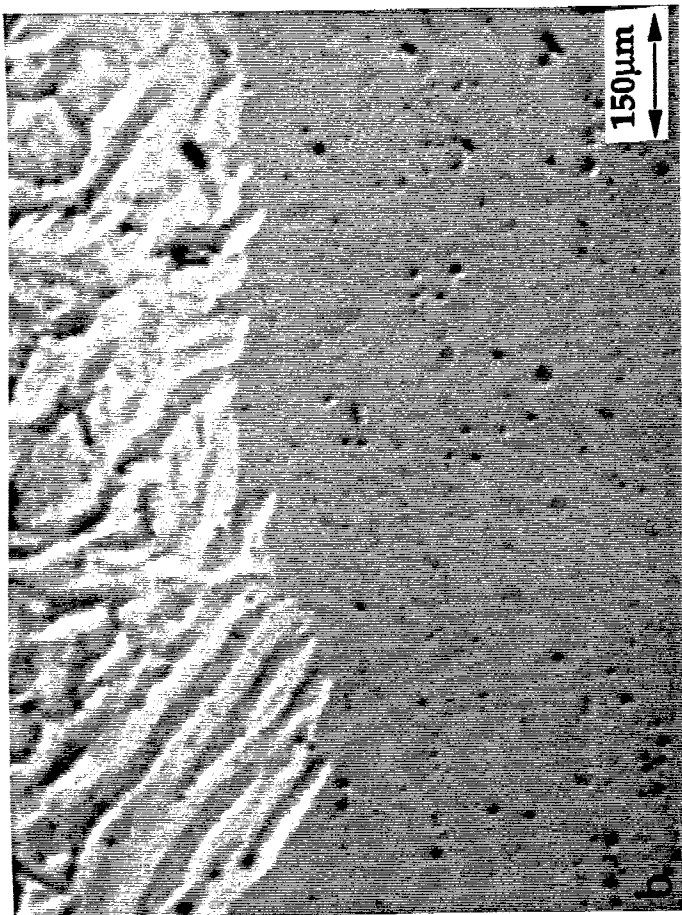


Figure 6



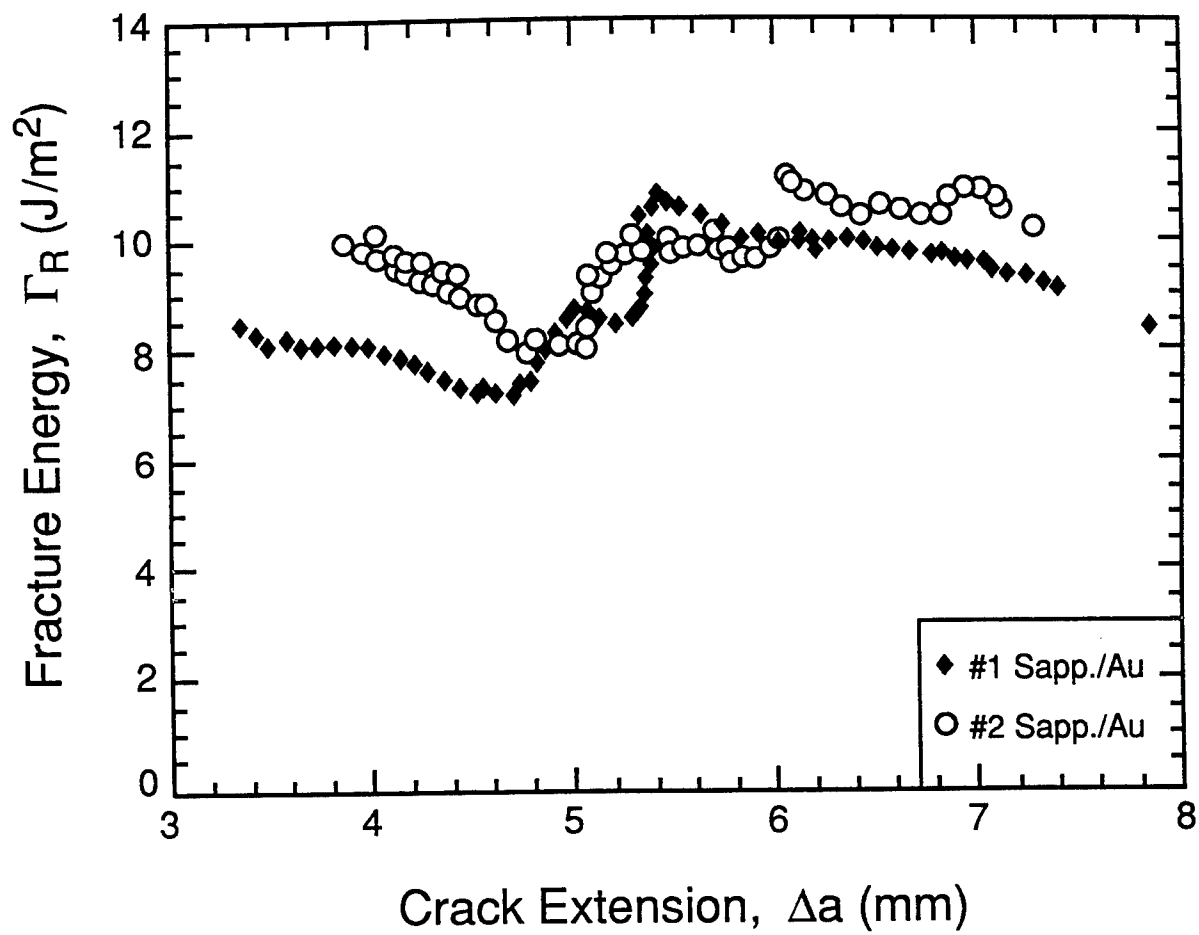
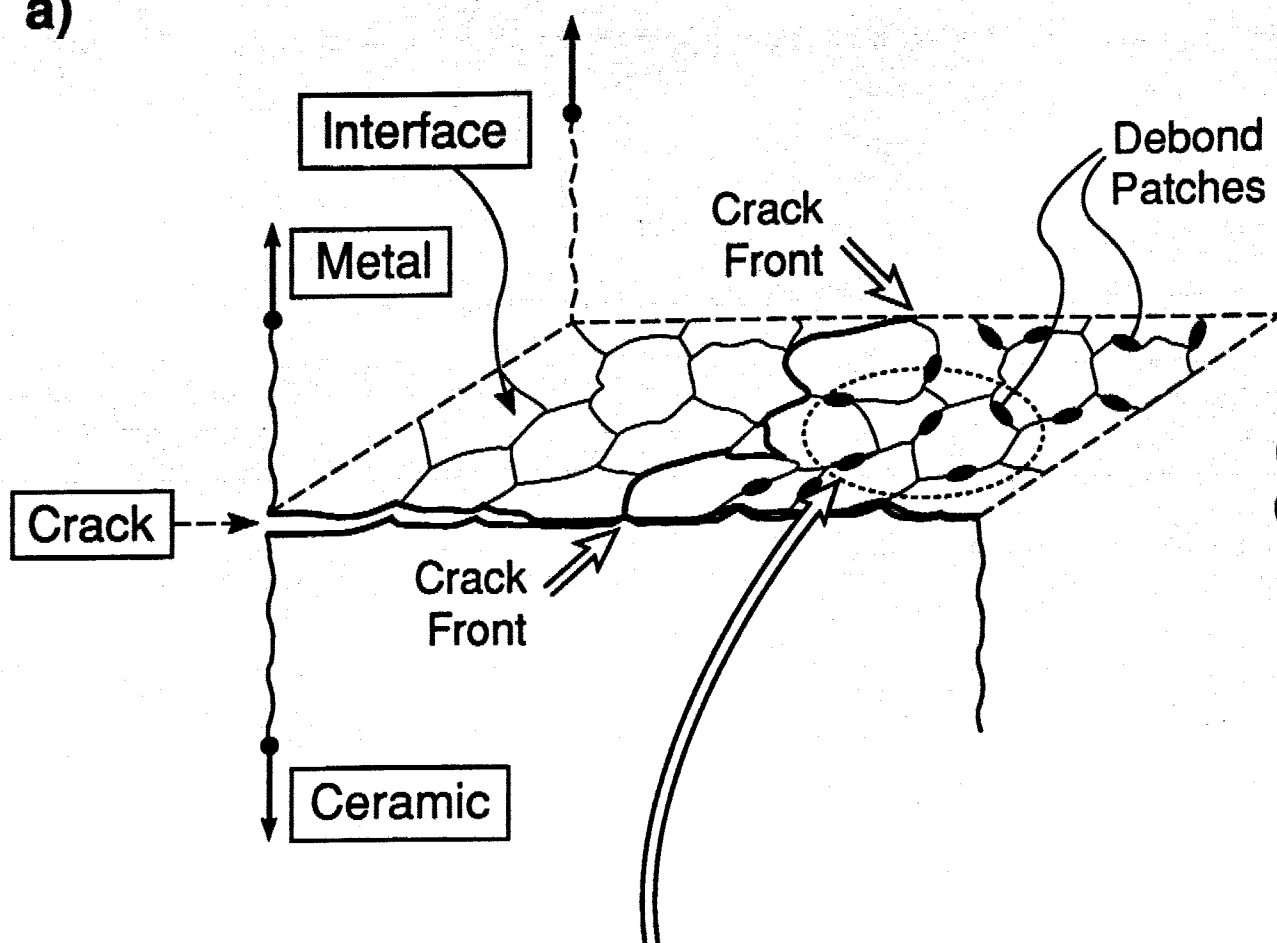


Figure 8

a)



b)

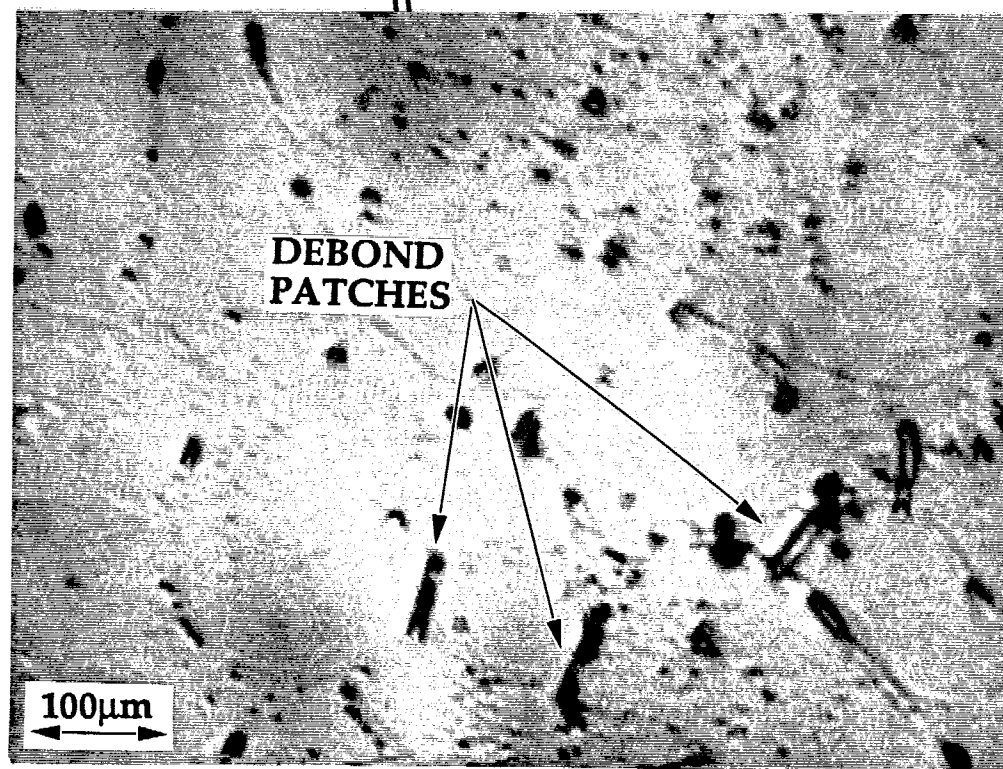
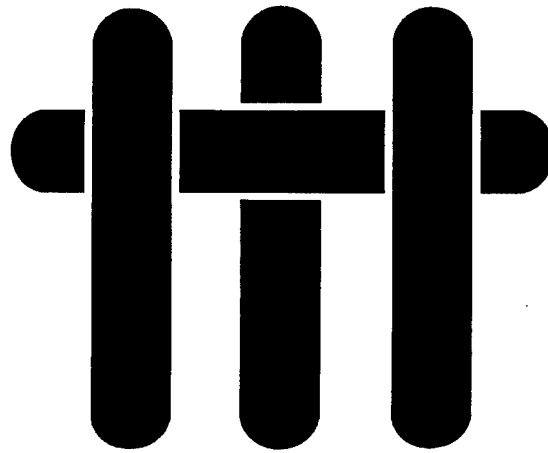


Figure 9

M A T E R I A L S



ANALYSIS OF THE DOUBLE CLEAVAGE DRILLED COMPRESSION SPECIMEN FOR INTERFACE FRACTURE ENERGY MEASUREMENTS OVER A RANGE OF MODE MIXITIES

by

Ming Y. He, Michelle R. Turner and Anthony G. Evans

Materials Department
College of Engineering
University of California
Santa Barbara, California 93106-5050

Submitted to Acta metallurgica et materialia
September 1994

ABSTRACT

The double cleavage drilled compression (DCDC) configuration has been analyzed using the finite element method. Mode I and mixed-mode configuration have been described and results presented for the energy release rate, the mixity angle and the crack opening displacement. The results have been expressed as simple analytical formulae having good accuracy. The application of the configuration to interface fracture measurements has been described.

1. INTRODUCTION

The double cleavage drilled compression (DCDC) specimen (Fig. 1a) has been developed for fracture mechanics studies on monolithic brittle materials.^{1,2} This specimen has many advantages, including compressive loading, mid-plane crack stability and auto-precracking. Moreover, it has additional advantages for measurements of the fracture energy of bimaterial interfaces, Γ_i , as elaborated in a companion paper.³ In particular, it allows Γ_i to be measured even when it exceeds the fracture toughness of the adjoining material, because of the stabilizing role of the compressive loads. It can also provide high-fidelity mode I and mixed mode data over several millimeters of crack extension, because of this crack stability feature.

A key requirement for applying this specimen is the availability of accurate stress intensity factor and energy release rate calibrations. A few calibration attempts have been made using either analytical or numerical approaches, but these have restricted scope.⁴⁻¹⁰ The analytical solutions^{4,5} are limited to a few specimen geometries and to short crack lengths (as elaborated below). Numerical results^{9,10} extend the crack length range, but are still restricted to a limited set of geometries. In this paper, the energy release rate G and crack opening displacement δ are systematically calculated for a full range of geometries and crack lengths. The finite element method is used for this purpose. Moreover, special requirements associated with measurements of the interface fracture energy are addressed. These include geometric variants capable of mixed-mode Γ_i measurements.

The fracture resistance of an interface generally depends on the mode mixity angle, ψ .¹¹ In order to fully characterize a given interface, a toughness curve, $\Gamma_i(\psi)$, must be determined. The loading phase ψ is defined as

$$\psi = \tan^{-1}(K_I/K_{II}) \quad (1)$$

where K_I and K_{II} are the mode I and mode II stress-intensity factors, respectively. For the DCDC configuration, a mixed-mode condition is achieved by offsetting the hole from the mid plane (Fig. 1b).

Dimensional analysis has indicated that the energy release rate can be expressed in the form^{4,5,8-10}

$$E\mathcal{G}/\pi\sigma^2R(1-\nu^2) = F_1(w/R, a/R, b/R) \quad (2)$$

where σ is the applied compressive stress, E is Young's modulus, R is the hole radius, $2w$ is the specimen width, a is the crack length, b is the hole offset displacement and F_1 is the function to be calculated (Fig. 1). The corresponding mixity angle ψ can be expressed as

$$\psi = \psi_1(b/R, w/R, a/R) \quad (3)$$

where ψ_1 is the function to be calculated. It will be shown that ψ_1 is a weak function of a/R , such that each choice of b/R and w/R defines a configuration with a specific mode mixity.

In addition to \mathcal{G} and ψ , it is useful to calculate the opening displacement at the crack/hole intersection, δ (Fig. 1), because measurements of this displacement can be used to evaluate the crack length.[‡] The associated non-dimensional form is

$$E\delta/R\sigma = \Delta(a/R, w/R, b/R) \quad (4)$$

[‡] This capability is helpful when the crack cannot be detected by optical methods.

where Δ is the function to be calculated.

2. THE FINITE ELEMENT MODEL

2.1 The Mesh

The calculations have been conducted using the finite element code, ABAQUS, with eight-noded isoparametric elements. All calculations have been made for an experimentally convenient aspect ratio, $L/w = 20$. The other geometries were varied within the ranges $2 \leq w/R \leq 4$, $2 \leq a/R \leq 15$ and $0 \leq b/R \leq 1$ (Fig. 1). Typical finite element meshes (Fig. 2) included either 487 elements and 1670 nodes (specimen a, mode I) or 1096 elements and 3737 nodes (specimen b, mixed mode). A fine, focused mesh with quarter-point crack tip elements served to model the singularity at the crack tip. A convergence study revealed that these meshes provided accurate values of K and G . The calculations were performed for cracks in monolithic materials. The results were then extended to interfacial cracks in specimens with a sandwich layer.

2.2 The Strain Energy Release Rate and Mode Mixity

Two techniques have been used to calculate the strain energy release rates. In the first, the J-integral was calculated by the domain integral method¹² for ten contours and an average value determined. In the second, the stress intensity factors K_I and K_{II} were obtained from the crack opening displacements, δ_x and δ_y , in accordance with

$$\begin{aligned} K_I &= \lim_{r \rightarrow 0} E \pi^{1/2} / (4\sqrt{2} (1 - \nu^2)) \delta_y / r^{1/2} \\ K_{II} &= \lim_{r \rightarrow 0} E \pi^{1/2} / (4\sqrt{2} (1 - \nu^2)) \delta_x / r^{1/2} \end{aligned} \quad (5)$$

The corresponding strain energy release rate was then obtained using

$$G = (K_I^2 + K_{II}^2)/E \quad (6)$$

The mode mixity was obtained using Eqn. (1). The agreement between the energy release rates J and G obtained by these two approaches provided an indicator of the quality of the results. In all calculations, the difference between J and G was found to be less than 1%.

3. THE MODE I CONFIGURATION

3.1 Strain Energy Release Rates

The numerical results show that the non-dimensional stress intensity factors, $\sigma\sqrt{\pi R}/K_I$, are linear functions of the crack length a/R , in the range, $w/R \leq a/R \leq 15$ (Fig. 3). By using the least square method to fit the calculations, the numerical results could be expressed as

$$\sigma(\pi R)^{1/2}/K_I = w/R + (0.235w/R - 0.259)a/R \quad (7a)$$

or

$$\bar{E}G/\sigma^2\pi R = [w/R + (0.235w/R - 0.259)a/R]^2 \quad (7b)$$

where $\bar{E} = E/(1 - \nu^2)$ for plane strain. The results expressed by Eqn. (7) are applicable within 1% *over the entire range of practical interest*, namely, $w/R \leq a/R \leq 15$, $2 \leq w/R \leq 4$. They are also in good agreement with previous FEM results and with experimental calibration,² as discussed later. But the present results extend over a much wider parameter range.

3.2 Crack Opening Displacements

The crack opening displacement, δ , is a linear function of the crack length where $a/R \geq 6$ (Fig. 4). By using the method of least squares, the results in this range ($6 \leq a/R \leq 15$) could be expressed as

$$E\delta/R\sigma = c_1 a/R + c_2 \quad (8)$$

where c_1 and c_2 are dimensionless functions of w/R (Fig. 5).

3.3 Stress Distributions

The stress fields are presented for one specimen geometry ($w/R = 3.0$, $L/w = 20$ and $a/R = 2 \rightarrow 15$). Under uniaxial compression along the y-axis, the σ_{yy} stress is compressive everywhere (Fig. 6a). The trends in σ_{yy} along the center line for two different crack lengths are indicated on Fig. 6b. The σ_{xx} stress contours (Fig. 7) show that there is a tensile region near the crack tip. Because this tensile region is very localized, the stress-intensity factor decreases as the crack length increases (under constant compression). There is also a tensile region near the hole. These latter stresses occur at the poles in the absence of a crack and are responsible for the initiation of cracks without the deliberate introduction of a precrack.

4. MIXED-MODE CONFIGURATION

4.1 Strain Energy Release Rates

By offsetting the hole from the mid plane, a mixed-mode loading condition is achieved (Fig. 1, specimen b). The numerical results for the energy release rate in the range, $w/R \leq a/R \leq 15$, $2.5 \leq w/R \leq 5.0$ may be expressed as

$$\bar{E}G/\sigma^2\pi R = [1.1 + d_1 w/R + (d_2 w/R - d_3)a/R]^{-2} \quad (9)$$

where d_i are dimensionless functions of the relative location of the hole, b/R (Table 1).

The loading phase ψ is a weak function of both the crack length and hole radius, but strongly dependent on the location of the hole, b/R (Fig. 8). A range of ψ between 0 and 64° can be achieved for reasonable values of b/R .

4.2 Stress Distributions

The stress fields are presented for a single geometry ($w/R = 3.0$, $L/w = 20$, $b/R = 1.0$ and $a/R = 5.0$). The stress, σ_{yy} , is again compressive everywhere. The σ_{xx} stress contours (Fig. 9) show that there are tensile regions near the crack tip and along the hole. The implication is that these specimens *must be precracked*; otherwise, additional mode I cracks might initiate from the center of the hole.

5. INTERFACE CONFIGURATIONS

5.1 Square Slots

For interface fracture studies, the circular hole configuration is not the most convenient, because holes must be made by diamond drilling after diffusion bonding.³ It is more convenient to fabricate specimens with square holes³ (Fig. 10). The effect of this change in hole geometry has been analyzed for mode I (specimen c, Fig. 10) and mixed-mode (specimen d, Fig. 10) configurations. The energy release rate results may be expressed as,

$$\bar{E}G/\sigma^2\pi R = [0.8w/R + (0.158w/R - 0.187)a/R]^{-2} \quad (10)$$

for mode I and

$$\bar{E}G/\sigma^2\pi R = [1.15 + 0.171w/R + (0.054w/R - 0.079)a/R]^{-2} \quad (11)$$

for mixed mode. For the latter, the loading phase ψ is a weak function of a/R and w/R . In the range $5 \leq a/R \leq 14$ and $2 \leq w/R \leq 4$, ψ varies from 52° to 57° .

5.2 Sandwich Specimens

The DCDC specimens discussed above can be used to study interface fracture by using a sandwich geometry, with a thin layer of one material between two beams of another material. For a very thin sandwich layer, the interface crack then has the same energy release rate as that for the monolithic body.¹³ The stress intensity factors for the interfacial crack, k_1 and k_2 , can be deduced by the nominal mode I and mode II intensity factors K_I and K_{II} for the monolithic material by using¹³

$$k_1 + ik_2 = \left\{ (1 - \alpha)/(1 - \beta) \right\}^{1/2} (K_I + K_{II}) h^{1/2} \epsilon^{i\omega(\alpha, \beta)} \quad (12)$$

where α and β are the Dundurs' parameters

$$\alpha = (\bar{E}_1 - \bar{E}_2)/(\bar{E}_1 + \bar{E}_2) \quad (13)$$

$$\beta = \frac{\mu_1(1 - 2\nu_2) - \mu_2(1 - 2\nu_1)}{2(\mu_1(1 - \nu_2) + \mu_2(1 - \nu_1))}$$

where μ is shear modulus and subscripts 1 and 2 correspond to the outer and sandwich layer materials, respectively. The parameter ϵ depends on β , according to

$$\varepsilon = (1/2\pi)\ln[(1-\beta)/(1+\beta)] \quad (14)$$

and ω is a function of α and β .¹³ With k_1 and k_2 determined in this way, both G and ψ can be obtained.¹³

5.3 Kinking

The condition needed to ensure that the crack remains at the interface (and not kink into the adjoining material) is that the fracture toughness ratio, Γ_i / Γ_m be less than a kinking transition ratio,^{14,15} summarized on Fig. 11, where Γ_i and Γ_m are fracture energies of the interface and adjoining material, respectively. For example, for a DCDC specimen, with a loading phase angle $\psi \approx 60^\circ$ ($w/R = 3$, $b/R = 1$, Fig. 8), the transition ratio is 0.55. That is, the matrix toughness must exceed that of the interface by a factor > 2 before the crack would kink out of the interface. This factor represents the upper limit of interface toughness that can be measured with the DCDC configuration (for each mode mixity). It is considerably larger than the equivalent factor for other test configurations.¹⁶

6. COMPARISON WITH OTHER SOLUTIONS

The present results have exposed the shortcomings of previous analytical models. One model⁵ has regarded the DCDC specimen as two vertical beams, each with a central segment having section reduced by the hole. This reduced section introduces bending moments into the beams. A key requirement for this model is the accurate estimation of the moment. The analytical model supposes that σ_{yy} along the net section is a *linear* function of the distance from the edge of the hole. The finite element results (Fig. 6b) show that $\sigma_{yy}(x)$ depends on the specimen geometry and crack length and stress is *only linear* in the specimen with a square slot. Moreover, the stress

concentration factor for the circular hole is higher than that for the square slot, such that the moment is also larger. These characteristics account for the disparity that G obtained from the analytical model for the circular hole is much higher than that obtained from the FEM analysis. In another analysis,⁷ the solution for the cracked strip problem was combined with the solution for the *exterior* circular hole problem. This approximation underestimates the σ_{yy} stresses and the moment and thus gives results for G much lower than the FEM results.

In a previous FEM analysis,¹⁰ results were obtained for only two geometries, $w/R = 3.75$ and 3.125 . The results for the former were expressed by a formula in good agreement with Eqn. (7a). However, the results for the latter differ by 10% from the present results and also differ from experimental calibrations.¹⁰

7. SUMMARY

Numerical calculations of the energy release rate, G , obtained for the double cleavage drilled compression configuration, have verified previous numerical solutions and extended them to a wide range of geometries. Simple analytical formulae have been used to express the trends with crack length, as well as hole size and shape.

It has been shown that the DCDC configuration containing either asymmetric cracks or holes provides mixed-mode behavior, with mixity angles, ψ , up to 67° . Results for G and ψ have been calculated for a range of geometric configurations, with either round or square holes. The extension of these results to interface fracture when sandwich DCDC configurations are used has been described. The application of the specimen to interface fracture energy measurements is discussed in a companion paper.³

ACKNOWLEDGEMENTS

This work was supported by the Office of Naval Research through Contract No. N-00014-93-I-0213. Provision of the ABAQUS finite element code by Hibbitt, Karlsson and Sorensen, Inc. of Providence, Rhode Island, is gratefully acknowledged.

TABLE 1

Values of d_i Coefficients For The Mixed-Mode Configuration

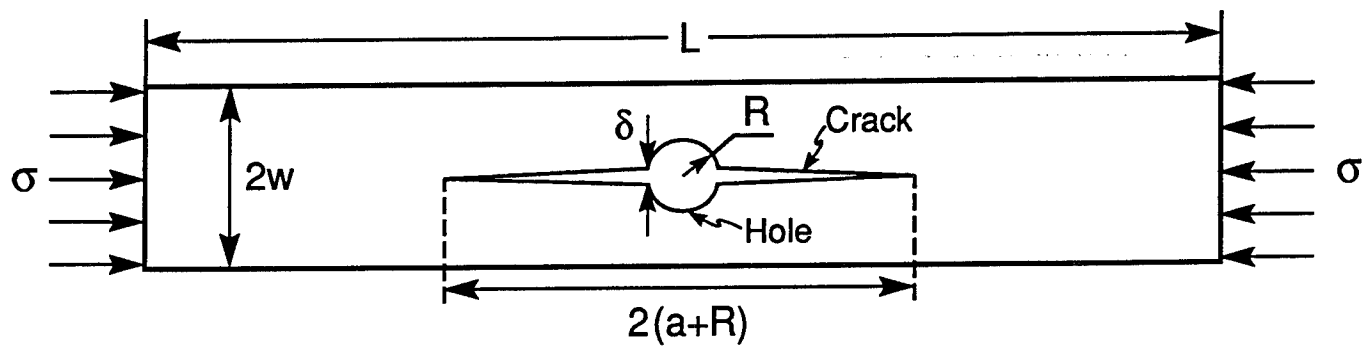
b/R	d_1	d_2	d_3
0.5	0.378	0.149	0.278
0.75	0.258	0.103	0.221
1.0	0.217	0.063	0.08

REFERENCES

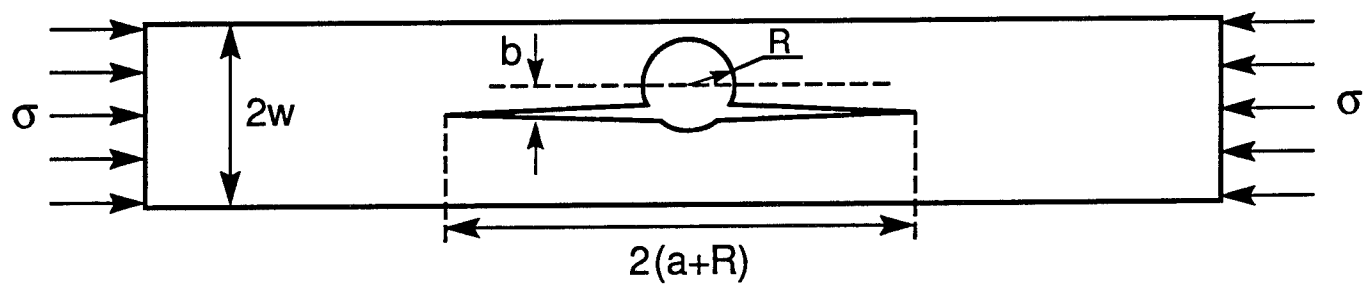
- [1] C. Jansson, "Specimen For Fracture Mechanics Studies On Glass," *Proc. 10th Int. Cong. On Glass* (pp. 10.23–10.30), Kyoto, Japan, 8–13 July 1974. Ceramic Society of Japan, Tokyo (1974).
- [2] C. Janssen, "Fracture Characteristics of DCDC Specimen." *Report No. R-8074*, Corning Glass Works, Corning, NH (1980).
- [3] M.R. Turner, M.Y. He and A.G. Evans, to be published.
- [4] T.A. Michalske and E.R. Fuller, Jr., *J. Am. Ceram. Soc.* **68**, 586 (1985).
- [5] C.G. Sammis and M.F. Ashby, *Acta metall.* **34**, 512 (1986).
- [6] W.L. Smith, "An Automated Test System for Studying Slow Crack Growth in Glass," *Closed Loop Mag.*, Spring, 18 (1987).
- [7] W.A. Warren, *Int. J. Frac.* **33**, 223 (1987).
- [8] T.W. Coyle, E.R. Fuller, Jr. and P. Swanson, *Ceramic Engineering and Science Proceeding*, **8**, 630 (1987).
- [9] Hongda Cai, K.T. Faber and E.R. Fuller, Jr., *J. Am. Ceram. Soc.* **75**, 3111 (1992).
- [10] T.A. Michalske, W.L. Smith and E.P. Chen, *Engineering Fracture Mechanics* **45**, 637 (1993).
- [11] J.W. Hutchinson and Z. Suo, "Mixed Mode Cracking in Layered Materials," *Advances in Applied Mechanics* **29**, 63, Academic Press, Inc. (1992).
- [12] C.F. Shih, B. Moran and T. Nakamura, *Int. J. Frac.* **30**, 79 (1986).
- [13] Z. Suo and J.W. Hutchinson, *Mat. Sci. Eng.* **A107**, 135 (1989).
- [14] M.Y. He and J.W. Hutchinson, *J. Appl. Mech.* **56**, 270 (1989).
- [15] M.Y. He, A. Bartlett, A.G. Evans and J.W. Hutchinson, *J. Am. Ceram. Soc.* **74**, 767 (1991).
- [16] A.G. Evans and B.J. Dalgleish, *Acta metall.* **40**, Suppl. S295 (1992).

FIGURE CAPTIONS

- Fig. 1. The DCDC specimen geometries (a) mode I, (b) mixed mode.
- Fig. 2. Typical finite element meshes (a) mode I, specimen a, (b) mixed-mode, specimen b.
- Fig. 3. Non-dimensional stress intensity factors $\sigma(\pi R)^{1/2}/K_I$ as a function of crack length a/R , plotted for three hole geometries.
- Fig. 4. The normalized crack opening displacement as a function of the crack length plotted for five hole geometries.
- Fig. 5. The crack opening coefficients (Eqn. 8) c_1 and c_2 plotted as a function of w/R .
- Fig. 6. The σ_{yy} stress contours for the mode I specimen: (a) stress contours for $w/R = 3, a/R = 9$; (b) stress distribution along the net section.
- Fig. 7. The σ_{xx} stress contours for the mode I, specimen a, with $w/R = 3, a/R = 9$.
- Fig. 8. The loading phase angle as a function of the crack length for mixed-mode specimen b.
- Fig. 9. The stress σ_{xx} contours for the mixed-mode, specimen b, with $w/R = 3, b/R = 1$ and $a/R = 5$.
- Fig. 10. DCDC specimen with a square slot: (a) Specimen c, mode I, (b) Specimen d, mixed mode.
- Fig. 11. The transition fracture toughness ratio as a function of loading phase angle ψ .



(a)



(b)

Figure 1

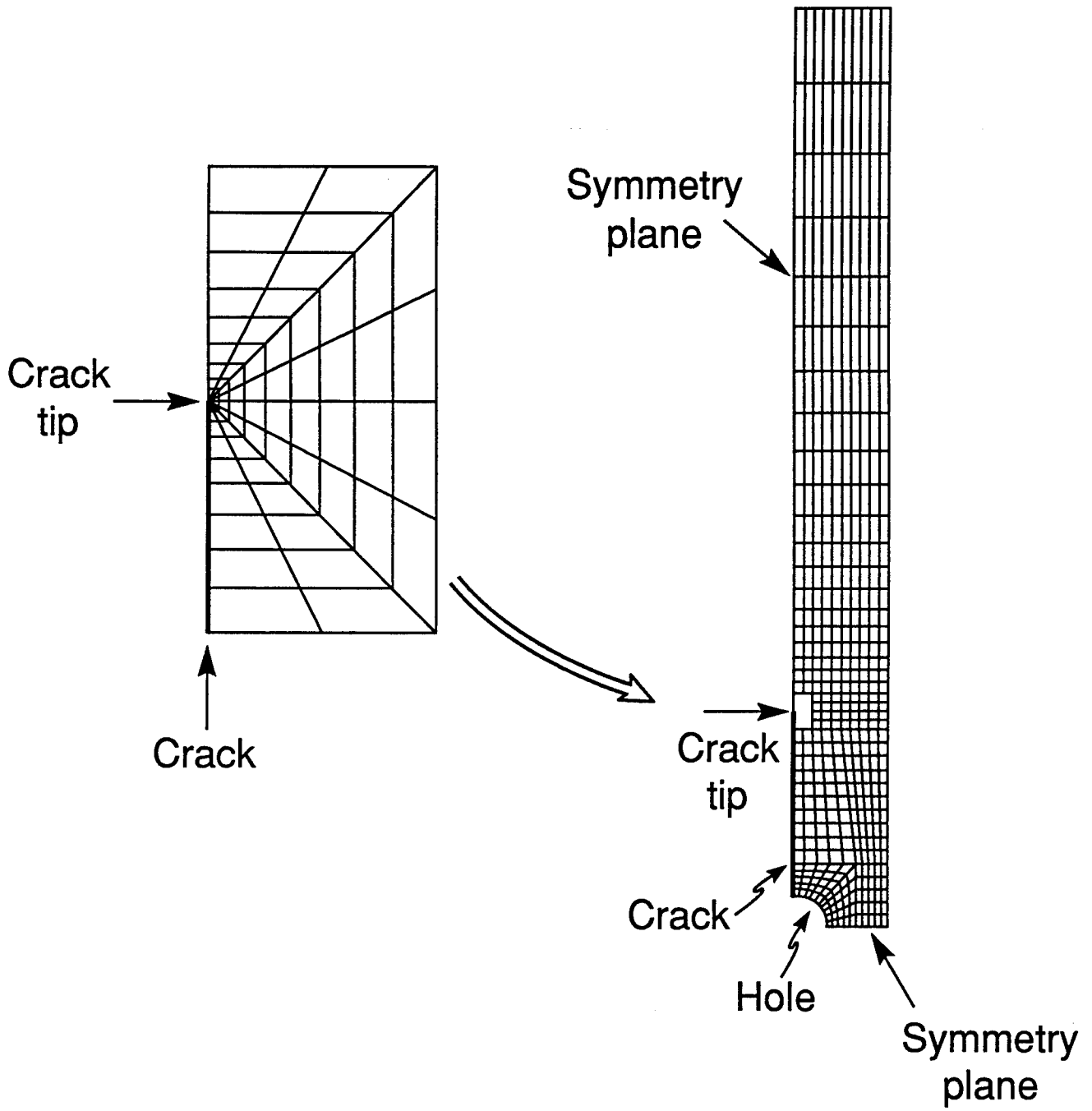


Figure 2a

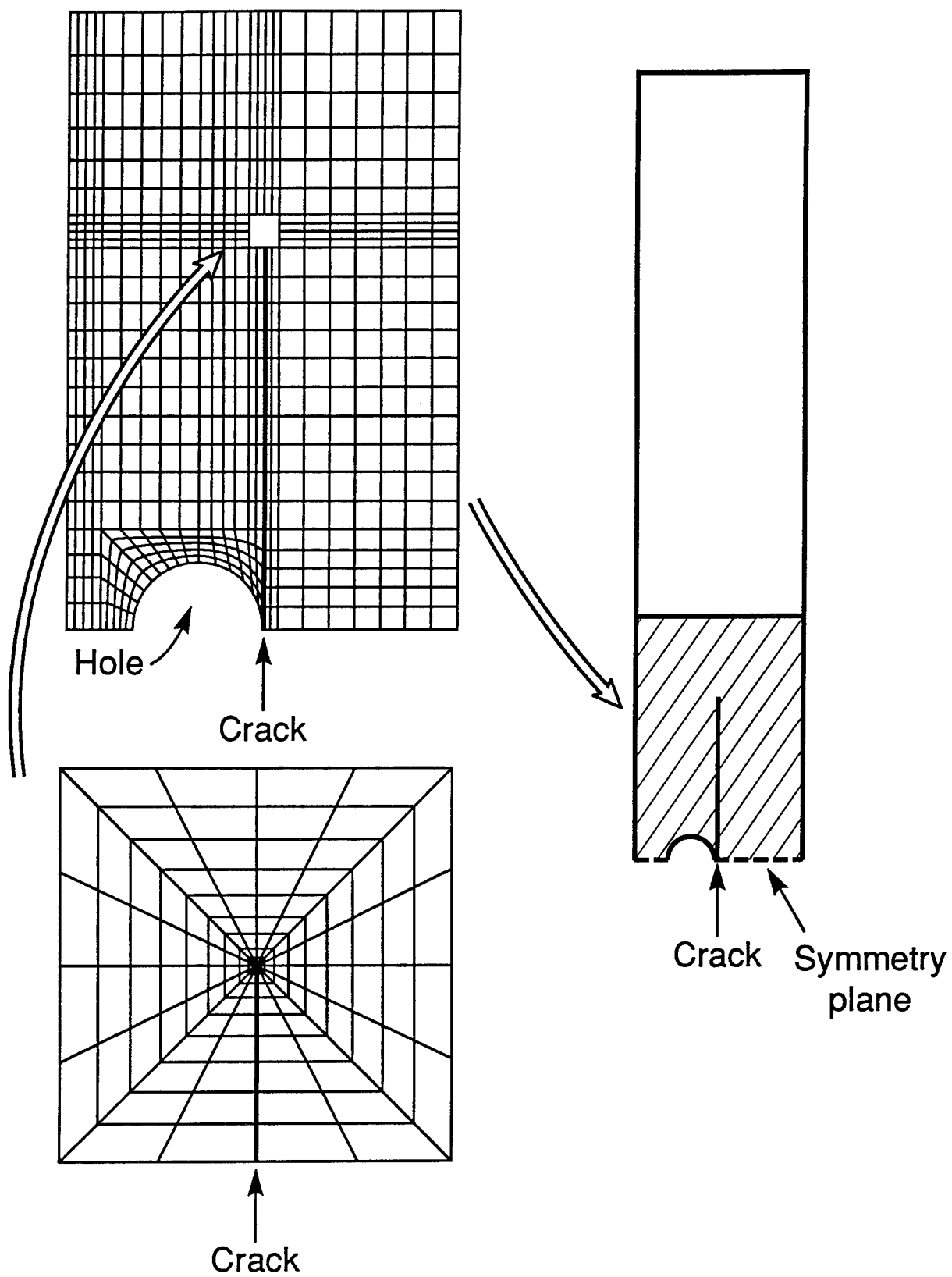


Figure 2b

Non-dimensional Stress Intensity Factors,

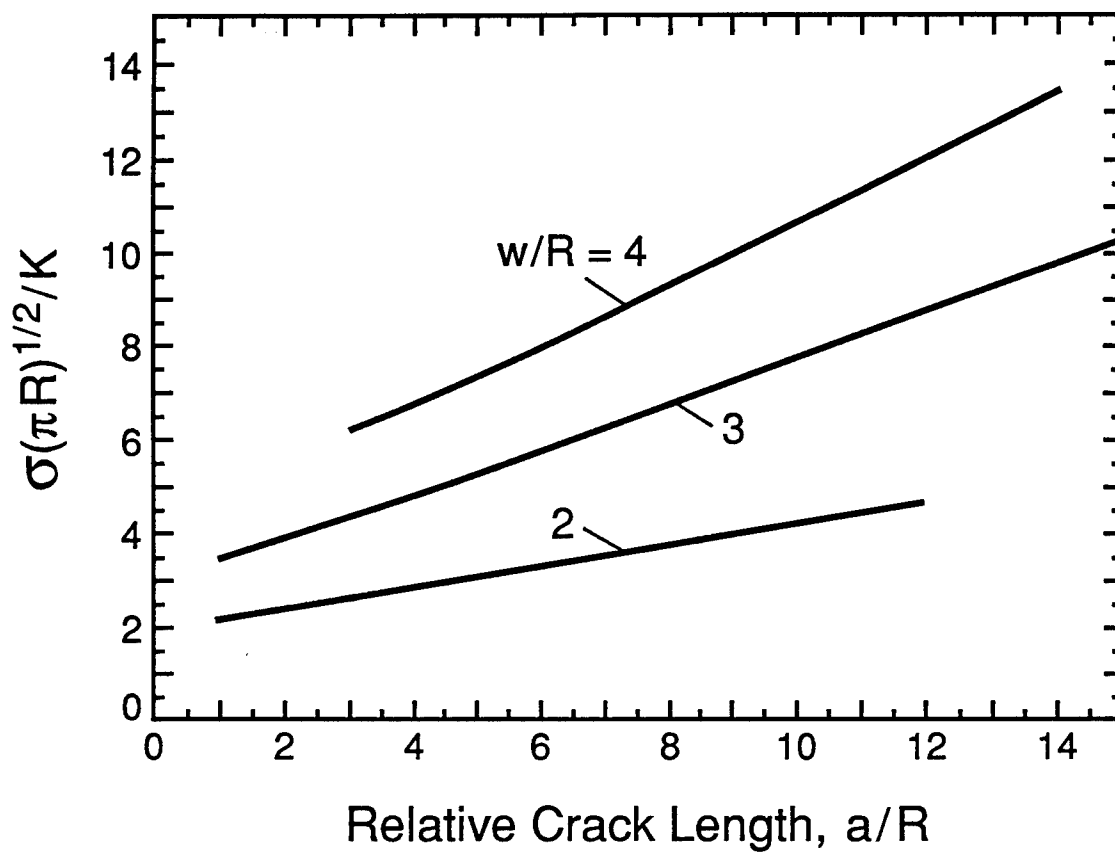


Figure 3

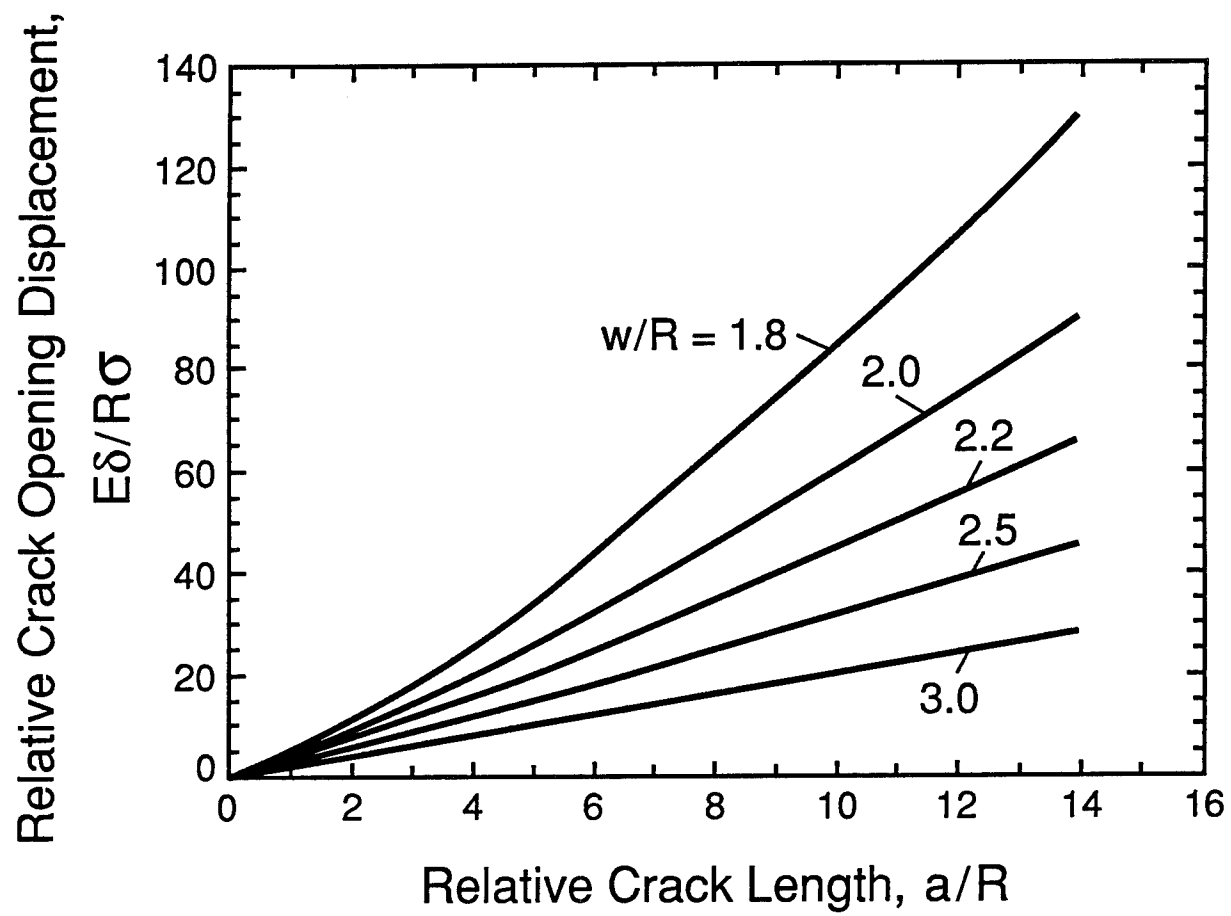


Figure 4

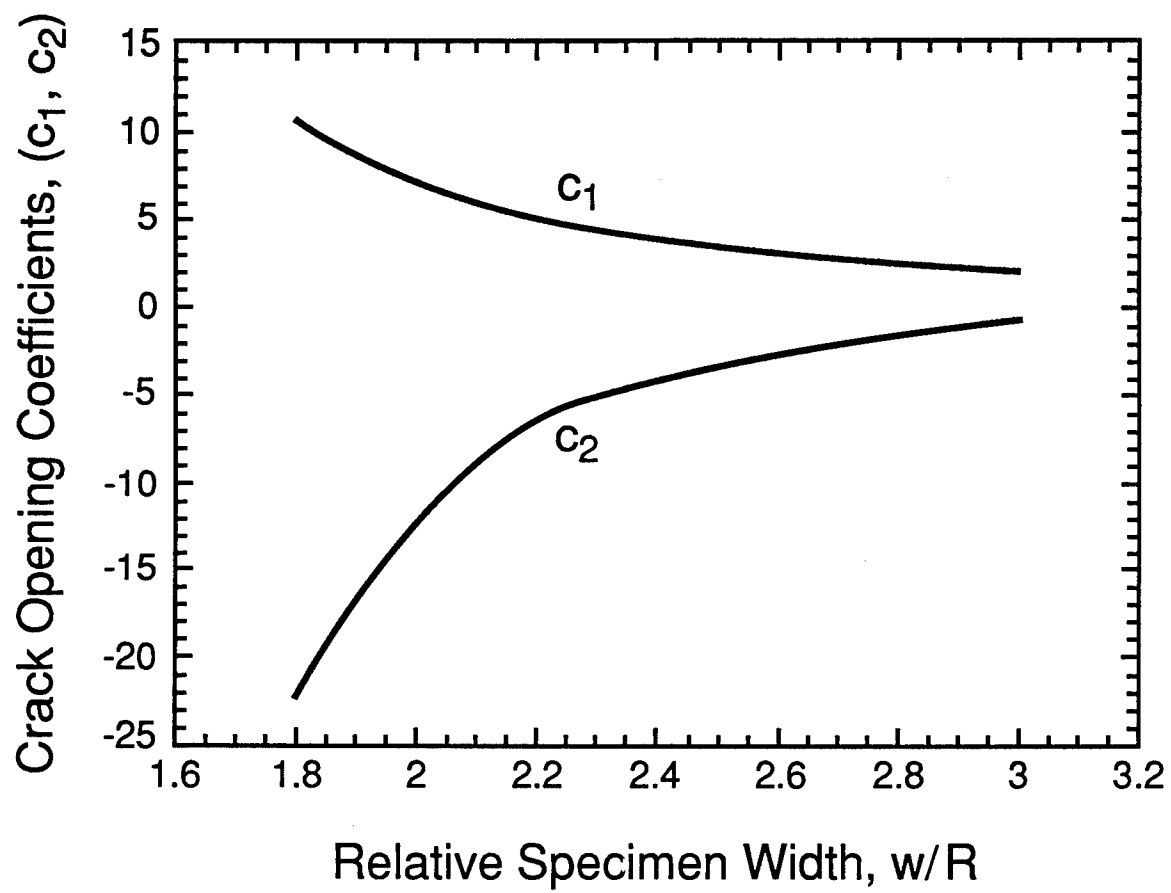


Figure 5

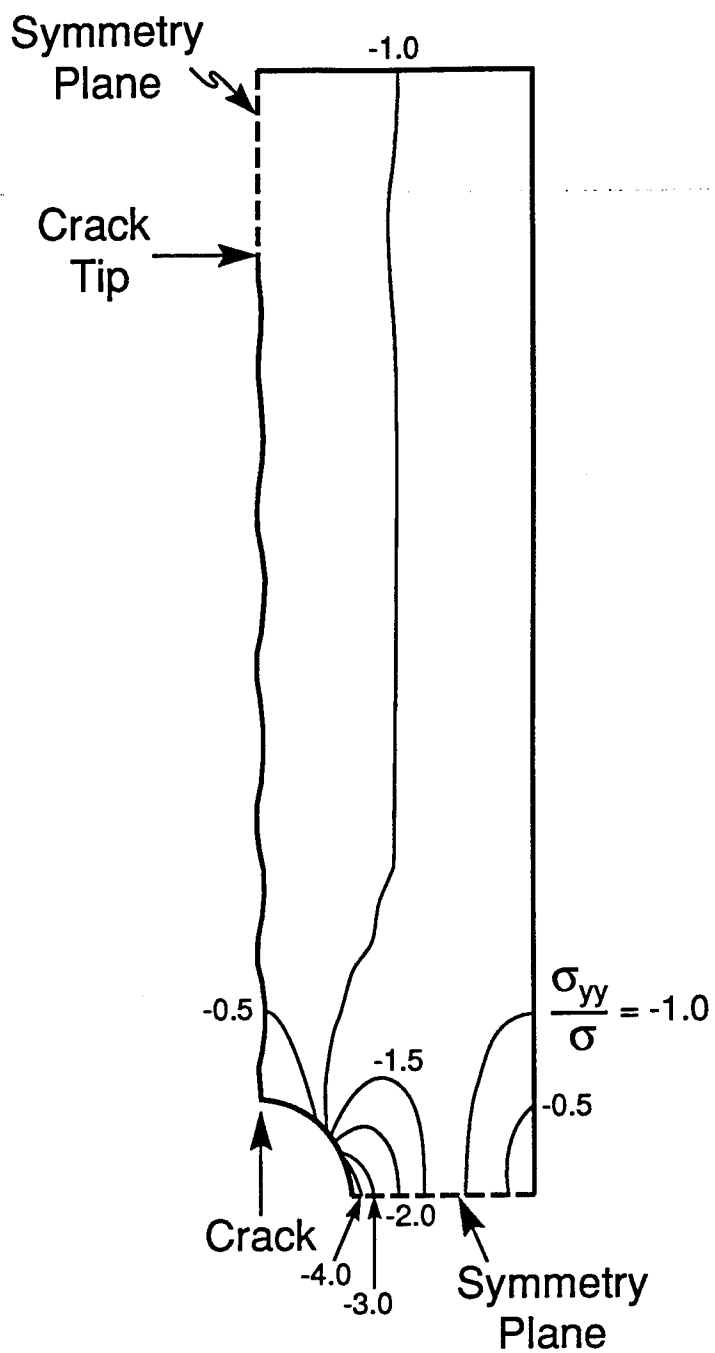


Figure 6a

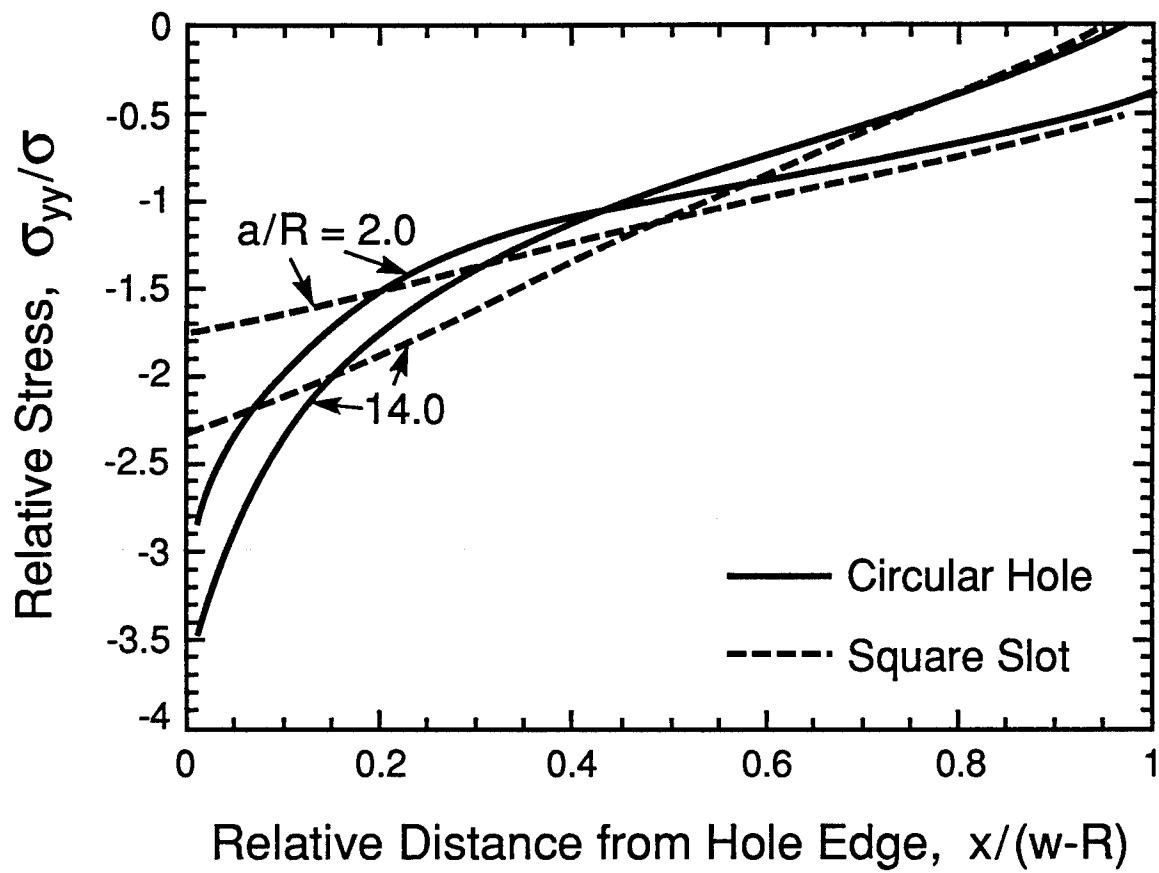


Figure 6b

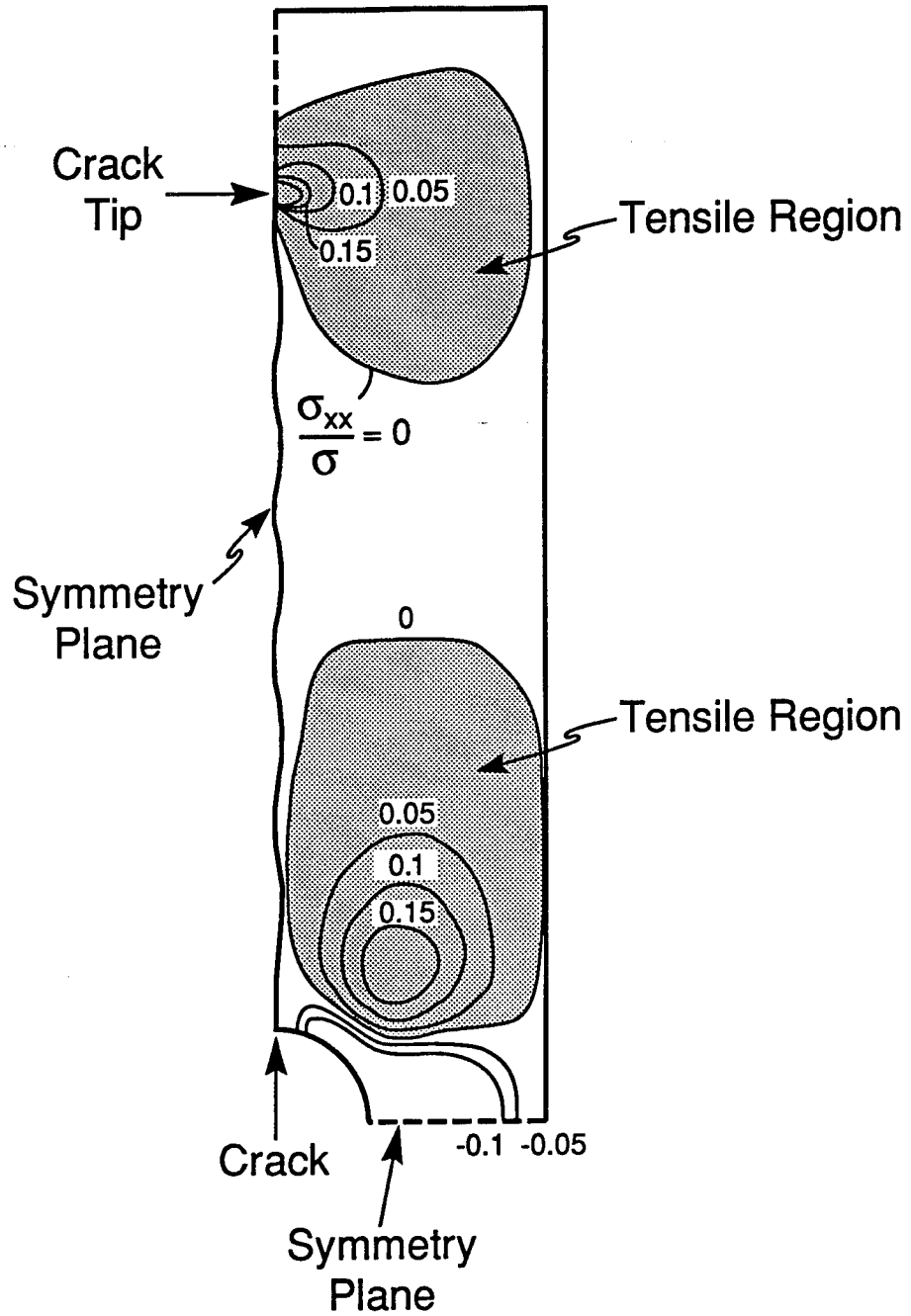


Figure 7

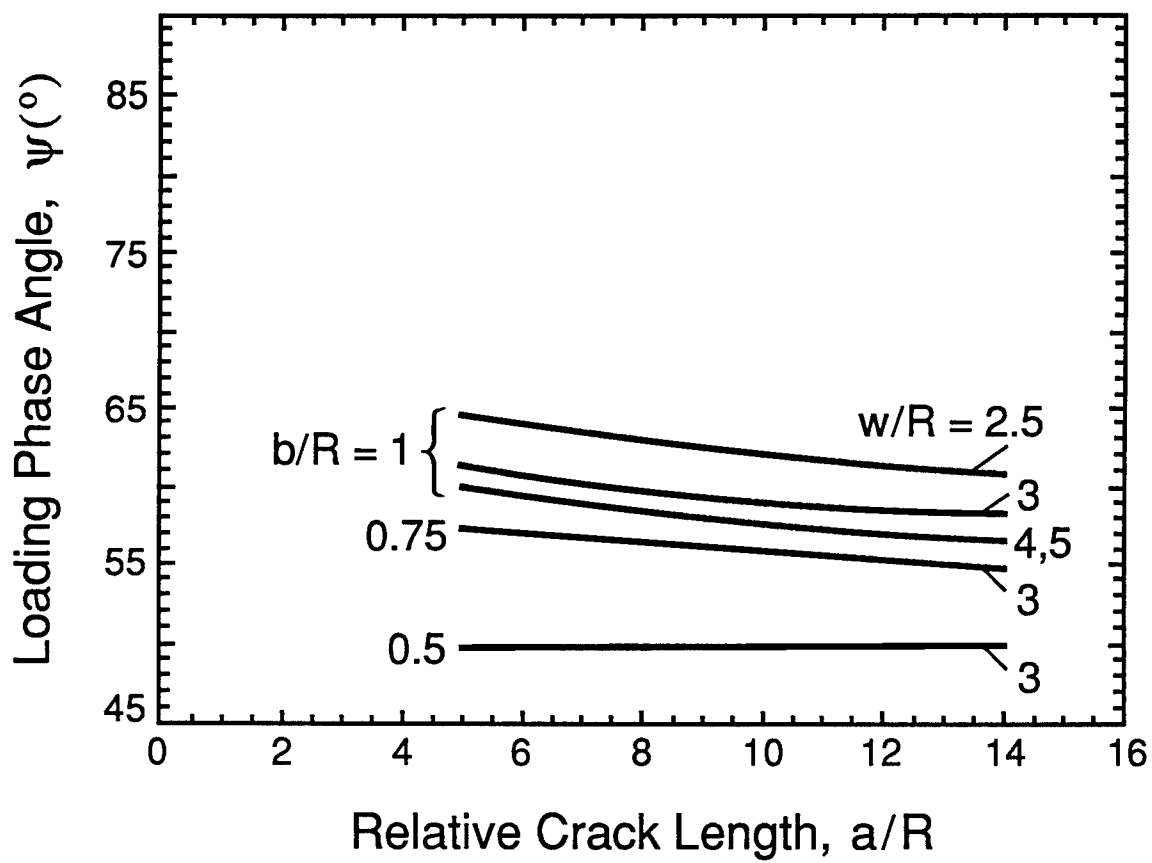


Figure 8

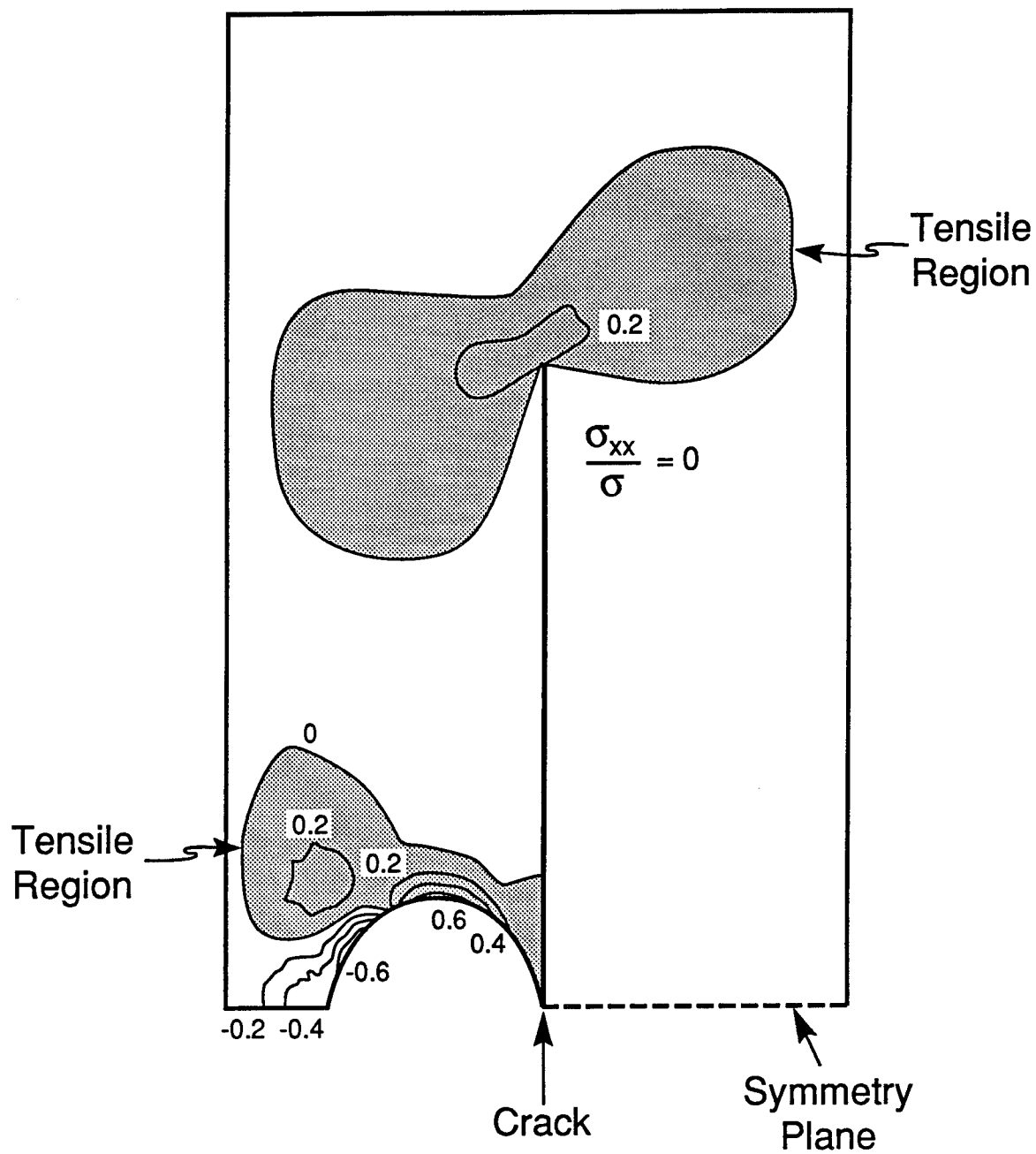
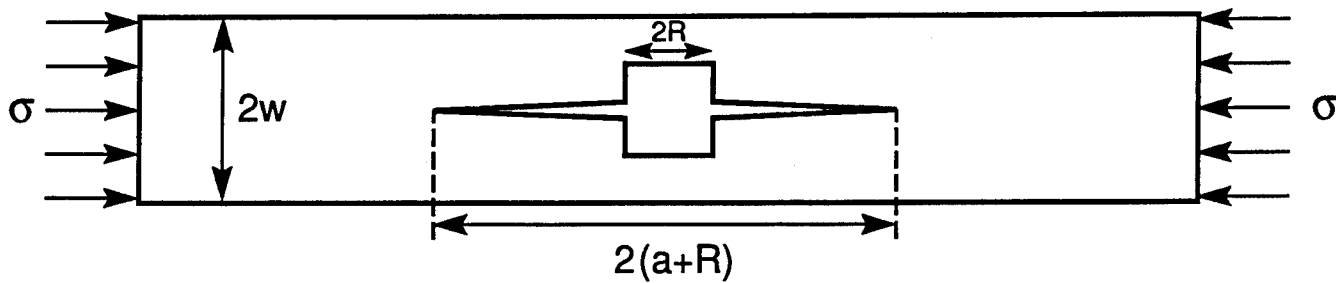
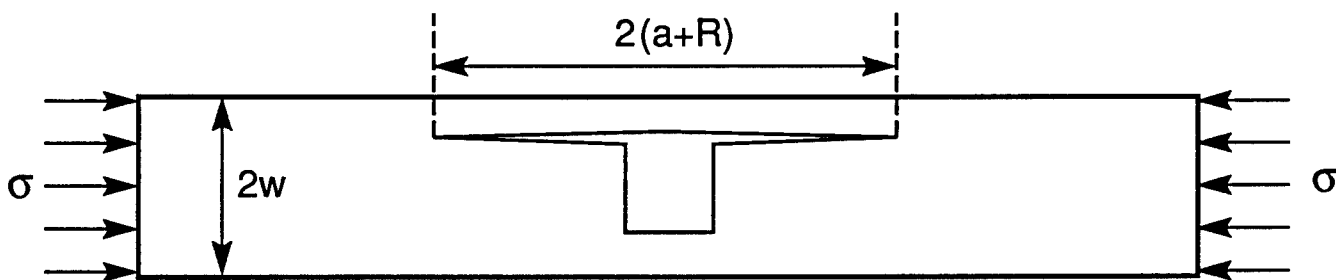


Figure 9



(a)



(b)

Figure 10

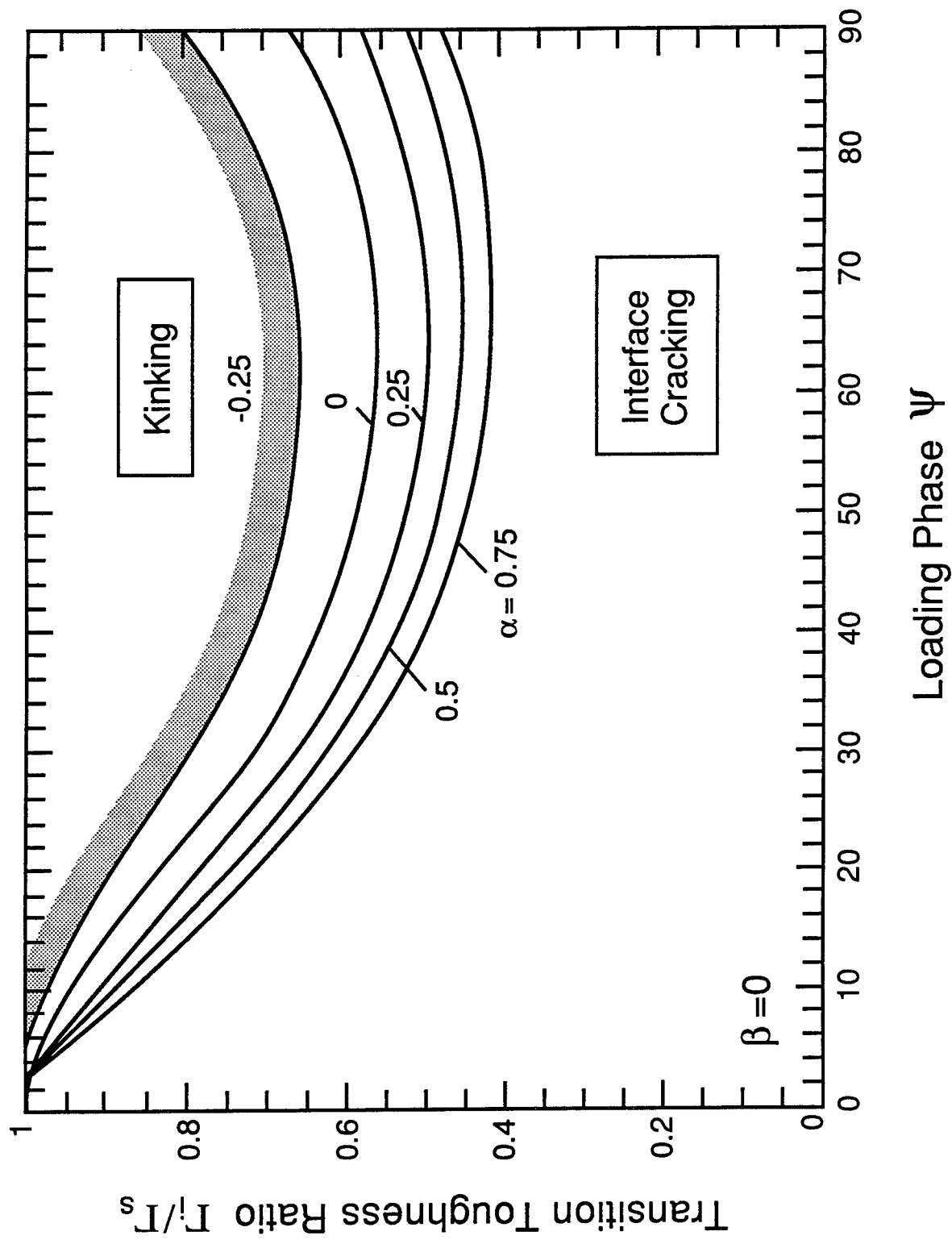
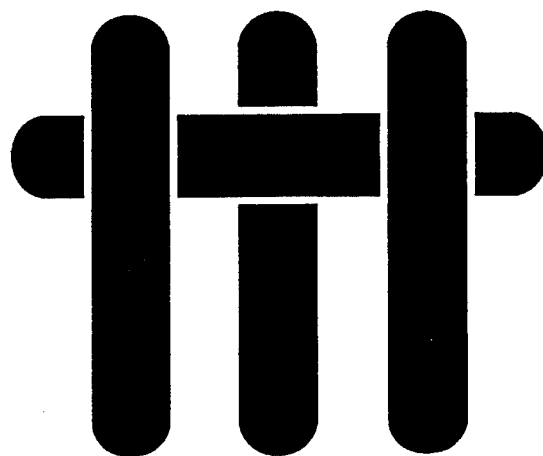


Figure 11

M A T E R I A L S



STRESS REDISTRIBUTION IN CERAMIC/METAL MULTILAYERS CONTAINING CRACKS

by

Q. Ma, M.C. Shaw, M.Y. He, B.J. Dalgleish, D.R. Clarke and A.G. Evans

Materials Department
College of Engineering
University of California, Santa Barbara
Santa Barbara, California 93106-5050

ABSTRACT

Multilayer systems comprising either Al or Cu bonded to sapphire have been used to evaluate stress redistribution effects around cracks, caused by slip in the metal. Single precracks have been introduced into the outermost sapphire layer and strain distributions measured around those cracks upon loading. Both moiré interferometry and (Cr^{3+}) fluorescence piezospectroscopy have been used for that purpose.

Finite element calculations of the plastic zone size, L_s , the crack opening displacement, δ , and the strains have been made, with the yield strengths of the metals, σ_o , regarded as unknowns. Comparison of L_s or δ with the measurements establishes σ_o . Once the relevant yield strengths have been determined, the calculated stresses and strains (as redistributed by slip in the metal layer) are found to be in reasonable correspondence with the values measured by either moiré interferometry or piezospectroscopy. Some small discrepancies remain, which have yet to be explained.

1. INTRODUCTION

Multilayer materials exhibit thermostructural characteristics dependent upon on the cracking sequence in the brittle layers.¹⁻⁴ When ductile interlayers are used that disperse the cracks, the materials can become damage tolerant.^{1,4-6} Less effective interlayers allow stress concentrations to persist. Dominant cracks¹ then form and degrade the structural performance. The phenomenon that governs the operative behaviors involve stress redistribution,² either by plastic slip within the metal layer or by debonding at the interface (Fig. 1). The present article emphasizes experimental methods for measuring redistributed stresses, with high spatial resolution. These measurements are compared with calculations,² to validate the stress redistribution mechanics.

The experimental emphasis is on two techniques capable of strain measurements with high spatial resolution. One method uses moiré interferometry. The other uses (Cr³⁺) fluorescence spectroscopy. The former measures the full in-plane strain tensor on the surface.⁷ The latter, which utilizes the piezospectroscopic shift of the R lines in alumina, provides a measure of the dilatational strain in the probed volume.^{8,9} In this work, the methods are applied to multilayers comprising alternate layers of Al₂O₃ single crystals (sapphire) with either Al or Cu. These materials are known to form well-bonded interfaces that rely on slip in the metal to redistribute stress.^{1,10,11} Numerical calculations are performed for geometric situations that duplicate the experiments

The emphasis is on well-bonded interfaces, even though slip is less effective than interface debonding at reducing stress concentrations^{2,4} (Fig. 1) because well-bonded interfaces are not prone to problems with delamination and hence, have superior transverse properties.

2. MATERIALS

Thin sapphire plates with C-axis normal to the plate thickness have been purchased, then mechanically ground and polished to optical flatness at a thickness of $\sim 100\text{ }\mu\text{m}$ by using diamond media. They were then annealed in air at 1100°C for 24 h to relieve residual stresses due to grinding. Foils of high purity Al and Cu (99.99%) have also been acquired and cold rolled to thicknesses of about 25 to $100\text{ }\mu\text{m}$. Multilayers with these constituents were produced by stacking the annealed sapphire plates and the metal foils within a vacuum furnace. A compressive stress of $\sim 2\text{ MPa}$ was imposed and the system slowly heated in order to diffusion bond the constituents.¹⁰ The temperature was maintained for $\sim 24\text{ h}$ and the system slowly cooled to room temperature.

The diffusion bonded plates were cut into rectangular beams (dimensions $25 \times 2.5 \times 2.1\text{ mm}$) suitable for flexure testing. The cut surfaces were mechanically polished to optical quality in order to facilitate measurements. On some specimens, the grids required for moiré measurements were attached to one of the side surfaces.^{7,11}

3. PROCEDURES

3.1 Mechanical Measurements

Prior to loading in four-point flexure, a precrack was introduced into the outermost sapphire layer. This was achieved by introducing a row of Knoop indentations along the center plane normal to the beam axis. A flexural load was then applied in a three-point configuration until the flaws beneath the indentations coalesced into a crack. This crack, when formed, extended unstably to the first $\text{Al}_2\text{O}_3/\text{metal}$ interface and then arrested.^{1,11} At this stage, the specimen was ready for strain measurements.

3.2 Strain Determination

The strain measuring procedure involves fixtures that imposed loads to the specimen and allowed *in situ* measurements either within an optical microprobe (fluorescence), as indicated on Fig. 2, or on an optical bench (moiré). The details have been described elsewhere.^{9,11} In this study, several tests were performed. All involved applying a bending moment to a precracked beam in four-point flexure with an inner span of 12 mm and an outer span of 22 mm. All strain measurements were conducted at loads lower than that needed to extend the precrack into the adjacent Al_2O_3 layer. When the tests were performed in the optical microprobe, scans were conducted under load in two orthogonal directions along three separate trajectories (Fig. 3). In the moiré tests, interference patterns were generated at fixed load. The tests were repeated at several different loads.

The two methods have an inherent preference for different spatial ranges. The moiré measurements emphasize strains in the region close to the crack ($x, y < 0.2 h_s$). The fluorescence measurements emphasize strains over a larger spatial range (x and y up to $10 h_s$) but with lower resolution in the zone close to the crack.

Various additional measurements were made. Among these was the crack opening displacement measured directly using the microscope of the optical microprobe.

4. RESULTS

4.1 Moiré Measurements

The distortion of the moiré patterns obtained upon unloading provide clear evidence of slip in the metal originating from the precrack and extending along the interface (Fig. 4). Such patterns allowed the slip length L_s to be measured as a function of load with high precision. Results obtained for Al layers of two different thicknesses

(Fig. 5) show that, when normalized by the precrack length (or sapphire layer thickness) h_s , there is a unique dependence of L_s/h_s on the applied (reference) stress σ with no effect of metal thickness. The shear, caused by bending, being defined as the maximum stress on the outer sapphire layer expected in the absence of the precrack.

The moiré patterns have a different characteristic when under load (Fig. 6). They indicate a strain concentration near the crack plane, which can be evaluated from the fringe spacings in the usual manner.⁷ The in-plane strains in the sapphire, ϵ_{xx} and ϵ_{yy} , have been obtained on material with a 25 μm thick Cu layer, both along the crack plane, OB and parallel to the interface, at $00'$ (Fig. 3). The results obtained at two different loads ($\sigma = 150$ and 250 MPa) are summarized in Figs. 7a,b. The results are restricted to the higher loads to enhance fidelity and resolution. The strains and positions are normalized using²

$$\begin{aligned}\mathcal{E}_{ij} &= \epsilon_{ij} E_s / \sigma (1 - \nu_s) \\ \mathcal{X} &= x/h_s \\ \mathcal{Y} &= y/h_s\end{aligned}\tag{1}$$

where E_s is the Young's modulus of the sapphire, ν_s is its Poisson's ratio and σ is the reference tensile stress. With these normalizations, there are no systematic influences of the stress on the measured strains (in the range 150–250 MPa), despite the plasticity in the metal.

4.2 Piezo-Spectroscopic Measurements

The piezo-spectroscopic shifts in the R2 fluorescence line $\Delta\nu$ have been measured in the sapphire on specimens with 25 μm thick Al layers. Measurements have been

made along the locations 00' and AA' (Fig. 3) at the three values of the reference stress indicated on Figs. 8a,b. The shifts are related to the in-plane stresses by⁹

$$\Delta v = \pi_a \sigma_{yy} + \pi_c \sigma_{xx} \quad (2)$$

where π_a , π_c are the piezospectroscopic coefficients in the crystallographic a and c directions, respectively: these have magnitude 2.72 and 2.11 (cm⁻¹/GPa).⁹

4.3 Crack Opening Displacements

The crack opening displacements have been measured under load. These are plotted on Fig. 9 as a function of the reference stress for both Al and Cu.

5. CALCULATIONS

The finite element method has been used to calculate the stress redistributions in plane stress by means of the ABAQUS code. The actual flexural geometry implemented in the present experiments was used. The mesh devised for this purpose is shown in Fig. 10. In the calculations, the yield strengths σ_0 of the Al and Cu are regarded as unknowns so calculations were performed for values between 10 and 100 MPa. A power law representation of the plasticity in the metal is used with a work hardening parameter n of either 4 or infinity (perfectly plastic). The sapphire was assumed to behave elastically. The interface is regarded as well-bonded.¹²

Preliminary calculations demonstrate the growth of the plane strain plastic zone L_s as the reference stress increases (Fig. 11). The extremity of the plastic zone shown in Fig. 11 is used to define L_s . This zone size, normalized by h_s , is superimposed on the data on Fig. 5 for both plane strain and plane stress conditions. It is apparent that a

yield stress σ_0 between 20 and 30 MPa gives a good fit to the measurements for the Al layer. From the same calculations, the average opening displacement of the crack, $\bar{\delta}$, is determined. Comparison with the microscopy measurements (Fig. 9) again indicates consistency for Al when σ_0 is about 20 MPa. The correspondence for Cu obtains when $\sigma_0 \approx 70$ MPa. In all subsequent calculations, the yield strengths were taken to be $\sigma_0 = 25$ MPa for Al and $\sigma_0 = 70$ MPa for Cu.

The stresses σ_{xx} and σ_{yy} are calculated along OO' and AA' with $\sigma_0 = 25$ MPa, to represent the stresses expected in Al/Al₂O₃ multilayers. These stresses are then used with Eqn. (2) to evaluate the R2 fluorescence peak shift, $\Delta\nu$. The calculations are compared with the fluorescence measurements in Fig. 8. The excellent correspondence indicates that strain redistribution can be accurately predicted once the yield strength of the Al has been established from either plastic zone size or crack opening displacement measurements.

The strains ϵ_{yy} and ϵ_{xx} , close to the crack, are calculated along the OO' and OB trajectories, either with $\sigma_0 = 70$ MPa to represent Cu or with $\sigma_0 = \infty$ (elastic). These are compared with the moiré measurements obtained on Cu/Al₂O₃ multilayers on Fig. 7. It is evident from the calculations that there is little effect of yielding in the Cu on the strains in the Al₂O₃, as elaborated elsewhere.^{1,2,4} In general, the experimental measurements are consistent with the calculations. The evident discrepancy is for $\epsilon_{xx}(x)$ at $y = 0$ (Fig. 7b). The differences between the measurements and the calculations are discussed below.

6. CONCLUDING REMARKS

The metal yield strengths determined from the comparisons between the measured and calculated values of the plastic zone size and crack opening displacement require comment. The yield strength found for Cu is typical of that measured on vapor

deposited thick Cu films, as well as on high purity, annealed Cu layers and foils. The value obtained for Al ($\sigma_0 \approx 25$ MPa) is lower than that usually expected for pure annealed Al, typically 70 MPa. However, since single crystals of pure Al can have yield strengths as low as 10 MPa, small values are not unprecedented.¹³ The inference is that considerable grain growth and extensive annealing during diffusion bonding have resulted in the lower yield strength.

The discrepancies between the $\epsilon_{xx}(x)$ moiré strain measurements for Cu/Al₂O₃ multilayers and the calculations are not yet understood. Measurement errors are probable, especially in the highly strained region near the crack front. However, the discrepancies in ϵ_{xx} are unlikely to be fully explained by such errors. An alternative possibility is that the metal deformation in the physically small region near the crack front cannot be represented by continuum plasticity. Instead, account must be taken of strain gradient plasticity.¹⁴ This phenomenon substantially elevates stresses in plastically deforming regions having small dimensions, $\lesssim 10$ μ m, and may result in larger ϵ_{xx} strains in the Al₂O₃.

Even though there are discrepancies between the measured and calculated strains for the Cu/Al₂O₃ layers, it is still evident that the ϵ_{yy} strains are similar to those expected solely from elasticity. The implication is that the level of stress reduction needed to fully suppress dominant crack formation from an initial surface flaw is not achieved within a multilayer having relatively thick ceramic layers, even when very soft metal interlayers are used. The only assurance, therefore, that a distributed damage mode can be realized in the absence of interface debonding is the use of a relatively large metal volume fraction, as elaborated elsewhere.¹¹ There are no obvious advantages to be derived from using thin (nanometers) multilayers. Moreover, there may be disadvantages because of the increased difficulty of plastic deformation in very thin metal layers.^{14,15}

REFERENCES

- [1] M.C. Shaw, D.B. Marshall, M.S. Dadkhah and A.G. Evans, *Acta Metall. Mater.*, **41** (1993) 3311.
- [2] K.S. Chan, M.Y. He and J.W. Hutchinson, *Mat. Sci. Eng.*, **A167** (1993) 57–64.
- [3] F.S. Shieu, R. Raj and S.L. Sass, *Acta Metall.*, **38**, (1990) 2215.
- [4] F.E. Heredia, M.Y. He, G.E. Lucas, A.G. Evans and D. Konitser, *Acta Metall. Mater.*, **41** (1993) 505.
- [5] W. Curtin, *J. Am. Ceram. Soc.*, **74**[11], 2837 (1991).
- [6] C. Cady, T.J. Mackin and A.G. Evans, *J. Am. Ceram. Soc.*, in press.
- [7] B. Han, *Optical Engineering*, **31** (1992) 1517.
- [8] S.E. Molis and D.R. Clarke, *J. Am. Ceram. Soc.*, **73** (1990) 3189.
- [9] Q. Ma and D.R. Clarke, *J. Am. Ceram. Soc.*, **76** (1993) 1433.
- [10] B.J. Dalgleish, K.P. Trumble and A.G. Evans, *Acta Metall.*, **37**[7] (1989) 1923–31.
- [11] M.C. Shaw, D.B. Marshall, B.J. Dalgleish, M.Y. He and A.G. Evans, *Acta Metall. Mater.*, submitted.
- [12] A.G. Evans and B.J. Dalgleish, *Acta Metall. Mater.*, **40** (1992) S295.
- [13] *Aluminum: Properties and Physical Metallurgy* (ed. J.E. Hatch) ASME, Metals Park, OH (1984) p. 2.
- [14] N.A. Fleck, G.M. Miller, M.F. Ashby and J.W. Hutchinson, *Acta Metall. Mater.*, **42** (1994) 475.
- [15] W.D. Nix, *Met. Trans.*, **20A** (1989) 2217.

FIGURE CAPTIONS

- Fig. 1. A schematic of a surface crack in a metal/ceramic multilayer indicating the relative effects of interface slip and debonding on the stress ahead of the crack.²
- Fig. 2. A schematic showing the loading arrangement used for R2 fluorescence measurements in the optical microprobe.
- Fig. 3. The locations used for stress measurement relative to the precrack: AA', 00' and OB.
- Fig. 4. A moiré pattern for Al/Al₂O₃, obtained after *unloading*, showing the region in which plastic slip has occurred. The curved line at the top center is a defect in the mask used to produce the grid.
- Fig. 5. The variation with applied stress of the slip length, normalized by the precrack length obtained for Al multilayers. Also shown are the predicted values for several yield strengths.
- Fig. 6. A typical moiré pattern sequence for Cu/Al₂O₃ multilayers as the load is increased: K refers to the nominal stress intensity factor.
- Fig. 7. Strain distributions for a Cu/Al₂O₃ multilayer obtained from the moiré measurements for a stress, $\sigma = 250$ MPa (a) along 00' (b) along OB. Both ϵ_{xx} and ϵ_{yy} are plotted. Also plotted are the calculated strains for plane stress, with $\sigma_0 = 70$ MPa and $n = 4$.
- Fig. 8. Piezospectroscopic peak shifts measured at three reference stresses for Al/Al₂O₃ multilayers along 00'. Also shown by the solid lines are the shifts calculated for a yield strength $\sigma_0 = 25$ MPa.
- Fig. 9. Measurements of the crack opening displacement. Also shown are the values predicted for the indicated yield strengths.
- Fig. 10. The finite element mesh used for the numerical calculations.

Fig. 11. Calculated plastic zone development and the crack opening displacements that occur upon applying a bending moment to Al/Al₂O₃ multilayers at the indicated reference stresses.

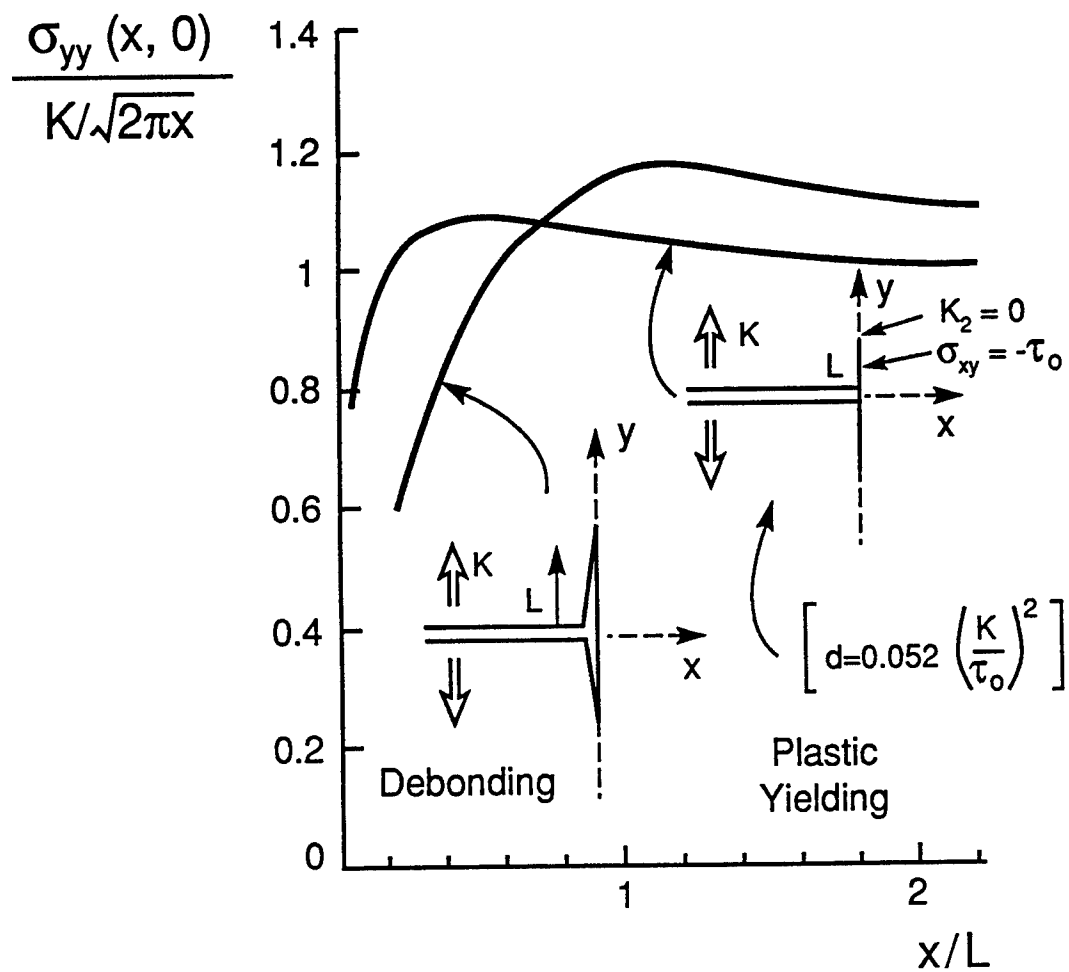


Figure 1

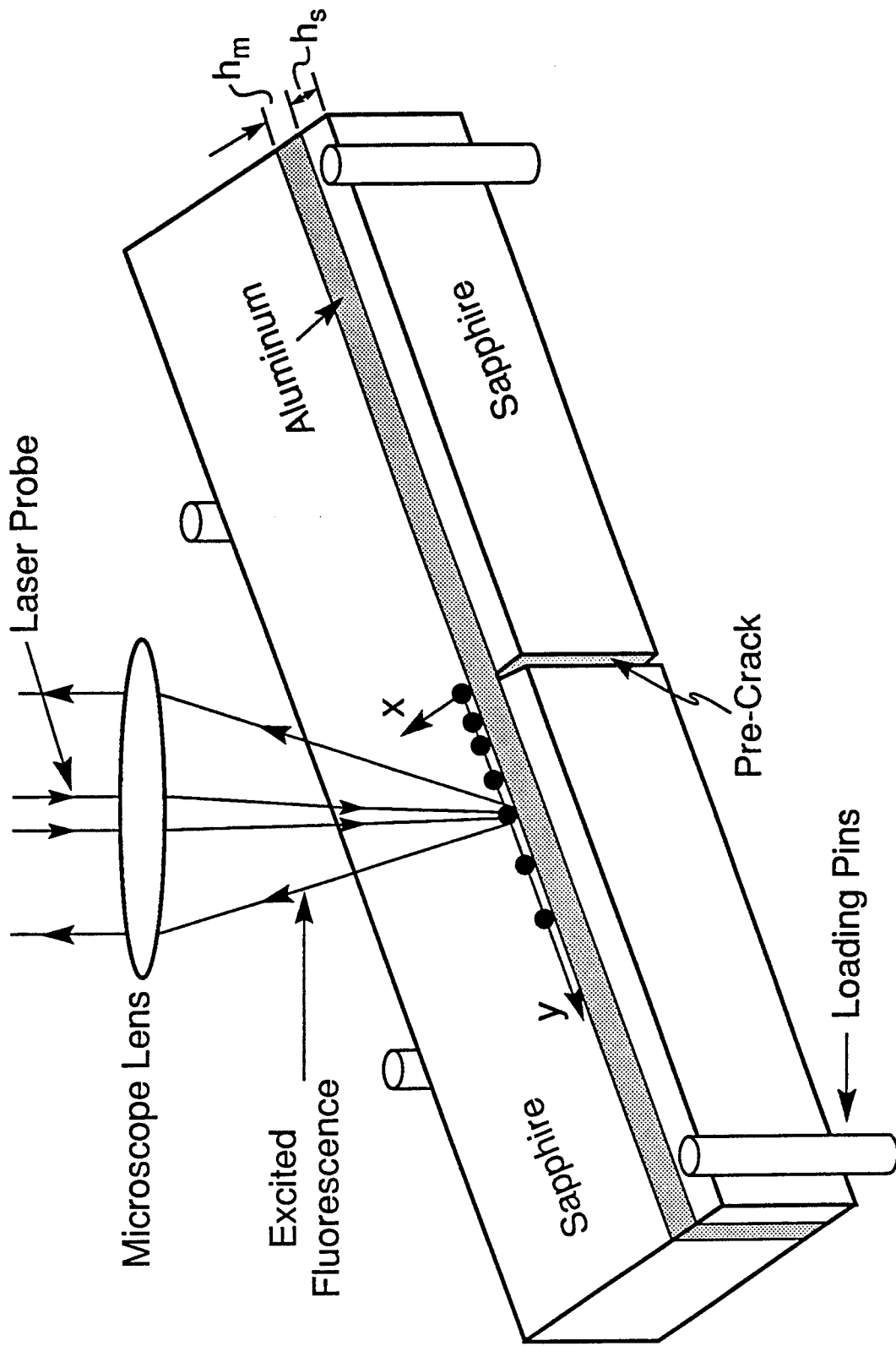


Figure 2

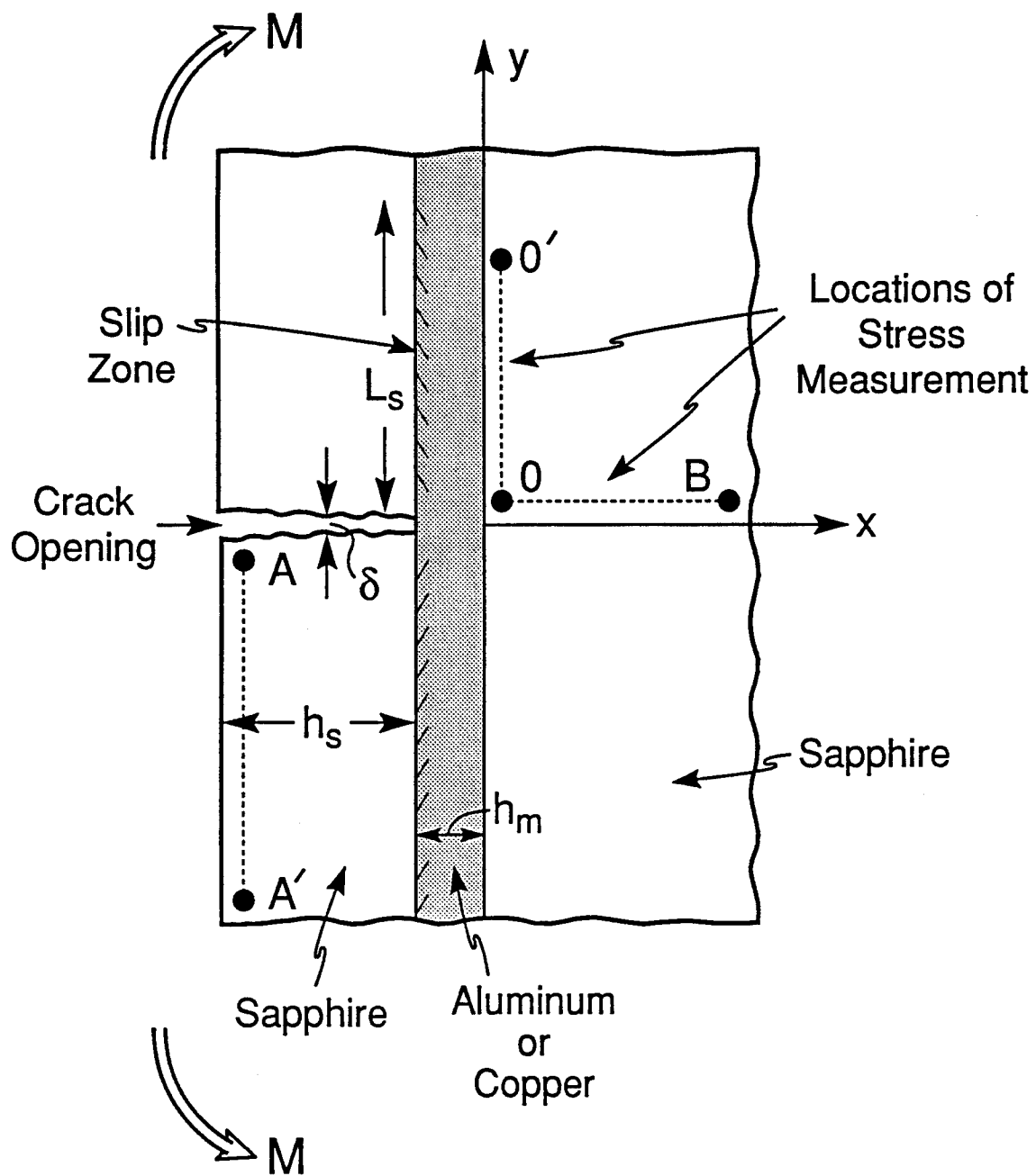


Figure 3



Figure 4

17-11-2017 14:10:10

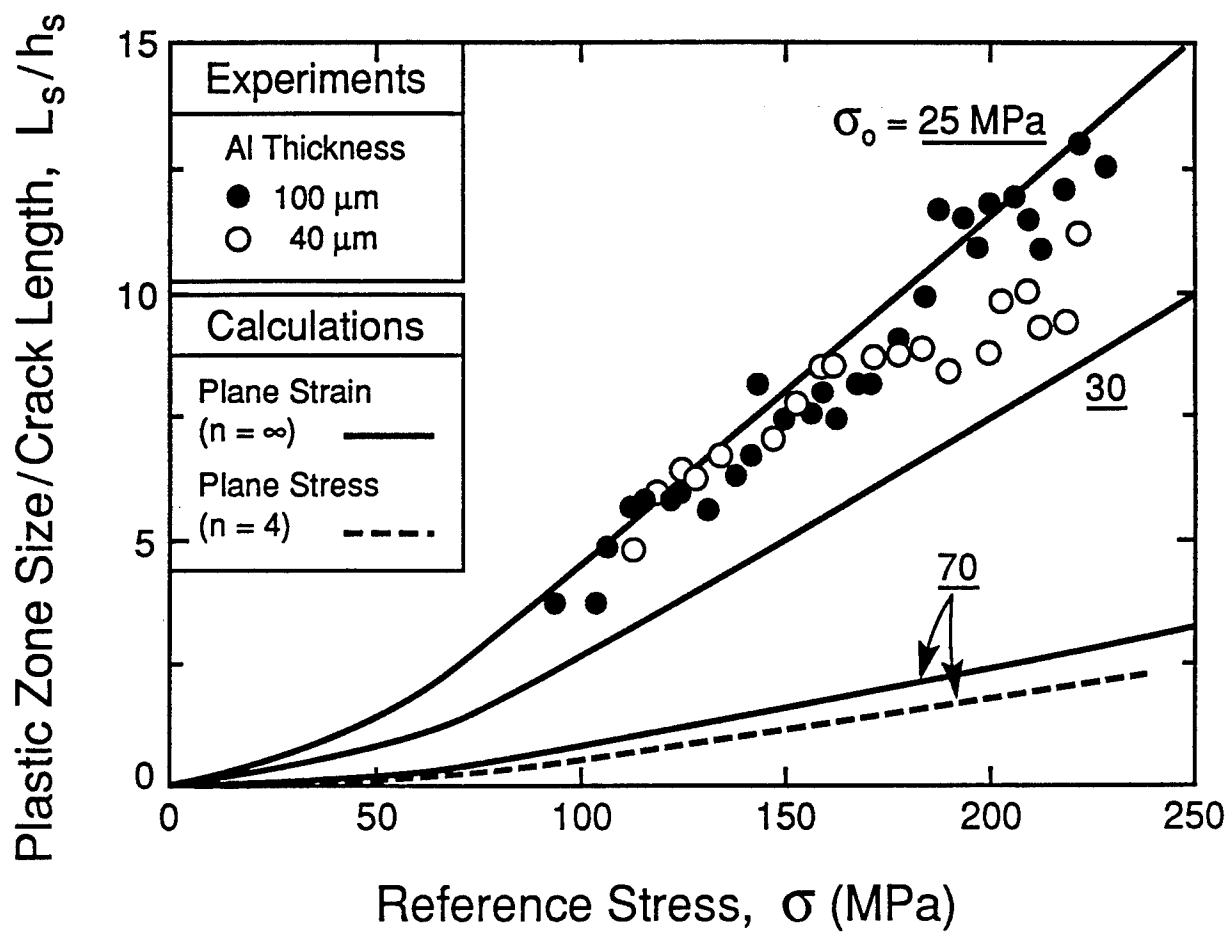


Figure 5

$K = 4.4$
(MPa \sqrt{m})

5.1

5.7

6.4

7.0

7.8

8.2

8.7

2 mm

Figure 6

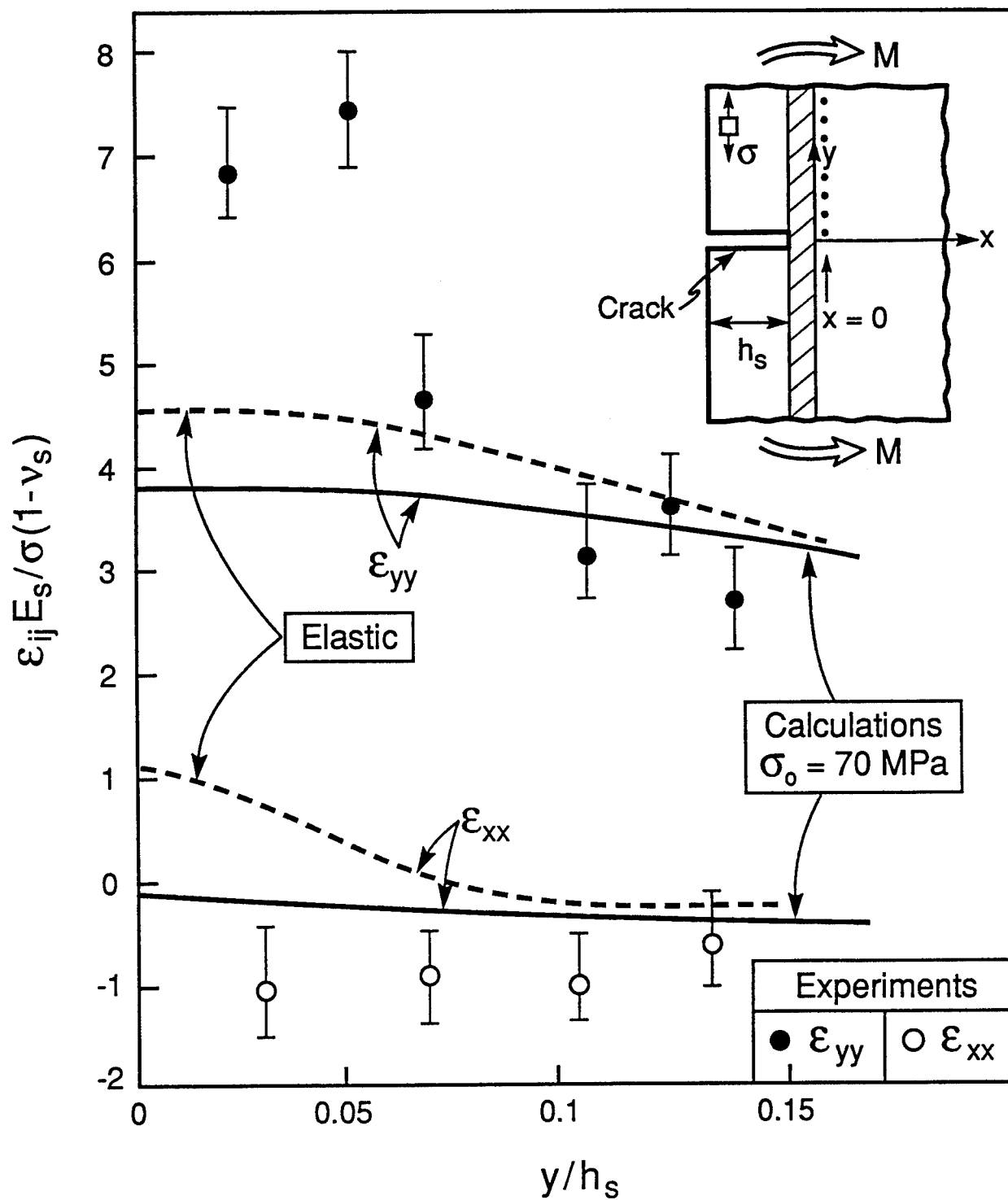


Figure 7a

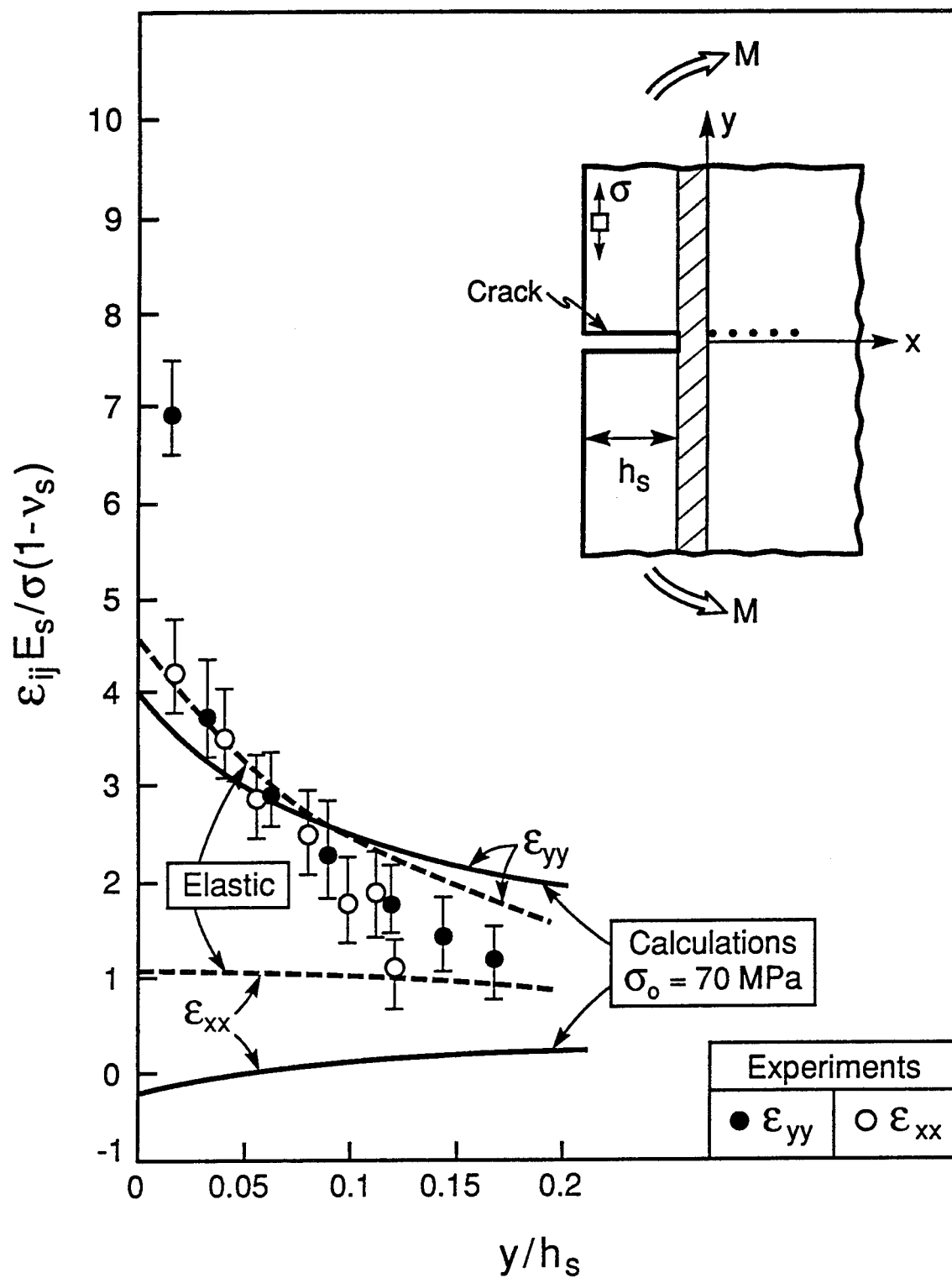


Figure 7b

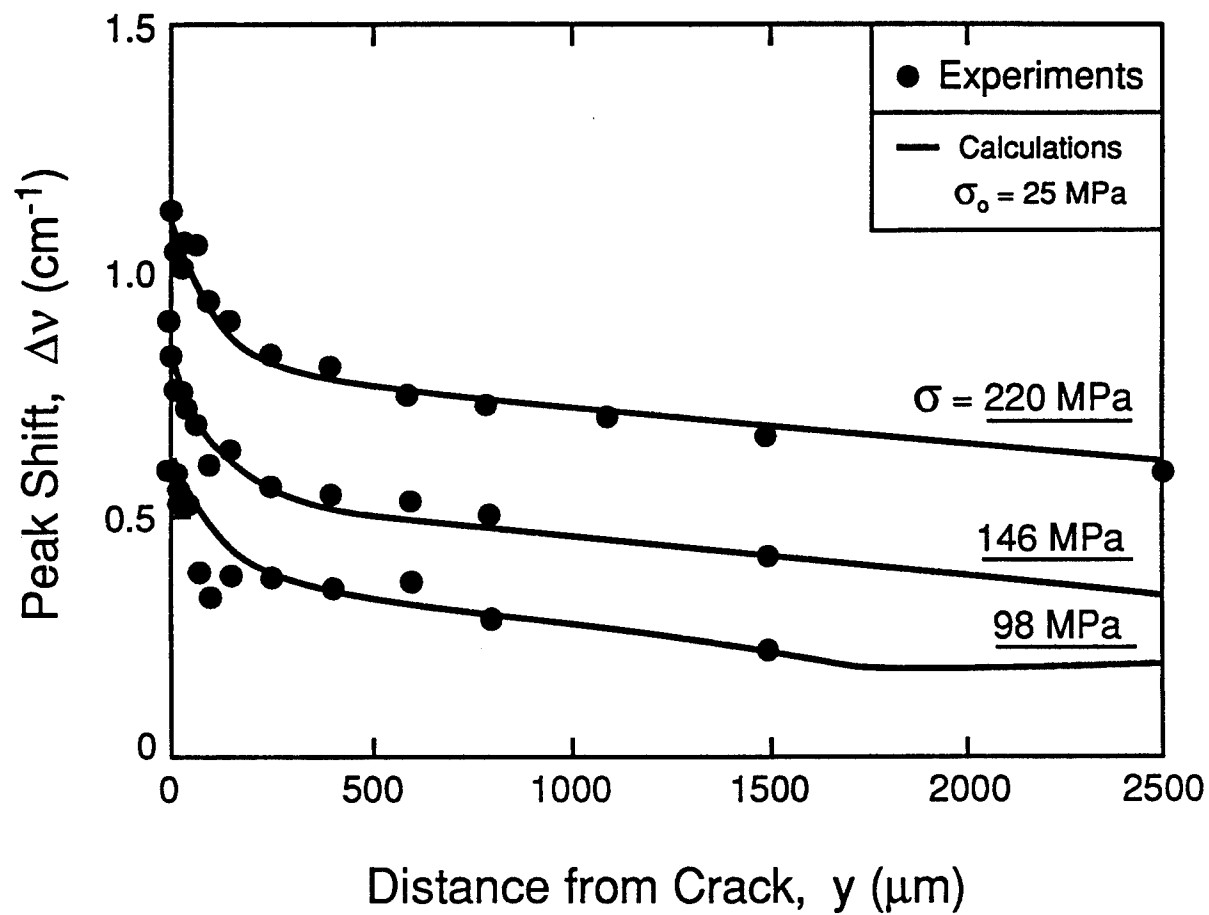


Figure 8

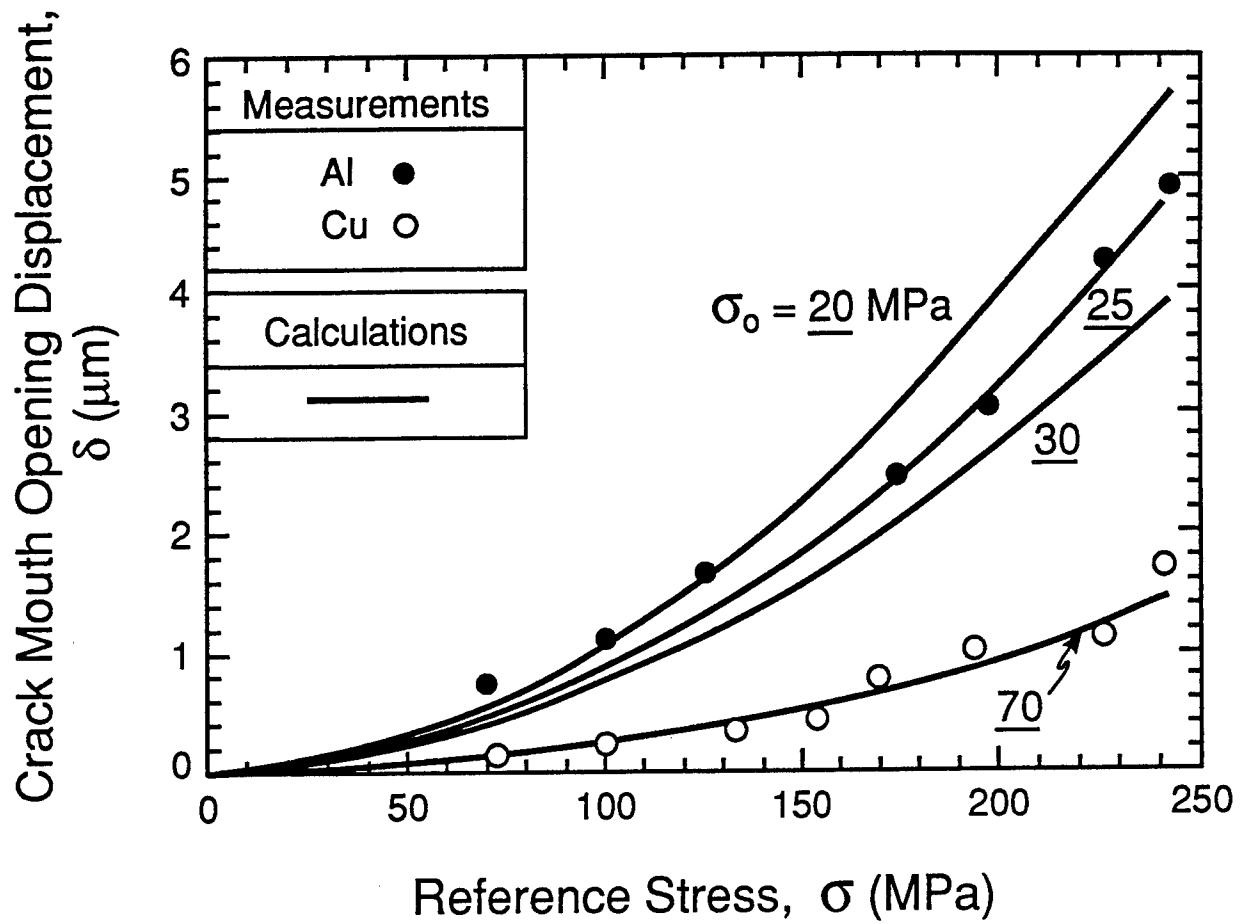


Figure 9

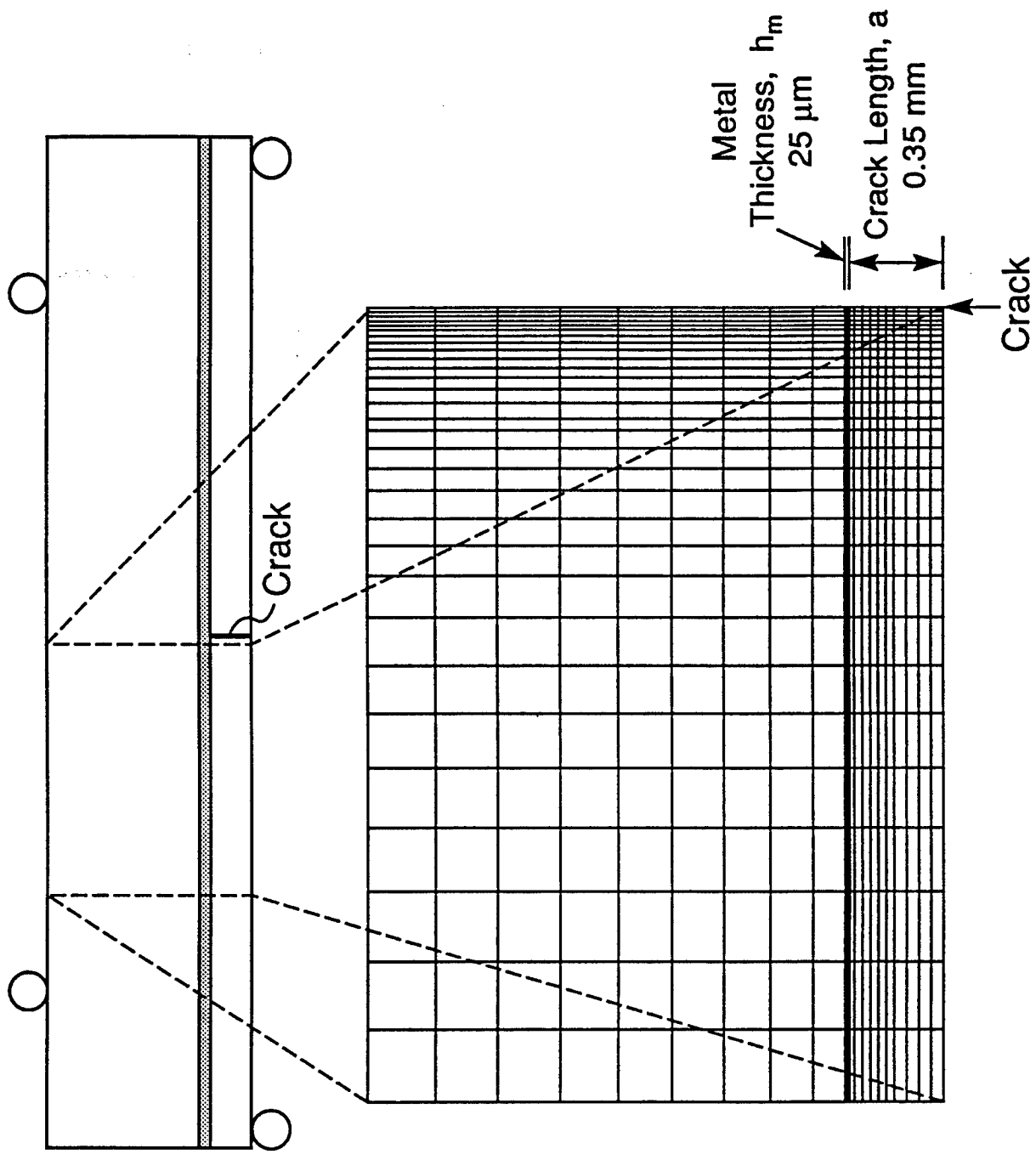


Figure 10

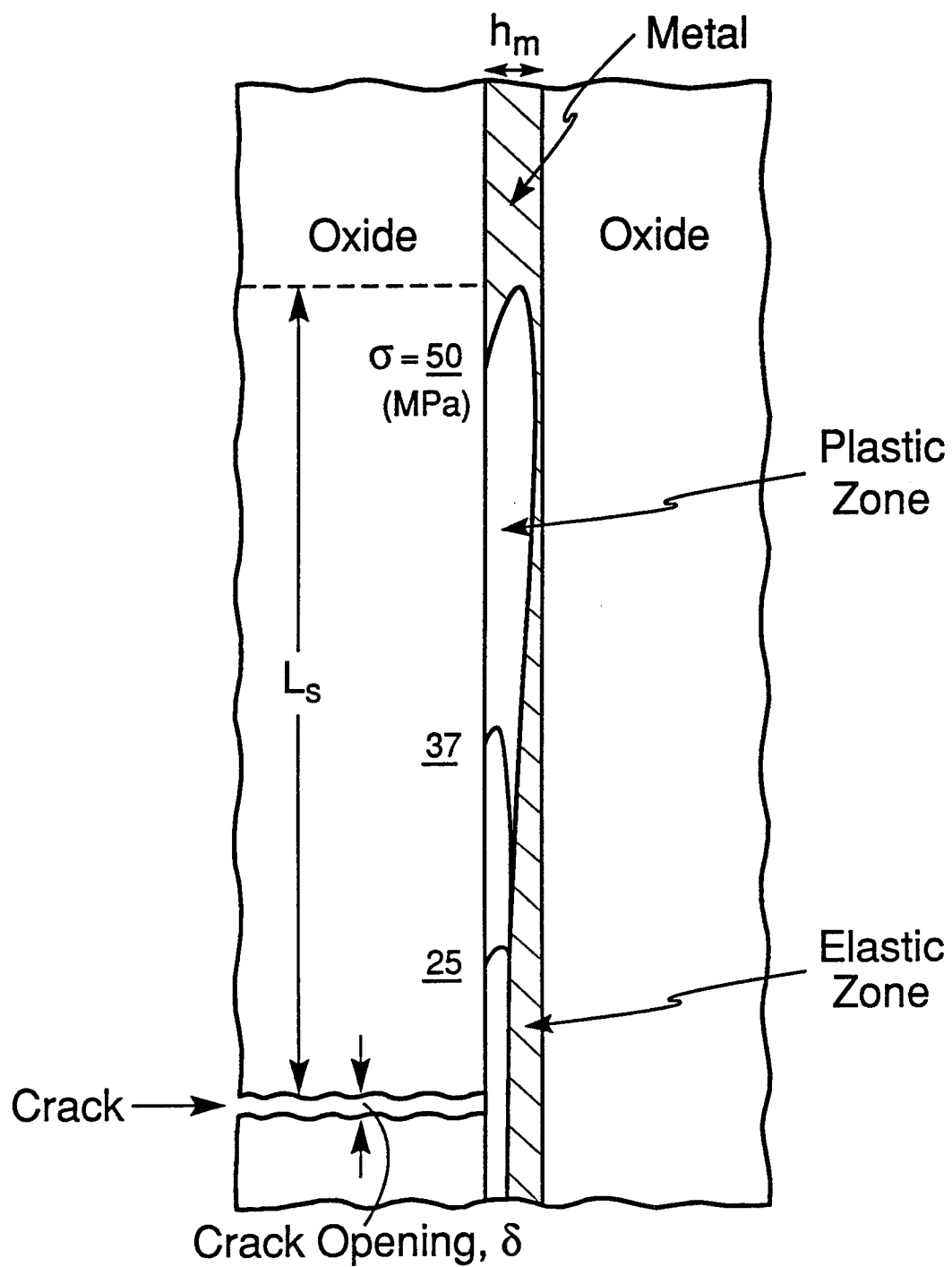
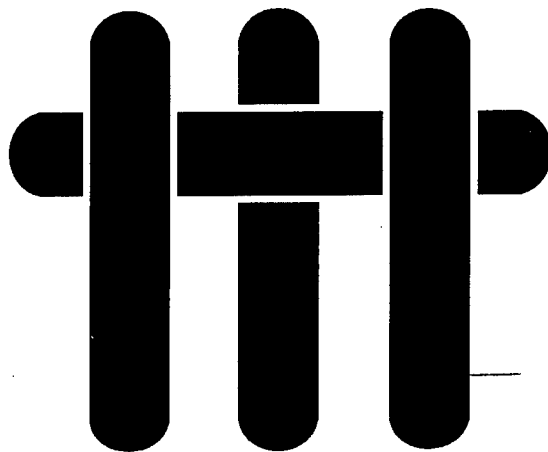


Figure 11

M A T E R I A L S



FATIGUE CRACK GROWTH AND STRESS REDISTRIBUTION AT INTERFACES

by

M.C. Shaw,^{†,‡} D.B. Marshall,[‡] B.J. Dalgleish,^{*} M.S. Dadkhah,[‡] M.Y. He,[†] and A.G. Evans[†]

[†]Materials Department
College of Engineering
University of California, Santa Barbara
Santa Barbara, California 93106-5050

[‡]Rockwell Science Center
Camino Dos Rios
Thousand Oaks, California 91360

^{*}Department of Materials Science
University of California, Berkeley
Berkeley, California 94720

ABSTRACT

The role of the interface in redistributing stress around cracks in multilayered ceramic/metal composites is investigated. The emphasis is on the different effects of interfacial debonding or of plastic slip in the metal phase adjacent to strongly bonded interfaces. The experiments are conducted on alumina/aluminum multilayered composites. Monotonic loading precracked test pieces causes plastic shear deformation within the aluminum layer at the tip of the notch without debonding. However, interfacial debonding can be induced by cyclic loading, in accordance with a classical fatigue mechanism. Measurements of the stress around the crack demonstrate that debonding is much more effective than slip at reducing the stress ahead of the crack.

1. INTRODUCTION

In layered materials with alternating ductile and brittle constituents, various modes of crack growth are possible.¹⁻⁶ Under in-plane loading, cracks form in the brittle layers. A crack in one layer may induce cracks in an adjacent layer. Whether or not this occurs depends upon the nature of the stress concentration transmitted across the intervening ductile material. If this stress concentration is large, a series of near-coplanar cracks form, which can be viewed as a single, *dominant crack*. Conversely, a weakened stress concentration allows *distributed damage*. The stress concentration may be reduced either by debonding at the interface between the brittle and ductile layers or plastic slip within the ductile layers. An asymptotic calculation⁶ (Fig. 1) predicts that debonding is more effective than slip at reducing the peak stress in the intact brittle layers and hence, should suppress crack renucleation. This prediction has yet to be verified by experiment.

The incidence of debonding, as opposed to slip adjacent to interfaces is influenced by the loading history. Interfaces that remain bonded upon monotonic loading may debond upon cyclic loading.⁷ Moreover, the ratio of mode II (shear) to mode I (tensile) loading acting upon an interface crack may affect the relative tendencies for debonding and slip.⁸

The three objectives of this study are as follows. (i) Contrast the debonding and sliding characteristics of interfaces subject to monotonic and cyclic loads. (ii) Examine the validity of models for the role of debonding and sliding on stress redistribution. This is achieved by comparing predicted stresses with measured stresses. For this purpose, the fluorescence spectroscopy method is used with aluminum oxide/Al multilayers. (iii) Establish the basic mechanism of cyclic debonding (fatigue) at metal/ceramic interfaces.

2. EXPERIMENTAL METHODS

2.1 Materials

Multilayered composites of Al and Al₂O₃ were prepared by diffusion bonding.^{1,4} For this purpose, thin discs of sapphire and polycrystalline Al₂O₃ were mechanically polished with diamond, to produce planar, parallel surfaces, which were then heat treated in air at 1000°C for 1 h to remove carbon based impurities. Thin sheets of Al (40, 100 or 250 µm thick) were prepared from 99.99% pure foils by cold rolling. These were interspersed between the sapphire and Al₂O₃ plates, with a sapphire layer on one outside surface and Al₂O₃ layers elsewhere. The layers were then vacuum hot pressed at temperatures of 640°C at a compressive stress of ~ 5 MPa for 48 h, resulting in a diffusion bond with essentially no residual porosity.

The diffusion-bonded discs were cut into beams suitable for flexural testing (dimensions ~ 3 x 3.5 x 50 mm) by using a diamond saw. Both side surfaces were polished to an optical finish to facilitate observations of interfacial debonding and crack growth, as well as for stress measurements.

2.2 Mechanical Tests

The location of the dominant crack in each specimen was pre-determined by placing a row of 50 N Knoop indentations, 500 µm apart, into the sapphire surface (Fig. 2). Direct observation of the specimen, using a long focal length optical microscope, revealed that these indentations produced precracks approximately 50-100 µm in length. The specimen was then loaded in four-point flexure with the indented surface in tension, within a fixture that permitted *in situ* monitoring of the side surfaces of the beams by using an optical microscope (Fig. 2). At a critical load, the flaws coalesced into a crack that propagated unstably, but arrested at the metal/sapphire interface.

These precracked specimens were loaded either monotonically or cyclically in four-point flexure. During each cyclic loading experiment, the range of load, ΔP , and the peak load, P_{\max} , were kept constant. The tests were interrupted after 1000, 5000 and 20,000–50,000 cycles to allow observation of the interface between the sapphire and the first aluminum layer. Interfacial debond cracks (Fig. 3a, b) were characterized by viewing through the transparent sapphire using an optical microscope. The growth rates of interfacial cracks were also determined in this manner. Following the cyclic experiments, the interfacial cracks were characterized further by scanning electron microscopy, after removal of the sapphire layer by fracture of the specimen.

2.3 Stress Measurement

After cycling, some specimens were reloaded in flexure, using a fixture located on the stage of a Raman microprobe.[†] This apparatus allows stress measurement by fluorescence spectroscopy within the Al_2O_3 .⁹ The loads were monitored using a miniature load cell. Chromium fluorescence spectra were collected at sites within the intact Al_2O_3 layer ahead of the precrack, as indicated in Fig. 2, with the specimen in both the loaded and unloaded states. Analysis of these spectra gave fluorescence peak locations that provided a measure of the stress in the Al_2O_3 layer: the relation between peak shift and stress was obtained from a separate series of calibration experiments (Section 4.1). In polycrystalline alumina, the method has ~ 20 MPa stress resolution and 100–200 μm spatial resolution.^{9–11}

In some cases, the precrack was extended into the underlying Al_2O_3 layers by monotonic loading. Again, cyclic loading experiments were conducted and the responses of the intervening Al layers were characterized by using both optical and scanning electron microscopy (SEM).

[†] Instruments SA, Model U1000.

3. INTERFACE RESPONSE

Monotonic loading of precracked specimens caused plastic slip within the metal layer at the tip of the precrack, prior to crack renucleation in the next Al_2O_3 layer. The characteristics of such plasticity have been measured using high-resolution strain mapping techniques.⁴ Cracks formed sequentially in adjacent polycrystalline Al_2O_3 layers, with increasing load. Each crack was nearly coplanar with the precrack. By considering this assembly as a dominant, mode I crack and by measuring its length, a nominal crack growth resistance, K_R , was determined from the applied loads (Fig. 4).

Cyclic loading of similar precracked specimens gave a different response. When the peak load was below that at which a crack renucleated in the next Al_2O_3 layer, *stable debonding* occurred along the sapphire/Al interface (Fig. 3). The crack growth rate, da/dN , was found to decrease slightly with increase in crack length, L_s , for a given load range, ΔP (typically by a factor of 2–4 after 20,000–50,000 cycles). After fracturing the specimen to remove the sapphire from the region above the interface fatigue crack, classical fatigue striations were observed by scanning electron microscopy on the Al crack surface (Fig. 5). In the case shown in Fig. 5, the striation spacing is about equal to the crack extension per cycle ($\sim 1 \mu\text{m}/\text{cycle}$). Moreover, the striations are strongly affected by crystallography, having different orientations in different grains (Fig. 5b). The basic crack growth mechanism thus appears to be similar to that occurring in monolithic alloys.¹²⁻¹⁵

The range of energy release rates, ΔG , applicable to each cyclic loading experiment was estimated from the load range, ΔP , by using a previous analysis of the flexural geometry (Fig. 2).^{16,17} The analysis provides solutions for steady-state cracks ($L_s/a_0 > 0.4$) in homogeneous elastic beams with no residual stress.¹⁷ The estimates were obtained by neglecting the effect of residual stress and plasticity in the metal on G

and by using the steady-state formulae. The present results were obtained for $0.2 < L_s/a_0 < 4.0$, except for the lower left point in Fig. 6, where $L_s/a_0 \sim 0.04$. Note that these results refer to mixed-mode cyclic debonding¹⁶ with a mode mixity, $\psi \approx 50^\circ$. These values of ΔG , in conjunction with the crack growth rates per cycle, da/dN , allow comparison with fatigue data for monolithic aluminum alloys obtained from the literature (Fig. 6 and Table I).¹⁸⁻²⁰ It is evident that the rates of cyclic interfacial debonding exceed the mode I fatigue crack growth rates for monolithic alloys, at all ΔG used during the present investigation. Therefore, *mixed-mode* fatigue crack growth can occur along strongly bonded metal/ceramic interfaces in preference to mode I crack growth through the alloy. These interface measurements complement data obtained previously in mode I.⁷

Conversely, in specimens that had been loaded monotonically to grow a crack through *several*, successive Al_2O_3 layers, subsequent cyclic loading caused rapid fatigue failure of the intervening, intact Al layers. This occurred by mode I cyclic growth emanating from cracks in the adjacent alumina layers (Fig. 7). Similar results have been reported for multilayered intermetallic/metal composites.²¹

4. STRESS MEASUREMENTS AND COMPARISON WITH THEORY

4.1 Piezospectroscopic Calibration

The relationship between the applied stress, σ_{ij} , and the fluorescence peak shift, Δv , is a tensorial relation,¹⁰

$$\Delta v = \Pi_{ij} \sigma_{ij} \quad (1)$$

where Π_{ij} are the piezospectroscopic coefficients. It has been shown that the off-diagonal components of Π_{ij} are negligibly small for the fluorescence peaks of chromium

in aluminum oxide.¹⁰ This expression may be further simplified for a polycrystalline material to¹⁰

$$\Delta v = Q \sigma_{kk} \quad (2)$$

where $Q = 1/3 (\Pi_{11} + \Pi_{22} + \Pi_{33})$ and σ_{kk} is the sum of the principal stresses, $\sigma_{kk} = \sigma_{11} + \sigma_{22} + \sigma_{33}$.

The coefficient, Q , for the stress dependence of the R_2 chromium fluorescence peak in the alumina used in the present case was calibrated by collecting spectra from the side surface of a polished alumina beam subjected to various levels of four-point flexural loading. These spectra were analyzed to yield the relative peak position as a function of applied stress (Fig. 8). From these results, $Q = 2.48 \pm 0.05 \text{ cm}^{-1}/\text{GPa}$: consistent with values previously reported for alumina ($2.46\text{--}2.52 \text{ cm}^{-1}/\text{GPa}$).¹⁰

4.2 Stresses

The distributions of stress before and after monotonic and cyclic loading were measured by optical fluorescence. In each specimen, the measurements were obtained from the first intact Al_2O_3 layer along a line $20 \mu\text{m}$ from the interface with the metal layer. Typical results are shown in Fig. 9. The stress distribution during monotonic loading (at $K = 7 \text{ MPa}\sqrt{\text{m}}$) exhibited a broad maximum ahead of the crack front. After unloading, the stress along the same line exhibited a minimum ahead of the crack front (Fig. 9). The measured peak stress at the maximum load is similar to that given by the solution for a homogeneous elastic body (Appendix A), consistent with previous measurements in other ceramic/metal multilayered composites.^{4,11} These have shown that slip in the metal layer does not diminish the σ_{yy} stress in the ceramic layer ahead of the crack tip (Fig. 1) significantly, unless the relative slip length, L_p/h , is large (> 10).⁶

After cyclic loading to attain a debond length, $L_s > 2 \text{ mm}$,[‡] the stress concentration ahead of the crack was found to be eliminated, within the sensitivity of the fluorescence measurements (Fig. 9). Comparison of this result with analysis is complicated by finite geometry effects: because of the large values of the ratio: debond length/precrack length, $L_s/h \approx 5$, the asymptotic solution (Fig. 1) is not relevant. A finite element solution has thus been obtained for the specific flexural geometry used in these tests. The solution (Fig. 10) establishes that, for $L_s/a_0 \approx 5$, the stress concentration ahead of the precrack is, indeed, eliminated. These measurements and calculations directly confirm that debonding is more effective than plastic slip at reducing the stress ahead of a crack in ceramic/metal multilayers.

5. FATIGUE CRACK TRAJECTORIES

Two trajectories are possible for a fatigue crack arrested at the interface (Fig. 11). The crack may propagate into the metal under essentially mode I conditions (Fig. 7). Alternatively, it may deflect and propagate along the interface (Fig. 3). The parameters controlling the choice between these two trajectories are the relative strain energy release rate ranges, ΔG , the crack growth rates, da/dN and the mode mixity, Ψ . For a surface crack, ΔG for mixed mode growth along the interface is *less* than ΔG for mode I growth through the Al alloy (Appendix B). Nevertheless, in flexural loading, for which $\Psi \approx 50^\circ$ ⁸ (Section 3), growth along the interface is preferred for both the Al/sapphire and the Al/polycrystalline alumina interfaces. This behavior arises because at given ΔG , the mixed-mode interfacial crack growth rate, da/dN is *larger* than the mode I growth rate through the alloy (Fig. 12), as elaborated in Appendix B.

[‡] ($\Delta K = 5 \text{ MPa}\sqrt{\text{m}}$ and $K_{\text{max}} = 7 \text{ MPa}\sqrt{\text{m}}$)

The preference for fatigue crack growth through the metal rather than along the interface when the metal layer is one of the intact ligaments remaining after monotonic cracking of several ceramic layers, as in Fig. 7, now remains to be explained. The relative values of ΔG for interfacial debonding and growth through the Al alloy are essentially the same as for the surface crack (Appendix B). One significant difference, however, is the mode mixity. For interfacial debonding at metal ligaments, the loading is mode II⁸ ($\Psi = 90^\circ$). It is likely that mode II cyclic debond rates are considerably lower than those measured in mixed mode, because of crack face contact.^{22,23} It is plausible that the debond rate is reduced to such a level that mode I ligament failure is preferred. If these arguments are correct, the effect of mode mixity on the cyclic debonding of the interface has major implications for the fatigue performance of multilayers.

The basic mechanisms that determine the different cyclic crack growth rates are governed by the cyclic stresses and strains that occur near the crack tip. For a crack near a bimaterial interface, the cyclic shear stresses can exceed those expected in a monolithic alloy.²⁴ These large stress amplitudes should coincide with a larger cyclic growth rate near the interface, at the equivalent loading mode. However, a comprehensive analysis that relates these stress amplitudes to crack growth for a range of mode mixities is needed to rationalize the behaviors found in this study.

6. CONCLUDING REMARKS

Two competing mechanisms of fatigue cracking have been observed in $\text{Al}_2\text{O}_3/\text{Al}$ multilayers. Mixed-mode cracks extend along the metal/ceramic interfaces, normal to the tip of a main crack, in accordance with a classical fatigue mechanism. Conversely, intact metal ligaments rupture rapidly by mode I fatigue crack growth. The interfacial cracking at the crack tip has the *beneficial* effect of reducing the stresses ahead of the

main crack and thereby suppressing further growth of that crack. The rupture of ligaments in the crack wake is detrimental, because it reduces the crack tip shielding imparted by the bridging ligaments. This duality in fatigue behavior might be exploited in order to optimize the fatigue resistance of metal/ceramic multilayers.

The mixed mode fatigue crack growth rate along the Al/Al₂O₃ interface exceeds the mode I rate in monolithic Al alloys. The large growth rate arises because of the enhanced shear stress amplitude at the tip when the crack is at a bimaterial interface.²⁵ Further analysis of the relationship between the growth rates in the interface and the alloy is in progress.

The experimental measurements of the relative effects of slip and debonding on stress redistribution ahead of a mode I crack are consistent with calculations.⁶ Debonding was found to be substantially more effective than slip at reducing the stress. The development of interfaces that experience controlled debonding upon either cyclic loading or monotonic loading thus represents an opportunity for achieving fracture and fatigue-resistant layered materials.

APPENDIX A

Fluorescence Measurements And Probe Size Effects

The signal intensity at a given frequency within a fluorescence spectrum of a stress-sensitive material is influenced by the state of stress of the material throughout the volume sampled by the probe. If stress gradients are significant within this volume, calculation of the fluorescence peak position requires a somewhat complicated calculation of the entire spectrum. To obtain an estimate of probe size effects in the present experiments, a simpler calculation, which assumes that the measured peak position is a weighted average of the peak positions from each element within the sampling volume, was used:

$$\sigma'_{kk}(x_o, y_o) = \int_{-y^*}^{y^*} \int_{-x^*}^{x^*} \sigma_{kk}(x, y) R(x_o - x, y_o - y) dx dy \bigg/ \int_{-y^*}^{y^*} \int_{-x^*}^{x^*} R(x, y) dx dy \quad (A1)$$

where $R(x-x_o, y-y_o)$ is the probe response function, $\sigma_{kk}(x, y)$ is the local stress field and x^* and y^* represent the boundaries of the region from which the probe collects information.

Previous studies have established that the stresses of interest for layered materials with strongly bonded interfaces are given to a good approximation by the asymptotic elastic field around a crack in a homogenous body.^{2,4} For mode I loading, the stress, $\sigma_{kk}(x, y)$ is, therefore,²⁵

$$\sigma_{kk}(x, y) = \left[K \sqrt{\left(\frac{2}{\pi(x^2 + y^2)^{3/2}} \right)} \right] \cos(\tan^{-1}(y/x)/2) \quad (A2)$$

where x and y are the Cartesian coordinates measured from the crack tip. In the present analysis, the measured stress is compared with this solution at the location directly opposite the precrack ($x = h_m, y = 0$), where Eqn. (A2) becomes

$$\sigma_{kk} = \frac{2K_I}{\sqrt{2\pi h_m}}. \quad (A3)$$

The response function was characterized experimentally by placing the probe on a horizontal surface of a thick beam of alumina, at a location immediately adjacent to a vertical free surface. The intensity of the signal was measured as the probe was translated away from the vertical surface, until the signal reached a level that did not change appreciably with further movement of the probe. The results were consistent with a response function of the form

$$R(x, y) = \exp[-(x^2 + y^2)/b^2] \quad (A4)$$

where b is a measure of the size of the volume of material sampled by the probe. The value of b ($\approx 200 \mu\text{m}$) is much larger than the area illuminated on the specimen surface (spot size $\sim 2 \mu\text{m}$); indirect illumination from internal scattering determined the volume from which the fluorescence signal was collected.

With the parameters pertinent to the data of Fig. 9 ($K_I = 7.0 \text{ MPa}\sqrt{\text{m}}$, $h_m = 250 \mu\text{m}$), the stress directly opposite the crack tip is, from Eqn. (A3), $\sigma_{kk}(h_m, 0) = 350 \text{ MPa}$. The stress given by Eqn. (A1), with the center of the probe at $(x_0, y_0) = (h_m, 0)$ is significantly lower: 325 MPa . However, both values are reasonably close to the value in Fig. 9 deduced from the measured peak shift ($360 \pm 20 \text{ MPa}$), consistent with the findings of previous studies.^{4,11}

APPENDIX B

Fatigue Crack Trajectory

The preferred path taken by a fatigue crack depends on the ratio of energy release rate ranges, $\Delta\mathcal{G}$, compared with the ratio of crack growth rates at the relevant phase angle, Ψ , for the different possible trajectories. For a surface crack, an interface debond is mixed mode ($\Psi \approx 50^\circ$).¹⁶ The comparison is thus made for mixed mode crack growth along the interface and mode I growth through the alloy (Fig. 6). The energy release rate range for mode I growth through the alloy is²⁶

$$\Delta\mathcal{G} \approx 1.26\pi a(\sigma_{\max}^2 - \sigma_{\min}^2)/E \quad (\text{B1})$$

where a is one-half the ceramic layer thickness, σ_{\max} and σ_{\min} are the maximum and minimum stresses applied during load cycling and E is the modulus of the ceramic. For mixed-mode growth along the interface, upon initial cyclic debonding²⁷

$$\Delta\mathcal{G}_{\text{I/II}} \approx 0.3\pi a(\sigma_{\max}^2 - \sigma_{\min}^2)/E. \quad (\text{B2})$$

Then, upon further growth, when steady state is reached ($\Delta\mathcal{G} = \Delta\mathcal{G}_{\text{ss}}$),¹⁶

$$\Delta\mathcal{G}_{\text{I/II}}^{\text{ss}} \approx 0.5a(\sigma_{\max}^2 - \sigma_{\min}^2)/E. \quad (\text{B3})$$

The ratio of energy release rates for mode I growth into the alloy and for mixed mode I/II growth along the interface, is thus in the range $4.2\text{--}2.5\pi$. Imposing this ratio onto the crack growth curves dictates whether interface debonding is preferred or vice versa

(Fig. 12). The present data for $\text{Al}_2\text{O}_3/\text{Al}$ (Fig. 6) indicate that interface crack growth is preferred, at least for ΔG in the range, $10 \rightarrow 10,000 \text{ Jm}^{-2}$.

For intact metal ligaments, the ΔG ratio is similar, with a somewhat larger value for mode I,²⁶

$$\Delta G_I \approx 2b(\sigma_{\max}^2 - \sigma_{\min}^2) [\tan(\pi a/2b)] / E. \quad (\text{B4})$$

where $2(b - a)$ is the ligament thickness. More importantly, the loading for an interface debond crack is now mode II. It is expected that the mode II debond growth rate, da/dN , is appreciably lower than that in mixed mode. Such reductions arise because of frictional contacts along the debond faces, as found in monolithic alloys in fatigue,²² and for monotonic interface debonding.²³ In this case, mode I growth through the alloy is preferred over interface debonding.

TABLE I**Interface Fatigue Crack Growth for Al/Al₂O₃**

Metal Layer Thickness (μm)	Energy Release Rate Range, ΔG (Jm^{-2})	Average Crack Growth Range, $d\bar{a}/dN$ (m/cycle)
40	13	2.9×10^{-8}
	144	1.0×10^{-8}
	180	1.5×10^{-6}
100	13	1.4×10^{-9}
	139	2.2×10^{-8}
250	4	2.8×10^{-9}
	130	3.4×10^{-8}

REFERENCES

- [1] B.J. Dalgleish, K.P. Trumble and A.G. Evans, "The Strength and Fracture of Alumina Bonded with Aluminum Alloys," *Acta Metall.*, **37**[7] (1989) 1923-31.
- [2] H.C. Cao and A.G. Evans, "On Crack Extension in Ductile/Brittle Laminates," *Acta Metall. Mater.*, **39**[12] (1991) 2997-3005.
- [3] M.Y. He, F.E. Heredia, M.C. Shaw, D.J. Wissuchek and A.G. Evans, *Acta Metall. Mater.*, **41** (1992) 369.
- [4] M.C. Shaw, D.B. Marshall, M.S. Dadkhah and A.G. Evans, *Acta Metall. Mater.*, **41**[11] (1993) 3311-22.
- [5] A.G. Evans and B.J. Dalgleish, *Acta Metall. Mater.*, **40** (1992) S295.
- [6] K.S. Chan, M.Y. He and J.W. Hutchinson, *Mat. Sci. Eng.*, in press.
- [7] R.M. Cannon, B.J. Dalgleish, R.H. Dauskart, T.S. Oh and R.O. Ritchie, *Acta Metall. Mater.*, **39**, (1991) 2145.
- [8] J.W. Hutchinson and Z. Suo, *Appl. Mech. Rev.*, **28** (1991).
- [9] S.E. Molis and D.R. Clarke, *J. Am. Ceram. Soc.*, **73** (1990) 3189.
- [10] Q. Ma and D.R. Clarke, *J. Am. Ceram. Soc.*, **76** (1993) 1433.
- [11] M.C. Shaw, A.G. Evans, D.B. Marshall, D.R. Clarke and Q. Ma, to be published.
- [12] R.M. Pelloux, *Trans. Quart., ASM*, **62**[1] (1969) 281.
- [13] R.W. Hertzberg and P.C. Paris, *Proceedings, International Fracture Conference, Sendai, Japan*, **1** (1965) 459.
- [14] R.C. Bates and W.G. Clark, Jr., *Trans. Quart., ASM* **62**[2] (1969) 380.
- [15] P.C. Paris, *Fatigue—An Interdisciplinary Approach*, Proceedings 10th Sagamore Conference, Syracuse University Press, Syracuse, NY (1964) p. 107.
- [16] P.G. Charalambides, J. Lund, R.M. McMeeking and A.G. Evans, *J. Appl. Mech.*, **56** (1989) 77-82.
- [17] P.G. Charalambides, H.C. Cao, J. Lund and A.G. Evans, *Mech. of Mtls.*, **8**[4] (1990) 269-83.
- [18] S.R. Swanson, F. Cicci and W. Hoppe, *ASTM STP 415* (1967) 312.
- [19] P.C. Paris and F. Erdogan, *J. Basic Eng. Trans., ASME, Series D*, **85**[4] (1963) 528.

- [20] Society of Materials Science, Japan, "Data Book on Fatigue Crack Growth Rates of Metallic Materials," [1] (1983).
- [21] K.T. Rao, R.O. Ritchie and G.R. Odette, *Acta Metall. Mater.*, **40** (1992) 353.
- [22] R.O. Ritchie, F.A. McClintock, H. Nayeib-Hashemi and M.A. Ritter, "Mode III Fatigue Crack Propagation in Low Alloy Steel," *Met. Trans. A*, Vol. **13A**, 1, 1982, pp. 101–110.
- [23] A.G. Evans and J.W. Hutchinson, *Acta Metall.*, **37** (1989) 909.
- [24] C. Woeltjen, C.F. Shih and S. Suresh, *Acta Metal. et Mater.*, **41** (1993) 2317.
- [25] B.R. Lawn and T. Wilshaw, *Fracture of Brittle Solids*, Cambridge Univ. Press (1975).
- [26] H. Tada, P.C. Paris and G.R. Irwin, *The Stress Analysis of Cracks Handbook*, Paris Productions (1985).
- [27] M.Y. He and J.W. Hutchinson, *Intl. Jnl. Solids Structures*, **25**[9] (1989) 1053–67.

FIGURE CAPTIONS

- Fig. 1. Effects of slip and debonding on the stress ahead of a semi-infinite crack.⁶
- Fig. 2. The specimen configuration and the locations used for stress measurement.
- Fig. 3. a) Optical micrographs of two Al/Al₂O₃ beams, the top beam subjected to a single load cycle, the lower beam subjected to 50,000 cycles of flexural fatigue.
b) Optical micrograph of an interface debond created from the precrack by cyclic loading, as viewed through the transparent outer sapphire layer.
- Fig. 4. Crack growth resistances measured for the multilayers used in the present study.
- Fig. 5. Scanning electron micrographs of fatigue striations observed in the aluminum layer after debonding and removal of the upper sapphire layer: a) within one grain, b) different orientations in different grains.
- Fig. 6. Plot of the average crack growth rate, $d\bar{a}/dN$ vs. ΔG for multilayers with different metal layer thicknesses. Also shown are data for Type 7075-T6 and 1100-TO aluminum alloys, taken from References 7 and 18-20.
- Fig. 7. Scanning electron micrograph of an aluminum ligament that failed in fatigue.
- Fig. 8. Piezospectroscopic calibration curve for the alumina used in the present investigation.
- Fig. 9. Stress ahead of precrack with load applied (nominal $K = 7 \text{ MPa}\sqrt{\text{m}}$) and unloaded. Comparison with and without debonding.
- Fig. 10. Effect of debonding in a flexural configuration on stresses ahead of the surface precrack.
- Fig. 11. Schematic illustrating possible fatigue crack trajectories: a) Mode I extension of cracks from cracked ceramic layers into the intervening metal layer and b), c) Extension of mode II cracks along the interface.

Fig. 12. Schematic of the effect of mode mixity on the relative crack growth rates for different crack trajectories. Also shown is the ratio of $\Delta\mathcal{G}$'s. For this case, interface debonding is preferred over mode I growth into the alloy.

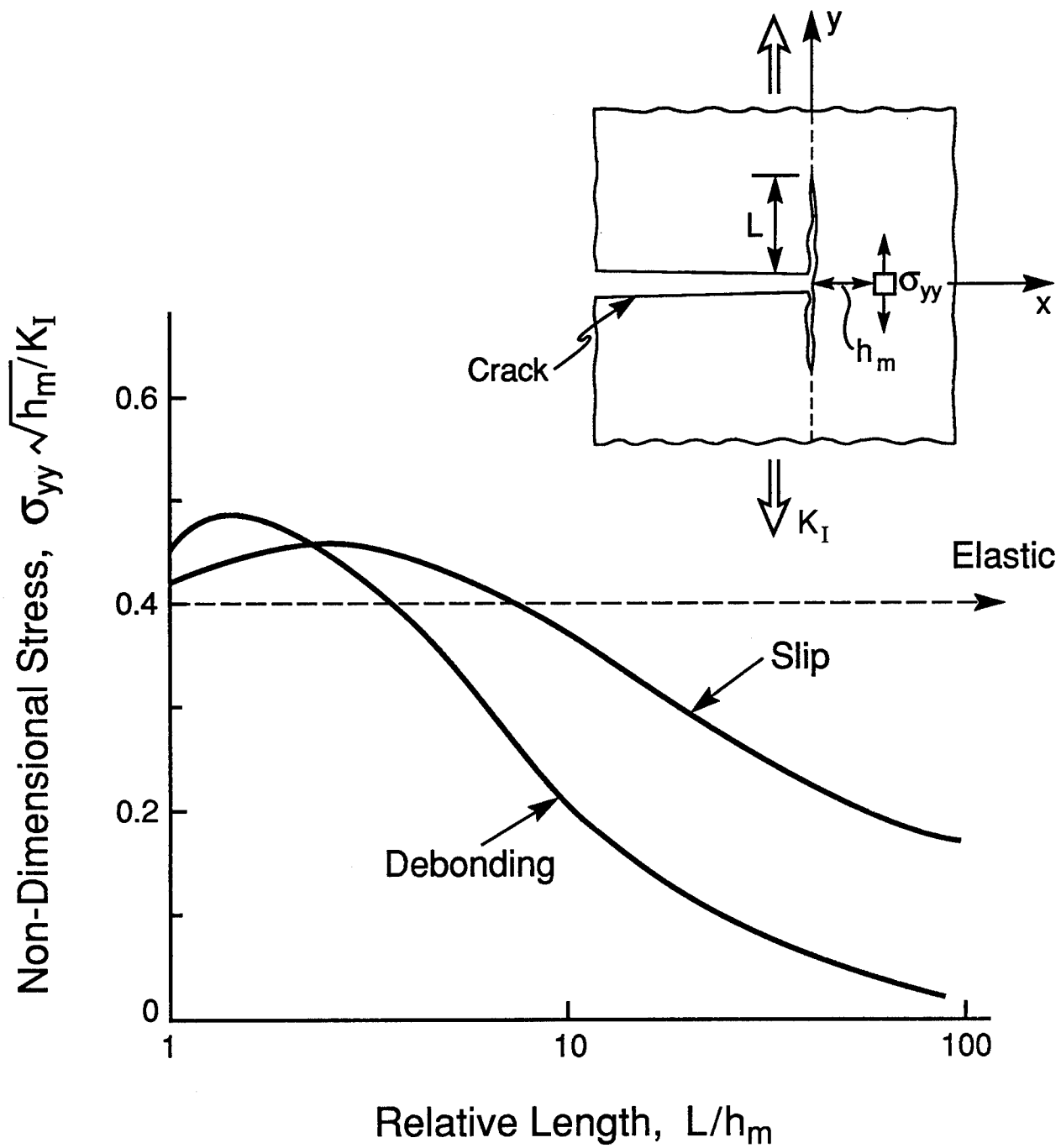


Figure 1

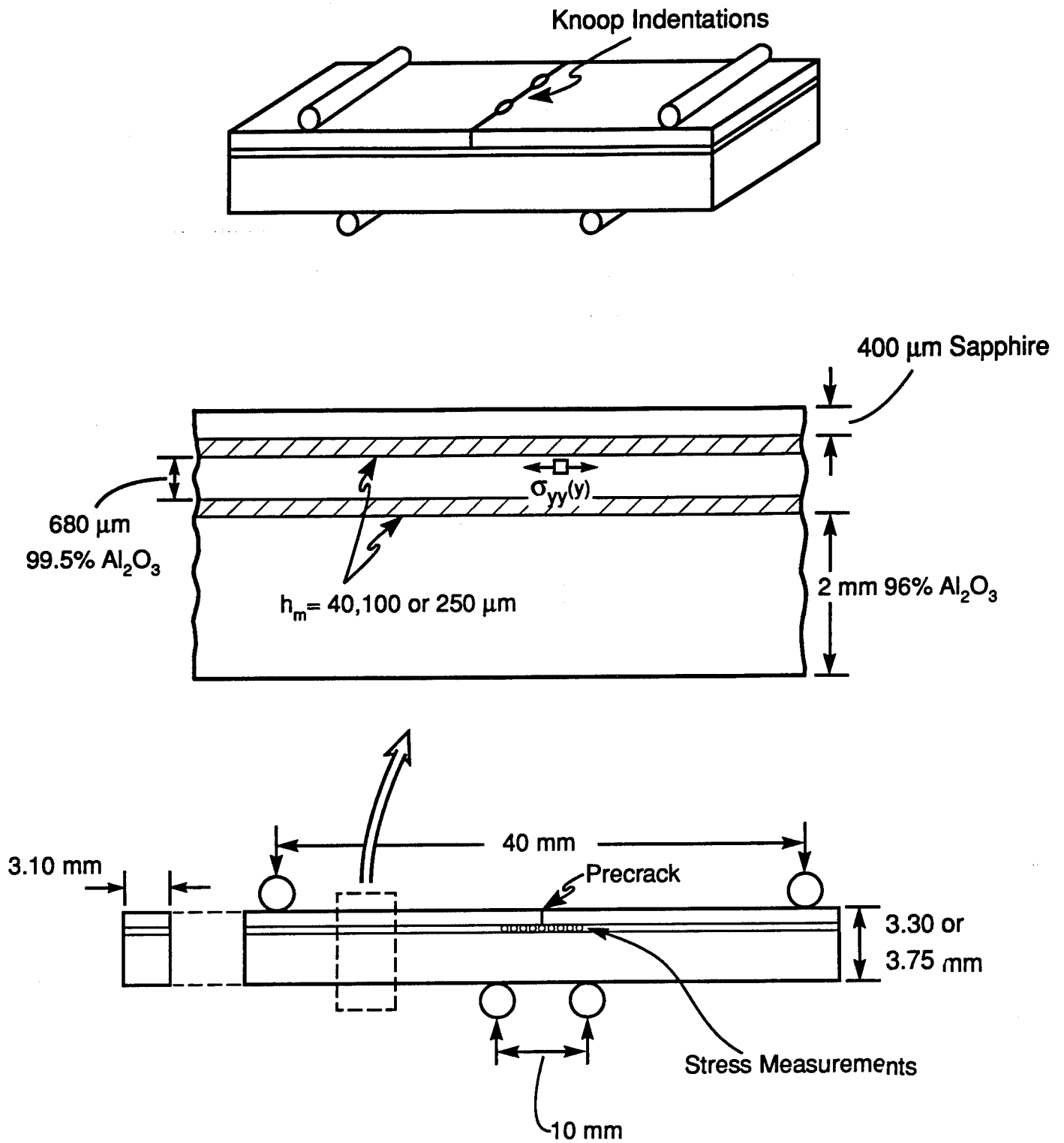
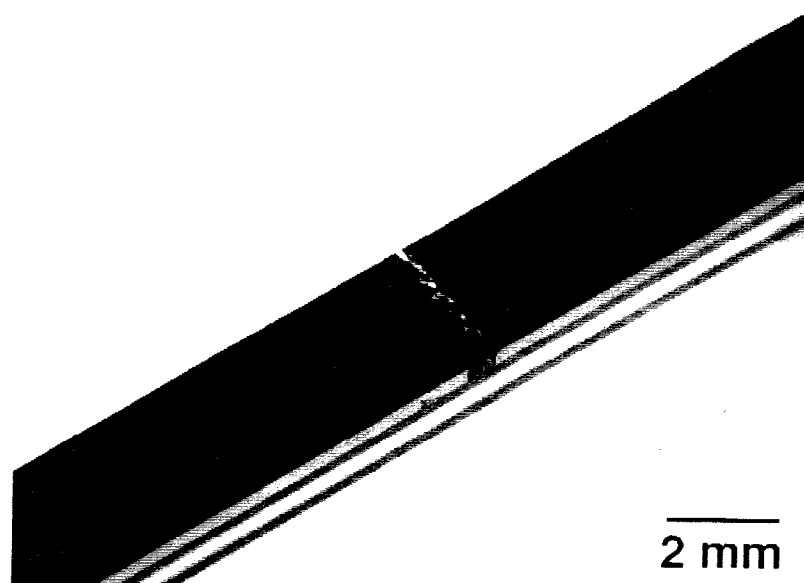
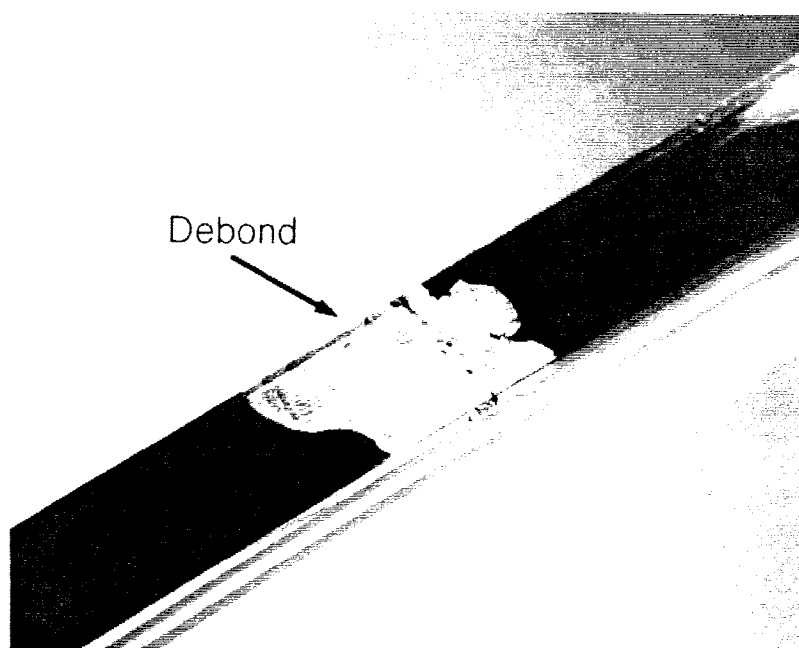


Figure 2



1 Load Cycle



50,000 Load Cycles

Figure 3(a)

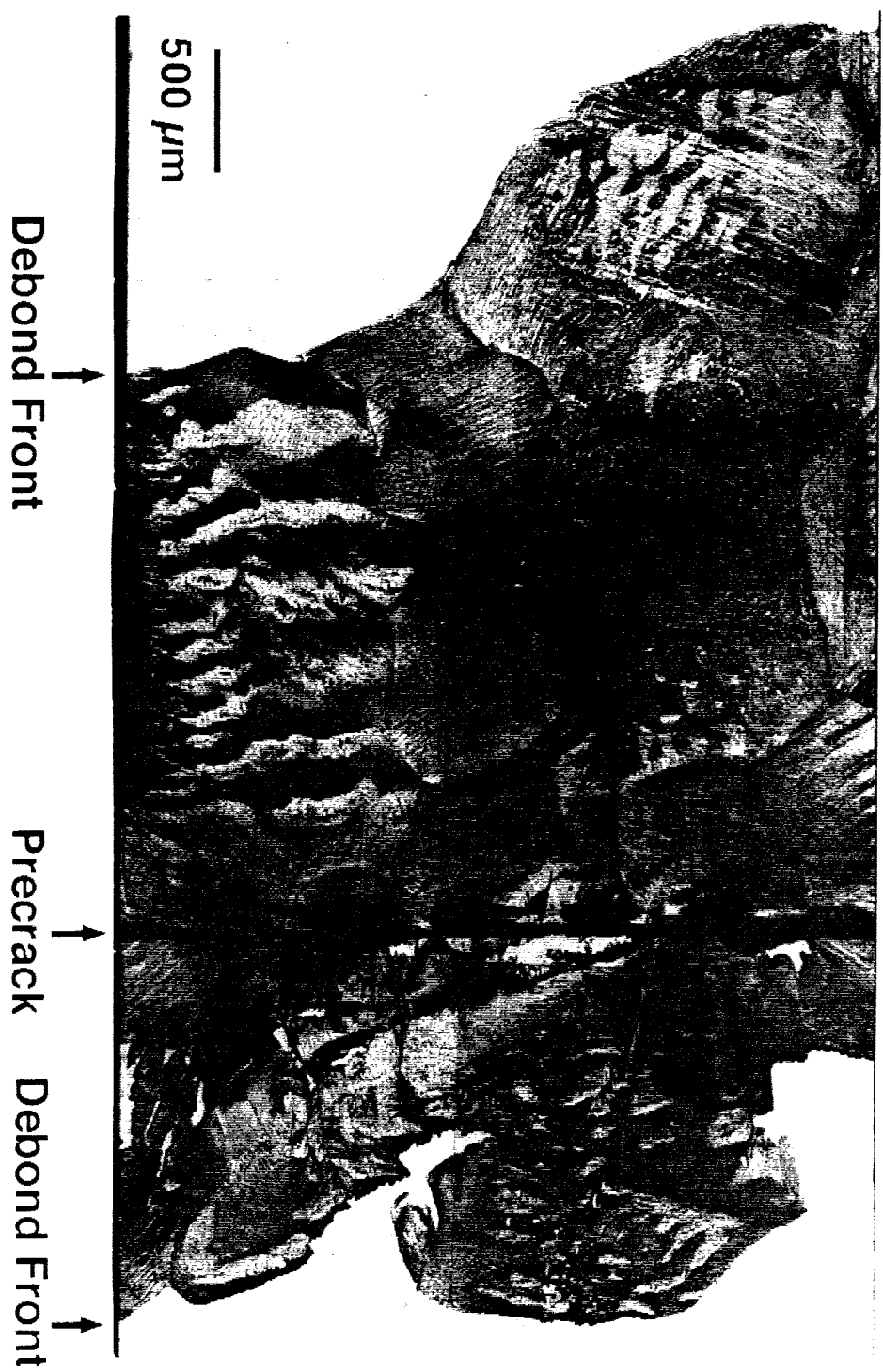


Figure 3(b)

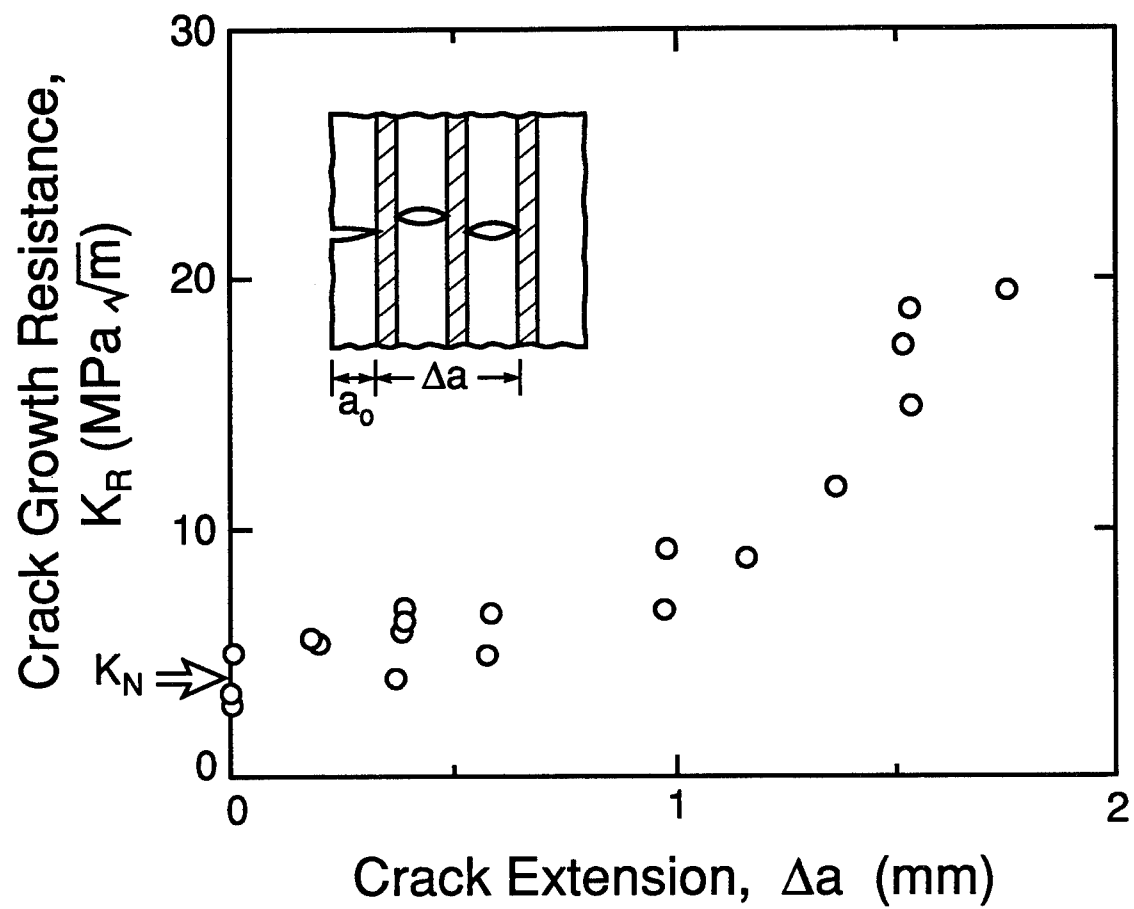
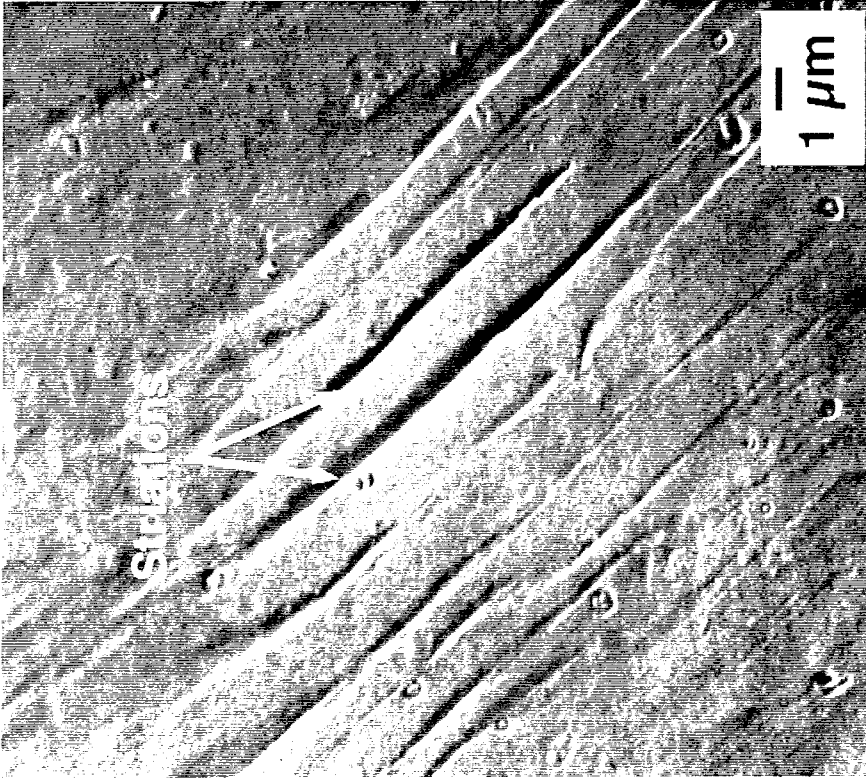
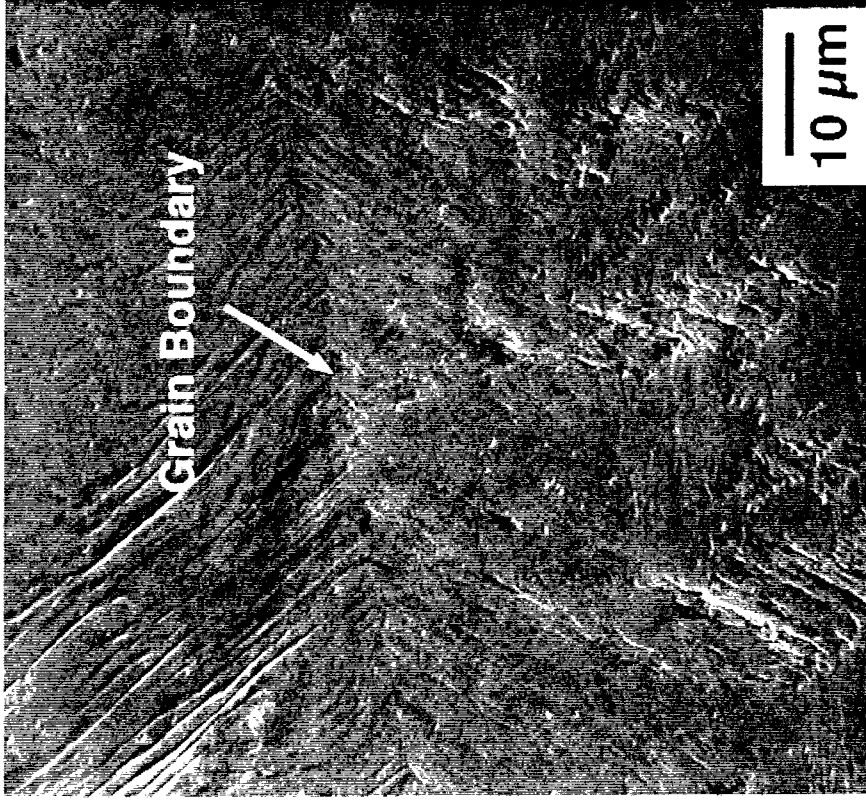


Figure 4



(a)



(b)

Figure 5

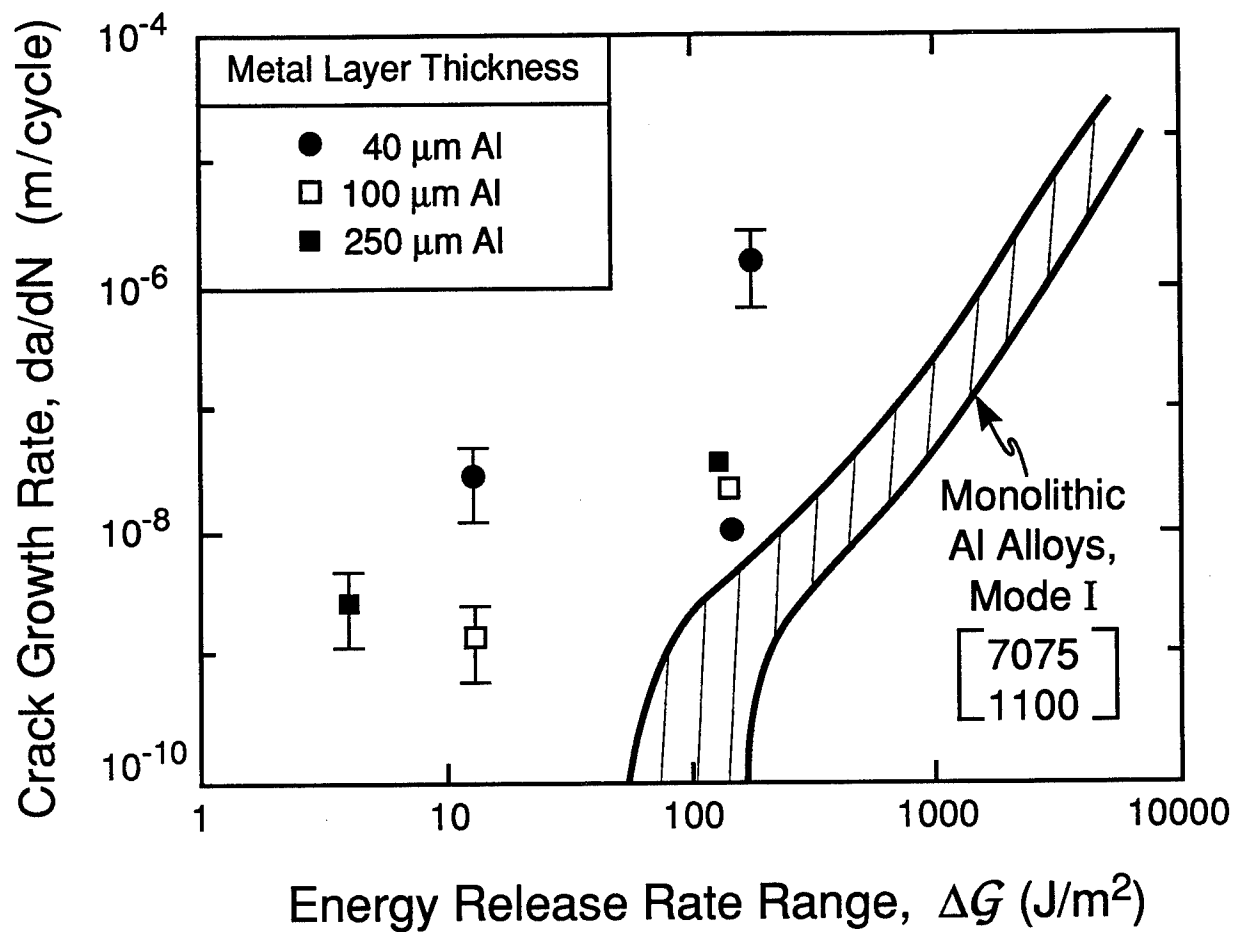


Figure 6

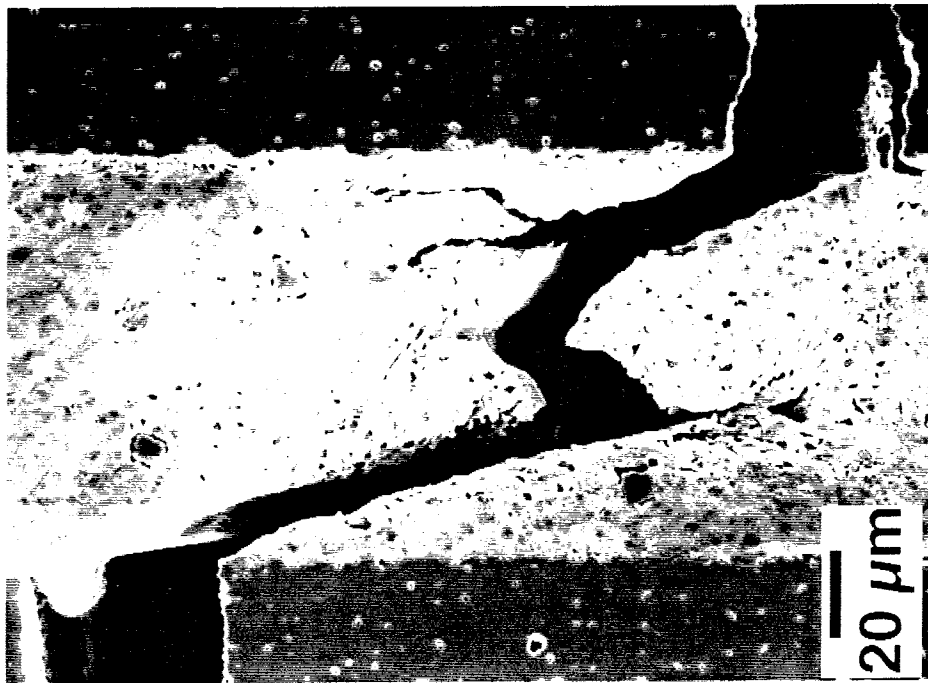


Figure 7

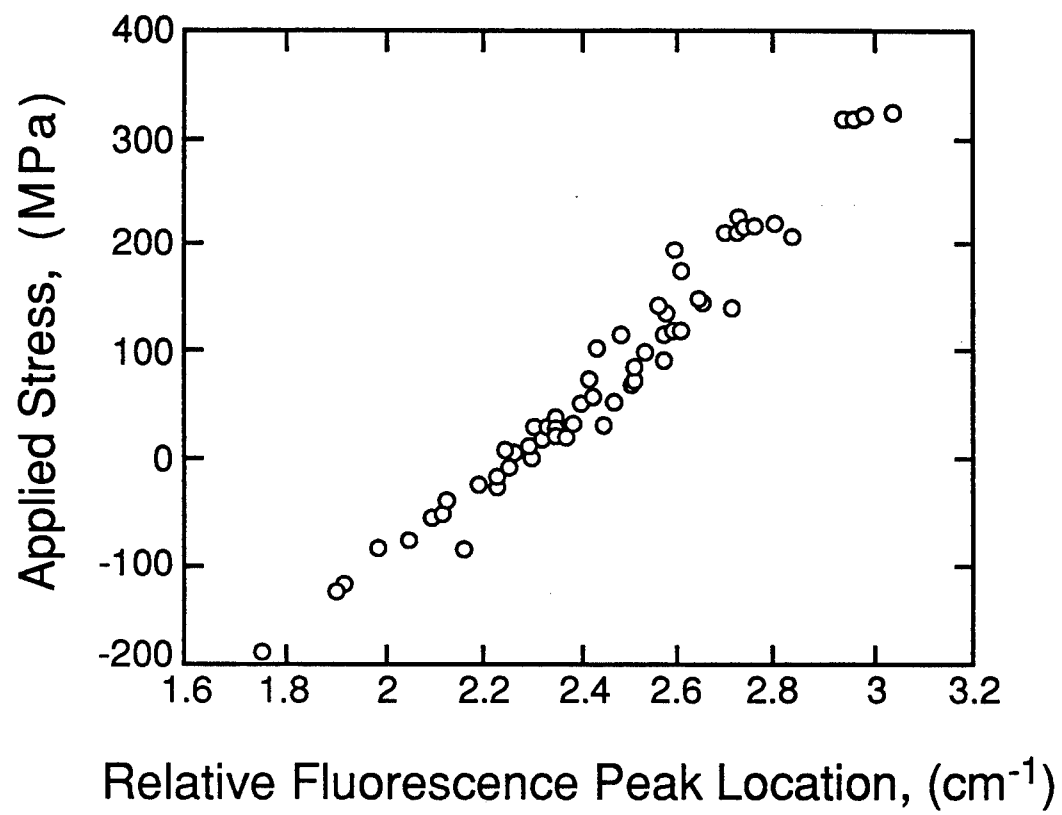


Figure 8

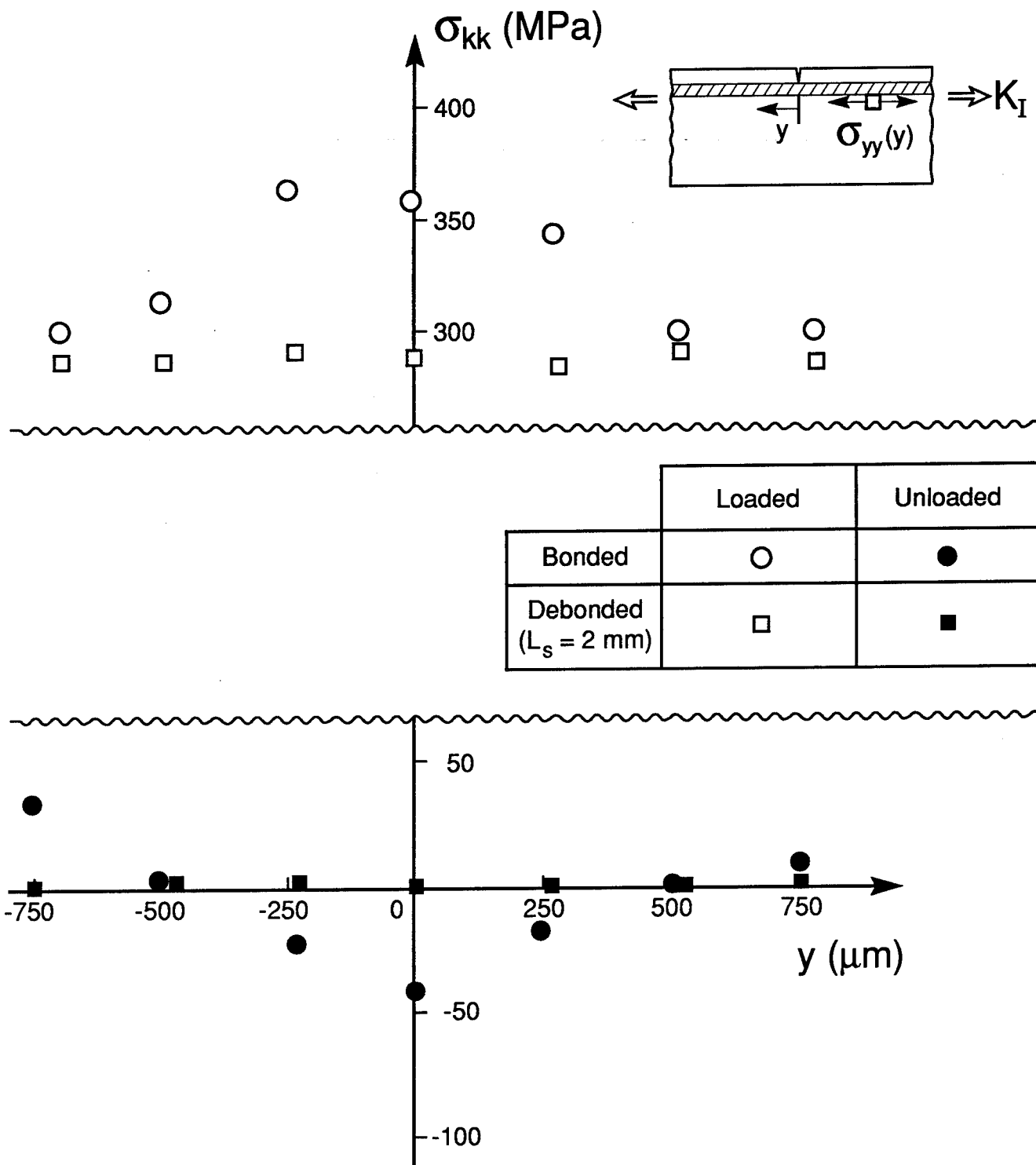


Figure 9

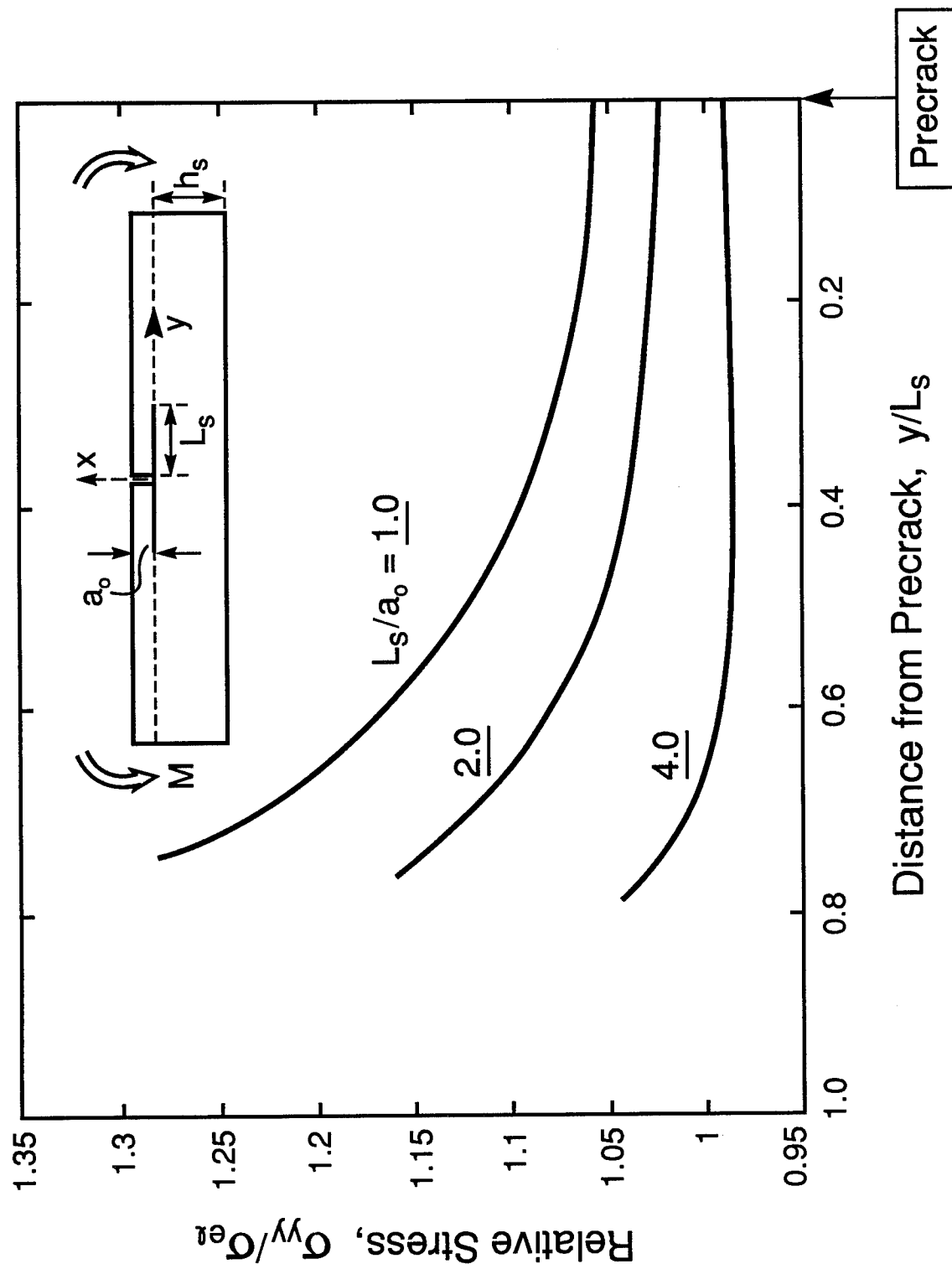


Figure 10

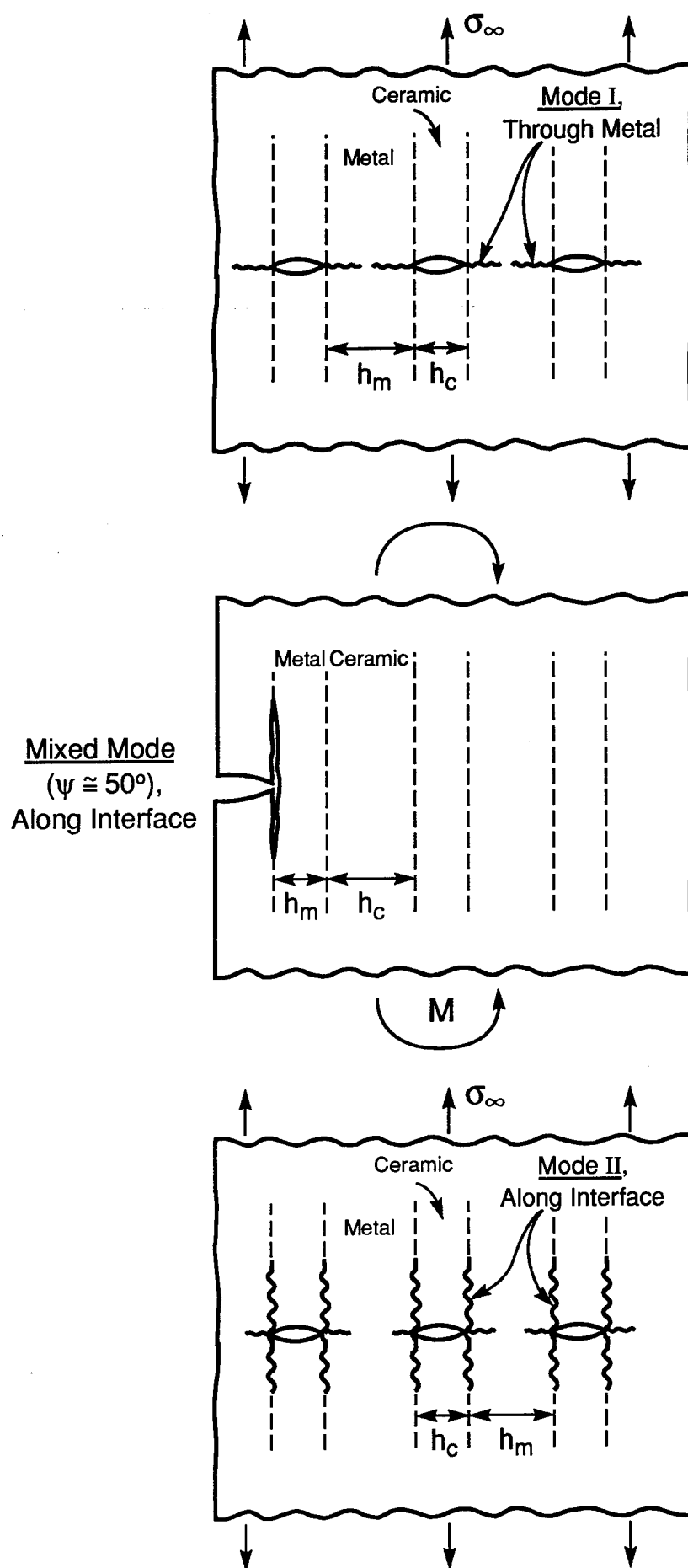


Figure 11

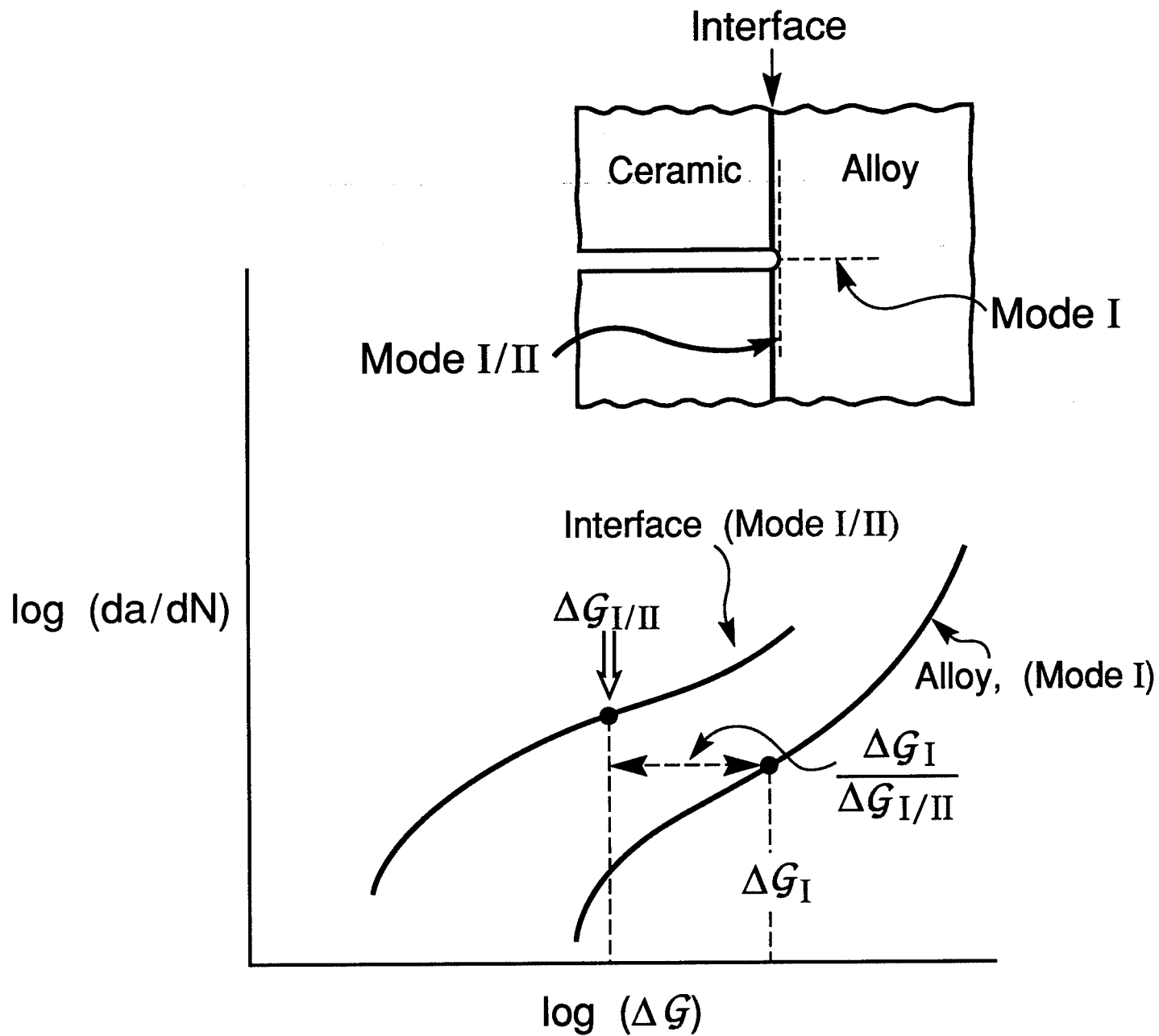
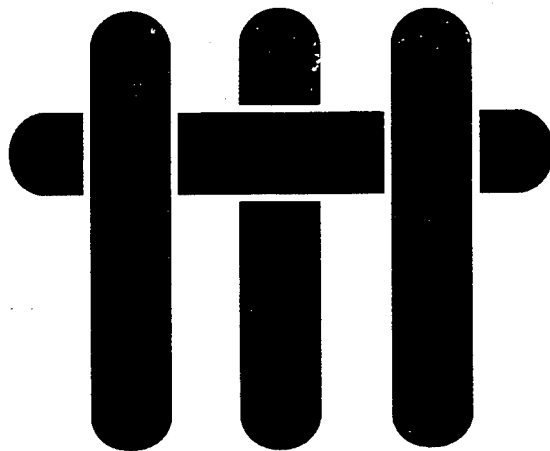


Figure 12

M A T E R I A L S



THE STRUCTURE AND THERMOMECHANICAL PROPERTIES OF $\text{Mo}/\text{Al}_2\text{O}_3$ INTERFACES

by

M.R. Turner, J.P.A. Löfvander, J.B. Davis and A.G. Evans
Materials Department
College of Engineering
University of California, Santa Barbara
Santa Barbara, California 93106-5050

ABSTRACT

The debonding and sliding resistances of interfaces formed between Mo and Al_2O_3 have been measured. The Mo/ Al_2O_3 interface exhibits a relatively low *interfacial fracture energy*, Γ_i , comparable in magnitude to the work of adhesion, W_{ad} . Debonding appears to occur with minimal plastic dissipation in the metal. Fine-scale plasticity phenomena occurring near the debond, within the Mo, are considered responsible for this behavior. The *sliding resistance* of the interface, subsequent to debonding, was found to depend on the shear yield strength of the Mo, consistent with observations of plastic grooving during fiber pull-out in composites containing Mo-coated sapphire fibers.

1. INTRODUCTION

The failure of interfaces between metals and oxides occurs by a variety of mechanisms.¹⁻³ In the absence of reaction products, some interfaces exhibit ductile fracture.^{1,4} Others fail by brittle debonding, but with plastic dissipation occurring in the metal.^{5,6} When reaction products form or interlayers exist, the behavior is usually brittle. The fracture occurs either *within* the reaction product or at one of the interfaces^{7,8} (usually, the metal/interphase interface).

Most bimaterial interfaces produced at high homologous temperatures exhibit a fracture energy, Γ_i , substantially larger than the work of adhesion, W_{ad} .^{1,9} Notable exceptions include the interfaces between Al_2O_3 and certain refractory metals, particularly Mo.^{1,10} These have fracture energies, $\Gamma_i \approx W_{ad}$. This phenomenon has not been explained. One motivation for the present study is to address the origin of the low fracture energy found for the Mo/ Al_2O_3 interface.

There are two basic approaches for creating a metal/oxide interface with a small debond energy. These approaches are evident from the basic correlation between the work of adhesion and the plastic dissipation¹⁰⁻¹²

$$\Gamma_i \approx W_{ad} \mathcal{P}(\hat{\sigma}/\sigma_o) \quad (1)$$

where the plastic dissipation parameter \mathcal{P} is a function of the ratio between the peak stress, $\hat{\sigma}$, needed to rupture the interface bonds and σ_o , the uniaxial yield strength of the matrix. Calculations conducted using continuum concepts predict variations in \mathcal{P} upon interface crack extension, Δa (Fig. 1).¹¹ Clearly, $\Gamma_i \rightarrow W_{ad}$, when $\hat{\sigma}/\sigma_o$ is small. Moreover, W_{ad} is related to the bond rupture stress by,^{10,12}

$$W_{ad} \approx \hat{\sigma} a_o / 2 \quad (2)$$

where a_0 is the separation distance of atoms across the interface. From Eqns. (1) and (2), it is evident that debonding can be encouraged either by having a small work of adhesion, or by using a high yield strength metal. These properties can be affected by segregation and alloying. Segregation changes $\hat{\sigma}$,¹⁰, whereas alloying influences σ_0 . Such effects are addressed for $\text{Al}_2\text{O}_3/\text{Mo}$ interfaces by measuring W_{ad} and σ_0 , and then relating these to measurements of Γ_i . In Mo, the strong influence of oxygen on flow strength and ductility,¹³ has special relevance.

The Mo/ Al_2O_3 interface also has thermomechanical characteristics consistent with those needed for Al_2O_3 fiber reinforcements, which impart high composite strength, as well as good fracture and fatigue resistance.¹³⁻¹⁶ In this application, not only are *small* values of Γ_i preferred, but also the sliding along debonded interfaces must occur with a controlled shear resistance, τ . This study addresses measurement of τ ¹⁷ and relationships with the interface structure.

2. MATERIALS AND PROCESSING

Interfaces between Mo and either sapphire or polycrystalline Al_2O_3 have been investigated. The sapphire used to create these interfaces had two basic geometries, either discs with basal plane orientation, or fibers with c-axis orientation.[‡] In some cases, polycrystalline Al_2O_3 plates, with two different compositions, have been used instead of sapphire.^{‡‡} Bodies comprising Mo-coated sapphire fibers in polycrystalline Al_2O_3 matrices produced from a high purity powder,^{‡‡‡} have also been studied.

Precautions have been taken to minimize the oxygen present in the Mo, by using high purity material and by conducting all steps of the bonding in environments with

[‡] Supplied by Sapphikon

^{‡‡} Coors AD-995 and Coors AD-96

^{‡‡‡} Sumitomo Chemical Company, Inc.

low oxygen partial pressure. The Mo was deposited onto the sapphire either by evaporation or sputtering from high purity (> 99.9%) targets. *Sputtered material* was deposited in an R.F. diode unit, in an atmosphere that comprised research grade argon at 6 millitorr working gas pressure. The top and bottom target voltages were maintained at 3kV and 0.5kV, respectively. Typical sputtered coating thicknesses were ~ 5 μm for planar substrates and 0.7–1.4 μm for fibers.** Coatings deposited by *electron beam evaporation* were produced at relatively high vacuum (<10⁻⁶ torr). Evaporated coating thicknesses were ~0.5 μm . A glow discharge cleaning procedure was used prior to deposition.

The coated discs were diffusion bonded at relatively high vacuum (< 10⁻⁶ torr). In some cases, a high purity (> 99.95%) Mo foil* (127 μm) was inserted between the Mo coated surfaces prior to bonding. The diffusion bonding was conducted at 1450°C for 12 h, using an applied pressure of 3–5 MPa. The fiber-containing composites were produced by hot pressing. For this purpose, the coated sapphire fibers were incorporated into an Al₂O₃ matrix and consolidated at 1500°C for 120 min., using an applied pressure of ~ 2 MPa.

3. ANALYTICAL TECHNIQUES

All interfaces were examined using transmission electron microscopy (TEM) techniques. For this purpose, electron transparent foils were prepared by cutting thin slices with a low speed diamond saw perpendicular either to the bonded surface or the fiber axis. These slices were ground to roughly 100 μm using diamond paste and 3 mm diameter discs were ultrasonically drilled. One side was polished with 3 μm diamond paste. The other side was dimple ground using 3 and 1 μm pastes, followed by a 1/4

** The fibers were rotated during coating at ~ 1 rpm.

* Johnson Mattheys

μm final polish. Subsequent thinning was accomplished by ion milling with Ar at 5kV, 1mA and 14° incidence angle. In many cases, thin foil cross-sections could not be produced because of the tendency to debond at the interfaces. In such cases, the coating was first removed from the substrate and mounted on a copper grid. All samples were examined* in a microscope equipped with a high take-off angle energy dispersive spectroscopy system. Crystallographic computations, simulations and indexing of diffraction patterns were carried out with the Diffract software. As-sputtered coatings were also examined using PEELS.

Scanning Auger microscopy (SAM) was used to characterize the interface chemistry, with spectra collected from debonded interfaces.† Depth profiles were performed by Ar ion sputtering of the Mo fracture surface. Debonded surfaces were also examined by scanning electron microscopy (SEM).** For this purpose, a thin carbon or gold layer was evaporated onto the surfaces. Chemical analyses were performed on surface features by using energy dispersive X-ray (EDS) methods.* The same surfaces were analyzed by X-ray diffraction methods.º

The morphology of the debond surfaces was established using atomic force microscopy (AFM).†

4. MECHANICAL MEASUREMENTS

The fracture energies of the Al_2O_3 / Mo interfaces were measured by using either four point flexure^{6,18} or Hertzian indentation.¹⁹ In both cases, interface debonding was monitored *in situ*, with an optical microscope focused through the sapphire layer. The

* JOEL 2000FX TEM at 200 kV

† Perkin Elmer PHI 660 Auger microscope

** Jeol SM840 SEM

* Tracor Northern TN5500 system

º Scintag XDS2000 diffractometer

† Nanoscope II from Digital Instruments

fracture energy, Γ_i was ascertained from the loads at which the cracks extended, as well as the specimen dimensions.^{18,19} For flexure tests, a pre-crack was introduced along the interface by propagating a controlled crack from a row of indentations emplaced on one of the sapphire surfaces.⁶ A typical debond region is depicted in Fig. 2. In systems produced with either the higher purity polycrystalline Al_2O_3 or sapphire, the loads at which these precracks extended gave debond energies in the range, $\Gamma_i \approx 1\text{--}4 \text{ Jm}^{-2}$. These results were insensitive to the Mo deposition method (sputtering or evaporation) and to the Mo thickness. Conversely, when the lower purity Al_2O_3 was used, Γ_i was substantially larger. It was typically in the range, $\Gamma_i = 10\text{--}20 \text{ Jm}^{-2}$.

The sliding behavior was measured on hot pressed fiber specimens by using a fiber push-through test method.^{10,17} Typical load-displacement curves involve a load drop, indicative of interface debonding, followed by fiber push-out (Fig. 3). The loads at which push-through displacements initiated (Fig. 3) gave the sliding resistance τ . It was found to be in the range, $\tau \approx 130\text{--}225 \text{ MPa}$. Grooves in the Mo were evident along the push-out zone (Fig. 4), indicative of plastic deformation occurring within the Mo.

The yield strength of the Mo subsequent to diffusion bonding was determined by microhardness measurements. The measurements were made at low loads, such that the indentation depth was less than 1/3 the Mo layer thickness. The results gave a hardness in the range, $H \approx 900 \text{ MPa}$ for the Mo foil after bonding. The corresponding uniaxial yield strength is,²¹ $\sigma_o \approx H/3 \approx 300 \text{ MPa}$. The sputtered coatings, deposited on the sapphire fibers, gave larger values of hardness, corresponding to $\sigma_o \approx 600 \text{ MPa}$.

5. INTERFACE STRUCTURE

The cross-section of an *as-deposited*, sputtered, Mo layer revealed a columnar growth structure with faceted grains, $\sim 100 \text{ nm}$ in diameter (Fig. 5). Diffraction patterns (Fig. 6) were consistent with the pattern simulated for randomly oriented grains with a

common $\langle 111 \rangle$ direction. Furthermore, PEELS results indicated the presence of thin oxide layers located both at the free surface and at the film/substrate interface.

All of the materials, regardless of the methods used to prepare the Mo, exhibited some metal oxide formation along the interfaces. Usually this oxide was *intermittent*. After debonding, the oxide was invariably attached to the sapphire, as evident from views of the sapphire side of a fracture surface (Fig. 7). Image analysis on sapphire fracture surfaces revealed an area of fraction of oxide grains of ≈ 0.2 . X-ray diffraction patterns obtained from these surfaces indicated that the oxide was MoO_2 . The presence of an oxide was further verified by SAM studies of the same surfaces.

In the system produced using the lower purity alumina (Fig. 8), the metal oxide layer was continuous, ~ 300 nm thick and could be analyzed by cross section TEM. This oxide phase was identified by tilting experiments, performed on single grains, to obtain diffraction patterns for the $[101]$, $[102]$, and the $[213]$ zone axes (Fig. 9a, b, c), which could be compared with patterns simulated for monoclinic MoO_2 (Fig. 9d, e, f). The simulations were achieved by using the space group, lattice parameters and fractional atom positions listed in Table I. The oxide consistently exhibited an orientation relationship with the sapphire substrates, exemplified by the diffraction pattern in Figs. 10a and b, which show the $[1\bar{1}00]$ sapphire // $[\bar{1}\bar{2}0]$ MoO_2 and $[2\bar{1}\bar{1}0]$ sapphire // $[\bar{3}\bar{2}0]$ MoO_2 , respectively. The orientation relationship may be described by

$$(0001)_{\text{Sapphire}} // (00\bar{1})_{\text{MoO}_2}$$

$$[\bar{1}\bar{2}10]_{\text{Sapphire}} // [010]_{\text{MoO}_2}$$

A structure diagram of the sapphire basal plane and the $(00\bar{1})$ plane in MoO_2 , oriented with the above crystallographic relationships indicate the resemblance of the oxygen sub-lattices (Fig. 11). The distance between two oxygen atoms along the $[\bar{1}\bar{2}10]$ direction

in sapphire is 4.76 Å. The distance between two oxygen atoms in the MoO₂ along the [010] direction is 4.86 Å. This misfit is less than 2% and supports the observed preference for this orientation relationship.

Also observed in this system was a continuous amorphous phase separating the MoO₂ layer from the Mo. These regions had chemical composition, 61 Si, 28 Al, 6 Ca, 3.5 Mg, 1.5 K (in atomic percent for metallic constituents only), as determined by EDS. The silicate was also observed throughout the Mo pore channels. In addition, MgAl₂O₄ spinel, with two distinct morphologies, was identified at the interface between the polycrystalline Al₂O₃ and the Mo (Fig. 12). These consisted of either block precipitates or a semicontinuous layer.

For bonds made with high purity Al₂O₃, a non-planar interface formed between the sapphire and the Mo (Fig. 13) with no apparent orientation relationship. A number of small (300–400 nm) MoO₂ grains were usually present throughout the sputtered Mo. The average grain diameter was 2–5 µm, indicating that there had been substantial grain growth during processing. Matching topographic features were evident in regions of direct contact between the sapphire and the Mo. These features formed by interface and surface diffusion, both in the Al₂O₃ and the Mo, during diffusion bonding.

Measurements of the profiles around the grain boundaries in the Mo, obtained both by TEM (Fig. 14) and AFM (Fig. 15) provided estimates of the dihedral angle. These are in the range, $130 \pm 14^\circ$. Non-matching features also exist, which relate to residual porosity at the interface. The area fraction of such porosity was ≈ 0.45 for the sputtered Mo.

The oxygen content measured by SAM ranged between 4 and 6 atom % throughout the layer, despite precautions taken to minimize access of oxygen. The solubility limit of oxygen in Mo is ~ 0.2 atom %. The presence of MoO₂ oxide grains in the Mo is consistent with these measurements.

6. DISCUSSION

6.1 Debonding

The measured debond energy appears to be relatively invariant and thus, insensitive to the amounts of either interface porosity or MoO₂ detected on the sapphire side of the debond surface. Such observations suggest that both the Mo/Al₂O₃ and the Mo/MoO₂ interfaces have low fracture energies. Conversely, failure *never* occurs at the Al₂O₃/MoO₂ interface. Its resistance to failure must be relatively high. This is consistent with the results of other investigations for oxide/oxide interfaces.¹⁰ Subsequent emphasis is given to the metal/oxide interfaces.

An attempt is made to understand the small value of Γ_i based on separate assessments of W_{ad} and σ_o , in accordance with the concepts expressed in Eqns. (1) and (2). The dihedral angle, ϕ , measurements provide one estimate of W_{ad} . These angles, established at high temperatures, relate the equilibrium interface energy, γ_i , to the Mo grain boundary energy, γ_b , through the relationship

$$\gamma_b = 2\gamma_i \cos \phi \quad (3)$$

Atomistic calculations²² suggest that γ_b for Mo is in the range, $\gamma_b = 1.2 \pm 0.6 \text{ Jm}^{-2}$. The interface energy is thus, $\gamma_i \approx 1.5 \pm 1.2 \text{ Jm}^{-2}$. The interface energy is, in turn, related to the work of adhesion by¹⁰

$$W_{ad} = \gamma_{oxide} + \gamma_{mo} - \gamma_i \quad (4)$$

where γ_{oxide} is the surface energy for either Al₂O₃ or MoO₂ and γ_{mo} is the Mo surface energy. Again, atomistic calculations provide the equilibrium energies:^{22,23}

$\gamma_{\text{mo}} \approx 2.0 \pm 0.2 \text{ Jm}^{-2}$ and $\gamma_{\text{Al}_2\text{O}_3} \approx 1 \pm 0.1 \text{ Jm}^{-2}$ for the basal plane. With these values, the work of adhesion is determined to be in the range, $W_{\text{ad}} = 1.7 \pm 1.1 \text{ Jm}^{-2}$.

This work of adhesion is typical of that found for many other metal/oxide interfaces.⁹ It is also similar in magnitude to the measured debond energies, Γ_i . Consequently, there is a minimal contribution to Γ_i from plastic dissipation. Yet, σ_o is only somewhat larger than the range found for other metal/oxide interfaces, which exhibit much larger debond energies, ($\Gamma_i \gg W_{\text{ad}}$). There is no obvious rationale, at this level of analysis, for the low Γ_i found for the Mo/Al₂O₃ interface. Further understanding must be based on more quantitative measurements and calculations.

The continuum plasticity analysis of crack growth (Fig. 1) requires that $\hat{\sigma}/\sigma_b \lesssim 3$, for the measured Γ_i/W_{ad} (1.5 \rightarrow 6.0). Consistency with Eqn. (2) thus requires that

$$\sigma_o a_o / W_{\text{ad}} \gtrsim 0.7 \quad (5)$$

For the Mo/Al₂O₃ interface, a_o is not known. However, for similar interfaces, such as Nb/Al₂O₃, atomistic calculations give, $a_o \approx 0.3 \text{ nm}$.²⁵ If this a_o is appropriate, since $W_{\text{ad}} \approx 1/2 - 2 \text{ Jm}^{-2}$ and $\sigma_o \approx 300\text{--}600 \text{ MPa}$, then $\sigma_o a_o / W_{\text{ad}}$ is in the range 0.05 \rightarrow 0.4. This does not satisfy Eqn. (5).[‡] A full understanding of the debond energy must involve fine-scale plasticity phenomena occurring near the interface crack front.^{1,24} The influence of this zone, width D , on the steady-state interface fracture energy (Fig. 16) provides perspective through the non-dimensional parameter, $D \sigma_o^2 / EW_{\text{ad}}$. Upon inserting measured values of Γ_i , W_{ad} and σ_o for the Mo/Al₂O₃ interface, Fig. 16 gives $D \approx 25 \text{ nm}$. Much larger values obtain for other metal/oxide interfaces ($D \approx 0.2 \mu\text{m}$ ²⁴) because of the strong sensitivity of D to yield strength ($D \sim \sigma_o^{-2}$, Fig. 16). This analysis

[‡] Moreover, in other metal/oxide interfaces, there is a more considerable discrepancy with Eqn (5).¹

reinforces the need to understand fine-scale plasticity and its association with D for different metal/oxide interfaces.

The interface between Mo and low purity polycrystalline Al_2O_3 has a considerably greater debond resistance than that between Mo and pure Al_2O_3 . The development of silicate phases in the bond zone (by viscous flow out of the alumina) appears to be responsible. In this case, the fracture energy is similar to that for the silicate phase itself ($\Gamma_i \approx 10 \text{ Jm}^{-2}$), which fractures as the bond separates. Similar results have been obtained for Pt/ Al_2O_3 interfaces.⁸ This behavior is probably responsible for the 'high strength' that occurs when low purity Al_2O_3 is bonded with Mo, for metal/ceramic seal technology.

6.2 Sliding

The observation of plastic grooving (Fig. 4), suggests that slip is controlled by shear yielding of the Mo. This should occur at a stress, $\tau \approx \sigma_o/\sqrt{3}$. Based on the hardness measurements for the sputtered Mo coatings ($\sigma_o \approx 600 \text{ MPa}$), sliding by shear yielding should occur at $\tau \approx 340 \text{ MPa}$. This is about twice the measured sliding resistance, $\tau \approx 130\text{--}225 \text{ MPa}$ (Fig. 3). However, sliding only occurs at contact points along the interface (Fig. 4). By normalizing the sliding resistance with the ratio of the *contact area to fiber surface area*, the lower measured values are compatible with a plastic grooving mechanism.

7. CONCLUSIONS

The mechanical properties of molybdenum/alumina interfaces have been investigated. The fracture energy Γ_i was compared to the work of adhesion, W_{ad} estimated using AFM and TEM techniques. The range of values obtained for W_{ad} are similar to measurements for other metal/ceramic systems. However, unlike other

systems, the measured fracture energy is similar to the work of adhesion, indicating that plastic dissipation in the molybdenum is minimal. Furthermore, fractographic examinations of failed interfaces show no discernible deformation. Yet, quantitative distinctions between Mo/Al₂O₃ and other metal/oxide interfaces, based on W_{ad} and the yield strength, σ_0 , have not been identified. However, the inference that the zone of fine-scale plasticity occurring near the interface is smaller for Mo/Al₂O₃, than other interfaces is considered relevant. A full understanding awaits further analysis of fine-scale plasticity.

The interfacial fracture energies were found to be sensitive to the alumina purity but only weakly dependent on the method used to prepare the Mo. The apparent insensitivity to the Mo processing conditions may result from the presence of oxygen (in solution and as oxides), which was invariably present throughout the metal layer and at the interfaces. The role of oxygen in the fracture process remains unclear, in part because it is difficult to eliminate. The effect of alumina impurities appears to be relatively straightforward. The fracture energy is increased when the silicate phase migrates from the polycrystalline alumina to the Mo/sapphire interface. For this case the interface exhibits the fracture resistance of the amorphous *interphase*.

The sliding resistance, τ , of the Mo/sapphire interface was found to be about half the shear yield strength of the metal. The basic scaling between τ and σ_0 has important ramifications for ductile coating concepts for ceramic matrix composites. Clearly, the coating yield strength emerges as a key parameter for controlling the interfacial sliding resistance.

TABLE I

Structure Type, Space Group, Lattice Parameters, Wyckoff Position and Fractional Atom Coordinates for the Structures Identified in This Study

Structure	Space Group	Unit cell (Å)	Atom	Fractional Coordinates		
Mo	$Im\bar{3}m$	$a = 3.1470$	Mo (2a)	0000	0000	0000
MoO ₂	$P2_1/c$	$a = 5.6109$ $b = 4.8562$ $c = 5.6285$ $\beta = 120.95$	Mo (4e) O ₁ (4e) O ₂ (4e)	2316 1123 3908	9916 2171 6969	0164 2335 2987
Al ₂ O ₃	$R\bar{3}c$	$a = 4.754$ $c = 12.99$	Al (12c) O (18e)	0000 3064	0000 0000	3523 2500
Al ₂ MgO ₄	$Fd\bar{3}m$	$a = 8.075$	Al (16d) Mg (8a) O (32e)	5000 1250 2510	5000 1250 2510	5000 1250 2510

REFERENCES

- [1] A.G. Evans and B.J. Dalgleish, *Acta Metall. Mater.*, **40** (1992) S295.
- [2] N.P. O'Dowd, M.G. Stout and C.F. Shih, *Phil. Mag. A*, **V66**[6] (1992) 1037-64.
- [3] B. Gibbeschg and G. Elsner, *Acta Metall. Mater.*, **40** (1992) 59.
- [4] B.J. Dalgleish, K.P. Trumble and A.G. Evans, *Acta Metall. Mater.*, **37** (1989) 1923.
- [5] G. Beltz and J.R. Rice, *Acta Metall. Mater.*, **40** (1992) S321-S331.
- [6] I.E. Reimanis, B.J. Dalgleish and A.G. Evans, *Acta Metall. Mater.*, **39** (1991) 3133.
- [7] A. Bartlett and A.G. Evans, *Acta Metall. Mater.*, **41** (1993) 497-504.
- [8] M. De Graef, M.R. Turner, B.J. Dalgleish and A.G. Evans, *Acta Metall. Mater.*, **40** (1991) S333.
- [9] A.G. Evans, M. Rühle, B.J. Dalgleish and P.G. Charalambides, *Mat. Sci. Eng.*, **A126** (1990) Se.
- [10] J.B. Davis, J.P.A. Löfvander, E. Bischoff, A.G. Evans and M.L. Emiliani, *J. Am. Ceram. Soc.*, **76**[5] (1993) 1249-57.
- [11] J.R. Rice and J.S. Wang, *Mat. Sci. Eng.*, **A107** (1989) 23-40.
- [12] V. Tvergaard and J.W. Hutchinson, *J. Mech. Phys. Solids*, **40**[6] (1992) 1377-97.
- [13] J.R. Smith, H. Schlosser, J. Ferrante, *Phys. Rev. B*, **44**[17] (1991) 9696-9699.
- [14] M.Y. He, A.G. Evans and W.A. Curtin, *Acta Metall. Mater.*, **41** (1993) 871.
- [15] D. Walls, G. Bao and F.W. Zok, *Scripta Metall. Mater.*, **25** (1991) 911.
- [16] O. Sbaizero, C. Hom, F.W. Zok and A.G. Evans, *J. Am. Ceram. Soc.*, **74**[1] (1991) 187-93.
- [17] P. Warren, T.J. Mackin and A.G. Evans, *Acta Metall. Mater.*, **40**[6] (1992) 1243-49.
- [18] P.G. Charalambides, J. Lund, R.M. McMeeking and A.G. Evans, *J. Appl. Mech.*, **111** (1989) 77.
- [19] J.B. Davis, G. Bao, H.C. Cao and A.G. Evans, *Acta Metall. Mater.*, **39**[5] (1991) 1019-24.
- [20] C. Liang and J.W. Hutchinson, *Mech. of Mtls.*, **14**[3] (1993) 207-21.
- [21] J.F.W. Bishop and R.J. Hill, *Phil. Mag.*, **42** (1951) 414.

- [22] D. Wolf, *Jnl. Appl. Phys.*, **69**[1] (1991) 185.
- [23] M. Finnis, to be published.
- [24] Z. Suo and C.F. Shih, *Acta Metall. Mater.*, **41** [5] (1993) 1551.

FIGURE CAPTIONS

- Fig. 1. Effects of the ratio of yield strength, σ_0 , to the bond strength, $\hat{\sigma}$, on the relative debond resistance of metal/ceramic interfaces (Tvergaard and Hutchinson):¹² calculations performed assuming continuum plasticity.
- Fig. 2. Optical observation of debonded region at Mo/sapphire interface.
- Fig. 3. Typical push-out curve for Mo-coated sapphire fibers in an Al_2O_3 matrix. τ is the sliding stress.
- Fig. 4. SEM image of push-out zone showing grooves on Mo.
- Fig. 5. TEM view of faceted Mo grains ~ 100 nm in diameter in as-deposited Mo film.
- Fig. 6. Diffraction patterns of sputtered Mo film, which indicate a common $\langle 111 \rangle$ zone; a) measured pattern, b) simulated pattern.
- Fig. 7. SEM image of sapphire fracture surface showing metal oxide attached to sapphire. The light grey grains are MoO_2 .
- Fig. 8. TEM image of continuous oxide layer formed with lower purity Al_2O_3 .
- Fig. 9. a-c) Diffraction patterns for the $[101]$, $[102]$ and $[213]$ zone axes.
d-f) Corresponding simulated patterns.
- Fig. 10. Diffraction patterns for Mo oxide indicating orientation relationships.
- Fig. 11. Oxygen sublattice of (0001) sapphire resembles that of (001) MoO_2 .
- Fig. 12. TEM imaged MgAl_2O_4 spinel at the interface between Al_2O_3 and Mo.
- Fig. 13. TEM image of a non-planar interface between sapphire and Mo with no orientation relationship.
- Fig. 14. TEM image of dihedral angles (arrowed) formed between a sapphire fiber and Mo grain boundaries.

Fig. 15. a) AFM trace across Mo grain boundaries at the interface. b) Corresponding image. The grain boundary at 0 is highlighted by the arrows on the trace in (a).

Fig. 16. Effects of fine-scale plasticity in a zone, width D , on the steady-state debond energy, Γ_s .

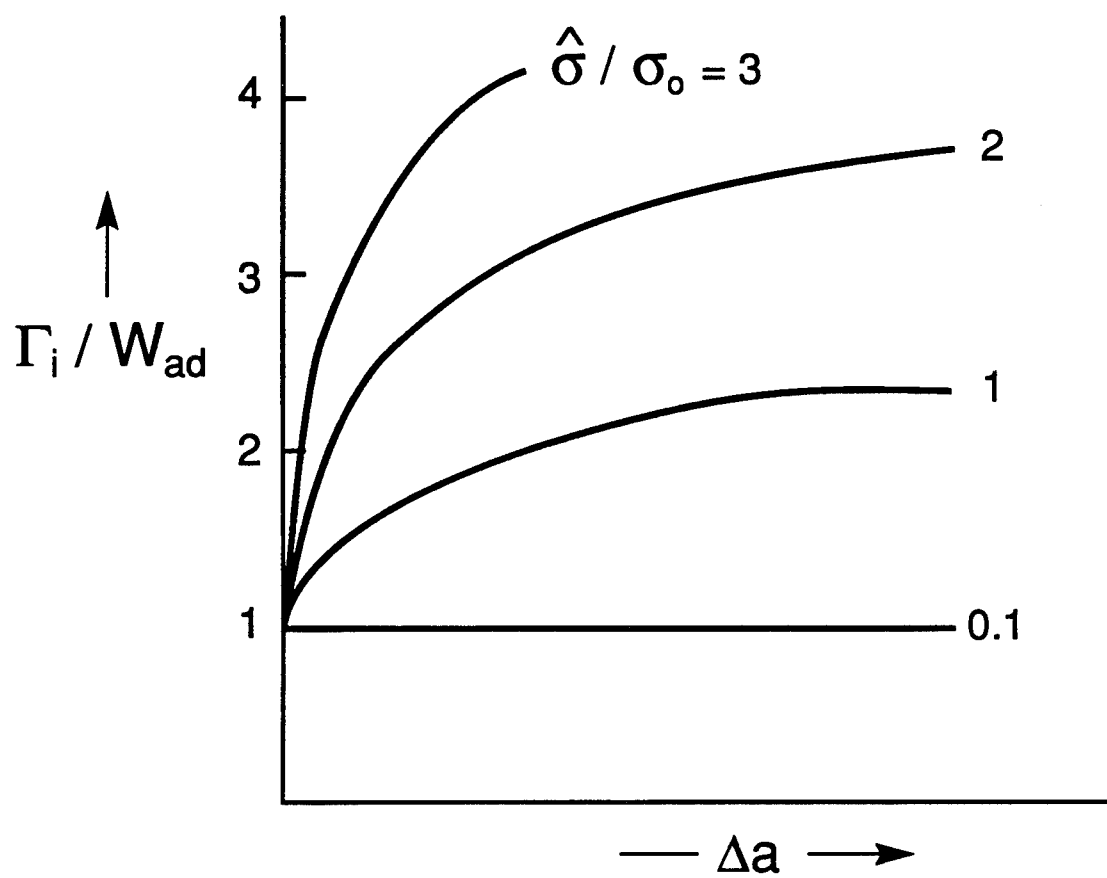


Figure 1

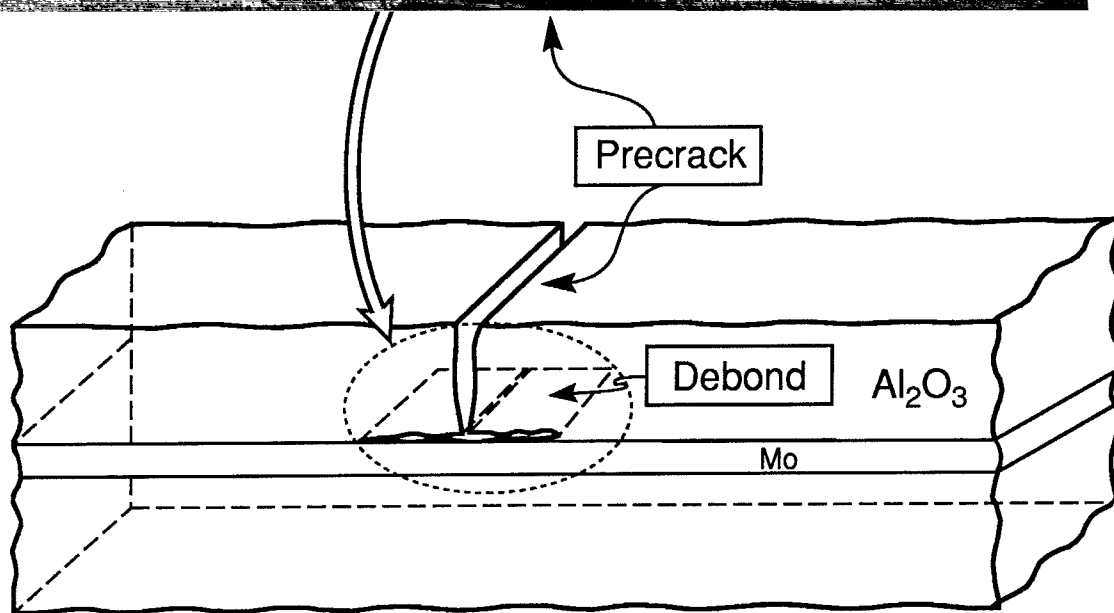
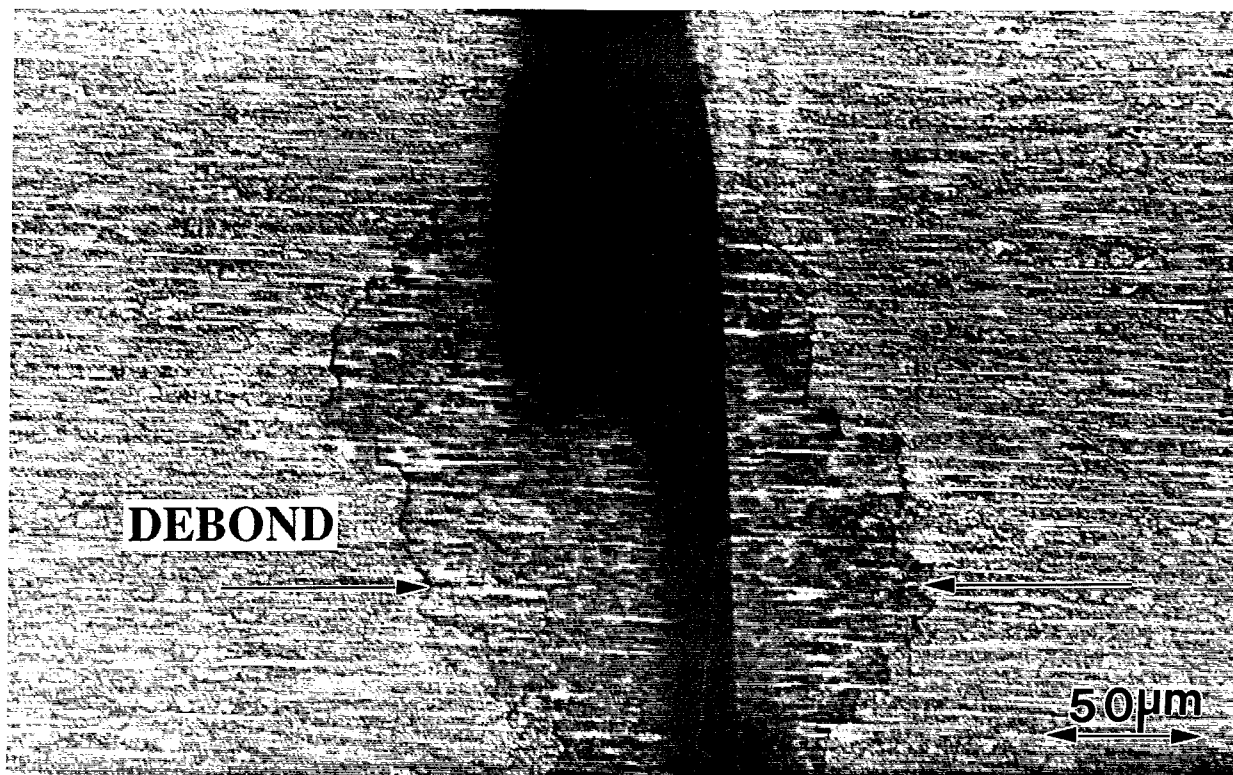


Figure 2

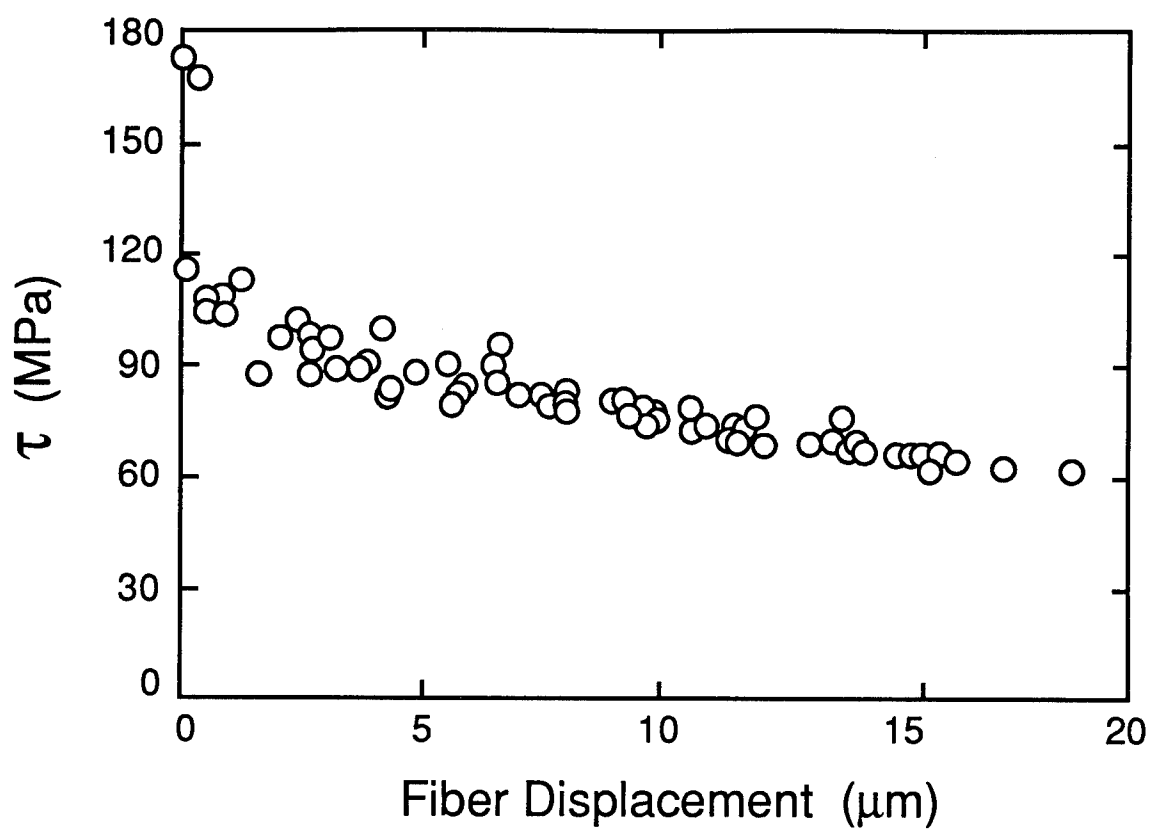


Figure 3

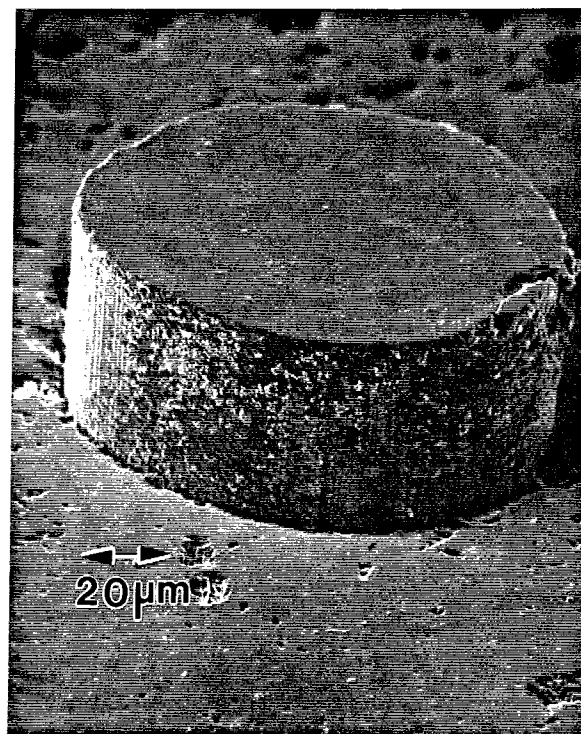


Figure 4

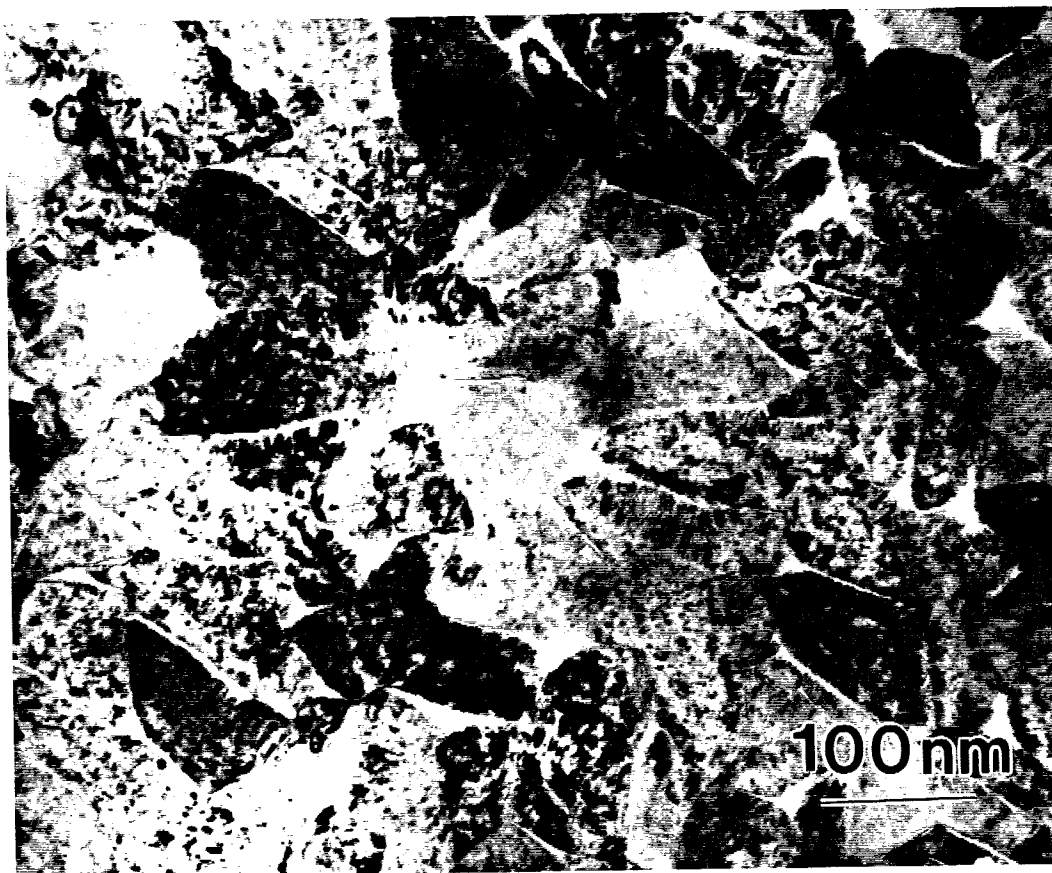


Figure 5

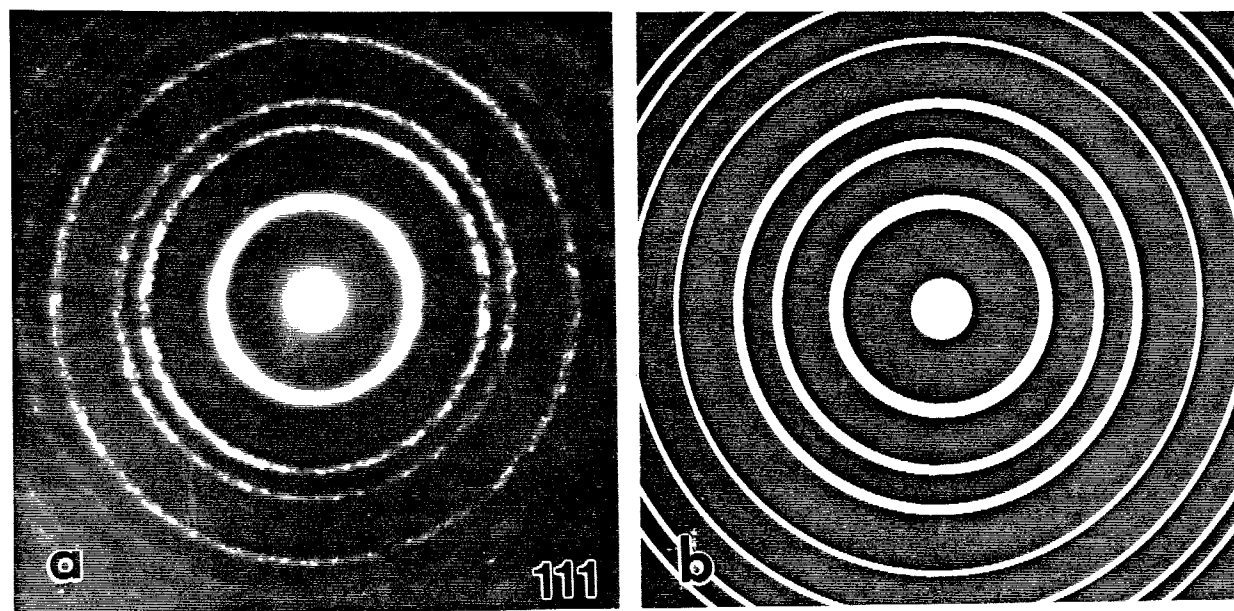


Figure 6

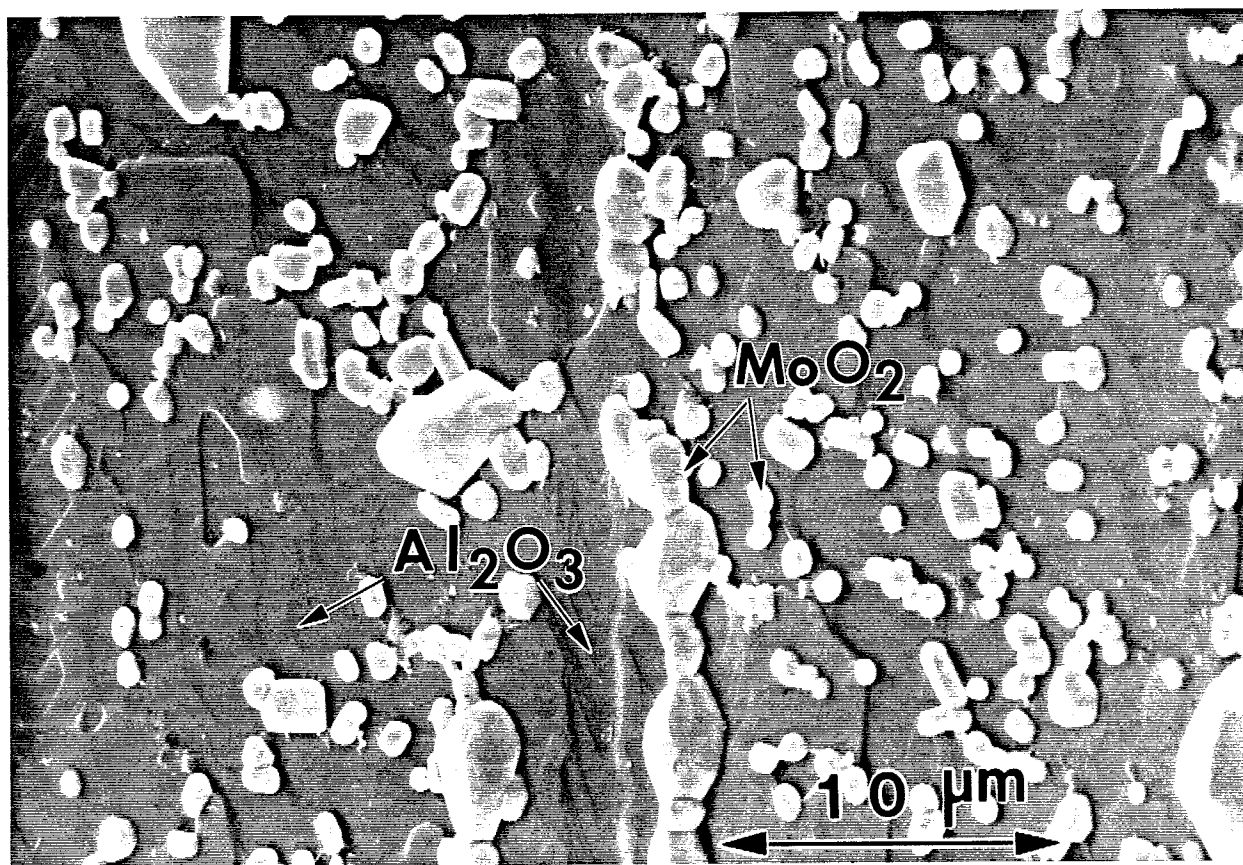


Figure 7

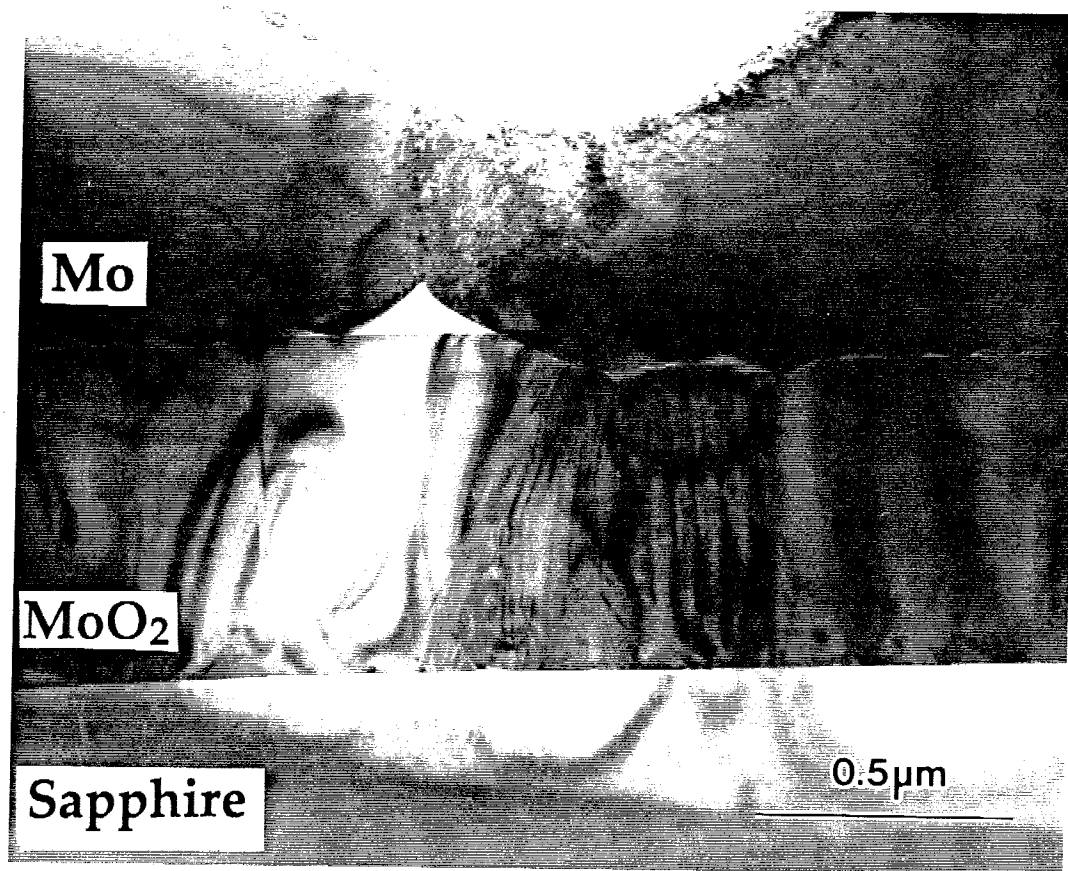


Figure 8

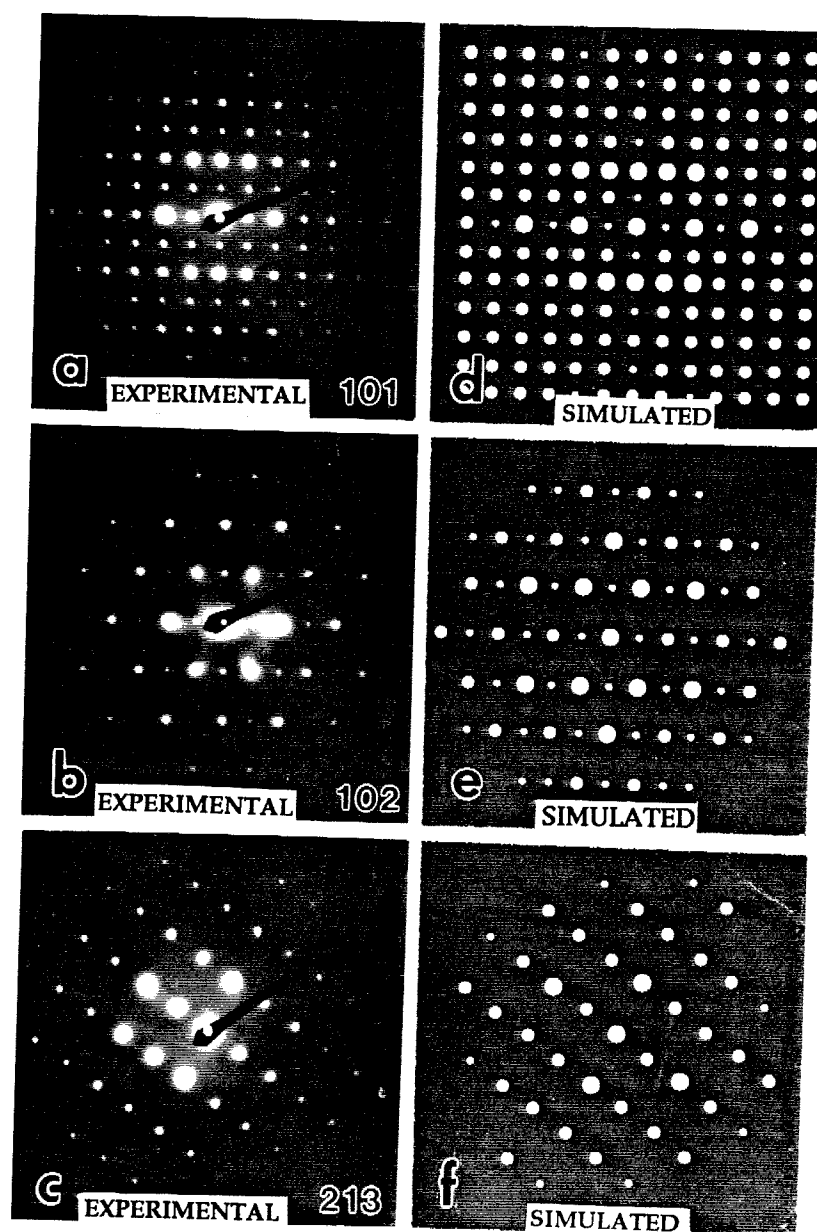


Figure 9

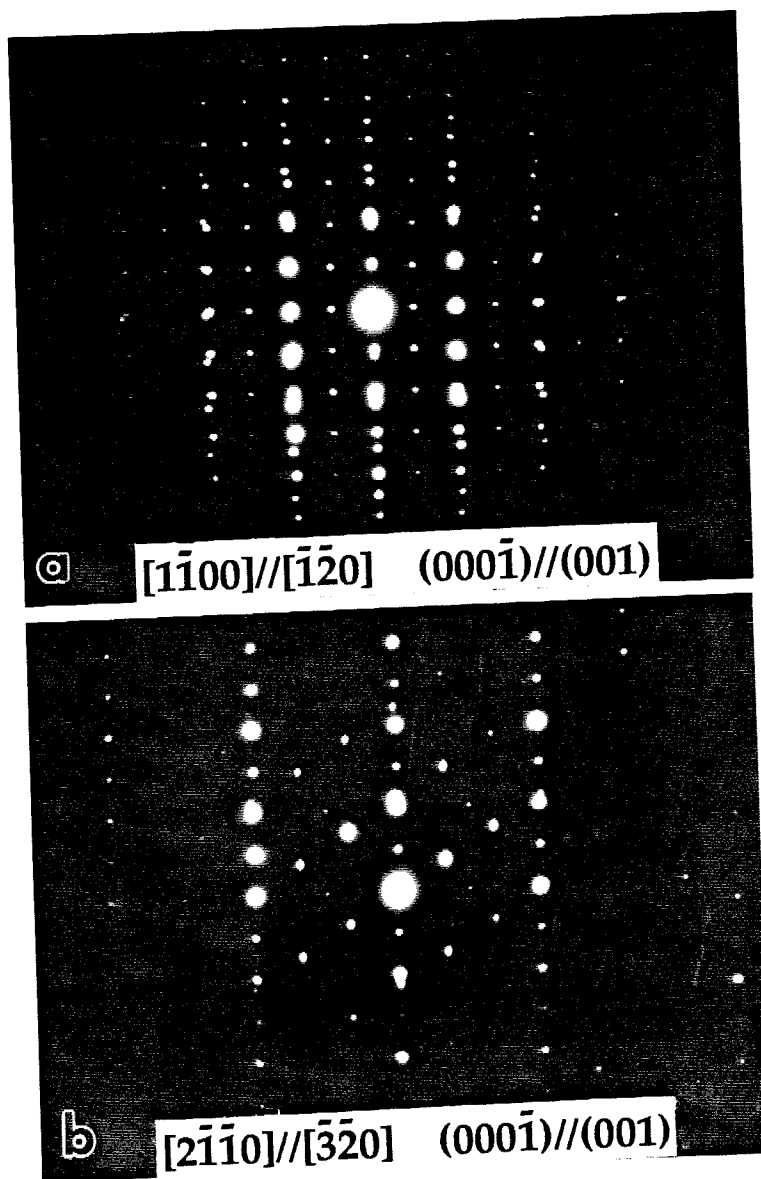
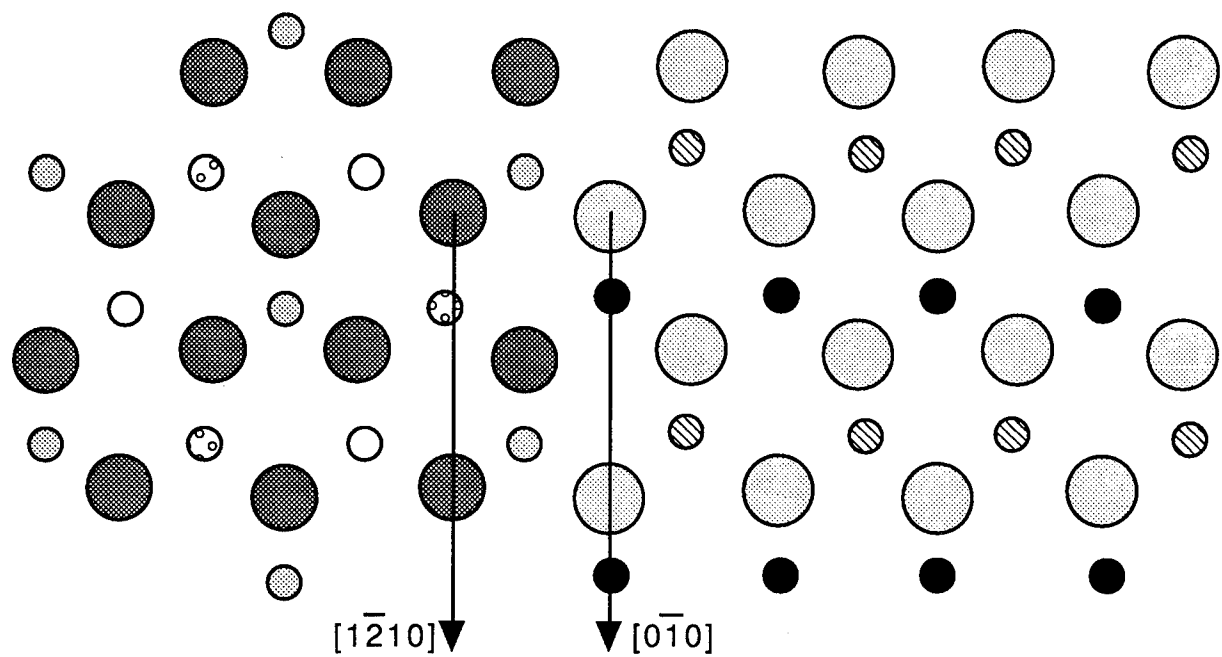




Figure 10





 O atom in sapphire in the plane

 O atom in MoO₂ (+/- 0.32Å)

 Mo 1.05-1.20Å above plane

 Mo 1.13-1.21Å below plane

 Al 0.85Å above plane

 Al 0.83Å below plane


 Al 1.32Å below plane

Figure 11

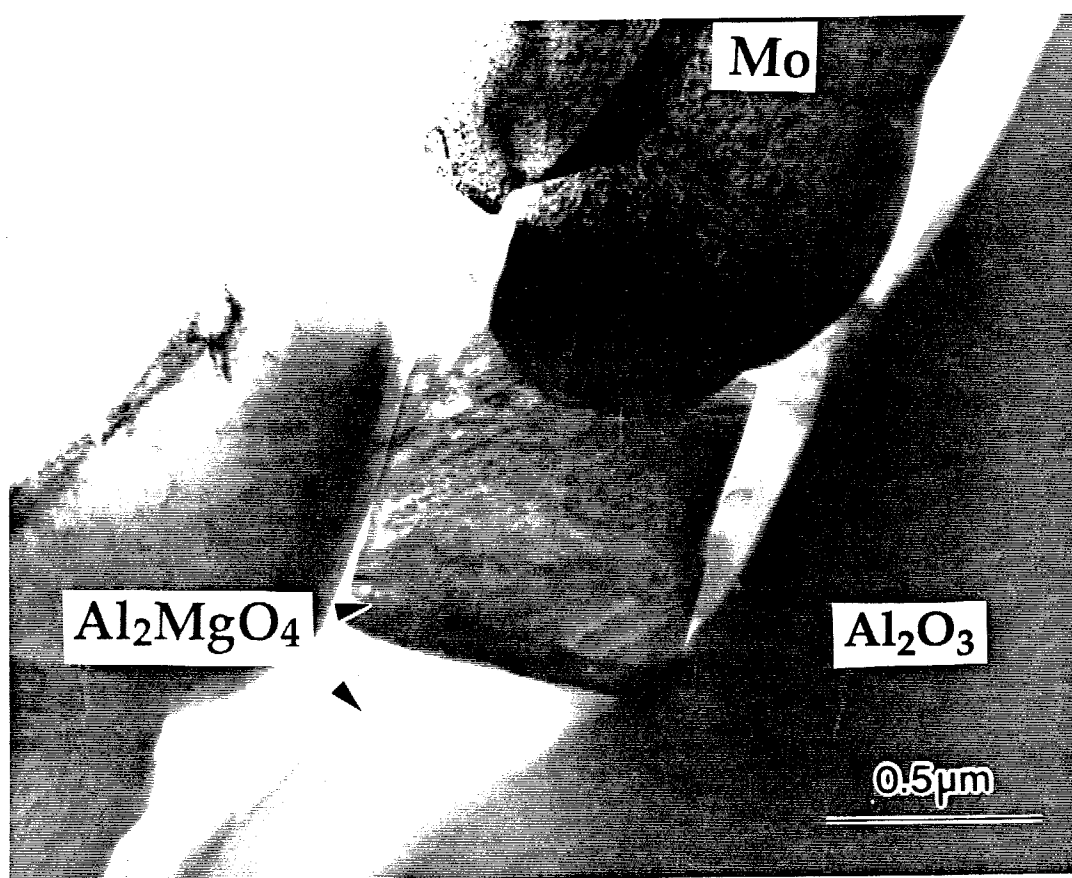


Figure 12

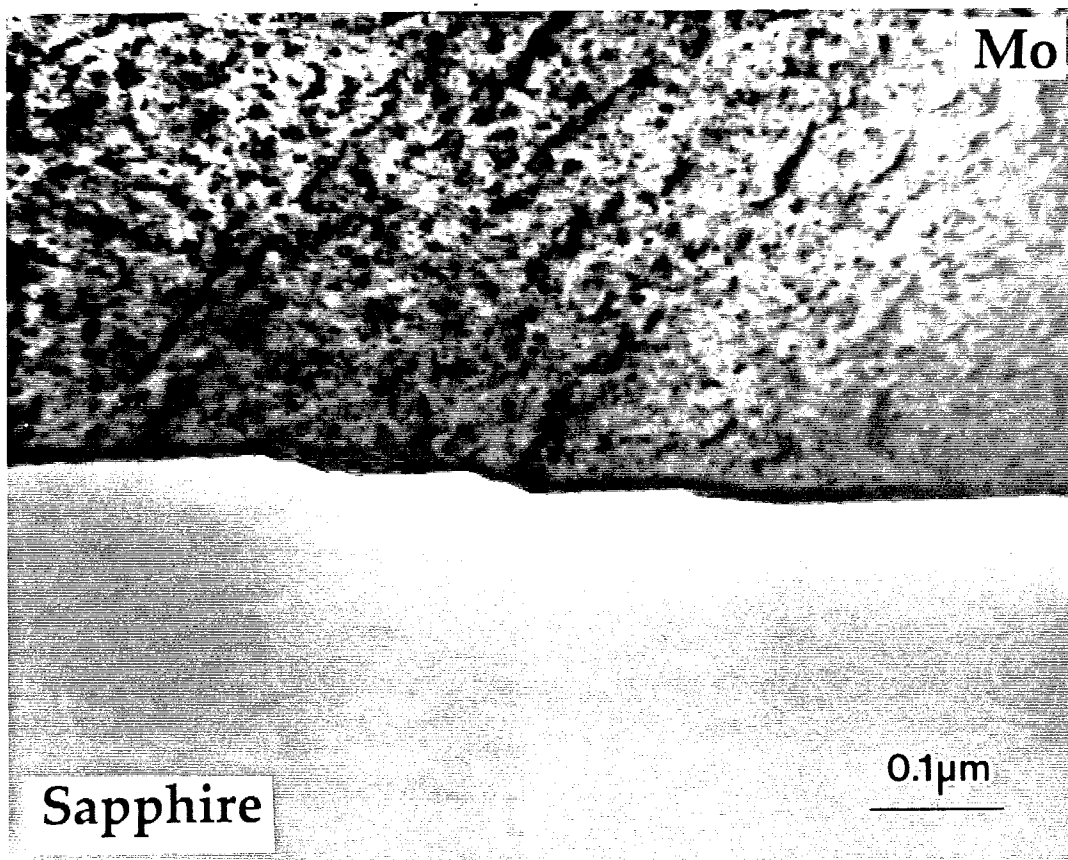


Figure 13

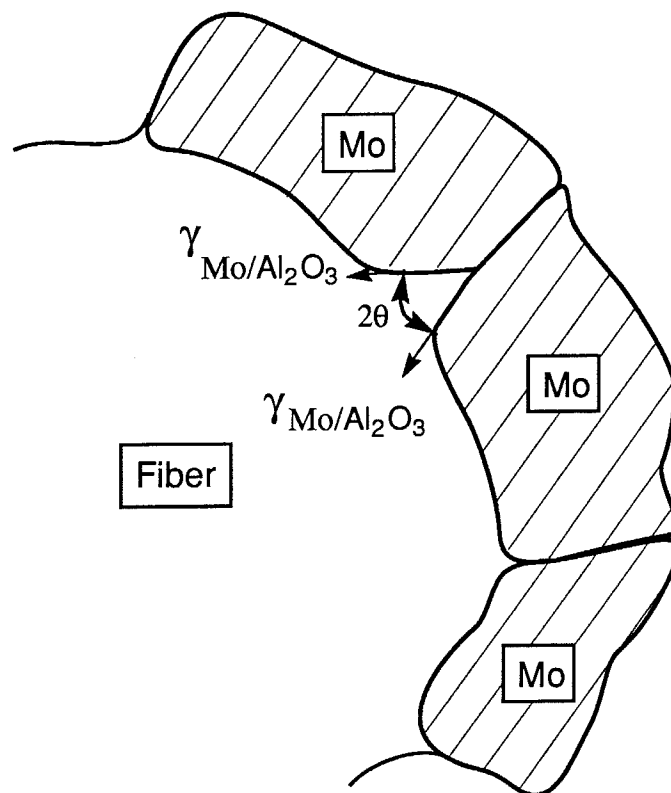
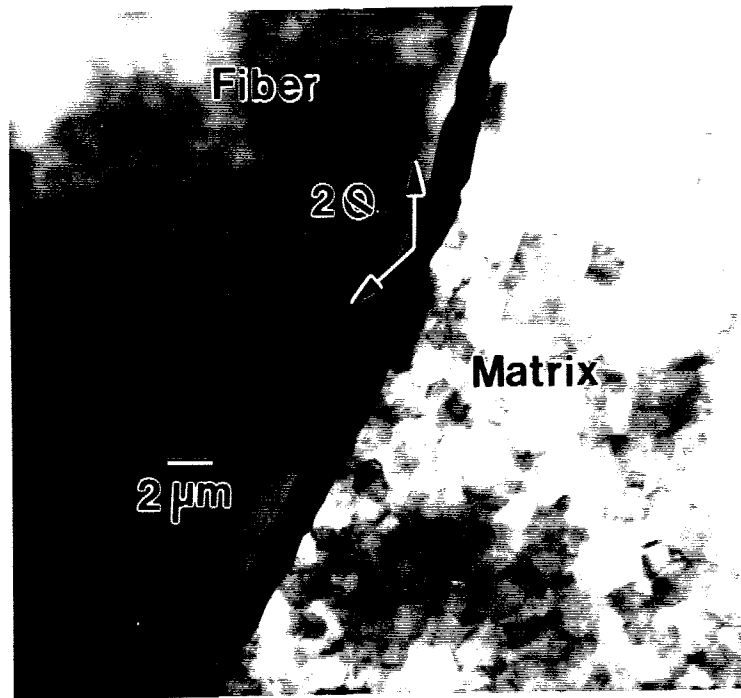


Figure 14

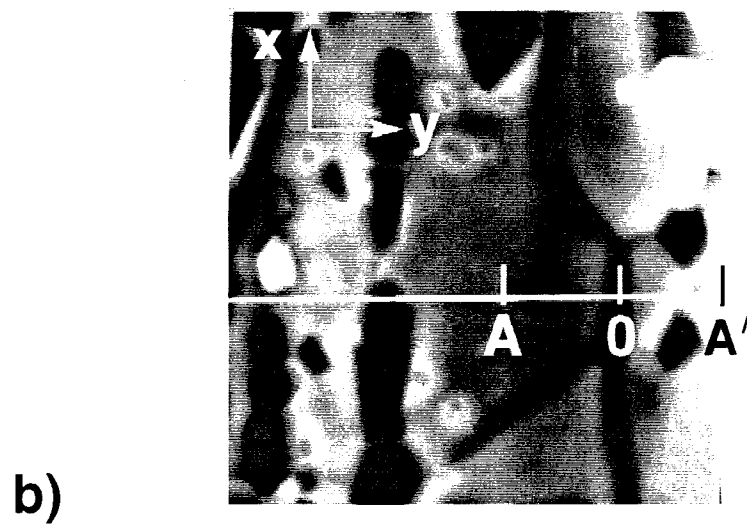
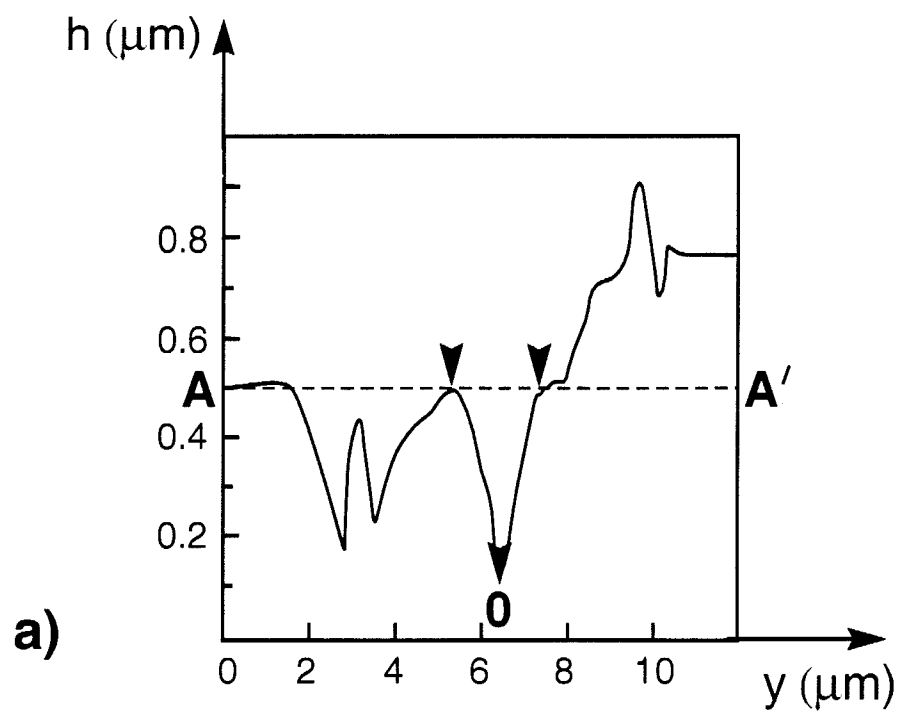


Figure 15

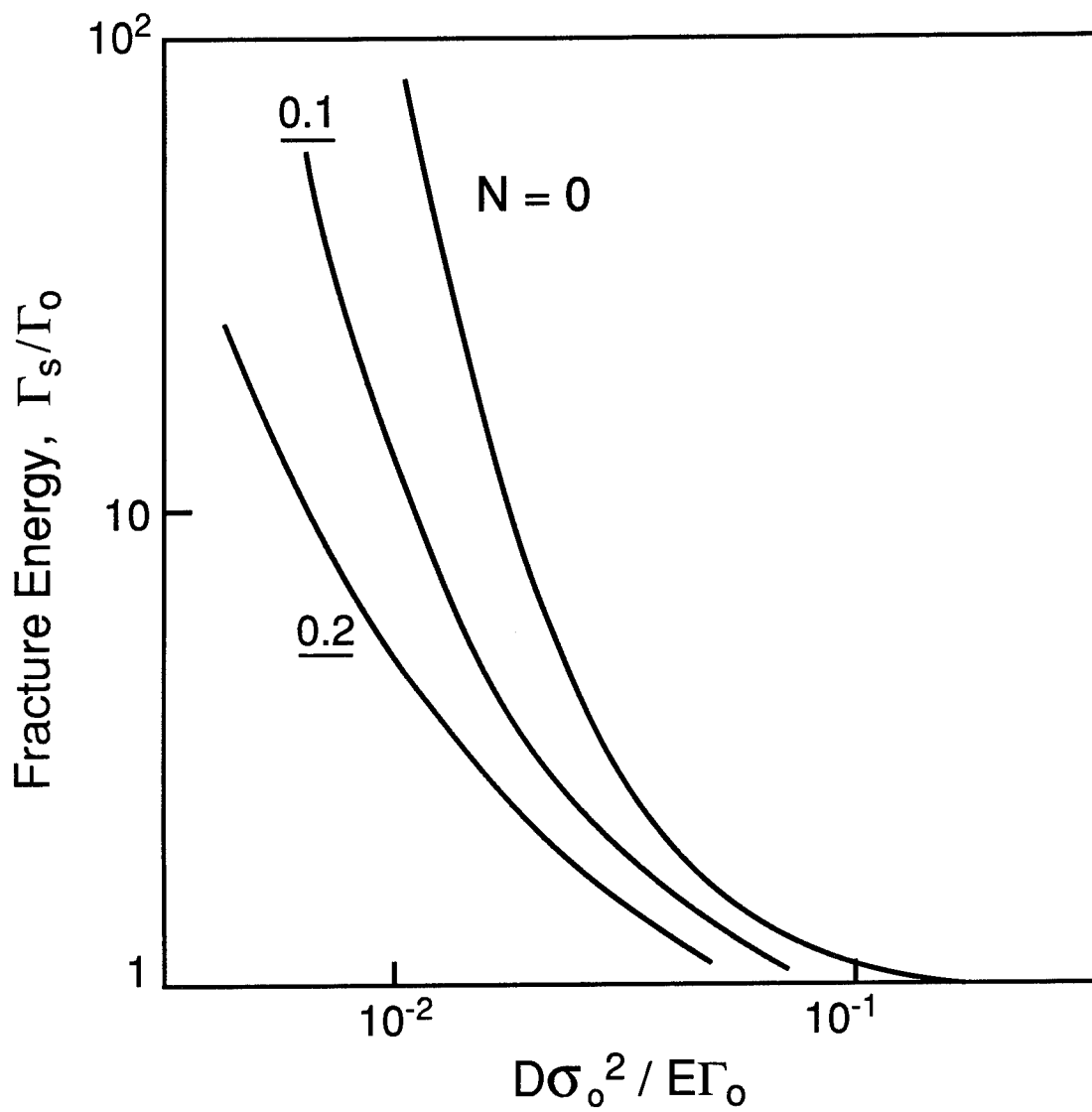


Figure 16

ICSHM4—PAPER 36

Preliminary Assessment of Mica as a High-temperature Fiber Coating for SiC Composites

ANA M. SEGADÃES, PAUL D. WARREN & ANTHONY G. EVANS

ABSTRACT *The potential of mica as a fiber coating for SiC fibers in a ceramic matrix composite has been explored. It has been shown that thermochemical effects are involved that degrade a thin layer of the coating upon consolidation. However, beyond the reaction layer, the debonding properties of the mica are retained.*

1. INTRODUCTION

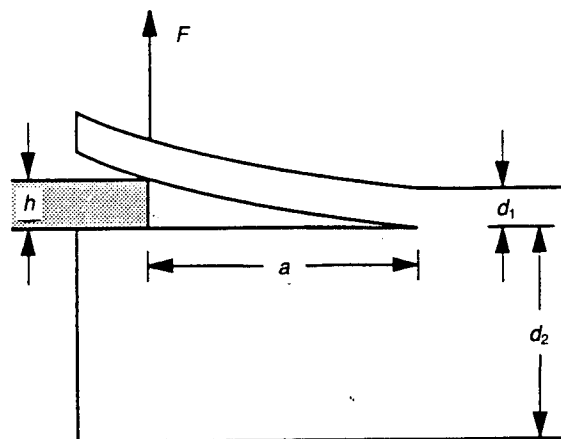
The mechanical properties of continuous fiber-reinforced ceramic matrix composites are now known to depend on the interface or coating between the fiber and the matrix [1-7]. The key characteristics of the coating that impart notch tolerance are the fracture energy, Γ_i , compared with that for the fiber, Γ_f , and the sliding resistance, τ , along the debonded faces [4, 6, 7]. Notably, it is required that $\Gamma_i/\Gamma_f \leq 1/4$ and that the sliding stress be in the approximate range $0 \leq \tau \leq 100$ MPa. Commonly, these coating characteristics have been achieved using either carbon or BN coatings [7-10]. Both coatings have problems at high temperature, especially when SiC fibers (e.g. Nicalon) are used, leading to oxidation and embrittlement [1, 11]. Various alternatives that might obviate the problem have been proposed for oxide fibers [2], based on the use of: (i) double coatings of oxides with either certain refractory metals (Mo, W, Cr) or with C; and (ii) porous or layered oxides. For non-oxide fibers, such as SiC or Si_3N_4 , the problem is more challenging because the fiber is susceptible to oxidation, resulting in SiO_2 layer formation with an associated volume expansion [11]. One proposal has been to use layered micaceous materials [12]. The intent of this study is to provide a preliminary assessment of the viability of this concept for a SiC-SiC composite.

The study has two specific objectives. The first is to examine the thermochemical compatibility between SiC and a common mica, phlogopite. The second is to measure the fracture energy of a mica layer, diffusion bonded to SiC, subjected to a mode mix equivalent to that associated with debonding at a crack front [2, 4], characterized by a phase angle of $\Psi \approx 50^\circ$.

2. MATERIALS

A 'high heat' grade phlogopite (from UNIMICA, NY) [13] was used and cleaved into sheets of various thicknesses (~ 65 - $100 \mu\text{m}$). X-ray diffraction gave a c -spacing of

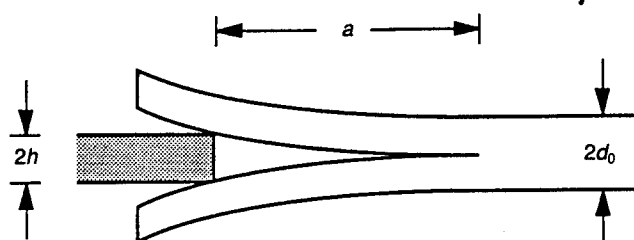
Ana M. Segadães, Departamento de Engenharia Cerâmica e do Vidro, Universidade de Aveiro 3800 Aveiro, Portugal. Paul D. Warren and Anthony G. Evans, Materials Department, College of Engineering, University of California, Santa Barbara, CA 93106-5050, USA.



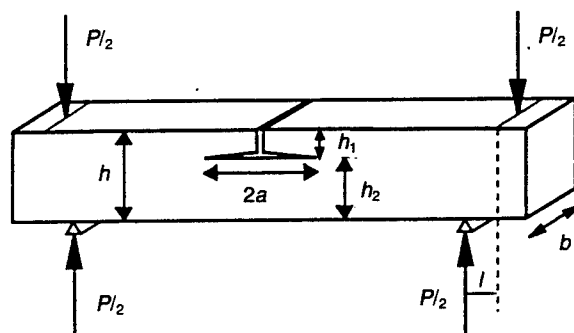
(a) Asymmetric Beam ($\Psi \approx -40^\circ$ for $d_2/d_1 \approx 10$)

$$G = 3E_{11}h^2d_0^3/4a^4$$

$$(2/d_0^3 = 1/d_1^3 + 1/d_2^3)$$



(b) Symmetric Beam ($\Psi = 0^\circ$)



(c) Flexure ($\Psi \approx 45^\circ$)

$$G = (3P^2l^2/2b^2E_{11}) \{1/h_2^3 - 1/[h_1^3 + h_2^3 + 3h_1h_2(h_1 + h_2)]\}$$

Figure 1. Test specimens used to measure the fracture energies at three different phase angles.

Table 1. Chemical Compositions (Weight Per Cent)*

	MgO	Al ₂ O ₃	SiO ₂	CaO	TiO ₂	Fe ₂ O ₃ ^b	MnO	Na ₂ O	K ₂ O	BaO	Loss on igni.
A	25.73	15.24	40.57	0.06	1.06	6.44	0.17	0.20	9.06	—	1.17
B	24.49	16.02	44.76	—	—	6.15	—	—	6.84	1.74	—
C	—	—	99.94	—	—	0.05	—	—	0.01	—	—
D	52.60	0.22	46.18	—	—	0.90	—	—	0.08	0.03	—

*A: Natural phlogopite, as cleaved, determined by X-ray fluorescence (trace elements rubidium, barium and niobium); B: phlogopite from open SiC-mica-SiC sandwich, after heat treatment (semi-quantitative EDS); C: SiC from open SiC-mica-SiC sandwich, after heat treatment (semi-quantitative EDS); D: secondary crystals grown on the edges of mica flakes at the SiC-mica interface, after heat treatment (semi-quantitative EDS).

^bTotal iron.

10.033 Å, consistent with the $\text{KMg}_3(\text{Si}_3\text{AlO}_{10})(\text{OH})_2$ phlogopite, 1M monoclinic polymorph. The chemical composition, obtained by X-ray fluorescence (sodium and potassium by flame photometry), is summarized in Table 1. The thermal expansion coefficient was found to be non-linear, with an average of $9.8 \times 10^{-6} \text{C}^{-1}$, between 138 and 810°C. The in-plane Young's modulus was determined as 154 GPa, obtained from load-strain measurements in four-point flexure with precision strain gauges bonded to the faces of the specimen. This value compares with 167 GPa calculated for

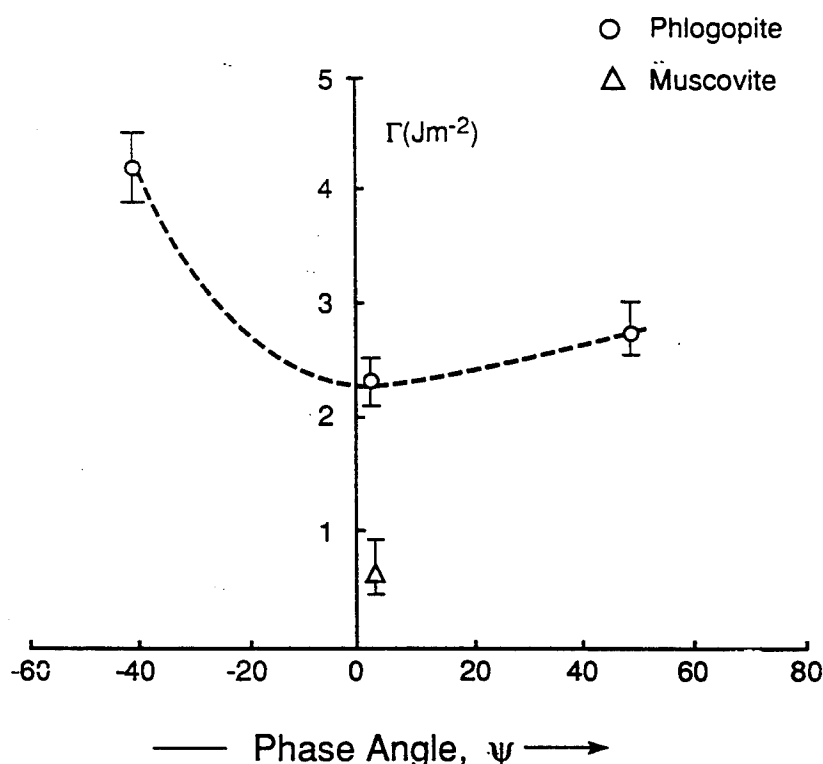


Figure 2. Fracture energies of phlogopite as a function of phase angle. Also shown is a literature result for muscovite [17, 18].

the basal plane using the single crystal elastic constants measured by Simmons and Wang [14] by assuming a hexagonal structure.

Argon sintered α -SiC was used as the other material (Hexoalloy from Carborundum, containing some boron and carbon). The thermal expansion coefficient was determined to be approximately linear and equal to $4.5 \times 10^{-6} \text{ } ^\circ\text{C}^{-1}$, between room temperature and $\sim 1100^\circ\text{C}$. X-ray diffraction indicated a predominantly 6H hexagonal polytype.

Planar SiC-mica interfaces were prepared by sandwiching a thin mica sheet between two lapped silicon carbide plates, followed by heat treatment subjected to uniaxial compression. The heat treatments were conducted in air, at 1100°C for 12 h (6°C min^{-1} heating rate, 3°C min^{-1} cooling rate), subjected to a stress of ~ 130 kPa.

3. FRACTURE ENERGIES

Measurements of the fracture energy of mica, Γ_i , have been made using three test geometries (Figure 1) having the approximate phase angles -40 , 0 and 45° [15, 16]. The tests performed by wedge loading (a glass slide was pushed through the split end of the mica strip and the equilibrium length of the crack measured) require independent measurements of crack length [15]. A systematic error is inherent in these measurements, because of the small crack opening displacements. Tests performed with the flexural specimen do not require crack length measurements [16] and are,

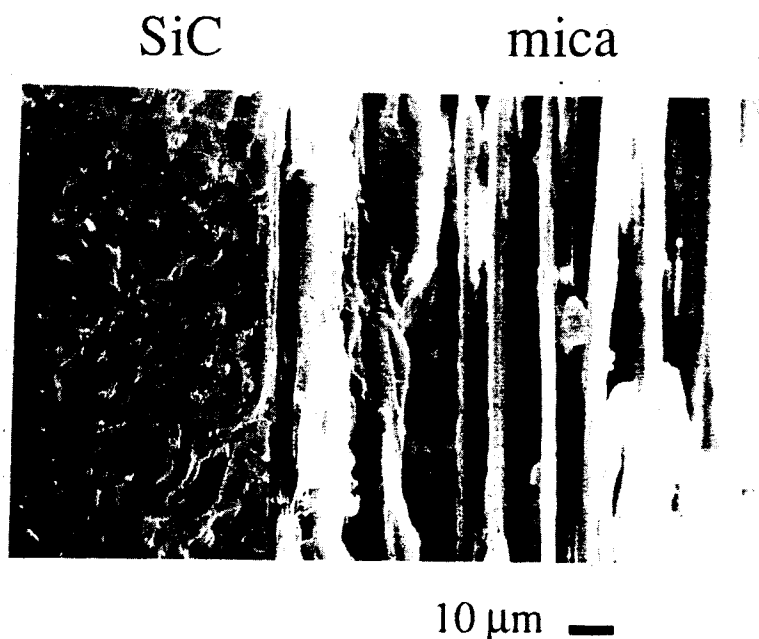


Figure 3. SEM cross-section view of the SiC-mica-SiC sandwich, showing mica's structural features still present in the mica layer.

consequently, more precise (it was found that a pre-crack was formed when razor-blade-inscribing the central notch on the rectangular mica strip and therefore no crack initiation was needed). The results are summarized in Figure 2. Little can be found in the current literature regarding the mechanical properties of phlogopite or, for that matter, any of the other mica minerals. Most information found concerns muscovite and, for comparison, Figure 2 also shows the results obtained in mode I on muscovite [17, 18]. The present measurements for phlogopite indicate significantly larger Γ_i than for muscovite.

4. CHARACTERIZATION

Micrographs of the cross-sectioned interface obtained by scanning electron microscopy (SEM) (Figure 3) indicated that reaction between the SiC and the mica is limited to a layer $<10\text{ }\mu\text{m}$ thick; otherwise, that the original mica structure is preserved. Superimposed energy dispersive spectroscopy (EDS) line scans for Mg, Al and K (Figure 4) establish that these distinctive mica elements did not diffuse into the SiC. Furthermore, semi-quantitative EDS analysis carried out on interface fracture surfaces (Figure 5) revealed a composition similar to the original mica prior to bonding (Table 1). Ultrasonic removal of the mica on either side of the fracture plane provided further details of the reaction layer (Figure 6). A convoluted morphology several micrometers

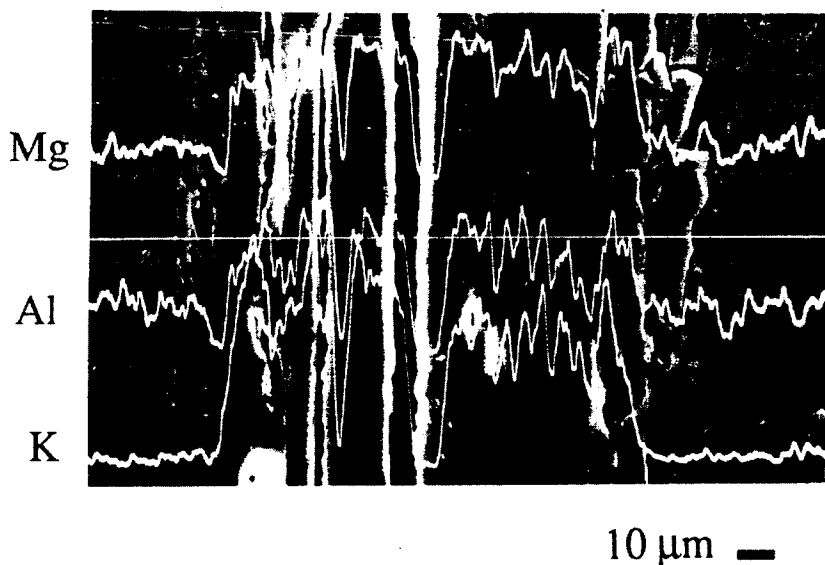


Figure 4. EDS line scans for Mg, Al and K on SEM cross-section of the SiC-mica-SiC sandwich.

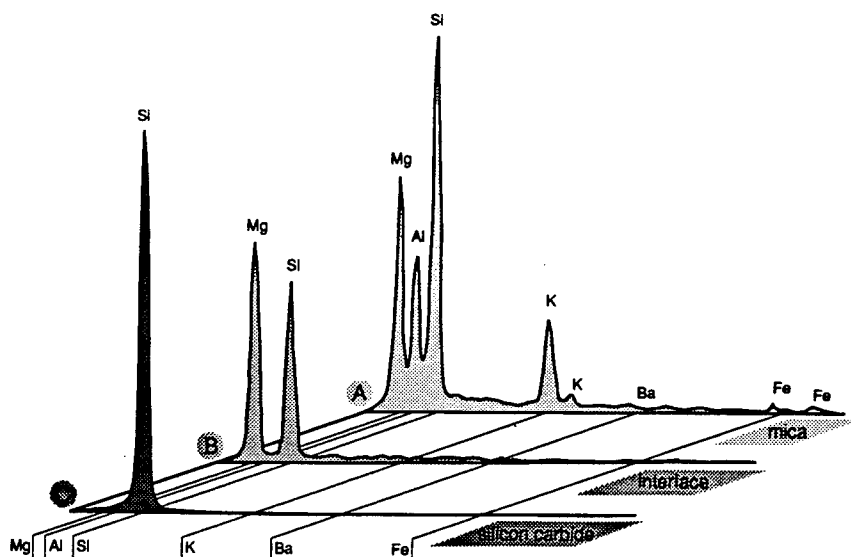


Figure 5. EDS spectra of: (A) phlogopite flakes, on open sandwich; (B) secondary crystals grown on the edges of mica flakes at the interface; and (C) sintered SiC, as seen through holes in the interface.

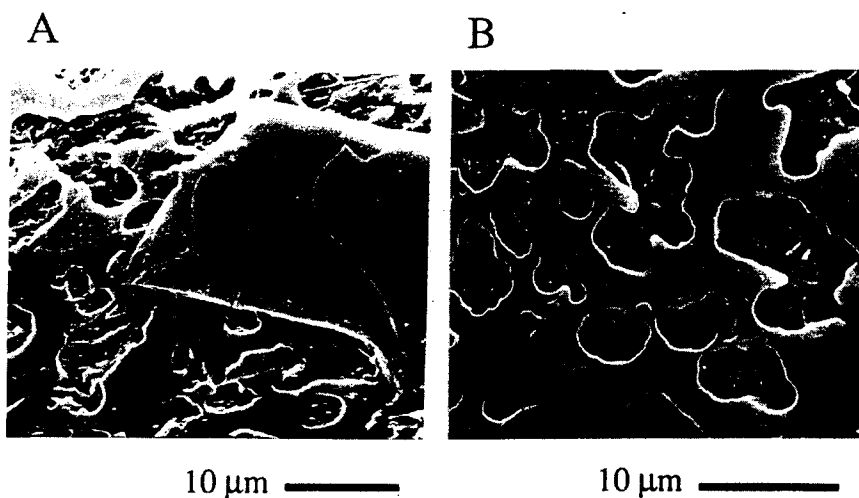


Figure 6. Reacted mica sheet on the SiC plate, from the mica side: (A) mica flake over the reacted mica sheet; (B) detail of the reacted mica sheet, showing the SiC through the holes in the film.

thick suggests that a liquid phase has formed. Semi-quantitative EDS analysis carried out inside the depressions indicates a SiC spectrum (Figure 6), whereas on the plateau,

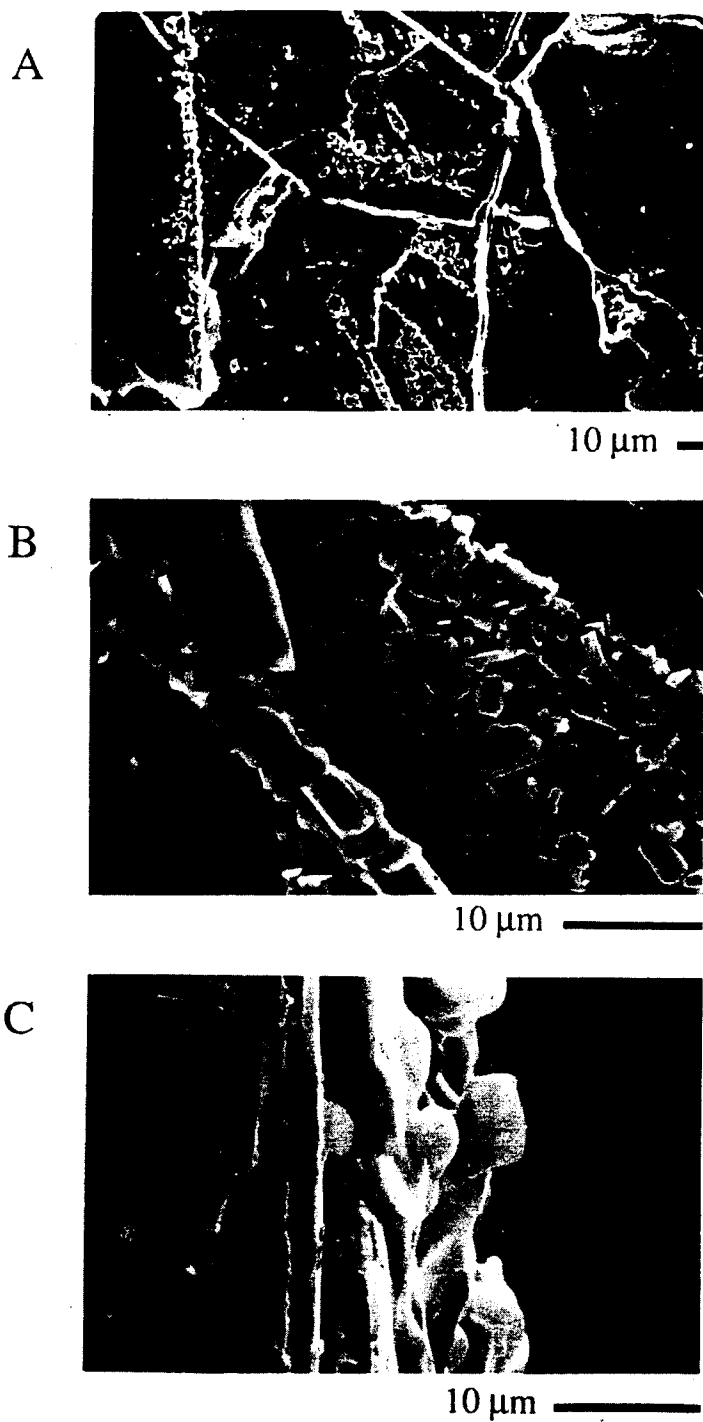


Figure 7. Reacted mica sheet on the SiC plate: (A) secondary phase crystals grown on the edges of mica flakes; (B) same as (A) (EDS analysis reveals a composition close to olivine, $(\text{Mg, Fe})_2\text{SiO}_4$); (C) same as (B), cross-section view.

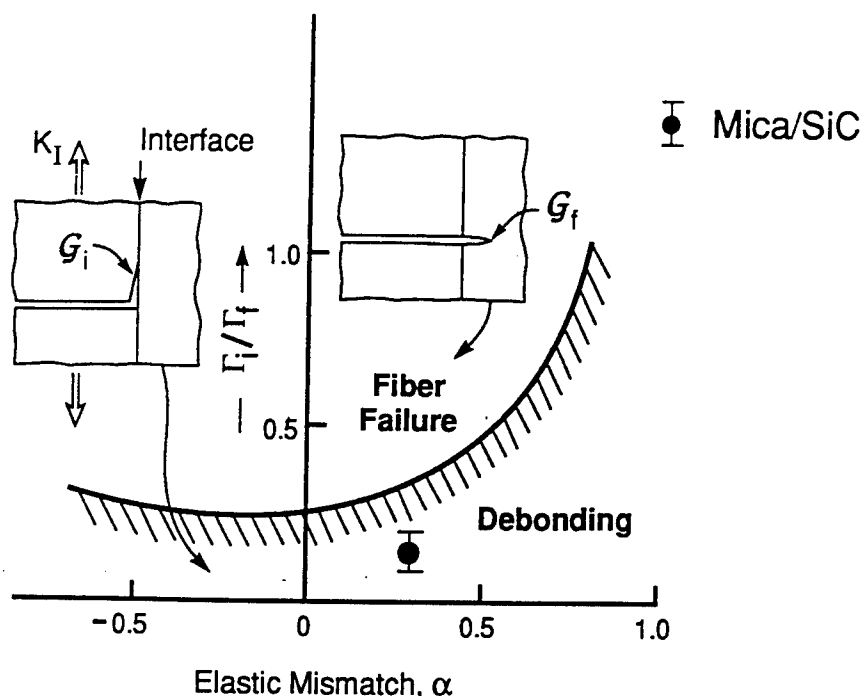


Figure 8. A debond diagram showing the location of the mica-SiC interface within the debond regime: in this diagram, α is an elastic mismatch parameter [4].

a mica-type spectrum is obtained, but with much decreased magnesium content. At higher magnifications, bright white globular crystals are found on the contours of the original mica flakes (Figure 7): EDS analysis reveals a composition close to olivine, $(\text{Mg,Fe})_2\text{SiO}_4$. This is one of the secondary phases expected from phlogopite breakdown, presumably caused by magnesium migration from the adjacent depleted layer (the magnesium does not diffuse into the SiC, Figure 4). The reaction seemingly disrupts the mica structure locally, such that components interact as independent oxides. The major oxide constituents are MgO , Al_2O_3 and SiO_2 (Table 1), and for this particular composition, a liquid phase would develop at 1365°C [19], the two solid phases remaining being enstatite ($\text{MgO}\cdot\text{SiO}_2$) and forsterite ($2\text{MgO}\cdot\text{SiO}_2$). The presence of the other mica constituents (especially iron oxide and K_2O) reduces the initial melting temperature below the theoretical value of 1365°C .

5. IMPLICATIONS AND CONCLUSIONS

The thermochemical issues associated with the use of mica fiber coatings in SiC-SiC composites, established by the present study, are as follows. A reaction occurs at 1100°C that results in a liquid phase which, in turn, facilitates diffusion bonding. While the associated details have not been addressed, it is apparent that magnesium diffusion is involved, as well as dissociation of the mica into its constituent oxides. The reaction layer is several micrometers thick. However, the integrity of the mica structure appears to be retained beyond this reaction zone. Furthermore, at lower processing temperatures, the reaction layer would undoubtedly be smaller. It is thus concluded that mica coatings are viable, but that thermochemical compatibility dictates

a minimum coating thickness in order to retain a discrete mica layer for debonding purposes.

The occurrence of debonding is examined by means of a debond diagram [4] (Figure 8). This diagram indicates that mica coatings in a SiC composite would allow debonding, even if they had an isotropic fracture energy. The anisotropy in Γ_i would further motivate debonding. However, the specifics cannot be addressed without knowledge of the fracture energy normal to the basal plane.

In summary, mica appears to have potential as a debond coating in SiC-SiC composites. Some reactions occur that lead to minimum requirements on coating thickness. There are also potential concerns about fiber degradation caused by the reactions. However, the key processing challenge is to orient the basal plane in the mica coatings parallel to the fiber surfaces.

ACKNOWLEDGEMENTS

The present work was supported by US DARPA No. 8-482490-25601-3 and by INVOTAN and Calouste Gulbenkian Foundation, Portugal, in the form of post-doctoral scholarships.

References

- [1] A.G. Evans and D.B. Marshall, *Acta Metall.*, 37, 2567 (1989).
- [2] A.G. Evans, F.W. Zok and J.B. Davis, *Compos. Sci. Technol.*, 42, 3 (1991).
- [3] R.W. Rice, J.R. Spann, D. Lewis and W. Coblenz, *Ceram. Eng. Sci. Proc.*, 5, 614 (1984).
- [4] M.-Y. He and J.W. Hutchinson, *Int. J. Solid. Struct.*, 25, 1053 (1989).
- [5] H.C. Cao, E. Bischoff, O. Sbaizero, M. Rühle, A.G. Evans, D.B. Marshall and J.J. Brennan, *J. Am. Ceram. Soc.*, 73, 1691 (1990).
- [6] J.W. Hutchinson and H. Jensen, *Mech. Mater.*, 9, 139 (1990).
- [7] R.W. Rice, *US Patent No. 4642271*, 10 February (1987).
- [8] D.C. Cranmer, *Am. Ceram. Soc. Bull.*, 68, 415 (1989).
- [9] B.A. Bender, D. Lewis, W. Coblenz and R.W. Rice, *Ceram. Eng. Sci. Proc.*, 5, 1513 (1984).
- [10] K.M. Prewo and J.J. Brennan, *J. Mater. Sci.*, 15, 463 (1980).
- [11] E. Bischoff, M. Rühle, O. Sbaizero and A.G. Evans, *J. Am. Ceram. Soc.*, 72, 741 (1989).
- [12] K. Chyung, Corning Research, private communication.
- [13] W.A. Deer, R.A. Howie and J. Zussman, *Rock-Forming Minerals*, Vol. 3, Sheet Silicates, John Wiley, New York (1965).
- [14] G. Simmons and H. Wang, *Single Crystal Elastic Constants and Calculated Aggregate Properties*, 2nd edn, MIT Press, Cambridge, MA, p. 139 (1971).
- [15] H.C. Cao and A.G. Evans, *Mech. Mater.*, 7, 295 (1989).
- [16] P.G. Charalambides, J. Lund, R.M. McMeeking and A.G. Evans, *J. Appl. Mech.*, 14, 77 (1989).
- [17] D.H. Roach, S. Lathabai and B.R. Lawn, *J. Am. Ceram. Soc.*, 71, 97 (1988).
- [18] K.T. Wan, N. Aimard, S. Lathabai, G.H. Horn and B.R. Lawn, *J. Mater. Res.*, 5, 172 (1990).
- [19] E.M. Levin, C.R. Robbins and H.F. McMurdie, *Phase Diagrams for Ceramists* (M.K. Reser, Ed.), Vol. 1, The American Ceramic Society, Columbus, OH (1974).

Structure and Properties at the Ferroelectric/Electrode Interface between Lead Zirconate Titanate and Copper

Heng C. Cao,* Marc De Graef,* and Anthony G. Evans*

Materials Department, College of Engineering, University of California, Santa Barbara, California 93106-5050

In advanced actuator systems, ferroelectric ceramics are usually made into multilayered stacks to obtain optimum performance. This is done by interlacing noble metals (such as Pt/Pd) with ceramic green sheet and cofiring. The present study proposes an alternative, more economic electrode. Copper has been successfully diffusion bonded to several PZT-based ferroelectric ceramics in a multilayer configuration. The microstructure and the relevant physical properties of the interfaces have been investigated. This has been achieved by using microscopy, as well as by mechanical and electrical characterization. These studies indicate that no reaction product forms at the interface and, furthermore, that the interface exhibits good cohesion.

I. Introduction

THE application of ferroelectric ceramics as actuators and sensors relies on multilayer concepts.¹⁻⁵ Electrodes, usually metal, alternate with the ferroelectric.¹⁻³ While the electrodes are often regarded as secondary to the actuator/sensor material, the ultimate performance of the system is strongly influenced by the electrical and mechanical characteristics of the electrode itself and particularly the electrode/ferroelectric interface.⁶ The interfacial zone has been considered to have an important influence on performance, through a multiplicity of potential degradation effects. These include fatigue, interface decohesion, and charge injection. Two factors have influenced the present research: (i) Most of the basic research on bimaterial interfaces has been on interfaces between metals and binary oxides, such as Al_2O_3 , ZrO_2 , and NiO .⁷⁻¹² There is minimal knowledge of interfaces between metals and complex oxides, such as ferroelectrics. Consequently, there are no rules that can be used to predict phenomena such as reaction product formation, interface decohesion, interface resistance, etc. (ii) Common electrode systems for PZT sensors and BaTiO_3 capacitors are typically noble metals (such as Pt and Ag). These materials may be susceptible to degradation effects¹ and are also expensive. For example, Ag is subject to migration that may lead to premature breakdown. Consequently, cofired multilayer actuators often use a Pd/Pt alloy, which is apparently resistant to migration, but still relatively expensive.

The present article represents a preliminary attempt to examine combined thermochemical and thermomechanical aspects of the interface between ferroelectric and metals, particularly inexpensive materials which have potential as electrodes. In this study, Cu is selected as the metallic phase within multilayer structures comprised of alternating layers of metal with either a ferroelectric or an antiferroelectric.

The major objective is to demonstrate that interfaces between Cu and ferroelectrics can be produced with minimal chemical reaction, while also having good resistance to decohesion and, moreover, that the interface can be produced subject to condi-

tions wherein the ferroelectric retains good polarization/field (*P/E*) characteristics. Phenomena involved in degradation are also characterized and analyzed, such as plastic deformation and microcracks.

II. Experimental Procedure

(1) Materials

Two oxide materials were used for this study. One was a hard piezoelectric (PZT C5500, Chanel Industries, Inc., Goleta, CA) with composition $\text{Pb}_{0.988}\text{Nb}_{0.024}(\text{Zr}_{0.528}\text{Ti}_{0.473})\text{O}_3$. The other was an antiferroelectric (PLSnZT) with chemical composition $\text{Pb}_{0.97}\text{La}_{0.02}(\text{Zr}_{0.66}\text{Ti}_{0.11}\text{Sn}_{0.23})\text{O}_3$. Thin plates of each material having dimensions 5 mm \times 8 mm and 2 mm thick were prepared by cutting from bulk sintered material, using a resin-bonded diamond wheel to minimize machining damage, and then surface ground. High-purity (99.98%) Cu foils, 25 μm thick were interspersed to form a multilayer (Fig. 1). The multilayered material was enclosed within copper foils. This enclosure created an equilibrium partial pressure of Pb during diffusion bonding. Pb loss was then confined to the edges, which were removed before testing. Bonding was conducted under vacuum at 1050°C for 10 h. A small pressure of about 5 MPa was maintained throughout. A slow cooling rate of about 3°C/min was used to alleviate residual stress. The bonded specimens were sectioned normal to the interface and polished.

(2) Microstructural Characterization

Transmission electron microscopy (TEM) was used to characterize the interfacial zone. For this purpose, thin sections were prepared using the off-center dimpling technique discussed elsewhere.⁹ Disks, 3 mm in diameter, with the interface region about 0.5 mm from the center of the dimple were ion-milled at 4 kV, using a 15° beam angle. Semicircular quartz shields were used to protect one side of the interface from the ion beams. The resulting samples showed a large hole adjacent to the interface in the ceramic (about 0.8 mm in diameter) with several interface regions sufficiently thin for TEM observations at 400 kV. Electron diffraction measurements, energy dispersive X-ray analysis (EDS), high-resolution imaging (HREM), and parallel electron energy loss spectroscopic measurements (PEELS) were all carried out on a JEOL 4000 FX side entry microscope.

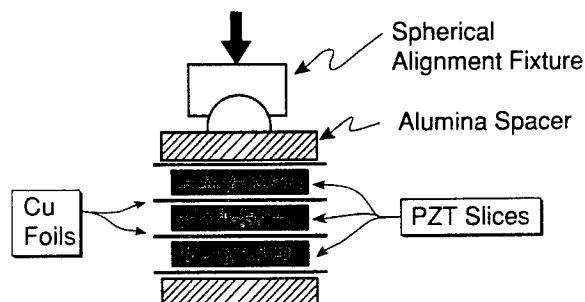


Fig. 1. Schematic showing the layout of Cu/PZT multilayered stack for diffusion bonding.

G. Messing—contributing editor

(3) Mechanical Measurements

The fracture resistance of the interface between the metal electrode and the ferroelectric was assessed by using an indentation technique. Previous studies have provided the basis for using this technique as an interface fracture resistance probe.⁸⁻¹⁰ A brief synopsis is presented here in order to facilitate interpretation. A Vickers hardness indentation is placed in the oxide, near the interface. The orientation is chosen to allow the formation of two orthogonal radial cracks that propagate normal and parallel to the interface. The distance of the indentation from the interface is chosen such that the radial crack which intersects the interface is *shorter* than the crack which extends away from the interface (Fig. 2).[†] This choice ensures that the stress intensity factor at the interfacial crack front exceeds the fracture toughness of the oxide. Experience with this technique¹⁰⁻¹² indicates that the radial crack causes decohesion when the interface debond energy, Γ_i , is relatively low and the interface fails by a brittle mechanism. Conversely, when the interface is strong and is subject to a ductile rupture mechanism, the interface crack blunts, without decohesion, and induces a zone of plastic deformation in the metal (Fig. 2). Consequently, the interface response to a radial crack, established by scanning electron microscopy (SEM), is used to classify the interface as either "weak" (when decohesion occurs) or "strong" (when blunting occurs without decohesion).

(4) Ferroelectric Characterization

Multilayer samples were incorporated into a Sawyer-Tower circuit in order to measure the polarization (P/E) behavior. For comparison, the $P-E$ curves were also measured by using thin slice samples with sputtered gold electrodes. The capacitance of the multilayer was also measured by using an LRC meter. In

addition, dielectric breakdown measurements were performed, by applying a high DC voltage across the specimen.

III. Interface Structure

In the antiferroelectric Cu-PLSnZT system, a low-magnification TEM view of the interfacial zone (Fig. 3(a)) indicates that the interaction zone is small. It is also apparent that the interface (arrowed) has convolutions up to 2 μm in amplitude. Faceted interfacial regions were identified at several locations (Fig. 3(b)). Diffraction and EDS established that these regions were pure Cu. There is no evident interdiffusion between the Cu and the oxide. PEELS measurements confirmed the absence of O in the Cu layer. In some Cu grains close to the interface, there is a weak N-edge. The origin of the N is unknown, but may have been present in the Cu foil. Dislocations are evident in the Cu, which had a substantially larger grain size than the ferroelectric material. Observations at high magnification were unable to identify a discrete copper oxide layer. Instead, ZrO_2 precipitates were evident at the interface (Fig. 4, arrowed regions). These were ~ 30 nm in diameter and occurred at a spacing of ~ 500 nm. All ZrO_2 particles protruded into the metal layer. The composition of these precipitates was established by means of combined EDS and PEELS analysis. An examination of defects that occur preferentially near the interface (Fig. 4(a)) indicated dislocations in the Cu at relatively low concentration and a much higher defect concentration in the oxide. These latter defects consisted of both dislocations and domain walls, which formed in a zone ~ 500 nm in width. The domain walls were identified by their fringe contrast, through features being asymmetric in the bright field and symmetric in dark-field imaging mode.

In the piezoelectric Cu/PZT, the interfacial zone exhibited similar undulations (Fig. 5(a)). EDS analysis of the metal again indicated an absence of cation interdiffusion from the oxide into the Cu. Several precipitates were evident along the interface, 40 to 100 nm in diameter. Electron diffraction analysis, combined with EDS, identified these particles as cubic ZrO_2 . A high defect concentration was again observed in the PZT close to the interface, consisting of both dislocations and domain walls (Fig. 5(b)).

In summary, the TEM studies have established that Cu does not exhibit appreciable interdiffusion with two typical ferroelectric oxides, upon diffusion bonding. The only evidence that some interaction has occurred is the existence of small, dispersed ZrO_2 precipitates along the interface. Since the ZrO_2 originates from the ferroelectric and there does not appear to be any change in the structure of the latter, near the interface, it is probable that there was dissolution of the other cations (Pb, Sn, Ti) and of oxygen into the Cu during bonding. However, this was not apparent at the detectability level achievable in the TEM. Dissolution of the oxide in the metal is a common phenomenon during diffusion bonding.⁷ Often the cations remain in solution in the metal, but oxide precipitation on cooling has also been observed, such as Al_2O_3 in Nb.⁷ The more important finding is that the ferroelectric retained integrity, both structural and chemical, up to the electrode interface. This factor should allow good ferroelectric performance.

The occurrence of defects in both ferroelectrics, near the interface, may have consequences for degradation, as elaborated below.

IV. Interface Integrity

Vickers indentations used within a load range between 5 and 30 N all gave behavior of the type illustrated in Fig. 6. Radial cracks that were initiated in the ferroelectric and extended to the interface *always* arrested at the interface without causing interface decohesion. Furthermore, the crack front at the interface exhibited plastic blunting. Analogies with other metal/oxide interfaces indicate that the interfaces between Cu and both PZT and PLSnZT are "strong." The closest analogy is with the Al/ Al_2O_3 system,^{11,12} which gives an identical interface response and which exhibits a ductile interface fracture mechanism.¹¹ "Strong" bonding has also been found between Cu and binary oxides.¹¹

[†]Consequently, the distance of the indent from the interface depends on the indentation load.

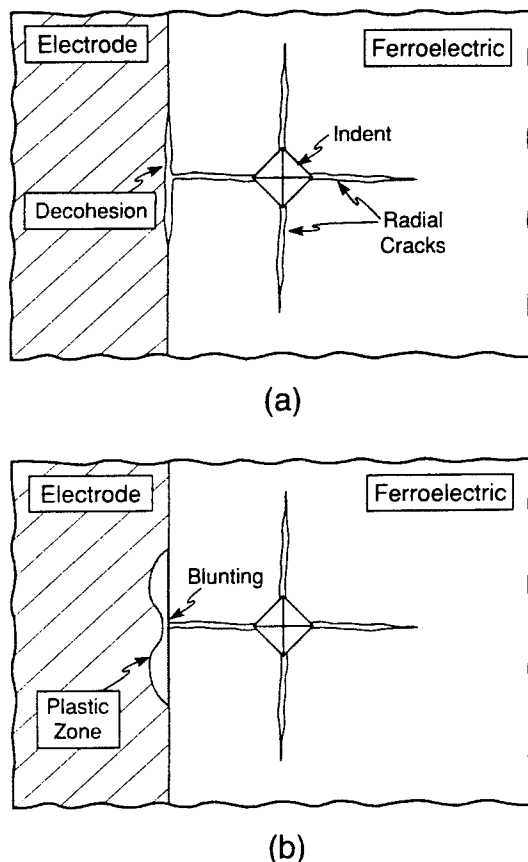


Fig. 2. Schematic illustrating indentation in a ferroelectric ceramic close to an interface: (a) "weak" interface, low Γ_i ; (b) "strong" interface, large Γ_i .

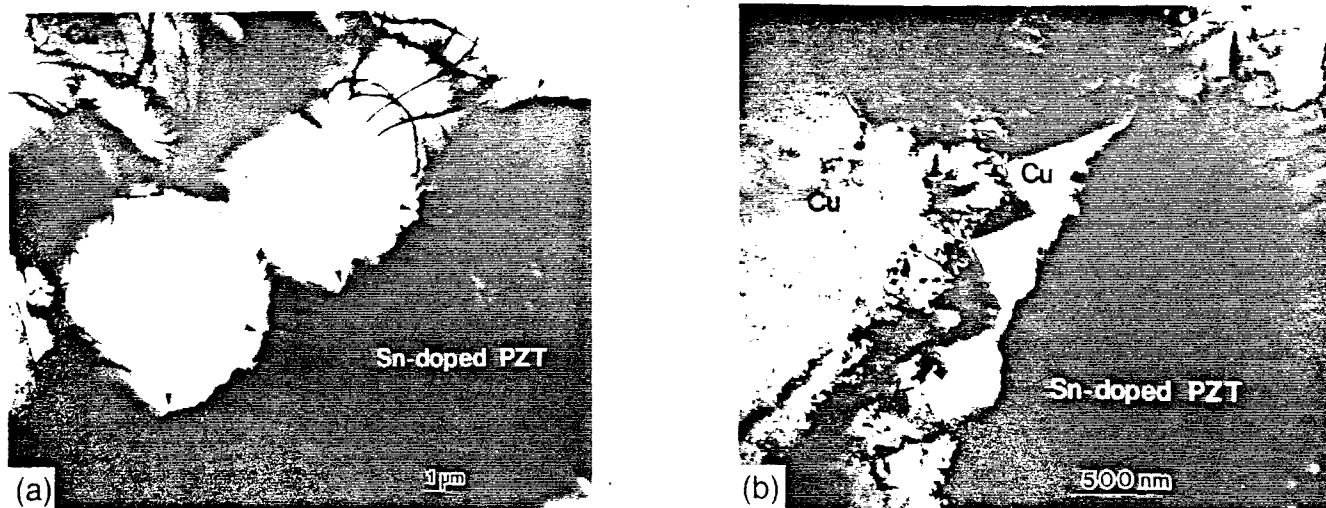


Fig. 3. (a) Low-magnification TEM micrograph indicating an interface between Cu and PLSnZT (arrows indicate locations of the interface). (b) Faceted Cu regions near the Cu/PLSnZT interface.

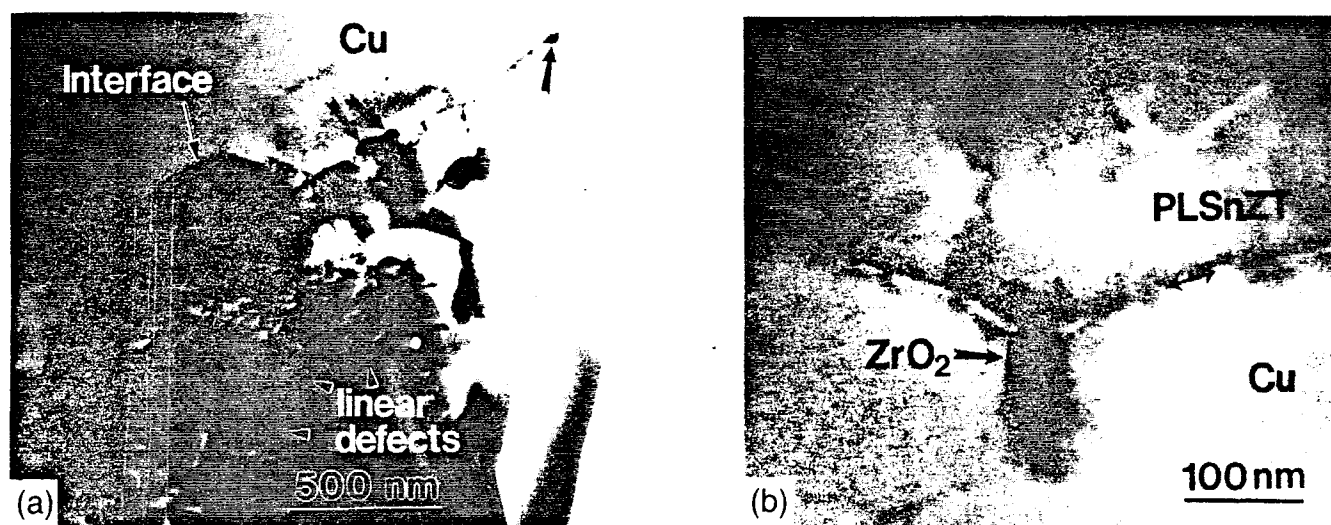


Fig. 4. (a) ZrO₂ precipitates (arrowed) are present at the Cu/PLSnZT interface. (b) A cube-shaped ZrO₂ precipitate at the interface, protruding into the metal layer.

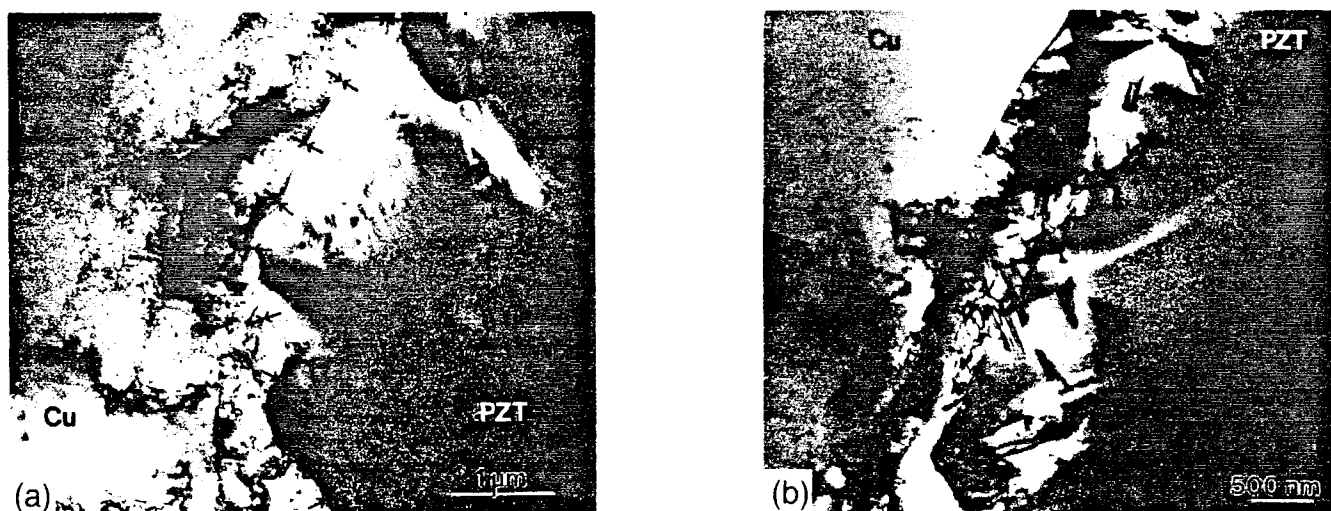


Fig. 5. (a) Interface (arrowed) between Cu and PZT. Ferroelectric domain walls are present in all PZT grains. (b) A high defect concentration in the PZT close to the interface.

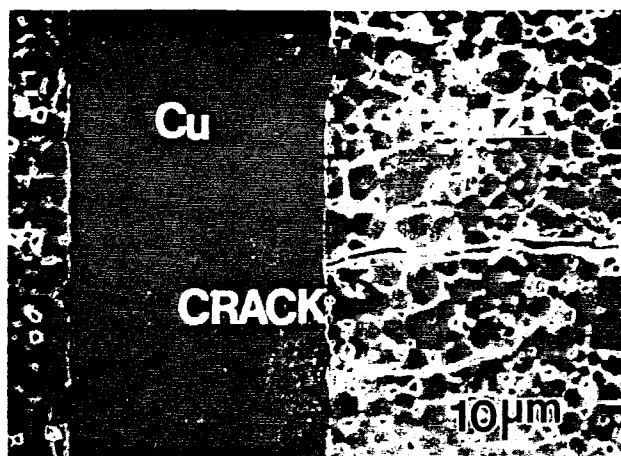


Fig. 6. Indentation crack arrests at the electrode/oxide interface and blunting takes place. No interface decohesion is observed (interfaces marked by arrows).

V. Ferroelectric Measurements

Capacitance measurements performed on the PZT multilayer gave values for the dielectric constant of PZT ($K = 1460$). This value is identical to that measured on the material with sputtered-gold electrodes prior to diffusion bonding. It also coincides with the value quoted by the manufacturer.¹³ The hysteresis loop width and the dielectric strength measured on the bonded multilayer were also identical to values obtained before bonding. It is thus concluded that the properties of the PZT were not degraded by diffusion bonding with Cu. The PLSnZT also exhibited properties after diffusion bonding with Cu, comparable to those measured with gold electrodes.

VI. Degradation Mechanisms

The occurrence of a high concentration of defects in both oxides within a narrow zone near the interface is of interest because these defects may have an important influence on actuator performance. It is believed that the defects form as a result of the thermal expansion mismatch between Cu and the ferroelectric. In order to rationalize defect formation, an analysis of thermal expansion misfit stresses is conducted.

Plastic deformation in either the metal or the ferroelectric is governed by the shear stresses.^{14,15} The local yielding around the interface suggested by the experimental observations must, therefore, be associated with shear stress concentrations. A concentration of shear stress near the interface only occurs near edges and surfaces.¹⁶ Furthermore, surfaces that intersect the interface are created when thin foils are produced for TEM. Consequently, the plastic deformation zones must evolve as the foils are generated. This thin foil effect is an important aspect of the interpretation of TEM observations.

The plastic deformation expected in the Cu should obey standard power law hardening in which the equivalent stress, σ^* , and equivalent plastic strain, ϵ^* , are related by¹⁴

$$\sigma^* = \sigma_0(\epsilon^*/\epsilon_0)^n \quad (1)$$

where σ_0 is the yield strength, ϵ_0 the yield strain, and n the work hardening coefficient. The magnitudes of these parameters for annealed Cu are given in Table I and plotted in Fig. 7.¹⁶ The deformation of the oxides obeys a different constitutive law, because the deformation mechanism is different.¹⁵ Recent experiments on piezoelectrics and antiferroelectrics have suggested the following two-term power law:¹⁵

$$\sigma^*/\sigma_0 = (\epsilon^*/\epsilon_0)^a + (\epsilon^*/\epsilon_0)^b \quad (2)$$

where the superscript $*$ again refers to deviatoric quantities, while a and b are hardening coefficients (given for PZT in Table I). A comparison of the plastic flow behavior of Cu and PZT is given in Fig. 7. Yielding is considered to occur when the equivalent stress exceeds the yield strength σ_0 of either constituent.

A finite element procedure (ABAQUS) has been used to analyze plastic strain contours in a Cu/PZT thin foil (thickness t). Geometric symmetry allows the calculations to be performed using a quarter of the cross section (Fig. 8). The plastic strain contours are computed as the specimen is cooled from the processing temperature. It is assumed that creep relaxation occurs at high temperatures, such that residual stresses do not begin to develop above $T \approx 0.7T_m$, with T_m being the melting point of the copper. The results (Fig. 9) indicate that there is a larger plastic zone in the PZT than in the Cu. Furthermore, the plastic strain in the PZT near the interface approaches 0.6%, the permanent saturation strain exhibited by PZT.¹⁵ The plastic zone size in the PZT is $R_p \approx t/2 \approx 400$ nm (Fig. 9).

Comparison of the calculations with the TEM observations (Figs. 4 and 5) indicates reasonable consistency. The calculated plastic zone size in the PZT (400 nm) is similar to the width of the defect zone found in the TEM (500 nm). This consistency confirms that the defects are caused by plastic deformation, induced by the thermal expansion mismatch between the electrode and the PZT.

The small zone of plastic deformation predicted to occur in the Cu, near the interface, is not readily apparent in the TEM. Dislocations clearly exist in the Cu (Figs. 4 and 5), but they are

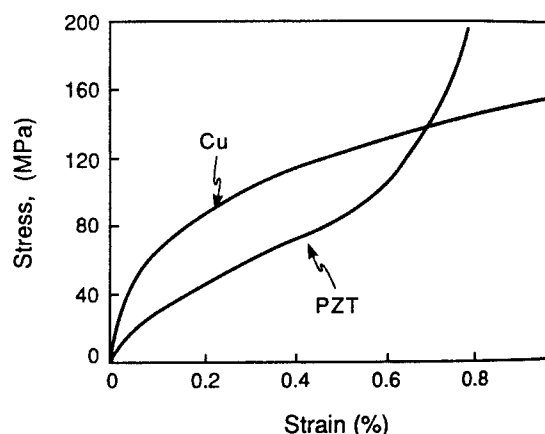


Fig. 7. Comparison of stress-strain curves for Cu and PZT.

Table I. Constitutive Properties of the Cu/PZT System

Material	Cu	PZT
Young's modulus, E (GPa)	130	80
Poisson's ratio, ν	0.34	0.4
Thermal expansion coefficient, α ($\times 10^{-6}$ K $^{-1}$)	16.6	1.8 ($T > T_c$) 9.0 ($T < T_c$)
Yield strength, σ_0 (MPa)	60	75
Reference strain, ϵ_0		0.65
Hardening exponents		
n	0.32	
a		0.7
b		12

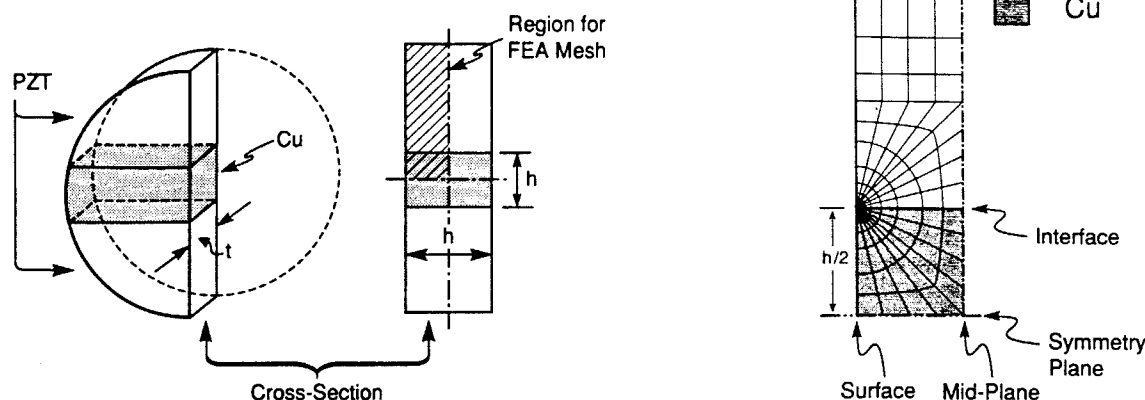


Fig. 8. Typical finite element mesh ($t/h = 1$).

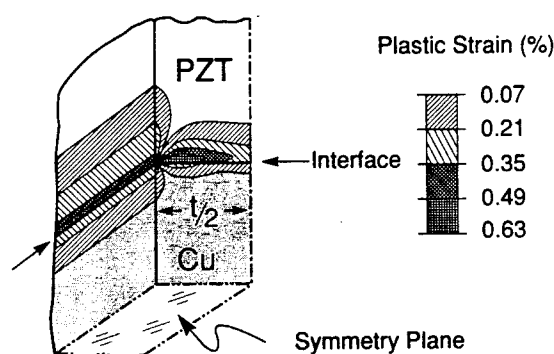


Fig. 9. Plastic strain contours in a Cu/PZT bond, caused by thermal mismatch straining ($t/h = 1$).

not confined to an interfacial zone. Confirmation that dislocation activity has occurred in the Cu upon thin foil formation would require more detailed study of the dislocation density in the Cu.

It is concluded that plastic deformation in the ferroelectric caused by thermal expansion mismatch is possible. However, it is a surface (or edge) phenomenon and should *not* occur homogeneously along the interface. This deformation may be a mechanism for degrading the material, through the gradual propagation of the plastic zone inward, from the edges, upon cyclic straining.¹⁷

VII. Concluding Remarks

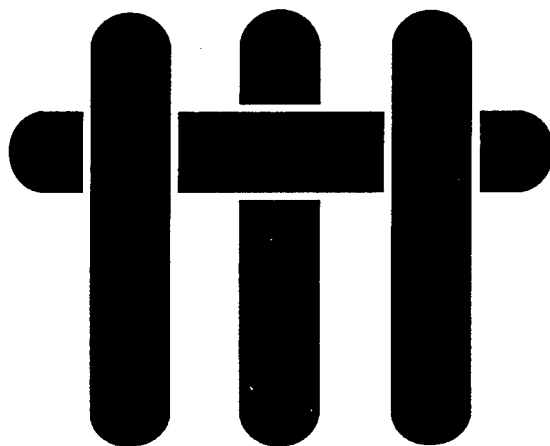
The present observations indicate that Cu has two desirable characteristics as an electrode for a multilayer actuator. There is minimal reaction at temperatures needed for diffusion bonding. The interface is strongly bonded and resistant to decohesion. However, a possible detriment is the occurrence of plastic deformation in the oxide, near the interface. Such deformation is an edge effect, associated with the thermal expansion mismatch,¹⁷ and arises because of the relatively large thermal

expansion coefficient of Cu combined with the low "yield strength" of the oxide. The concern is that superposed effects of electric field, during operation, may result in damage that spreads from the edge.

References

- ¹S. R. Winzer, N. Shanker, and A. P. Ritter, "Designing Cofired Multilayered Electrostrictive Actuators for Reliability," *J. Am. Ceram. Soc.*, **72**, 2246-57 (1990).
- ²L. E. Cross, "Piezoelectric and Electrostrictive Sensors and Actuators for Adaptive Structures and Smart Materials"; pp. 1-20 in *ONR Annual Report*. Pennsylvania State University, State College, PA, 1990.
- ³D. P. Skinner, R. E. Newnham, and L. E. Cross, "Flexible Composite Transducers," *Mater. Res. Bull.*, **13**, 599 (1978).
- ⁴W. A. Smith, A. A. Shaulov, R. F. Rosar, and B. M. Singer, "Composite Piezoelectrics for Ultrasonic Transducers"; pp. 231-49 in *Proceedings of the 6th IEEE Symposium on Applications of Ferroelectrics*, Lehigh University, June 8-11, 1986.
- ⁵M. Ealy and C. Wheeler, "A Standardized Electrodisplative Transducer"; presented at the SPIE Symposium on Aerospace Sensing, Orlando, FL, March 1989.
- ⁶W. J. Menz and R. Anderson, AT&T Bell Laboratory Report, 1978.
- ⁷M. Rühle, A. G. Evans, M. F. Ashby, and J. P. Hirth, "Metal Ceramic Interfaces," *Acta Scr. Metall. Proc. Ser.*, **4**, 1-120 (1990).
- ⁸I. E. Reimanis, B. J. Dalgleish, and A. G. Evans, "The Fracture Resistance of a Model Metal/Ceramic Interface," *Acta Metall.*, **39**, 3133-41 (1991).
- ⁹M. De Graef, B. J. Dalgleish, M. R. Turner, and A. G. Evans, "Interfaces Between Alumina and Platinum: Structure and Fracture Resistance," *Acta Metall. Mater.*, **40**, 5333 (1992).
- ¹⁰A. G. Evans, M. C. Lu, S. Schmauder, and M. Rühle, "Some Aspects of the Strength of Metal/Ceramic Bonded Systems," *Acta Metall.*, **34**, 1643 (1986).
- ¹¹A. G. Evans and B. J. Dalgleish, "The Fracture Resistance of Metal/Ceramic Interfaces," *Acta Metall. Mater.*, **40**, 295 (1992).
- ¹²B. J. Dalgleish, K. P. Trumble, and A. G. Evans, "The Strength and Fracture of Alumina Bonded with Aluminum Alloys," *Acta Metall.*, **37**, 1923 (1989).
- ¹³Catalogue, Channel Industries, Inc., Goleta, CA.
- ¹⁴J. H. Hollomon, "Tensile Deformation," *Trans. AIME*, **162**, 268 (1945).
- ¹⁵H. C. Cao and A. G. Evans, "Nonlinear Deformation of Ferroelectric Ceramics," *J. Am. Ceram. Soc.*, **76**, 890 (1993).
- ¹⁶R. W. Hertzberg, *Deformation and Fracture Mechanics of Engineering Materials*, 2nd ed. Wiley, New York, 1983.
- ¹⁷H. C. Cao, M. D. Thouless, and A. G. Evans, "Residual Stresses and Cracking in Brittle Solids Bonded with a Thin Ductile Layer," *Acta Metall.*, **36** [8] 2037-46 (1988).

M A T E R I A L S



EFFECTS OF COMPOSITE PROCESSING ON THE STRENGTH OF SAPPHIRE FIBER-REINFORCED COMPOSITES

by

J.B. Davis, J. Yang and A.G. Evans
Materials Department
College of Engineering
University of California, Santa Barbara
Santa Barbara, California 93106-5050

ABSTRACT

The current interest in tough, high-temperature materials has motivated fiber coating development for sapphire fiber-reinforced alumina composites. For this system, it has been demonstrated that the interfacial properties can be controlled with coatings which can be eliminated from the interface subsequent to composite consolidation. However, these fugitive coatings can contribute to the high temperature strength degradation of sapphire fibers. Such degradation, which compromises the composite strength and toughness, is the focus of the current investigation. It has been observed that, in some cases, by selecting appropriate composite processing conditions, such effects can be minimized. But overcoming fiber strength loss remains an important issue.

1. INTRODUCTION

The current limitations to the advancement of ceramic matrix composites are associated with the development of high strength, oxidation and creep resistant fiber-reinforcements and the control of the interfacial debonding and sliding behaviors. One approach to reinforcements has been to develop single crystal oxide fibers. The most thoroughly studied of these is sapphire. One promising class of coating is fugitive,¹⁻² whereby the coating is removed from the interface subsequent to composite consolidation in order to leave a gap between the fiber and matrix. Carbon and molybdenum are examples of such coatings. The coating thickness and resulting gap size are used to manipulate the interfacial sliding resistance. However, the coating chemistry and thickness can affect the surface morphology of the fibers during either composite processing or subsequent exposures to high temperatures. This can lead to pronounced changes in fiber strengths. Such effects are the focus of this investigation.

This study has five essential elements. (i) Uncoated fibers were heat treated and their strengths measured in order to classify inherent strength degradation mechanisms. (ii) Coated fibers were given similar heat treatments and tested to establish additional degradation phenomena that may arise. (iii) Fibers with thick fugitive coatings of C and Mo were introduced into an alumina matrix by hot pressing. The fibers were removed by using the fugitive character of the coating. The withdrawn fibers were tested. These tests identified new degradation mechanisms that may operate with this coating. (iv) Unidirectional composites were fabricated with several coating thicknesses. The tensile properties of the composite were measured and fiber push-out tests performed. These tests indicated whether there are other strength loss phenomena associated with composite consolidation. They also allowed correlation to be made between composite behavior, the fiber strength and the interface debonding/sliding resistance. (v) The fiber

morphological changes were examined in order to provide an understanding of the mechanisms involved.

2. EXPERIMENTAL PROCEDURES

2.1 Fiber Strength Tests

The fibers were obtained from a single spool of Saphikon sapphire fiber (diameter $\sim 130 \mu\text{m}$). Their tensile strengths were measured for several fiber conditions by using a commercially available fiber testing machine* and a one-inch gauge length. The first set was tested in the as-received state. The second was washed in cold water followed by acetone and ethanol, and then subjected to the series of heat-treatments summarized in Table I. The remaining two sets were first washed and then coated with either Mo or C to a thickness of $\sim 10\text{--}15 \mu\text{m}$. These were hot pressed into a high purity alumina matrix using the conditions specified in Table I. After hot pressing, the composites were heat treated at 1100°C in air for $\sim 2 \text{ h}$ to remove the coatings from the interfaces. The fibers were extracted from the matrix and their strengths were measured directly.

Fiber strength data sets were comprised of ~ 20 measurements. While this set size is too small to give an accurate determination of the fiber strength distribution parameters, it is sufficient to establish definitive trends in the median fiber strength.^{3,4}

2.2 Composite Specimen Fabrication

Unidirectional alumina matrix composites containing Mo coated sapphire fibers were produced for correlating composite behavior with the properties of the fibers and interfaces. Coatings with three thicknesses (0.2 , 0.7 and $1.4 \mu\text{m}$) were used. Composites were produced by hot isostatic pressing (HIPing). These have been made by first

* Micropull Sciences, Thousand Oaks, California

fabricating a preform comprising coated fibers within a slurry of the matrix material. These composites were sealed in an evacuated niobium can. Consolidation was achieved at a pressure of 30 MPa at 1350°C for 30 min (Fig. 1). Dog-bone shaped tensile specimens were diamond machined from the consolidated composite and the coatings were removed from the interface by heat-treating in air at 1150°C for 50 h.

2.3 Microstructural Characterization

Scanning electron microscopy (SEM) techniques with energy dispersive X-ray analysis were used to identify the strength limiting flaws for each data set. In addition, the morphologies of heat-treated fibers were examined in a field emission scanning electron microscope (JEOL 6300F) in order to classify and compare various surface and fracture features.

The interfaces in the composites were examined by transmission electron microscopy (TEM). For this purpose, electron transparent foils were prepared as described elsewhere. After tensile testing, the fiber pull-out length distributions were measured from scanning electron micrographs and the surface features of the fibers characterized. In addition, interactions between the fibers and the matrix were also classified.

2.4 Composite Testing

Tension tests were performed on the composite in a fixture located within a scanning electron microscope (Fig. 2). The forces were measured from a load cell. The behavior at small strains was monitored from strain gauges affixed to the specimen. At larger strains, the specimen displacement was measured with an LVDT. These strain data were compared with photomicrographic measurements.

The interfacial sliding resistances were measured by using the fiber push-through technique.⁶

3. FIBER STRENGTHS

The fibers in the as-received condition were found to have a median strength, $\bar{S} \approx 2.7$ GPa, and a Weibull modulus, $m \approx 6.5$ (Fig. 3a), consistent with values reported in the literature.⁵ After heating the washed, uncoated fibers to successively higher temperatures (1250°C, 1350°C and 1450°C), there were small, though significant, reductions in either the mean strength, \bar{S} , or the Weibull modulus, m , (Fig. 3b, Table I). Conversely, extracted fibers originally coated with Mo showed considerable strength loss, at all heat-treatment temperatures (Fig. 3b). The fibers originally coated with carbon exhibited a smaller reduction in median strength but had the most substantial strength *variability*, reflected in the highest coefficient of variation and the low Weibull modulus ($m \approx 2.6$).

4. FIBER MORPHOLOGY

Upon heat treatment, the fiber morphology was found to be strongly influenced by both diffusional effects and chemical reactions, especially in the presence of either fiber coatings or a composite matrix. There are four basic phenomena (Fig. 4), each exemplified by the observations presented below. (i) Surface diffusion causes fiber faceting, even in isolated fibers. (ii) Thin polycrystalline coatings, when chemically inert (no reaction products), are morphologically unstable and develop holes. Equilibrium at the hole edges then motivates surface diffusion and induces the formation of ridges on the fibers. (iii) Chemical reactions occur between the coating and the fiber resulting in fiber surface damage. This may produce either solid or gaseous reaction products. (iv) After a coating has either become discontinuous during composite consolidation or has been removed by oxidation, the matrix may sinter to the

fiber. This results in localized bonding, causing matrix grains to remain attached to the fiber during pull-out, upon composite testing.

4.1 Uncoated Fibers

The fibers display sinusoidal diameter modulations along their length with characteristic wavelengths and amplitudes, described elsewhere.⁶ Flaws observed in the as-received fibers were primarily associated with porosity. Pores develop during fiber growth and have been observed within the fibers and at the fiber surfaces (Fig. 5). The strength range is consistent with calculations for cylindrical rods containing cracks having the same dimensions as the pores⁷ (Fig. 6).

The surface features were altered by high temperature heat-treatments. The fibers facet (Fig. 7), illustrating the inherent morphological instability of single crystal fibers. Frequently, local surface damage was evident resulting from chemical reactions (Fig. 8a). These sites usually correlate with failure origins and account for the strength loss. Energy dispersive X-ray spectroscopy measurements identified Si and Mg at these sites (Fig. 8b). Two likely sources of contamination include the incomplete removal of the fiber sizing and reactions with inorganic contaminants that condense onto the fiber surfaces during heat treatment in the air furnace. Such contaminant reactions are avoidable upon encapsulation of the fibers and are of moderate practical concern.

4.2 Carbon Coated Fibers

The heat treated carbon coated fibers displayed surface regions indicative of a chemical reaction between the coating and the fiber, localized near fiber ends and at locations where the coatings were discontinuous. The reaction product, identified by X-ray analysis as Al_4C_3 , severely degraded the fiber surface. The extent of reaction increased with temperature (Fig. 9). In addition, accentuated fiber facetting occurred near the reaction sites.

Thermodynamic calculations (Appendix I) indicate that alumina and C can react to form volatile aluminum suboxides at temperatures as low as 1100°C, at least when heat treatments are conducted in an open system.⁸⁻¹¹ The progress of these reactions requires a means of removing CO from the reaction site, consistent with the reactions being preferentially located at the fiber ends and at coating discontinuities. This tendency for localized attack is presumably responsible for the strength *variability* of the fibers. Some fibers were relatively undamaged in the gauge section and exhibit strengths similar to the uncoated fibers heat treated to the same temperature. Others were damaged in the gauge length associated with areas where the coating was discontinuous.

4.3 Mo Coated Fibers

Observations of the extracted Mo coated fibers reveal substantial changes in surface morphology. At least two phenomena contribute. The first involves the breakup of the polycrystalline Mo coating.^{12,13} The Mo/Al₂O₃ interface then forms ridges on the surface of the sapphire, at the Mo grain edges. This process proceeds by *surface and interface diffusion*. The ridges are visible when the coating is chemically etched from the fibers (Fig. 10). They heighten as the heat treatment temperature increases. Upon removing the coating, further heat treatment causes the ridges to become unstable. The morphology then resembles fiber facetting, but with an additional surface roughness that originates with the ridges.

A second potential phenomenon involves the dissolution of alumina in Mo. If it occurs, the same morphological changes discussed above would proceed, but the kinetics could be more rapid than those for interface diffusion. Such dissolution has been well documented for Nb/Al₂O₃ interfaces¹⁴ and has also been reported to occur for Mo/Al₂O₃ at temperatures similar to those used in this study.¹⁵ However, Mo dissolution not been verified, because high resolution TEM specimens are difficult to produce without interface debonding.

The large strength reduction found for the Mo coated fibers is presumed to relate to the ridges and troughs formed by diffusion or dissolution. It has not been possible to quantify the measured strengths, because an appropriate surface flaw model has not been developed. However, the general trend toward a lower strength with increased ridge height, as the temperature increases, suggests a model based on the stress intensification caused by ridges and troughs.

4.4 Fibers Within A Composite

Thin (0.2 and 0.7 μm) Mo fiber coatings do not remain continuous after composite consolidation (Fig. 11). Consequently, submicron thick Mo fiber coatings permit the fibers to sinter to the matrix, during HIPing, in those areas where the coating has become discontinuous. The thicker (1.4 μm) Mo coatings are continuous (Fig. 11), but the thickness is non-uniform. For these coatings, local sintering of the fiber to the matrix does not occur upon HIPing, but can still occur *after the coating has been removed*. In such cases, upon debonding, some matrix grains remain attached to the fiber, with associated ridge formation and fiber damage (Fig. 12). Chipping of the fibers can also occur (Fig. 13). Such visual evidence of fiber, matrix sintering allows measurement of the sintered regions to give the area fraction of fiber bonded to the matrix, designated f_A (Table II). In some locations, additional features are evident, manifest as large ridges and troughs between neighboring sintered sites (Fig. 14).

Sintered areas resist debonding and increase the interfacial fracture energy in proportion to the area fraction of bonding. Moreover, when the matrix sinters to the fibers, the resulting damage (Figs. 12, 13) reduces the fiber strength. The relatively large depth of these damaged regions compared with the size of the ridges and troughs found for the extracted Mo coated fibers (Fig. 10) suggests that the strengths may be substantially lower in the HIPed composites. The magnitude of the additional strength reduction is implied from analyses conducted below.

Localized sintering would also induce residual stress upon cooling, because of the thermal expansion mismatch between c-axis sapphire and polycrystalline Al_2O_3 . Such stresses should be of order 100 MPa and may influence trough formation (Appendix II).

5. COMPOSITE PROPERTIES

Composites with Mo coated fibers were tested after removing the Mo. All failed from a single dominant crack because of the low fiber volume fractions ($f < 0.20$). However, the fracture resistance and the extent of fiber pull-out were very different for the three coating thicknesses (Table II). The specimens with thin ($0.2 \mu\text{m}$) gaps had low toughness and exhibited co-planar fracture (Fig. 15a), with no pull-out. Conversely, appreciable pull-out was evident for the two larger interfacial gaps (Figs. 15b,c). Moreover, the material with the $1.4 \mu\text{m}$ interface gaps exhibited substantially more pull-out (average pull-out length, $\bar{h} \sim 640 \mu\text{m}$) than the material with the $0.7 \mu\text{m}$ gaps ($\bar{h} \sim 90 \mu\text{m}$). A typical load-displacement curve for these materials illustrates the fiber pull-out contribution to the composite fracture resistance (Fig. 16). The magnitude of the fracture dissipation is $\sim 40 \text{ k Jm}^{-2}$. The associated ultimate tensile strengths (UTS), summarized in Table I indicate a similar trend, with the larger gap giving a considerably higher UTS.

The corresponding push-out behaviors are summarized in Fig. 17. The composite with the thinnest coating did not exhibit push-out. The inability of this interface to slide and pull-out results from sintering. Conversely, sliding was induced in the other two composites. Both materials exhibited essentially the same sliding resistance. This similarity suggests that sliding is dominated by local variations in the coating thickness, rather than by the average gap width.

6. ANALYSIS

6.1 Method and Assumptions

An attempt is made to interpret the above composite behavior in terms of the fiber strength degradation phenomena, discussed above, in conjunction with related trends in interface properties. For this purpose, three basic assumptions are made and used together with models of interface debonding and sliding, as well as fiber pull-out. It is assumed that, when the fiber sinters to the matrix, debonding occurs when the energy release rate reaches the mode I fracture energy of the fine-grained alumina polycrystals ($\Gamma_c \approx 25 \text{ Jm}^{-2}$). The debond energy Γ_i is then,

$$\Gamma_i \approx f_A \Gamma_c \quad (1)$$

with f_A given in Table II. It is also assumed that a sliding zone exists behind the debond, subject to a constant sliding resistance, τ . In this case, the debond length, ℓ , at stress, σ , is¹⁶

$$\ell = \frac{R(1-f)}{2\tau f}(\sigma - \sigma_i) \quad (2)$$

where R is the fiber radius, f is the fiber volume fraction and σ_i is the debond stress given by,

$$\sigma_i = \frac{1}{c_1} \sqrt{E\Gamma_i/R} - \sigma^T \left(\frac{c_2}{c_1} \right) \quad (3)$$

where σ^T is the axial misfit stress caused by thermal expansion mismatch and c_1 and c_2 are constants defined by Hutchinson and Jensen.¹⁶

Finally, it is assumed that fiber failure occurs *within the debond zone*, in accordance with weakest link statistics. The fiber pull-out length \bar{h} should then be related to ℓ . The relationship between ℓ and \bar{h} is considered to be similar to that derived by Curtin,¹⁷

$$\bar{h} = \ell \lambda'(\text{m}) \quad (4)$$

where λ' is a function of the Weibull modulus of the fibers. Equation (4) must be a lower bound for the pull-out length when a non-zero debond energy obtains.

6.2 Interpretation

The preceding formulae allow an understanding and rationalization of the observation that composites with the 0.7 μm gap have smaller pull-out lengths than materials with a 1.4 μm gap, but yet have similar sliding resistance. There are two factors involved. (i) A smaller debond length is expected with the narrower gap, because of the larger debond resistance induced by the more extensive fiber/matrix sintering. Slip is limited by the debond length. (ii) Fiber weakening occurs when matrix grains sinter to the fibers and create damage sites (Figs. 12, 13).

The measured UTS, σ_u , may be inserted into Eqn. (2) and, upon using Eqns. (1) and (3), the debond lengths at failure may be estimated. The results (Table II) verify that a considerably larger debond length develops for the composite with the wider interface gap. Moreover, the proportionality constant, λ' , between the pull-out length, \bar{h} , and the debond length ℓ (Eqn. 4) is similar for both materials.

The strengths of the fibers in the composite S_c is of order,

$$S_c \approx \sigma_u / f \quad (5)$$

These strengths (Table II) are considerably lower than those measured on the extracted fibers with the thick coatings. It is implied that the strengths have been markedly degraded by sintering of the matrix to the fibers. Furthermore, because S_c represents the strength measured at a gauge length of order the debond length,¹⁷ even smaller values would obtain at a 1" gauge length.

7. SUMMARY

Single crystal sapphire fibers have been suggested as a high strength reinforcement for ceramic matrix composites. Interfaces have been developed based on a fugitive coating concept which satisfies the fiber debonding and sliding conditions for toughness enhancement. However, the strengths of the fibers are reduced by the presence of the coatings and are further reduced upon forming a composite. The mechanisms for the strength loss of coated fibers include: i) gas phase reactions with the coating which produce aluminum sub-oxides and etch the fibers ii) chemical reactions which form solid state reaction products and iii) facetting or ridging by surface diffusion. Carbon coated fibers are susceptible to the first two modes of degradation. However, it should be possible to minimize these effects by selecting composite processing conditions that provide a controlled CO/CO₂ atmosphere. For the Mo coatings, the degradation mechanisms are primarily of the third type and more difficult to eliminate.

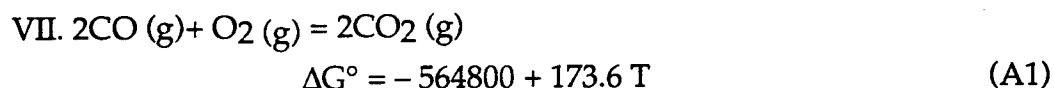
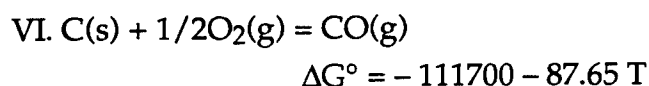
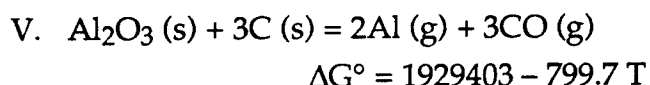
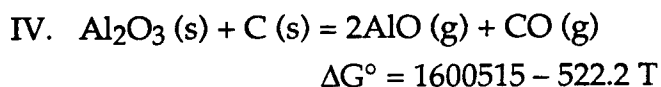
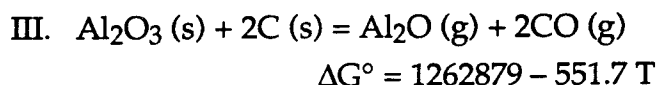
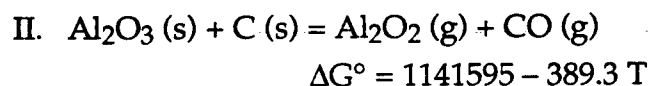
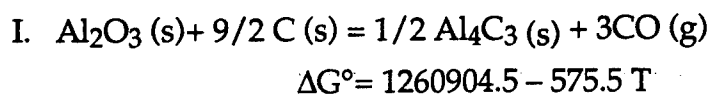
Additional fiber strength reduction results after composite processing with thin coatings, due to localized sintering of the matrix to the fiber. Such bonding affects the surface of the fibers. It also imposes a residual stress, which may further alter the surface morphology. It is believed that this strength loss could be minimized by

manipulating the matrix microstructure and chemistry (by incorporating segregants) to reduce the sintering potential.

APPENDIX I

Thermodynamic Calculations

For alumina to be reduced by carbon during diffusion bonding, a maximum pressure for the reaction system can be determined. The chemical reactions of interest and their standard free energies, * ΔG° (J/ mole), per mole of CO, are as follows:



where T is the temperature. Reaction I was calculated to have the lowest free energy for the temperature range of interest (1250°C–1450°C). Furthermore, since this reaction

* Thermodynamic data are taken from references 8-11.

involves the formation of one gaseous species, the equilibrium CO partial pressure can be determined as a function of temperature.[#] The equilibrium CO partial pressure is calculated (Table A.1), using

$$P_{\text{co}} = \exp\left[\frac{\Delta G^\circ}{3RT}\right] \quad (\text{A2})$$

For Reaction I to proceed, the CO partial pressures in the system must not exceed the equilibrium values. Such pressures cannot develop in the vacuum system used for the present experiments, indicating that the reaction is likely to occur.

With P_{co} specified at its equilibrium value, the partial pressures of the aluminum suboxides can be determined for Reactions II to V (Table AII). From these results, it is apparent that both Al_2O and Al have significant partial pressures under conditions that also permit the formation of Al_4C_3 . The formation of these volatile phases could occur by reaction with CO in regions adjacent to the C coating, consistent with the observation of rapid facetting near discontinuities in the coating (Fig. 9).

[#] It is assumed that the buffer system described by reactions VI and VII does not dictate the CO partial pressure in the system.

APPENDIX II

Crack-Like Surface Instabilities

Recent analyses have shown that surface perturbations can grow into crack-like flaws, by surface diffusion, in bodies subject to stress.¹⁹ The flux is provided by the strain energy contribution to the chemical potential, which can exceed the surface curvature term, at sufficiently high stress. The consequence is that there is a critical stress, σ_c , above which such flaws can develop. The surface troughs observed in some of the fibers may be caused by this phenomenon. In order to explore this possibility, analysis of the critical stress is performed.

The basic requirement for the development of crack-like flaws is that the change in strain energy, dU , upon crack extension, da , exceed the increase in surface energy, dU_s , as in the original Griffith analysis. This condition defines the critical stress. For an array of surface flaws of depth, a , and separation, b , the energy release rate at stress, σ , is⁷

$$\frac{dU}{da} = \left(\frac{\sigma^2 \pi b}{E} \right) F(a/b) \quad (B1)$$

where the function $F(a/b)$ is plotted on Fig. A1. The corresponding change in surface energy is

$$\frac{dU}{da} = 2\gamma_s \quad (B2)$$

where γ_s is the surface energy per unit area. Hence, for flaw growth to be possible,

$$dU/da \geq dU_s/da \quad (B3)$$

resulting in a critical stress,

$$\sigma_c = \sqrt{\frac{2E\gamma_s}{\pi b} F(a/b)} \quad (B4)$$

For flaws with depths in the micron range to extend in sapphire, Eqn. (A4) indicates that stresses of order 500 MPa are required (Fig. A2). While such stresses are unlikely, the mechanism has not been ruled out because of the morphological similarity of the observed trough with the profile predicted for diffusive crack growth.

TABLE I
Fiber Strength Data

Heat Treatment*		Median Strength (GPa)	Coefficient of Variation	Weibull Modulus
As-Received		2.9	0.13	6.5
Uncoated	1250°C	2.6	0.10	9.8
	1350°C	2.0	0.15	6.8
	1450°C	2.1	0.18	5.8
Mo Coated: Extracted	1250°C	1.9	0.16	6.2
	1350°C	1.4	0.32	2.2
	1450°C	1.0	0.33	3.2
C Coated: Extracted	1450°C	1.6	0.38	2.6

* With the exception of the As-Received set, all fibers were heated in an air furnace at 1150°C for 2 hours subsequent to the heat treatments shown above.

TABLE II

Constituent Properties of Composite

Coating Thickness (μm)	Measured				Inferred		
	τ (MPa)	\bar{h} (μm)	Area Fraction of Fiber Bonded to Matrix f_A	UTS (MPa)	S_c (GPa)	ℓ (μm)	λ' (m)
0.7	17	90	~ 0.05	22	0.1	250	0.3
1.4	15	640	~ 0.01	79	0.4	1000	0.7

TABLE AI

Equilibrium Partial Pressure of CO for Reaction I

T (°C)	pCO (atm)
1250	$4.0 \cdot 10^{-5}$
1350	$3.1 \cdot 10^{-4}$
1450	$1.9 \cdot 10^{-3}$

TABLE AII

Partial Pressures of Gas Phases for the Aluminum Oxide/Carbon System*

T (°C)	pCO (atm)	pAl ₂ O ₂ (atm)	pAl (atm)	pAl ₂ O (atm)	pAlO (atm)
1250	4.0•10 ⁻⁵	3.0•10 ⁻¹⁵	2.0•10 ⁻⁶	1.6•10 ⁻⁶	2.3•10 ⁻¹²
1350	3.1•10 ⁻⁴	1.3•10 ⁻¹³	1.2•10 ⁻⁵	1.4•10 ⁻⁵	4.0•10 ⁻¹¹
1450	1.9•10 ⁻³	2.8•10 ⁻¹²	5.0•10 ⁻⁴	1.3•10 ⁻⁴	5.0•10 ⁻¹⁰

* These results are in reasonable agreement with literature values. (Ref.: Sprague in Ref. of High Temp. Sys. vol. 1., ed. G.S. Bahn, Gordon & Breach (1964).

REFERENCES

- [1] T. Mah, K. Keller, T.A. Parthasarathy and J. Guth, *Ceram. Eng. Sci. Proc.*, **12** [9-10] pp. 1802-15 (1991).
- [2] J.B. Davis, J.P.A. Löfvander, E. Bischoff, A.G. Evans and M.L. Emiliani, *J. Am. Ceram. Soc.*, **76** [5] 1249-57 (1993).
- [3] K. Trustrum, and A. De S. Jayatilaka, *J. Mat. Sci.*, **14** 1080-1084 (1979).
- [4] J.R. Porter, *MRS Symp. Proc.*, **273** 315-324 (1992).
- [5] E. Trembauer and R. Tressler, *HITEMP Conference Proceedings* (1992).
- [6] T.J. Mackin, J. Yang and P.D. Warren, *J. Am. Ceram. Soc.*, **75** [12] 3358-62 (1992).
- [7] H. Tada, P.C. Paris and C.R. Irwin, *The Stress Analysis of Cracks Handbook*, Del Research Corp., Pennsylvania (1973).
- [8] L.M. Foster, G. Long and M.S. Hunter, *J. Am. Ceram. Soc.*, **39** [1] 1-11 (1956).
- [9] D.R. Stull and H. Prophet, *JANAF Thermochemical Tables*, 2nd ed., NSRDS-NBS 37, U.S. Department of Commerce, Washington, D.C., 1971.
- [10] I. Barin and O. Knacke, *Thermochemical Properties of Inorganic Substances*, Springer-Verlag, New York, 1973.
- [11] I. Barin, O. Knacke, and O. Kubaschewski, *Thermochemical Properties of Inorganic Substances, Supplement*, Springer-Verlag, New York, 1977.
- [12] W.W. Mullins, *Journal of Applied Physics*, **28** [3] 333-339 (1957).
- [13] K.T. Miller, F.F. Lange and D.B. Marshall, *Mat. Res. Soc. Proc. Sym. on Ultrastr. Proc.*, **121** [3] 823-30 (1988) and *J. Mater. Res.*, **1** [5] 151-60 (1990).
- [14] M. Rühle and A.G. Evans, *Materials Science and Engineering*, A107 187-197 (1989).
- [15] G.H.M. Gubbels, *Materials Science and Engineering*, A135 (1991) 135-139.
- [16] J. W. Hutchinson and H. M. Jensen, *Mech. Mtls.*, **9** 139 (1990).
- [17] W.A. Curtin, *J. Am. Ceram. Soc.*, **74** [11] 2837-45 (1991).
- [18] M.Y. He, A. Bartlett, A.G. Evans and J.W. Hutchinson, *J. Am. Ceram. Soc.*, **74** [4] 767-71 (1991).

- [19] W.H. Yang and D.J. Srolovitz, "Crack-Like Surface Instabilities in Stressed Solids," *Phys. Rev. Lett.*, in press.

FIGURE CAPTIONS

- Fig. 1. Cross section of composite produced by HIPing.
- Fig. 2. Composite tensile test geometry for *in situ* studies in the SEM.
- Fig. 3. a) Fiber strength data plotted as the cumulative probability of fracture.
b) Effect of heat treatment on median strengths and standard deviation.
- Fig. 4. Schematic representations of the surface morphology changes found to occur when coated sapphire fibers are heat treated.
- Fig. 5. Pores observed on the surface of a sapphire fiber.
- Fig. 6. Fiber strength predictions obtained upon assuming that the porous behaviors are penny-cracks. The fracture energy for sapphire was assumed to be 15 Jm^{-2} . Typical pore diameters are $\sim 1 \text{ }\mu\text{m}$.
- Fig. 7. Facets observed on the surfaces of uncoated, heat treated fibers.
- Fig. 8. a) Surface damage was observed on uncoated, heat-treated fibers near the failure plane. A chemical reaction has occurred between the fiber and the contaminant. b) The reaction site examined by EDS, reveals Si and Mg.
- Fig. 9. The fiber surface degradation (near the coating edge) for the carbon coated fibers increases with the heat-treatment temperature. a) Surface features of a fiber heated in vacuum for 2 h at 1250°C . b) Surface features of a fiber heated in vacuum for 2 h at 1350°C . c) Surface features of a fiber heated in vacuum for 2 h at 1450°C .
- Fig. 10. Ridges on the sapphire surface observed when Mo coated fibers were heat treated. The coating has been chemically etched from the fiber surface.
- Fig. 11. TEM micrographs reveal that a) $0.7 \text{ }\mu\text{m}$ thick Mo coatings do not remain continuous during HIPing. b) $1.4 \text{ }\mu\text{m}$ thick Mo coatings are continuous.
- Fig. 12. A view of a section of the fiber surface after pull-out. Matrix grains which sinter to the fiber remain attached.

- Fig. 13. Surface grooves observed on sapphire fibers in HIPed composites, after fiber pull-out. Also evident are the patches that sintered and then debonded.
- Fig. 14. Sliding between the matrix and fiber during pull-out degrades the fiber surface by forming a chip.
- Fig. 15. a) Extensive bonding between the fiber and matrix led to co-planar fracture of the composite produced with $0.2\text{ }\mu\text{m}$ thick gaps.
b) Composites produced with the $0.7\text{ }\mu\text{m}$ thick coatings exhibited moderate fiber pull-out.
c) The greatest extent of fiber pull-out was found for the composites produced with $1.4\text{ }\mu\text{m}$ thick coatings.
- Fig. 16. Load-displacement curve for composite produced with $1.4\text{ }\mu\text{m}$ thick interface gaps reveals contribution to crack growth resistance from fiber pull-out. The corresponding energy dissipation is 40 kJm^{-2} .
- Fig. 17. Shear resistance of interface measurements by fiber push-out.
- Fig. A1 The strain energy density function for an array of surface cracks.
- Fig. A2 The critical stress required for deepening of surface troughs by surface diffusion.

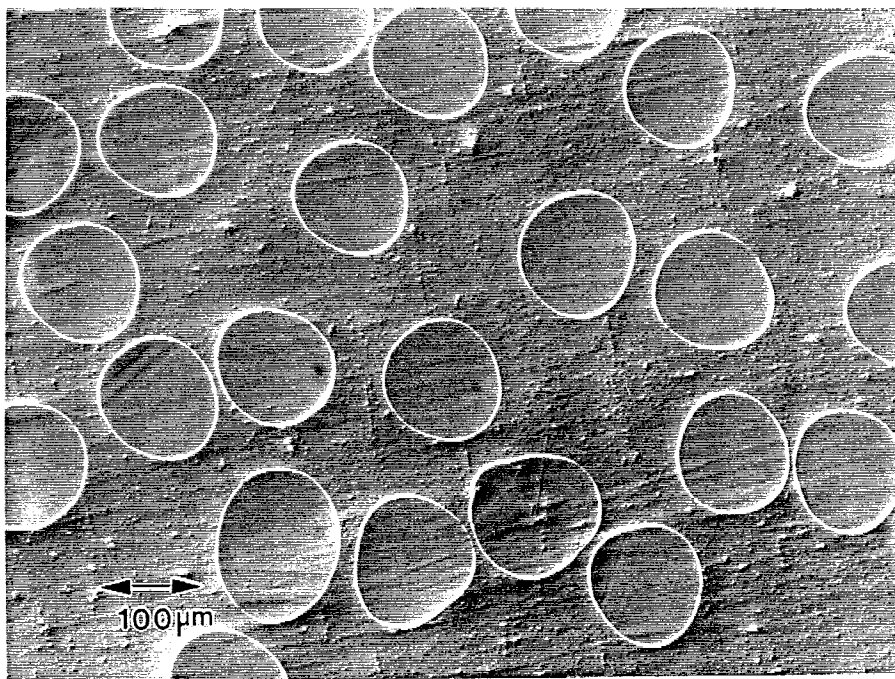


Figure 1

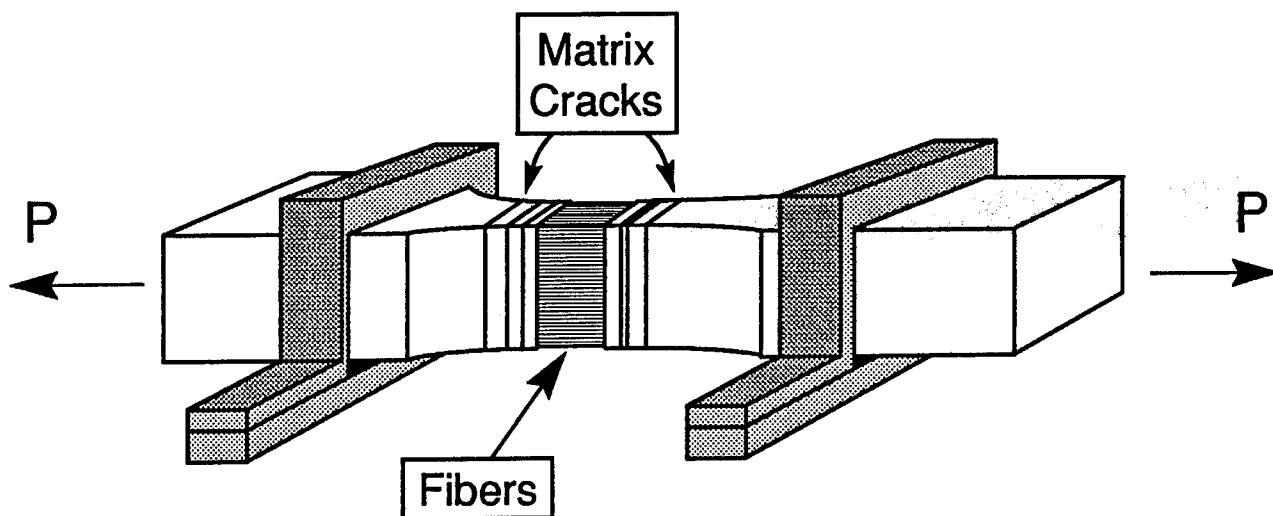


Figure 2

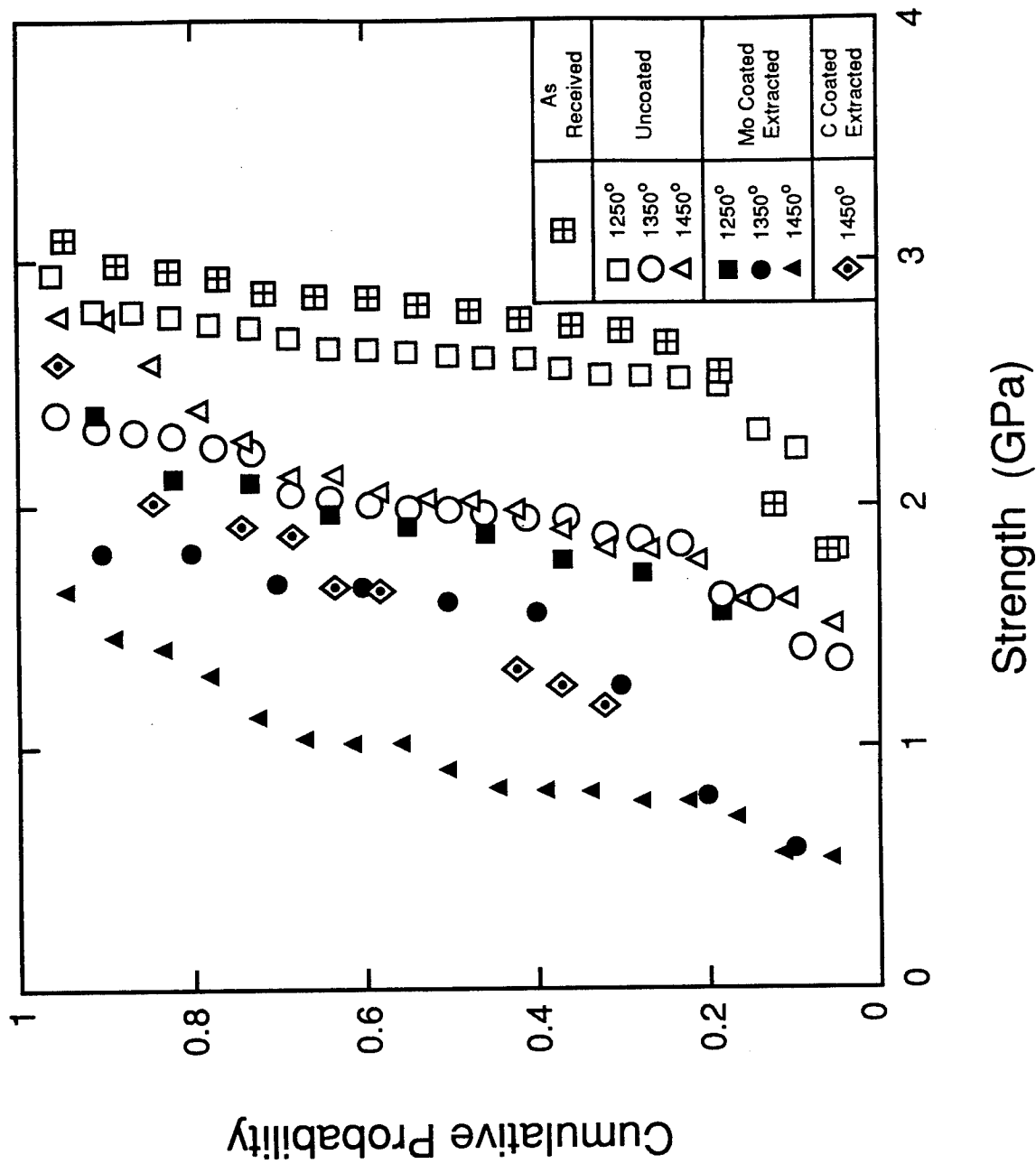


Figure 3a

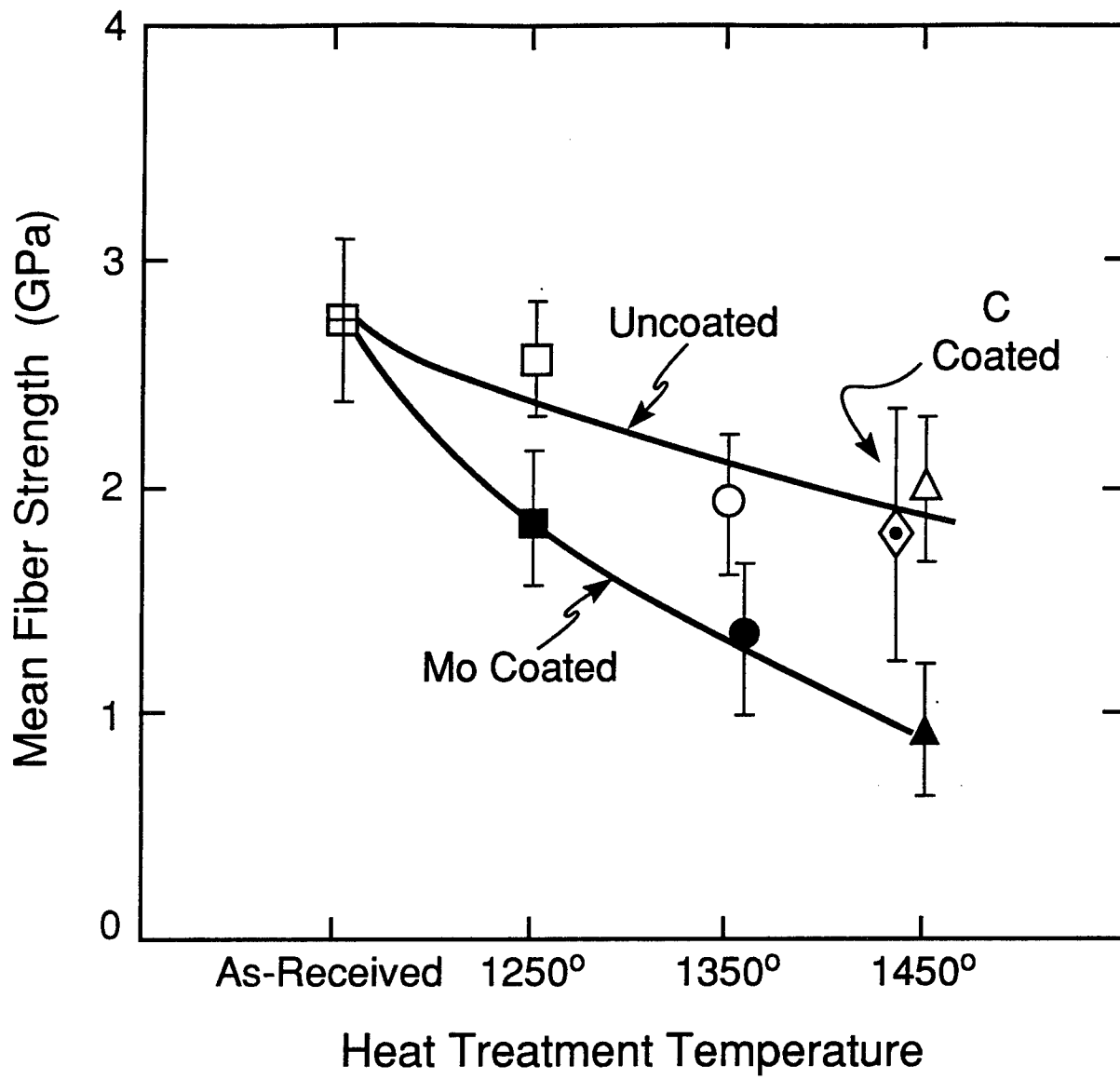


Figure 3b

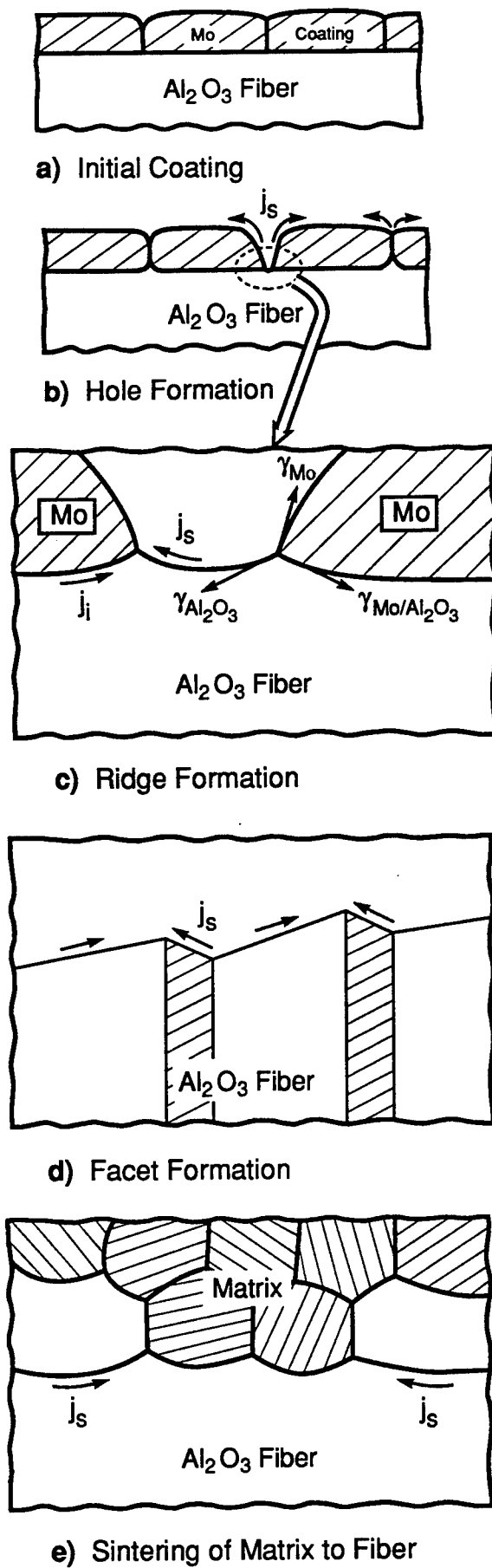


Figure 4

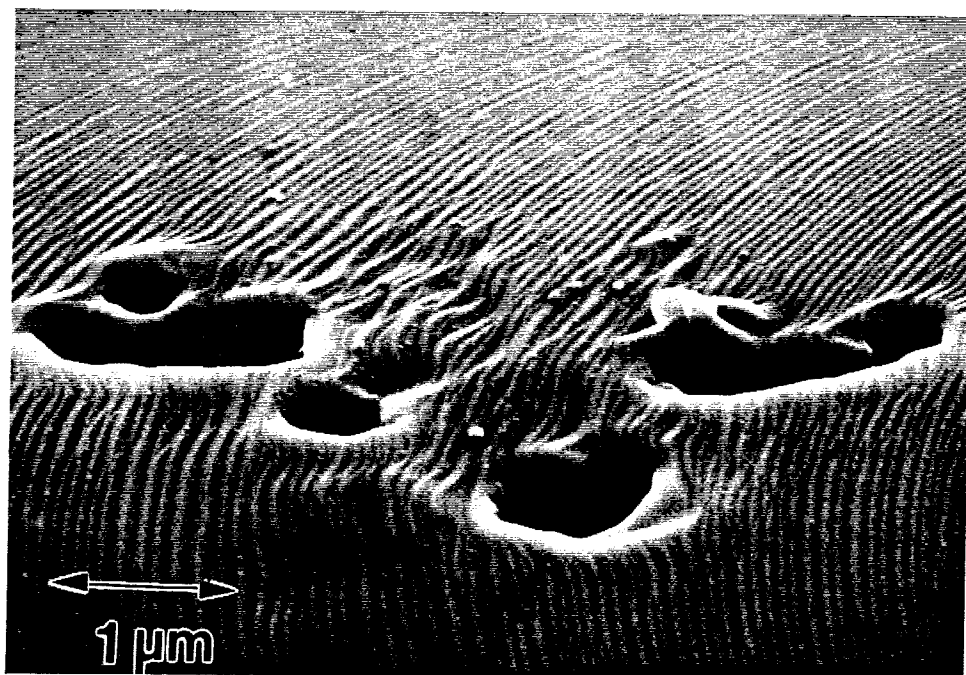


Figure 5

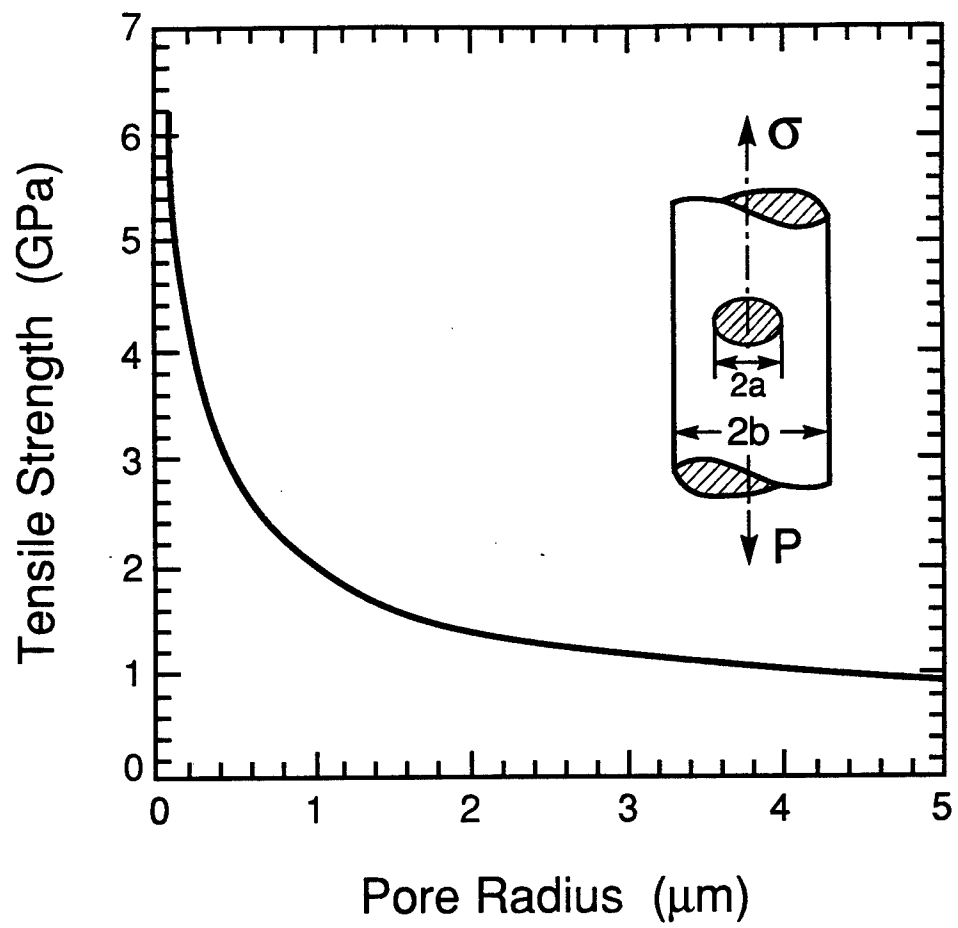


Figure 6

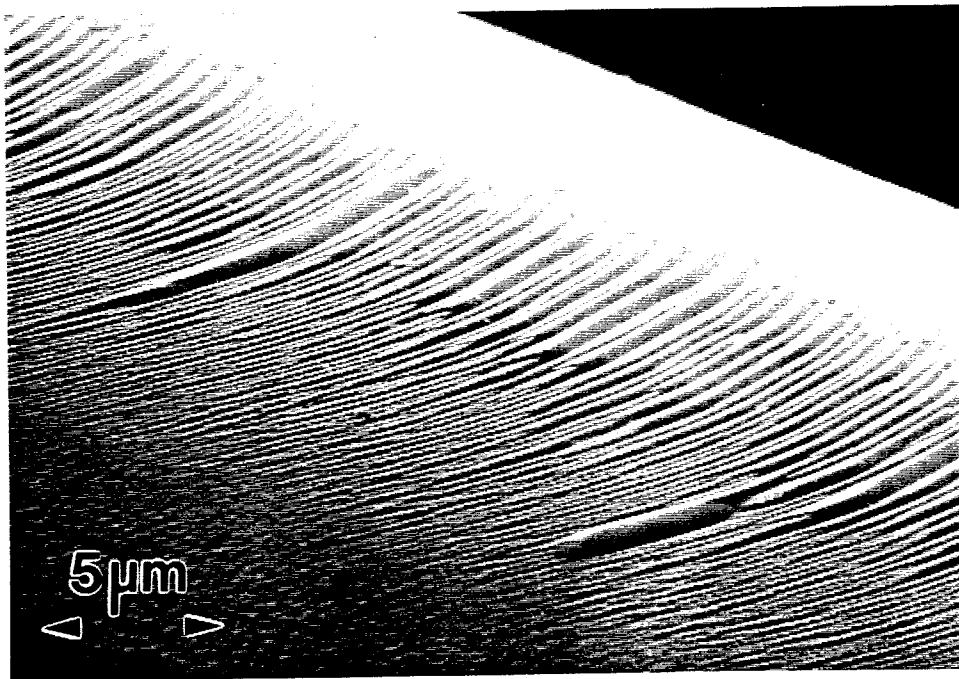


Figure 7

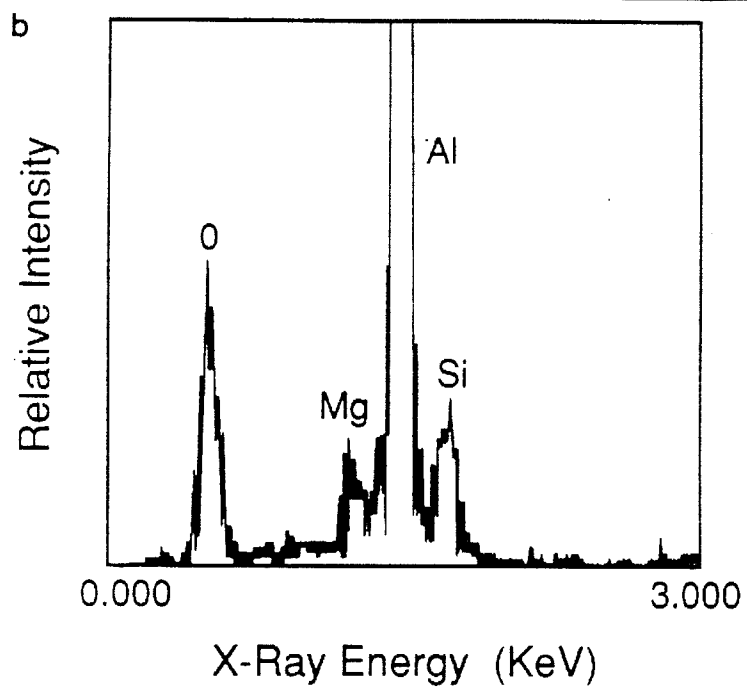
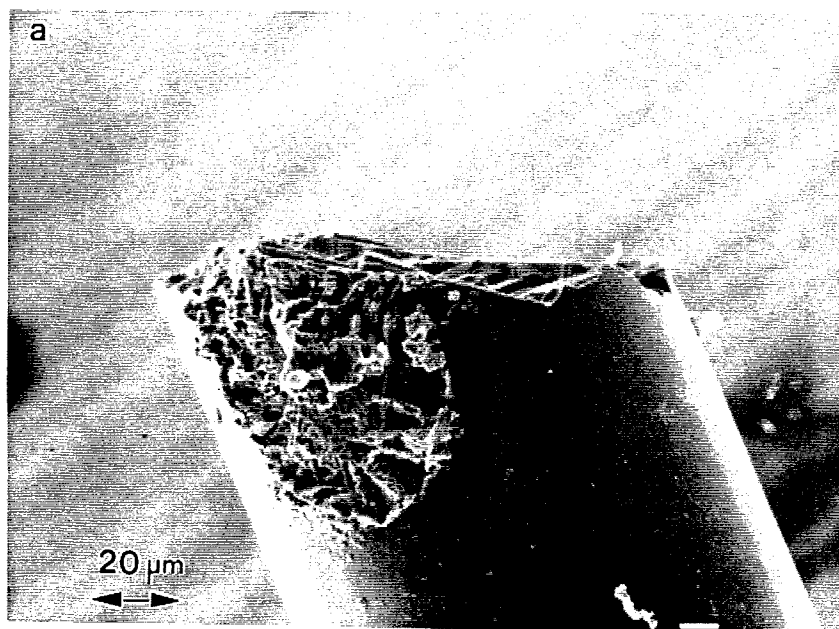


Figure 8

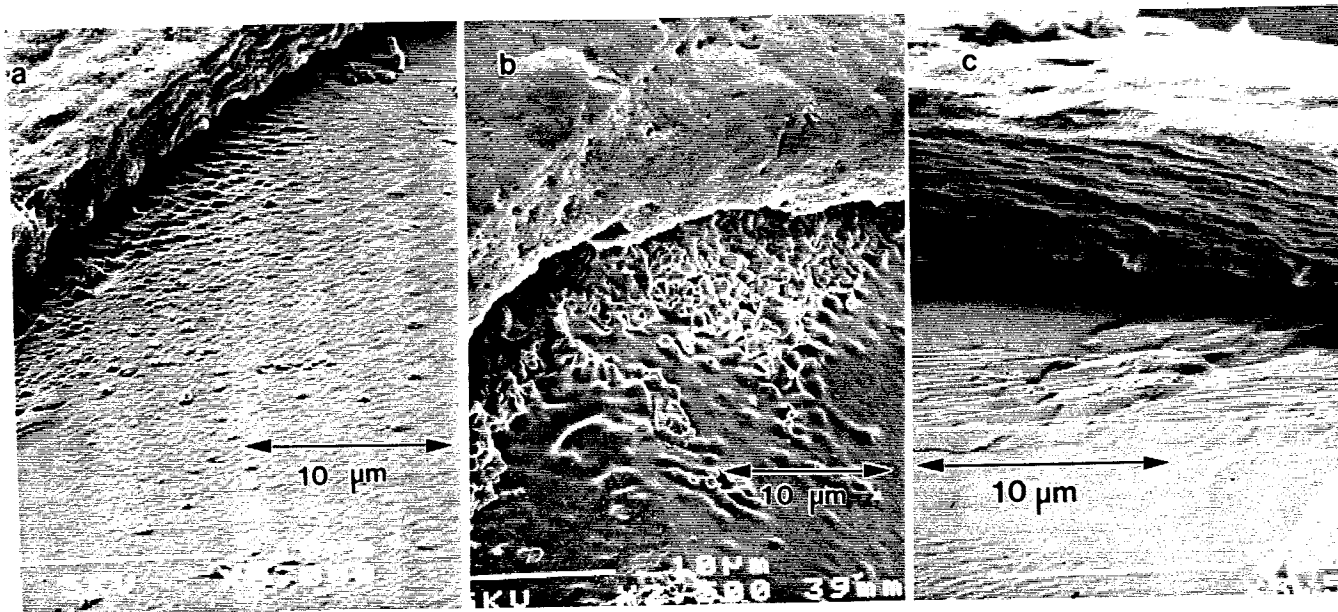


Figure 9

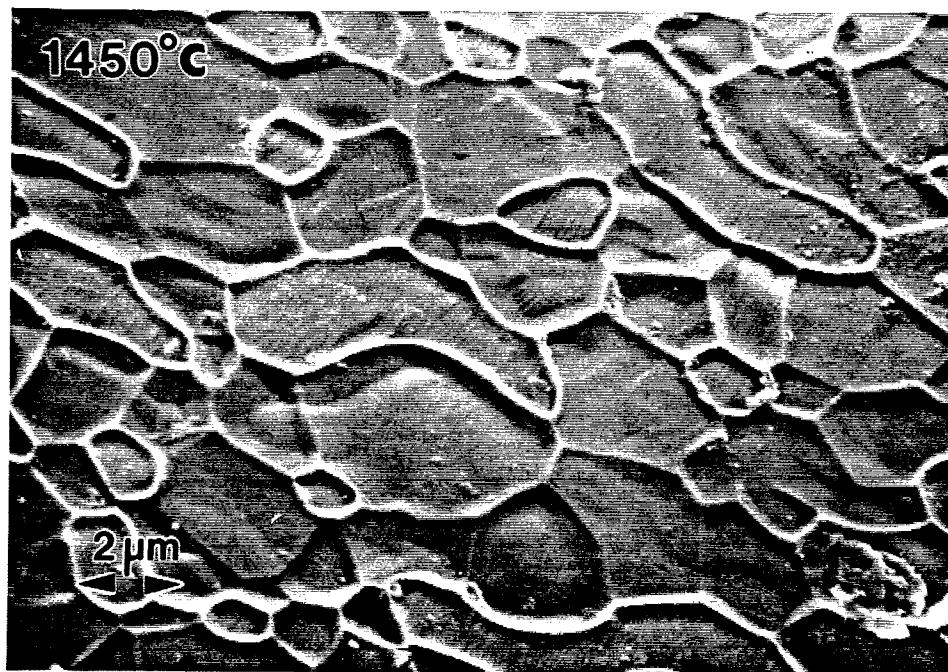


Figure 10

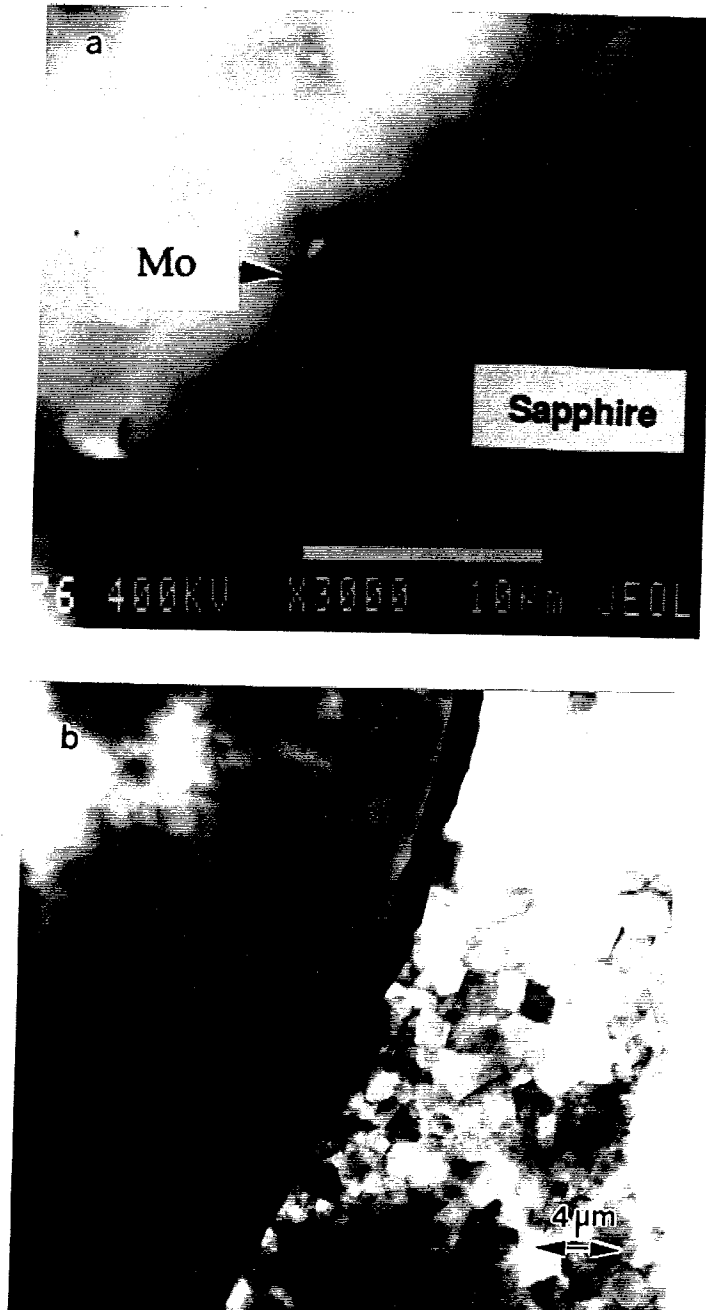


Figure 11

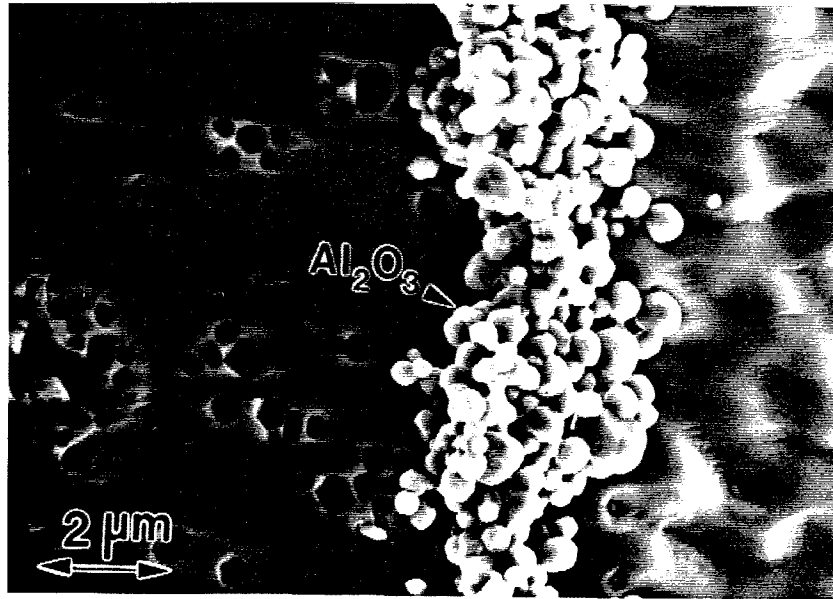


Figure 12

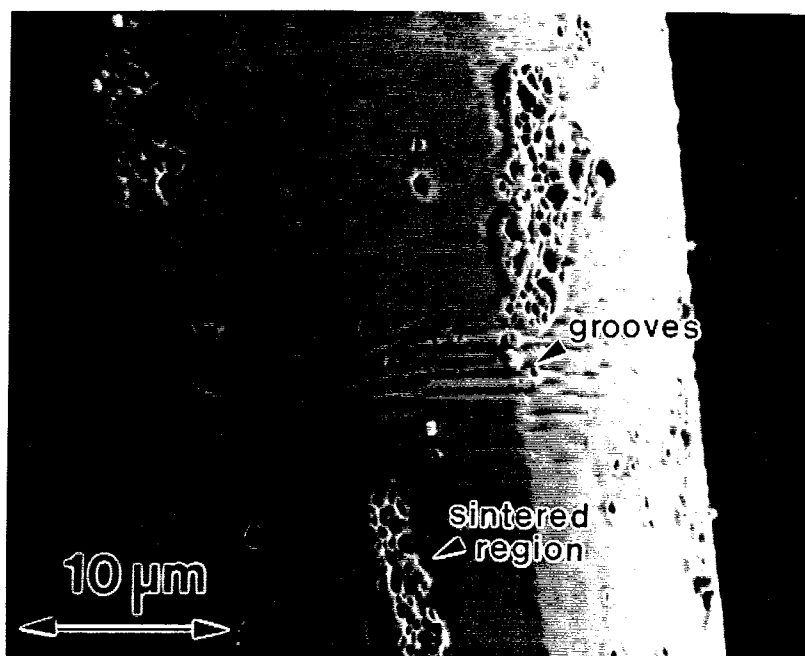


Figure 13

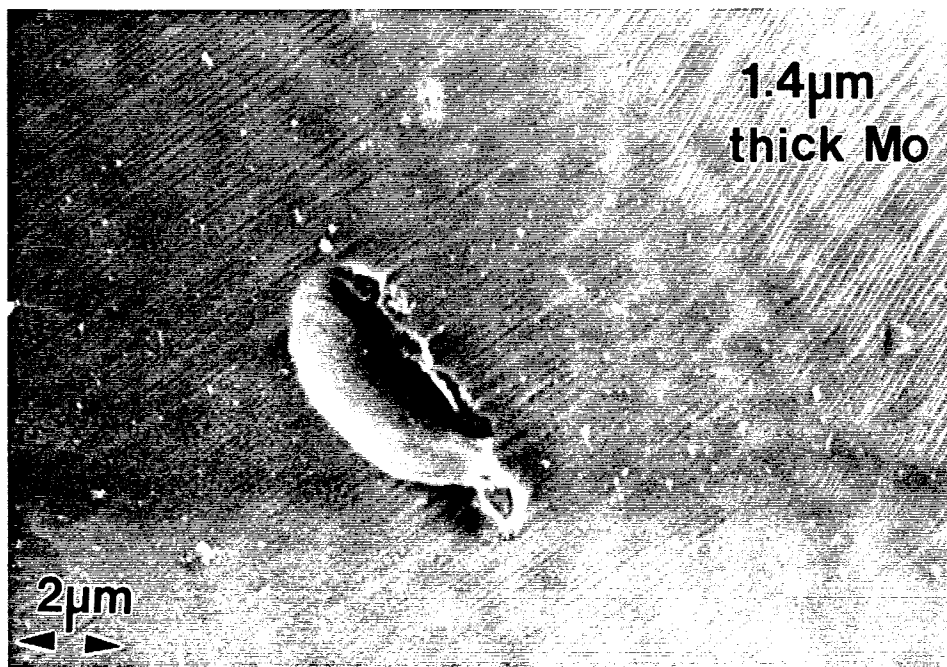


Figure 14

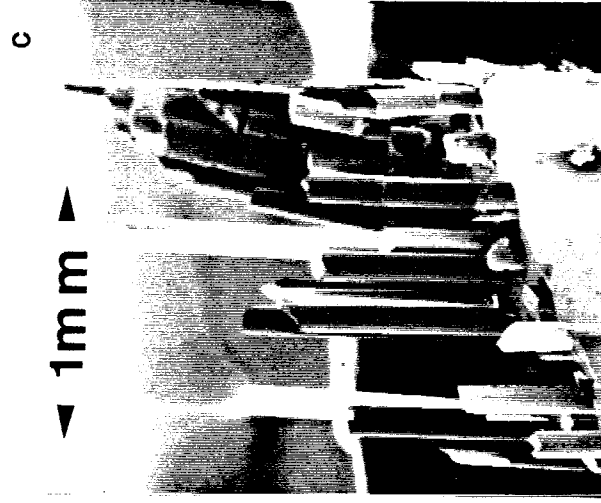
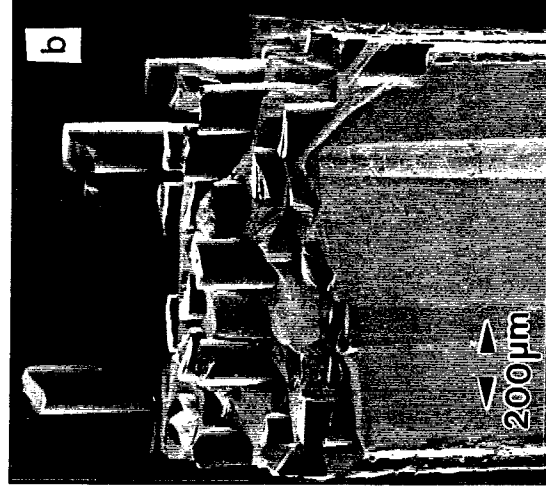
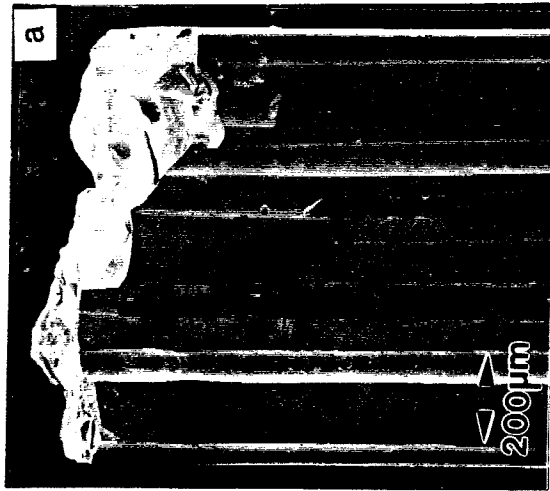


Figure 15

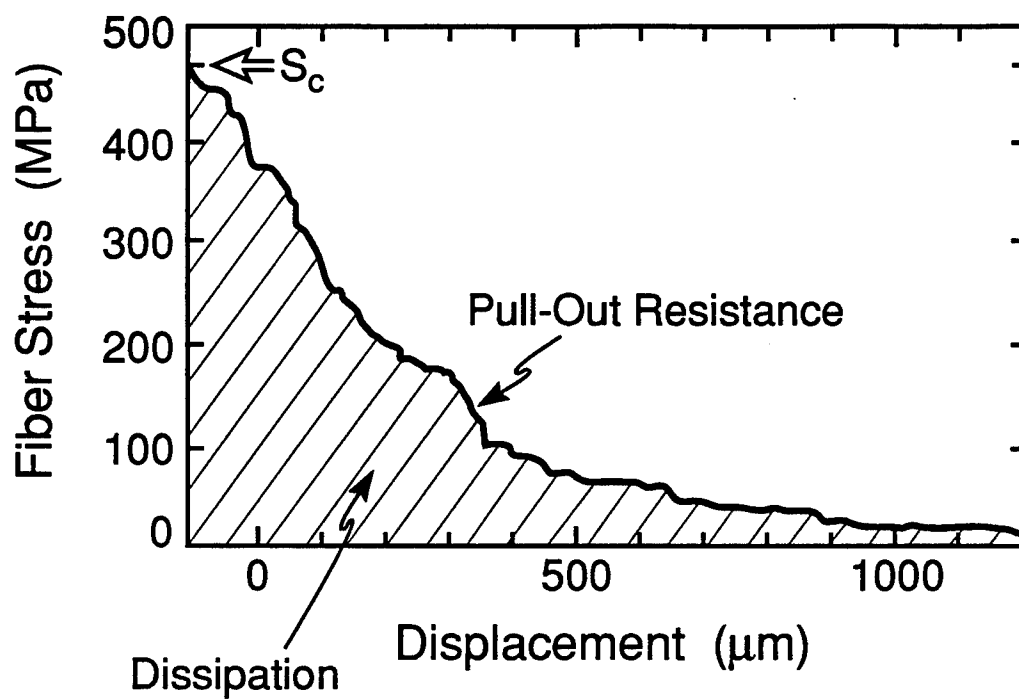


Figure 16

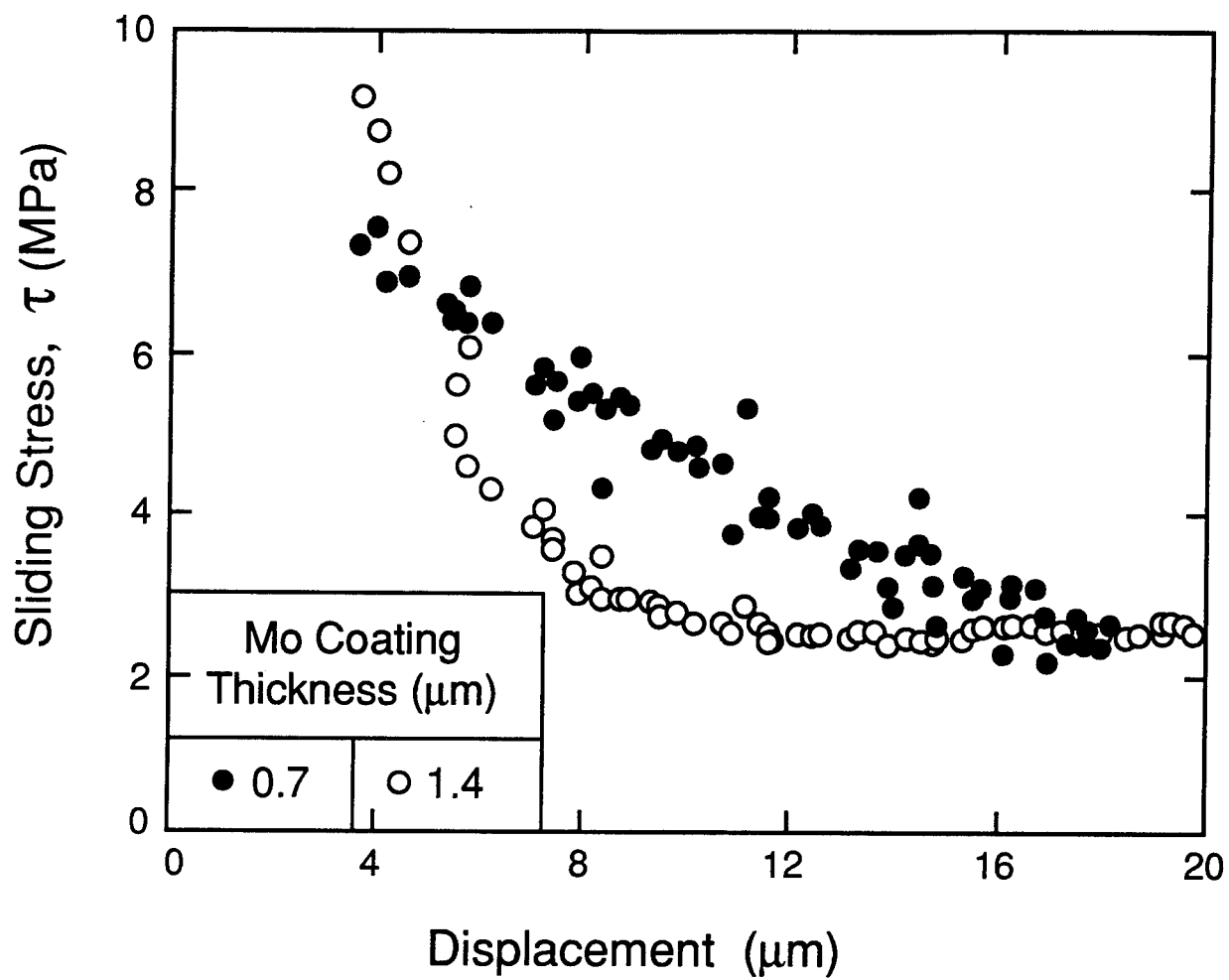


Figure 17

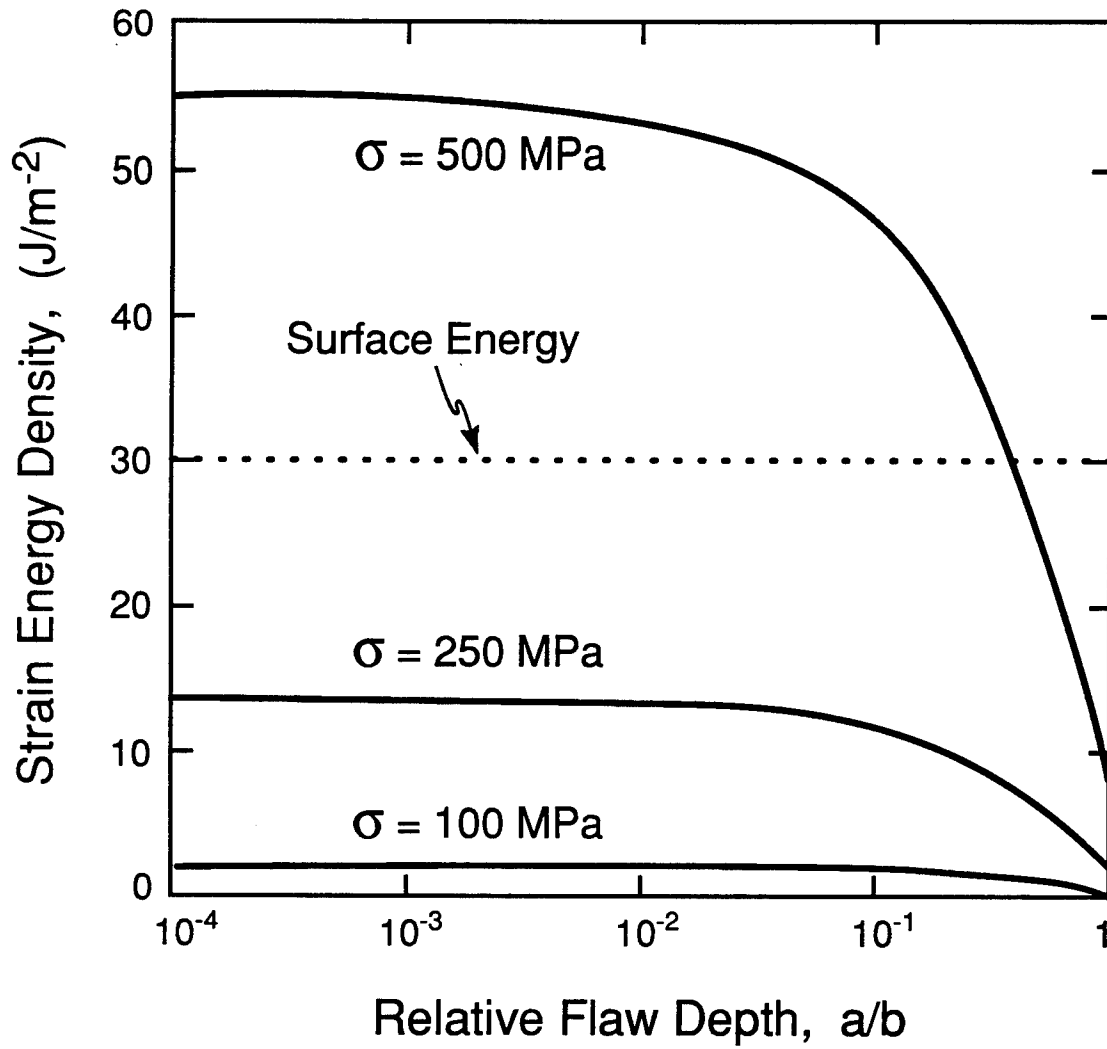


Figure A1

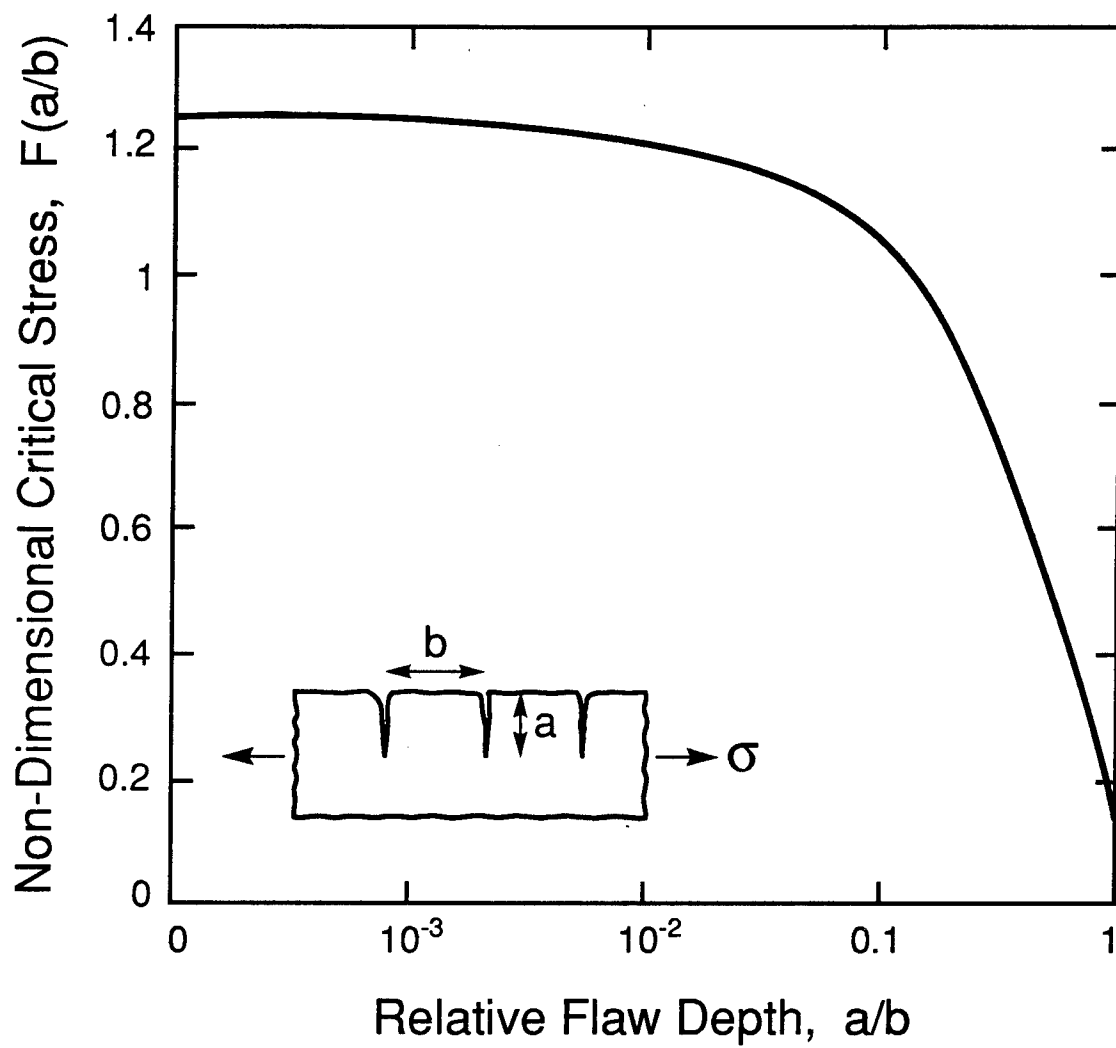
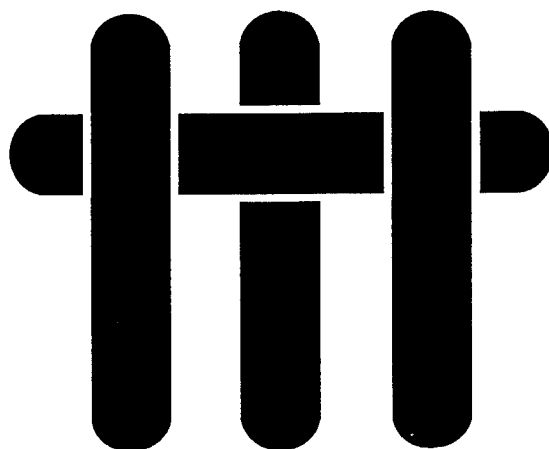


Figure A2

M A T E R I A L S



A Simple Method For Measuring Surface Strains Around Cracks

b y

D. J. Wissuchek,⁺ T. J. Mackin,⁺⁺ M. DeGraef,⁺⁺⁺
G. E. Lucas,⁺ and A. G. Evans⁺

⁺ Materials Department
College of Engineering
University of California
Santa Barbara, CA 93106-5050

⁺⁺ Department of Mechanical and Industrial Engineering
The University of Illinois at Urbana-Champaign
1206 W. Green St.
Urbana, IL 61801

⁺⁺⁺ Department of Materials Science and Engineering
Carnegie Mellon University
Pittsburgh, PA 15213-3890

A Simple Method For Measuring Surface Strains Around Cracks

ABSTRACT

A simple system has been developed to measure surface strains that occur during in-situ deformation of mechanical test specimens. The system uses photolithographically deposited displacement markers and computer image recognition routines to determine in-plane displacements and strains from digital images. The strain calculating routines are integrated into a simple, mouse driven software package that facilitates the transformation from digital images to useful strain field information. Additional routines have been developed to determine crack tip stress fields, and J integrals.

Crack tip stress intensities have been calculated from strain maps obtained for traction free cracks in stainless steel. The J integrals were found to be independent of contour and consistent with applied stress intensities. Crack tip stress intensities were calculated for bridged cracks in lamellar TiAl. The toughening effect of the bridging zones was determined by including the bridged region in the contours. Resistance curves generated from strain maps were consistent with those measured during mechanical testing.

1. INTRODUCTION

Qualitative descriptions of the deformation and fracture behavior of most materials systems are easily obtainable from in-situ observations of deforming specimens and mechanical test data. When more quantitative information about

deformation phenomena is required, surface strain maps become invaluable tools¹⁻⁶. A new system has been developed for this purpose. This system is compatible with conventional computer image manipulation routines used with photographs taken during insitu mechanical testing. The system, named DAiSIES for Displacement And Strain Image Evaluation System, has been developed as a fast and user friendly software-based system that accurately determines surface displacements and strains from digital images. It obviates the limitations involved with other systems, such as the extensive hardware and specimen constraints present in either Moire interferometry¹ or automated photogrammetry systems^{5,6}. The DAiSIES procedure is described in this article and examples of its application to crack problems are presented.

The DAiSIES system uses an array of uniform photolithographically deposited markers. Digitized images of the surface are produced, and the center of gravity of each marker is found through image recognition routines. These routines assign a single pixel location to each marker. The differences between the reference and deformed images are computed. Surface feature, such as particulates or fiber ends, could also be used as the displacement markers if the surface features have good optical contrast. The program is a simple mouse-driven operation with built-in plotting routines that greatly facilitate the transformation from digitized images to deformation and strain maps. Different algorithms that account for discontinuities, such as cracks, are available for computing strains from displacement information. The user is free to choose the appropriate algorithm to match the material's deformation behavior.

The procedures used in conjunction with DAiSIES are described below and illustrated for two materials: stainless steel, and lamellar TiAl. A particular emphasis is given to strains around cracks tips, which relate to the mechanisms of crack growth.

2. PROCEDURE

2.1 Grid Deposition

The specimens to be tested are first polished to a 1 μm surface finish. An array of high optical contrast markers is developed on the surface via photolithographic methods. This is done by spin coating with a 1.1 μm layer of Hoechst Celanese 4110k positive photoresist. A mask is aligned to cover the region of interest and the photoresist exposed for 18 seconds at a uv power of 7.7 mW/cm² and then developed. An electron beam evaporator is used to deposit 100-120 nm of metal on the surface of the sample. The metal is chosen for high optical contrast and good cohesive properties with the base material. The photoresist is lifted off with acetone. The final grid consists of 1-2 μm circular markers with 10 μm period. These are arranged either in a square array or in a 2-d fractal pattern. The fractal pattern is well suited for observing displacements over large areas, because each marker can be defined as a kernel of more than one circular marker.

The surface of samples with a large degree of surface roughness are planarized by coating with a thin (~5 μm) polyimide film before applying the photoresist. For instance, metal matrix composites often have surfaces with pulled-out fibers. Undulations are of a scale larger than the photolithographic markers and the grid does not develop directly on the areas with pulled out fibers. A thin polyimide coating eliminates the problems brought about by inhomogeneous surfaces, and still allows the microstructure to be viewed during mechanical testing.

2.2 Measurements and Analysis

Survey photographs were taken at 200x and 400x magnification on an inverted optical microscope. When crack behavior is of interest, notched specimens with sharp fatigue precracks were used. These precracks were sufficiently long that relatively small loads could be used to propagate the cracks in an in-situ testing fixture located on an optical microscope. In each test, the applied load and load point displacement were continuously monitored. Periodically, the crosshead was stopped

and photographs were taken of the region around the crack tip.

Images of the crack tip region in the undeformed and deformed sample were digitized with an Eikonix digitizer, which produces a 512×512 pixel image. Several adjustments were made to the digitized images using a Macintosh computer and the Image⁷ software package. Contrast and brightness of the digital images were adjusted, and a binary image created with the background appearing white and the markers appearing black. The center of gravity routine was used to determine exact pixel locations of each marker, and a data file produced for each image.

The data files are used as input for the strain mapping routines, which are written in Interactive Data Language (IDL)⁸, and currently running on a workstation. DAiSIES reassembles binary representations of the reference (undeformed) and deformed images from these data files. The user identifies a point in each array which becomes the point of zero displacement. The images are aligned using this as a reference, enabling points in the undeformed array to be paired with their partners in the deformed array. The user is given the option of removing rotational errors from the two arrays. DAiSIES also includes routines for removing points from the reference or distorted array so that each marker in the reference array has a corresponding strain marker in the distorted array. The user iterates between reference and distorted arrays, eliminating points from each, until each marker has a partner. Finally, a map of displacement vectors is generated from the reference and deformed arrays.

3. STRAIN CALCULATIONS

A nearest neighbor algorithm is used to calculate strains at each marker, by fitting a polynomial surface to the displacements of the 9 nearest neighbors. Polynomial warping routines are used with displacement information to determine the matrix coefficients, $kx(i,j)$ and $ky(i,j)$ of the equations⁹:

$$x_i = \sum_{i,j} kx(i,j)x_o^j y_o^i \quad (1)$$

$$y_i = \sum_{i,j} ky(i,j)x_o^j y_o^i \quad (2)$$

where x_o and y_o are the coordinates of the reference points, x_i and y_i are the coordinates of the distorted points, and the dimensions i and j are equal to the degree of the polynomial used in the fit. Once the matrix coefficients are found, the strains are found by differentiating equations 1 and 2 with respect to x_o and y_o . For small strains,¹⁰

$$\epsilon_{xx} \equiv \frac{\partial u}{\partial x_o} = \frac{\partial(x_i - x_o)}{\partial x_o} = \frac{\partial}{\partial x_o} \sum_{i,j} kx(i,j)x_o^j y_o^i - 1 \quad (3a)$$

$$\epsilon_{yy} \equiv \frac{\partial v}{\partial y_o} = \frac{\partial(y_i - y_o)}{\partial y_o} = \frac{\partial}{\partial y_o} \sum_{i,j} ky(i,j)x_o^j y_o^i - 1 \quad (3b)$$

$$\gamma_{xy} \equiv \frac{1}{2} \left(\frac{\partial v}{\partial x_o} + \frac{\partial u}{\partial y_o} \right) = \frac{1}{2} \left(\frac{\partial}{\partial x_o} \sum_{i,j} ky(i,j)x_o^j y_o^i + \frac{\partial}{\partial y_o} \sum_{i,j} kx(i,j)x_o^j y_o^i \right) \quad (3c)$$

Quadratic surface fits are used to determine strains in regions with large gradients, such as near crack tips. Otherwise, linear surfaces are fit to the displacement data in order to minimize the effects of noise. When cracks exist, provisions are made to avoid selecting nearest neighbors across a crack plane. Otherwise the strain values in the crack tip region would be inflated. Alternative algorithms are available for situations where no cracks are present.

For situations involving large strains the Lagrangian tensor gives a more accurate measure of true strain:¹¹

$$\eta_{xx} = \frac{\partial u}{\partial x} + \frac{1}{2} \left(\left(\frac{\partial u}{\partial x} \right)^2 + \left(\frac{\partial v}{\partial x} \right)^2 \right) \quad (4a)$$

$$\eta_{yy} = \frac{\partial v}{\partial y} + \frac{1}{2} \left(\left(\frac{\partial v}{\partial y} \right)^2 + \left(\frac{\partial u}{\partial y} \right)^2 \right) \quad (4b)$$

$$\eta_{xy} = \frac{1}{2} \left(\frac{\partial u}{\partial x} + \frac{\partial v}{\partial y} \right) + \frac{1}{2} \left(\frac{\partial u}{\partial x} \frac{\partial u}{\partial y} + \frac{\partial v}{\partial x} \frac{\partial v}{\partial y} \right) \quad (4c)$$

The DAiSIES routine includes these Lagrangian terms.

The J integral¹² can be calculated from surface strain information and a constitutive law. The tip value is calculated by drawing a rectangular contour around the crack tip and summing the contributions from the horizontal (J_H) and vertical (J_V) branches of the contour¹³,

$$J_v = \int_{v1} \left[W - \left(\sigma_{xx} \frac{\partial u}{\partial x} + \tau_{xy} \frac{\partial v}{\partial x} \right) \right] dy - \int_{v2} \left[W - \left(\sigma_{xx} \frac{\partial u}{\partial x} + \tau_{xy} \frac{\partial v}{\partial x} \right) \right] dy \quad (5a)$$

$$J_H = \int_{H1} \left(\sigma_{yy} \frac{\partial v}{\partial x} + \tau_{xy} \frac{\partial u}{\partial x} \right) dx - \int_{H2} \left(\sigma_{xx} \frac{\partial u}{\partial x} + \tau_{xy} \frac{\partial v}{\partial x} \right) dx \quad (5b)$$

Here, W is the strain energy density, which is defined as:

$$W = \int_0^{\epsilon_{ij}} \sigma_{ij} d\epsilon_{ij} \quad (6)$$

The strains are calculated in the DAiSIES routine, and the stresses are calculated by using J2 deformation theory (see appendix). When desired, the strain energy release rates calculated with the J integral can be converted to crack tip stress intensities:

$$K = \sqrt{E' J} \quad (7)$$

where $E' = E$ for plane stress and $E' = E/(1-\nu^2)$ for plane strain.

4. CALIBRATION AND VALIDATION

The DAiSIES mapping procedure has been calibrated and validated by first using mathematically generated strain data to deform arrays of reference markers. The deformed arrays were then used along with reference arrays as input into the DAiSIES program. The expected (calculated) strains were plotted along with the values determined from DAiSIES, so that problems with the strain calculating algorithms could be easily seen as deviations in the contour plots. This has been an effective means of checking the mapping procedure, because it incorporates the same single pixel noise in marker location that constitutes the largest source of errors in real test samples.

When the HRR field equations¹⁴⁻¹⁵ are used with finite element data¹⁶ to generate model crack tip strains for a mode 1 crack tip field, the agreement between the calculated strains and the mapped strains is quite good. The behavior is exemplified in Figure 1, which compares calculated and mapped strain fields for a power law hardening material with a strain hardening exponent, $n = 5$. The largest deviation between the calculated and mapped strain fields is in the area directly ahead of the crack tip where there is a sharp strain gradient. Avoiding this area when drawing J

integral contours decreases scatter.

Calculations performed for an input K field of $18.7 \text{ MPa}\sqrt{\text{m}}$ over a variety of rectangular J integral contours yields mapped stress intensity values of $19.2 \pm 1 \text{ MPa}\sqrt{\text{m}}$ (Figure 2). The small error is probably due to the edge effects in the contouring routine, as the model crack tip is located close to the edge of the mapped field.

Additional verifications of the J integral routines were performed on a stainless steel sample containing a fatigue precrack (Figures 2-4) and having the uniaxial tensile behavior summarized in Table 1. This specimen was tested in-situ on an optical microscope. When the applied stress intensity was $12.4 \text{ MPa}\sqrt{\text{m}}$, DAiSIES yielded a mapped stress intensity of $12.7 \pm 2 \text{ MPa}\sqrt{\text{m}}$, averaged over all valid J contours. Moreover, for the same crack tip at an applied stress intensity, $K = 23.8 \text{ MPa}\sqrt{\text{m}}$, DAiSIES yielded a mapped stress intensity of $23.9 \pm 2.5 \text{ MPa}\sqrt{\text{m}}$.

5. COMPARISON WITH OTHER SYSTEMS

5.1 Strain Measurements

Moire interferometry systems,¹ and several digital image processing techniques²⁻⁶ are currently used to measure surface displacements from in-situ mechanical tests. In each method, the position of a set of reference features in an unstrained state are compared to the position of the features when a load is imposed. Automated stereoimaging systems, such as HASMAP at Rockwell International Science Center and DISMAP at Southwest Research Institute, use random sample surface features as displacement markers. In Moire interferometry, a fine grid of lines is introduced onto the surface of the sample (the active grating). This grid is compared with a grid that is not attached to the sample (the reference grating). The shifting of the active grating with respect to the reference grating creates an optical fringe pattern. Each fringe is a contour of constant displacement.

DAiSIES offers several advantages over these systems. Moire

interferometry requires a sophisticated laser optics system with resulting specimen geometry constraints. By contrast, DAiSIES uses information obtained from photographs taken from any specimen while under load. Automated stereoimaging systems require that a large number of reference photos be taken to capture the features in the same optical field in the deformed frame as in the reference frame, because of aberrations in the magnifying systems. By contrast, the use of photolithographic markers makes it possible to use one photographic negative as the reference frame for every distorted frame. The effects of aberrations in the magnification system are eliminated, since minimal shifting is necessary to align the reference and deformed arrays.

The best absolute measure of resolution is the minimum strain that can be detected in a given image. This is based on the minimum displacement that can be detected and the image size. DAiSIES has the capability of detecting 0.5 pixel displacements in 2048x2048 array size for a strain resolution of $\sim 2.5 \times 10^{-4}$. In practice, dealing with digital images of this scale becomes cumbersome and slows the computation process. The system is usually operated at a resolution of 1 pixel in 512 or a strain resolution of 0.2%. This resolution is sufficient for detecting the plastic strains that occur in crack tip fields in most structural materials. HASMAP and Moire generally cite strain sensitivities in the 10^{-4} range.

The spatial resolution of DAiSIES is a function mainly of the magnification at which the reference photos are taken. This magnification is in turn determined by the distribution of high contrast features across the surface of the specimen. With the current photolithographic grids and assuming that a 20×20 set of these features are captured in a reference frame, displacements of $0.1 \mu\text{m}$ can be detected. DAiSIES also has the capabilities of using TEM lattice fringe images or STM atomic images as reference and distorted arrays. In cases such as these, sub-angstrom displacements can be detected and mapped.

5.2 J-Integral Determination

The J-integral is path independent for a traction free, stationary crack.⁹ Moreover, any closed contour that is not drawn around a singularity should yield a J value of zero.⁹ These requirements provide a check on the accuracy of the method. Deviations between different J contours can also be minimized by recognizing problem areas in the strain mapping routines and avoiding contours that intersect these areas. The greatest inaccuracies occur very close to crack tips and near the edges of images.

The specific accuracy of DAiSIES crack tip J-integral routines has been shown on both the model HRR crack tip fields and on real strain fields in stainless steel. Mean crack tip stress intensities taken from a variety of J contours are accurate to within 10 percent of modeled or applied values. The standard deviations of these measurements are also less than 10 percent of the modeled or applied stress intensities.

6. APPLICATIONS

The new method has been used to address the crack growth resistance of a lamellar alloy, Ti-48Al-2Cr-2Nb. This alloy exhibits a resistance curve (Figure 5) with an initiation toughnesses in the range of 14-20 MPa \sqrt{m} . This increases to ~ 30-35 MPa \sqrt{m} upon crack extension.¹⁴⁻¹⁶ The specific values of the initiation toughness and the subsequent resistance curve behavior in this alloy are dependent on the crack growth direction with respect to lamellar and grain orientation. Crack growth is impeded at grain or lamellar colony boundaries as the crack changes direction onto planes of low crack growth resistance, such as lamellar interfaces. These effects give rise to the varying values between specimens.

The initiation toughness has been attributed to slip and twinning, whereas the rising resistance has been regarded as a ligament bridging phenomenon. Further understanding of these behaviors can be made by evaluating J contours at different

locations behind the crack front. For this purpose, strain maps and J-integral data have been generated from a three point bend specimen. Strain maps of this material (Figures 6-7) show anisotropic fields ahead of the crack, with the most prominent strains on the side of the crack where the angle between the lamellae planes and the crack propagation direction is the smallest.

The toughening effect of the bridging ligaments has been evaluated by including varying lengths of the bridged zone in the J integral calculations. Two such assessments have been made (Figure 5). The first was for a crack that had extended 40 μm from a fatigued precrack. The J integral contours were drawn at the crack tip and up to 80 μm behind the tip, for an applied stress intensity, $K = 24 \text{ MPa}\sqrt{\text{m}}$. The tip toughness was found to be 13.1 $\text{MPa}\sqrt{\text{m}}$. Moreover, the applied value was achieved at $\sim 20 \mu\text{m}$ from the tip and then remained nearly constant. The implication is that bridging ligaments are present up to 20 μm behind the crack tip. This finding is consistent with the microstructure, because the crack crosses a grain boundary and changes direction at an extension of 20 μm from the precrack. The second assessment was performed on the same crack after it had extended 380 μm from the precrack at an applied stress intensity of 32 $\text{MPa}\sqrt{\text{m}}$. This crack was also found to have a tip toughness of $\sim 13 \text{ MPa}\sqrt{\text{m}}$. Subsequently, the K value increased steadily up to 24 $\text{MPa}\sqrt{\text{m}}$ at $\sim 80 \mu\text{m}$ from the tip. In this specific test, the in-situ photographs only allowed measurement to be made up to 80 μm from the crack front. The implication is that the bridging zone length at this crack extension exceeds 80 μm , such that the applied K is only attained at greater distances from the crack tip.

Strain mapped resistance curves were reconstructed from the above tests by plotting the K values against the length of bridging zone included within the contours. These curves are plotted along with the curve determined directly from the applied loads and the crack length (Figure 5). The mapped tip values for the initiation toughness are similar to the lowest of the range of values determined from the applied

load. The relatively high initiation toughness measured from the applied loads on this particular sample was due to precrack arrest at the grain boundary outlined in Figure 8. For crack extensions between 10 and 80 μm , the strain mapped results are consistent with curves obtained by direct measurement. The further use of this method to understand the toughening mechanisms present in this material are discussed elsewhere.²¹

7. SUMMARY

DAiSIES is a fast and simple system developed for evaluating surface strains in deforming materials from photographs taken during the deformation process. DAiSIES is particularly suited to determining strains at crack tips and integrated routines are available for calculating crack tip toughnesses using a J Integral approach. Mapped strains of model arrays show excellent agreement with expected values. Moreover, crack tip stress intensity values obtained from stainless steel specimens show good agreement with the known applied values, accurate to within 10 percent.

The ability of DAiSIES for producing stain maps and determining crack tip toughnesses has been demonstrated. DAiSIES is currently being used to evaluate shear strains in weak ceramic matrix composite layers, to evaluate crack tip strains and toughness values in metal matrix composites, to observe deformations due to interfacial cracks in ceramic/metal bilayers, and to evaluate bridging ligament toughening in lamellar TiAl.²¹ Additional routines are being added to determine the mode I and mode II contributions to toughness and to determine out of plane displacements that occur during material deformation.

APPENDIX

Deformation Theory Used to Determine Stresses From Strains²²

J2 deformation theory is used to calculate the stresses at points on the surface of a sample where strain information is available. If the uniaxial tensile behavior of the material and the stress state are known, stresses can be calculated from the in-plane strains. Assuming that the elastic strain near the crack tip are negligible with respect to the total strain, J2 deformation theory states that for a given stress state, the stresses and plastic strains are proportional such that:

$$\varepsilon_{ij} = f(\sigma_e) s_{ij} \quad (A1)$$

where s_{ij} the stress deviator, ε_{ij} is the strain tensor, and σ_e is the equivalent stress defined as:

$$\sigma_e^2 = \frac{3}{2} s_{ij} s_{ij} \quad (A2)$$

Under tensile loading :

$$s_{ij} = \frac{2}{3} \sigma_{11} \quad (A3)$$

such that equation (A1) becomes,

$$\varepsilon_{11} = f(\sigma_e) \frac{2}{3} \sigma_{11} \quad (A4)$$

The plastic strain for uniaxial loading can be described by:

$$\frac{\varepsilon_{11}}{\varepsilon_0} = \alpha \left(\frac{\sigma_{11}}{\sigma_0} \right)^n \quad (A5)$$

where σ_0 is the tensile yield strength, α and n are material constants, and ϵ_0 is the uniaxial yield strain. Now, $f(\sigma_e)$ can be determined from equations (A4) and (A5) yielding the generalized stress-strain law:

$$\frac{\epsilon_{ij}}{\epsilon_0} = \frac{3}{2} \alpha \left(\frac{\sigma_e}{\sigma_0} \right)^{n-1} \frac{s_{ij}}{\sigma_0} \quad (A6)$$

Formula (A6) allows the stresses to be determined from the in-plane strains.

References

1. D. Post, Optical Engineering, 1985, **24** [3], 663
2. B.N. Cox, W. L. Morris, , and M. R. James, 1986, Proc. Nondestructive Testing and Evaluation of Advanced Materials and Composites, Colorado Springs, CO, 25
3. R.B. Joshi, A.E. Bayoumi, H. M. Zbib, Experimental Mechanics, 1992, **32** [2], 117
4. K. Hatanaka, T. Fujimitsu, and H. Inoue, Experimental Mechanics, 1992, **32** [3], 211
5. M. R. James, W. L. Morris, B. N. Cox, and M. S. Dadkhah, Micromechanics: Experimental Techniques, ASTM AMD 102, 1989, 89
6. D. L. Davidson, K. S. Chan, and R. A. Page, Micromechanics: Experimental Techniques, ASTM AMD 102, 1989, 73
7. Copyright 1994 National Institute of Health
8. Copyright 1989-1994 Research Systems Inc.
9. E.L. Hall, Computer Image Processing and Recognition, Academic Press, 1979, 186
10. S.P. Timoshenko and J.N. Goodier, Theory of Elasticity, McGraw Hill, 1951, 6
11. L.E. Malvern, Introduction to the Mechanics of a Continuous Medium, Prentice Hall, 1969, 160
12. J.R. Rice, ASME Journal of Applied Mechanics, 1968, **35**, 379
13. M. S. Dadkhah, A. S. Kobayashi, and W. L. Morris , ASTM Data Ser., STP 1131, 1992, 135
14. J. W. Hutchinson, J. Mech. and Phys. Solids, 1968, **16**, 13
15. J. R. Rice, and G. F. Rosengren, J. Mech. and Phys. Solids, 1968, **16**, 1
16. C. F. Shih,, ASTM Data Ser., STP 560, 1974, 187
17. H. E. Deve, A. G. Evans, and D. S. Shih, Acta Metall., 1992, **40**, 1259
18. K.S. Chan, Metall. Trans. A, 1993, **24A**, 569
19. K.S. Chan and Y-W. Kim, Metall. Trans. A., 1994, **25A**, 1217
20. Y. W. Kim, Acta Metall. Mater., 1992, **40**, 1121
21. D. J. Wissuchek, work in progress
22. J. W. Hutchinson, Nonlinear Fracture Mechanics, Technical University of Denmark, 1979

Figure Captions:

Figure 1. Comparison between calculated and mapped ϵ_{yy} strain contours for an HRR crack tip field in a strain hardening material.^{14,15}

Figure 2. Digital image of a crack tip in stainless steel specimen at $K_{\text{applied}} = 23.8 \text{ MPa}\sqrt{\text{m}}$ with superimposed displacement vectors.

Figure 3. Crack tip in stainless steel specimen at $K_{\text{applied}} = 23.8 \text{ MPa}\sqrt{\text{m}}$ with the resulting shear strain field.

Figure 4. Crack tip in stainless steel specimen at $K_{\text{applied}} = 23.8 \text{ MPa}\sqrt{\text{m}}$ with the resulting ϵ_{yy} field.

Figure 5. The range of resistance curves obtained from mechanical test data compared with results generated from strain maps at two different crack lengths.

Figure 6. Digital image of a crack tip in lamellar TiAl with superimposed displacement vectors.

Figure 7. Crack tip in lamellar TiAl with resulting shear field.

Figure 8. Digital image of crack tip deviation at a grain boundary with lamellar orientations indicated.

Table 1. Material tensile data used for J integral determination.

Table I

Deformation Parameters (Eqn. A5)

	Stainless Steel	Lamellar TiAl^{20, 21}
E (GPa)	175	190
σ_o (MPa)	320	400
n	5.6	3.5
α	8.8	1.4

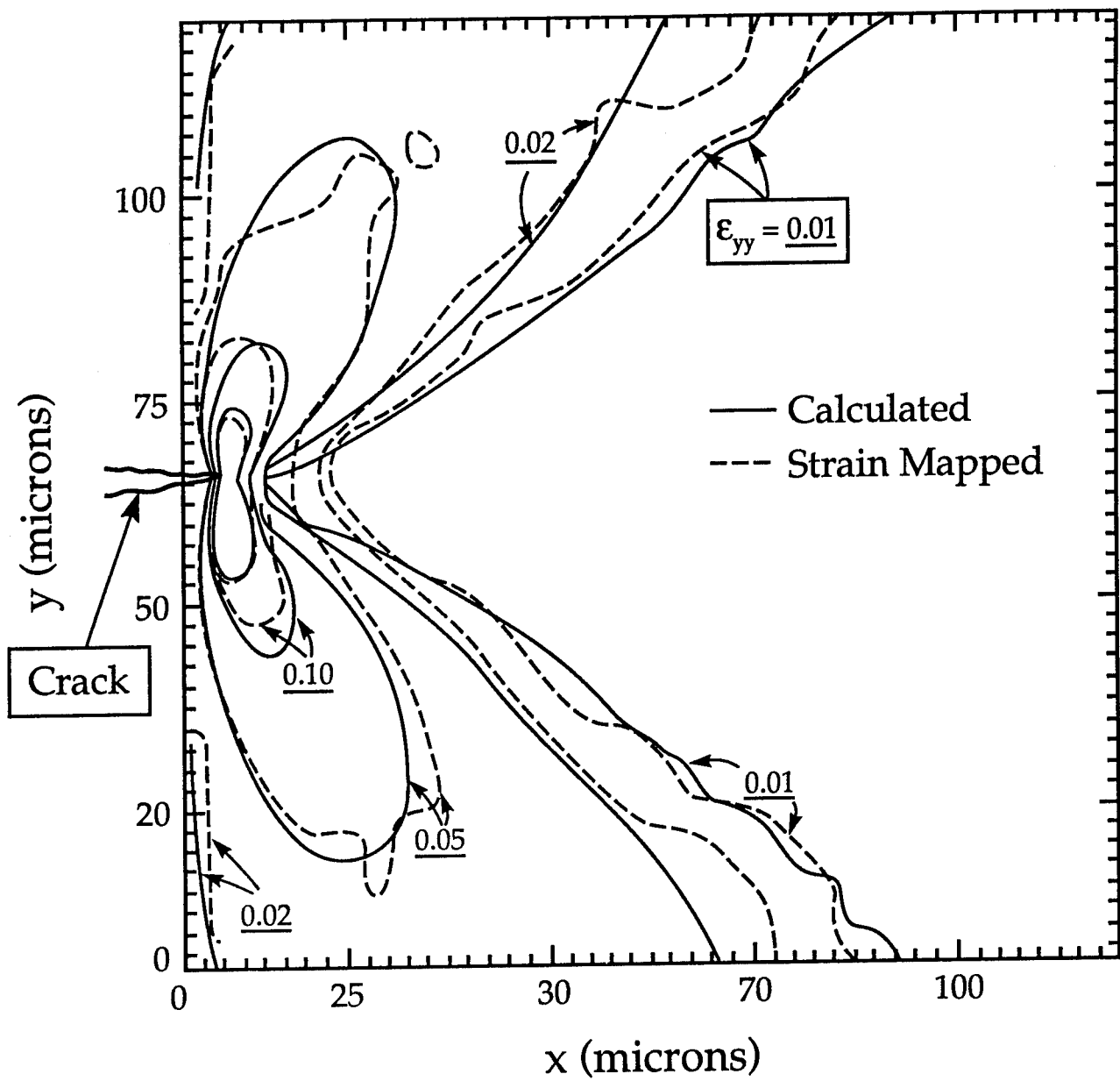


Figure 1

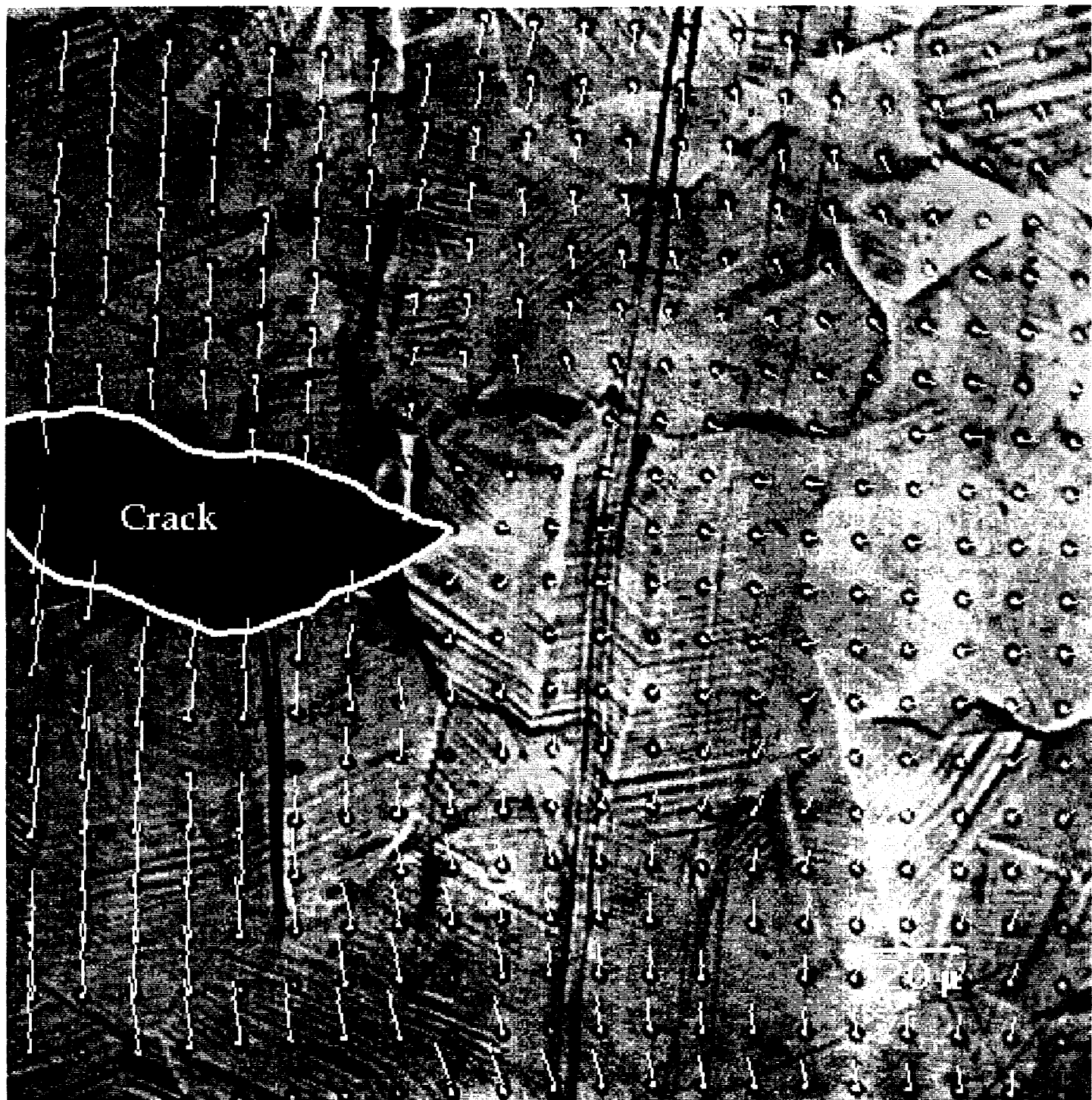


Figure 2

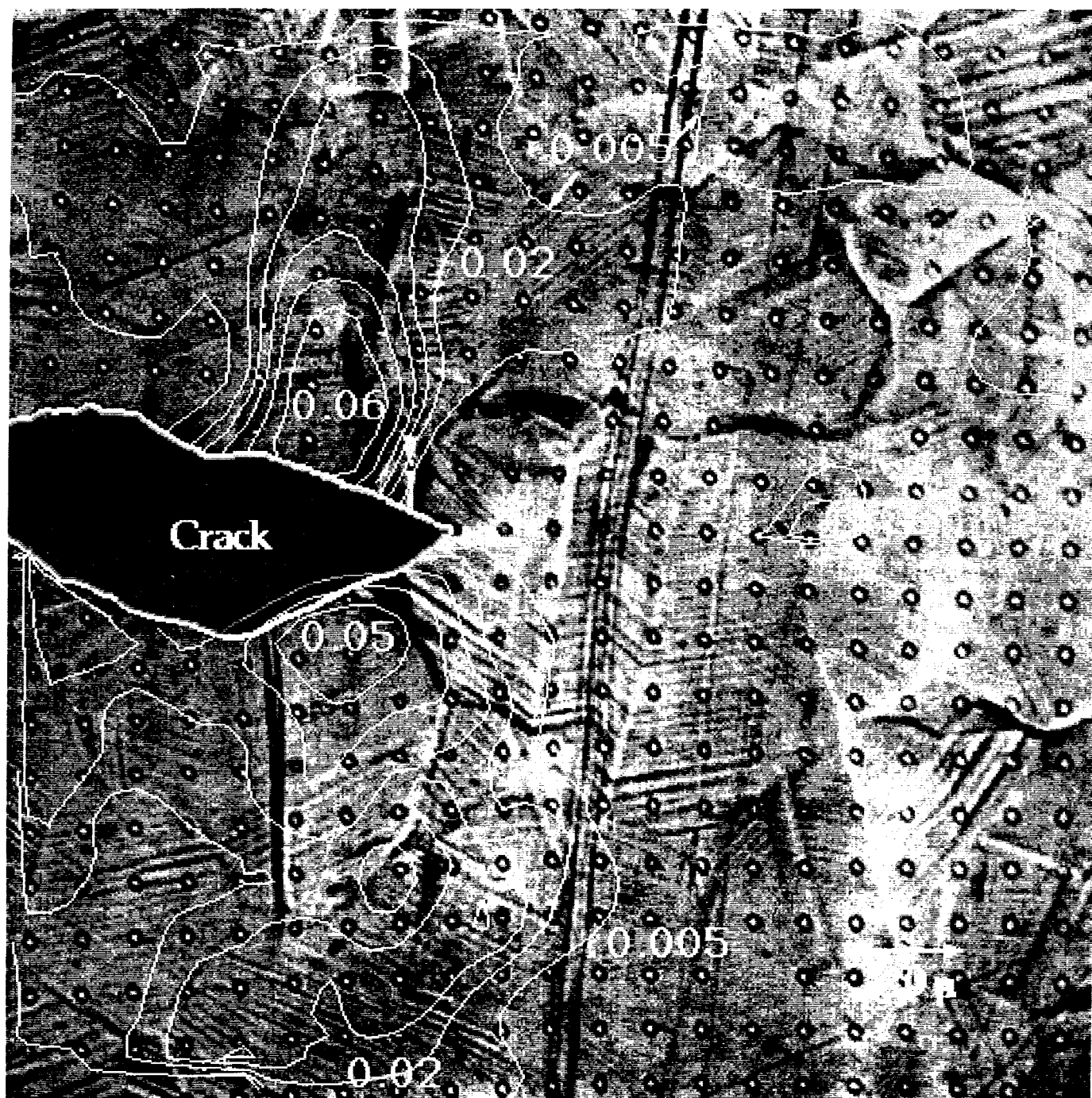


Figure 3

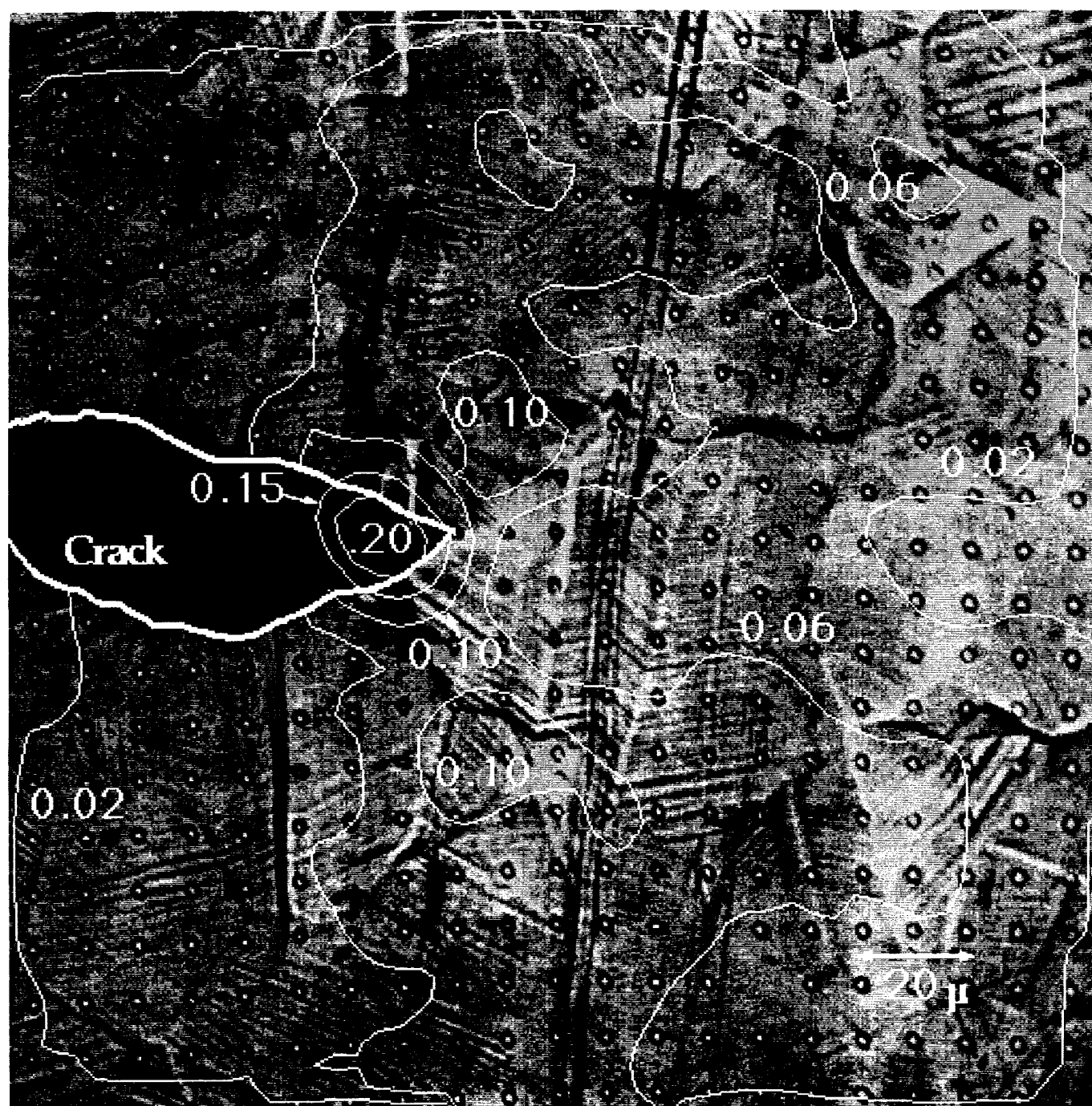


Figure 4

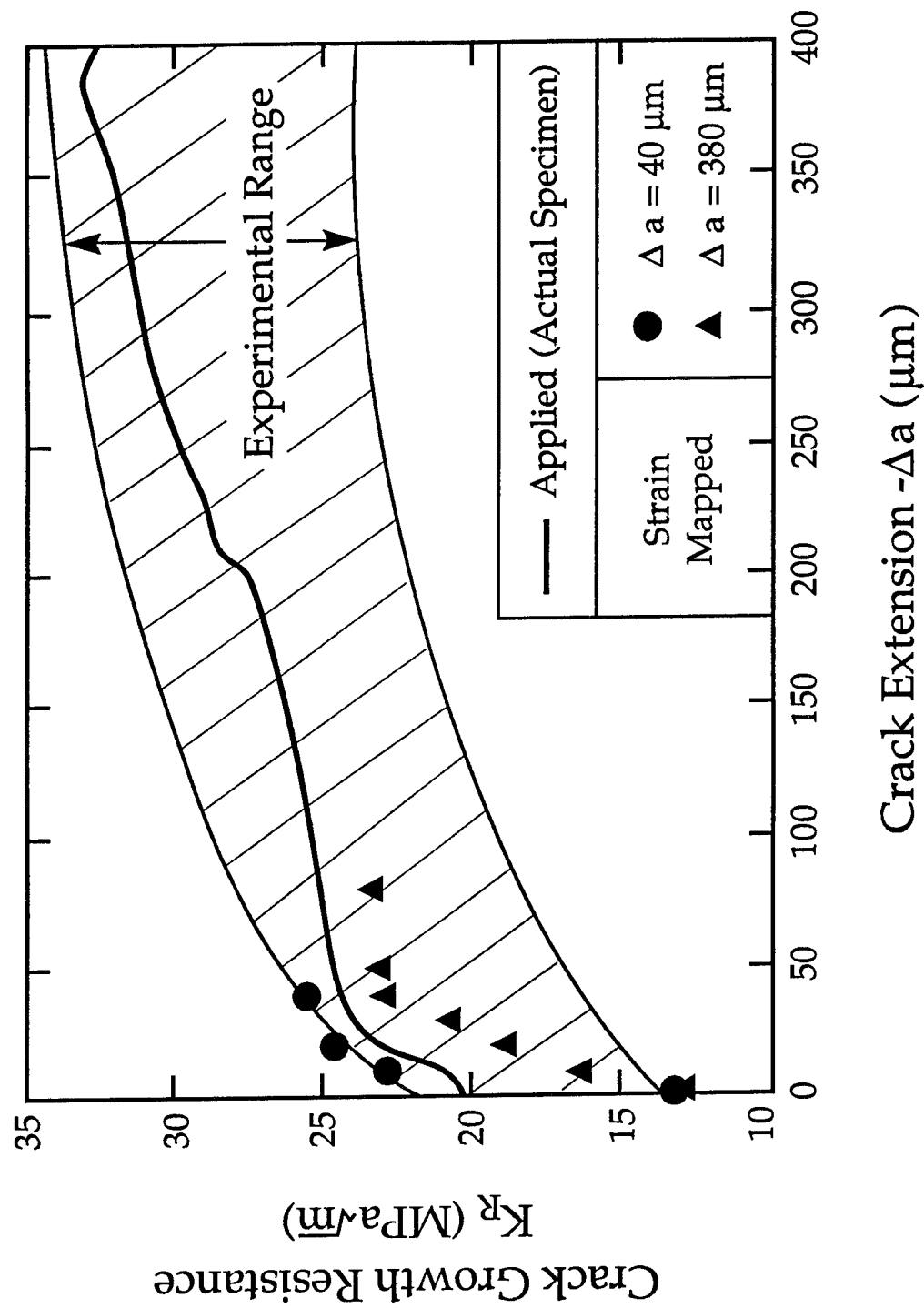


Figure 5

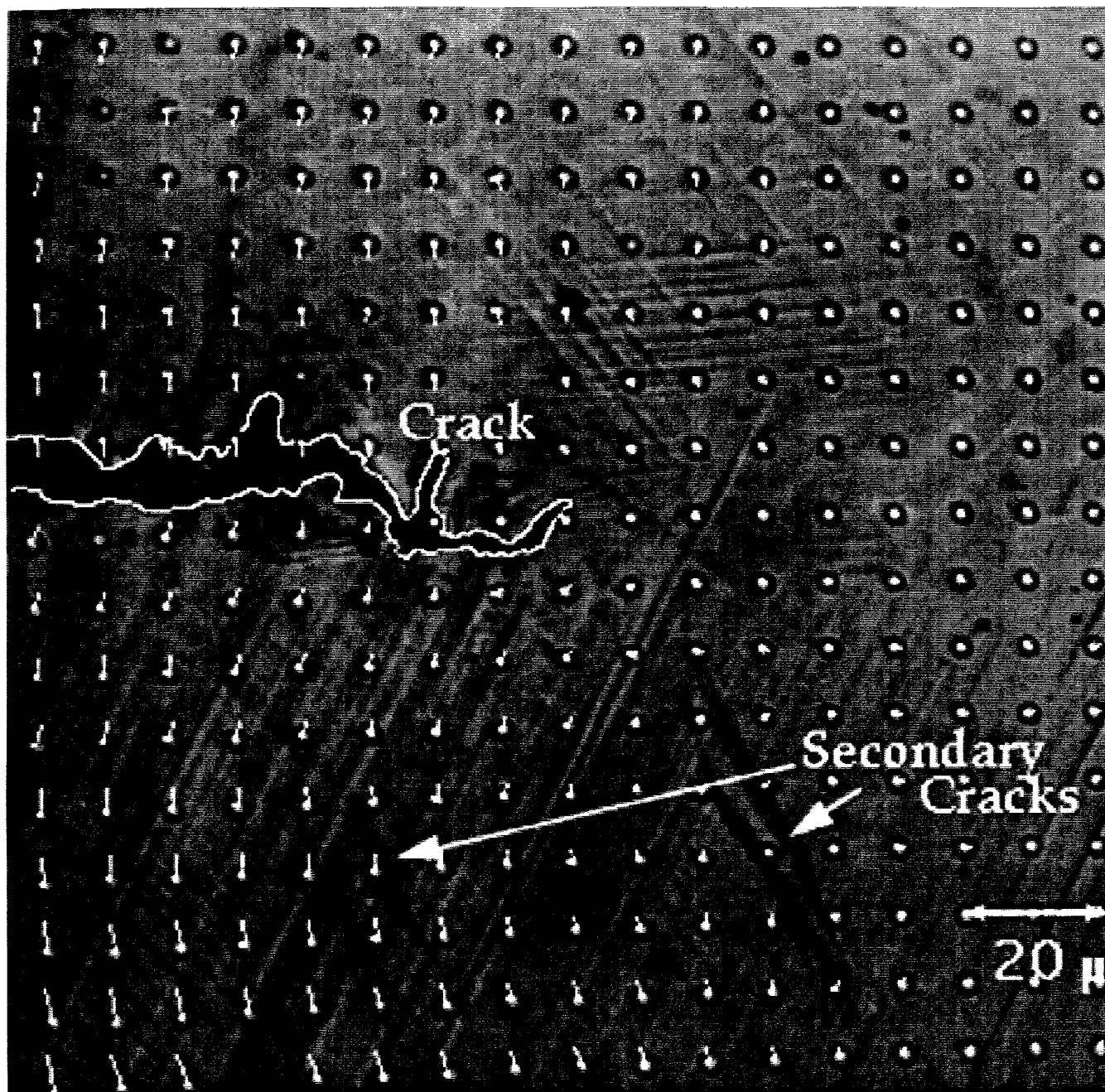


Figure 6

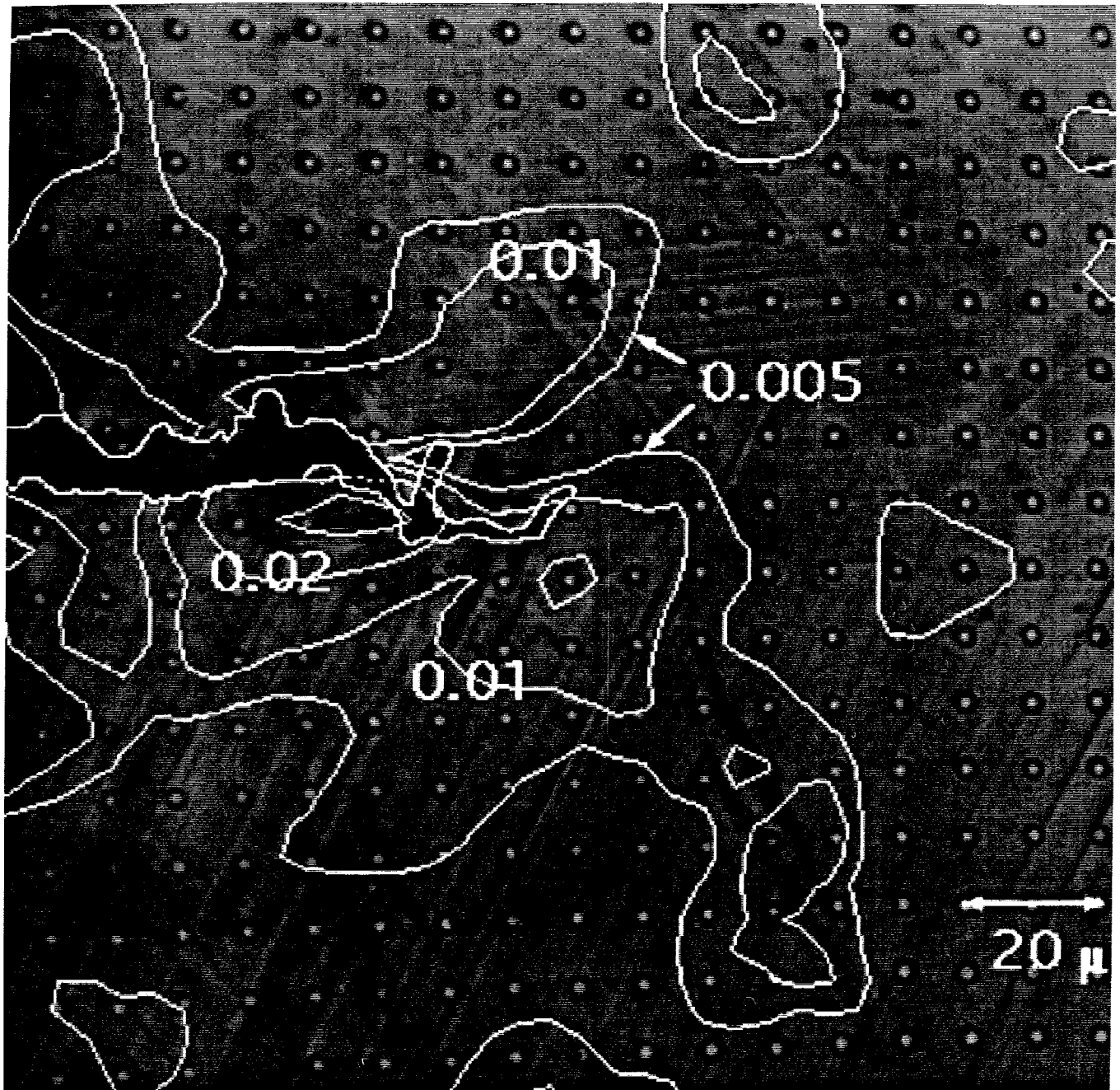


Figure 7

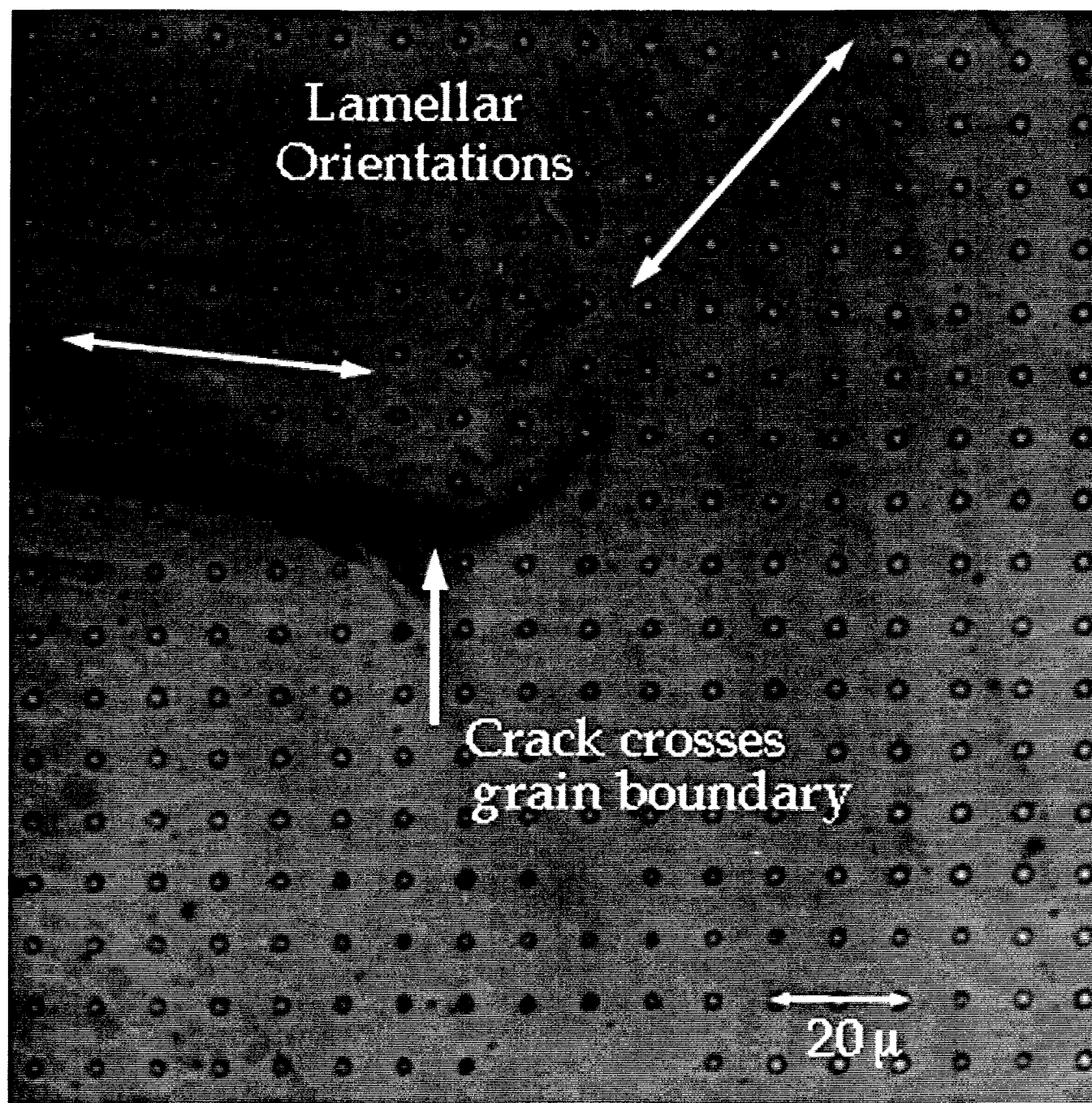


Figure 8



CRACKING AND DAMAGE MECHANISMS IN CERAMIC/METAL MULTILAYERS

M. C. SHAW^{1,2}, D. B. MARSHALL², M. S. DADKHAH² and A. G. EVANS¹

¹Materials Department, College of Engineering, University of California, Santa Barbara, CA 93106-5050
and ²Rockwell International Science Center, 1049 Camino Dos Rios, Thousand Oaks, CA 91360, U.S.A.

(Received 10 November 1992)

Abstract—Investigations of cracking in multilayered ceramic/metal composites are presented. Two aspects are considered: crack renucleation across intact single metal layers and subsequent crack extension. Crack renucleation criteria are determined and compared with predictions. High-resolution strain-mapping techniques are employed to determine the surface strain fields surrounding cracks. Good agreement is found between these experimental measurements and the predictions of a small-scale yielding model. Subsequent crack progression occurs either by the extension of a dominant, nearly planar crack or by the formation of a zone of periodically spaced cracks. Both patterns are analyzed. The dominant cracking behavior is found to depend on the volume fraction and yield strength of the metal.

1. INTRODUCTION

The macroscopic mechanical properties of layered metal/ceramic composites are governed by the mechanisms of deformation and damage that occur upon loading [1–6]. Especially important is the manner in which cracks that first form in brittle layers communicate further damage to the neighboring layers. Two limiting responses have been identified: global and local load sharing [1]. When global load sharing applies, the stress redistribution caused by a crack results in a uniformly increased stress in all of the remaining uncracked layers. Consequently, a straightforward stochastic approach can be used to characterize the mechanical properties, leading to a damage mechanics representation. Conversely, local load sharing results in a stress concentration around an initial crack formed within one layer, which causes damage to progress laterally, often as a dominant mode I crack. In this case, large-scale bridging mechanics is appropriate. As yet, there is no fundamental understanding of the properties of the layers and of the interfaces that govern the occurrence of these extreme behaviors (or of intermediate mechanisms). The present article addresses the criterion that governs this fracture mechanism transition.

A previous study provided some understanding of the stress fields around a crack within a ductile–brittle layered composite [2]. For a crack located in a brittle layer with its tip incident upon a ductile layer (as illustrated in Fig. 1), two limits were identified: (i) a small-scale yielding (SSY) limit, wherein the plastic zone extends completely through the ductile

layer but only a small distance (compared with the crack length) along the layer and (ii) a large-scale yielding (LSY), or shear lag (SL) limit, characterized by the plastic zone extending a relatively large distance normal to the crack. The SSY limit exhibits relatively large stress concentrations and is expected to result in local load sharing. The LSY limit is typified by much smaller stress concentrations and may allow global load sharing. Investigation of these stress fields (including their relationship with the cracking sequence) should provide insight into the transition in mechanism. The present study describes experimental approaches for measuring the stress and displacement fields around such cracks, and compares the results with calculated stress fields.

2. EXPERIMENTAL

2.1. Materials

Metal/ceramic multilayers were produced by vacuum diffusion bonding precleaned metal and ceramic sheets. Bonding was conducted at homologous temperatures for the metal, $T/T_m \sim 0.9$, for ~ 24 h, with an applied compression ~ 2 MPa, in a vacuum ($\sim 10^{-6}$ torr). The composites were prepared from two grades of aluminum oxide,[†] one of higher strength than the other, bonded to high purity aluminum or copper. These systems have strongly bonded interfaces [3]. The properties of the constituents are summarized in Table 1. The thicknesses of the layers, as well as the ratios of the metal thickness, h_m , to the ceramic thickness, h_c , were varied, but in all cases, a total multilayer thickness of 4–8 mm was used. The range of systems and diffusion bonding conditions are summarized in Table 2. Some specimens with relatively thick (2 mm) Al_2O_3 outer layers were used

[†]Coors ADS-995, which is relatively pure and has high flexural strength, and Coors ADS-96, which is less pure and has lower strength.

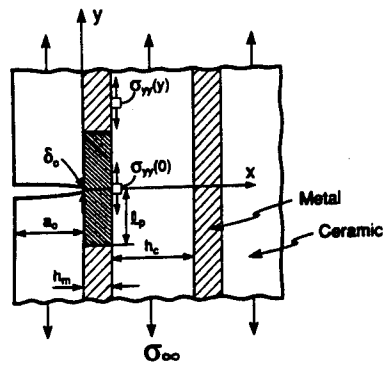


Fig. 1. Schematic illustrating the crack geometry and the parameters measured in the experiments.

in order to establish a well-developed crack prior to testing [Fig. 2(a)].

2.2. Measurements

In situ observations of crack growth in the multilayered composites were obtained on beam specimens with notches cut to a depth of ~50% of the thickness of the outer ceramic layer with a diamond saw. The specimens were polished optically flat on one face to allow observations of crack growth. Cracks were initiated from the root of the notch and then extended stably to the interface using a loading fixture attached to the stage of an optical microscope [Fig. 2(a)]. Most tests were done in ambient air. However, to examine environmental susceptibility, a few tests on the $\text{Al}_2\text{O}_3/\text{Al}$ materials were done in dry N_2 . High magnification micrographs were obtained from the crack tip region during loading. In all cases, cracks were oriented with the crack plane perpendicular to the layers (Figs 1 and 2) and the loads were applied in four-point flexure. Typical specimen dimensions were $1 \times 8 \times 30$ mm, with the inner and outer loading point separations being 10 and 25 mm. The nominal mode I stress intensity factors K_I were evaluated from the measured loads, crack lengths and specimen

dimensions by using the calibration for an elastically homogeneous beam (Section 4.1) [7].

Optical micrographs of the crack tip region were analyzed to determine the opening displacement, δ_o , of the cracked ceramic layer adjacent to the metal, the strain, ϵ_{yy} , in the neighboring ceramic layer, and the plastic zone size, l_p (Fig. 1). This was achieved by measuring differential displacements of corresponding image features in pairs of micrographs: one taken at zero load (the reference) and the other obtained under load. Two image analysis techniques were used: stereo viewing of pairs of micrographs [8] and a computerized image comparison procedure [9] (HASMAR-High Accuracy Strain MAPing). The latter technique determines full-field maps of in-plane displacements, which can be differentiated to produce the in-plane strain fields. Since both methods measure differential displacements, their sensitivity is much greater than the point-to-point resolution of the micrographs.†

Strain distributions were also measured using microscopic high-resolution moiré interferometry. The procedure involved depositing a diffraction grating on the specimen surface and forming a moiré interference pattern between the specimen grating and a fixed reference grating during loading of the specimen [10, 11]. The moiré image consists of fringes which define contours of constant displacement, with the increment between fringes being equal to one-half of the grating period. A fringe multiplication technique was used [10] to increase the differential displacement resolution to 36 nm/fringe. Interferographs were obtained in two orthogonal directions, x or y (Fig. 1), by using two interpenetrating diffraction gratings oriented at 90° . The strains ϵ_{yy} were determined by measuring fringe spacings along a line within the ceramic layer, 5 μm from the interface. The $\sigma_{yy}(y)$ stress was then estimated using the plane stress relation [12]

$$(1 - \nu^2)\sigma_{yy}(y) = E[\epsilon_{yy}(y) + \nu\epsilon_{xx}(y)] \quad (1)$$

where ν is Poisson's ratio and E is Young's modulus of the Al_2O_3 .

†Displacement resolution of 10 nm is achieved from optical micrographs.

Table 1. Properties of constituents

Constituent	Thermal expansion coefficient $\alpha (\times 10^{-6} \text{ } ^\circ\text{C}^{-1})$	Young's modulus E (GPa)	Uniaxial yield strength σ_0 (MPa)	Work hardening coefficient n
Al_2O_3	8	380	—	—
Al	25	70	50	0.2
Cu	17	120	70	0.3

Table 2. Summary of diffusion bonding conditions

Multilayer	Bonding temperature ($^\circ\text{C}$)	Bonding pressure (MPa)	Bonding time (h)	Al_2O_3 thickness (μm)	Metal thickness (μm)
	620	1.5	20	45	250
A/ Al_2O_3	655	2.6	20	680	8, 25, 50, 100, 250
				125	250
				680	8, 25, 100, 250
Cu/ Al_2O_3	940	1	24	480	25, 130

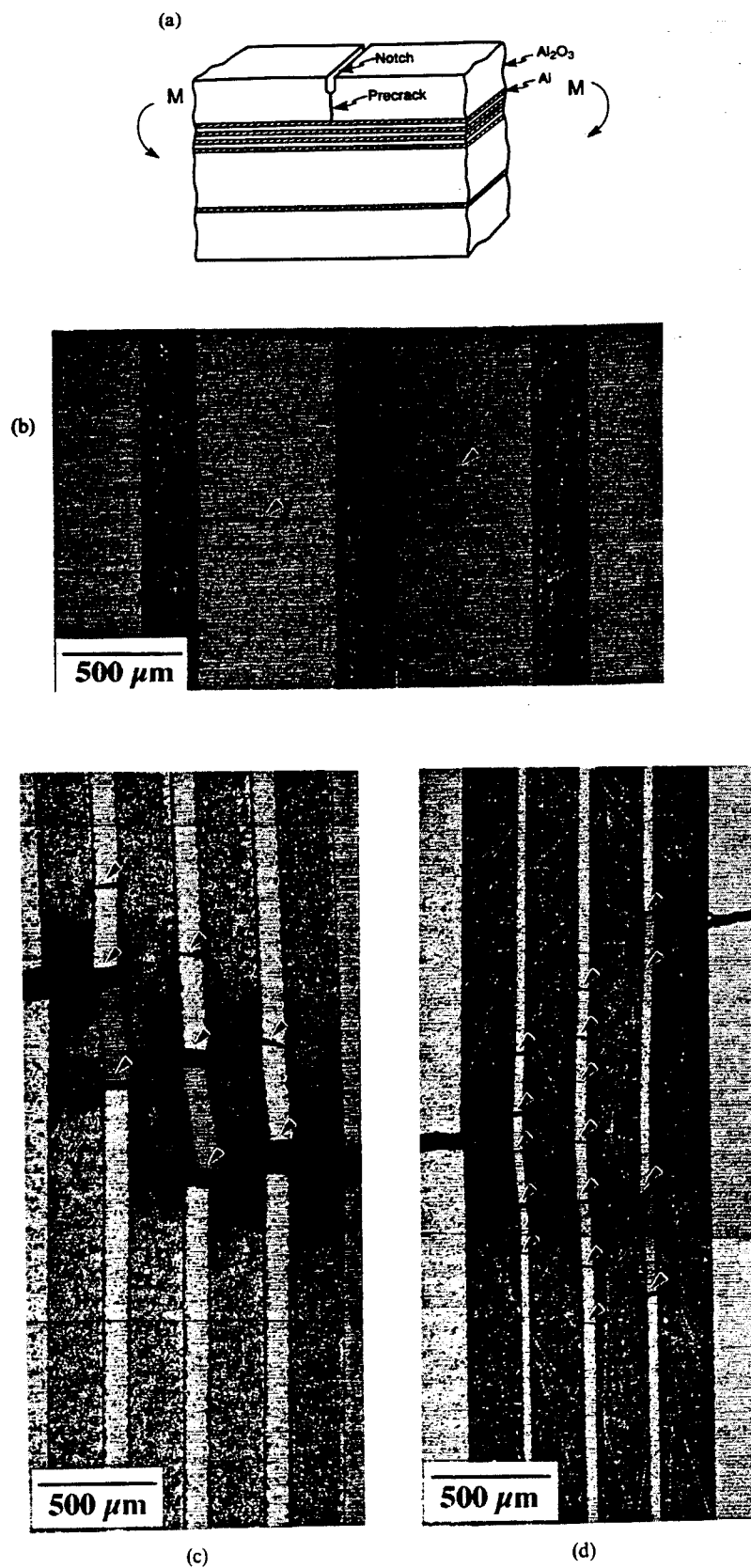


Fig. 2. (a) Schematic illustrating the specimen type and loading geometry where *M* is the applied bending moment. (b, c, d) Cracking patterns determined by optical microscopy: (b) single crack in a system with Al/480 μm Al₂O₃, (c) multiple cracking in composites with Al/125 μm Al₂O₃ and (d) Al/45 μm Al₂O₃. Arrows indicate the crack locations. All three composites contained 250 μm thick Al layers.



Fig. 3. Scanning electron micrographs of fracture surfaces of Al/Al₂O₃ multilayers, showing a single aluminum layer sandwiched between two alumina layers.

In materials with relatively thick Al₂O₃ layers (>480 μm), average strains, $\bar{\epsilon}_{yy}$, were measured with strain gauges, over an area $\approx 0.6 \times 0.25$ mm.

The strength distribution of the higher strength alumina was measured using four-point flexural loading of specimens cut from as-received plates (680 μm thick) and from plates that had been surface-ground to reduce their thickness to 450 μm. The strength distribution of the lower strength alumina was also measured using four-point flexural loading of specimens cut from as-received plates (2 mm thick). The cumulative probability of failure, $\Phi(S)$, was determined (using order statistics) as a function of the nominal strength, S , for both types of alumina, by using the volume flaw solution (see Section 3) [13]

$$-\ln[1 - \Phi(S)] = (S/S_0)^m (Lhw/V_0) \times (m+2)/4(m+1)^2 \quad (2)$$

where L is the test span, w is the specimen width and h is the specimen thickness, with V_0 being a reference volume (taken to be 1 m³) and S_0 and m the reference strength and shape parameters.

3. RESULTS

3.1. Crack growth

In multilayered composites with low volume fractions of metal ($f_m < 0.3$), a single crack formed in each ceramic layer ahead of the notch during fracture of precracked beams [Fig. 2(b)]. No interfacial debonding occurred in any of the composites, during either crack renucleation or subsequent fracture, despite extensive plastic stretching of the metal layers (Fig. 3). Furthermore, the cracks renucleated sequentially in adjoining layers on nearly the same plane as the notch. The damage is thus viewed as a dominant mode I crack, with the crack tip taken to be the edge of the furthest cracked ceramic layer. A nominal stress intensity factor K_I can then be defined as the loading parameter.

The growth of mode I cracks in systems containing ceramic layers of thickness greater than that of the

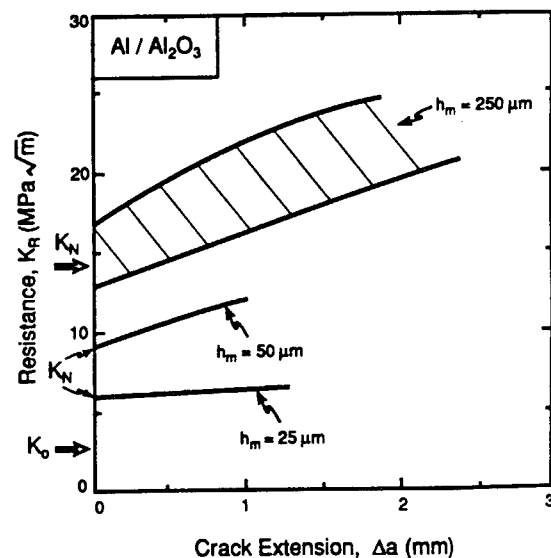
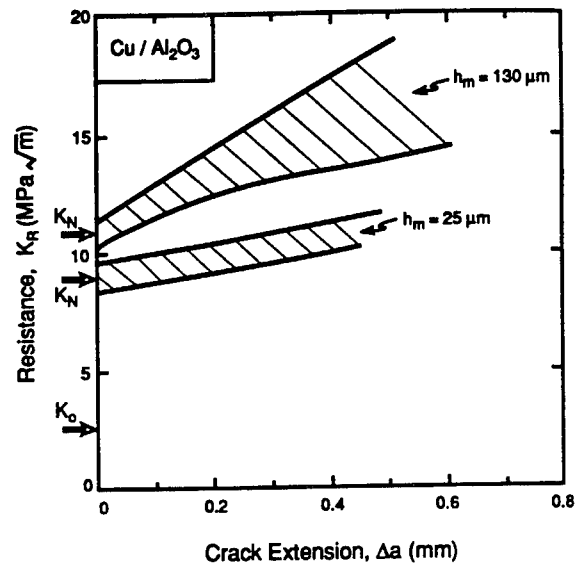


Fig. 4. Measured crack growth resistance, K_R , as a function of crack extension, Δa , for several multilayered composites.

metal layers ($h_c = 450\text{--}680\text{ }\mu\text{m}$, $h_m = 8\text{--}250\text{ }\mu\text{m}$) may be represented by resistance curves (Fig. 4). Two values of the stress intensity factor characterize crack growth: (i) that needed for initial crack renucleation across intact metal layers, K_N , and (ii) that needed for subsequent crack growth, K_R . Initial crack growth is controlled by crack renucleation in the ceramic layer ahead of the crack tip, whereas K_R increases during

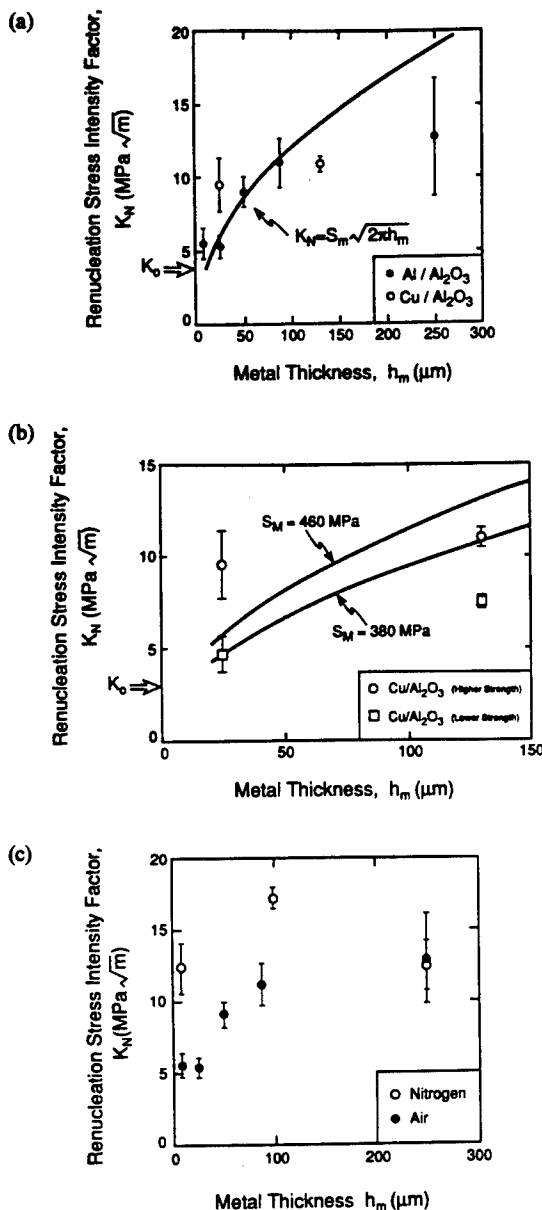


Fig. 5. (a) Crack renucleation stress intensity factor, K_N , as a function of metal layer thickness, h_m , for (a) composites fabricated from the higher strength alumina and tested in an air environment. Also shown is the SSY prediction for a median ceramic strength, $S_m = 460\text{ MPa}$. (b) K_N for copper/alumina composites fabricated from either the higher strength or lower strength alumina and tested in an environment. Also shown are the SSY predictions for K_N for median ceramic strengths of $S_m = 460\text{ MPa}$ and $S_m = 380\text{ MPa}$. (c) K_N for aluminum/alumina multilayers fabricated from the higher strength alumina tested in air and dry nitrogen.

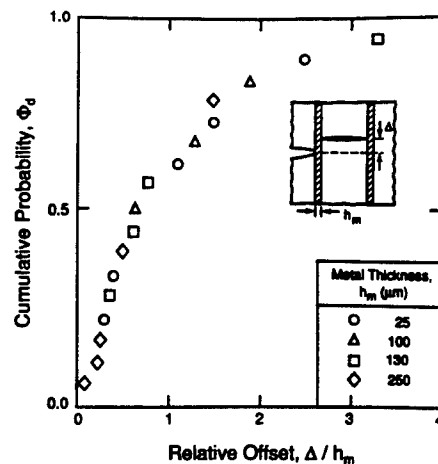


Fig. 6. Cumulative distribution, Φ_d , of the offset, Δ , in crack renucleation location normalized by the metal layer thickness, h_m , for multilayers with a range of metal layer thicknesses.

subsequent crack growth because of the bridging effect of intact metal layers in the crack wake. For a given material combination and environment (Fig. 5), the renucleation resistance increased with the thickness of the metal layers. The values of K_N ranged between 5 and 17 MPa $\sqrt{\text{m}}$, in all cases, higher than the fracture toughness of alumina [14] ($K_0 \sim 3.5$ to 4 MPa $\sqrt{\text{m}}$) [Fig. 5(a)]. The values of K_N were also systematically higher in Cu/Al₂O₃ composites containing the higher strength Al₂O₃ than in equivalent composites with the lower strength Al₂O₃ [Fig. 5(b)]. Testing of the Al/Al₂O₃ composites in air resulted in lower values of K_N than testing in dry N₂, implying a sensitivity of crack renucleation to moisture [Fig. 5(c)].

Finally, the locations at which the cracks renucleated were usually offset from the crack plane in the previously cracked Al₂O₃ layer. The offset distances, Δ , measured for composites with metal layers of various thicknesses are shown in Fig. 6 as a single probability distribution, plotted as a function of Δ normalized by the thickness, h_m , of the metal layers. The results indicate that Δ scales with h_m .

3.2. Crack tip opening displacements

The stationary crack tip opening displacements, δ_0 , were determined by stereoscopy from *in situ* optical micrographs obtained before cracks renucleated in the ceramic layer ahead of the precrack. For each specimen, δ_0 was found to increase with increasing K_I , following the proportionality, $\delta_0 \propto K_I^2$ [Fig. 7(a)]. This proportionality suggests that the data may be compared with the solution for a homogeneous metal in the small scale yielding limit, given by [15, 16]

$$\delta_0 \equiv \frac{HK_1^2}{E_m \sigma_0}, \quad (3)$$

where E_m and σ_0 are the Young's modulus and uniaxial yield strength of the metal and H is a

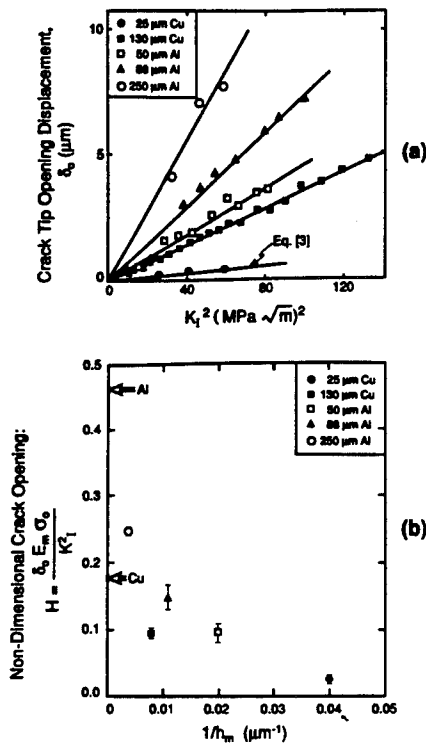


Fig. 7. (a) Crack tip opening displacements, δ_0 , as a function of the square of the applied stress intensity factor, K_1^2 , for several multilayer systems. Also shown is the prediction [equation (3)]. (b) The non-dimensional parameter, $H = \delta_0 E_m \sigma_0 / K_1^2$ as a function of inverse metal layer thickness for several different multilayer systems.

non-dimensional parameter. For homogeneous metals, H depends only on the work hardening coefficient, and typically has values of 0.48 for aluminum and 0.18 for copper [16, 17]. It is apparent from Fig. 7(b) that smaller values of H obtain for all of the layered materials. Moreover, the magnitude of H decreases with decreasing metal layer thickness [Fig. 7(b)] and, at given layer thickness, is lower for the multilayers containing copper than for those containing aluminum, consistent with the trend in H for the homogeneous metals.

3.3. Strain measurements

The average strains, $\bar{\epsilon}_{yy}$, measured using strain gauges in the Al_2O_3 layers directly opposite the precrack increased with increasing K_1 (Fig. 8). Both the magnitude of the strain and the rate of increase in strain, at given K_1 , increased with decreasing metal layer thickness.

A moiré interference micrograph showing fringes of constant displacement in the vertical (y) direction, obtained from the region surrounding a crack tip in a multilayered $\text{Cu}/\text{Al}_2\text{O}_3$ composite, is shown in Fig. 9. The stresses, σ_{yy} , along the edge of the Al_2O_3 layer ahead of the crack tip, evaluated from the micrographs [by using equation (1)] are plotted in Fig. 10, along with theoretical predictions to be discussed in the following section. The data obtained

at each of three values of the applied stress intensity factor indicate that local stress concentrations exist ahead of the crack tip, with peaks offset symmetrically by approximately $50 \mu\text{m}$ from the crack plane. The magnitude of the peak stress increases linearly with K_1 . The strains, ϵ_{yy} , in the metal layer displayed a similar distribution as those in the intact ceramic layer, but were much larger in magnitude with a plastic zone that extended beyond the field of view ($\pm 350 \mu\text{m}$).

The distribution of shear strains (as determined by HASMAP) around a crack in another $\text{Cu}/\text{Al}_2\text{O}_3$ multilayered composite with thicker copper layers ($130 \mu\text{m}$) is shown in Fig. 11. A zone of localized plastic strain within the copper layer ahead of the crack tip is evident. The zone extends to the side of the crack to a distance approximately 7 times the metal layer thickness ($l_p \approx 1 \text{ mm}$).

3.4. Multiple cracking

In composites with larger volume fractions of metal ($f_m > 0.7$), multiple cracks formed within the Al_2O_3 layers [Fig. 2(c, d)] after initial renucleation from the precrack. Furthermore, in multilayers with the highest metal volume fraction [$f_m = 0.85$, Fig. 2(d)], lateral spreading of multiple cracks within the same brittle layer often occurred in preference to forward progression of the main crack. In all cases, the crack density eventually saturated within a damage zone $\sim 2 \text{ mm}$ in total width [approximately twice the width of the region of the specimen containing the thin ceramic layers, Fig. 2(a)], with the distribution, Φ_m , of crack spacings shown in Fig. 12. It is evident that the mean crack spacing at saturation, l_s , increases as the alumina layer thickness increases.

3.5. Alumina strengths

The strength distributions measured on the as-sintered and surface-ground specimens of the higher strength Al_2O_3 were indistinguishable [Fig. 13(a)],

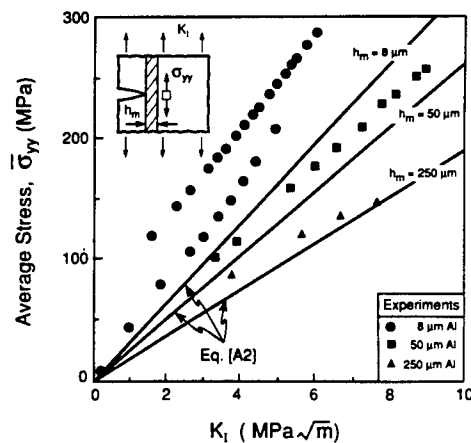


Fig. 8. Average stresses, $\bar{\sigma}_{yy}$, in ceramic layers directly opposite the crack determined with a strain gauge, for several multilayers. Also shown are the predictions for $\bar{\sigma}_{yy}$ from equation (A2).

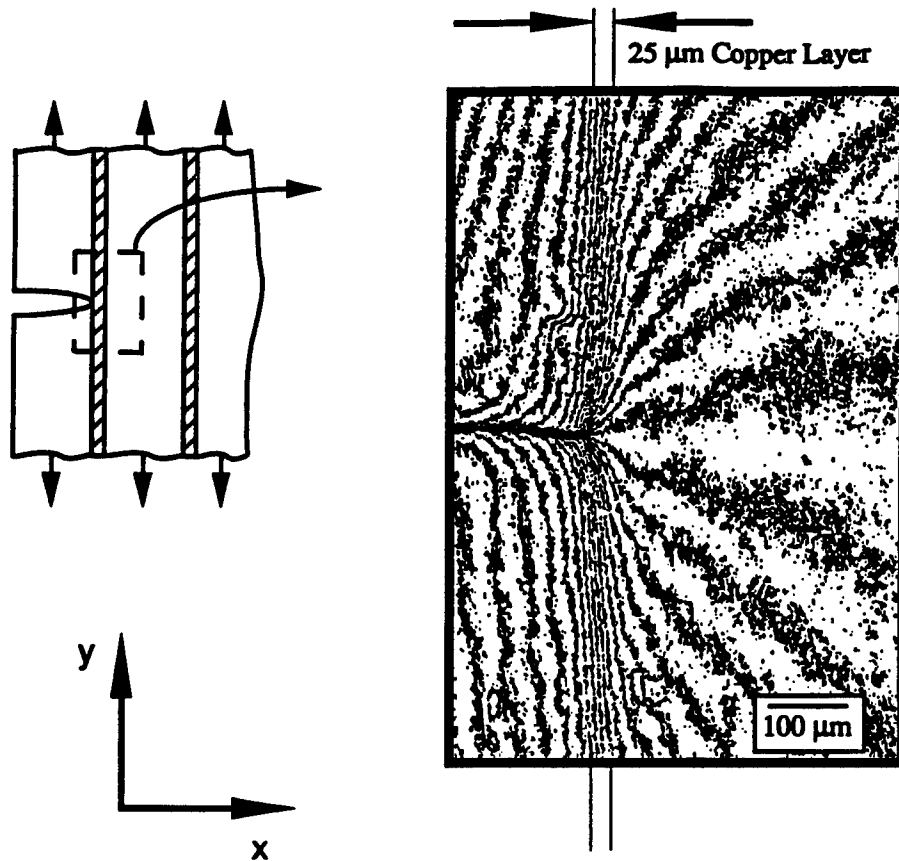


Fig. 9. High-resolution moiré interferograph of the crack tip region in a Cu/Al₂O₃ multilayer when subjected to an applied stress intensity factor of $K_I = 7.7 \text{ MPa}\sqrt{\text{m}}$. Each fringe represents a contour of constant differential displacement of 36 nm in the vertical direction (y -direction).

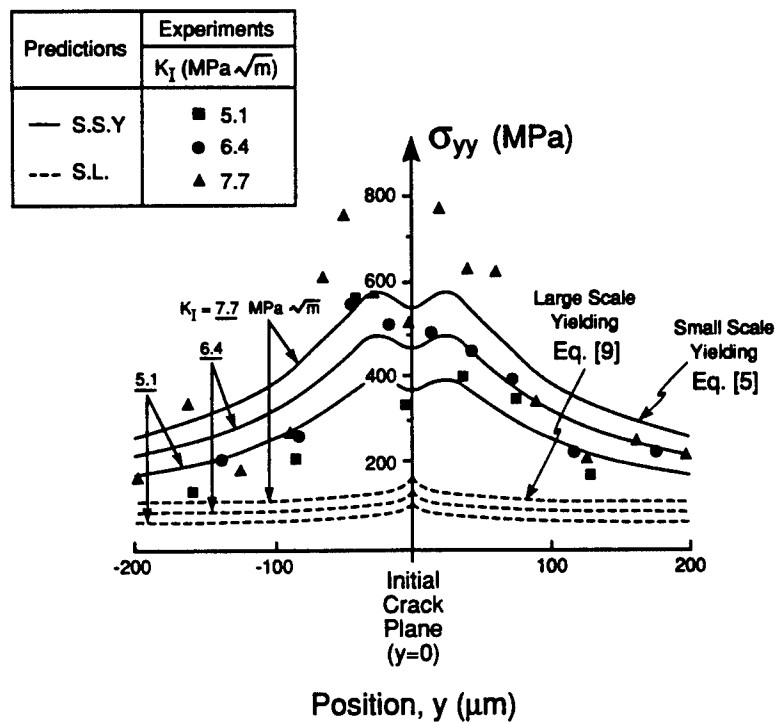


Fig. 10. Stress distributions, $\sigma_{yy}(y)$, obtained by moiré interferometry at three loads ($K_I = 5.1, 6.4$ and $7.7 \text{ MPa}\sqrt{\text{m}}$). Comparisons with SSY and LSY predictions are also shown.

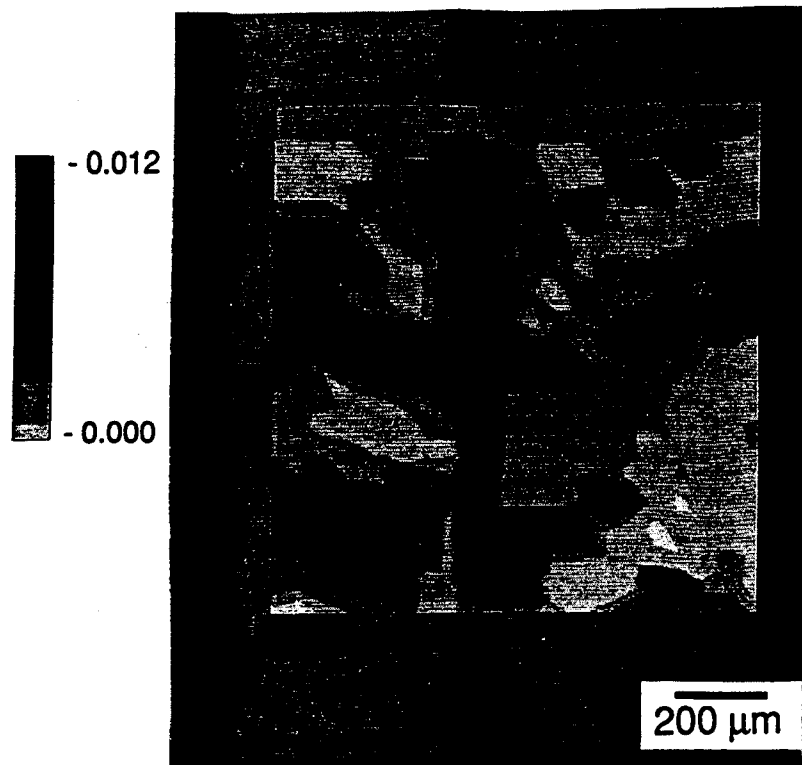


Fig. 11. Contour map of the in-plane shear strain distribution, ϵ_{xy} , measured by HASMAP just before crack renucleation in a copper/alumina multilayer. The contour intervals represent a strain of 6×10^{-4} .

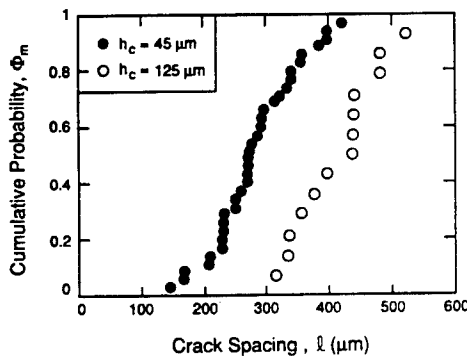


Fig. 12. Distribution, Φ_m , of crack spacings, at saturation, from several multiply cracked aluminum/alumina specimens containing 45 and 125 μm thick alumina layers with 250 μm thick aluminum layers.

suggesting that the strength is controlled by volume flaws.[†] The data from both types of specimens were combined, and the magnitudes of the shape parameter, m , and the reference strength, S_0 , were ascertained by fitting equation (2) to the data, giving $V_0 S_0^m = 2.9 \times 10^{11} \text{ MPa}^m \cdot \text{m}^3$. The corresponding median strength is, $S_m = 460 \text{ MPa}$. For the lower strength Al_2O_3 (as-sintered), $V_0 S_0^m = 1.2 \times 10^9 \text{ MPa}^m \cdot \text{m}^3$ and the median strength is, $S_m = 380 \text{ MPa}$ [Fig. 13(b)].

[†]Although it is possible that the surface flaw distributions were the same within the measurement accuracy, it is considered unlikely.

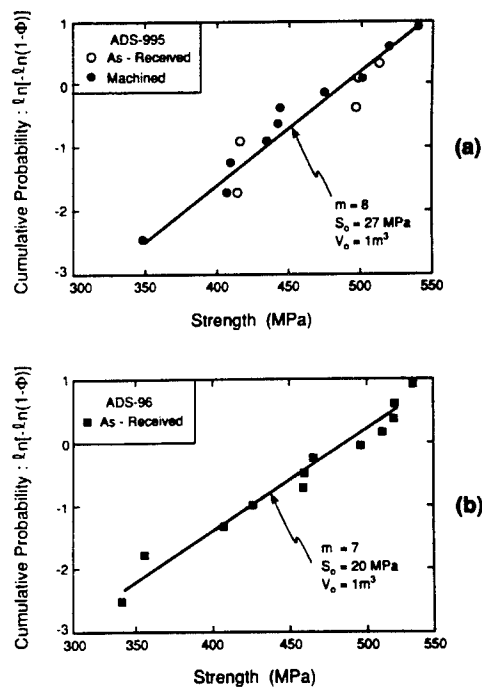


Fig. 13. Cumulative failure probabilities (a) for plates of the higher strength Al_2O_3 in the as-received and machined conditions, and (b) plates of the lower strength alumina in the as-received condition.

4. COMPARISON WITH MODELS

4.1. Crack tip stresses

Two limiting solutions have been identified for the stresses, $\sigma_{yy}(x, y)$, within intact brittle layers ahead of the crack tip in layered metal/ceramic composites. In the small-scale yielding (SSY) limit, the stresses along the crack plane closely approximate the elastic solution [2]

$$\sigma_{yy}(x, 0) \approx K_I / \sqrt{2\pi x} \quad (x \geq h_m) \quad (4)$$

where K_I is computed for an elastically homogeneous medium. This result holds even when the plastic zone extends both through the metal layer and laterally up to a distance several times the metal layer thickness. The corresponding stresses in the intact ceramic layer alongside the metal/ceramic interface ($x = h_m$) are given by [18]

$$\sigma_{ij} = \frac{K_I}{\sqrt{2\pi r}} f_{ij}(\theta), \quad (5)$$

with

$$\sigma_{yy}(r, \theta) = \frac{K_I}{\sqrt{2\pi r}} \left(\cos\left(\frac{\theta}{2}\right) \left[1 + \sin\left(\frac{\theta}{2}\right) \sin\left(\frac{3\theta}{2}\right) \right] \right)$$

where r and θ are the radial and angular coordinates from the crack tip (Fig. 1)

$$r = \sqrt{h_m^2 + y^2} \\ \theta = \arctan\left(\frac{y}{h_m}\right). \quad (6)$$

An estimate of the size of the slip zone, obtained by equating σ_{xy} to the shear yield strength of the metal [with $K_I = \sigma_\infty \sqrt{\pi a_0}$ in equation (5)], is [2]

$$l_p/a_0 \approx 0.38(\sigma_\infty/\sigma_0)^2 \quad (7)$$

where σ_∞ is the applied tensile stress and a_0 is the length of the precrack. For larger slip lengths, corresponding to large-scale yielding (LSY), a finite element analysis has been used to evaluate the stresses [2]. The peak stress in the ceramic layer is [2]

$$\sigma_{yy}(h_m, 0) \approx \sigma_\infty \left[1 + \frac{5.8}{\ln(l_p/h_m)} \right]. \quad (8)$$

The distribution of σ_{yy} stresses in the intact ceramic layer for $0.05 \leq (y/l_p) \leq 1$ is [2]

$$\sigma_{yy}(h_m, y) \approx \sigma_\infty \left[1 - 5.8 \left(\frac{a_0}{w} \right) Q \frac{\ln(y/l_p)}{\ln(l_p/h_m)} \right] \quad (9)$$

where Q is a dimensionless parameter and w is the specimen width [2]. The corresponding slip length is

$$l_p/a_0 = \sqrt{3\sigma_\infty/\sigma_0}. \quad (10)$$

The predicted stresses, given by equations (5) and (9), are compared with the moiré interferometry data

†A more rigorous analysis would entail statistical analysis of fracture, using the measured strength distribution of the Al_2O_3 layers and the nonuniform stress field of Eqn. (5). Preliminary calculations indicate that the present simplification does not result in significant error.

in Fig. 10. The SSY predictions agree reasonably well with the experimental results, including the locations of the peak stress which are offset from the crack plane. Conversely, the LSY solution substantially underestimates the magnitudes of the stresses and fails to predict the location of maximum stress. Additionally, the SSY predictions are compared with the strain gauge measurements, made over a range of loads (Fig. 8; Appendix A). Again, the SSY predictions agree reasonably well with the data.

The stress distributions at $x = h_m$ in the ceramic layer ahead of the crack tip can be used in conjunction with the measured strength of the ceramic to predict failure of the ceramic layer and thus, the renucleation stress intensity factor, K_N . A simple estimate is obtained by equating the stress (at $x = h_m, y = 0$) from equation (5) to the median strength, S_m , of the Al_2O_3 layers.† For small-scale yielding, this gives

$$K_N = S_m \sqrt{2\pi h_m}. \quad (11)$$

The prediction of equation (11), with $S_m = 460$ MPa (from Fig. 13), agrees reasonably well with measured values of K_N for materials with metal layers of various thicknesses [Fig. 5(a)]. Furthermore, the decrease in K_N in multilayers fabricated from the lower strength alumina [Fig. 5(b)] also is consistent with the predicted decrease in K_N resulting from a lower S_m . These correlations with the SSY predictions apply even though the normalized plastic zone size extends up to $l_p/a_0 \approx 2$ (Fig. 11). Consequently, the SSY stresses seemingly apply over a wider range of plastic zone sizes than had been expected [2], although these findings are consistent with recent calculations [19].

4.2. Multiple cracking

4.2.1. Transition from single to multiple crack-

ing. The criterion for the transition from single to multiple cracking is a key design parameter for this class of multilayered composites. Since the present experiments indicate that SSY conditions dominate, this transition does not appear to be related to the onset of LSY conditions. Instead, it is suggested that the transition occurs when new cracks are formed in the Al_2O_3 layers in the crack wake. For wake cracking to occur preferentially, the local stresses in the wake must exceed those ahead of the crack, as well as reach the fracture strength of the ceramic layers. These stresses are influenced by two contributions: the K-field of the main crack tip and the bridging tractions exerted by the intact, but plastically stretched, metal layers. The stresses associated with the K-field are always smaller in the wake than ahead of the crack tip. However, the contribution from the bridging tractions can be sufficient to make the wake stress larger than the tip stress. This contribution depends on the magnitude of the bridging tractions, T , the relative area over which the tractions are applied (the volume fraction of the metal) and the absolute thicknesses of the individual layers. The

magnitude of T is known to depend on the metal yield strength and the local crack opening [20, 21].

A simple model for wake cracking, involving a primary crack traversing three ceramic layers and partially bridged by two intact metal layers, is analyzed in Appendix B (Fig. B1). Approximate analytical solutions for the wake stresses as a function of distance from the crack plane, for this particular geometry (Fig. B2), indicate that the stress increases from zero at the crack faces to a maximum at a characteristic distance from the crack plane, and then decreases. The characteristic distance could dictate the crack spacing within the zone of multiple cracking. The analysis reveals that as the volume fraction of metal increases, the location of the larger peak stress changes from the brittle layer ahead of the crack tip to the crack wake, provided that the metal flow strength is sufficiently high (Fig. B2). This trend is qualitatively constant with the observations in Section 3.

4.2.2. Multiple crack density. An important measure of the extent of crack damage relevant to a damage mechanics formulation is the crack density, ρ . No attempt is made here to understand the evolution of ρ . However, some appreciation for the applicability of damage mechanics may be gained by comparing the measured crack spacings with values predicted by fragment length analysis [1]. Stochastic analysis of multiple cracking in bimaterial systems with sliding interfaces [1] indicates that the crack density saturates and that the saturation density, ρ_s , is related to the interfacial shear stress, τ , as well as a characteristic ceramic layer strength, S_c , through the relationship

$$\rho_s = \lambda(m)\tau/(h_c S_c) \quad (12)$$

where λ is a dimensionless coefficient of order unity [1], and, for a well-bonded interface, τ is the shear flow strength of the metal ($\tau \approx \sigma_0/\sqrt{3}$). The characteristic strength, S_c (Appendix C), is [1]

$$S_c = (\lambda\tau V_0 S_0^m / h_c^2 w)^{1/(m+1)}. \quad (13)$$

Therefore, equation (12) can be written

$$\rho_s = \left(\frac{\lambda^m \tau^m h_c^{(1-m)w}}{V_0 S_0^m} \right)^{1/(m+1)}. \quad (14)$$

With the relevant parameters for the $\text{Al}_2\text{O}_3/\text{Al}$ system [$V_0 S_0^m = 2.9 \times 10^{11} \text{ MPa} \cdot \text{m}^3$, $\tau \approx 30 \text{ MPa}$, $\lambda(m=8) \approx 1.6$], the saturation crack spacings for multilayered specimens with $45 \mu\text{m}$ and $125 \mu\text{m}$ thickness alumina layers are predicted from equation (14) to be $\sim 0.8 \text{ mm}$ and $\sim 1.7 \text{ mm}$, respectively. Although these are larger than the measured spacings, they are in the same range and they scale correctly (Fig. 12). A damage approach based on the stochastics of the brittle layers, coupled with interfacial slip, thus appears to be a potentially viable procedure for characterizing the properties associated with multiple cracking.

5. CONCLUSIONS

Crack growth and damage accumulation in strongly bonded ceramic/metal multilayers have been investigated, with particular emphasis on the criterion for crack advance, as well as on crack extension patterns. Crack renucleation beyond intervening metal layers is found to be governed by the small-scale yielding stress field. Plastic flow within the metal layers exerts a minimal influence, despite clear evidence of plasticity in the metal layers prior to crack renucleation. The metal layers therefore act simply to separate the intact ceramic layer from the crack tip by a distance corresponding to the metal layer thickness. This behavior leads to a simple inverse-square root dependence of the crack renucleation resistance, K_N , on the metal layer thickness, h_m . These conclusions establish that crack renucleation results from a significant stress concentration associated with cracks in adjacent brittle layers.

Damage develops either as a dominant crack, or as periodic cracks, depending on the volume fraction, layer thickness and yield strength of the metal. As the volume fraction of metal increases, at constant ceramic layer thickness, the stresses in the crack wake increase, whereas the stresses in the intact layer ahead of the crack tip decrease. This trend in stress leads to a transition in cracking mechanism with increasing volume fraction of metal, whenever the metal layers have sufficiently high yield strength. Specifically, for low metal volume fractions, mode I extension of a primary crack occurs, whereas for high metal volume fractions, periodic multiple cracking occurs.

When multiple cracking dominates, a damage mechanics approach for characterizing properties appears to be viable. To assess the validity of such an approach, a simple model has been used to relate the saturation crack density, ρ_s , to the intrinsic flow properties of the metal, the strength characteristics of the brittle layers and the geometry of the multilayers. The predictions of the model are qualitatively consistent with the measured trends.

Acknowledgements—The authors gratefully acknowledge the assistance of Dr B. J. Dalgleish in preparation of the copper/alumina multilayers, and for many valuable discussions. This work was supported by Rockwell International Research and Development funding and by the Office of Naval Research, Contract No. N00014-90-J-1300.

REFERENCES

1. W. A. Curtin, *J. Mater. Sci.* **26**, 5239 (1991).
2. H. C. Cao and A. G. Evans, *Acta metall. mater.* **39**, 2997 (1991).
3. B. J. Dalgleish, K. P. Trumble and A. G. Evans, *Acta metall.* **37**, 1923 (1989).
4. M. S. Hu and A. G. Evans, *Acta metall.* **37**, 917 (1989).
5. D. C. Agrawal and R. Raj, *Acta metall.* **37**, 1265 (1989).
6. F. S. Shieu, R. Raj and S. L. Sass, *Acta metall.* **38**, 2215 (1990).

7. H. Tada, P. C. Paris and G. R. Irwin, *The Stress Analysis of Cracks Handbook*. Paris Productions, St Louis, MO (1985).
8. D. R. Williams, D. L. Davidson and J. Lankford, *Exp. Mech.* 4 (1980).
9. M. R. James, W. L. Morris and B. N. Cox, *Exp. Mech.* 30, 60 (1990).
10. B. Han, *Optical Engng* 31, 1517 (1992).
11. M. S. Dadkhah, B. Han and M. C. Shaw, to be published.
12. S. P. Timoshenko and J. N. Goodier, *Theory of Elasticity*. McGraw-Hill, New York (1934).
13. N. A. Weil and I. M. Daniel, *J. Am. Ceram. Soc.* 47, 268 (1964).
14. L. A. Simpson and G. J. Merrett, *J. Mater. Sci. Lett.* 9, 685 (1974).
15. J. R. Rice and M. A. Johnson, *Inelastic Behavior of Solids* (edited by M. F. Kanninen, W. F. Adler, A. R. Rosenfield and W. F. Jaffee), pp. 641-672. McGraw-Hill, New York (1969).
16. J. W. Hutchinson, Dept. Solid Mechanics, Technical Univ. of Denmark (1979).
17. R. A. Hertzberg, *Deformation and Fracture Mechanics of Engineering Materials*. Wiley, New York (1983).
18. B. R. Lawn and T. Wilshaw, *Fracture of Brittle Solids*. Cambridge Univ. Press (1975).
19. K. S. Chan, M. Y. He and J. W. Hutchinson, *Mater. Sci. Engng.* In press.
20. D. B. Marshall, B. N. Cox and A. G. Evans, *Acta metall.* 33, 3013 (1985).
21. A. G. Evans and R. M. McMeeking, *Acta metall.* 34, 2435 (1986).
22. T. J. Roark, *Formulas for Stress and Strain*. McGraw-Hill, New York (1954).

APPENDIX A

Comparison of Predicted Stresses with Strain Gauge Measurements

The strain gauge data provide a measure of the average stress, $\bar{\sigma}_{yy}$, within the region bounded by the strain gauge, i.e. $h_m < x < h_m + d$, where d is the width of the strain gauge. For the stress field given by the small-scale yielding limit [2]

$$\bar{\sigma}_{yy} = \frac{1}{d} \int_{h_m}^{h_m+d} \frac{K}{\sqrt{2\pi x}} dx. \quad (A1)$$

Integration gives

$$\bar{\sigma}_{yy} = \sqrt{\frac{2}{\pi}} \frac{K}{\sqrt{d}} \left(\sqrt{\frac{h_m}{d} + 1} - \sqrt{\frac{h_m}{d}} \right) \equiv \frac{K}{\sqrt{2\pi d}}. \quad (A2)$$

where

$$\bar{d} = \left[\frac{d}{2[\sqrt{h_m + d} - \sqrt{h_m}]} \right]^2. \quad (A3)$$

Equation (A2) is compared with measurements for materials with aluminum layers of different thickness in Fig. 8.

APPENDIX B

Multiple Cracking Analysis

The mode of damage evolution (single or multiple cracking) depends on the relative magnitudes of the stresses in the ceramic layers ahead of and behind the crack tip. These depend, in turn, on the thickness of the metal and ceramic layers, the crack length, the strength distribution of the ceramic, and the flow properties of the metal. To assess the effect of changing the volume fraction of metal, these stresses are estimated for the specific composite geometry shown in Fig. B1.

The stresses were estimated by regarding the effect of the intact metal bridging ligaments as crack closure tractions, T , acting on the crack faces (Fig. B1). In general, the magnitude of T depends on the local crack opening, the flow properties of the metal and interfacial debonding. However, for the purpose of illustrating the transition in behavior, T is taken to be a constant ($T = 1.5\sigma_\infty$) in the present analysis. Assuming that the stress concentration due to the crack tip is given by a K field, and assuming elastic homogeneity, the crack tip stresses are [18]

$$\sigma_{tip} = \frac{K_{tip}}{\sqrt{2\pi r}} f(\theta) \quad (B1)$$

where K_{tip} is the local stress intensity factor given by [20]

$$K_{tip} = 2 \sqrt{\frac{a}{\pi}} \int_0^1 \frac{[\sigma_\infty - T(X)] dX}{\sqrt{1-X^2}} \quad (B2)$$

where $X = 1 + x/a$ (Fig. B1). The stresses in the crack wake along the line normal to the crack at $x = -(h_m + h_c)$ are given by the superposition of two components, one due to the crack tip stress concentration, equation (B1), and the other due to the traction T [18, 22]

$$\sigma_{wake} = \frac{K_{tip}}{\sqrt{2\pi r}} f(\theta) + g(f_m, r, \theta, T) \quad (B3)$$

where $f(\theta)$ is given by equation (5) and the function $g(f_m, r, \theta, T)$ accounts for the wake stresses arising from the crack bridging tractions applied to the surface of an elastic half space over the intervals, $-2(h_c + h_m) < x < -(2h_c + h_m)$, and $-(h_c + h_m) < x < -h_c$ [22],

$$g(f_m, r, \theta, T) = T(\alpha_1 + \alpha_2 + \sin \alpha_1 + \sin \alpha_2)/\pi \quad (B4)$$

with

$$\alpha_1 = \arctan\left(\frac{h_m}{y}\right)$$

$$\alpha_2 = \arctan\left(\frac{h_m + h_c}{y}\right) - \arctan\left(\frac{h_c}{y}\right)$$

with h_m , h_c , and y defined in Fig. 1.

The stresses in the ceramic layers ahead of the crack tip (σ_A) and in the crack wake (σ_B) are plotted as a function of distance from the crack plane in Fig. B2 for various values of f_m . The stress distributions at both locations pass through a maximum at a distance from the crack plane of several times h_c . At small values of f_m , the maximum stress is larger ahead of the crack than in the wake, thus favoring growth

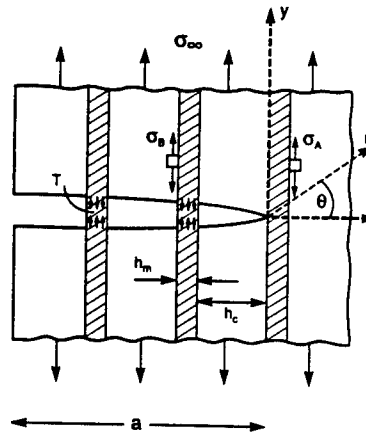


Fig. B1. Schematic of the crack configuration analyzed in Appendix B.

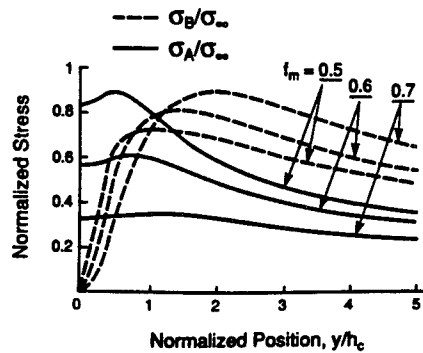


Fig. B2. Approximate analytical solutions for crack tip and crack wake stresses for the crack geometry shown in Fig. B1 with various volume fractions of metal, f_m , and with bridging tractions taken to be $T = 1.5\sigma_\infty$.

of a single crack. Conversely, at large f_m , the maximum stress is larger in the wake, leading to multiple cracking. The transition occurs at $f_m \approx 0.6$, for the particular value of T and the crack and layer geometries chosen here, for illustrative purposes.

APPENDIX C

Characteristic Ceramic Layer Strength

For a power law strength distribution in the brittle layers, the fraction, P , of flaws that can cause failure at stress S in a volume V is given by

$$P(V, S) = \frac{V}{V_0} (S/S_0)^m. \quad (C1)$$

At the point of crack saturation [1], $S = S_c$,

$$P(V_s, S_c) = \frac{V_s}{V_0} (S_c/S_0)^m = 1 \quad (C2)$$

where V_s is the volume of material between the cracks. Using equation (12), V_s can be reexpressed as

$$V_s = \frac{h_c^2 S_c w}{\lambda \tau}. \quad (C3)$$

Combining equations (C2) and (C3) yields

$$S_c = \left(\frac{\lambda \tau V_0 S_0^m}{h_c^2 w} \right)^{1/(m+1)}. \quad (C4)$$